# *Deconvolution of small molecule pleiotropic effects during immunomodulation*


Hannah Unsworth

Hertford College

Chemistry in Cells Doctoral Training Programme

Department of Chemistry and Department of Physiology, Anatomy and Genetics

University of Oxford

This dissertation is submitted for the degree of Doctor of Philosophy

October 2025

## Declaration of authorship

The work presented in this thesis is my own, except where otherwise stated. No part of this thesis has been submitted for any other degree at this or any other university.

*Hannah Unsworth*

October 2025

## Acknowledgements

I would first like to thank the Chemistry in Cells team and the Wellcome Trust for providing me with the opportunity to pursue a DPhil at Oxford.

I would like to express my deepest gratitude to Paul and Angie for their continual support and guidance throughout my 4 years at Oxford. Thank you for challenging me to become a better scientist, and nurturing an incredibly welcoming research environment in both your groups. Your ongoing mentorship as I progress into the next stage of my career has been invaluable.

Thank you to my collaborators, Dr Steven Huband, Dr Mathieu-Benoit Voisin and Dr Ayman Al Haj Zen, without whom this research would not have been possible.

A HUGE thanks to both my research groups in Oxford, I could not have made it through without you. To the whole AJR group, thank you for supporting my caffeine addiction with our innumerable trips to Horsebox. A special thanks to Carole for being my lab fairy godmother, waving your wand and getting sh*t done. Thank you to Pol, Helen, Marc, Ríona, Josh and Ciaran for the much-needed squash sessions to get out my frustration over failed reactions. An extra special thanks to Marc, Ríona and Caroline who were always up for good wine and good food, providing the perfect distraction after long days in the lab. To Christophe, who taught a lowly chemist how to keep cells alive, I honestly would not have been able to complete this DPhil without you. Thank you so much for your time and patience, I hope you're proud of the cosplay biologist I've become.

Thank you to my parents and sister for their support and enthusiasm for my research, even though you have no idea what I'm doing half the time. The weeks you spent reading and researching my transfer report to try and understand meant the world to me.

To Adam, thank you for putting life into perspective and reminding me that I am more than my research. You have been my biggest supporter, encouraging me to persevere through the sometimes seemingly endless lows of this DPhil. Your love has been unconditional – even though I feel like I've been pushing it with the late nights and constant mess. I am so excited for the next chapter of our lives to start, let's get to New Zealand!

And finally, in the immortal word of Snoop Dogg – I wanna thank me!

## Abstract

Ischaemic heart disease is one of the leading causes of death worldwide, and is rapidly growing in prevalence. Despite improvements in response and treatment times, individuals who suffer from cardiac ischaemic injury are at risk of developing chronic heart failure. The development of regenerative therapeutics which harness endogenous recovery mechanisms to optimise repair of the injured heart after ischaemic injury are highly desired. One emerging mechanism *via* modulation of the immune response demonstrates great promise as a potential mediator of cardiac regeneration. The lymphatic system plays a significant immunomodulatory role in the transportation and clearance of immune cells. In the heart, the efficient clearance of immune cells post-ischaemic injury is linked to reduced fibrotic scarring and improved cardiac function, ultimately resulting in a more effective recovery after a myocardial infarction. This immune cell clearance is enhanced by lymphangiogenesis, which is the growth of new lymphatic vessels from pre-existing vasculature. This research has identified a small molecule, fingolimod, which induces lymphangiogenesis while also demonstrating previously reported pleiotropic effects upon both the lymphatic and immune system (i.e. T-lymphocyte sequestration in lymph nodes and T-lymphocyte migration inhibition).

The aim of this research was to deconvolute the potentially tissue-specific activity of fingolimod, to distinguish the mechanisms of action responsible for these immunomodulatory effects of interest. Phenotypic assays of lymphangiogenesis and T-lymphocyte migration were developed and optimised to aid this endeavour. Preliminary studies suggested that fingolimod's metabolite, fingolimod phosphate is responsible for the immunomodulatory effects on both the lymphatic and immune system. Further

pharmacological evaluation of fingolimod phosphate's mechanisms of action demonstrated that these phenotypic effects were independent of fingolimod's canonically associated sphingosine-1-phosphate receptors, but were dependent on another G-protein coupled receptor. The apelin receptor was identified as a target of interest, related to fingolimod's lymphangiogenic effect. This observation was supported by CETSA, pharmacological inhibition studies, siRNA knockdown studies and downstream pathway analysis.

To further decipher fingolimod phosphate's targets of phenotypic interest in an unbiased manner, fingolimod-derived chemical probes with a sustained functional effect were designed and synthesised, utilising photoaffinity labelling technology. A structurally similar but functionally inactive photoaffinity labelling probe was also synthesised and validated, with the intention of acting as a necessary negative control. There were significant attempts made to synthesise an iridium photocatalytic photoaffinity probe, to map fingolimod's microenvironment, in addition to its direct targets. However, challenges in selectively modifying the sterically-hindered headgroup of fingolimod impeded this synthesis.

The validated photoaffinity probe was used to assess the direct targets of fingolimod in lymphatic endothelial cells. Proteomic analysis of probe-enriched proteins revealed novel interaction partners of fingolimod related to both its lymphangiogenic and migratory phenotypes. These findings also provided insight into the potential origins of fingolimod's adverse side effects, as well as pleiotropic effects relating to other disease areas (i.e. diabetes, Alzheimer's disease). These discoveries highlight the importance of target deconvolution in the development of effective therapeutics.

## Table of Contents

## Abbreviations and Symbols

| | |
|---|---|
| **°** | degree |
| **°C** | degree Celsius |
| **ΔG** | Gibbs free energy difference |
| **μm** | Micrometre |
| **μM** | Micromolar |
| **μL** | Microlitre |
| **2MeTHF** | 2-Methyltetrahydrofuran |
| **Å** | Angstrom, $10^{-10}$ metres |
| **AA** | Amino acid |
| **Aβ** | Amyloid-β |
| **AD** | Alzheimer's disease |
| **AGC** | Automatic gain control |
| **AIBN** | Azobisisobutyronitrile |
| **ANOVA** | Analysis of variance |
| **APC** | Antigen-presenting cell |
| **APCI** | Atmospheric pressure chemical ionisation |
| **APLNR** | Apelin receptor |
| ***app*** | Apparent |
| APP | Amyloid precursor protein |
| **aq.** | Aqueous |
| **BCA** | Bicinchoninic Acid |
| **Boc** | *tert*-Butyl carbonate |
| **Bpin** | Pinacolboronate |
| **BRET** | Bioluminescence resonance energy transfer |
| **BSA** | Bovine Serum Albumin |
| **CALB** | Candida Antarctica Lipase B |
| **CALCRL** | Calcitonin receptor-like receptor |
| **cat.** | Catalytic |
| **CDI** | Carbonyldiimidazole |

| | |
|---|---|
| **CuAAC** | Copper(I)-catalysed azide-alkyne cycloaddition |
| **CETSA** | Cellular thermal shift assay |
| **CerS2** | Ceramide Synthase 2 |
| **CHAPS** | (3-((3-Cholamidopropyl) dimethylammonio)-1-propanesulfonate) |
| **CHD** | Coronary Heart Disease |
| **CID** | Collision-induced dissociation |
| **CMC** | Critical micelle concentration |
| **CX3CL1** | C-X3-C motif chemokine ligand 1 |
| **CX3CR1** | C-X3-C motif chemokine receptor 1 |
| **d** | Doublet |
| **Da** | Dalton |
| **DAMPs** | Damage-associated membrane patterns |
| **DAPI** | 4′,6-Diamidino-2-phenylindole dihydrochloride |
| **DBCO** | Dibenzocyclooctyne-amine |
| **DC** | Dendritic cell |
| **DCC** | *N,N'*-Dicyclohexylcarbodiimide |
| **DCE** | Dichloroethane |
| **DET** | Dexter energy transfer |
| **DIPEA** | *N,N*-Diisopropylethylamine |
| **DMAP** | 4-Dimethylaminopyridine |
| **DMF** | Dimethylformamide |
| **DMSO** | Dimethylsulfoxide |
| **DPPA** | Diphenylphosphonium azide |

| | |
|---|---|
| **dppf** | 1,1′-Bis(diphenylphosphino)ferrocene |
| **DTT** | Dithiothreitol |
| **EAE** | Experimental autoimmune encephalomyelitis |
| **ECM** | Extracellular matrix |
| **EDC** | 1-Ethyl-3-(3-dimethylaminopropyl)carbodiimide |
| **EDTA** | Ethylenediaminetetraacetic acid |
| **EGF** | Epidermal growth factor |
| **EGM2-d** | Endothelial growth medium-2 depleted of VEGF, EGF and FGF |
| **EGM2MV** | Endothelial cell growth medium-2 |
| **EI** | Electron ionisation |
| **Em** | Emission |
| **eq** | Equivalents |
| **ESI** | Electrospray ionisation |
| **Ex** | Excitation |
| **FAC** | Final adjusted concentration |
| **FACS** | Fluorescence-activated cell sorting |
| **FAME** | Fingolimod-associate macular oedema |
| **FBS** | Fetal Bovine Serum |
| **FC** | Fold-change |
| **FDR** | False discovery rate |
| **FGF** | Fibroblast growth factor |
| **Fing-P** | Fingolimod phosphate |
| **FRET** | Förster resonance energy transfer |
| **FT-IR** | Fourier Transform Infrared Spectroscopy |
| **g** | Gram |
| **GAPDH** | Glyceraldehyde 3-phosphate dehydrogenase |
| **GC** | Gas chromatography |
| **GO** | Gene ontology |

| | |
|---|---|
| **GPCR** | G-protein coupled receptor |
| **h** | Hour(s) |
| **HAA** | Hydroaminoalkylation |
| **HATU** | Hexafluorophosphate azabenzotriazole tetramethyl uronium |
| **HCD** | High energy collision dissociation |
| **HDAC5** | Histone Deacetylase 5 |
| **HMBC** | Heteronuclear Multiple Bond Correlation |
| **HMPA** | Hexamethylphosphoramide |
| **HOSA** | Hydroxylamine-*O*-sulfonic acid |
| **HPLC** | High performance liquid chromatography |
| **HRP** | Horseradish peroxidase |
| **HUVECs** | Human umbilical vein endothelial cells |
| **Hz** | Hertz |
| **IDE** | Insulin-degrading enzyme |
| **IPA** | Isopropyl alcohol |
| **IR** | Infrared spectroscopy |
| ***J*** | Coupling constant |
| **KD** | Knockdown |
| **kDa** | Kilodalton |
| **KO** | Knockout |
| **kV** | Kilovolt |
| **LCMS** | Liquid chromatography–mass spectrometry |
| **LCMS/MS** | Liquid chromatography–tandem mass spectrometry |
| **LDL** | Low-density lipoprotein |
| **LECs** | Lymphatic endothelial cells |
| **LGALS1** | Galectin 1 |
| **LN** | Lymph node |
| **LiHMDS** | Lithium bis(trimethylsilyl)amide |

| | |
|---|---|
| **LRMS** | Low resolution mass spectroscopy |
| **LYVE1** | Lymphatic vessel endothelial hyaluronan receptor 1 |
| **m** | Multiplet |
| **M** | Molar |
| **mbar** | Millibar |
| **MHz** | Megahertz |
| **MI** | Myocardial infarction |
| **min** | Minute(s) |
| **mg** | Milligram |
| **mL** | Millilitre |
| **mm** | Milimetre |
| **mM** | Millimolar |
| **mmol** | Millimole |
| **MMPs** | Matrix metalloproteinases |
| **MOA** | Mode of action |
| **MOE** | Molecular Operating Environment |
| **MRC1** | Macrophage mannose receptor 1 |
| **MS** | Mass spectrometry |
| **ms** | Millisecond |
| **MTT** | 3-(4,5-Di methyl thiazol-2-yl)-2,5-diphenyltetrazolium bromide |
| **MW** | Microwave |
| **m/z** | Mass-to-charge ratio |
| **NA** | Numerical aperture |
| **NHC** | N-heterocyclic carbene |
| **NK** | Natural killer |
| **nm** | Nanometre |
| **nM** | Nanomolar |
| **NP-40** | Nonidet® P-40 |
| **ns** | Nanosecond |
| **PAL** | Photoaffinity labelling |

| | |
|---|---|
| **PBS** | Phosphate buffer solution |
| **PCC** | Pyridinium chlorochromate |
| **PD** | Pull-down |
| **PEG** | Poly(ethylene glycol) |
| **PEPPSI** | Pyridine-Enhanced Precatalyst Preparation Stabilization and Initiation |
| **PFA** | Paraformaldehyde |
| **PFP** | Pentafluorophenyl |
| **PG** | Protecting group |
| **PHA-L** | Phytohemagglutinin-L |
| **PLPP3** | Phospholipid phosphatase 3 |
| ***p*NB** | *para*-Nitrobenzyl |
| **ppm** | Parts per million |
| ***p*-TSA** | *para*-Toluenesulfonic acid |
| **PTX** | Pertussis toxin |
| **PVDF** | Polyvinylidene difluoride |
| **q** | Scattering vector |
| **quant.** | quantitative |
| **RAAS** | Renin-Angiotensin-Aldosterone System |
| **RIPA** | Radioimmunoprecipitation assay buffer |
| **ROS** | Reactive oxygen species |
| **rpm** | Revolutions per minute |
| **RRMS** | Relapsing-remitting multiple sclerosis |
| **rt** | Room temperature |
| **s** | Singlet |
| **S1P** | Sphingosine-1-phosphate |
| **S1PR** | Sphingosine-1-phosphate receptor |
| **SAR** | Structure-activity relationship |
| **sat.** | Saturated |
| **SAXS** | Small-angle x-ray scattering |
| **SD** | Standard deviation |

| | |
|---|---|
| **SDS** | Sodium dodecyl sulphate |
| **SDS-PAGE** | Sodium Dodecyl Sulfate-Polyacrylamide Gel Electrophoresis |
| **SEM** | 2-(trimethylsilyl)Ethoxymethyl |
| **sem** | Standard error margin |
| **SNP** | Single nucleotide polymorphism |
| **SPAAC** | Strain-promoted azide-alkyne cycloaddition |
| **SPHK2** | Sphingosine kinase 2 |
| **SPS** | Synchronous Precursor Selection |
| **STAB1** | Stabilin 1 |
| **T** | Time |
| **t** | Triplet |
| **$t_{1/2}$** | Half-life |
| **TAMRA** | 5-Carboxytetramethylrhodamine |
| **TBDMS** | *tert*-Butyldimethylsilyl |
| **TBTA** | Tris[(1-benzyl-1H-1,2,3-triazol-4-yl)methyl]ami |
| **TCEP** | Tris(2-carboxyethyl)phosphine hydrochloride |
| **TCR** | T-cell receptor |
| **Tf** | Triflate |
| **TFA** | Trifluoroacetic acid |
| **TFAA** | Trifluoroacetic anhydride |
| **THF** | Tetrahydrofuran |
| **TIPS** | Triisopropylsilyl |
| **TLC** | Thin layer chromatography |
| **TM** | Transmembrane |
| **TMS** | Trimethylsilyl |
| **TMT-MS** | Tandem mass tag mass spectrometry |
| **ToF** | Time of flight |
| **Tris** | Tris(hydroxymethyl)aminomethane |

| | |
|---|---|
| **UV** | Ultraviolet |
| **UPLC** | Ultra Performance Liquid Chromatography |
| **VEGFC** | Vascular Endothelial Growth Factor C |
| **VEGFR** | Vascular Endothelial Growth Factor Receptor |
| $\nu_{max}$ | Wavenumber |
| **waterLOGSY** | Water Ligand Observed via Gradient SpectroscopY |
| **WT** | Wildtype |
| **YAP** | Yes-associated protein |

# Chapter 1

## Introduction

# 1 Introduction

## 1.1 Cardiac ischaemic injury

Ischemic heart disease, also called coronary heart disease (CHD), occurs when a region of the cardiac muscle (myocardium) becomes starved of oxygen. This ischaemic event is commonly caused by the narrowing or obstruction of the coronary arteries which supply oxygen-rich blood from the lungs to the heart (Figure 1.1).[4] This narrowing of the coronary arteries is caused by the build-up of fatty, cholesterol-rich deposits called atheromas around the arterial walls.[5] Over time, these atheromas develop into a hardened plaque which narrows and rigidifies the artery. As these plaques grow, they can break away as a blood clot, leading to arterial thrombosis and the pathological restriction of blood flow to the myocardium, causing a myocardial infarction (MI), or heart attack. The evolution towards a MI occurs when cardiac tissue downstream of the blockage becomes necrotic.[6] Post-MI, the deposition of fibrotic scarring reduces the overall cardiac function, leading to the subsequent progression into cardiac hypertrophy and heart failure. CHD can arise from a variety of acquired or genetic risk factors. In most cases, the development of CHD in a patient can be attributed to acquired risk factors, many of which are interlinked. Poor lifestyle factors, such as a lack of physical exercise, high-fat diet and smoking,[7-9] can increase the propensity towards CHD. There are also a number of genetic risk factors which are associated with CHD, not all of which are well understood. Some of these observed risk factors present as a genetic predisposition towards heart disease (i.e. chr9p21, type 1 diabetes),[10, 11] whereas others have a direct pathological cause and effect to which it can be attributed (i.e familial hypercholesterolemia).[12]

There is no cure for ischaemic heart disease beyond preventative lifestyle choices, symptomatic treatments and surgical interventions to slow the disease progression. Heart disease remains the number one cause of death globally and CHD has an astounding global prevalence, affecting over 250 million people worldwide.[13] Hence there is a huge unmet need for curative treatments to combat cardiac ischaemic injury.

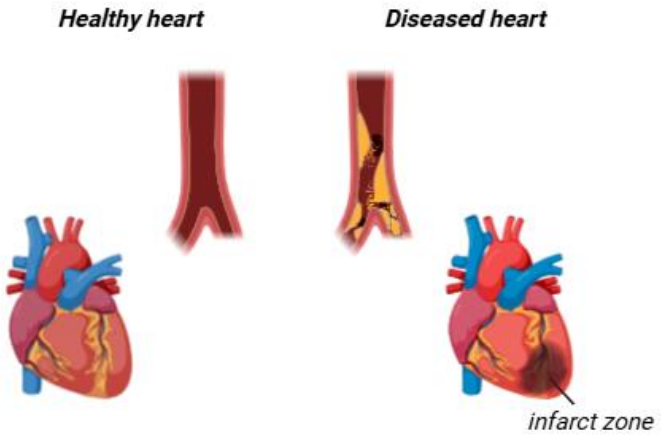


***Figure 1.1: Schematic depiction of a healthy heart compared to an infarcted heart.*** *Healthy hearts possess clear, non-obstructed arteries, whereas infarcted hearts have coronary arteries occluded with atheromas and thrombosis. This blockade of the coronary artery results in a lack of oxygenated blood reaching the downstream myocardium, leading to necrosis.*

### 1.1.1 Timeline of a Myocardial Infarction

Once myocardial infarction happens, upon occlusion or narrowing of the coronary arteries, cardiomyocytes and vascular endothelial cells downstream of the blockage become ischaemic and begin to die.[6] The most common mechanism of cardiomyocyte cell death immediately after a MI is coagulation necrosis.[14, 15] Necrosis is defined as an uncontrolled form of cell death whereby the cell becomes metabolically compromised and ATP-starved, leading to protease leakage from lysosomes and subsequent cellular degradation.[16] This is usually followed by cell membrane rupture and the release of intracellular contents, triggering an innate immune response. In the case of coagulation necrosis, the cellular architecture remains intact, but the intracellular proteins become denatured, preventing proteolytic degradation.[14] This is

observed physiologically as firm, white coagulated tissue. This region of ischaemic tissue is called the infarct zone. The released damage-associated membrane patterns (DAMPs) trigger the innate immune response and mobilisation of immune cells from bone marrow/splenic reservoirs. These immune cells invade the injured heart and initially present with a pro-inflammatory phenotype.[17] This phase of the immune response is characterized by the clearance of necrotic tissue from the infarct zone and the degradation of the extracellular matrix (ECM) by matrix metalloproteinases (MMPs).[18] However, an excessive pro-inflammatory response can result in the clearance of healthy cardiomyocytes, expanding the infarct zone and exacerbating the injury.[19] Following the inflammatory phase, recruited immune cells adopt a more reparative phenotype and activate fibroblasts to proliferate and differentiate into myofibroblasts. These myofibroblasts replace the necrotic tissue and promote the secretion of a collagen-based scar to maintain the structural integrity of the heart and prevent cardiac rupture.[20] Neovascularisation of both blood and lymphatic vessels occurs to induce reperfusion of the infarcted tissue, and modulate inflammation. Angiogenesis (i.e. growth of new blood vessels) into the infarct zone post-MI facilitates the redistribution of oxygenated and nutrient-rich blood to the heart, while also enabling direct immune cell infiltration.[21] Lymphangiogenesis (i.e. growth of new lymphatic vasculature) into the infarct zone enhances immune cell clearance, stimulating inflammation resolution.[22] The scar tissue begins to mature after a couple of weeks, with extensive crosslinking of the collagen ECM occurring, alongside cardiac remodelling. The excessive collagen deposited around the scar tissue impairs its contractility and elasticity. Coupled with the lack of conductivity with the survived tissue, this can lead to arrhythmia which in-turn can be lethal.[23] Thus, adverse cardiac remodelling can hinder the overall function and cardiac output of the heart. This

suboptimal repair mechanism that the body adopts after a MI can lead to a plethora of long-term complications.

The pro-inflammatory and reparative pathways which are triggered post-MI are regulated by the complex interplay between immune cells that make up the innate and adaptive immune response. As such, a greater understanding of the spatiotemporal roles that each immune cell plays in the heart after a MI could provide insight into new therapeutic targets to aid cardiac recovery.

### 1.1.2 Immune response after a Myocardial Infarction

Upon cardiomyocyte cell death, in response to ischaemic injury, the innate immune response is triggered by pro-inflammatory and apoptotic signalling by necrotic cardiomyocytes, damaged ECM and cell debris.[24] The release of cleaved complement proteins (C5a) and cytokines (histamine, TNF$\alpha$ and IL-1$\beta$) recruits the initial influx of neutrophils from reservoirs in the spleen and bone marrow to the site of injury in the heart.[25-28] Neutrophils can enter the periphery of the infarct site within hours of a MI, but their migration to the centre of the necrotic tissue can be hindered by its non-perfused nature. Their population peaks around day 3 post-MI, beginning to decline at day 5 and nearly absent by day 7 (Figure 1.2).[29] DAMPs activate the neutrophils, promoting their release of reactive oxygen species (ROS) and proteases, perpetuating the immune response.[30] Excessive build-up of neutrophils at the site of injury or their delayed clearance can be detrimental to cardiac recovery, due to their role in maladaptive cardiac remodelling.[31, 32]

Neutrophils recruit monocytes through the secretion of proteoglycans and cathepsin G.[33] In addition, neutrophils release pro-inflammatory cytokines which increases the expression of

adhesion receptors on the surface of endothelial cells and activates integrins on the surface of monocytes, potentiating the system towards increased immune cell infiltration.[34] Upon recruitment to the site of infarct, monocytes initially differentiate into M1-type macrophages (day 1-3 post-MI),[29, 35] which display a pro-inflammatory phenotype. These M1-type macrophages participate in crucial phagocytotic events, clearing cell debris and apoptotic neutrophils,[36] while also degrading ECM.[37] However, excessive cell clearance can lead to the expansion of the infarcted zone, exacerbating the injury.[38] Over time (days 5-7 post-MI),[29] the macrophage population primarily adopts a reparative M2-type phenotype, which promotes ECM deposition, myofibroblast proliferation and angiogenesis.[39] Whilst M2 macrophages are canonically associated with a cardioprotective phenotype, their persistent activation can lead to excessive ECM and fibrosis deposition which results in adverse cardiac remodelling.

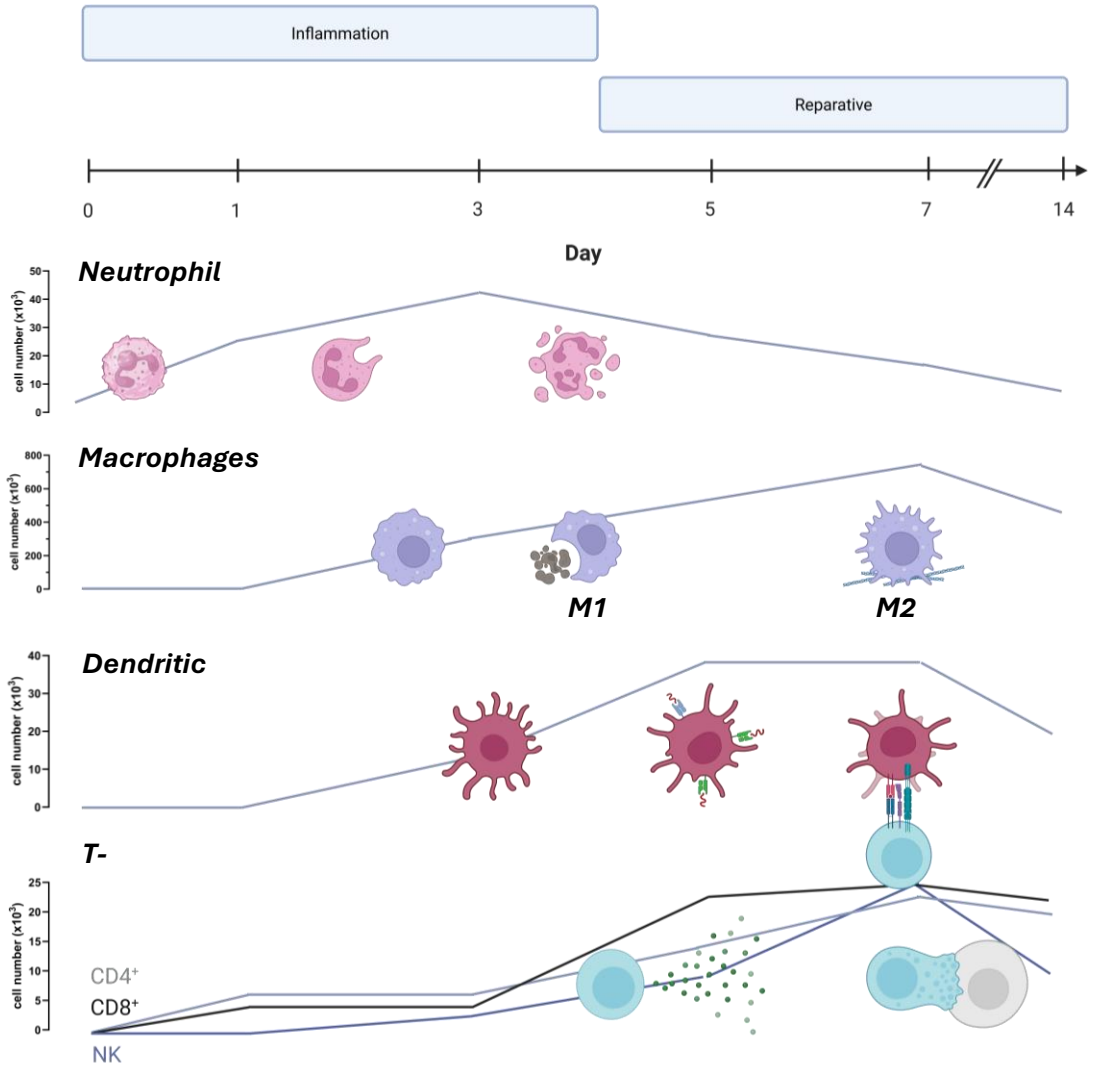


***Figure 1.2: Timeline of the immune response after a myocardial infarction.*** *A schematic depiction of the immune cell infiltration timeline into the infarct zone after a myocardial infarction in adult mice. Expression levels quantified by Yan et al are depicted.[29] Neutrophils enter the heart within hours of the infarction, clearing cell debris before undergoing apoptosis. Neutrophil signalling and apoptosis triggers macrophage infiltration. Macrophages phagocytose the cell debris before shifting from a M1 to a M2 phenotype, aiding reparative ECM deposition. Dendritic cells take up cardiac specific antigens and present them to naïve T-lymphocytes in secondary lymphoid organs, triggering their activation and migration to the heart. Circulating T-lymphocytes migrate to the heart first, releasing both pro- and anti-inflammatory signalling molecules. Cytotoxic T-lymphocytes can trigger cell death in healthy cardiomyocytes. Dendritic cell-activated T-lymphocytes infiltrate later, making up the majority of the T-lymphocyte population.*

During the secondary wave of the immune response, monocytes can also differentiate into dendritic cells (DCs), with the majority of the population being myeloid DCs, originating from

the spleen.[40-42] DCs are immunoregulatory cells which bridge the gap between the innate and adaptive immune response. They possess the ability to phagocytose, in addition to exhibiting cardiac-specific pro-inflammatory antigens on their cell surface, acting as an antigen-presenting cell (APC). As an APC, DCs can induce T-lymphocyte activation through direct contact of the presented-antigen with the T-cell receptor (TCR).[42, 43] DCs also play a crucial role as a modulator of monocyte/macrophage homeostasis, controlling their population levels and relative M1/M2 phenotype proportions.[44] Conversely, prolonged mature DC infiltration in the myocardium deteriorates left ventricle cardiac remodelling,[45] likely due to the stimulation of an excessive inflammatory response which can induce secondary myocardial injury, such as myocarditis.[46, 47]

Upon activation by DCs in secondary lymphoid organs (i.e. lymph nodes and spleen), T-lymphocytes are recruited to the site of injury (day 7 post-MI).[29] There are various subpopulations of T-lymphocytes that can display a pro-inflammatory/effector role or a regulatory anti-inflammatory role. T-lymphocytes are primarily divided into $CD4^+$ or $CD8^+$ T-lymphocytes, depending on their surface expression of either biomarker. $CD4^+$ T-lymphocytes can be further divided into 3 subtypes which have been shown to have a major influence in myocardial infarction recovery, Th1, Th2 and Tregs. Th1 cells portray a pro-inflammatory phenotype and play a role in cell debris clearance after a MI, however, like most pro-inflammatory immune cells their prolonged presence can exacerbate the damage caused by a MI.[48] Th2 cells play a role in tissue regeneration regulation as they secrete mediators which promote the shift of macrophages towards a M2-phenotype.[49] A more pronounced Th2-immunity in patients is conducive to improved recovery after a MI and reduced risk of heart failure,[50] potentially due to IL-5 secretion and eosinophil recruitment.[51] Tregs are a class of

regulatory $CD4^+$ T-lymphocytes which primarily demonstrate a cardioprotective effect.[52] They play an indispensable role in the homeostasis of pro- vs anti-inflammatory immunity, favouring the progression towards Th2 and M2 phenotypes.[53] Tregs and Th1 cells are the predominant $CD4^+$ populations present in the heart 7 days post-MI.[29] $CD8^+$ T-lymphocytes of note in the context of MI recovery are cytotoxic T-lymphocytes and natural killer (NK) T-lymphocytes. Cytotoxic T-lymphocytes have been shown to recognise and kill healthy cardiomyocytes,[19, 54] aggravating the ischaemic injury further. Whereas NK T-lymphocytes are part of the innate immune response and participate in a regulatory role, releasing cardioprotective cytokines (i.e. IL-10) to dampen the chronic inflammatory response after a MI.[55]

To summarise, the acute innate inflammatory response is essential for the clearance of necrotic cardiomyocytes post-ischaemic injury. However, prolonged exposure of these pro-inflammatory populations (neutrophils, M1 macrophages, Th1 and cytotoxic $CD8^+$ T-lymphocytes) can worsen the injury by increasing the infarct size and promoting the progression towards a chronic inflammatory state. After the initial inflammation phase, the localised immune cell populations evolve towards a more reparative state. These anti-inflammatory populations (M2 macrophages, Th2) promote proliferation of myofibroblasts to replace the dead tissue and deposit a collagen-rich ECM to stabilise the hearts' structure, preventing rupture. Yet, the excessive stimulation of these recovery mechanisms can result in adverse cardiac remodelling which hinders the cardiac output of the heart and can lead to further complications. There are several immunoregulatory populations (Tregs, NK T-lymphocytes, DCs) which are responsible for the homeostasis between the inflammatory and reparative mechanisms involved in cardiac recovery.

It is evident that more research into the fine balance between pro- and anti-inflammatory immunity post-MI is required. A greater understanding will allow us to decipher the optimal immunomodulatory response, which is conducive to improved cardiac recovery. Spatiotemporal cell-type specific control over the different immune cell populations involved in ischaemic injury recovery demonstrates great therapeutic potential.

### 1.1.3 Long term consequences of cardiac ischaemic injury

As previously stated, the endogenous repair mechanisms which are triggered in response to ischaemic injury are suboptimal. The acute inflammatory response requires carefully balanced regulation, and any slight deviation can initiate the evolution into a chronic state. This commonly observed transition towards chronic inflammation can exacerbate the initial ischaemic injury, with healthy cardiomyocytes being targeted by cytotoxic and phagocytotic immune cells, resulting in the growth of the original infarct zone.[54, 56] Additionally, the overwhelming pro-inflammatory signalling subsequently hinders the reparative response mechanisms and a prolonged inflammatory response post-MI leads to increased cardiomyocyte cell death. [26]

The reparative phase is also essential for limiting cardiac damage following MI. Inadequate ECM deposition and delayed revascularisation results in a weakened fibrotic scar that is prone to cardiac rupture.[57] Equally, a premature deviation towards the reparative phase before thorough cell debris clearance by pro-inflammatory immune cells can be similarly devastating. Excessive fibrosis can affect the contractility of the repaired heart, thereby hindering its function. These complications are observed physiologically as adverse cardiac remodelling, whereby the ineffective repair and regeneration of the injured heart results in its inadequate function, leading to further complications. The high proportion of collagen within

the fibrotic scar tissue reduces the contractility and conductivity of the fibrotic tissue.[58] The extent of fibrosis can also be increased by insufficient neovascularisation of the infarcted zone, leading to secondary ischaemic events.[59]

Heart remodelling is also the consequence of the heart experiencing increased mechanical stress upon the cell wall, causing it to stretch, in order to maintain the required levels of blood circulation.[60, 61] This leads to increased chamber dilation which correlates to poor prognosis in patients.[62-65] In response to stress, cardiomyocytes may undergo hypertrophy, whereby non-infarcted healthy cardiomyocytes proliferate to compensate for the loss of contractile tissue.[66] This initial compensation is beneficial, as it reduces the overall load and stress on the myocardial wall. Cardiac hypertrophy has also been linked to metabolic remodelling in cardiomyocytes due to energy starvation.[67] Nonetheless, continual myocardium thickening results in stiffening of the muscle and the development of diastolic heart failure.[68]

In summary, the main features of adverse cardiac remodelling are (i) excessive cardiomyocyte loss resulting in a larger infarct, wall thinning and chamber dilation (ii) extensive fibrosis demonstrating impaired contractility and conductivity (iii) mechanical stress and impaired metabolism leading to myocardial hypertrophy and functional impairment. All these complications increase the risk of experiencing another heart attack and developing heart failure. The common progression of this type of heart disease is also responsible for its extremely high rate of morbidity, underscoring the need for improved treatments.

### 1.1.4 Current treatments for cardiac ischaemic injury

Despite the severity and prevalence of ischaemic injury, there are currently no available treatments which reverse the damage caused by adverse cardiac remodelling. The majority of treatments on the market focus on preventative measures, reperfusion therapy or surgical intervention to slow the progression of the disease towards heart failure.

#### 1.1.4.1 Preventative treatments

The available preventative treatments focus primarily on reducing the likelihood of an ischaemic event from occurring,[69] by combatting the development of atherosclerosis and thrombosis. Statins lower the circulating LDL cholesterol, reducing atheroma formation. Similarly, anti-platelet and anti-coagulation therapies are carefully used to prevent blood clot formation and subsequent thrombosis. In addition, anti-hypertensive drugs work by lowering blood pressure and consequently lower the risk of CHD. At-risk patients are commonly prescribed a combination of preventative treatments, along with recommended lifestyle changes to lower the likelihood of coronary artery occlusion and ischaemic injury.

#### 1.1.4.2 Post-ischaemia treatments and their complications

Post-MI, most treatments concentrate on mitigating risk factors to reduce the risk of adverse disease progression, while also working to re-administer blood flow to the heart. Thrombolytic drugs are administered to remove the coronary blockage and enable infarct reperfusion.[70] However, caution must be taken when inducing reperfusion, as paradoxically the re-establishment of blood flow can exacerbate the injury in what is known as ischaemia-reperfusion injury.[71] The rapid influx of oxygenated blood leads to a substantial increase in

ROS which play a role in tissue damage. In addition, reperfusion significantly enhances early neutrophil infiltration, which similarly has a detrimental effect on ischaemia recovery.[72]

Sodium glucose co-transporter 2 (SGLT2) inhibitors, while initially developed as a treatment for type 2 diabetes, are used to slow the progression of heart failure.[73] Inhibition of SGLT2 displays many cardioprotective effects, including improved energy metabolism,[74] reduced inflammation,[75] and reduced cardiac hypertrophy.[76] These combined effects contribute towards a marked reduction in hospitalisations and morbidities in post-MI patients.[77, 78]

#### 1.1.4.3 Surgical intervention

In parallel with the available pharmaceutical treatments, surgical intervention is also a possibility. To restore blood flow to the heart, a less invasive surgery such as an angioplasty or stent insertion can be performed to widen the occluded vessel. In extreme cases, such as multiple vessel or left main coronary artery blockage, a bypass surgery may be required as a long-term solution if the less invasive methods are ineffective. Bypass surgery involves the relocation of blood vessels from elsewhere in the body to the heart to bypass occluded arteries and restore blood flow. Furthermore, in severe cases a heart transplant may be necessary for end-stage heart failure patients. Despite the success rate of these surgeries,[79, 80] like all invasive procedures they carry their own inherent risks, particularly in older patients with underlying health issues.

There is an unmet need for new ischaemic injury therapies which tackle the underlying issues of cardiac remodelling and chronic inflammation, to enhance our endogenous recovery mechanisms in cardiac repair and regeneration after a heart attack.

## 1.2 Cardiac regeneration

The definitive cure in cardiac ischaemia would be complete cardiomyocyte regeneration, to replace fibrotic scarring and reverse poor cardiac remodelling. Human cardiac regeneration has been postulated by academics and medical professionals for nearly a century,[81] however, it was only with the advancement of surgical procedures and *in utero* monitoring that the first cases of human foetal and neonatal cardiac regeneration were observed. The first reported case of neonatal cardiac regeneration followed by a severe MI was in 1980,[82] since then there have been several more documented cases observed.[83-87] In 2015, a new-born baby suffered a severe thrombotic occlusion of the left anterior descending artery approximately 2 h after birth.[88] After thrombolytic reperfusion treatment, the new-born made a full recovery, with a cardiac function indistinguishable from a healthy child of a similar age. These case studies exemplify that humans exhibit the endogenous mechanisms required for complete cardiac regeneration, but they are lost very quickly after birth. This is a trait which is shared with other mammalian species (i.e. mice and pigs). Due to the rarity of neonatal MI and the ethical implications, the cardiac repair mechanisms that are adopted in human neonates cannot be studied in any great depth. As such, animal models of fish and mammalian neonates have provided a promising insight into regeneration.[89]

### 1.2.1 Animal models of cardiac regeneration

Many mammalian neonates retain cardiac regeneration potential, however this is lost within 7 days of birth.[90] When comparing their differences in innate immune response, neonatal mice release more anti-inflammatory cytokines (IL-10, IL-6),[91, 92] and histamines to encourage DCs and T-lymphocytes to adopt a reparative phenotype (Figure 1.3a).[92] Moreover, in neonates endothelial cells possess less surface adhesion receptors (i.e selectins), which reduces immune

cell infiltration.[93] Whereas adult mice exhibit a stronger inflammatory response and excessive fibrotic scarring.[94] However, one exception to this observation is the spiny mouse that can regenerate as an adult. [95] One key difference which has been observed in spiny mice is the superior neovascularisation of both blood and lymphatic vessels into the infarcted tissue post-MI.[95] Moreover, the scar tissue in spiny mice has a higher cardiomyocyte density and is composed of misaligned and less compacted collagen, resulting in a thicker but more permissive scar.[96] In addition, the cardiomyocyte phenotype in adult spiny mice resembles that of neonatal cardiomyocytes in laboratory house mice.[95] The improved vascularisation, differential cardiomyocyte expression and distinct scar composition could all be potential strategies to explore in the drive for human adult cardiac regeneration.

Adult zebrafish also have the capacity to regenerate their heart (Figure 1.3b).[97] However, this does not extend to all small teleost fish; for example the Japanese rice fish, medaka, is unable to regenerate its heart. It is evident that differences in the immune response triggered after ischaemic injury, between the two fish, may underlie differences in regenerative capacity.[98] Medaka fish demonstrate a neutrophil-dominant inflammatory phase with a delayed and diminished reparative macrophage recruitment. Conversely, the zebrafish exhibits a moderated neutrophil response and early macrophage infiltration. These observations are conducive to a subdued pro-inflammatory response, which as indicated previously, can be cardioprotective.

The Mexican tetra fish represents another valuable model for studying heart regeneration, owing to its evolutionary divergence into surface-dwelling and cave-dwelling subspecies. The cave-dwelling fish are incapable of cardiac regeneration while the surface fish have retained their capacity to completely recover after cardiac injury (Figure 1.3c).[99] Whilst cardiomyocytes

from both subspecies proliferate to the same extent, the cave fish exhibit a larger immune response after ischaemic injury and a more substantial fibrotic scar. Another evolutionary deviation which could explain the difference in cardiac regeneration between the two species is the altered metabolism observed in cave fish. To overcome long periods of food scarcity and a nutrient deficient diet, the cave fish have a reduced metabolism, higher energy storage and insulin resistance.[100] This diabetic-like phenotype could be linked to the reduced cardiac regeneration potential of the cave fish.

There are many possible attributes which could be responsible for the ability of some species to regenerate their heart, over others. The likely cause is a combination of multiple factors which generate an environment conducive to cardiac regeneration. Nonetheless, a recurring theme throughout the known literature is the importance of a controlled immune response, with an emphasis on more reparative and proliferative mechanisms. This underscores the central role of immune regulation, making immunomodulation a key mechanism to explore to promote cardiac regeneration

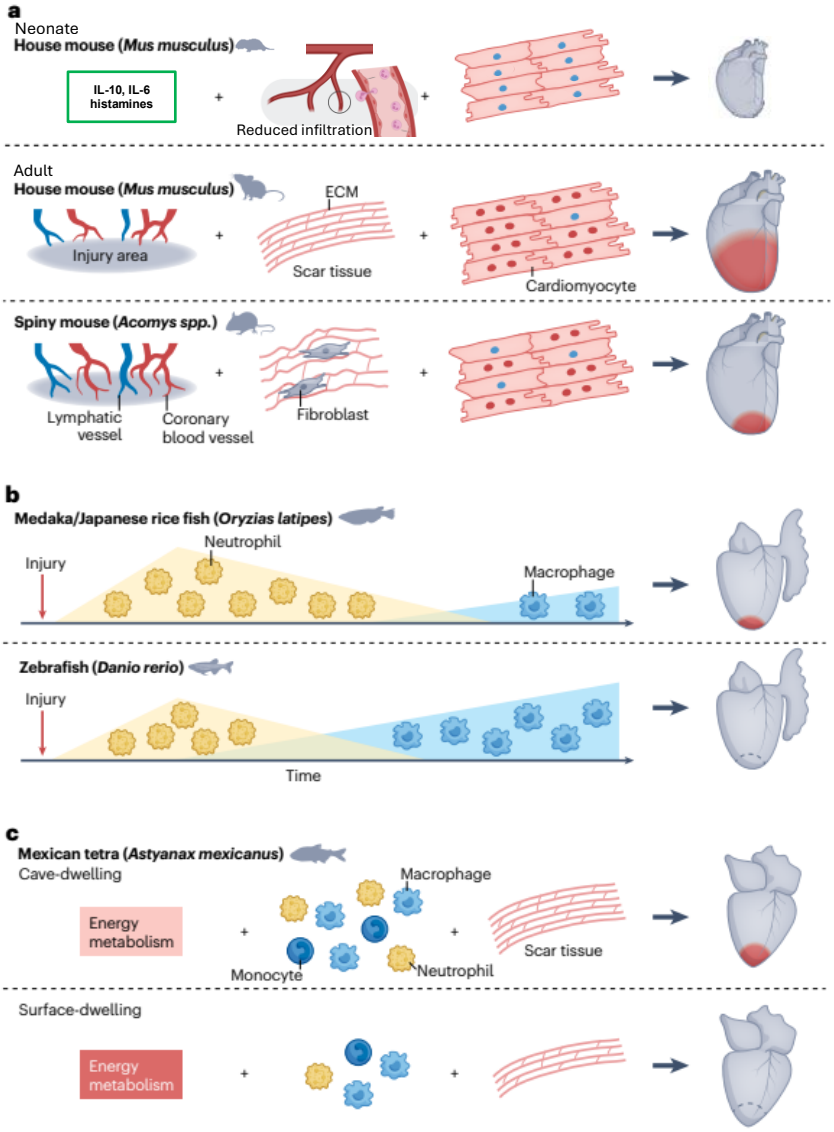


***Figure 1.3: Animal models of cardiac regeneration adapted from Weinberger et al.***[101] *(a) Spiny mice demonstrate improved cardiac regeneration over laboratory mice due to their increased neovascularisation, less compacted collagen scarring and immature cardiomyocyte phenotype (b) Zebrafish can regenerate their heart due to their favourable immune response characterised by reduced neutrophil recruitment and early macrophage infiltration (c) The surface dwelling population of the Mexican tetra have evolved different metabolic pathways, have a diminished immune response and reduced scarring which could justify their high cardiac regeneration potential.*

### 1.2.2 Role of immunomodulation in cardiac regeneration

As previously discussed, there are certain pro-inflammatory immune cells present in the injured heart post-MI which exacerbate the injury. Therefore, it could be beneficial if these populations were therapeutically targeted to diminish their presence within the infarcted heart.

Controlled depletion of neutrophils post-MI is a potential avenue of exploration, however, attempts to completely block neutrophil infiltration into the injured heart post-MI showed no therapeutic benefit.[101] Neutrophils have an influence upon the polarisation of macrophages, and some studies indicate that neutrophils could comprise two sub-populations, N1/2 (similar to the M1/2 macrophage populations). Whilst N1 populations enact a pro-inflammatory effect, N2 play a more proliferative role. Subsequently, it is clear that a complete blockade upon neutrophil infiltration into the injured heart would disregard the potentially beneficial and regulatory roles that they play. This exemplary situation can be applied to several subsets of immune cells present after MI (i.e. macrophages, T-lymphocytes). Therefore, an alternative therapeutic strategy could perceive a mechanism whereby immune cell clearance from the injured heart is made more efficient. This would allow for the initial benefits of an acute inflammation response to be enacted, succeeded by efficient clearance before the immunity evolves to a more chronic state. As afferent lymphatic capillaries within the heart are responsible for the clearance of immune cells from the tissue, it is of interest to study their role in cardiac regeneration.

### 1.2.2.1 Cardiac lymphatic system

Cardiac lymphatics are comprised of a network of vessels located throughout the atria and ventricles. Afferent lymphatic capillaries are smaller blind-ended vessels which are responsible for the clearance of fluid and immune cells from the tissue to the draining lymph nodes.[102] The tips of lymphatic capillaries are comprised of oak leaf shaped lymphatic endothelial cells (LECs) with intercellular button-like junctions (Figure 1.4), with predominant CD31 surface expression and intermittent tight junction proteins (i.e. CD144, claudin-5, occludin).[103] As the capillaries progress towards collecting vessels, the morphology of the cellular interaction adopts a tight zipper-like junction, comprised of solely tight junction proteins. Developmentally, the vascular endothelial growth factor C (VEGFC) and its receptor vascular endothelial growth factor receptor 3 (VEGFR3) are essential for lymphatic development in embryos.[104, 105] The growth of new lymphatic vessels from pre-existing vasculature is termed lymphangiogenesis, and their role in response to MI recovery and cardiac regeneration has been explored.[106]

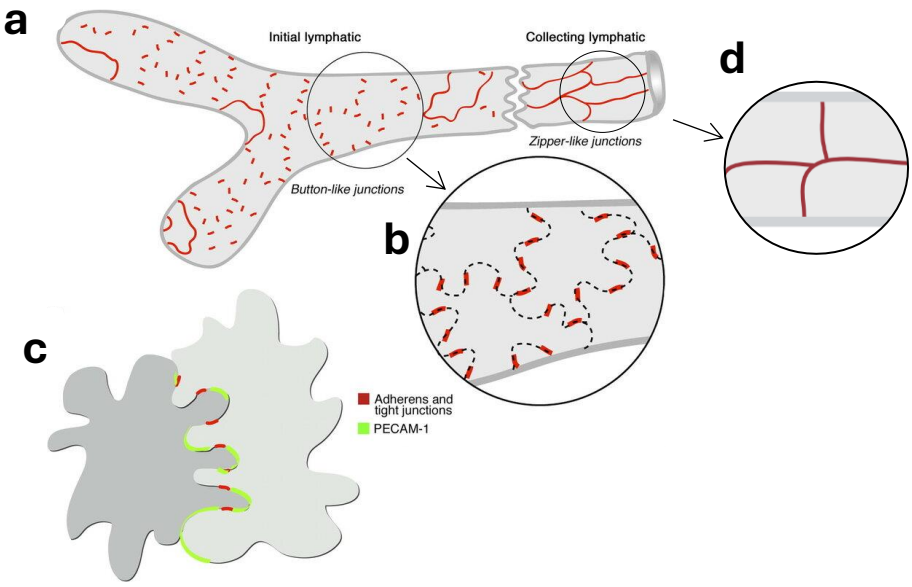


***Figure 1.4: Lymphatic vessel junctions adapted from Baluk et al.***[103] *(a) Schematic of lymphatic capillaries with button-like junctions and collecting lymphatic vessels with zipper-like junctions (b) Highlighting the oak-leaf shaped LECs and button junctions in lymphatic capillaries (c) Adhesion protein composition of button-like junctions with alternating PECAM-1 (CD31, green) and tight junction proteins (red) (d) Highlighting the zipper-like junctions of collecting lymphatic vessels.*

### 1.2.2.2 Role of lymphangiogenesis in cardiac repair and regeneration

It has previously been demonstrated in a MI mouse model, that treatment with pro-lymphangiogenic VEGFC-C156S at time of injury and during the first week, showed significant improvement in cardiac function relative to vehicle control.[107] By inducing lymphangiogenic growth, increased inflammatory resolution was achieved. Enhanced neutrophil clearance was observed as well as significant displacement of macrophages and dendritic cells in a LYVE1 (lymphatic vessel endothelial hyaluronan receptor 1) dependent manner.[63] Conversely, knocking out LYVE1 in mice with an increased immune cell load in the injured heart demonstrated severely impaired cardiac recovery post-MI,[22] recapitulating the essential immunomodulatory role the lymphatic system plays after ischaemic injury.

Whilst VEGFC has shown therapeutic potential, it was administered as a synthetic protein which has a short half-life and potential off-target effects, reducing its *in vivo* efficacy and

diminishing its potential as a drug-of-choice. Additionally, proteins are a costly and time-consuming modality to produce. Therefore, it would be more desirable to identify a small molecule therapeutic which could similarly induce lymphangiogenesis, improve immune cell clearance and enhance cardiac recovery.

## 1.3 Fingolimod

### 1.3.1 Development of fingolimod

Fingolimod (Gilenya®, FTY720) is a small molecule anti-inflammatory drug first developed by researchers at Kyoto University, in collaboration with Taito and Yoshitomi Pharmaceutical Industries. It was progressed through clinical trials and subsequently to market by Novartis, gaining FDA approval in 2010 for relapsing-remitting multiple sclerosis (RRMS).[108] The initial development of fingolimod was derived from the fungal metabolite, myriocin (Table 1.1, Entry **1**), which was identified as a powerful immunosuppressant, reducing T-lymphocyte activity and proliferation in transplanted mice.[109] Initial structural development of myriocin aimed to simplify the molecule. It was observed that the ketone at $C_{14}$ (Entry **2**) wasn't necessary for immunosuppression, whereas the unsaturation at $C_6/C_7$ was important (Entries **3**).[110] Similarly, lactonization of the acid showed no change in efficacy, implying that the acid was non-essential (Entry **4**), whereas acetylation of the head group alcohols (Entry **5**) or amine (Entry **6**) greatly ablated the activity. The chiral alcohol at $C_4$ wasn't necessary for immunosuppressive activity (Entry **7**).[111] *In vivo* studies showed that entry **2** was most effective at inhibiting allo-reactive cytotoxic T-lymphocyte generation in a murine transplantation model. [110]

***Table 1.1: Structure-activity relationship studies on the immunosuppressive influence of myriocin***

| *Entry* | *Structure* | *$IC_{50}$ ($\mu g/mL$)‡* | *% inh** |
|---|---|---|---|
| 1 | 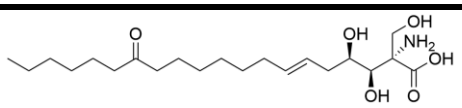 *myriocin* | 0.0032 | 79.6 |
| 2 | 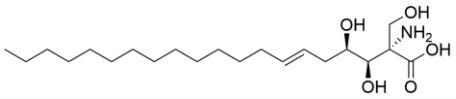 | 0.00075 | 95.7 |
| 3 | 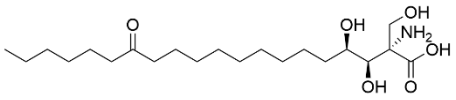 | 0.02 | - |
| 4 | 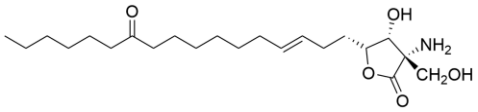 | 0.005 | - |
| 5 | 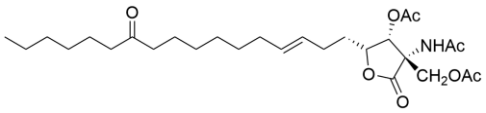 | 32 | - |
| 6 | 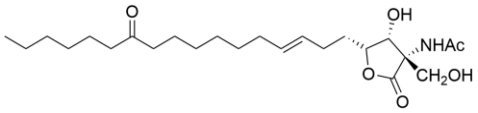 | 0.22 | - |
| 7 | 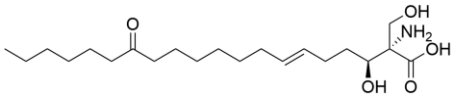 | 0.0022 | - |

‡ *in a mouse allogenic mixed lymphocyte model (in vitro)*[110]
* *% inhibition of the generation of allo-reactive cytotoxic T-lymphocytes at 0.3 mg/kg dose (in vivo)*[110]

Utilising this accumulated structure-activity relationship (SAR) data, simplification of the myriocin structure through removal of the chiral centres and unnecessary branching, led to the first generation of 2-amino-1,3-propanediols.[112] These derivatives showed similar efficacy to myriocin, but with reduced toxicity.[113] Lipophilic chain length studies highlighted a

'goldilocks' zone, with carbon chain lengths of 14-16 exhibiting the highest efficacy both *in vitro* and *in vivo* (Figure 1.5).

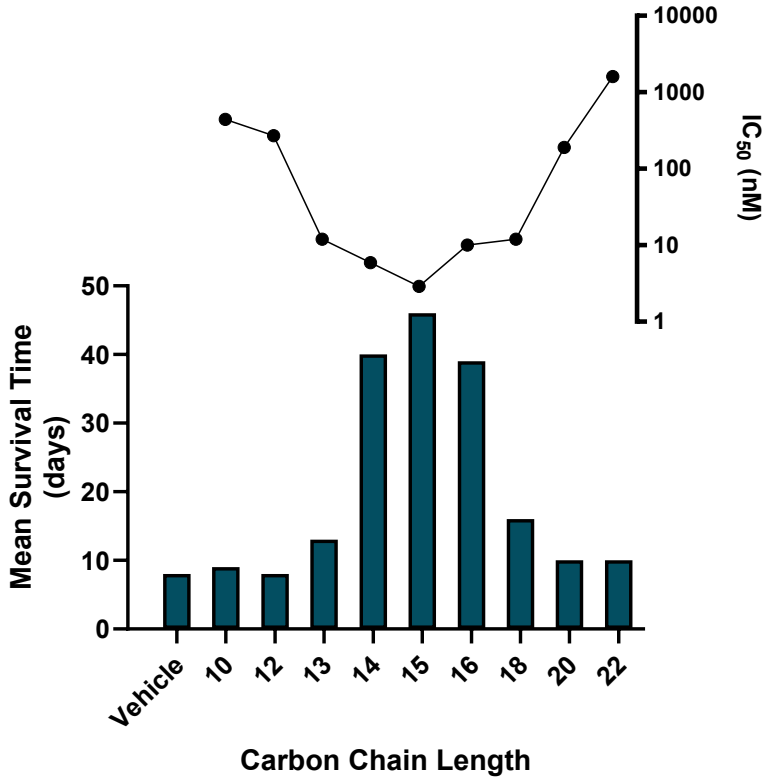


***Figure 1.5: Immunosuppressive effect of 2-amino-1,3-propanediol series.***[112] *In vitro murine allogenic mixed lymphocyte model (scatter plot) and in vivo rat allogenic transplantation survival (bar chart).*

Ultimately, tetradecyl-2-amino-1,3-propanediol (14-carbon chain) was chosen as the preferred molecule for future studies. Subsequent rigidification of the carbon skeleton with the addition of a benzene ring led to the generation of fingolimod (Scheme 1.1).[114]

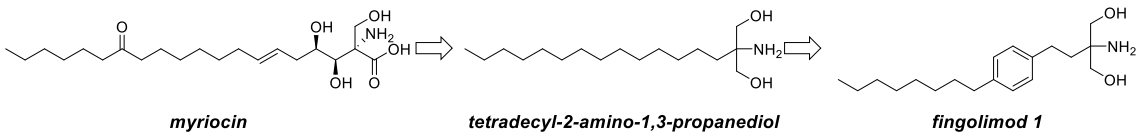


***Scheme 1.1: Evolution of myriocin to fingolimod***

It was later determined that fingolimod's immunomodulatory effect stemmed from its sequestration of circulating mature T-lymphocytes within lymph nodes (LNs), preventing their infiltration into transplanted tissue.[115, 116] Due to the structural similarity between fingolimod and sphingosine-1-phosphate (S1P; Scheme 1.2), it was proposed and subsequently shown, that fingolimod's mechanism of action proceeded *via* agonism of the sphingosine-1-phosphate receptor (S1PR) family.[117] It was also demonstrated that fingolimod's activity was dependent on its enantioselective phosphorylation into (*S*)-fingolimod-phosphate (Fing-P) by sphingosine kinase 2 (SPHK2).[118, 119] This transformation is in equilibrium with phospholipid phosphatase 3 (PLPP3), which removes the phosphate from Fing-P.[120]

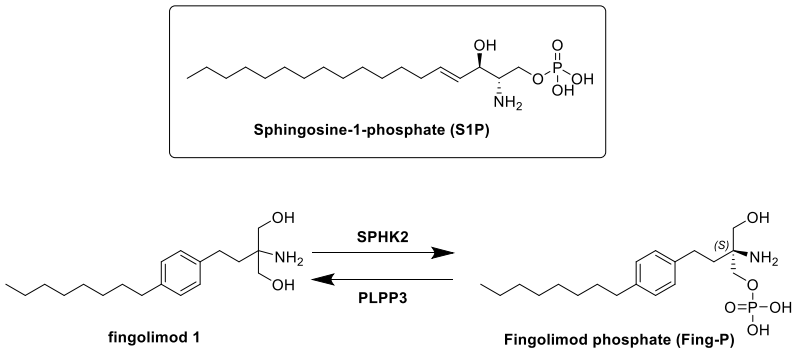


***Scheme 1.2: Cellular metabolism of fingolimod.*** *The structure of sphingosine-1-phosphate (S1P) is illustrated (in the box), highlighting the structural similarity to Fingolimod-phosphate (Fing-P) which led to the hypothesis that Fing-P could be a substrate for the sphingosine-1-phosphate receptor (S1PR) family. Fingolimod is phosphorylated by sphingosine kinase 2 (SPHK2) to yield Fing-P; Fing-P is de-phosphorylated by phospholipid phosphatase 3 (PLPP3).*

Whilst early pre-clinical studies into fingolimod's immunosuppressive effect focused on post-transplantation survival, fingolimod did not pass phase III clinical trials for renal transplantation due to insufficient efficacy.[121] As such, alternative uses for fingolimod's immunosuppressive phenotype were explored. Several pre-clinical studies demonstrated fingolimod's implication as a treatment for RRMS in animal experimental autoimmune encephalomyelitis (EAE) models.[122-124] After demonstrating promising long-term efficacy and manageable adverse side effects in clinical trials,[125-127] fingolimod was brought to market under the trade name Gilenya in 2010, for the treatment of RRMS.

### 1.3.2 Fingolimod and Sphingosine-1-phosphate receptors

S1P is the common endogenous ligand of the S1PRs family of G-protein coupled receptors (GPCRs).[128] However, each of the SIPR family members is associated with a different set of G-proteins, [129] explaining the observed differences in their downstream pathways and phenotypes. Fingolimod's phosphorylated metabolite, Fing-P, acts as a potent agonist towards 4 out of 5 of the S1PR family of receptors ($S1P_1$, $S1P_4$, $S1P_5$: $EC_{50}$ ~ 0.3 – 0.6 nM) and $S1P_3$: $EC_{50}$ ~ 3 nM). [117, 130] However, there is some ambiguity surrounding the true mechanism of action of fingolimod's immunomodulation through the S1PRs. Following Fing-P's initial agonism, S1PRs are rapidly (15-45 mins) internalised, rendering fingolimod as a simultaneous functional antagonist of S1PR family.[131]

$S1PR_1$ is universally expressed across all studied tissue types. This receptor has been shown to play a role in vascular development and neurogenesis as well as lymphocyte trafficking as stipulated previously.[132, 133] $S1PR_3$ is expressed universally, but with a higher abundance in smooth muscle tissue, which aligns with the various regulatory roles it's been shown to enact upon the heart.[134-137] $S1PR_4$ is highly expressed in lymphoid tissue,[138] playing a mediatory role

upon T-lymphocyte proliferation and cytokine signalling.[139] $S1PR_5$ is predominantly expressed in the brain and the spleen, but has low level expression in most tissue types,[140, 141] and is known to regulate NK cell trafficking and maintain the integrity of the blood-brain barrier.[142, 143]

Despite the canonical association of fingolimod with the S1PR family, it is a highly promiscuous molecule, likely due to its generic lipid-like structure. In the literature, fingolimod has been linked to a vast number of proteins and pathways within numerous cell types and disease settings.[144-148] As a drug, fingolimod exhibits a long list of documented side effects associated with its administration.[149] As such, a cautious approach should be taken when deciphering any phenotypic effects of fingolimod to avoid making assumptions about its mechanism of action.

### 1.3.3 Adverse side effects of fingolimod

Despite the FDA approval of fingolimod as a treatment for RRMS, there have been many reported adverse side effects associated with long-term administration of the drug.[150] Some of these effects can be attributed to fingolimod's immunosuppressive phenotype. Patients who are treated with fingolimod have an increased likelihood of developing opportunistic infections such as cryptococcal, herpes simplex virus, nasopharyngitis and various encephalopathies.[151-155] Fingolimod treatment has been associated with asymptomatic bradycardia, but this usually returns to normal after a month. Investigations into this indication revealed that fingolimod's agonism of $S1PR_3$ is responsible, inadvertently triggering activation of a G-protein coupled potassium channel in the heart.[156]

However, of note are the adverse effects with no known indication attributable to S1PR agonism, implying the existence of non-selective, off-target phenotypes. RRMS patients receiving fingolimod treatment commonly report ophthalmological side effects, in particular fingolimod-associate macular oedema (FAME).[157] There have also been multiple observed instances of basal cell carcinoma in patients receiving fingolimod treatment,[151] similarly *via* an unknown mechanism of action. Alongside the disease implications of fingolimod treatment, there have been several fingolimod-induced observations reported on a cellular level.

### 1.3.4 Fingolimod and immunomodulation

In the context of pleiotropic immunomodulatory effects, fingolimod treatment has been shown to modulate a variety of processes. Treatment with fingolimod inhibits the transendothelial migration of T-lymphocytes into peripheral afferent lymphatics *in vivo*.[158] T-lymphocytes appear to accumulate at the basal membrane of the lymphatic endothelium. This observation suggests that the inhibitory effect of fingolimod resides in the disruption of transendothelial migration rather than an interference of chemotaxis or surface adhesion. Alternatively, fingolimod could trigger aggregation of the T-lymphocytes, interfering with their ability to migrate. Additionally, $S1PR_1$-deficient lymphocytes migrate normally, showing that $S1PR_1$ is not needed for T-lymphocyte ingression.[158] Furthermore, fingolimod inhibited migration 4-7 fold more than S1P or a selective $S1PR_1$ agonist,[158] again implying that the inhibitory effects of fingolimod are more complex than just $S1PR_1$ modulation. Interestingly, migration across blood endothelium is not affected by fingolimod treatment, further implying the presence of pleiotropic effects within LECs.[158]

Fingolimod has also been shown in the literature to induce angiogenesis,[159] whilst selective $S1PR_1$ agonists have demonstrated reduced angiogenic sprouting.[160] Due to the history of their

shared signalling pathways,[161] fingolimod was chosen as a test compound in a screen to identify lymphangiogenic modulators*, and was shown to induce lymphangiogenic sprouting at 1 μM.

In addition, there has been reported evidence of fingolimod's therapeutic potential in stroke recovery.[162, 163] However, its mechanism of action is not known. Due to the pathological similarity between cardiac ischaemic injury and strokes, it could be worth investigating whether a common fingolimod-induced beneficial mechanism of action exists.

As previously stipulated, fingolimod has been linked to several immunomodulatory phenotypes which could be therapeutically manipulated to aid MI recovery (i.e. inducing lymphangiogenesis and inhibiting T-lymphocyte ingression). Whilst fingolimod is canonically associated with the S1PR family of GPCRs, there is preliminary evidence to suggest that fingolimod's mechanism of action is *via* a unique target, potentially in a cell-type specific manner. It is important in pathway deconvolution, to resist making assumptions about a promiscuous small molecule's efficacious target. Compounds with a lipid-like structure have been shown to exhibit alternative modes of action within immune cells, contrary to their primary target.[164]

Therefore, a technique which could directly determine the interaction partners of fingolimod within an immunomodulatory context would be a powerful tool.

## 1.4 Drug-protein interactome mapping techniques

Current techniques to probe the interaction between a small molecule and the proteome have advanced our ability to identify both the desired and adverse targets of those drugs. These

* *unpublished, Dr Christophe Ravaud*

techniques include FRET/BRET-based approaches,[165] radiolabelled & lanthanide-based ligands,[166, 167] thermal profiling,[168, 169] phage display,[170] affinity/activity-based protein profiling,[171, 172] and Chem-seq.[173] These tools provide a greater understanding of drug-protein interactions, allowing a more tailored approach to the drug development pipeline. These techniques have also provided a foundation for predictive network-based tools which infer the interactome of drugs based on both the pharmacogenomic properties of the small molecule and the biological characteristics of proteins.[174-176] However, these techniques have limitations with scalability, bias towards high abundance proteins, disruption of natural binding and prior target knowledge requirements. This has led to the development of covalent proximity labelling target identification methodologies.

### 1.4.1 Photoaffinity labelling

Photoaffinity labelling (PAL) was developed in the 1970s as a technique to identify drug-protein interactions within a cellular setting.[177] The basic principle of PAL exploits the ability of certain photolabile functionalities to form highly reactive species (i.e. carbene, nitrene, diradical, ketene), capable of crosslinking in response to irradiation. Within a cellular setting, these reactive intermediates are capable of forming irreversible covalent interactions with proximal biomacromolecules. The short half-life of these reactive species within an aqueous cellular environment restricts labelling to the immediate locality of the small molecule probe. Incorporation of biorthogonal tags to the crosslinking small molecule allows further functionalisation of these targets with affinity handles to aid in their isolation, or dyes for continual monitoring. While this technique started as a way to evaluate drug-protein interactions, the PAL methodology has since been expanded to examine a variety of subcellular exchanges. To date, PAL has been used to identify interactions between

antibodies, proteins, small molecule drugs, lipids, transcription factors, oligonucleotides, carbohydrates and chromatin.[178-184] Commonly used photoaffinity functionalities include phenylazides, pyrones, benzophenones, diazirines and cyclobutane diazirines (PALBOX). These modalities can undergo further modification (i.e. electron-withdrawing neighbours) to ensure the required stabilisation of their subsequent reactive intermediates (Scheme 1.3). This stabilisation allows finetuning of the reactive intermediate half-lives to reduce their diffusion radius and non-specific labelling, while still allowing substantial labelling to occur.

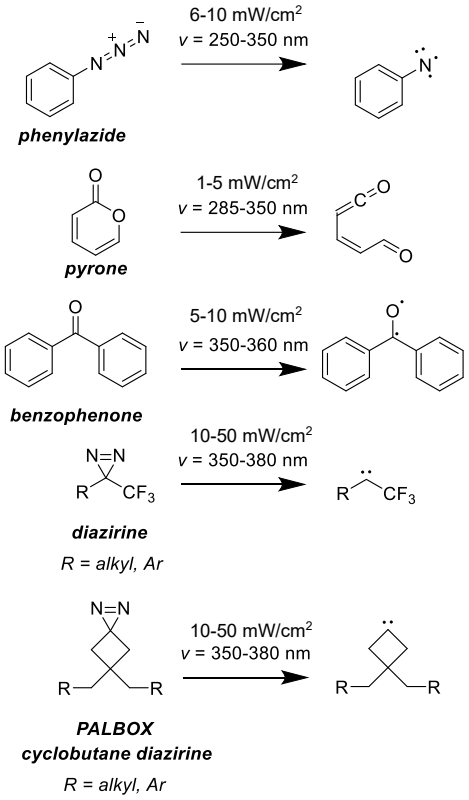


***Scheme 1.3: Photoactivatable groups utilised in photoaffinity labelling.*** *Different modalities which decompose into reactive intermediates upon irradiation. These reactive intermediates are capable of cross-linking to biomacromolecules in situ.*

The diazirine functionality is a popular choice as a photoactivatable group when designing a small molecule PAL probe. Due to its small size, there is minimal interference with target binding and enables the probe to remain as structurally similar to the natural ligand as

feasibly possible. The diazirine also requires a relatively long wavelength of activation (365 nm) compared to other photoactivatable groups, reducing the risk of photodamage to the cell. Upon irradiation, diazirines decompose into carbenes which insert into C-H bonds.[185] However, the preference for amino acid (AA) insertion varies depending on the nature of the carbene (Scheme 1.4). Aryl carbenes insert into all AAs equally, whereas alkyl carbenes preferentially insert into acidic (40-60%) and polar (<20%) AAs,[186] which could result in biased labelling. One inherent issue of the reactivity of the resultant alkyl/aryl carbene is its susceptibility towards intramolecular 1,2-hydride shift to generate the 'quenched' alkene product.[187] This reactivity can be negated by the absence of a β-H or the introduction of a conformationally constrained system with a higher energy barrier to overcome for alkene formation. Such is the case for the so-called PALBOX cyclobutane diazirines.[188, 189] Whilst PALBOX demonstrated more selective protein labelling,[189] the size of the modification and the complexity of the synthesis can be undesirable.

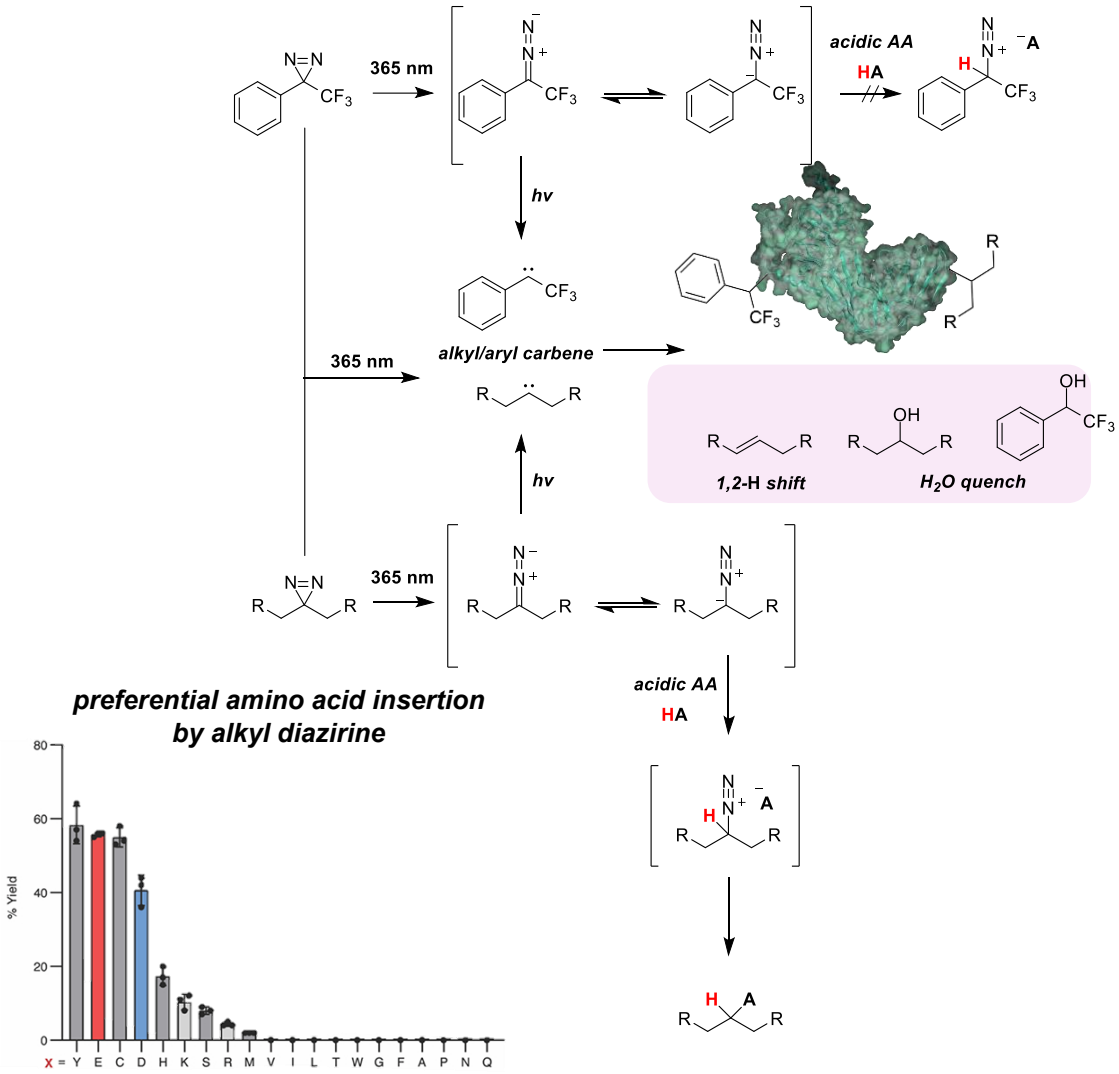


***Scheme 1.4: Decomposition and insertion pathways of alkyl and aryl diazirine (adapted from West et al)[186].*** *Diazirines undergo decomposition upon 365 nm irradiation to carbenes and diazo derivatives. Carbenes can undergo non-productive quenching (blue box) or addition into C-H of proximal biomacromolecules. Alkyl diazo intermediates selectively insert into acidic amino acid (AA) residues. The graph, from West et al,[186] illustrates the relative extent of insertion with different amino acids, demonstrating a clear preference for acidic AA (i.e. tyrosine [Y], glutamate [E], cysteine [C], aspartate [D] etc.).*

Upon probe incubation, irradiation and subsequent labelling of target proteins, it is necessary to isolate them for further analysis. Incorporation of an alkyne tag allows biorthogonal 'click' chemistry to be utilised to add a biotin affinity handle. The copper(I)-catalysed azide-alkyne cycloaddition (CuAAC) click reaction promotes the conversion of a terminal alkyne and biotin-linked azide into a 1,2,3-triazole linkage (Scheme 1.5). Exploiting the high affinity of

biotin for streptavidin/neutravidin allows 'pull down' of labelled proteins for identification *via* immunoblotting and proteomics. To further explore the subcellular localisation of the target proteins, strain-promoted azide-alkyne cycloaddition (SPAAC) is a live cell compatible alternative to CuAAC. The use of a highly strained alkyne (i.e. DBCO) promotes the [1,3]-dipolar Huisgen cycloaddition without the need for a cytotoxic copper source, CuSO4. When utilising SPAAC, a fluorophore tag can be added to visualise the subcellular localisation of target proteins.

To probe for drug-protein interactions, *in vitro* cells are dosed with the bifunctional chemical probe, for a select period, allowing the probe to interact and bind to its target proteins. Upon irradiation, any proteins in the proximity of the probe are irreversibly crosslinked. The appropriate click chemistry is performed depending on the chosen avenue (i.e. fluorophore or biotin tag). Neutravidin pull-down allows isolation of target proteins. Immunoblotting is utilised to screen for both known and speculated target proteins. Proteomics provides a thorough analysis of all isolated target proteins. Once targets are identified they are validated in binding and inhibitor/knock out studies.

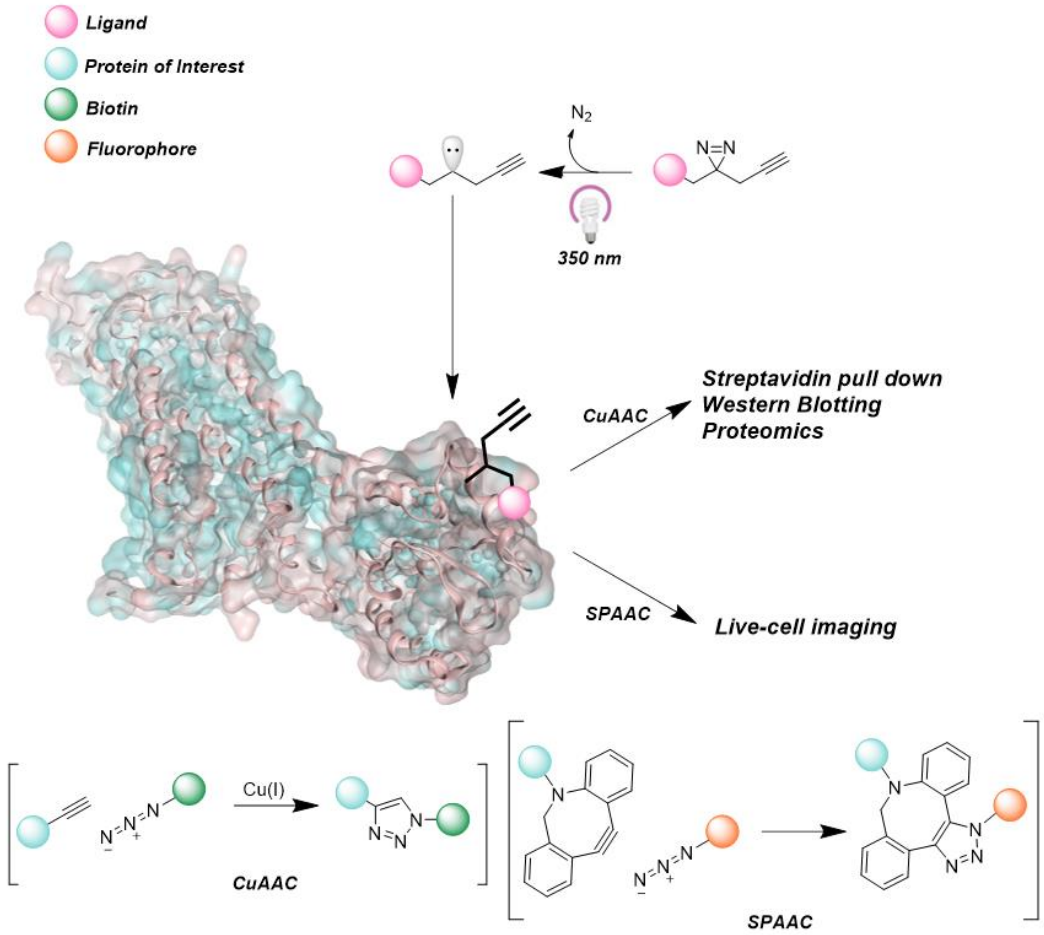


***Scheme 1.5: Small molecule photoaffinity labelling of a protein.*** *Upon irradiation by UV light (350 nm) the diazirine undergoes nitrogen elimination to form a highly reactive carbene. The carbene will covalently label the protein its ligand is bound to. The alkyne click handle can be used to attach a biotin tag (CuAAC) for further proteomic elucidation, or it can be used to attach a fluorophore (SPAAC) for live-cell imaging.*

### 1.4.2 Iridium-based photocatalytic affinity probes

An emerging advancement in the field of photoaffinity labelling is the development of catalytic photoaffinity probes.[184] One major drawback of standard photoaffinity labelling is the poor signal-to-noise ratio. This limitation is due to a combination of two significant factors; firstly, a large proportion of the reactive intermediates do not label proteins as they are rapidly quenched by surrounding water molecules; and secondly, due to the nature of the labelling technique there is only one labelling event per protein which increases the likelihood of sample loss during the rigorous washing steps involved in protein isolation. This inherent

disadvantage makes it difficult to identify target proteins which have a naturally low cellular abundance. In 2020, the MacMillan group developed the first catalytic photoaffinity probes which addressed these limitations (Scheme 1.6).[184, 190] Their new technology links an iridium photocatalyst to the target ligand, which requires a less harsh blue light (450 nm) irradiation to activate. Upon photonic absorption, the iridium photocatalyst progresses through a Dexter energy transfer (DET) mechanism to excite the diazirine, triggering $N_2$ elimination and carbene formation. As the efficiency of DETs are highly sensitive to distance, only diazirines within a 1 nm radius of the iridium photocatalyst are activated, resulting in high precision protein labelling with a theoretical labelling radius of approximately 5 nm.[191] However, it is worth noting that whilst the average protein is approximately 4-5 nm and therefore encapsulated within this labelling radius, protein complexes are usually >10 nm. As such, the tight diffusion radius of the reactive carbene intermediate may not be able to capture all protein-protein interactions of interest. Consequently, it may be of interest to utilise a photoreactive group with a larger diffusion radius.

By separating the ligand binding portion of the probe from the labelling part of the probe, one probe molecule can theoretically promote the labelling of the same protein multiple times, however, this has not been observed in practise. The more reasonable explanation for the observed signal amplification is the shear excess of diazirine co-dosed with the photocatalytic probe, increasing the likelihood of successful labelling vs quenching. The separation of affinity and crosslinking modalities also permits labelling of neighbouring proteins which has huge implications for interactome mapping and pathway elucidation.

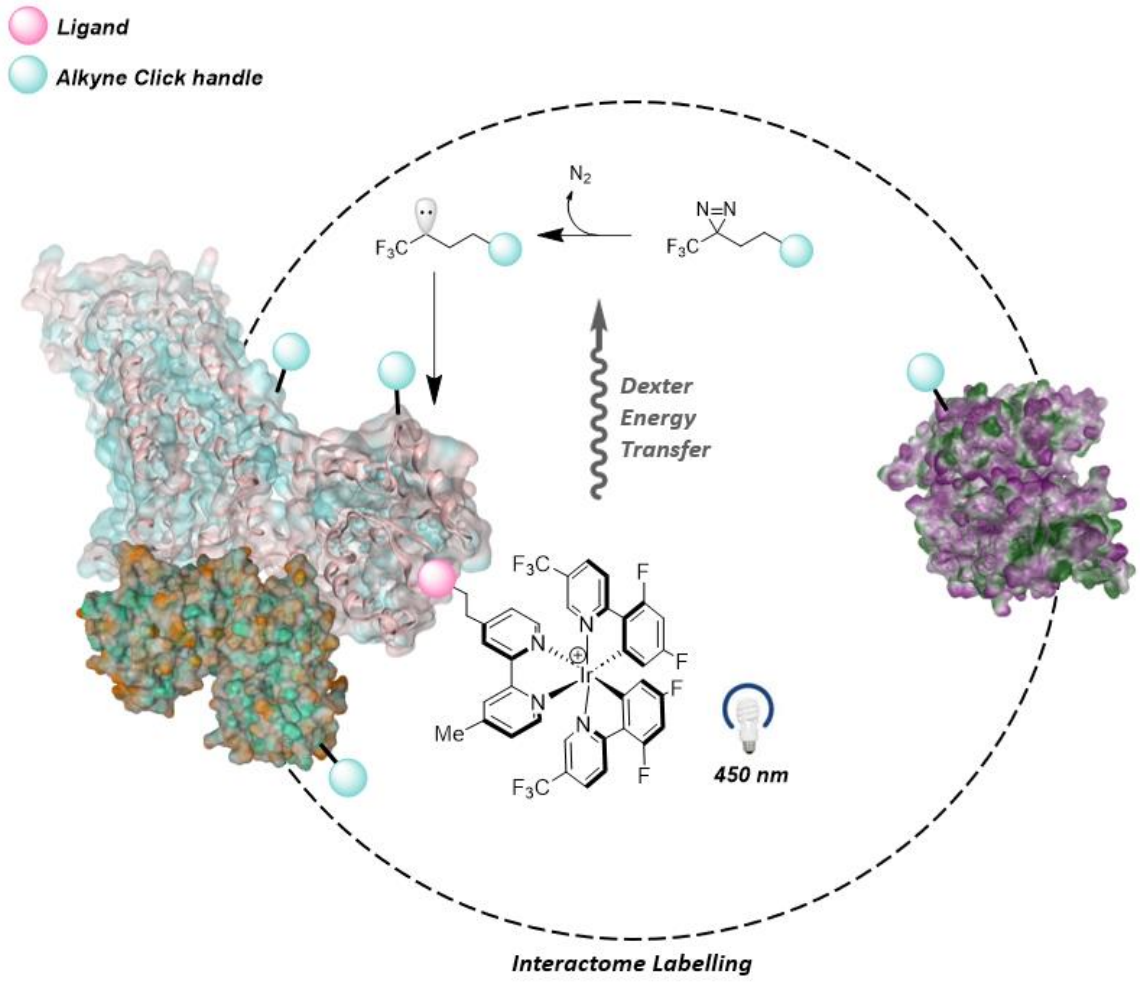


***Scheme 1.6: Photocatalytic photoaffinity labelling.*** *Upon irradiation by blue light (450 nm), the iridium photocatalyst undergoes a Dexter Energy Transfer which excites the diazirine (radius <1 nm). The excited diazirine immediately eliminates nitrogen gas and decomposes into a reactive carbene species, which covalently labels any proximal protein. Labelling radius of approximately 5 nm.*

However, as interaction does not directly correlate to function, it is important to further validate any identified targets (Figure 1.6). Confidence in the deconvolution of a small molecule's mechanism of action requires the use of several orthogonal assays which ascertain the link between interaction and desired function. To facilitate this, it is necessary to have access to reliable phenotypic assays which can distinguish between differences in functional effect. With a reliable functional assay in hand, knockdown (KD) or knockout (KO) studies can be performed to assess the involvement of a target protein in the phenotypic event of

interest. Similarly, inhibition studies can be performed using known small molecule antagonists or function-blocking antibodies. If the downstream indications of the identified target are well reported, then downstream pathway analysis can be performed using a transcriptional or phosphoproteomic readout.

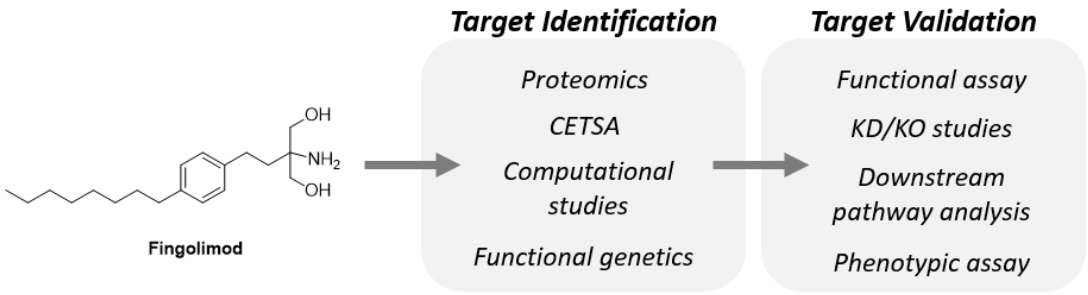


***Figure 1.6: Schematic depiction of potential orthogonal studies which can be performed to deconvolute the mechanism of action of a small molecule.***

However, to achieve this functional validation a reliable phenotypic assay is necessary.

## 1.5 Phenotypic models of lymphangiogenesis and T-lymphocyte ingression

### 1.5.1 Phenotypic models of lymphangiogenesis

To assess the functionality of any synthesised analogues, negative controls or representative probes, it is necessary to develop phenotypic assays to ensure they have the desired effect. There are various models available to assess (lymph)angiogenic growth.[192] Cell proliferation assays work on the assumption that increased endothelial proliferation correlates to increased lymphangiogenesis.[193] This assay is the simplest model of lymphangiogenesis and is practically undemanding, however, it is limited by the lack of physiological and morphological information available regarding how/why the lymphatic endothelium is growing. Corneal neovascularisation has been a useful *in vivo* model of angiogenesis, as it

exploits the absence of vasculature present in the cornea.[194] The lack of capillaries in the cornea allows for easy detection of pro-angiogenic treatments. Whilst the cornea is also devoid of lymphatic vessels, they are difficult to detect without further labelling, limiting its application. Furthermore, the use of Matrigel plugs, whereby Matrigel containing lymphangiogenic factors is injected *in vivo*, can be used to subsequently monitor lymphatic vessel invasion.[195] Whilst physiologically relevant, this assay has limited application in higher throughput identification of hit compounds. A compromise between practicality and relevance can be obtained with 2D/3D lymphatic growth assays.[196, 197] Tubulogenic/plexus formation assays can be utilised to assess the self-organisation of LECs and their ability to form pseudo-vessel architecture. Finally, spheroid and lymphatic ring assays allow for the visualisation of tipped lymphatic sprouts and new lymphatic vasculature, making them a more relevant model of lymphangiogenesis.

### 1.5.2 Phenotypic models of T-lymphocyte ingress

As indicated previously, phenotypic models are essential to ensure a sustained effect upon structural modification. There are several established models which have been utilised to assess immune cell migration and chemotaxis *in vitro*. Cell motility assays can be used to assess the movement of immune cells in response to different treatments or conditions.[198] However, these models fail to capture the vital interplay between immune cells and the endothelium through which they migrate. Boyden chamber/Transwell insert migration assays permit the co-culturing of different cell types to overcome this issue. These assays facilitate the formation of an endothelial monolayer upon a porous membrane, through which immune cells can migrate in response to chemotactic modulators. There is substantial literature precedent for their capability to measure immune cell migration through lymphatic

endothelium.[199-201] A more physiologically relevant assay, which incorporates flow and 3D vasculature, is the microvessel-on-a-chip assay. Despite the more laborious experimental set-up, this approach would provide an environment compatible with T-lymphocyte ingression in a system conducive to live imaging. Whilst this technique has been applied extensively to blood vasculature,[202-206] there has been little evidence of its use to mimic lymphatics.[207-209] The limited literature has a predominant focus on tumour metastasis, hence, there is an opportunity to build upon this technique and explore its application towards immune cell migration.

## 1.6 Aims and Hypothesis

The therapeutic benefits of strategic lymphangiogenesis after cardiac ischaemic injury is well-precedented. A prior screening of small molecules in a screen of lymphangiogenic modulators uncovered various 'hits' of interest, with potential distinct mechanisms of action. Among these hits was the anti-inflammatory drug, fingolimod. Fingolimod was chosen as the focus of this research due to its various immunomodulatory effects of interest, in addition to its pro-lymphangiogenic effect. Fingolimod is known to sequester T-lymphocytes within lymph nodes in a $S1PR_1$-dependent manner. However, the mechanism through which fingolimod inhibits T-lymphocyte migration from the tissue into afferent lymphatic capillaries, or the pathway through which it promotes lymphangiogenesis remain to be elucidated. What this research aims to uncover are the underlying mechanisms which govern fingolimod's lymphangiogenic effect and its inhibitory influence upon T-lymphocyte ingression.

It is hypothesised that fingolimod acts *via* unique and distinct pathways to induce these pleiotropic phenotypes, within both the lymphatic endothelium and T-lymphocytes, potentially in a tissue-dependent manner.

Therefore, it is the aim of this research to utilise photoaffinity labelling technology to decipher the direct targets of fingolimod responsible for these effects, within T-lymphocytes and the lymphatic endothelium. The use of photocatalytic PAL technology will enable visualisation of the microenvironment of fingolimod's targets, providing a broader understanding of its successive pathways. To complement the design of these PAL probes, phenotypic assays will be developed to assist in the validation of their sustained functional effect. Tandem mass tag mass spectrometry (TMT-MS) proteomics will decipher fingolimod's interactome. Upon target identification, orthogonal investigations will be used to link fingolimod's interactions with its functional effects and potential mechanisms of action which promote the lymphangiogenic and anti-migratory phenotypes observed.

# Chapter 2

## Materials and Methods

# 2 Materials and Methods

## Software

Ligand docking studies were performed using Molecular Operating Environment (MOE) 2020.0901 software. Protein structures were obtained from the PDB database, as a Legacy PDB format. Protein structures were prepared using QuickPrep. Prior literature precedent was used to identify the binding site which was defined using dummy atoms. Ligand databases were uploaded and energy minimised before docking. Ligands were docked against the dummy atoms, taking into account ligands already present (i.e. ADP). A triangle matcher placement method was used, coupled with an induced fit refinement. 5000 poses were docked, and the top 50 were reported. A GBVI/WSA dG scoring method was used to calculate the binding free energy (ΔG). Schematic figures were generated using BioRender. Graphs were generated using GraphPad Prism 10. Functional enrichment analysis was performed using STRING and Metascape. STRING analysis generated a full network of interactions generated from all sources with a medium confidence threshold.

## Cell culture

Primary human dermal microvascular lymphatic endothelial cells (CC-2543; Lonza) were maintained in endothelial cell growth medium-2 (EGM2MV, CC-3162; Lonza) at 37 °C and 5% $CO_2$, following supplier instructions. For all experiments cells were used at passage 6-8.

Jurkat clone E6-1 (TIB-152; ATCC) were maintained in ATCC-modification RPMI-1640 media (A1049101; ATCC) with 10% FBS at 37 °C and 5% $CO_2$, following supplier instructions. For all experiments cells were used between passage 5-10.

## Cell viability

Treated cells were incubated with RealTime Glo™ MT Cell Viability Assay (G9711; Promega) and cell viability was assessed using PHERAstar (BMG Labtech).

## Jurkat activation

A 12-well plate was coated with αhCD3 (1 μg/mL, OKT3, 16-0037-81; eBioscience) in PBS for 2 h, at 37 °C and 5% $CO_2$. PBS was removed and Jurkat cells (2 x$10^6$ cells/mL) were added with αhCD28 (5 μg/mL, CD28.2, 16-0289-85; eBioscience). The cells were incubated for 48 h, at 37 °C and 5% $CO_2$. Activation was confirmed by biomarker expression (CD69, TCRαβ) using FACS.

## Immunocytochemistry

Cells were fixed with 4% PFA, permeabilised with 0.1% Triton in PBS, blocked with 10% serum in 0.1% Tween in PBS and incubated with primary antibodies at 4 °C overnight. Cells were washed with PBS then incubated with secondary antibodies at room temperature for 1 h. After PBS washes the cells were imaged with ImageXpress® Pico Automated Cell Imaging System (Molecular Devices).

| *1° Antibody* | *Target Species* | *Host Species* | *Clone* | *Supplier* | *Cat. No.* |
|---|---|---|---|---|---|
| CD31 | Human | Sheep | - | bio-techne | AF806 |
| CD144 | Human | Goat | - | bio-techne | AF938 |
| Prox-1 | Human | Rabbit | - | Proteintech | 11067-2-AP |
| PDPN | Human | Rat | - | AngioBio | 11-009 |
| HDAC5 | Human | Mouse | 1B9E6 | Proteintech | 68437-1-IG |
| SPHK2 | Human | Rabbit | - | Proteintech | 17096-1-AP |

| *2° Antibody* | ***Target Species*** | ***Host Species*** | ***Fluorophore*** | ***Supplier*** | ***Cat. No.*** |
|---|---|---|---|---|---|
| anti-Mouse IgG | Mouse | Donkey | AlexaFluor488 | Invitrogen | A-21202 |
| anti-Rabbit IgG (H&L) | Rabbit | Goat | AlexaFluor488 | Invitrogen | A-11008 |
| anti-Mouse IgG (H&L) | Mouse | Donkey | AlexaFluor555 | Invitrogen | A-31570 |
| anti-Rat IgG (H&L) | Rat | Donkey | AlexaFluor647 | Invitrogen | A78947 |
| anti-Sheep IgG (H&L) | Sheep | Donkey | AlexaFluor488 | Invitrogen | A11015 |
| anti-Goat IgG (H&L) | Goat | Donkey | AlexaFluor488 | Invitrogen | A32814 |

## Transwell Migration

LECs were cultured to confluency on the bottom face of polyethylene terephthalate 24-well Transwell cell culture inserts (3 μm pore size, 8 x$10^5$ pores/$cm^2$, 351151; Corning) in EGM2MV (Lonza) media for 48 h, at 37 °C and 5% $CO_2$. TNF$\alpha$ (1 ng/mL, PHC3015; Fisher Scientific) was added to the LEC media 12 h before migration experiment. For cell migration, 1 x $10^5$ pre-activated Jurkat cells in 250 μL of EGM2MV +/- treatment were added to the top chamber of the Transwell insert. The number of Jurkat cells which migrated to the bottom chamber after 4 h were counted using flow cytometry (BD FACS Aria III). Migrated cells were stained for 7-AAD, CD3, CD69 and TCR$\alpha\beta$. The percentage migration was calculated using the equation below.

$$\%\ Migration = \frac{No.\ of\ cells\ counted\ in\ bottom\ chamber\ after\ 4\ h}{No.\ of\ cells\ added\ to\ top\ chamber\ at\ the\ start\ of\ the\ experiment}\ x\ 100$$

### Microvessel-on-a-chip Preparation

All the channels of the OrganoPlate (40004-400-B; Mimetas) were washed with PBS and to the middle channel was added 1.68 μL of the preprepared ECM gel (full protocol in SI). Once polymerised, the lymphatic vessel channel was coated with 40 μL fibronectin (10 μg/mL; 1918-FN; R&D Systems) and incubated overnight at 37 °C and 5% CO2. The fibronectin was removed, and the channel was washed twice with PBS and once with EGM2MV (Lonza). Then 9 x $10^4$ LECs in 3 μL of EGM2MV were added to the top channel and 50 μL EGM2MV was added to all inlets and outlets. The OrganoPlate was cultured at a 75° inclination for 3 h. Once LECs had adhered to the collagen the OrganoPlate was placed on a OrganoFlow rocker (14° inclination; 8 min) for 4-5 days, with media changes every 2 days, until the microvessel had formed.

For Jurkat migration studies, the LEC tubule was activated 12 h before with EGM2MV contained 1 ng/mL TNF$\alpha$. 9 x $10^4$ fluorescently labelled Jurkats were seeded in 8 μL Matrigel (7.5 mg/mL; A1413302; Gibco) in the bottom channel, EGM2MV +/- treatment was added to each inlet/outlet and the plate was incubated on an OrganoFlow rocker for 3 days at 37 °C and 5% CO2. The LEC tubule was stained with $\alpha$hCD31 (ab9498; Abcam) and anti-mouse IgG AF568 (A-11004; Invitrogen) and visualised by confocal microscopy.

### Spheroid Sprouting Assay

LECs were seeded at 4.8 x $10^5$ cells/well in an AggreWell™ plate (34415; StemCell Technologies) in EGM2-d media (EGM2MV depleted of VEGF, EGF and FGF, Lonza) and allowed to aggregate into spheroids for 24 h. The spheroids were embedded and seeded in 25 μL Type 1 Collagen (VitroCol; Advanced Biomatrix) per well in 384-well plate (6057300; PerkinElmer). After 1 h, the collagen was polymerised and 40 μL of EGM2-d +/- treatment

were added for either 6 or 24 h. The spheroids were then fixed with 4% PFA, permeabilised with 0.1% Triton in PBS, and then stained with AlexaFluor488 Phalloidin (A12379; Invitrogen) and DAPI (D9542, Sigma) in 0.1% Tween in PBS. The spheroids were imaged using ImageXpress® Pico Automated Cell Imaging System (Molecular Devices) and the images were analysed using ImageJ. The spheroids and sprouts were counted manually.

### Plexus Formation Assay

LECs were seeded at 3 x$10^4$ cells/well in a 384-well plate (6057300; PerkinElmer). The following day, 25 μL of Type 1 Collagen (VitroCol; Advanced Biomatrix) was added. Once polymerised, the LECs were treated for 24 h. The plexus were fixed with 4% PFA, permeabilised with 0.1% Triton in PBS, and then stained with AlexaFluor488 Phalloidin (A12379; Invitrogen) and DAPI (D9542, Sigma) in 0.1% Tween in PBS. The plexus were imaged using ImageXpress® Pico Automated Cell Imaging System (Molecular Devices) and the images were analysed using ImageJ.

### Jurkat Aggregation Assay

Pre-activated Jurkats were seeded at 1 x$10^5$ cells/well in a 384-well plate (6057300; PerkinElmer). Treatment was added and after 4 h the cells were imaged using ImageXpress® Pico Automated Cell Imaging System (Molecular Devices). The images were analysed using Fiji.

### Flow Cytometry

Staining was performed with the antibodies listed below. Cells were analysed using a flow cytometer (BD FACS Aria III).

| *Conjugated Antibody* | *Target Species* | *Clone* | *Fluorophore* | *Supplier* | *Cat. No.* |
|---|---|---|---|---|---|
| CD3 | Human | HIT31 | FITC | Biolegend | 300305 |
| CD4 | Human | OKT4 | APC | Biolegend | 317415 |
| CD8 | Human | SK1 | Pacific Blue | Biolegend | 344717 |
| CD69 | Human | FN50 | PE/Cy7 | Biolegend | 310911 |
| TCR$\alpha\beta$ | Human | IP26 | PE | Biolegend | 306707 |
| 7-AAD | - | - | - | Biolegend | 420-403 |
| ICAM-1 | Human | 15.2 | FITC | TONBO | 35-0549-T025 |
| VCAM-1 | Human | REA269 | PE | Miltenyi Biotec | 130-122-008 |
| E-selectin | Human | REA280 | APC | Miltenyi Biotec | 130-104-685 |
| CCR7 | Human | G043H7 | Pacific Blue | Biolegend | 353209 |
| CXCR4 | Human | QA18A64 | PE | Biolegend | 304503 |
| *1° Antibody* | ***Target Species*** | ***Clone*** | ***Host Species*** | ***Supplier*** | ***Cat. No.*** |
| S1PR1 | Human | - | Rabbit | Proteintech | 29318-1-AP |
| S1PR3 | Human | 776897 | Mouse | R&D Systems | MAB75241 |
| S1PR4 | Human | 1012512 | Mouse | R&D Systems | MAB10321 |
| S1PR5 | Human | 282503 | Mouse | R&D Systems | MAB3964 |
| CX3CR1 | Human | K0124E1 | Mouse | Biolegend | 355701 |
| *2° Antibody* | ***Target Species*** | ***Host Species*** | ***Fluorophore*** | ***Supplier*** | ***Cat. No.*** |
| anti-mouse IgG (H&L) | Mouse | Goat | AlexaFluor488 | Invitrogen | A-11029 |
| anti-rabbit IgG (H&L) | Rabbit | Goat | AlexaFluor488 | Invitrogen | A-11008 |

### Knockdown of LECs by siRNA transfection

LECs were seeded at 5 x $10^4$ in a 12 well-plate and grown in EGM2MV (Lonza) media at 37 °C and 5% $CO_2$, until 70% confluency. Pooled targeting siRNAs and non-targeting controls were purchased from ThermoFisher (Silencer Select siRNA). siRNAs were complexed with Lipofectamine RNAiMAX (Invitrogen), and transfection was performed according to the manufacturer's instructions. 1-3 days after the transfection, the cells were lysed and protein was extracted to measure the efficiency of the knockdown by Western blot.

### Western Blot

Cells were harvested and washed three times with PBS. The cell pellets were lysed with RIPA buffer (50 mM Tris, pH 7.5, 1% NP40, 150 mM NaCl, 0.5% sodium deoxycholate, 1% SDS, protease inhibitor cocktail). Lysates were centrifuged and the protein amounts in supernatants were measured by BCA assay (23227; ThermoFisher). The supernatants were heat denatured for 5 min, subjected to SDS-PAGE (XP04200BOX; Invitrogen), and transferred onto a PVDF membrane (1704156; Bio-Rad). The membrane was blocked with a TBST buffer (10 mM Tris, pH 7.4, 150 mM NaCl, 0.1% Tween-20) containing 5% skim milk at rt for 1 h. Then the membrane was incubated with the primary antibodies at 4 °C overnight, then washed and incubated with secondary antibodies at rt for 1 h. The signals were detected using the enhanced chemiluminescence method (WBLUR0100; Merck) by a Bio-Rad ChemiDoc MP imaging system. The relative abundances were quantified by ImageJ.

| *1° Antibody* | *Target Species* | *Clone* | *Host Species* | *Supplier* | *Cat. No.* |
|---|---|---|---|---|---|
| S1PR1 | Human | - | Rabbit | Proteintech | 29318-1-AP |
| APLNR | Human | - | Rabbit | Proteintech | 20341-1-AP |
| CX3CR1 | Human | - | Rabbit | Proteintech | 29819-1-AP |
| SPHK2 | Human | - | Rabbit | Proteintech | 17096-1-AP |
| LYVE-1 | Human | - | Rabbit | AngioBio | 11-032 |
| THEM6 | Human | - | Rabbit | Novus Biologicals | NBP2-24492SS |
| GAPDH | Human | - | Mouse | Abcam | Ab8245 |
| SOD1 | Human | - | Rabbit | Cell Signalling Technologies | 2770 |
| *2° Antibody* | ***Target Species*** | ***Host Species*** | ***Reporter*** | ***Supplier*** | ***Cat. No.*** |
| anti-rabbit IgG (H&L) | Rabbit | Goat | HRP | Cell Signalling Technologies | 7074 |
| anti-mouse IgG (H&L) | Mouse | Horse | HRP | Cell Signalling Technologies | 7076 |
| anti-biotin | Human | Goat | HRP | Cell Signalling Technologies | 7075 |

## qRT-PCR

Total RNA was reverse transcribed using oligo-dT primers and Superscript III RT (Invitrogen). qRT-PCR analysis was performed on a ViiA 7 Real-Time PCR System (Thermo Fisher Scientific) using Fast SYBR™ Green Master Mix (4385612; Applied Biosystems). Data were normalized to *36b4* housekeeping gene expression. Fold change in gene expression was determined by the $2^{-\Delta\Delta CT}$ method.[210] Primer sequences are listed below. GAPDH was used as a housekeeper gene.

| *Gene* | *Forward (5′-3′)* | *Reverse (5′-3′)* |
|---|---|---|
| ***36b4*** | CTACAACCCTGAAGAAGTGCTTG | CAATCTGCAGACAGACACTGG |
| ***Cd31*** | TGCAGTGGTTATCATCGGAGTG | CGTTGTTGGAGTTCAGAAGTGG |
| ***Lyve1*** | CTGGGTTGGAGATGGATTCG | TCAGGACACCCACCCCATTT |
| ***Pdpn*** | GACACTGAGACTACAGGTTTGG | GCCAGACTTATAGCGGTCTTC |
| ***Vegfr3*** | CCATCGAGAGTCTGGACAGC | CCGGGATGGTGGTCACATAG |

*Note:- Pooled primers should be used to avoid non-specific annealing events which can lead to misinterpreted data*

**Cellular Thermal Shift Assay (CETSA)**

LECs grown to confluency in a 10 cm dish were treated with fingolimod (3 μM) or DMSO (0.1%) for 4 h, scrapped and pelleted. The pellets were resuspended in PBS (360 μL) and divided into 9, 40 μL for each temperature (46, 49, 52, 55, 58, 61, 64, 67, 70 °C). Each aliquot was heated to the indicated temperature for 3 min, left at rt for 3 min, then 10 μL 5% NP-40 in PBS was added and the samples were immediately flash frozen in liquid $N_2$. The samples underwent two freeze/thaw cycles, were centrifuged at 20,000 xg at 4 °C for 20 mins and supernatants subjected to SDS-PAGE.

**Photoaffinity labelling for Western blot analysis**

LECs were seeded at 7.5 x $10^5$ in a 10 cm dish until confluent, then dosed with treatment in 5 mL EGM2-d (Lonza) for 1 h. The cells were then washed with PBS and irradiated (5 min, 365 nm) on ice. Cells were then lysed in 300 μL lysis buffer (1% NP-40, 0.1% SDS in PBS) with added protease inhibitor cocktail (cOmplete™, 11697498001; Roche) at 4 °C for 30 min. Lysates were centrifuged and the protein amounts in supernatants were measured by BCA assay

(23227; ThermoFisher) and normalised to 1 mg/mL. 300 μg of lysate per sample were then were heat denatured for 5 min, the samples were then clicked to biotin-azide (FAC of 0.1 mM from 10 mM in DMSO stock) with $CuSO_4$ (FAC of 1 mM, from 50 mM in $H_2O$ stock), TCEP (FAC of 1 mM, from 50 mM in $H_2O$ stock) and TBTA (FAC of 0.1 mM, from 10 mM in DMSO stock) for 1 h at rt, 700 rpm shaking. The lysates were quenched with EDTA and filtered through 10 kDa centrifugal filters (UFC5010; Amicon). The lysates were incubated overnight at 4 °C with 75 μL pre-washed neutravidin magnetic beads (78152104010150; Cytiva). The supernatant was removed, the beads were washed 3 times with 500 μL 0.2% SDS in PBS, 3 times with 500 μL 1 M NaCl in $dH_2O$, 3 times with 500 μL 10% EtOH in $dH_2O$ and then heated to 95 °C for 10 min in 40 μL Laemmli buffer + 5% β-mercaptoethanol. The samples were analysed by Western blot.

*Note:- Check the pH of TCEP stock solutions before use (pH 6.0-7.5) to ensure efficient Click*

**Photoaffinity labelling for proteomics**

LECs were seeded at 7.5 x $10^5$ in a 10 cm dish until confluent, then dosed with treatment in 5 mL EGM2-d (Lonza) for 1 h. The cells were then washed with PBS and irradiated (5 min, 365 nm) on ice. Cells were then lysed in 300 μL lysis buffer (1% NP-40, 0.1% SDS in PBS, protease inhibitor cocktail) at 4 °C for 30 min. Lysates were centrifuged and the protein amounts in supernatants were measured by BCA assay (23227; ThermoFisher) and normalised to 1 mg/mL. 1 mg of lysate per sample were then were heat denatured for 5 min, the samples were then clicked to biotin-azide (FAC of 0.1 mM from 10 mM in DMSO stock) with $CuSO_4$ (FAC of 1 mM, from 50 mM in $H_2O$ stock), TCEP (FAC of 1 mM, from 50 mM in $H_2O$ stock) and TBTA (FAC of 0.1 mM, from 10 mM in DMSO stock) for 1 h at rt, 700 rpm shaking. The lysates were quenched with EDTA and filtered through 10 kDa centrifugal filters (UFC5010; Amicon).

The lysates were incubated overnight at 4 °C with 250 μL pre-washed neutravidin magnetic beads (78152104010150; Cytiva). The supernatant was removed, the beads were washed 3 times with 500 μL 0.2% SDS in PBS, 3 times with 500 μL 1 M NaCl in $dH_2O$, 3 times with 500 μL 10% EtOH in $dH_2O$. The beads were stored at −20 °C until shipment to University of Bristol Proteomics Facility.

*Note:- Check the pH of TCEP stock solutions before use (pH 6.0-7.5) to ensure efficient Click*

**In-gel fluorescence**

Irradiated cells were harvested and washed three times with PBS. The cell pellets were lysed with lysis buffer (1% NP-40, 0.1% SDS in PBS, protease inhibitor cocktail) at 4 °C for 30 min. Lysates were centrifuged and the protein amounts in supernatants were measured by BCA assay (23227; ThermoFisher) and normalised to 1 mg/mL. 50 μg of lysate per sample were then were heat denatured for 5 min, the samples were then clicked to TAMRA-azide (FAC of 0.1 mM from 10 mM in DMSO stock) with CuSO4 (FAC of 1 mM, from 50 mM in $H_2O$ stock), TCEP (FAC of 1 mM, from 50 mM in $H_2O$ stock) and TBTA (FAC of 0.1 mM, from 10 mM in DMSO stock) for 1 h at rt, 700 rpm shaking. The samples were quenched with EDTA and subjected to SDS-PAGE (NP0315BOX; Invitrogen) and imaged using LiCOR Odyssey. Total protein staining was achieved using Coomassie (161-0436; Bio-Rad).

*Note:- Check the pH of TCEP stock solutions before use (pH 6.0-7.5) to ensure efficient Click*

***In Vivo* Studies**

*In vivo* studies were performed with Dr Benoit-Voisin at QMUL.

## Sample preparation for imaging

Spleens were harvested from WT C57BL/6 male donor mice (8 weeks old), disrupted in PBS containing 0.5% FBS + 2mM of EDTA and filtered through 70 μm mesh nylon strainer (Fisher Scientific, 11597522). The single cell suspension was centrifuged at 500 xg for 10 mins and resuspended in ACK lysis buffer to remove red blood cells. Leukocyte pellet was then centrifuged (500 xg) and resuspended at 1 x $10^8$ cells/mL in RPMI media + 10% FBS. $CD3^+$ T-lymphocytes were isolated using EasySep™ Mouse T Cell Isolation Kit (StemCell Technologies; 19851). Isolated T-lymphocytes were cultured and activated at 2 x $10^6$ cells/mL in RPMI + 10% FBS + IL-2 (5 ng/mL) + αmCD28 (5 μg/mL, 102101; Biolegend) in a αmCD3 (1 μg/mL, 100201; Biolegend) coated 6-well plate for 48 h. T-lymphocytes were stained with CFSE (1mM) for 30 min at 37 °C in PBS, resuspended in either vehicle or fingolimod (1 mg/kg) treated medium and intradermally injected into the ear pinnae at 2.5 x$10^6$/ear. 5 h later the draining auricular LNs and ears were harvested and fixed with 4% PFA at 4 °C for 24 h. The LNs and ears were then split into two halves and permeabilised in PBS + 20% FBS + 0.5% Triton X-100 for 4 h at rt. Tissues where then immunostained in PBS + 5% FBS at 4 °C with an anti-mouse Lyve-1 (ThermoFisher, 14-0443-82) conjugated to AlexaFluor555 and anti-mouse αSMA (ears, 614855; Biolegend) or anti-mouse HEV (LNs, MECA-79, 120807; Biolegend) conjugated to AlexaFluor647 at 4 °C overnight. Tissues were then washed 3 times for 1 h/wash in PBS and then mounted on slides for subsequent confocal imaging.

**Image acquisition**

Tissues from LNs and ears were imaged using confocal microscopes from the Advanced Bio-Imaging at QMUL. Ears were visualised under a Leica SP8 DIVE system 25x water immersion motCORR (NA:1) objective and with corresponding SP laser lines at a speed of 8,000 Hz, a line averaging of 4, a zoom factor of 1 and in sequential scanning mode for individual fluorochromes (AlexaFluor488 Ex: 488 nm/Em: 505-550 nm, AlexaFluor555 Ex: 561 nm/Em: 550-561 nm and AlexaFluor647 Ex: 632 nm/Em: 575-624 nm). Images resolution was set at 1024×1024 pixels in the x×y planes with an average of ~200 focal planes; corresponding to a voxel size of 0.35×0.35×0.5 μm in x×y×z planes, respectively. Around 10-12 regions were acquired for each ear.

Halved LNs were imaged with a Nikon Spinning Disk CSU-W1 SoRa system to generate x, y, z image tile scans of each halved LNs using a 10x air objective, NA:0.45 , camera resolution of 2048x2048 (0.68μm/pixels) by field of view, binning 1x1, 12-bit depth with a total image size variating according to the size of LNs, and with sequential recording under spinning disk mode(pinhole size of 50 μm) for individual fluorochromes (AlexaFluor488 Ex: 488 nm Em filter: 525-550 nm; AlexaFluor555 Ex: 568 nm Em filter: 593-640 nm; AlexaFluor647 Ex: 647 nm Em filter: 716-740 nm).

Quantification of CFSE-labelled T cells was performed with the 3D-reconstructing image processing software IMARIS™ (Bitplane, Switzerland). In the ear images, the T cell number within the interstitium was counted using the spot detection algorithm of the IMARIS™ software and normalised to the size the imaged tissue region. Intravasated donor T cells were identified and quantified manually within the LYVE1$^{+}$ lymphatic vessels and normalised to the volume of the vessel for individual images. Data are expressed as the number of tissue-

located and intravasated donor T cells per given volume of tissue or lymphatic vessel, respectively. Donor T-cell number within the LNs were also quantified manually and normalised to the imaged surface area of halved LNs using segmentation (Ilastik). Data are presented as mean ± sem per mouse and condition (vehicle vs fingolimod-treated cells).

**waterLOGSY**

Following the protocol detailed by Bataille *et al*,[211] a 10 mM solution of fingolimod in $d_6$-dmso was prepared, resuspended in 0.5 mL PBS or EGM2MV and transferred into a 3 mm NMR tube. All NMR experiments were performed on a 600 MHz Bruker NEO 600 machine. A standard $^1$H NMR spectrum with $H_2O$ suppression was recorded, followed by a $^1$H waterLOGSY NMR spectrum.

**SAXS**

SAXS experiments were performed with Dr Huband at the University of Warwick. Small-angle X-ray scattering (SAXS) measurements were made using a Xenocs Xeuss 2.0 equipped with a micro-focus Cu K$\alpha$ source collimated with Scatterless slits. The scattering was measured using a Pilatus 300k detector. Sample to detector distances of 0.987(3) m and 2.496(5) m were tested giving q ranges of 0.007 to 0.39 Å$^{-1}$ and 0.003 to 0.15 Å$^{-1}$. The magnitude of the scattering vector (q) is given by $q = (4\pi\sin\theta)/\lambda$, where $2\theta$ is the angle between the incident and scattered X-rays and $\lambda$ is the wavelength of the incident X-rays. The samples and backgrounds were mounted in 1mm thick borosilicate glass capillaries and measured for 2 h (0.987(3) m setup) or 10 min (2.496(5) m) setup. Xenocs XSACT software was used to integrate the raw 2D detector images into 1D q vs intensity files.

**TMT-MS Proteomics**

All proteomics experiments were performed at University of Bristol Proteomics Facility by Dr Kate Heesom.

## TMT Labelling and High pH reversed-phase chromatography

Immuno-isolated samples were reduced (10 mM TCEP, 55 °C for 1 h), alkylated (18.75 mM iodoacetamide, rt for 30 min) and then digested from the beads with trypsin (1.25 μg trypsin; 37 °C, overnight). The resulting peptides were labelled with Tandem Mass Tag (TMTpro) 12-plex reagents according to the manufacturer's protocol (Thermo Fisher Scientific, Loughborough, LE11 5RG, UK) and the labelled samples pooled.

The pooled sample was evaporated to dryness, resuspended in 5% formic acid and then desalted using a SepPak cartridge according to the manufacturer's instructions (Waters, Milford, Massachusetts, USA). Eluate from the SepPak cartridge was again evaporated to dryness and resuspended in buffer A (20 mM ammonium hydroxide, pH 10) prior to fractionation by high pH reversed-phase chromatography using an Ultimate 3000 liquid chromatography system (Thermo Scientific). In brief, the sample was loaded onto an XBridge BEH C18 Column (130 Å, 3.5 μm, 2.1 mm x 150 mm, Waters, UK) in buffer A and peptides eluted with an increasing gradient of buffer B (20 mM ammonium hydroxide in acetonitrile, pH 10) from 0-95% over 60 min. The resulting fractions (concatenated into 6 in total) were evaporated to dryness and resuspended in 1% formic acid prior to analysis by nano-LC MSMS using an Orbitrap Fusion Tribrid mass spectrometer (Thermo Scientific).

## Nano-LC Mass Spectrometry

High pH RP fractions were further fractionated using an Ultimate 3000 nano-LC system in line with an Orbitrap Fusion Tribrid mass spectrometer (Thermo Scientific). In brief, peptides

in 1% (vol/vol) formic acid were injected onto an Acclaim PepMap C18 nano-trap column (Thermo Scientific). After washing with 0.5% (vol/vol) acetonitrile 0.1% (vol/vol) formic acid peptides were resolved on a 250 mm × 75 μm Acclaim PepMap C18 reverse phase analytical column (Thermo Scientific) over a 150 min organic gradient, using 7 gradient segments (1-6% solvent B over 1 min, 6-15% B over 58 min, 15-32%B over 58 min, 32-40%B over 5 min, 40-90%B over 1 min, held at 90%B for 6 min and then reduced to 1%B over 1 min) with a flow rate of 300 nl $min^{-1}$. Solvent A was 0.1% formic acid and Solvent B was aqueous 80% acetonitrile in 0.1% formic acid. Peptides were ionized by nano-electrospray ionization at 2.0 kV using a stainless-steel emitter with an internal diameter of 30 μm (Thermo Scientific) and a capillary temperature of 275 °C.

All spectra were acquired using an Orbitrap Fusion Tribrid mass spectrometer controlled by Xcalibur 2.1 software (Thermo Scientific) and operated in data-dependent acquisition mode using an SPS-MS3 workflow. FTMS1 spectra were collected at a resolution of 120,000, with an automatic gain control (AGC) target of 200,000 and a max injection time of 50 ms. Precursors were filtered with an intensity threshold of 5,000, according to charge state (to include charge states 2-7) and with monoisotopic peak determination set to peptide. Previously interrogated precursors were excluded using a dynamic window (60 s +/-10 ppm). The MS2 precursors were isolated with a quadrupole isolation window of 1.2 m/z. ITMS2 spectra were collected with an AGC target of 10,000, max injection time of 70 ms and CID collision energy of 35%.

For FTMS3 analysis, the Orbitrap was operated at 50,000 resolution with an AGC target of 50,000 and a max injection time of 105 ms. Precursors were fragmented by high energy collision dissociation (HCD) at a normalised collision energy of 60% to ensure maximal TMT

reporter ion yield. Synchronous Precursor Selection (SPS) was enabled to include up to 10 MS2 fragment ions in the FTMS3 scan.

## Data Analysis

The raw data files were processed and quantified using Proteome Discoverer software v2.4 (Thermo Scientific) and searched against the UniProt Human database (downloaded January 2025; 83095 sequences) using the SEQUEST HT algorithm. Peptide precursor mass tolerance was set at 10 ppm, and MS/MS tolerance was set at 0.6 Da. Search criteria included oxidation of methionine (+15.995 Da), acetylation of the protein N-terminus (+42.011 Da), methionine loss from the protein N-terminus (-131.04 Da) and methionine loss plus acetylation of the protein N-terminus (-89.03 Da) as variable modifications and carbamidomethylation of cysteine (+57.021 Da) and the addition of the TMTpro mass tag (+304.207 Da) to peptide N-termini and lysine as fixed modifications. Searches were performed with full tryptic digestion and a maximum of 2 missed cleavages were allowed. The reverse database search option was enabled and all data was filtered to satisfy false discovery rate (FDR) of 5%.

# Chapter 3

## Optimisation of Immunomodulatory Phenotypic Assays

# 3 Optimisation of Immunomodulatory Phenotypic Assays

## 3.1 Characterisation of commercial lymphatic cell line

The chosen commercial lymphatic cell line, used for the entirety of this research, was a cultured primary line isolated from adult human dermal microvasculature, with an advertised 99% $CD31^{+}PDPN^{+}$ phenotype (Lonza). The cells were characterised to ensure they displayed a consistent lymphatic phenotype across the passages of interest (P6-8). qPCR confirmed the RNA expression of key lymphatic genes (CD31, LYVE1, podoplanin [PDPN], Prox-1),[212] however, there was an observable decrease in Prox-1 and PDPN mRNA levels by passage 8 (Figure 3.1a). Therefore, it was investigated whether this transcriptional decline correlated directly to protein levels. The expression of lymphatic biomarkers (CD31, LYVE1, VEGFR3, PDPN) were assessed by FACS (Figure 3.1b), and there was no observable decline in biomarker levels from passage 6-8. Immunocytochemistry was also used to confirm the protein expression of the nuclear-localised transcription factor, Prox-1, and the cytosolic PDPN (Figure 3.1c). Phalloidin staining of filamentous actin permitted visualisation of the lymphatic cell cytoskeleton and DAPI staining confirmed the co-localisation of Prox-1 within the nucleus. The presence of these biomarkers confirmed the lineage of the cell line as present within the lymphatic endothelium. The levels of Prox-1 and PDPN did not appear to significantly diminish across all passages of interest.

Assessment of the biomarker expression confirmed the cell line was predominantly in lymphatic origin. Whilst a slight decline in Prox-1 and PDPN was observed on a transcriptional level, this did not correlate to protein expression. Therefore, it was determined

that the lymphatic phenotype was maintained to a satisfactory degree across the necessary passages (6-8).

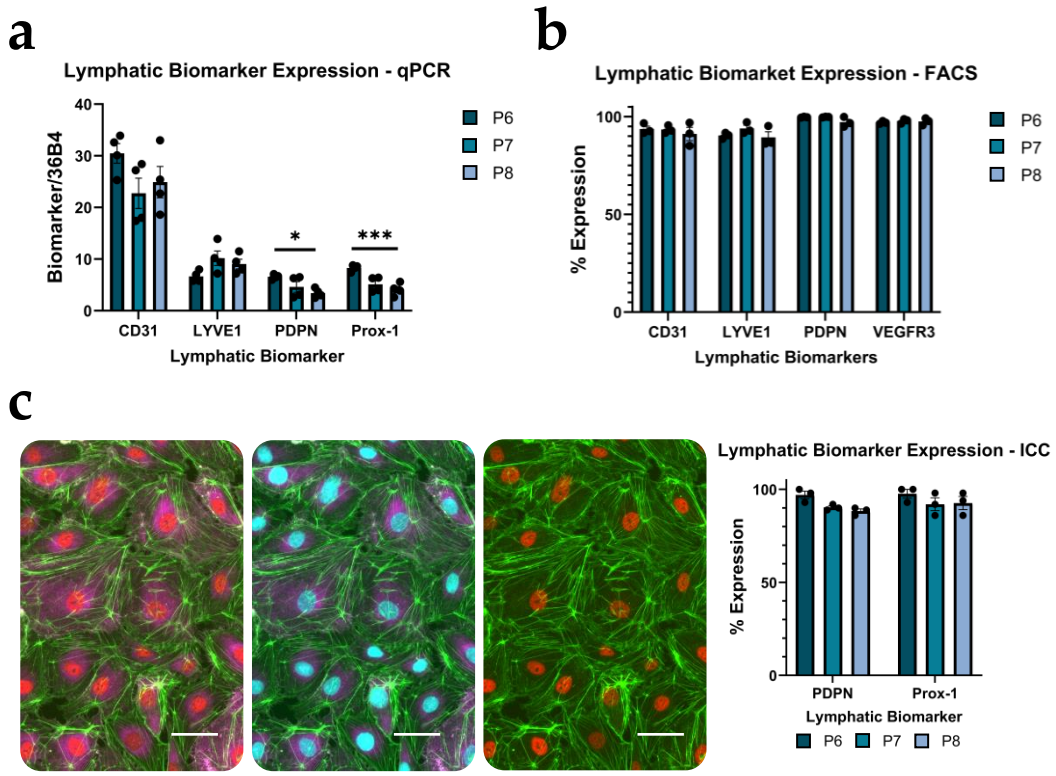


***Figure 3.1: Characterisation of the commercial lymphatic endothelial cells (LECs) at passage 6-8.*** *(a) mRNA expression levels in LECs over passages 6-8 as measured by qPCR. N=4. Statistical analysis performed using one-way ANOVA. * = P<0.05, *** = P<0.005. (b) Protein expression levels in LECs over passages 6-8 as measured by flow cytometry. N=3 (c) Immunocytochemistry of LEC monolayer, staining with DAPI (cyan), Phalloidin (green), Podoplanin (magenta) and Prox-1 (red). Scale bars = 50 µm. Expression was quantified using ImageJ. N=3. Error bars = sem.*

## 3.2 Optimisation of a phenotypic model of lymphangiogenesis

It was necessary to develop a robust phenotypic assay to quantitatively measure the pro-lymphangiogenic effect of any synthesised compounds, including structurally modified PAL probes and negative control analogues.

A plexus formation assay assesses the ability of a lymphatic endothelium monolayer to form tubule networks when seeded with a supportive ECM. This assay was initially explored due

to its compatibility with robust compound screening. As described previously,[213] lymphatic endothelium monolayers were encapsulated in a type-1 collagen matrix to provide stability and structural support for network formation (Figure 3.2). The monolayers were treated for 24 h, and the resultant networks were stained with Phalloidin and imaged with an automated cell imaging microscope.

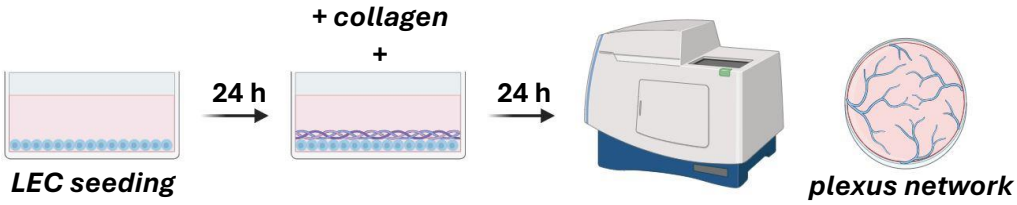


***Figure 3.2: Plexus formation assay.*** *Schematic diagram illustrating the plexus formation assay setup, a LEC monolayer was embedded in type-1 collagen and dosed for 24 h with treatment. The resultant plexus was fixed, stained with Phalloidin and imaged.*

Initial LEC seeding density was explored to optimise tube formation in the plexus assay (Figure 3.3a-b). LECs were grown and cultured in a growth factor-depleted media (no VEGF, EGF or FGF) to control against lymphangiogenic effects which were independent of compound treatment. As a control, 0.1% DMSO treatment was used to establish a baseline network formation threshold, while treatment with a known pro-lymphangiogenic factor, VEGFC,[214] was chosen to probe a maximal observable response. After dosing for 24 h, cells were stained with Phalloidin and the extent of the plexus formation was evaluated qualitatively. The lymphatic endothelium developed visually promising interconnecting networks; however, it was difficult to compare between control and treatments as they were not visibly distinctly different. Therefore, to quantify the plexus networks the AngiogenesisAnalyzer ImageJ plugin was utilised (Figure 3.3c);[215] images were converted into a binary skeletal "tree" and the complexity of the networks was determined by quantifying a

variety of factors including the number of *junctions*, *branches*, *nodes* and *segments* (a section of the vasculature connecting two junctions).[215] Under both DMSO and VEGFC-treated conditions, there was a density-dependent increase in the complexity of the networks, as expected (Figure 3.3d). However, no significant difference between DMSO and VEGFC-treated networks was observed, and therefore the plexus formation assay could not be used to confidently analyse a lymphangiogenic effect in response to treatment. Despite this setback, the plexus networks could provide an extra degree of observational clarity that the pro-lymphangiogenic effects were conducive to structural network formation, rather than random proliferation. Due to these limitations of the plexus formation assay, alternative phenotypic models of lymphangiogenesis were explored.

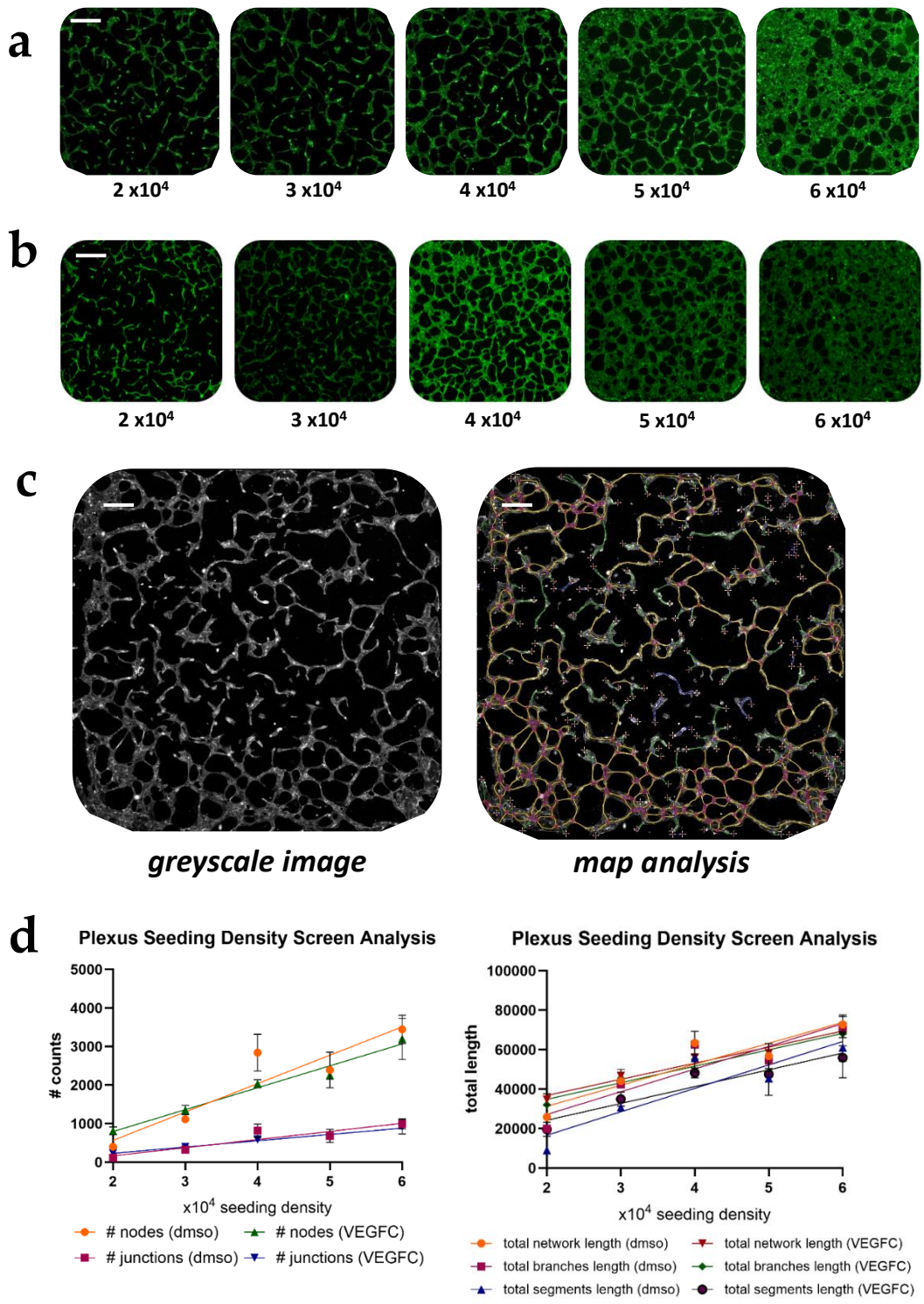


***Figure 3.3: Analysis of lymphatic endothelial plexus formation assay.*** *LECs were seeded at varying densities (2-6 x $10^4$cells) for 24 h, embedded in collagen and treated with either (a) 0.1% DMSO or (b) VEGFC (200 ng/mL) for a further 24 h. The networks were fixed and stained with Phalloidin (green). Scale bar is 500 µm (c) Image analysis workflow using the AngiogenesisAnalyzer ImageJ plugin counted the number of branches (green), junctions (dark blue), nodes (red) and segments (yellow) as well as quantified their length. Scale bar is 250 µm (d) The analysed networks were quantified to compare the number of junctions, branches and segments between the different seeding densities in response to 0.1% DMSO (baseline) and 200 ng/mL VEGFC (positive control) treatment. Trendlines depicted are a linear fit. Error bars = sem.*

The spheroid sprouting assay is a 3D *in vitro* model which enables the culture of lymphatic endothelial spheroids in a physiologically relevant ECM which facilitates lymphangiogenic growth and sprouting (Figure 3.4a).[216] LECs are cultured in Aggrewell™ plates to form spheroids which are then isolated and seeded with an ECM of choice and treated before fixation. Previous optimisation of this assay by Dr Christophe Ravaud with the Lonza lymphatic cell line demonstrated preferential and more defined sprouting when co-cultured with a type 1 collagen ECM over Matrigel, which is consistent with previous reports that type 1 collagen accelerates lymphatic endothelial tube formation.[217] Type 1 collagen is the more physiologically relevant ECM for lymphangiogenesis studies due to its prominence in connective tissue as a supportive network for lymphatic capillaries.[218] The LEC spheroids were similarly grown and cultured in a growth factor-depleted media. Typical use of this assay generally proceeds with a 24 h treatment dosing window before spheroid sprouting quantification and analysis occurs, however, Trowbridge *et al* reported in their initial disclosure of the photocatalytic probe methodology that the iridium catalyst can become cytotoxic after 6 h.[182] It was therefore necessary to ensure that the spheroid sprouting assay could display significant treatment distinction within this timeframe.

The relative extent of spheroid sprouting in response to treatment was quantified by manual counting of the number of sprouts per spheroid per well, which was then converted into a fold change value relative to the baseline sprouting level observed after vehicle dosage (Equation 1).

$$Fold\ change\ in\ sprouting = \frac{sprouts\ in\ treated\ well\ /\ spheroids\ in\ treated\ well}{sprouts\ in\ dmso\ well\ /\ spheroids\ in\ dmso\ well} \qquad Eq.\ 1$$

Spheroid sprouting was observed within the desired 6 h time frame in a dose-dependent manner in response to pro-lymphangiogenic factor, VEGFC, however this response was more modest than initially anticipated (Figure 3.4b-c). Therefore, in the search for a positive control compound which had a more pronounced pro-lymphangiogenic effect upon the spheroids, SB431542, a potent TGF-β inhibitor known to enhance lymphangiogenesis, was chosen.[219] SB431542 had previously been detected as a positive inducer of lymphangiogenesis in a preliminary screen.[†] SB431542 demonstrated a significant increase in sprouting (~8-fold) and was therefore used as a positive reference condition for all future spheroid sprouting assays (Figure 3.4d).

In an attempt to streamline the analysis of the spheroid sprouting data, the AngiogenesisAnalyzer ImageJ plugin was utilised to automate the counting of the spheroids and their sprouts.[215] Unfortunately, when comparing the automated output to the manual counting there were significant discrepancies. In some instances, there were clear, observable sprouts which were not detected by the software and therefore not counted (Figure 3.4e, red arrows). Also of concern were the occurrences whereby unavoidable artefacts (i.e. bubbles, dust, disaggregated spheroids) were misinterpreted as sprouts or spheroids (Figure 3.4e, white arrows). These artefacts could not be corrected for with manual post-imaging contrast modifications. Therefore, it was decided that the spheroid sprouting should be manually counted, while this would be a time-consuming endeavour, it was necessary to ensure confidence in the quantified results.

[†] *Dr Christophe Ravaud, unpublished results*

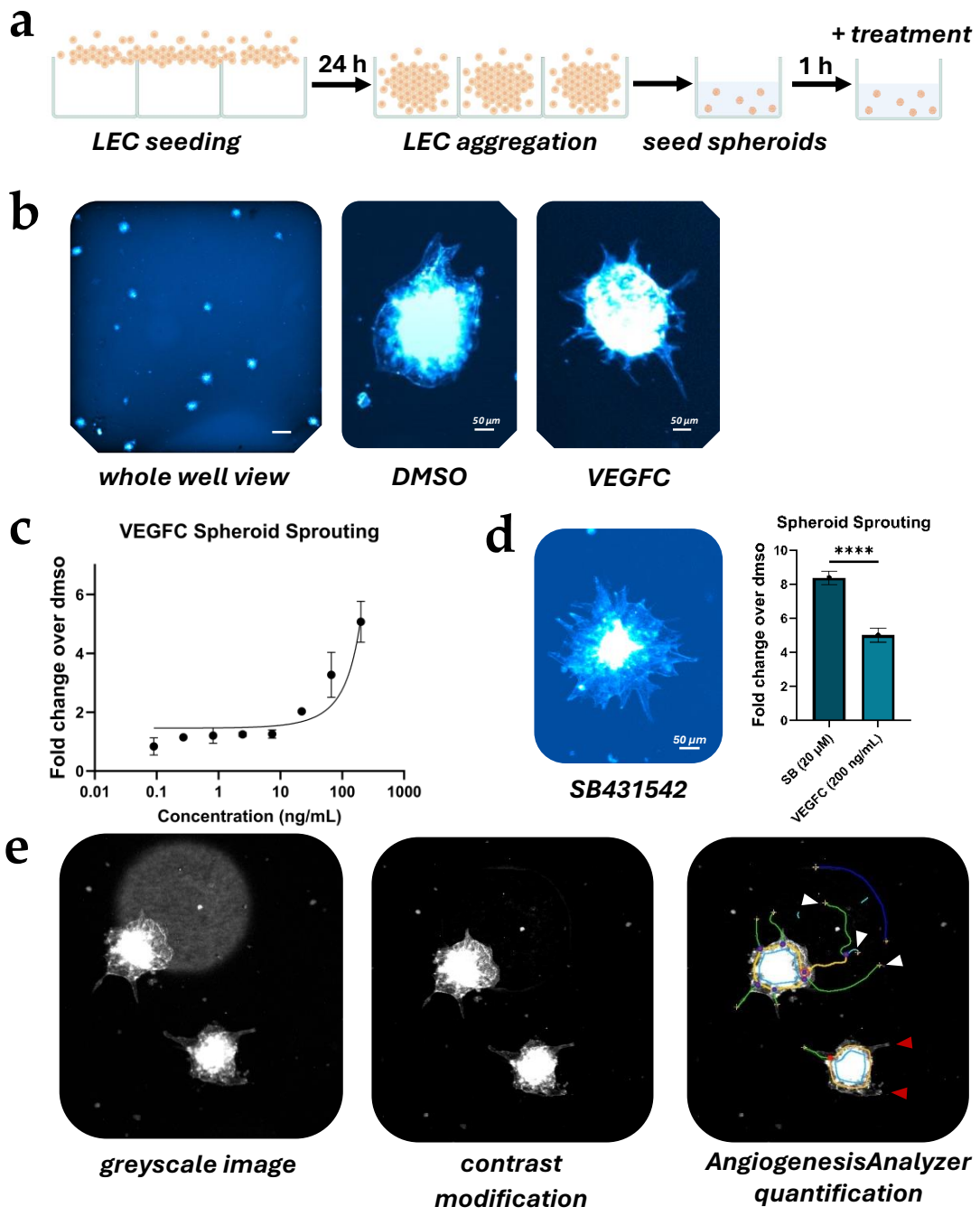


***Figure 3.4: Spheroid sprouting assay as a phenotypic model for lymphangiogenesis*** *(a) Schematic depiction of the LEC spheroid sprouting assay experimental set up. LECs were seeded in Aggrewell™ plates for 24 h to form spheroids which were collected and embedded in type 1 collagen before treatment for 6 h. The spheroids were fixed, stained for Phalloidin (blue) and imaged (b) Whole well and enhanced images of sprouting spheroids in response to 0.1% DMSO vehicle, 1.7 µM fingolimod and 200 ng/mL VEGFC treatment. (c) Spheroid sprouting in response to a serial dilution of VEGFC (N=3). Error bars = sem (d) Sprouting in response to improved positive control 20 µM SB431542 (N=4). Scale bar is 500 µm. Error bars = sem. Statistical analysis performed on raw data using a Student's t-test. **** = P<0.001 (e) AngiogenesisAnalyzer quantification of a greyscale image of the spheroids which then underwent post-imaging enhancement and artefact subtraction before analysis; cyan = spheroid, green = sprout. Discrepancies between the manual and automated counting are illustrated with arrows. White arrows highlight false positive artefacts. Red arrows indicate false negative sprouts.*

During the development of reliable lymphangiogenic models, both a qualitative and quantitative assay were developed. The plexus formation assay permitted the visualisation of a cohesive lymphatic network, whilst the spheroid sprouting assay permitted the observation and quantification of pro-lymphangiogenic sprouting. The spheroid sprouting assay met the requirement for a quantifiable measurement within a 6 h treatment window. Whilst automated analysis of these assays could not be achieved due to the existence of unavoidable artefacts, manual assessment increased the confidence and reliability of these assays as a measure of lymphangiogenesis.

### 3.2.1 Confirmation of fingolimod's lymphangiogenic effect

With the spheroid sprouting assay optimised as a model of lymphangiogenesis, it was necessary to recapitulate the initial findings of the library screen‡ and confirm fingolimod's pro-lymphangiogenic effect. Fingolimod induced sprouting of LEC spheroids in a dose-dependent manner, with a measurable $EC_{50}$ of 1.67 μM (Figure 3.5). Also, of consideration was whether fingolimod or its metabolite Fing-P was the bioactive form responsible for the lymphangiogenic phenotype. This finding would provide a valuable insight into the design process of future PAL probes. To assess this, spheroids were treated with a serial dilution of fingolimod co-dosed with a selective SPHK2 inhibitor, SLM 6031434 (2 μM).[220, 221] It was observed that co-dosing with a SPHK2 inhibitor completely ablated fingolimod's pro-lymphangiogenic effect (Figure 3.5), suggesting that it is the metabolite, Fing-P, which is responsible for the lymphangiogenic phenotype.

‡ Dr Christophe Ravaud, *unpublished data*

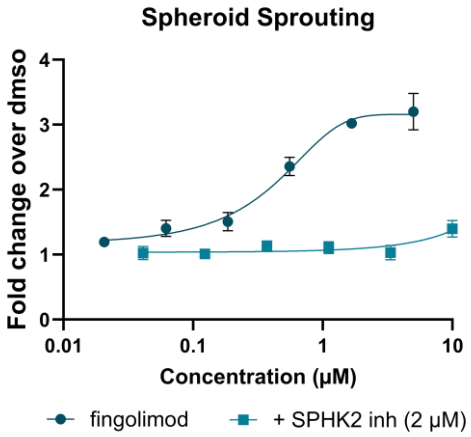


***Figure 3.5: Co-dosing lymphangiogenesis studies of fingolimod with a SPHK2 inhibitor.*** *Observed fold change in sprouting per spheroid relative to DMSO control in response to a serial dilution of fingolimod co-dosed with a selective SPHK2 inhibitor (2 μM). N=3. Error bars = sem.*

With this in mind, it would be crucial that any active PAL probes remained a substrate for SPHK2 to facilitate their phosphorylation and subsequent activation. Contrastingly, blocking this site of phosphorylation could be an avenue worth exploring in the design of structurally similar but functionally inactive control probes.

## 3.3 Optimisation of a phenotypic model of T-lymphocyte migration

### 3.3.1 Optimisation of Transwell migration assay

A robust phenotypic model of T-lymphocyte migration was required to assess fingolimod's inhibitory effect on T-lymphocyte ingression. Transwell inserts are commonly used to monitor immune cell chemotaxis,[222] however, they have recently been explored as a model of transendothelial migration of T-lymphocytes across the lymphatic endothelium.[223] Lymphatic endothelial cells can be seeded on the underside of the inserts to mimic a basal to apical transmigration of T-lymphocytes (Figure 3.6a), a model of T-lymphocyte ingression (i.e. the migration of cells from tissue into a lymphatic vessel). The Transwell inserts are comprised of a porous membrane and a 3 μm pore size was selected to ensure the assay only captured active

migration through the endothelium, versus passive diffusion through large gaps in the membrane, as advised by the manufacturer (Corning).

Previous protocols recommended a seeding density of 5 x $10^5$ LECs per insert, with a growth period of 48 h to cultivate a confluent monolayer.[224] To test this, the inserts were fixed and stained after 48 h with the endothelial cell biomarker CD31,[225] which confirmed the presence of an intact monolayer (Figure 3.6b). Additional staining with lymphatic junction marker, CD144, confirmed that the monolayer formed tightly connected intercellular junctions (Figure 3.6b).[103]

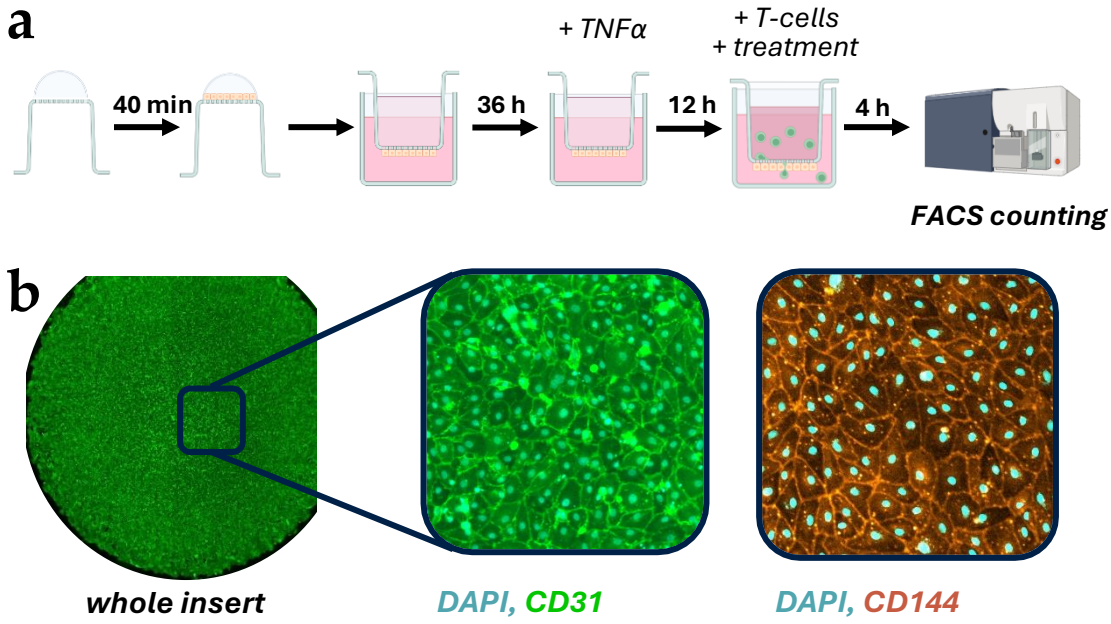


***Figure 3.6: Optimisation of Transwell migration assay as a phenotypic model of T-lymphocyte ingression.*** *(a) Schematic depiction of experimental set up, LECs (orange) were seeded on the underside of the insert and allowed to attach for 40 mins, the inserts were inverted in fresh media to grow for 48 h. 12 h before migration TNFα (1 ng/mL) was added to activate LECs. αCD3/CD28-activated Jurkats (green) were added to the top chamber and allowed to migrate for 4 h, after which the migrated cells were collected from the bottom chamber, stained with αCD3 FITC antibody and counted using FACS (b) Fluorescent imaging of the insert coated with an intact LEC monolayer, CD31 (green) highlighting an intact monolayer, DAPI (cyan) and, CD144 (orange) expression confirming tight junction formation.*

The Transwell migration assay would enable modelling of T-lymphocyte migration through the lymphatic endothelium. Our T-lymphocyte cell line of choice were E6.1 Jurkats, a clone of the immortalised human lymphoblastic leukemic Jurkat line, which were originally derived from the peripheral blood of a 14-year-old male with acute T-lymphocyte leukaemia.[226] Jurkats are commonly used in the literature to study T-lymphocyte signalling,[227, 228] function,[229, 230] and migration,[231, 232] due to their rapidly proliferative and readily available nature. Jurkats provide a more practical alternative to primary human T-lymphocytes, although their use is limited by their genetic instability which can lead to variability in their function and behaviour over time in culture.[233] Therefore, the culturing of the Jurkats was limited to passage 10, as recommended.[234]

There are many methods which have been used in the literature to quantify cell migration through Transwell inserts. The most common techniques are flow cytometry, whole cell fluorescence readings or lysed cell DNA quantification.[235-237] This approach requires the co-culturing of Jurkats and LECs, as such, treatment of lysed cells with a DNA dye (e.g. CyQUANT) which incurs the risk of artefacts from detached LECs during the washing steps of the protocol, was ignored. Using a cell-impermeable dye (e.g. CellTracker) coupled with a light-blocking Transwell membrane is an efficient way to measure cell migration into the lower chamber.[236] However, in initial studies utilising CellTracker, some leakage of dye was observed when visualising the migration by microscopy. In addition, this method of measuring fluorescently labelled Jurkats would require light blocking inserts, which are considerably more expensive than the transparent alternatives, making them an unfavourable method for migration quantification. Therefore, flow cytometry was chosen as the method of

quantification to measure the extent of Jurkat migration through the LEC monolayer and into the bottom chamber.

Preliminary trials attempted to establish a baseline migration level of 3-5%, as had previously been reported in the literature for Jurkat migration.[238-240] Unfortunately, minimal migration (0.005%) of untreated Jurkats was observed after 4 h (Figure 3.7a). The loading Jurkat density of 1 x $10^6$ was high, and could be encouraging Jurkat aggregation which would hinder transendothelial migration. Therefore, lower Jurkat densities (1-5 x $10^5$) were explored. While there was a slight improvement in migration observed when the input Jurkat density was lowered to 1 x $10^5$ (0.55%), this was not a substantial enough baseline migration. Increasing the permeability of the lymphatic endothelial monolayer could aid Jurkat migration; to achieve this LEC activation was explored. It had previously been demonstrated that TNF$\alpha$-mediated activation of LECs induces the upregulation of surface adhesion receptors, ICAM-1, VCAM-1 and E-selectin.[241] These receptors are key for the surface adhesion and subsequent transendothelial migration of immune cells through the lymphatic endothelium.[242] Due to the short-lived nature of E-selectin expression ($t_{1/2}$ ≈ 4 h), it was decided that 12 h prior to transmigration would be an optimal timeframe for TNF$\alpha$-mediated LEC activation, ensuring adequate receptor expression levels as confirmed by FACS (Figure 3.7b). Unfortunately, while activation of the lymphatic endothelium did significantly increase migration (1.0%), further improvements were required to ensure a substantial baseline migration.

Activation of the Jurkats was also investigated as T-lymphocyte activation is known to influence migration propensity. Upon activation, T-lymphocytes exhibit an increased expression of key adhesion and chemokine receptors, compared to naïve lymphocytes, which facilitates their tendency to migrate.[243] There are various stimulants capable of inducing

activation of T-lymphocytes. For instance, phytohemagglutinin-L (PHA-L) is a lectin extracted from legumes which binds to carbohydrates on TCR to trigger T-lymphocyte activation *via* an antigen-independent mechanism.[244] Furthermore, in an attempt to adopt a more physiologically relevant environment, it was investigated whether the presence of pro-inflammatory cytokines (IFN$\gamma$, IL-6, TNF$\alpha$ and IL-1$\beta$) which are abundant in the heart after a MI,[245] could induce T-lymphocyte activation in an *in vitro* setting. Finally, the most widely used mode of T-lymphocyte activation involves mimicking APCs with co-stimulation of TCR and CD3 by $\alpha$CD28 and $\alpha$CD3 antibodies, respectively.[246] The extent of activation was measured by activated T-lymphocyte biomarker, CD69,[247] expression at 24 h (Appendix I) and 48 h timepoints (Figure 3.7c). There was no change in CD69 expression after 48 h incubation of the Jurkats with pro-inflammatory cytokines. However, CD69 expression increased comparably after 48 h incubation with both PHA-L and $\alpha$CD28/CD3, confirming their ability to activate this Jurkat cell line. Consequently, it was deemed that $\alpha$CD28/CD3 stimulation generated a more uniform population and was a more physiologically relevant means of activating the Jurkats. Therefore, $\alpha$CD28/CD3 activation of Jurkats was used in all further transmigration studies. While Jurkat activation alone did not achieve the desired level of migration (1.2%), the dual activation of both the LECs and Jurkat cells resolved the issues of T-lymphocyte migration, with an observed baseline migration of 4.3% (Figure 3.7a).

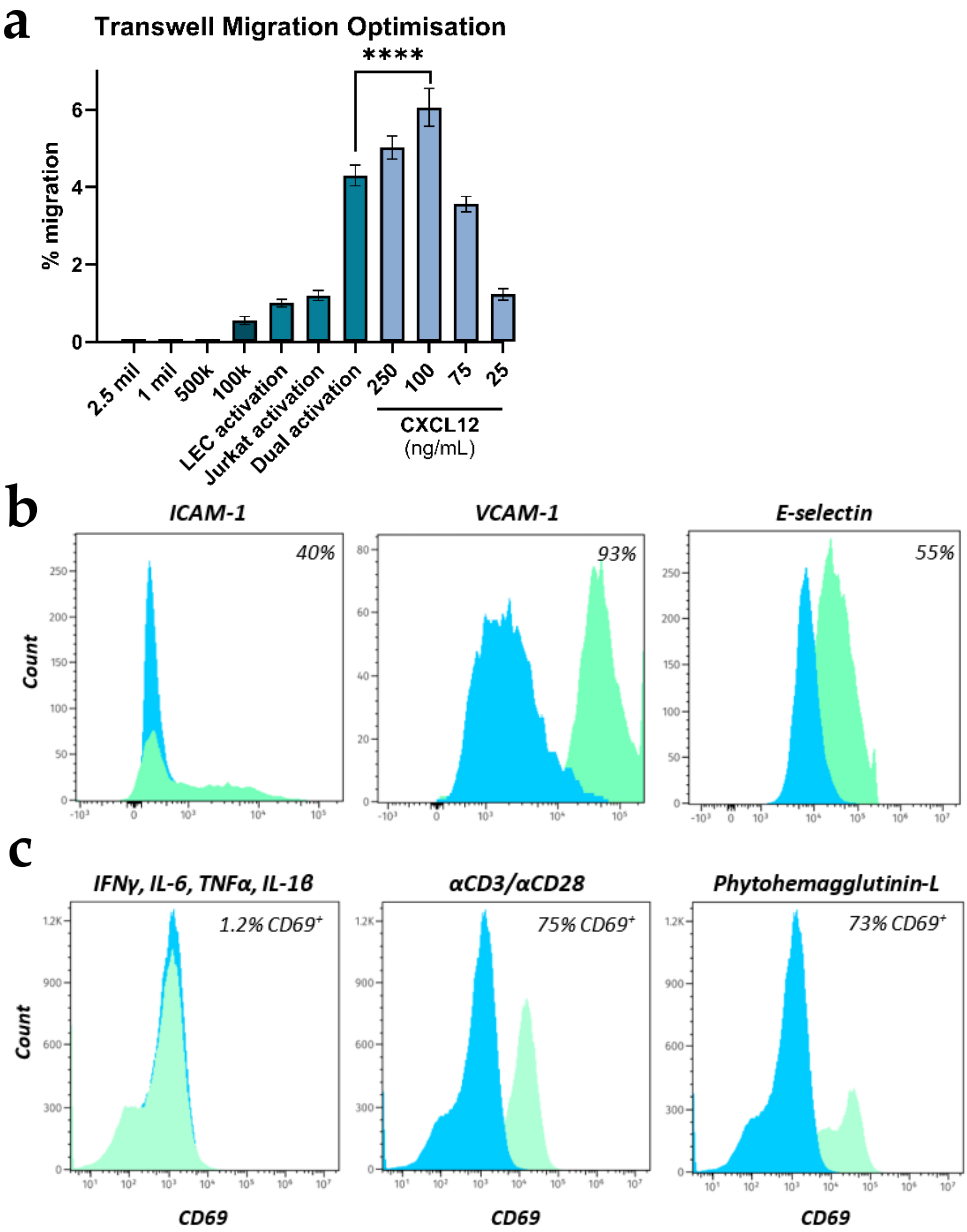


***Figure 3.7: Optimisation of Transwell migration assay as a phenotypic model of T-lymphocyte ingression.*** *(a) Optimisation of Jurkat migration through Transwell insert into the bottom chamber, as counted by FACS. % of input (1 x $10^5$ Jurkats unless stated otherwise). Statistical analysis using Student's t-test. **** = P<0.001 (b) Expression of ICAM-1, VCAM-1 and E-selectin (CD62E) on LECs before (blue) and after (green) 12 h TNFα treatment (1 ng/mL), measured by FACS. Analysed with FlowJo v11 (c) Expression of surface activation marker CD69 on Jurkats before (blue) and after (green) 48 h activation treatments, measured by FACS. Analysed with FlowJo v11. Gating strategy in Appendix.*

To ensure the robustness of the migration assay, a positive migratory control was needed to act as a continual reference to assess the validity of the assay. There are several known chemokines which function as T-lymphocyte chemoattractants. Due to the $CD4^+CD8^-CXCR4^+$ phenotype of our activated Jurkat cell line (Appendix II), CXCL12 was tested in the Transwell migration assay as it has been shown to bind to CXCR4 to trigger chemotaxis in $CD4^+$ T-lymphocytes.[248-250] Under the optimised experimental conditions, CXCL12 increased Jurkat migration (6.1%), at an optimal concentration of 100 ng/mL, with an observable bell-shaped dose response effect commonly associated with chemotaxis (Figure 3.7a).[251]

After optimisation of the Transwell migration assay, a desired baseline migration of 4.3% was achieved, which increased to 6.1% upon stimulation with a chemoattractant. This level of Jurkat migration and response to stimulus provided confidence in the established experimental set-up. Therefore, this optimised assay was used for all further quantification of Jurkat transendothelial migration through the lymphatic endothelium in response to different treatments.

### 3.3.2 Confirmation of fingolimod's inhibition of T-lymphocyte migration

Fingolimod significantly inhibited migration of Jurkats in the Transwell assay in a dose-dependent manner up to 1 μM (Figure 3.8), however, at higher concentrations fingolimod lost its inhibitory effect with a return to baseline migration at 5 μM. This observation was intriguing, and investigations into the cause of this decline in activity will be highlighted later in the chapter.

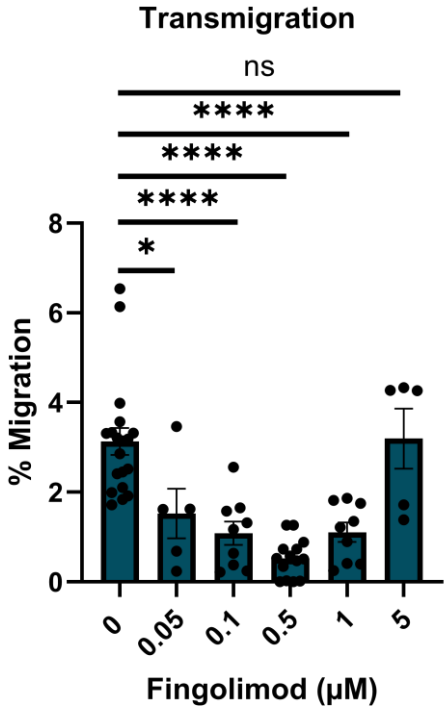


***Figure 3.8: Investigating the influence of fingolimod on T-lymphocyte migration.*** *Migration of T-lymphocytes in response to fingolimod treatment. N>3. Statistical tests using a one-way ANOVA and multiple comparison tests. **** = P<0.001, * = P<0.05, ns = P>0.05. Error bars = sem.*

To further investigate the potential mechanism of action of fingolimod's inhibitory effect on T-lymphocyte migration, co-dosing experiments with SPHK2 inhibitor, SLM6031434,[220, 221] were performed. SPHK2 inhibition was shown to block fingolimod's inhibitory effect upon T-lymphocyte migration (Figure 3.9), suggesting that Fing-P was the bioactive form. Coupled with the observations from the lymphangiogenesis studies, it is evident that phosphorylation of fingolimod is a key attribute towards its immunomodulatory phenotypic efficacy.

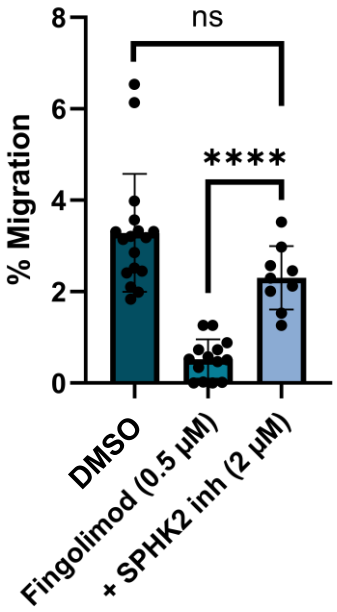


***Figure 3.9: Co-dosing fingolimod with a SPHK2 inhibitor inhibits its inhibitory effect on T-lymphocyte transmigration.*** *Migration of T-lymphocytes in response to treatment with fingolimod (0.5 µM) co-dosed with a SPHK2 inhibitor, SLM6031434 (2 µM). N≥3. Statistical tests using a one-way ANOVA and multiple comparison tests. **** = P<0.001, ns = P>0.05. Error bars = sem.*

These migration studies were performed over a 4 h timeframe as it has commonly been reported that a 4 h migration window is sufficient to capture the transendothelial movement of T-lymphocytes through a Transwell insert.[252, 253] To confirm this, a migration time course was performed. This would allow the determination of an optimal window to observe fingolimod's inhibitory influence. There appeared to be a slow onset in T-lymphocyte migration that increased significantly at 4 h (Figure 3.10). This level of migration plateaued after 4 h, reaffirming the literature observations, and this migration window was maintained in all further migration studies.

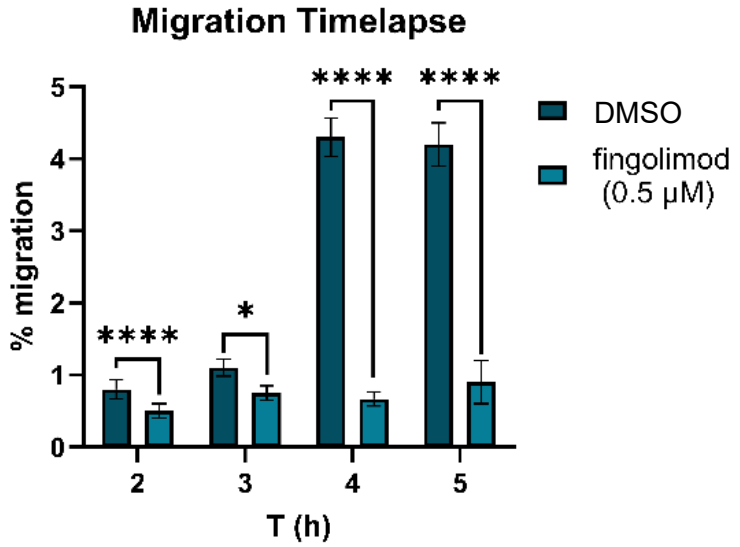


***Figure 3.10: Optimisation of the timeframe of the Transwell migration assay.*** *Time course migration study of Jurkat migration through to bottom chamber, as counted by FACS. Error bars = sem. Statistical analysis performed using Student's t-test. * = P<0.05, **** = P<0.001.*

### 3.3.3 Investigations into fingolimod's activity profile

The loss of fingolimod's efficacy at higher concentrations was an interesting observation which warranted a more in-depth investigation as to the cause. It was initially hypothesised that this observation could be due to the toxicity of fingolimod, which has been previously reported in other cell lines.[254, 255] Therefore, MTT mitochondrial metabolism studies were performed on fingolimod (Figure 3.11), to assess the level of cell viability within the time frame of these experiments (6 h). Up to 10 µM, fingolimod demonstrated no significant drop in cell viability in either cell line within 6 h, therefore the loss of the inhibitory effect of fingolimod could not be attributed to cell death.

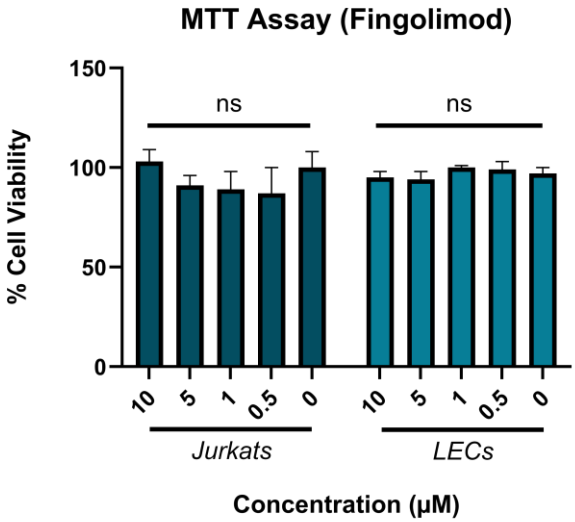


***Figure 3.11: Investigating the toxicity of fingolimod on Jurkats and lymphatic endothelial cells.*** *MTT mitochondrial metabolism cell viability assay of Jurkats and LECs treated for 6 h with fingolimod. N=3. Statistical tests using a one-way ANOVA. ns = P>0.05. Error bars = sem.*

An alternative explanation was potentially due to the amphiphilic, surfactant-like nature of fingolimod, leading to micelles or aggregates at higher concentrations (5-10 μM), above its critical micelle concentration (CMC). This aggregation would lower the bioavailable free fraction of fingolimod in solution, which could explain the loss of effect at higher doses. It is precedented that fingolimod forms micelles in water at 75 μM,[256] therefore it was investigated whether the CMC could be lower under the experimental conditions. The presence of salts in the media increases the ionic strength of the solution which has been shown to lower the CMC.[257] It is also possible that the presence of cell membrane phospholipids could enable heteromicelle formation, which could increase the total surfactant concentration in solution,[258] also lowering the observable CMC of fingolimod. To test this hypothesis, waterLOGSY experiments were performed following a previously established protocol.[259] WaterLOGSY is an NMR technique which relies on the principle that excited water molecules undergo a transfer of $^{1}H$ magnetism to small molecules in solution *via* a positive nuclear Overhauser effect. This is observed as an increase in signal intensity. Upon aggregation, this transfer of

magnetism yields a negative nuclear Overhauser effect due to the slower tumbling rates of the larger aggregate. This is observed as a decrease or inversion in signal intensity (Figure 3.12a). WaterLOGSY experiments were attempted in EGM-2MV media however the background signals were too complex to interpret anything meaningful from the spectra (Appendix III). Therefore, PBS was used as the solution for the subsequent waterLOGSY experiments. The resultant spectra did not show a complete inversion of peaks which would have been indicative of a strong aggregator, nonetheless, there was a decrease in the positive signal intensity (Figure 3.12b-c). Whilst not conclusive, the data suggests that fingolimod is a weak aggregator in PBS.

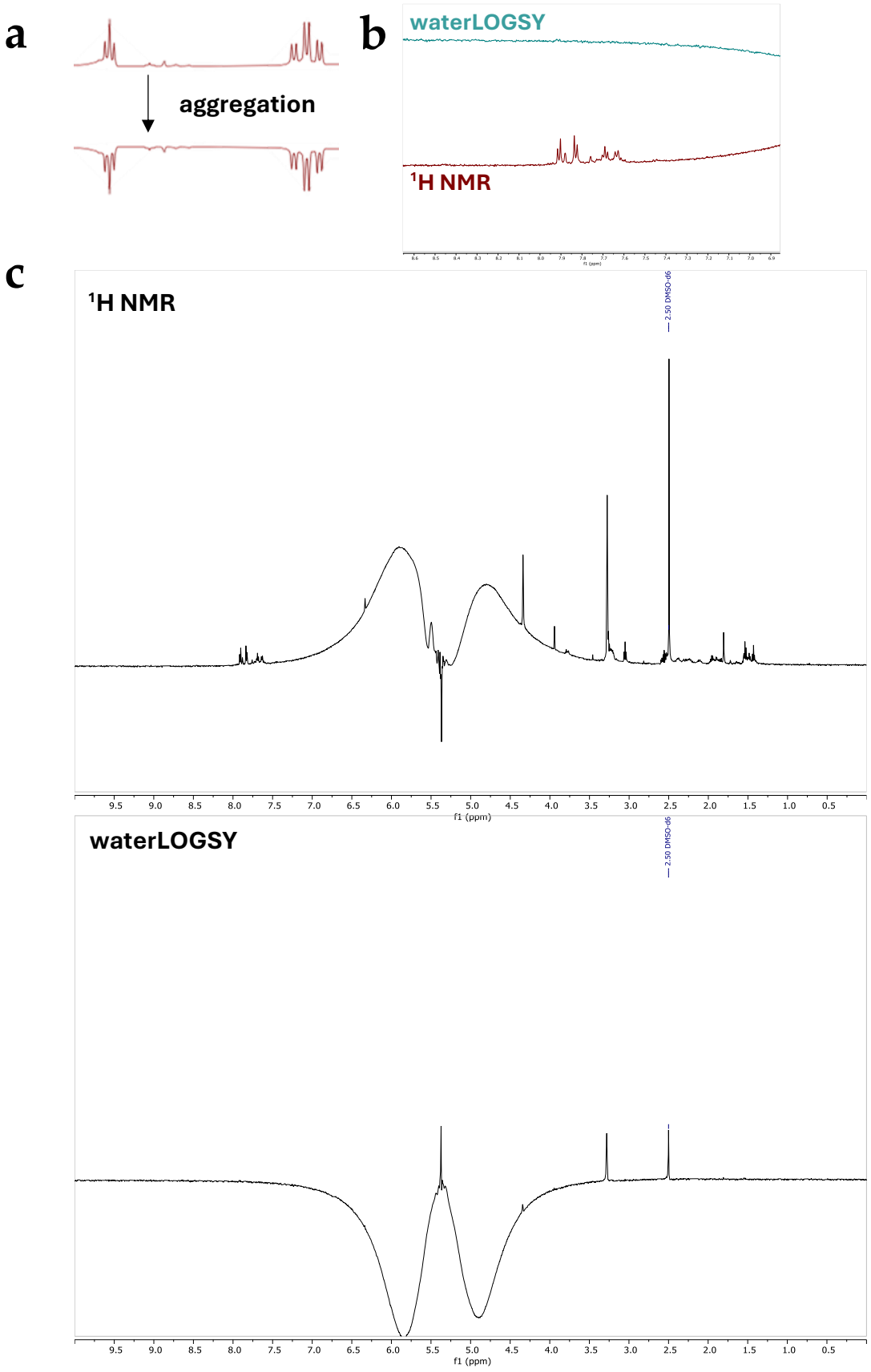


***Figure 3.12: WaterLOGSY studies show fingolimod is a weak aggregator in PBS.*** *(a) Schematic depiction of waterLOGSY spectra inversion upon compound aggregation (b) close up of stacked spectra in the aromatic region (9.1-7.0 ppm) (c) $^{1}$H NMR spectra (32 scans) and waterLOGSY spectra (1024 scans) of fingolimod (500 µM) in PBS.*

One of the limitations of waterLOGSY as a method to measure aggregation is its sensitivity. As a consequence, these studies were performed at a concentration of 500 μM fingolimod, which is significantly higher than the phenotypically relevant dosages. Therefore, the more sensitive technique of small angle x-ray scattering (SAXS) was explored (Figure 3.13a) and these experiments were performed in collaboration with Dr Huband at the University of Warwick. The core principle of SAXS requires a monochromatic and unidirectional beam of x-rays (0.1 – 0.2 nm) to be passed through a sample. As the x-rays interact with the sample, they are scattered. The extent of scattering is monitored by a detector and can be used to extract structural information about the size and morphology of the sample. Using a DMSO-treated supernatant as a background control, SAXS experiments were performed to assess the presence of fingolimod aggregation (Figure 3.13b-c). Unfortunately, no discrepancies in scattering could be detected when comparing the background control vs fingolimod-treated samples. There are multiple potential explanations for this observation: (i) fingolimod does not aggregate at the tested concentrations, therefore, there must be an alternative reason for the loss of activity at higher concentrations; (ii) if fingolimod is forming micelles they could be too small to detect amongst the background noise of the media additives; (iii) rather than forming a spherical micelle structure, fingolimod could be forming a monolayer at the liquid-air interface which could not be detected using this technique.

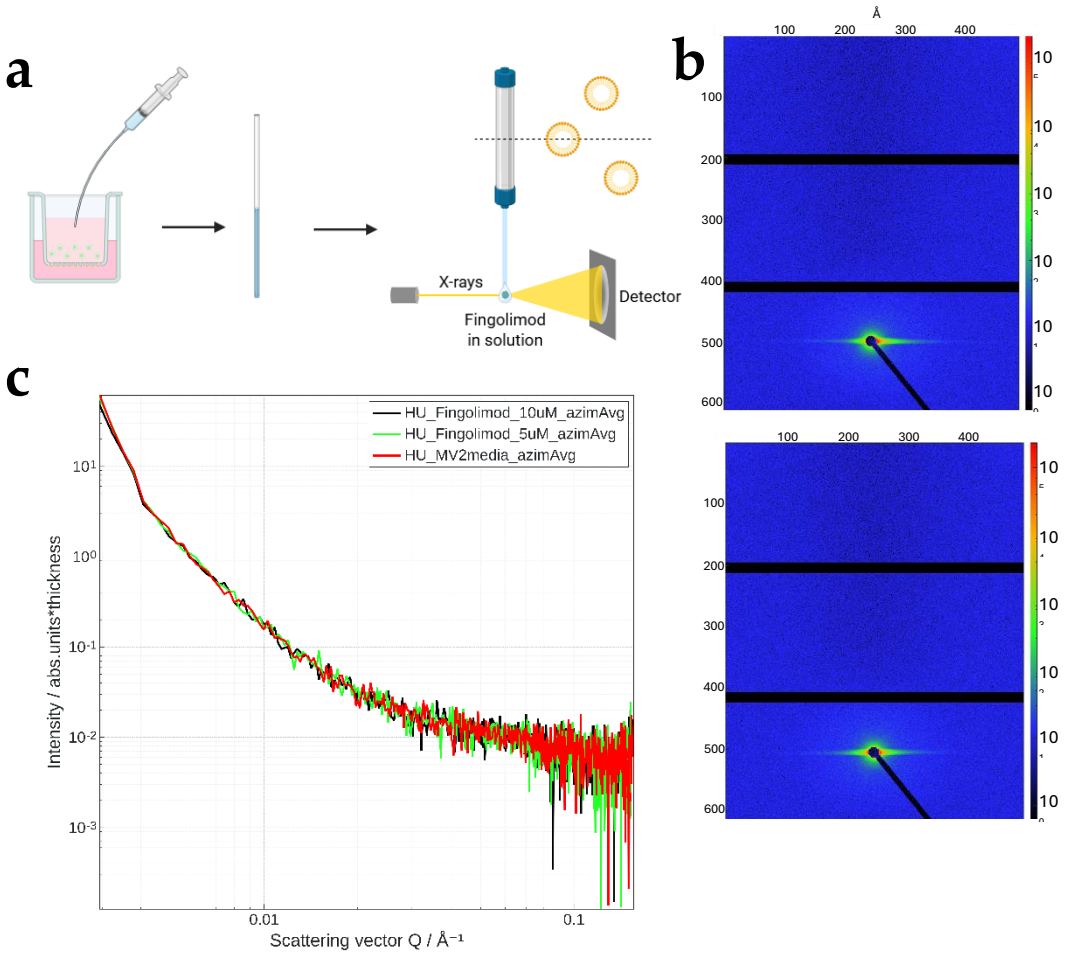


***Figure 3.13: Small-angle x-ray scattering (SAXS) experiments could not determine fingolimod aggregation*** *(a) Schematic depiction of SAXS experimental set up. Supernatant from a Transwell migration insert was transferred to a capillary tube. A monochromatic polarised beam of x-rays were shone through the sample and the resultant scattering was detected (b) 2D SAXS diffraction of 10 µM fingolimod (top) and DMSO (bottom) treated supernatant. Colour scale depicts log(counts) (c) 1D SAXS profile for DMSO (red), 5 µM fingolimod (green) and 10 µM fingolimod (black) treated supernatant. SAXS experiments were performed by Dr Huband.*

If fingolimod was not forming micelles or aggregates, then a potential explanation could be that at higher concentrations fingolimod is desensitising its target receptor, potentially through receptor internalisation or negative feedback signalling. To investigate this hypothesis further, washout experiments could have been performed, however it was decided to prioritise other experiments.

### 3.3.4 Development of Microvessel-on-a-chip assay

The Transwell migration assay provided a medium throughput model with which to test the phenotypic effect of fingolimod and its analogues towards T-lymphocyte ingression. Nevertheless, as previously observed (Figure 3.6b), the junctions formed within the monolayer were tight rather than the typical button-like junctions present in lymphatic capillary tips.[260] In addition, whilst a gravitationally-induced flow can be introduced by varying the volume of media in the top and bottom chambers, there is no physiological interstitial flow present in this model of migration, which has been shown to affect immune cell adhesion and lymphatic permeability.[261] Therefore, a more physiologically relevant assay was devised to rigorously test the phenotypic effect of select compounds of interest.

In the field of microfluidics, microvessel-on-a-chip assays have shown great promise as an improved model of vessel formation, function and physiology.[262] These assays facilitate the formation of a vessel with an intact lumen upon an ECM basement membrane which can be placed on rockers to mimic both luminal and interstitial flow. These assays have recently been commercialised, which has facilitated the broader use of these chips, overcoming the need to design and 3D print the moulds yourself. While the vessels themselves are much larger in comparison to native lymphatic capillaries, 200 μm in diameter versus 60 μm,[263] they are conducive to live imaging which can be utilised to monitor real-time migration events. Mimetas™ 3-channel chips were chosen due to their co-culturing capacity, and they have previously been used to grow lymphatic vessels using an immortalised lymphatic cell line (Figure 3.14).[264] However, the growth of these vessels using our own commercial LEC cell line

required extensive optimisation with the assistance of an experienced collaborator, Dr Al Haj Zen at HBKU in Qatar, who developed a robust protocol that enabled a reliable vessel growth.

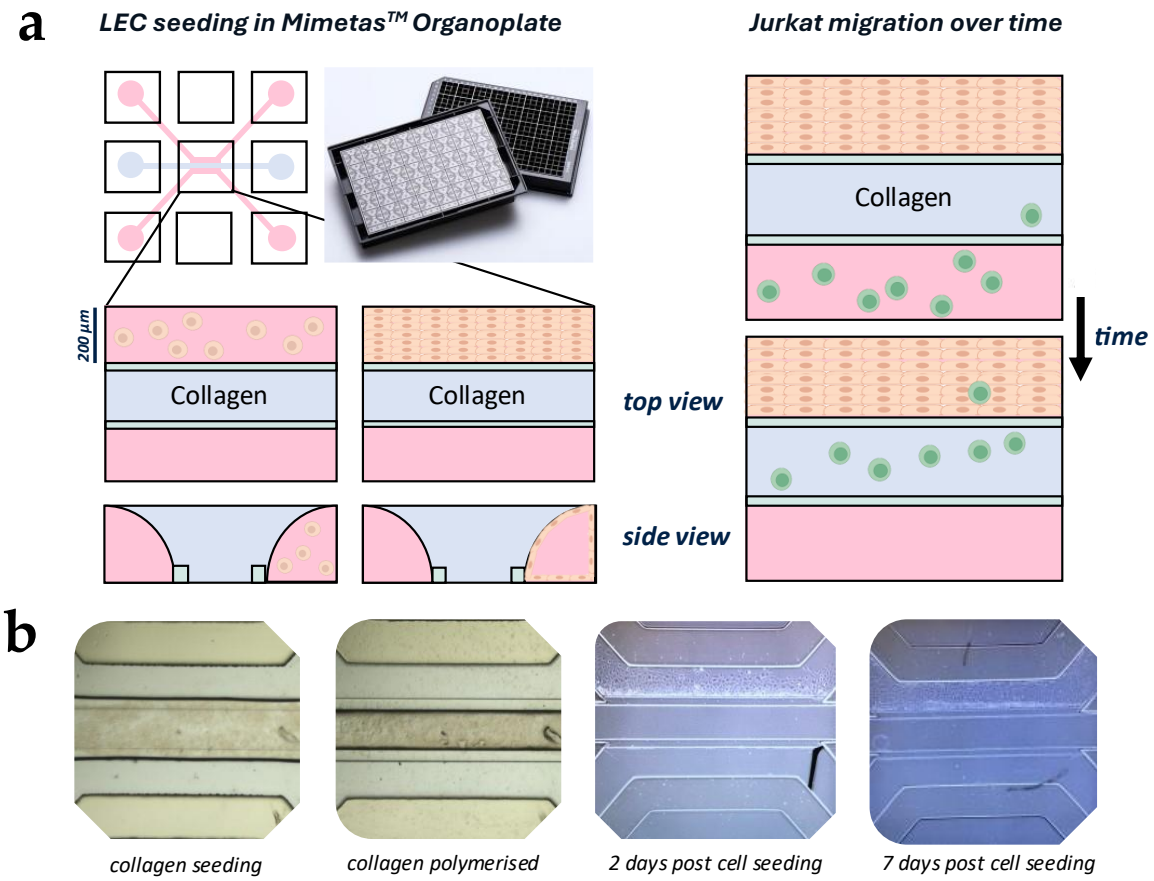


***Figure 3.14: Mimetas™ 3-channel chip used for microvessel-on-a-chip studies.*** *(a) Schematic depiction of the experimental set up of the microvessel-on-a-chip assay with the Mimetas™ 3 channel chip. 7 days after LEC seeding, an intact LEC vessel forms. Upon seeding Jurkats in the opposing channel, they undergo migration through the extracellular matrix, towards the lymphatic vessel (b) Brightfield images of the different stages of chip preparation and vessel formation.*

Dr Al Haj Zen performed a screen of ECMs and discovered that Matrigel alone was an unsuitable ECM as it lacked the structural integrity required to allow LEC seeding and vessel formation (Figure 3.15). In contrast, type 1 collagen (3 mg/mL) or a 3:1 ratio of Matrigel to type 1 collagen provided the necessary rigidity required for lymphatic vessel formation. I attempted both automated and manual loading of the ECM to compare reliability and repeatability between the two methods, and it was observed that manual loading of the ECM

was essential as a 'by-eye' approach ensured the correct volume was loaded, which prevented the overflow of the ECM into other channels.

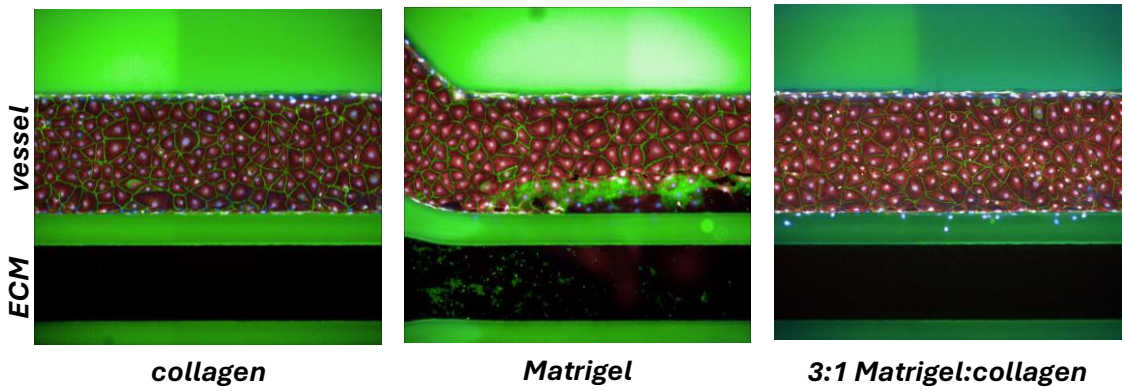


***Figure 3.15: Optimisation of extracellular matrix for lymphatic vessel formation in microvessel-on-a-chip.*** *Images of lymphatic vessels, grown after 7 days of culture in the presence of different extracellular matrices. LECs were stained with CellMask™ Deep Red (red), CD144 (green) and DAPI (cyan). Images obtained by Dr Al Haj Zen.*

Dr Al Haj Zen discovered that additional coatings of fibronectin were required to aid LEC attachment to facilitate vessel formation. With these additional alterations, it was possible to grow intact vessels within 7 days of LEC seeding and confocal imaging confirmed the formation of a luminal vessel (Figure 3.16).

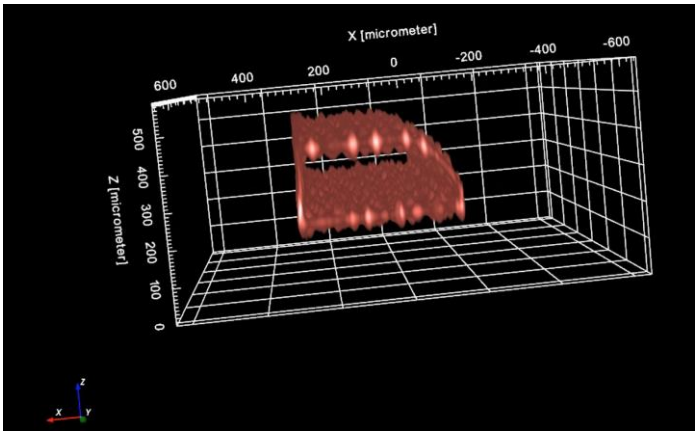


***Figure 3.16: Microvessel-on-a-chip enables luminal vessel formation.*** *Image taken from a 3D reconstruction of confocal Z-stacks of a lymphatic vessel grown over 7 days in the presence of a collagen (3 mg/mL) extracellular matrix. Original Z-stack images obtained by Dr Al Haj Zen.*

However, upon the initiation of co-culturing studies with Jurkats, it became evident that the use of a solely collagen-based ECM did not facilitate T-lymphocyte invasion towards the lymphatic vessel (Figure 3.17). However, a 3:1 ratio of Matrigel to type 1 collagen provided the ideal compromise between the rigidity and permeability required for an invasive migration model. The medium in which T-lymphocytes were seeded also appeared to play a vital role in their propensity to migrate. T-lymphocytes administered in EGM-MV2 media displayed a greatly reduced level of invasion, relative to Matrigel or the Matrigel/collagen mix, which themselves displayed a similar migratory profile. As such, Matrigel was chosen as the preferred medium in which to seed Jurkats in the co-cultured model.

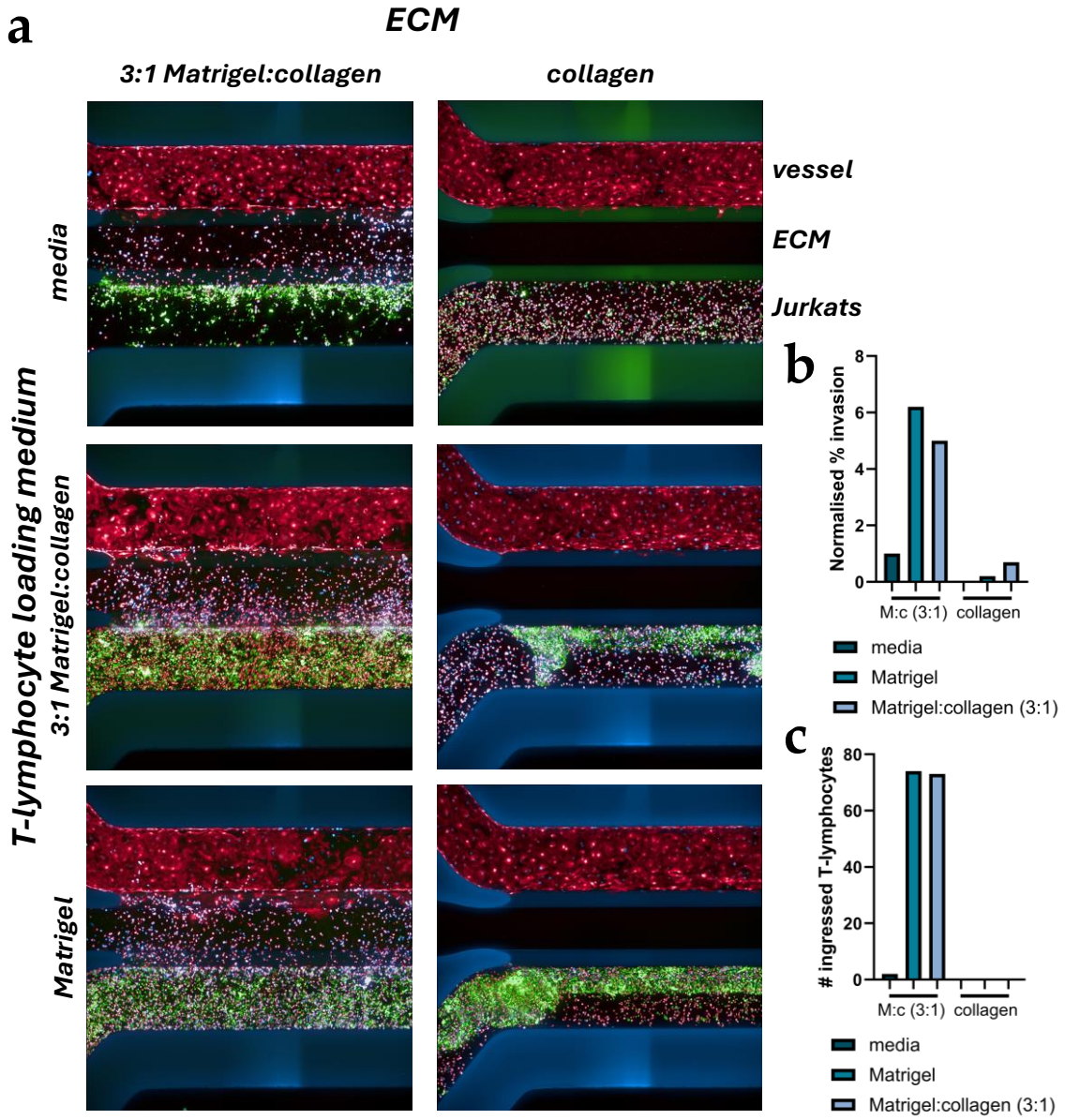


***Figure 3.17: T-lymphocyte invasion in co-cultured lymphatic microvessel-on-a-chip studies.*** *(a) A lymphatic vessel was cultured in the presence of either a 3:1 Matrigel:collagen (left) or collagen (right) ECM for 7 days. Upon vessel formation, Jurkats were seeded in the opposing channel in either media (top), 3:1 Matrigel:collagen (middle) or Matrigel (bottom). Lymphatic vessels were stained with CellMask™ Deep Red (red) and DAPI (cyan). T-lymphocytes were labelled with GFP using a lentiviral induction. Images were obtained by Dr Al Haj Zen. (b) Quantification of T-lymphocyte invasion into the ECM (c) Quantification of T-lymphocyte ingression into lymphatic vessel.*

The optimisation of microvessel-on-a-chip microfluidics provided an ECM-supported 3D lymphatic vessel through which co-cultured T-lymphocytes could migrate. This platform was

conducive to confocal imaging and would allow live visualisation of T-lymphocyte migration through the lymphatic endothelium in response to different treatments.

With the phenotypic assays optimised and fingolimod's immunomodulatory effects validated, the PAL probes and their negative control analogues could be developed. The observation that Fing-P was the bioactive molecule responsible for the immunomodulatory phenotypes would enable a more informed design approach to be adopted (as discussed in Chapter 4).

# Chapter 4

## *Design and Synthesis of Fingolimod-derived Photoaffinity Probes*

# 4 Design and Synthesis of Fingolimod-derived Photoaffinity Probes

## 4.1 Design of photoaffinity labelling probes

To decipher both the direct targets of fingolimod and their interactome, a series of PAL probes were designed. It was essential that any modifications had a minimal impact on binding interactions to ensure retention of the desired phenotypes. Previous studies into fingolimod's efficacy had suggested that fingolimod's metabolite, Fing-P, was the bioactive form. Therefore, it would be crucial that any synthesised probes should remain a substrate for SPHK2. As such, it was decided that the pro-*S* alcohol of the fingolimod headgroup should remain free for phosphorylation by SPHK2 (Scheme 4.1).

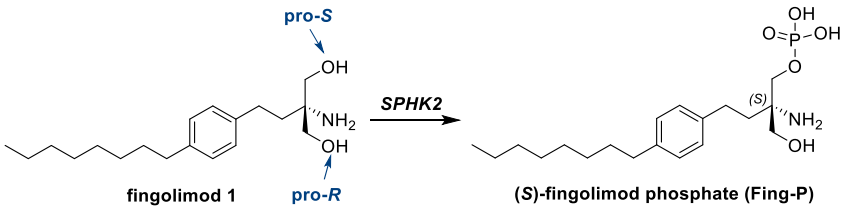


***Scheme 4.1: Fingolimod undergoes SPHK2-mediated phosphorylation of its pro-(S) alcohol to yield the phenotypically active fingolimod phosphate (Fing-P).***

When designing the photocatalytic probe, choosing the correct exit vector to connect fingolimod to the iridium photocatalyst was essential for the retention of its activity. Information was obtained from fingolimod's known binding mode to $S1PR_1$. Cryo-EM structures of fingolimod co-crystalised with $S1PR_1$ have been obtained by Xu et al (PDB: 7WF7) and show that fingolimod binds to the transmembrane helical region of the protein, with the lipophilic tail buried deep within the pocket placing the polar head group in a more solvent exposed region near the binding pocket entrance (Figure 4.1).[265] This is a common binding motif of lipid-like small molecules, therefore, it was predicted that fingolimod would

likely bind other target proteins in a similar way.[266] It was also evident in the crystal structure of $S1PR_1$ that the amine of the fingolimod head group can participate in hydrogen-bonding interactions within the protein binding pocket. Disruption of these interactions could attenuate the probe's affinity towards its target proteins and alter the basicity of the molecule, which could impact its permeability and subcellular distribution.

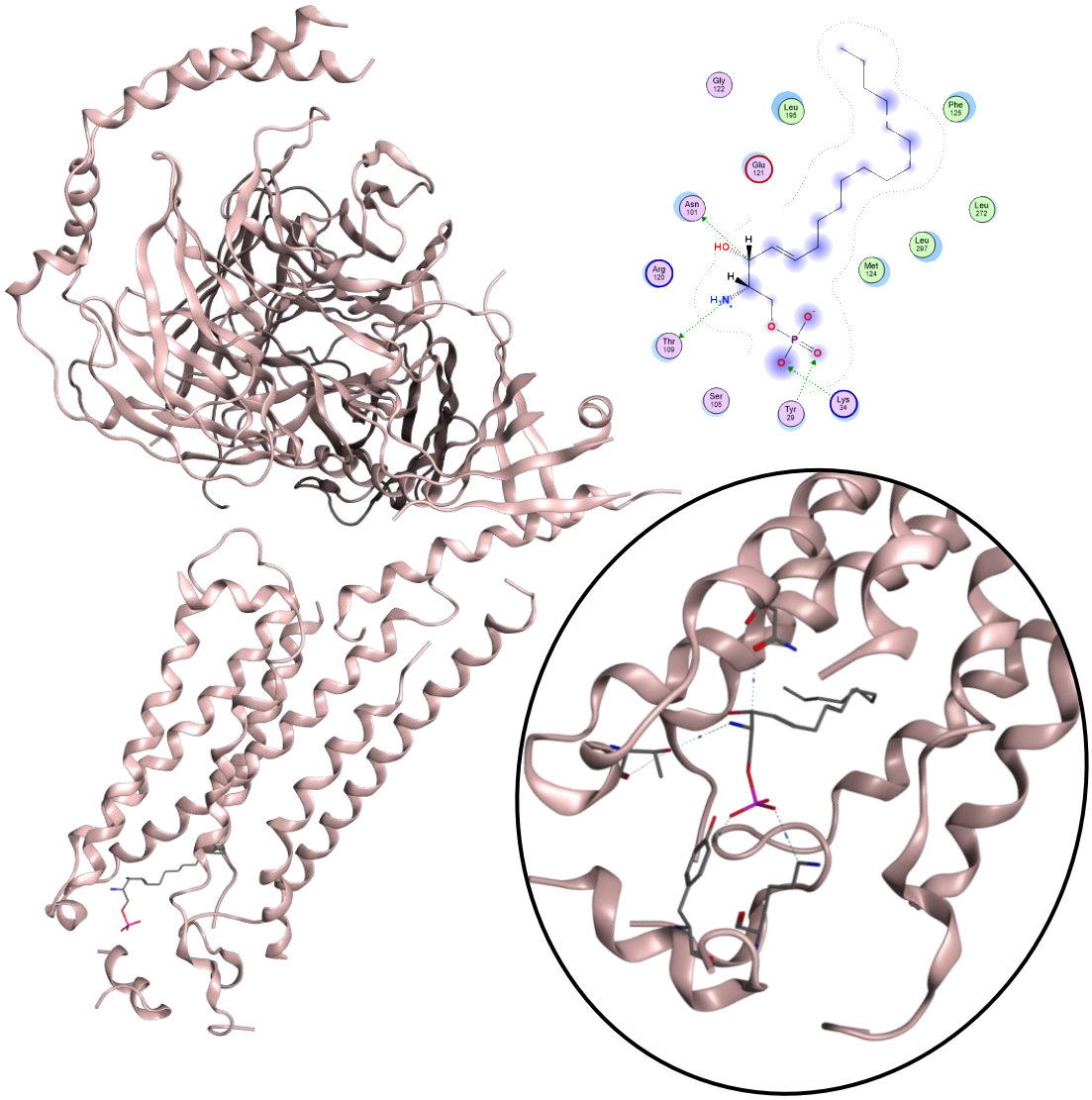


***Figure 4.1: Fingolimod phosphate co-crystalised with $S1PR_1$ (PDB: 7WF7) by Wu et al.[267]*** *Key electrostatic interactions between the pocket residues and the phosphate and amine of the head group are highlighted.*

An experimental crystal structure of SPHK2 has not yet been obtained, however, its isozyme SPHK1 has been crystalised with ADP (PDB: 3VZD).[267] Docking studies of $^{t}$BuPEG$_2$-linked

fingolimod with SPHK1 similarly demonstrate the positioning of the headgroup towards the solvent exposed opening of the substrate binding pocket, proximal to the predicted ATP-binding domain, with space for synthetic expansion from the serinol head group (Figure 4.2). SPHK1 is commonly used as a homology model of SPHK2 due to their similar structure.[268] In fact, crystallography studies have demonstrated that the SPHK2 binding pocket is much more tolerant towards substrate expansion, relative to SPHK1.[268] This is proposed to be due to the substitution of the sterically demanding Phe374 in SPHK1 for a smaller cysteine residue in SPHK2.[269]

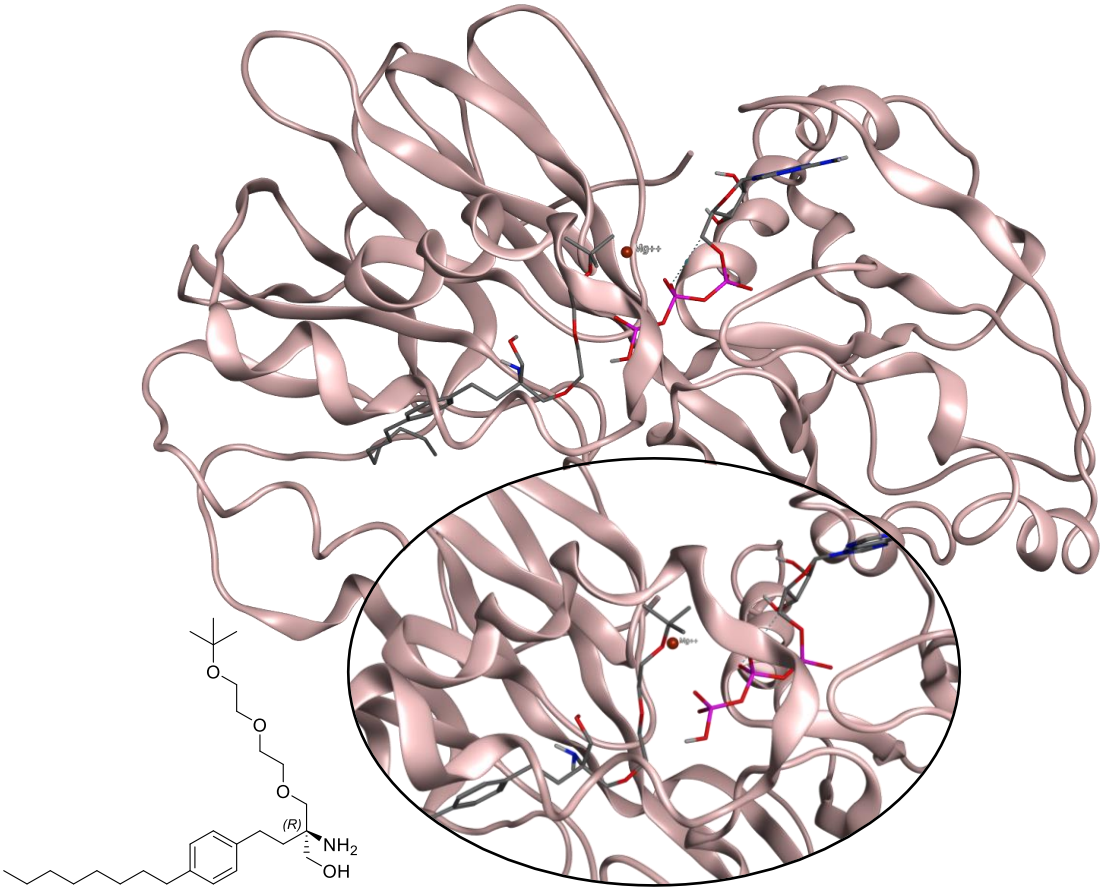


***Figure 4.2: Docking of $^{t}$BuPEG$_2$-Fingolimod in SPHK1 (PDB:3VZD) co-crystalised with ATP.***[269] *SPHK1 was used as a homology model of SPHK2, co-crystallised with ATP to highlight its binding region in the kinase. tBuPEG$_2$-Fingolimod was docked in the SPHK1-binding pocket by MOE, using a triangle matcher/induced fit method. A GBVI/WSA scoring was used to calculate ΔG of the interaction. ΔG= −7.5899 kcal/mol. RMSD = 1.7675 Å.*

This *in silico* data provided confidence in the decision to focus synthetic efforts on the expansion from fingolimod's pro-(*R*) alcohol to generate the photocatalytic PAL probe. Additionally, previous SAR surrounding fingolimod's immunomodulatory effect upon circulating T-lymphocytes shows that the pro-(*R*) alcohol is not required for activity. Compound **2** induced a comparable reduction in circulating T-lymphocytes *in vivo*,[270] similarly, morpholino analogue **3** showed a SPHK2-dependent decrease in blood lymphocytes as well.[271] Whilst this SAR relates to fingolimod's sequestration of T-

lymphocytes in the LNs, it provides an insight into the substrate tolerance of SPHK2 and the aptitude of the pro-(*R*) alcohol for expansion. Attempts to dock PAL probe (*R*)-**4** were unsuccessful due to the large, complex iridium photocatalyst which possesses many degrees of freedom which lowered the resolution and the confidence in the docking poses.

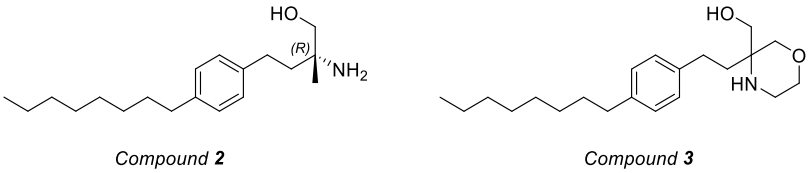


*Compound **2*** *Compound **3***

***Figure 4.3: Structural analogues of fingolimod which display similar immunomodulatory efficacy.***

With these criteria in mind, two fingolimod-derived probe designs were devised, incorporating expansion from the pro-(*R*) alcohol (Figure 4.4). Photocatalytic probe **4** involved the incorporation of a $PEG_3$ chain linked to the iridium photocatalyst, whilst PAL probe **5** was modified to include an ether-linked alkyl diazirine alkyne moiety.

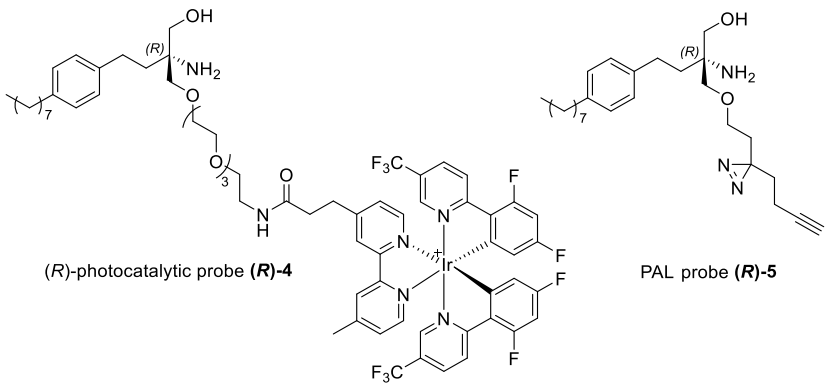


***Figure 4.4: Initial photoaffinity probe designs.***

Structurally similar but functionally inactive negative controls would be essential to enable deconvolution of the proteomic data, and to decipher which target proteins were responsible for the differing phenotypic effects of interest. The synthesis of multiple orthogonal negative control probes would allow differentiation between the migratory and lymphangiogenic effects of fingolimod. Due to the lipid-like nature of fingolimod, it was hypothesised that the length of the hydrophobic tail could be modulated to distinguish protein binding selectivity,[272] therefore truncated fingolimod analogues were designed as potential negative controls (Figure 4.5, analogues **6** & **7**). This hypothesis was also supported by the previous SAR studies performed in the development of fingolimod, which indicated that alkyl chain length played a role in the efficacy of the drug (Figure 1.5). In parallel, modification of the polar head group to block the site of activity-dependent SPHK2-mediated phosphorylation was also explored (Figure 4.5, analogue **8**). To complement the suggested photocatalytic probe **(*R*)-4**, its enantiomer **(*S*)-4** was proposed as a structure-matched negative control probe with an obstructed phosphorylation site (Figure 4.5). Similarly, the enantiomeric (*S*)-PAL probe **(*S*)-5** was also proposed as a potentially inactive PAL probe.

However, it is important to consider whether the significant structural changes being made to the PAL probes will alter their biological function relative to the parent compound. In particular, the addition of the iridium photocatalyst could interfere with the solubility, permeability, subcellular localisation, phosphorylation state and the bioactivity of the probe. As such, it is important to fully validate the synthesised probes to endure they maintain the desired phenotype.

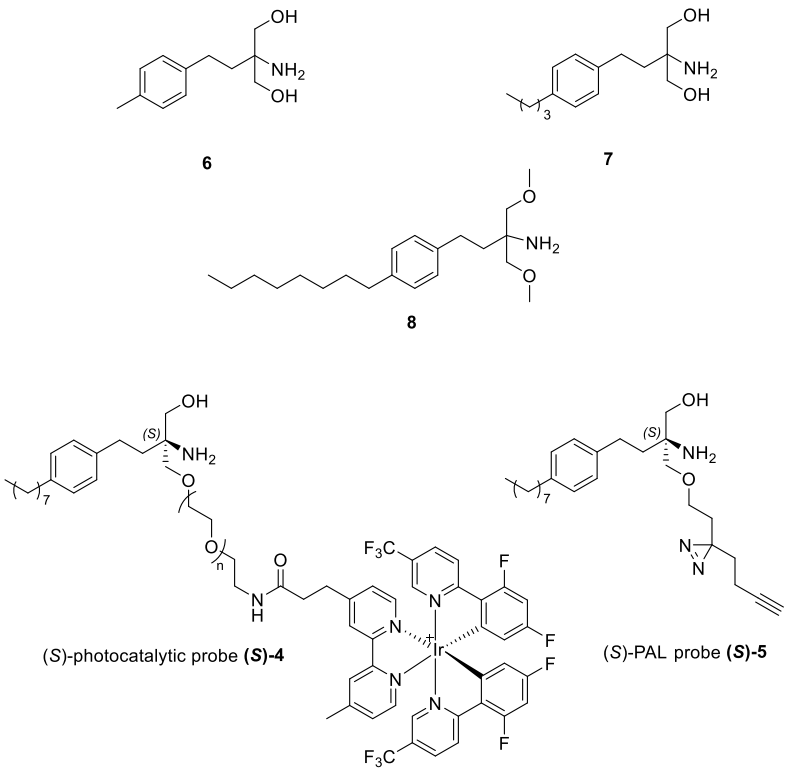


***Figure 4.5: Structure-matched negative control analogue designs.*** *Truncation of the lipophilic alkyl chain (**6** & **7**) or methylation of the polar head group (**8**) to interfere with SPHK2-mediated phosphorylation. Matched enantiomeric photoaffinity probe **(S)-5** and photocatalytic probe **(S)-4** were also designed with an obstructed phosphorylation site.*

## 4.2 Synthesis of fingolimod

A previously reported literature syntheses of fingolimod demonstrated that it can be synthesised from acetamidomalonate **9** (Scheme 4.2).[273] In an attempt to streamline the synthesis and improve the yield, a convergent synthesis was devised whereby the acetamidomalonate headgroup was incorporated into an acyl chloride for a Friedel-Crafts Acylation.

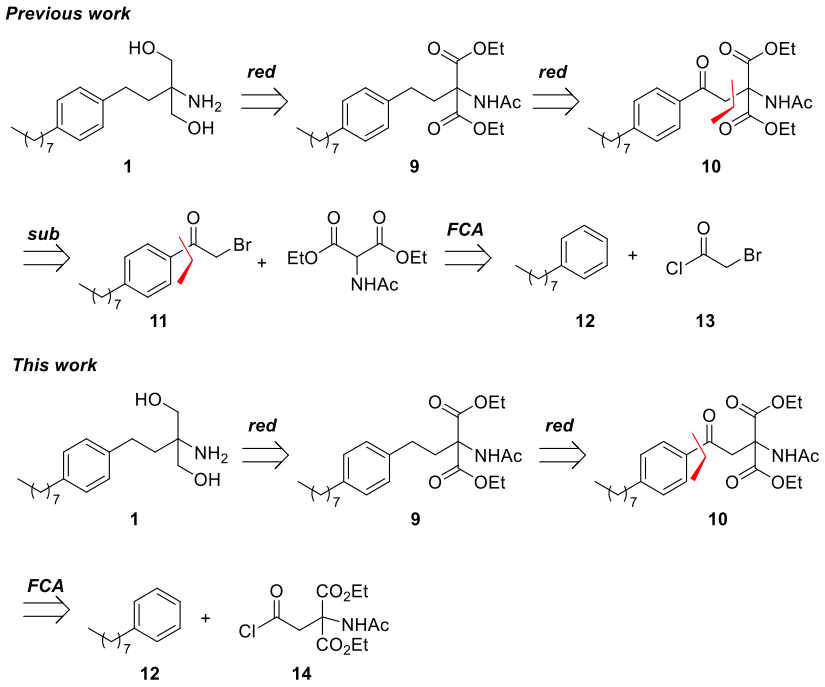


***Scheme 4.2: Retrosynthetic analysis of fingolimod, adapting a known literature synthesis by Kiuchi et al, to facilitate a convergent synthesis***

Nucleophilic substitution of bromide **15** and *tert*-butyl ester hydrolysis generated carboxylic acid precursor **17** in reasonable yields (Scheme 4.3). Treatment of the acid **17** with thionyl chloride led to acyl chloride formation *in situ* as confirmed by mass spectrometry (MS). However, upon isolation of the acyl chloride, significant hydrolysis back to the carboxylic acid was observed. Therefore, a one-pot activation/Friedel-Crafts protocol was attempted, both *via* the acyl chloride and the anhydride intermediate, but no conversion was observed.

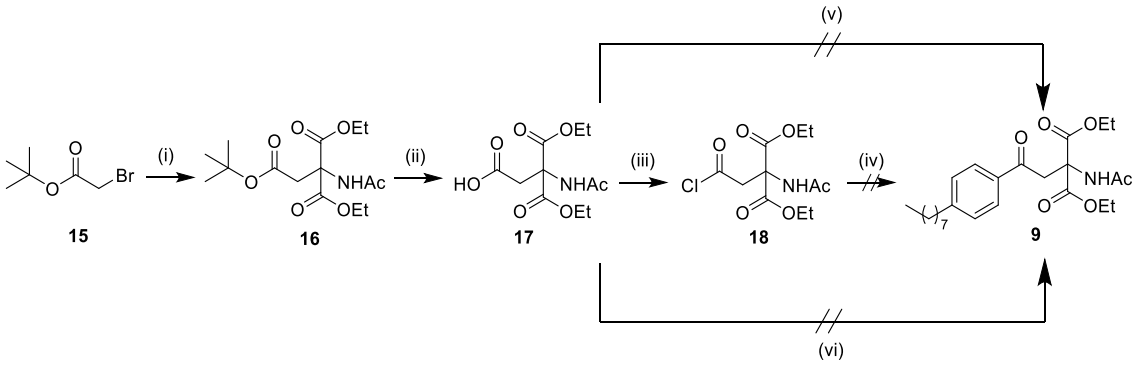

***Scheme 4.3: Reagents and conditions**: (i) diethylacetamidomalonate (3.0 eq), NaH (4.5 eq), THF:DMF, rt-65 °C, 24 h, 64% (ii) TFA, $CH_2Cl_2$, rt, 30 min, 97% (iii) $SOCl_2$, $CH_2Cl_2$, rt, 1 h, 100% (iv) $AlCl_3$ (1.4 eq), c-hexane, rt, 16 h (v) $SOCl_2$ (2.0 eq), c-hexane, rt then $AlCl_3$ (1.4 eq), octylbenzene (1.0 eq), rt-60 °C, 16 h (vi) octylbenzene (2.0 eq), TFAA:$H_3PO_4$ (4:1), reflux, 2 h.*

To overcome these issues, it was decided to continue with the reported linear synthesis, which would bypass the problematic later-stage acylation (Scheme 4.4).[273]

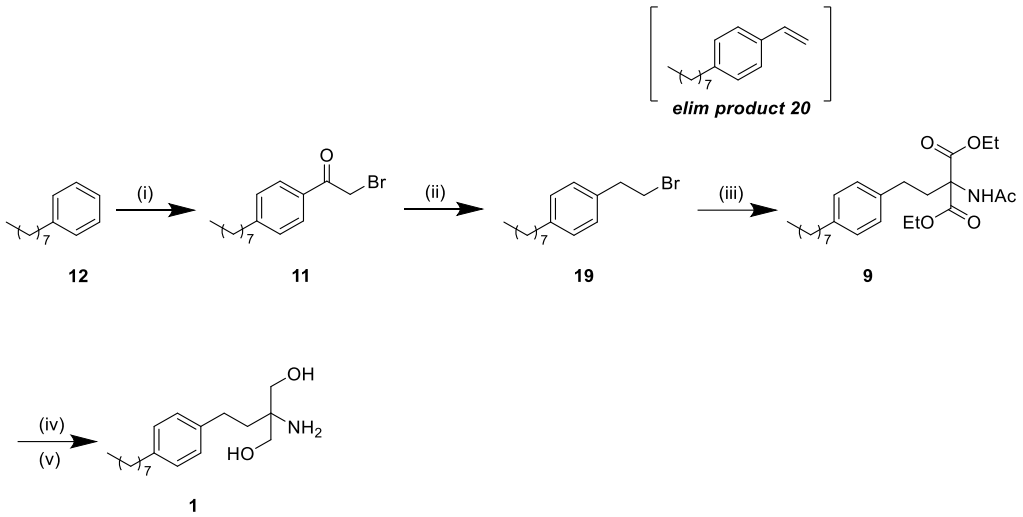


***Scheme 4.4: Reagents and conditions:** (i) $AlCl_3$ (1.4 eq), c-hexane, 10 °C-rt, 16 h, 96% (ii) $HSiEt_3$ (2.2 eq), TFA, 10 °C-rt, 16 h; 91% (iii) diethylacetamidomalonate (1.5 eq), $Cs_2CO_3$ (3.0 eq), DMSO, 60 °C, 24 h, 55% (vi) $NaBH_4$ (3.0 eq), THF, rt, 16 h (v) NaOH, MeOH, 70 °C, 5 h, over 2 steps 60%.*

Starting from alkyl benzene **12**, a Friedel-Crafts acylation with bromoacetyl chloride yielded $\alpha$-bromoketone **11.** This bromoketone was then converted to bromide **19** *via* a triethylsilane-mediated ketone reduction in good yield. The alkylation of diethylaminoacetamidomalonate with bromide **19** required further optimisation to minimise the formation of a styrene side product **20** *via* a competing elimination reaction (Table 4.1). Lowering the reaction temperature and employing an aprotic polar solvent favoured the substitution reaction (Entries **4**-**6**). The insolubility of the malonate anion generated *in situ* also proved problematic, therefore addition of DMF (Entries **7-8**) was trialled but ultimately DMSO was chosen as the optimal solvent to overcome these issues (Entry **9**). Once optimised, a $NaBH_4$-mediated reduction and acetamide deprotection yielded fingolimod in 29% overall yield.

***Table 4.1: Conditions trialled for the alkylation of alkyl bromide 19 with diethylacetamidomalonate.***

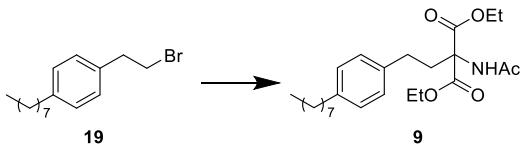


| *Entry* | *Solvent* | *T (°C)* | *Scale (mmol)* | *Base* | *20:9** | *Yield‡* |
|---|---|---|---|---|---|---|
| 1 | EtOH | 80 | 1.50 | NaOEt | 36:1 | 5% |
| 2 | dry EtOH | 80 | 0.07 | NaOEt | 2:9 | - |
| 3 | dry THF | 80 | 0.07 | NaOEt | 2:13 | - |
| 4 | dry MeCN | 65 | 0.07 | NaOEt | 1:8 | - |
| 5 | dry THF | 65 | 0.07 | NaOEt | 1:25 | - |
| 6 | dry THF | 65 | 0.07 | NaH | 1:50 | 12% |
| 7 | dry THF:DMF (3:1) | 65 | 1.68 | NaH | 1:50 | 16% |
| 8 | dry THF:DMF (1:1) | 65 | 1.68 | NaH | 1:50 | 45% |
| 9 | DMSO | 65 | 1.68 | $Cs_2CO_3$ | 1:50 | 55% |

** as determined by $^1$H NMR*
*‡ isolated yield*

A shorter synthetic route towards fingolimod employed the novel photocatalytic hydroaminoalkylation (HAA) methodology developed by Askey *et al*.[274] This methodology proceeded *via* photocatalytic activation by 427 nm light to facilitate formation of a serinol $\alpha$-amino radical which undergoes terminal addition to the styrene to generate the desired product (Scheme 4.5).

This methodology has been shown to work over a broad scope of amine and styrene reagents, showing promise for its compatibility with our desired synthetic route. To test the methodology, fingolimod was synthesised from serinol and *para*-octyl styrene. *Para*-octyl styrene **20** was freshly synthesised due to its propensity for polymerisation. This was achieved

by modifying the reaction conditions of the previous fingolimod synthesis (Scheme 4.4) to favour elimination over nucleophilic substitution, by increasing the reaction temperature (60 -> 80 °C), switching to a protic solvent (DMSO -> EtOH) and stronger base ($Cs_2CO_3$ -> NaOH). This modified route achieved synthesis of fingolimod in 4 steps, with an overall yield of 49%.

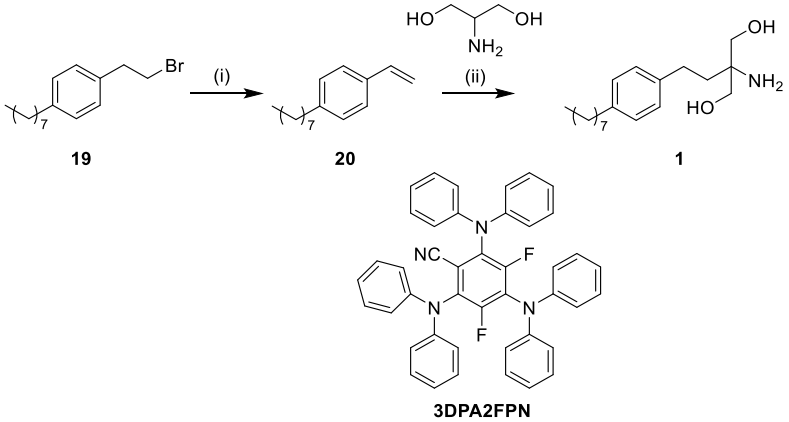


***Scheme 4.5: Reaction conditions:*** (i) NaOH (2.0 eq), EtOH, 80 °C, 90% (ii) serinol (1.0 eq), $[NBu_4][N_3]$ (10 mol%), 3DPA2FPN (1 mol%), DMF (0.15 M), rt, 427 nm, 20 h, 60%.

## 4.3 Synthetic routes towards a fingolimod-derived photocatalytic probe

As previously mentioned, it was desirable to develop a photocatalytic probe capable of microenvironment mapping to try and understand more about the pathways being modulated in response to fingolimod.[182] It was important to consider the *in cellulo* enantioselective metabolism of fingolimod to the bioactive Fing-P during the design of both active and inactive probes. If possible, a facile synthesis of both enantiomers of the ether-linked fingolimod photocatalytic probe **4** would hopefully allow for a structure-matched pair of functional and inactive probe compounds (Figures 4.4 & 4.5). It was postulated that photocatalytic probe **(*R*)-4** could be synthesised from octylstyrene **20** and a functionalised serinol head group (Scheme 4.6).

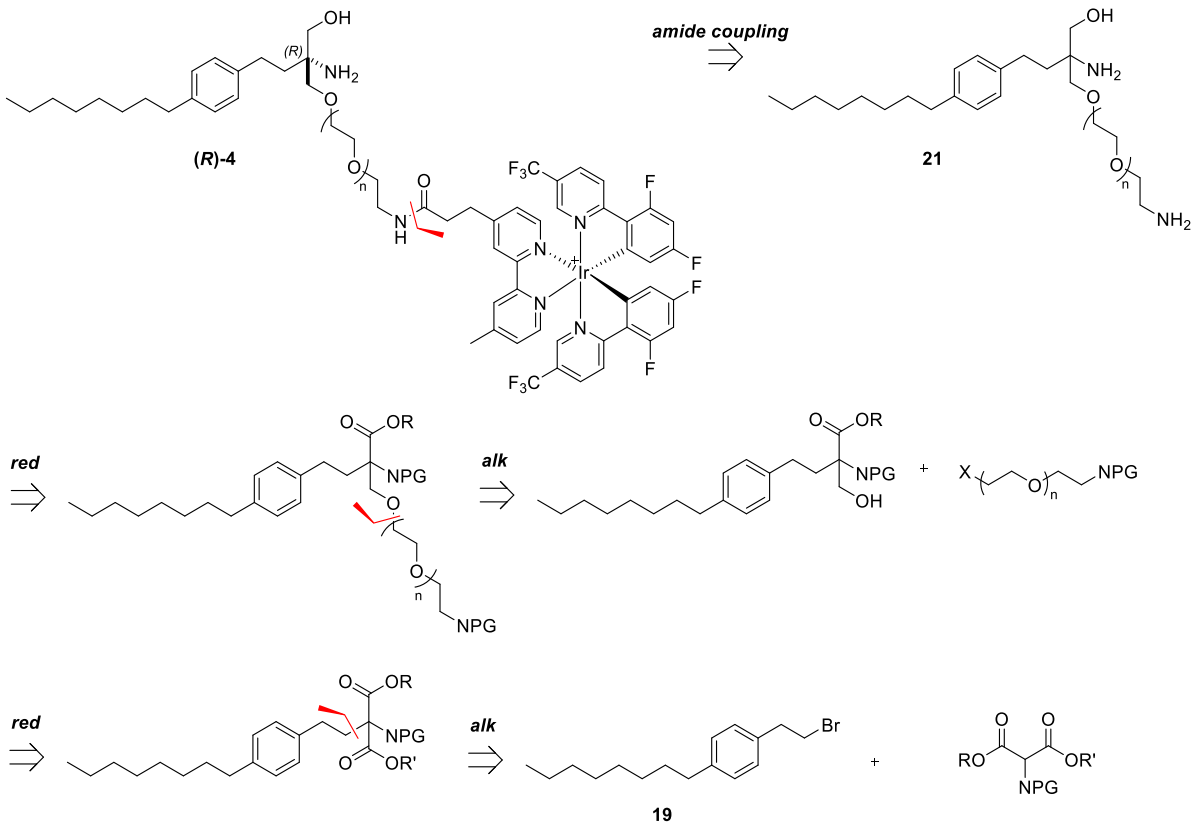


***Scheme 4.6: Retrosynthetic analysis of the iridium-coordinated photocatalytic probe (R)-4.***

To generate the necessarily PEG-functionalised serinol derivative, selective modification of the malonate prior to alkylation was explored as it was theorised that differing esters would provide orthogonal handles for modification (Scheme 4.6). Literature precedent reported that the reduction of a pentafluorophenyl (PFP) ester in the presence of an ethyl ester could be performed with $SmI_2{\cdot}H_2O$.[275] Malonate **23** was synthesised *via* monohydrolysis of diethylacetamidomalonate and subsequent esterification (Scheme 4.7). Nonetheless, alkylation of malonate **23** to yield compound **24** was unsuccessful. $D_2O$ quenching MS experiments were performed to assess whether the PFP malonate **23** was being deprotonated. However, after exposure to a variety of bases (NaH, $Et_3N$, $Cs_2CO_3$, DBU) at differing temperatures (50-80 °C) and reaction times (30 min-24 h), no deuterated PFP malonate adducts were observed by MS. This was surprising, as PFP esters have been shown to increase $\alpha$-H

acidity.[276] Therefore, it is speculated that the added steric hindrance around the tertiary centre could be a contributing factor to the lack of reactivity at this position.

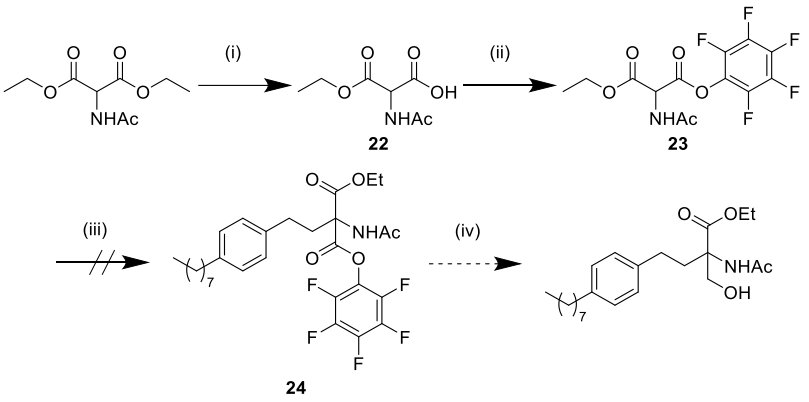


***Scheme 4.7: Reagents and conditions:*** *(i) KOH (1.0 eq), 1,4-dioxane, rt, 3 h, 87% (ii) pentafluorophenol (1.5 eq), DCC (1.1 eq), CH2Cl2, 0 °C-rt, 24 h, 45% (iii) NaH (2.0 eq),* ***19*** *(1.0 eq), THF:DMF, 65 °C, 24 h (iv) SmI2 (0.1 M in THF),* THF, $H_2O$ (25 eq), $N_2$, rt, 15 min.

It was then theorised that the less-bulky serinol head group of fingolimod could be modified directly, streamlining the synthesis. The protection of 1,2-amino alcohols as various heterocycles is well established in the literature,[277-279] and upon amine protection this would provide a handle for mono-alkylation of the free alcohol (Scheme 4.8).[277-282] The conversion of fingolimod to oxazolidine **25** was unsuccessful under both Brønsted (Table 4.2, Entry **1**) and Lewis (Entry **2**) acidic conditions, with only starting material and the monoalkylated acyclic intermediate **28** being observed. A biocatalytic route (Entry **3**) was attempted with *Candida Antarctica Lipase B* (CALB) and dimethylcarbonate but there was no observed conversion. Oxazolidinone **26** synthesis was attempted with carbonyldiimidazole (CDI), benzylchloroformate and triphosgene (Entries **4-6**), however, it was only successful when using diphosgene (Entry **7**) which demonstrated excellent conversion, likely due to its more reactive nature. Oxazolidinone **26** was Boc-protected to facilitate selective functionalisation of the primary alcohol.

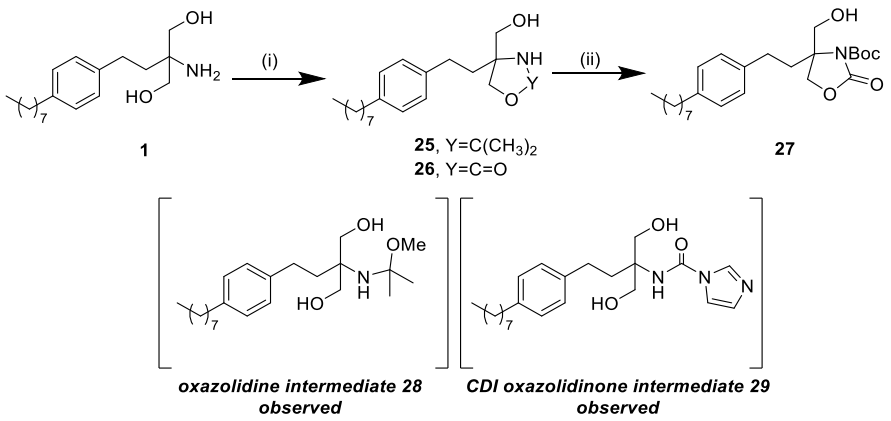


***Scheme 4.8: Reagents and conditions:*** *(i) see* ***Table 4.2*** *(ii) $(Boc)_2O$, $Et_3N$, rt, 3 h (49%)*

***Table 4.2: Routes attempted for the cyclisation of fingolimod***

| *Entry* | *Reaction conditions (i)* | *Yield* | *Prod* |
|---|---|---|---|
| 1 | dimethoxypropane (2.0 eq), *p*-TSA (0.1 eq), acetone, 24 h, reflux, 4Å molecular sieves | nr | **25** |
| 2 | dimethoxypropane (2.0 eq), $BF_3 \bullet Et_2O$ (0.1 eq), acetone, 24 h, reflux, 4Å molecular sieves | nr | **25** |
| 3 | CALB, dimethylcarbonate (2.0 eq), 1,4-dioxane, rt, 24 h | nr | **25** |
| 4 | CDI (1.0 eq), anh. THF, 24 h, 0-50 °C, 4Å molecular sieves | nr | **26** |
| 5 | benzylchloroformate (3.0 eq), 2.0 M NaOH, rt, 2 d | nr | **26** |
| 6 | triphosgene (1.0 eq), $Et_3N$ (2.0 eq), THF, 0 °C-rt, 6 h | nr | **26** |
| 7 | diphosgene (1.0 eq), 6.0 M NaOH, rt, 6 h | 82% | **26** |

A variety of synthetic routes were explored to achieve the selective functionalisation of the free alcohol of oxazolidinone **27** (Table 4.3). Initial studies attempted to methylate the primary alcohol utilising methyl iodide and various bases (Entries **1-2**), however these were unsuccessful and only starting material remained. Trimethyloxonium tetrafluoroborate was used as a more electrophilic methylating agent (Entry **3**), however this also yielded no desired conversion. In an attempt to reverse the reactivity at this position, mesylation (Entry **4**) and

Appel iodination (Entry **5**) of alcohol **27** were attempted to generate a suitable leaving group for nucleophilic substitution. Nonetheless, likely due to the steric hindrance around the alcohol group, no functionalisation was observed. To generate an alternative potential negative control species, instead of blocking the free alcohol it was attempted to remove the alcohol to develop a probe analogous to compound **2** (Figure 4.3). This was attempted *via* a radical deoxygenation of a brominated (Entry **6**) or Barton-McCombie intermediate (Entry **7**), however, this was again unsuccessful and chemical manipulation of this oxazolidinone intermediate was abandoned.

***Table 4.3: Synthetic attempts to functionalise oxazolidinone 27***

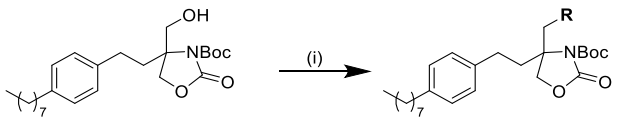


**27**

| *Entry* | *R =* | *Reaction conditions (i)* | *Yield* |
|---|---|---|---|
| 1 | OMe | NaH, MeI, THF | nr |
| 2 | OMe | *n*BuLi, MeI THF | nr |
| 3 | OMe | Proton sponge, $[Me_3O][BF_4]$, $CH_2Cl_2$ | nr |
| 4 | OMs | MsCl, DIPEA, DCM | nr |
| 5 | I | $PPh_3$, $I_2$, imidazole, THF | nr |
| 6 | H | $PBr_3$, AIBN, $Bu_3SnH$, DCE, toluene, reflux | nr |
| 7 | H | Phenylchlorothioformate, pyridine, DMAP, AIBN, $Bu_3SnH$, toluene | nr |

An alternative synthetic route was devised to enable selective alkylation of only one alcohol in the serinol head group through modification of the malonate head group *via* mono ester hydrolysis and chemoselective reduction. Limiting the equivalents and rate of KOH addition

provided control to achieve monohydrolysis of **9** in good yield (Scheme 4.9). From the carboxylic acid derivative **30**, two routes of selective reduction were explored; borane-mediated carboxylic acid reduction and $LiBH_4$-mediated ester reduction, both to the primary alcohol. Selective acid **30** reduction to give alcohol **32** showed poor conversion, whereas acid **31** was successfully synthesised in 40% yield, by NMR. However, separation of the alcohol product from acid was problematic. These complications with purification as well as the relative successes of parallel routes resulted in this synthesis being abandonned.

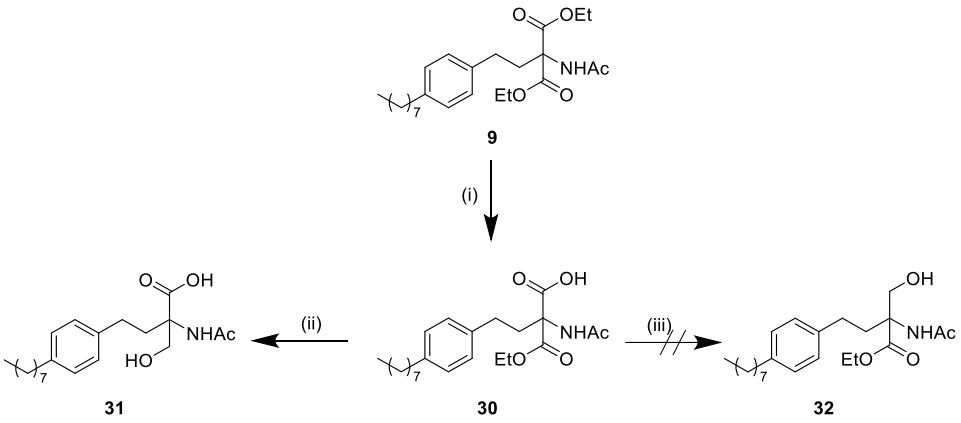


***Scheme 4.9: Reagents and conditions:*** *(i) 1.0 M KOH, 1,4-diozane, rt, 3 h, 87% (ii) $LiBH_4$ (2.0 eq), THF:iPrOH, 10 °C, 2 h, 40% (iii) $BH_3$·THF, 0 °C, $N_2$, 2 h*

Throughout the synthetic routes attempted there were numerous complications due to the steric hindrance around the quaternary head group in fingolimod and its analogues. Therefore, a different disconnection was proposed which would allow modification of a less hindered tertiary head group which could undergo late-stage addition. This route would also minimise the inherent purification issues with such a polar, lipid-like small molecule. It was proposed to utilise the HAA methodology to facilitate this route (Scheme 4.10).

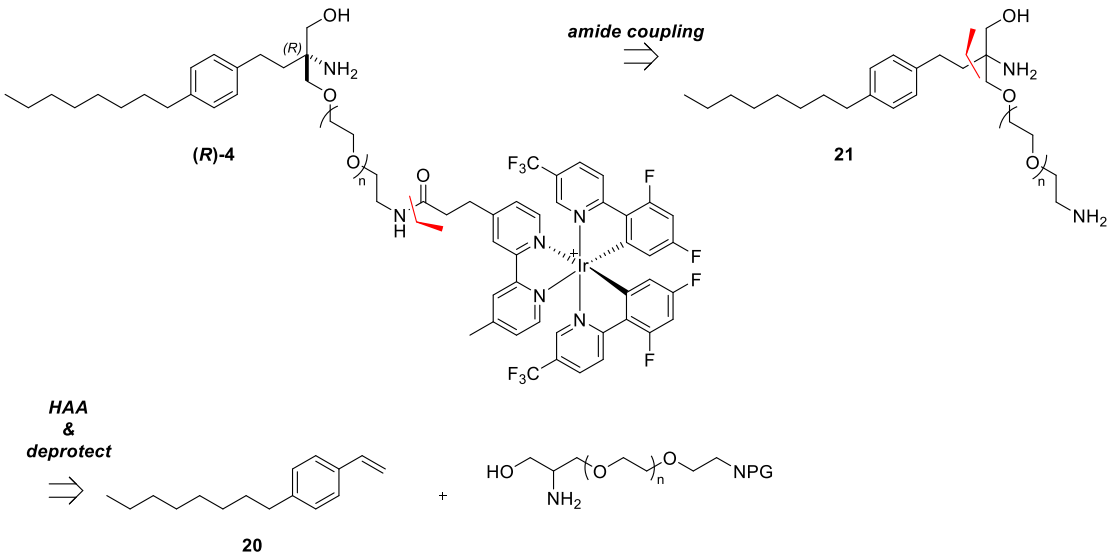


***Scheme 4.10: Retrosynthetic analysis of the iridium-coordinated photocatalytic probe (R)-4, incorporating HAA chemistry.***

The previously rationalised designs for the photocatalytic probe **(*R*)-4** would require a serinol derived headgroup, desymmetrised with the addition of an ether-linked PEG linker with an orthogonal handle for subsequent coupling of the iridium catalyst. The initial designs incorporated a $PEG_3$ chain with a terminal azide which could be reduced and subsequently coupled to the bipyridyl iridium ligand. To generate the desired linker, tetrapropyleneglycol was mesylated followed by selective azide substitution to generate linker **34** which underwent nucleophilic substitution with *N*-trityl serine methyl ester to yield ester **35** (Scheme 4.11). $LiBH_4$-mediated reduction and subsequent acid-catalysed trityl deprotection yielded primary amine **36** as the desired HAA precursor. Unfortunately, azide **37** was not compatible with the HAA step, with no desired product observed, potentially due to competing radical mechanisms.[283, 284] Therefore, an alternative handle was designed to allow late-stage incorporation of the iridium photocatalyst.

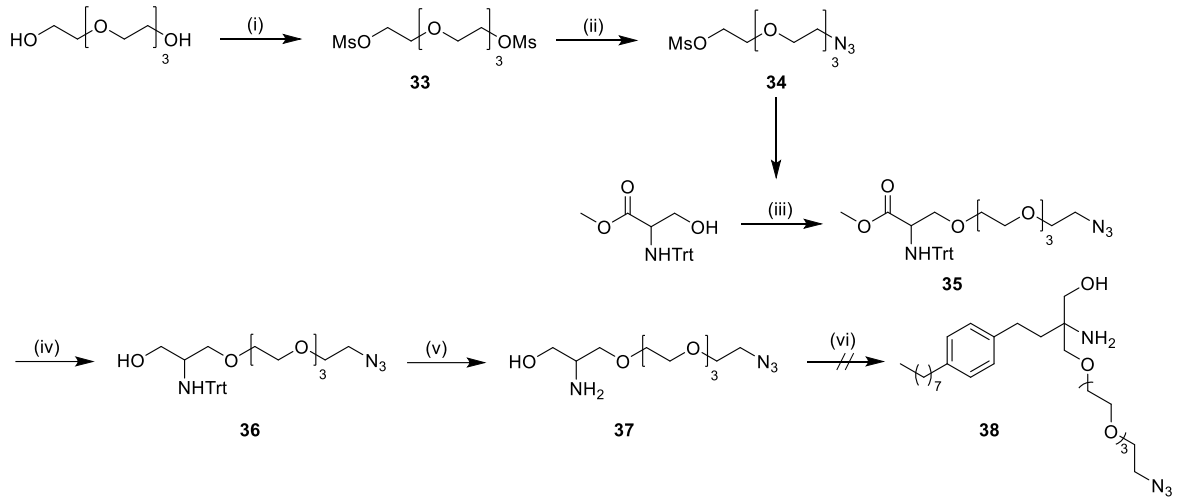


***Scheme 4.11: Reaction conditions:*** *(i) Mesyl chloride (2.3 eq), $Et_3N$ (2.4 eq), 2-MeTHF, 0 °C-rt, 4 h, 72% (ii) $NaN_3$ (1.1 eq), EtOH, 80 °C, 16 h, 22% (iii) methyl tritylserinate (1.1 eq), NaH (1.2 eq), DMF, 0-40 °C, 6 h, 49% (iv) $LiBH_4$ (2.0 eq), THF, 0 °C-rt, 4 h (v) $CH_2Cl_2$:TFA (2:1), rt, 1 h, 37% over 2 steps (vi) 3DPA2FBN (1 mol%), $[NBu_4][N_3]$ (10 mol%), DMF, 427 nm, rt, 20 h.*

A benzyl-protected amine was deemed a compatible handle for iridium catalyst coordination, due to the orthogonality of its deprotection with trityl. Benzylamine **40** was synthesised *via* reductive amination of amine **39** with benzaldehyde (Scheme 4.12). Unfortunately, attempts to selectively mesylate the alcohol were unsuccessful with the major observed product being the double mesylation product. To overcome this, a bulkier tosylate was proposed to shift the regioselectivity of the protection towards the less hindered alcohol. This was successful, with tosylate **41** synthesised in good yields. Attempts to substitute this tosylate with *N*-trityl serine methyl ester were unsuccessful, with no reaction observed even at higher temperatures (120 °C). Therefore, an alternative route to probe **(*R*)-4** was explored.

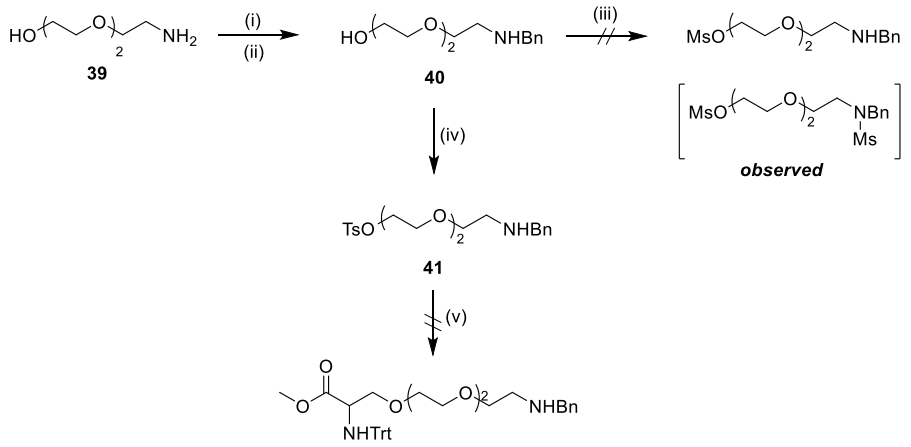


***Scheme 4.12: Reaction conditions:*** *(i) benzaldehyde (1.2 eq), $CH_2Cl_2$, 4 Å molecular sieves, rt, 18 h (ii) $NaBH_4$ (2.0 eq), THF, rt, 3 h, 58% over 2 steps (iii) MsCl (1.0 eq), NaH (2.0 eq), THF, 0 °C-rt, 4 h (iv) TsCl (1.0 eq), NaH (2.0 eq), THF, 0 °C-rt, 4 h, 78% (v) N-trityl serine methyl ester (1.2 eq), NaH (1.5 eq), DMF, 120 °C, 48 h.*

Due to the incompatibility of *N*-trityl serine methyl ester to form the tertiary centre of the serinol head group, an alternative scaffold was explored. It was hypothesised than an aziridine could pose as a complementary electrophile for a ring opening addition of the PEG linker (Scheme 4.13).[285] Aziridine **43** was synthesised from alcohol **42** under dilute basic conditions (0.05 M) to prevent competing intermolecular cyclisation or polymerisation reactions. Ring opening of the aziridine with alcohol **40** yielded a mixture of the desired amine **44** but also the sequential ring closing product **45**. Attempts to reopen the aziridine with hydroxide anions in the presence of Lewis acid catalysts were unsuccessful, making this a low yielding step as a result. Lithium naphthalenide-mediated detosylation of **44** yielded primary amine precursor **46,** which was subjected to HAA conditions to produce fingolimod derivative **47**. The low yielding nature of this chemistry meant that the deprotected amine **48** could not be isolated after hydrogenation, due to the small scale and potential chelation of the product to the palladium catalyst during purification.

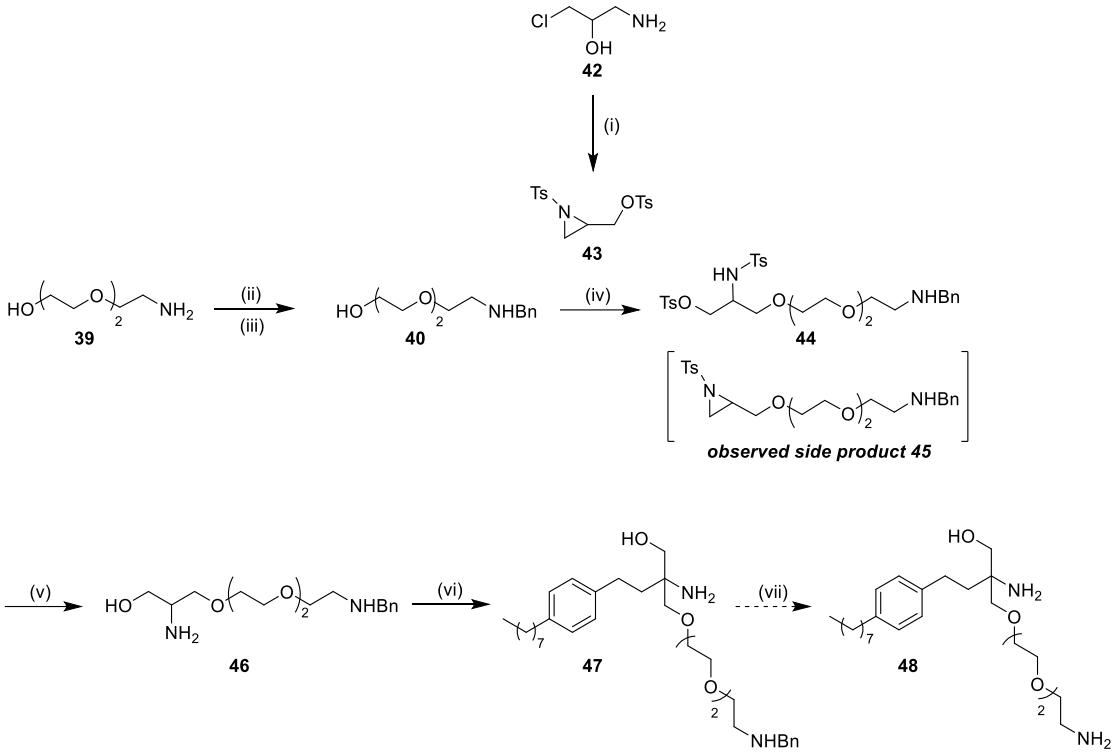


***Scheme 4.13: Reaction conditions:*** *(i) TsCl (1.2 eq), $Et_3N$ (2.0 eq), $CH_2Cl_2$ (0.1 M), rt, 6 h then addition of TsCl (1.2 eq), KOH (2.0 eq), $H_2O$ (0.05 M), rt , 18 h, 81% (ii) benzaldehyde (1.2 eq), $CH_2Cl_2$, 4 Å molecular sieves, rt, 18 h (iii) $NaBH_4$ (2.0 eq), THF, rt, 3 h, 58% over 2 steps (iv) KO$^t$Bu (2.0 eq), DMF, 120 °C, 18 h,* ***44:*** *16%,* ***45:*** *19% (v) Li (10 eq), naphthalene (10 eq), THF, –78-0 °C, 2 h, 43% (vi)* ***20*** *(1.0 eq), 3DPA2FBN (1 mol%), $[NBu_4][N_3]$ (10 mol%), DMF, 427 nm, rt, 20 h, 1% (vii) Pd/C, $H_2$, MeOH, rt, 2 h.*

Due to time limitations, exploration towards a fingolimod-derived photoaffinity probe was prioritised, and this route was discontinued. However, with adequate re-scaling, the penultimate coupling of amine **48** to the iridium ligand and subsequent iridium coordination, could yield the desired fingolimod-derived photocatalytic probe to be used in future labelling studies to probe the microenvironment of fingolimod's targets.

## 4.4 Synthetic routes towards a fingolimod photoaffinity labelling probe

The initial design of PAL probe **(*R*)-5** incorporated an ether-linked diazirine alkyne to the pro-(*R*) alcohol of fingolimod's head group. However, due to the aforementioned lack of success trying to functionalise fingolimod's head group, an alternative design was explored (Figure 4.6). The diazirine moiety was still the most favourable photolabile functionality to integrate

into the PAL probe design **49**. The diazirine was placed at the benzylic position proximal to the polar head group of fingolimod, this was justified in part by the broader reactivity of benzylic diazirines relative to alkyl diazirines,[286] but also with the intention of minimising electrostatic interference and improving synthetic tractability. Moreover, to minimise hydrophobic interaction interference, the alkyne handle was placed at the terminal position of the already lipophilic alkyl tail of fingolimod.

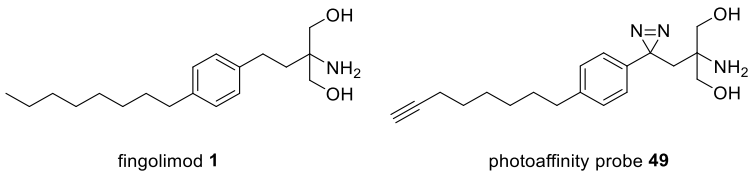


***Figure 4.6: Second generation photoaffinity probe design.*** *Photoaffinity probe **49** consists of a benzylic diazirine proximal to the polar head group, and a terminal alkyne.*

Docking studies were performed to assess whether the structural modifications present in probe **49** would still be tolerated, therefore $S1PR_1$ was used as a model protein in which to dock **49** (Figure 4.7). Fortunately, the benzylic diazirine appeared to be tolerated, with the added potential to act as a hydrogen bond acceptor.

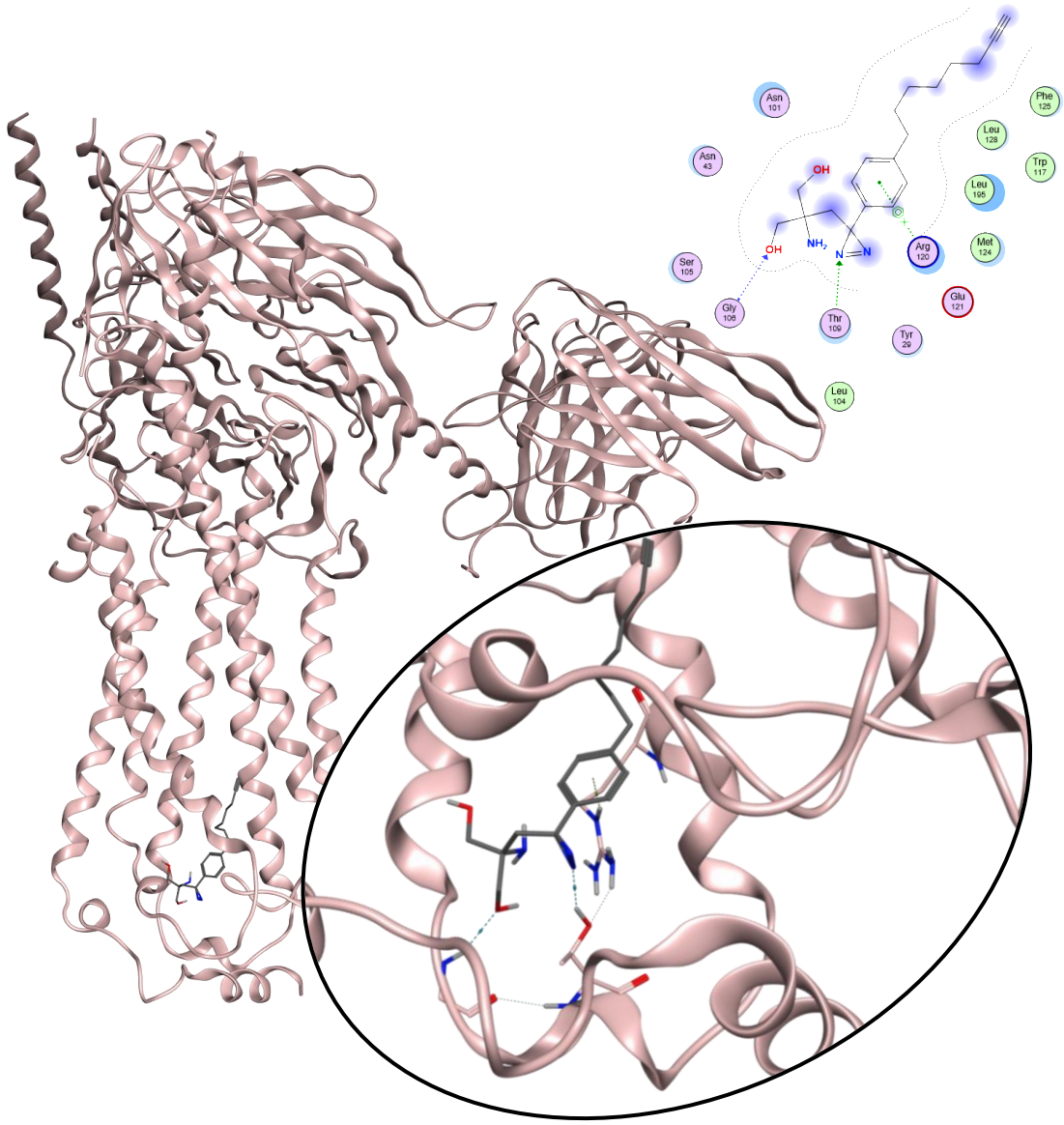


***Figure 4.7: Docking of PAL probe 49 in S1PR$_1$ (PDB: 7WF7).***[267] *Key electrostatic interactions between the pocket residues and the diazirine are highlighted. PAL probe* ***49*** *was docked in the S1PR$_1$-binding pocket by MOE, using triangle matcher/induced fit method. A GBVI/WSA scoring was used to calculate ΔG of the interaction. ΔG = −8.4526 kcal/mol. RMSD = 1.6537 Å.*

From a retrosynthetic analysis it was presumed that the diazirine could be synthesised from benzylic ketone **50** (Scheme 4.14). Previously utilised chemistry (Scheme 4.4) could be used to generate **50** from the terminal alkyne precursor **52**, which in turn could be generated from bromide **53**.

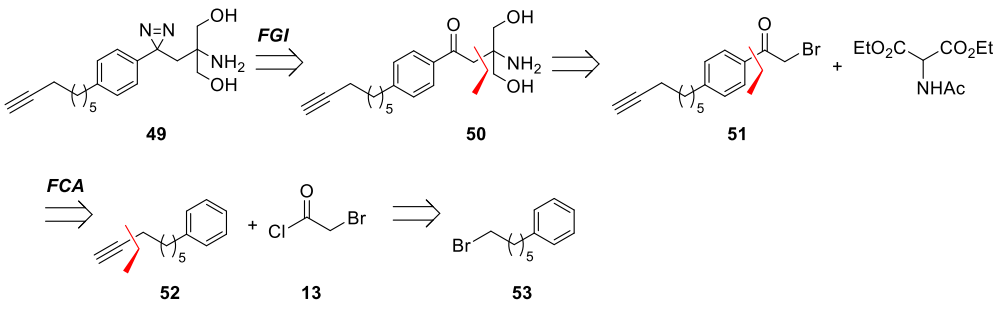


***Scheme 4.14: Retrosynthetic analysis of PAL probe 49, aiming to incorporate the terminal alkyne early in the synthesis***

Before synthesising alkyne **51**, there were concerns over the nucleophilic terminal alkyne interfering with the desired Friedel-Crafts acylation. To circumvent this issue silyl-protected alkynes **54** and **55** were synthesised from alkyl bromide **53** in good yields (Scheme 4.15). However, the subsequent Friedel-Crafts acylation failed to produce the desired product. As previously discussed, terminal alkynes are susceptible to acylation, generating vinyl chlorides.[287] Hence, it was believed that the acidic Friedel-Crafts conditions promoted deprotection of the alkyne, allowing acylation of the alkyne to occur. This hypothesis is based on MS evidence ($[M+H]^+$ 463 m/z) and NMR analysis of the observed crude which showed the appearance of two peaks with an alkene chemical shift (6.56 & 6.23 ppm, Appendix IV), characteristic of a mixture of *E*/*Z* *β*-chlorovinyl ketone **56**.[287,288] Monitoring of the reaction by MS revealed that silyl deprotection occurred prior to acylation on the benzene ring. Milder Friedel-Crafts conditions utilising $AgNO_3$ were trialled,[289] however, deprotection and alkyne addition were still observed, therefore an alternative route was pursued to install the terminal alkyne at a later-stage in the synthesis to avoid its incompatibility with Friedel-Crafts acylation.

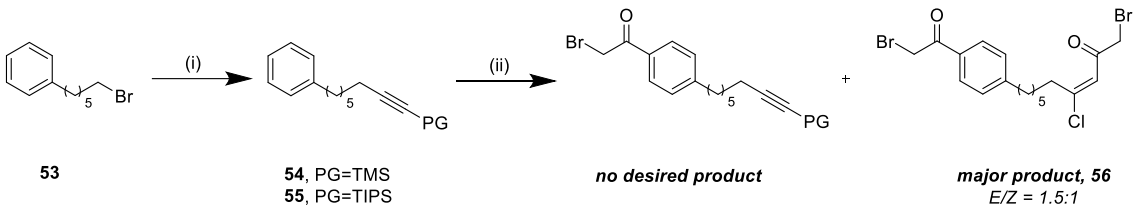


***Scheme 4.15: Reaction conditions:*** *(i) silyl acetylene (1.2 eq), n-BuLi 2.5 M in THF (1.2 eq), HMPA (1.1 eq), THF, −78 °C-rt, 16 h,* ***54:*** *96%,* ***55:*** *75% (ii) 2-bromoacetyl chloride (1.0 eq), $AlCl_3$ (1.0 eq), c-hexane, rt, 16 h.*

To overcome these issues of chemoselectivity, a new synthetic route was designed that incorporated the alkyne at a later stage. (Scheme 4.16). It was hypothesised that proceeding *via* a protected alcohol would be a more suitable handle for alkyne substitution. This proposed route would require a protected alcohol that was stable under both acidic and basic conditions.

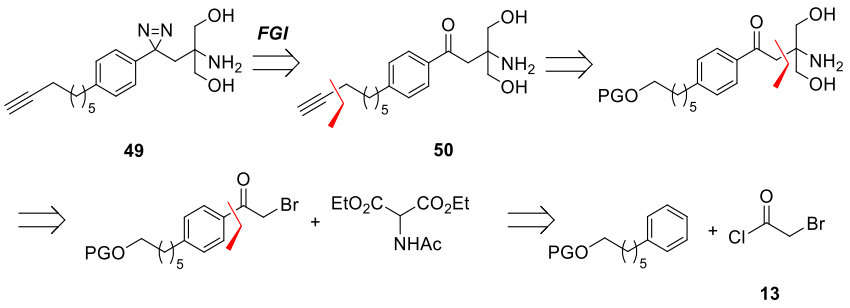


***Scheme 4.16: Retrosynthetic analysis of fingolimod-derived PAL probe 49, utilising a protected alcohol as a handle for late-stage terminal alkyne incorporation.***

A variety of protecting groups were screened, based on prior literature precedent (Table 4.4, Scheme 4.17).[290] Protecting 6-phenylhexanol as a methyl (**57**) or allyl ether (**58**) proved compatible with both the Friedel-Crafts acylation and malonate alkylation. Whereas, SEM (**59**), *para*-nitrobenzyl (**60**) and TBDMS (**61**) protecting groups all demonstrated cleavage under Friedel-Crafts conditions. Due to the harsh nature of the $BBr_3$-mediated deprotection of methyl ethers, it was decided that the allyl protecting group was a more suitable choice. A

Tsuji-Trost allylic deprotection of **64** yielded the primary alcohol **65** which was transformed into alkyl halides **66** and **67** *via* poor yielding Appel reactions. Subsequent attempts to install the terminal alkyne *via* a nucleophilic substitution were unsuccessful, with conversion of the starting material to a major by-product which failed to be characterised with any confidence. A Sonogashira cross-coupling with alkyl iodide **67**, was also attempted employing a Pd/N-heterocyclic carbene-based PEPPSI catalyst to facilitate the coupling of the unactivated alkyl iodide. This cross-coupling was successful and provided desired product **68** in 70% yield. Reaction efficiency was not significantly improved upon by increasing the bulkiness (iPr -> iPent) of the NHC ligand, which has been previously reported to encourage reductive elimination leading to higher catalyst turnover.[291] However, the low yielding iodination made scale up of this route difficult and alternative methods of functionalising the primary alcohol to facilitate alkyne insertion were explored.

***Table 4.4: Conditions used in the protection of 6-phenylhexanol***

| *Product* | *Conditions (i)* | *Yield* |
|---|---|---|
| 57 | NaH, MeI, THF, 0 °C-rt, 2 h | quant. |
| 58 | NaH, allyl bromide, THF, 0 °C-rt, 2 h | 94% |
| 59 | DIPEA, SEMCl, $CH_2Cl_2$, rt, 1 h | 96% |
| 60 | $K_2CO_3$, 4-nitrobenzyl bromide, rt, 16 h | quant |
| 61 | Imidazole, TBDPSCl, $CH_2CL_2$, rt, 2 h | 99% |

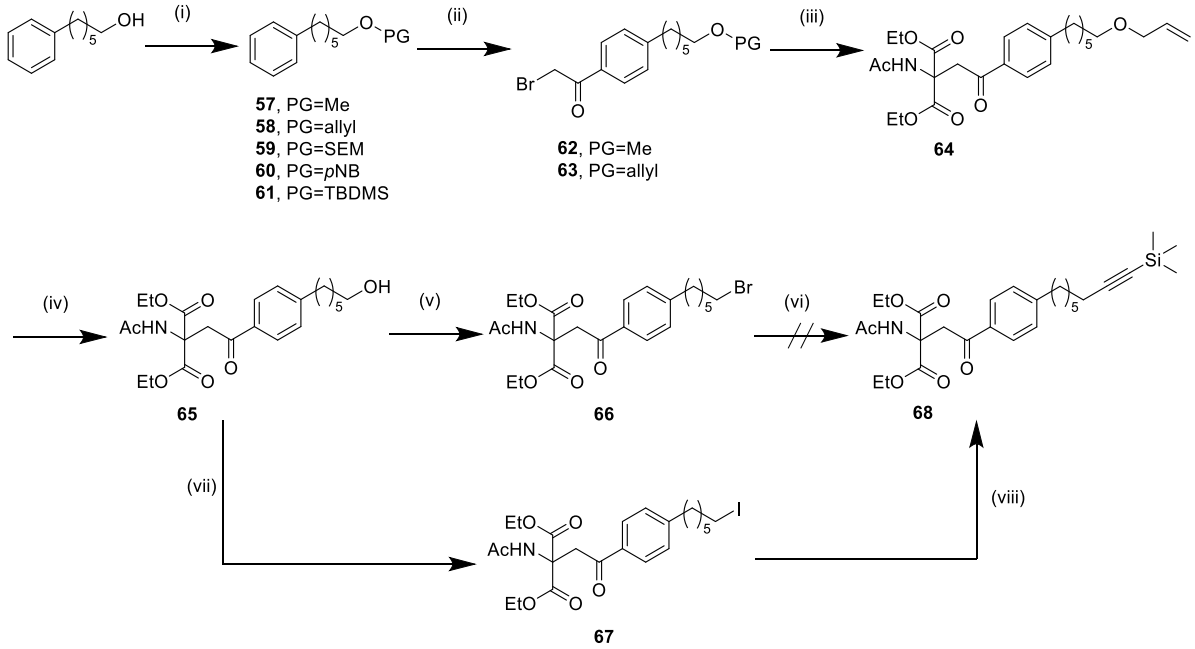


***Scheme 4.17: Reaction conditions:*** (i) see Table **4.4** (ii) 2-bromo acetyl chloride (1.0 eq), $AlCl_3$ (1.0 eq), c-hexane, rt, 16 h, **57:** 44% **58:** 41% (iii) diethyl acetamidomalonate (2.0 eq), $Cs_2CO_3$ (2.2 eq), DMSO, 60 °C, 16 h, 25% (iv) $Pd(PPh_3)_4$ (10 mol%), DMBA (2.0 eq), MeOH, rt, 16 h, 82% (v) $PPh_3$ (3.2 eq), $CBr_4$ (3.2 eq), $CH_2Cl_2$, 0 °C-rt, 48 h, 15% (vi) TMS acetylene (1.2 eq), *n*BuLi (2.5 M, 1.2 eq), HMPA (1.2 eq), THF, −78 °C-rt, 16 h (vii) $PPh_3$ (1.2 eq), $I_2$ (1.2 eq), imidazole (1.2 eq), $CH_2Cl_2$, 0 °C-rt, 48 h, 10% (viii) Pd-PEPPSI-iPr (10 mol%), CuI (7 mol%), $Cs_2CO_3$ (1.4 eq), TMS acetylene (2.0 eq), $Et_2O$:DMF (2:1), 40 °C, 16h, 70%.

The Bestmann-Ohira modification of the Seyferth-Gilbert homologation enables the facile conversion of an aldehyde to a terminal alkyne *via* a diazophosphonate intermediate and sequential eliminations in a Wittig-type manner.[292] A PCC-mediated oxidation of **65** yielded the desired aldehyde **69**, which under Bestmann-Ohira conditions led to selective

transformation over the benzylic ketone into the desired terminal alkyne **70** (Scheme 4.18). A global $LiAlH_4$-mediated reduction yielded benzylic alcohol **71**. Initial attempts to oxidise **71** to the desired ketone, employing freshly prepared $MnO_2$ as an oxidant were unsuccessful, with no conversion of starting material observed. It was first thought that the polar head group of the molecule could be sequestering the $MnO_2$ through chelation, but using excess $MnO_2$ still did not facilitate any oxidation and spiking the reaction mixture with benzyl alcohol led to conversion to benzaldehyde. It was then hypothesised that this position could be too sterically hindered for the oxidation to occur. Nonetheless, when less sterically demanding oxidative conditions were attempted ($NaBr/H_2O_2/AcOH$) no conversion was observed either. In an attempt to circumvent issues of undesired benzylic ketone reduction, the cyclic acetal **72** was synthesised, however alkyl bromide **72** was too sterically hindered to allow malonate substitution, so this route was abandoned.

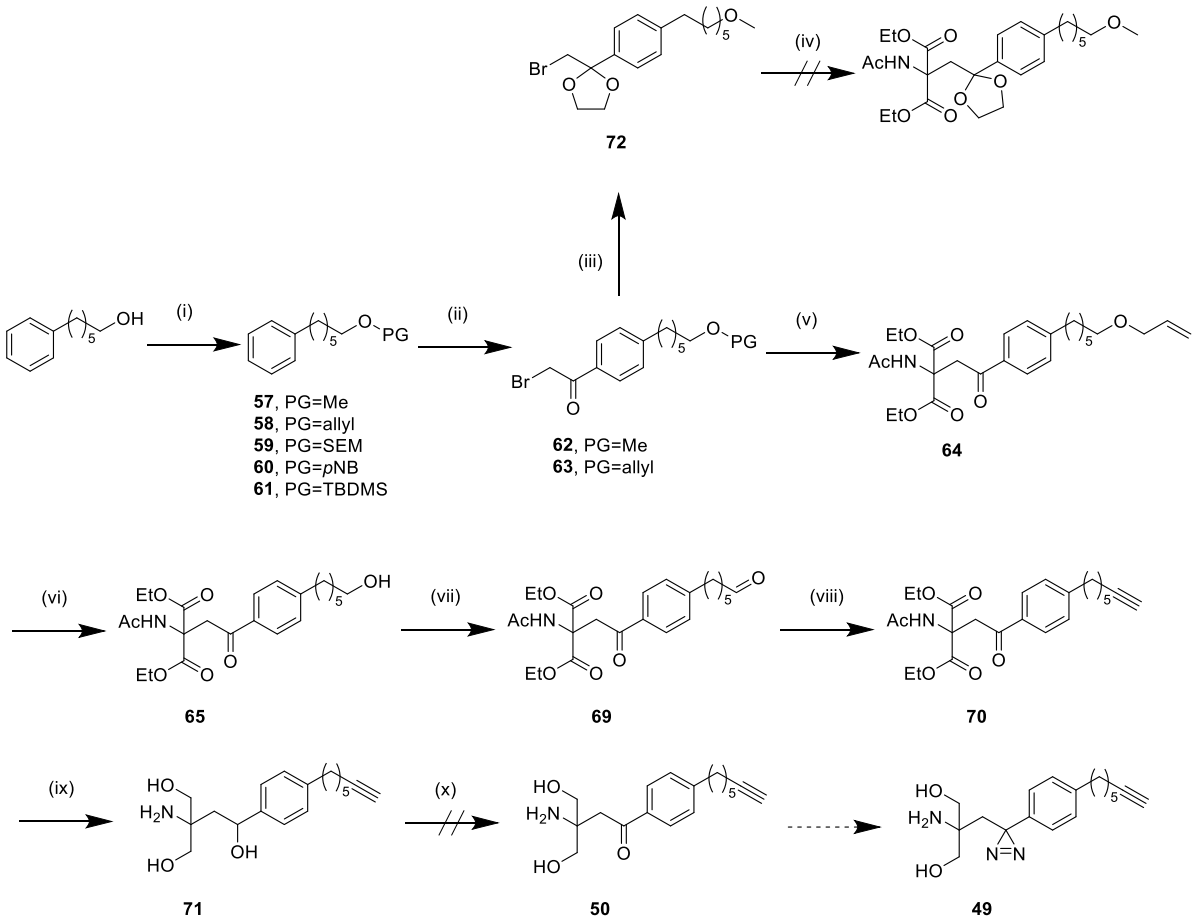


***Scheme 4.18: Reaction conditions:*** *(i) see* ***Table 4.4*** *(ii) 2-bromo acetyl chloride (1.0 eq), $AlCl_3$ (1.0 eq), c-hexane, rt, 16 h,* **62:** 44% **63:** 41% *(iii) ethylene glycol (1.5 eq), pTSA (1.0 eq), benzene, 90 °C, 48 h, 85% (iv) & (v) diethyl acetamidomalonate (2.0 eq), $Cs_2CO_3$ (2.2 eq), DMSO, 60 °C, 16 h,* ***64:*** *25% (vi) $Pd(PPh_3)_4$ (10 mol%), DMBA (2.0 eq), MeOH, rt, 16 h, 82% (vii) PCC (2.0 eq), DMSO (couple drops), $CH_2Cl_2$, rt, 16 h, 95% (viii) Bestmann-Ohira reagent (1.2 eq), $K_2CO_3$ (2.0 eq), MeOH, rt, 16 h, 16% (ix) $NaBH_4$ (4.0 eq), THF, rt, 16 h, 16% (x) $MnO_2$ (2.0 eq), THF, rt, 16 h.*

It was then decided to re-think the design strategy of the PAL probe as the positioning of the diazirine at the benzylic position proximal to the polar head group was repeatedly proving to be problematic. Therefore, the new PAL probe design **73** proposed placing the diazirine at the opposing benzylic position (Figure 4.8).

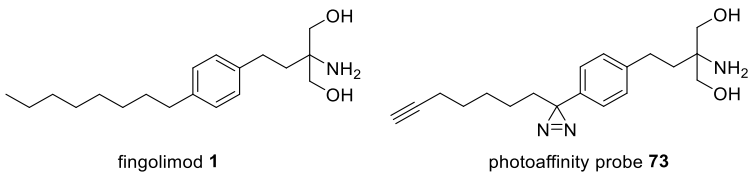


***Figure 4.8: Third generation of photoaffinity labelling probes.*** *The PAL probe design* ***73*** *incorporated a diazirine at the opposing benzylic position lateral to the polar head group.*

It was proposed that similar Bestmann-Ohira chemistry could be utilised for late-stage terminal alkyne incorporation from an acetal-protected aldehyde (Scheme 4.19). This functionalised alkyl chain could be introduced *via* Sonogashira coupling, allowing for selective hydration of the alkyne to yield the necessary benzylic ketone for diazirine formation. There are several precedented synthetic routes which facilitate the conversion of a ketone to a diazirine. Starting from the tosyloxime derivative, in the presence of lithium amide/ $NH_{3\,(l)}$ yields the desired diazirine in a one-pot reaction.[295] Similarly, the reaction of a ketone and LiHMDS/$NH_{3\,(l)}$ generates the diaziridine precursor which can be readily oxidised under basic conditions (i.e. KOH) to form the desired diazirine. However, the most commonly utilised synthetic route proceeds via $NH_3$-mediated imine formation and nucleophilic HOSA attack, followed by cyclisation and sulphate elimination to yield the diaziridine precursor which can be oxidised.

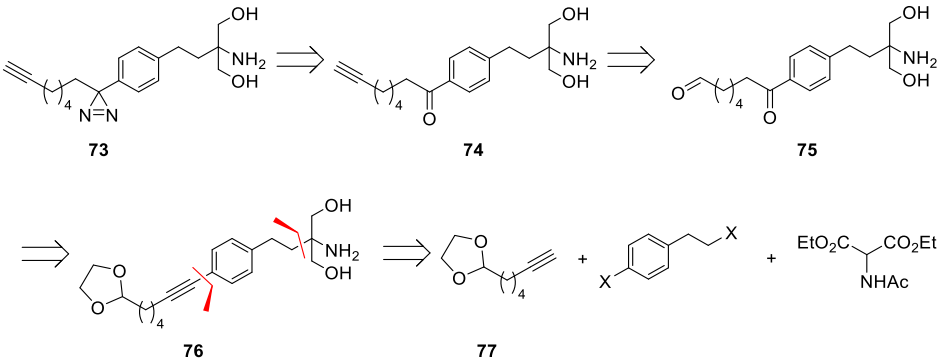


***Scheme 4.19: Retrosynthetic analysis of the second-generation design for PAL probe 73, facilitating late-stage incorporation of the terminal alkyne to overcome previous issues with regioselectivity.***

To facilitate the Sonogashira coupling, a terminal alkyne incorporating a protected aldehyde was required. Alkyne **77** was synthesised from hept-6-yn-1-ol, through a PCC-mediated oxidation and cyclic acetal formation (Scheme 4.20). Following precedented routes (Scheme 4.4), aryl bromide **88** was synthesised by Friedel-Crafts acylation, silane reduction and malonate alkylation. Attempts were made to synthesise the aryl iodide **86** due to its favoured reactivity for Sonogashira couplings, however substantial dehalogenation was observed after triethylsilane-mediated reduction. Similarly, triflate **87** was also explored as a highly reactive Sonogashira coupling reagent. From methoxy **85**, acid-catalysed demethylation yielded phenol **86**, however, efforts to form the triflate with a variety of triflating agents were unsuccessful. Despite this, the aryl bromide **88** demonstrated adequate reactivity towards alkyne **77** under Sonogashira coupling conditions and provided acetal **90** in 17% yield. Selective RedAl-mediated ester reduction yielded the diol **91**, however, despite promising indications using model substrates, the Au(I)-catalysed alkyne hydration yielded regioisomer **93**. Due to the time-consuming nature of this synthetic route, coupled with low yielding steps and expensive starting materials, an alternative route was devised to prepare the required PAL probe **73**.

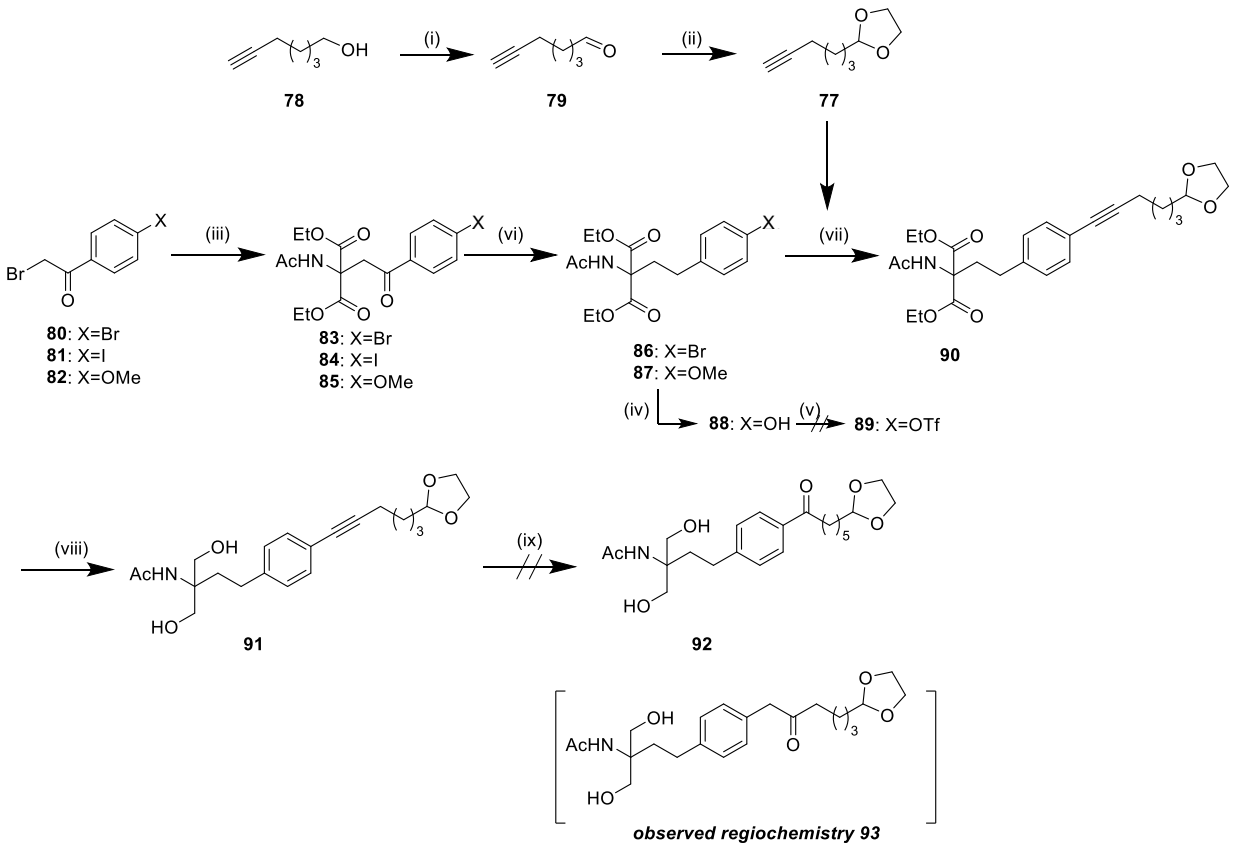


***Scheme 4.20: Reaction conditions:*** *(i) PCC (2.0 eq), $CH_2Cl_2$, rt, 16 h, quant. (ii) ethylene glycol (1.2 eq), pTSA (1.0 eq), benzene, 90 °C, 48 h, quant. (iii) diethyl acetamidomalonate (2.0 eq), Cs2CO3 (2.2 eq), DMSO, 60 °C, 16 h,* ***83:*** *30%,* ***84:*** *3%,* ***85:*** *70% (iv) $BBr_3$ (1.0 M, 3.0 eq), $CH_2Cl_2$, −5 °C-rt, 18 h, 85% (v) TfCl/$Tf_2O$/N,N-Bis(trifluoromethylsulfonyl)aniline (2.0 eq), $K_2CO_3$ (3.0 eq), THF, $N_2$, 0 °C-rt, 18 h (vi) $HSiEt_3$ (2.0 eq), TFA, rt, 16 h,* ***86:*** *45%,* ***87:*** *85% (vii) $Pd(PPh_3)_4$ (0.4 eq), CuI (0.2 eq), $Et_3N$ (10 eq), DMF, 80 °C, 16 h, 10% (viii) RedAl (5.0 eq), THF, 0 °C, 30 mins, 17% (ix) [(iPr)AuCl] (1000 ppm), $AgSbF_6$ (cat.), 1,4-dioxane:$H_2O$ (2:1), 120 °C, 16 h.*

To synthesise PAL probe **73**, it was postulated that benzylic ketone **74** could be synthesised from a Weinreb amide *via* a Grignard reaction with a complementary aryl bromide (Scheme 4.21).

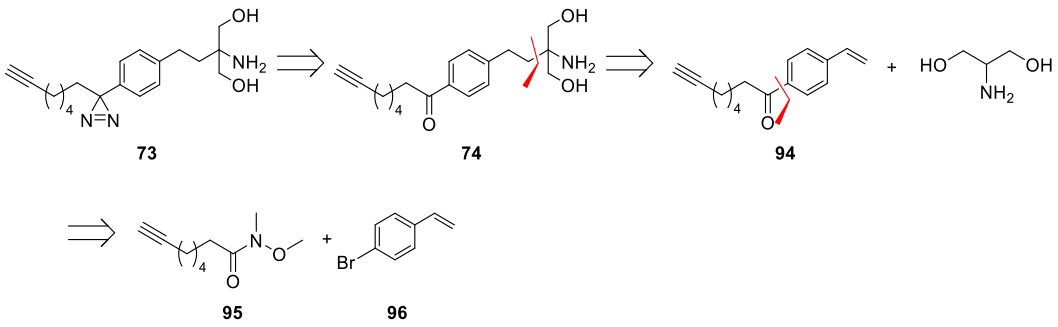


***Scheme 4.21: Retrosynthetic analysis of PAL probe 73, via hydroaminoalkylation***

Oct-7-yn-1-ol was oxidised with Jones reagent to yield carboxylic acid **97**, followed by amide coupling to synthesise Weinreb amide **95** (Scheme 4.22). After $I_2$-mediated activation of Mg granules, the organomagnesium reagent derived from bromide **96** was prepared *in situ*, before addition of the Weinreb to yield ketone **94** in 20% yield. Photocatalytic HAA with serinol enabled the incorporation of the amino diol head group and led to the formation of ketone **76** in 74% yield. Prior to the conversion of the benzylic ketone to a diazirine, the ketone was activated as a benzylimine,[293] followed by addition of condensed liquid ammonia and hydroxylamine-O-sulfonic acid (HOSA), however the diaziridine intermediate was not observed. It was suspected that the free amine of the serinol head group, as a competing nucleophile,[294] could be interfering with the diaziridine formation, so the diazirine formation was attempted with the styrene precursor **94**, as it had been confirmed that the diazirine would be photostable under the wavelength used in the subsequent photocatalytic HAA step (427 nm). Unfortunately, the formation of diazirine **98** was unsuccessful. The major side product of the reaction was isolated and characterised as amide **99**. It has been previously observed that due to the migratory aptitude of the electron-rich phenyl, the sulphonyl oxime intermediate can undergo an irreversible Beckmann rearrangement to form an *N*-aryl amide.[295-298]

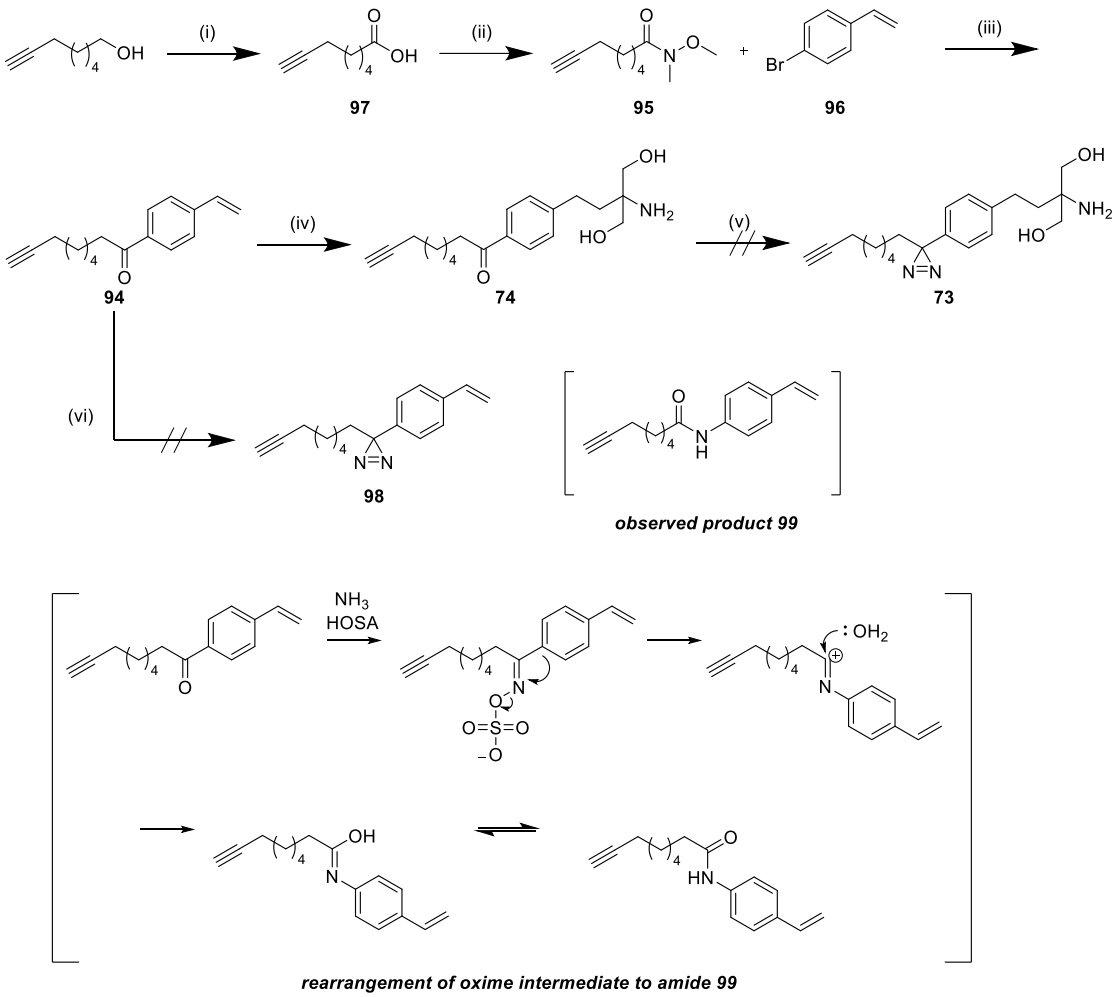


***Scheme 4.22: Reaction conditions:*** *Jones reagent (1.2 eq), acetone, 0 °C, 16 h, 77% (ii) NHMeOMe•HCl (1.2 eq), EDC•HCl (1.2 eq), DMAP (cat.), $Et_3N$ (1.2 eq), $CH_2Cl_2$, 0 °C-rt, 16 h, 87% (iii) Mg (8.0 eq), $I_2$ (cat), THF, −78 °C-rt, 16 h, 20% (iv) serinol (1.0 eq), 3DPA2FBN (1 mol%), $[NBu_4][N_3]$ (10 mol%), DMF, 427 nm, rt, 20 h, 74% (v) & (vi) benzylamine (3.0 eq), $ZnCl_2$ (5 mol%), toluene, 120 °C, 12 h then HOSA (2.2 eq), $NH_3$ (sat), MeOH, −20 °C, 16 h then $Et_3N$ (2.0 eq), $I_2$, MeOH, rt, 16 h. In brackets, the proposed Beckmann rearrangement to yield the isolated amide.*

Once again, the design of the PAL probe was re-evaluated and the diazirine was re-positioned one carbon along the chain, in the β position, to overcome the issues observed with the benzylic position (PAL probe **100**, Figure 4.9).

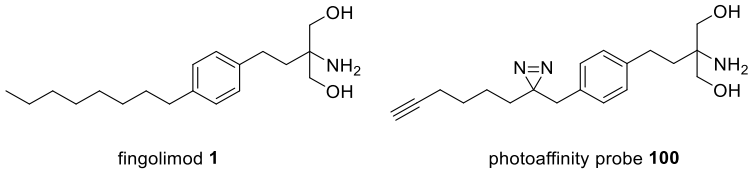


***Figure 4.9: Fourth generation photoaffinity labelling probe design.*** *Photoaffinity probe **100** consisted of a diazirine placed in the β-position relative to the phenyl.*

To synthesise PAL probe **100** it was proposed to employ the precedented Grignard and HAA chemistry, with appropriately modified reagents **102** and **103** (Scheme 4.23).

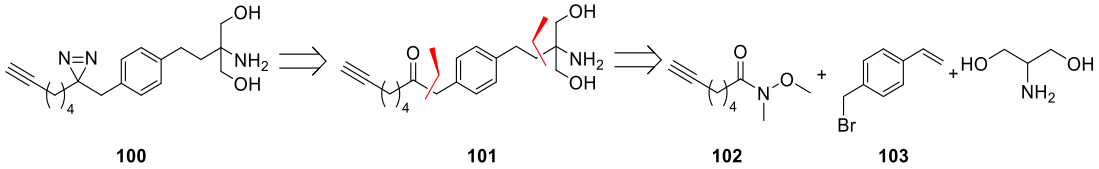


***Scheme 4.23: Retrosynthetic analysis of the third-generation design of PAL probe 100.***

Following the route shown in Scheme 4.24, bromination of alcohol **104** yielded benzylic bromide **103** in good yields. The required Weinreb amide **102** was synthesised from 6-heptynoic acid *via* an amide coupling in 87% yield. The addition of the organomagnesium derived from benzylic bromide **103** to Weinreb amide **102** was attempted; however, no desired product was observed and mostly unreacted benzyl bromide **103** remained. Alternative magnesium activation methods were explored, including $I_2$, 1,2-dibromoethane and Brown's mechanical activation,[299] but this failed to improve the route.

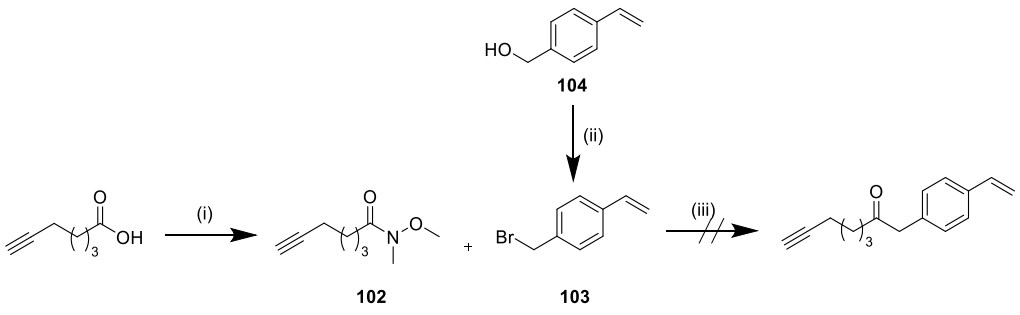


***Scheme 4.24: Reaction conditions:*** *NHMeOMe•HCl (1.2 eq), $Et_3N$ (1.2 eq), EDC•HCl (1.2 eq), DMAP (cat), $CH_2Cl_2$, rt, 18 h, 87% (ii) $PBr_3$ (4.0 eq), $Et_2O$, 0 °C, 18 h, 81% (iii) Mg (8.0 eq), alkylBr (4.0 eq), $I_2$ (cat), 1,2-dibromoethane (cat), THF, −78-0 °C, 18 h.*

Therefore, it was proposed to reverse the reactivity of the reagents employed and use alkyl chloride **105** and Weinreb amide **107** (Scheme 4.25). TMS-protection of 6-chloro-1-hexyne yielded the desired chloride **105**. A Suzuki cross-coupling between methyl 4-bromophenylacetate and potassium vinyltrifluoroborate yielded styrene **106** in good yield. A subsequent ester hydrolysis and amide coupling generated Weinreb amide **107** as the required Grignard reagent. The ensuing Grignard reaction, nonetheless, was unsuccessful with no desired ketone product formed. A large quantity of unreacted Weinreb amide was isolated, which implied an issue with the generation or stability of the alkylmagnesium chloride. We hypothesise that the 6-carbon chain length potentiates the alkyl Grignard towards an intramolecular cyclisation, both a *4-exo-tet* cyclisation to a cyclobutane and a *5-exo-dig* cyclisation to the cyclopentane are precedented,[300-301] therefore it was proposed to reduce the carbon chain length by one carbon to avoid these potential issues. The Grignard synthesis with the TMS-protected 5-chloro-1-pentyne was successful and generated ketone **109** with good yield. Base-promoted silyl deprotection and photocatalytic HAA produced the penultimate PAL probe intermediate **101**. Due to the susceptibility of the styrene towards oxidation, the 2-step HOSA-mediated diazirine synthetic conditions were chosen preferentially over the one-pot *tert*-butyl hypochlorite method developed by Ibert *et al*.[302] Initial trials were unsuccessful with a large quantity of the oxime intermediate **112** being observed, however, by switching to freshly prepared anhydrous HOSA the diaziridine intermediate formation was observed. The diaziridine was subjected to both Ag(I) oxide and $I_2$/$Et_3N$ oxidative conditions to assess the reaction compatibility. $Ag^+$ has precedented alkynophilicity due to its ability to participate in π-coordination making it prone to undesired side reactions and transformations.[303] Whereas, elemental iodine readily enters into a reversible equilibrium with styrene to form the di-iodo derivative.[304] Unfortunately, under

both conditions, oxidation of the diaziridine to the desired diazirine was not observed, which is believed to be due to the incompatibility of the styrene with these oxidative conditions. These findings led to the final redesign of the PAL probe.

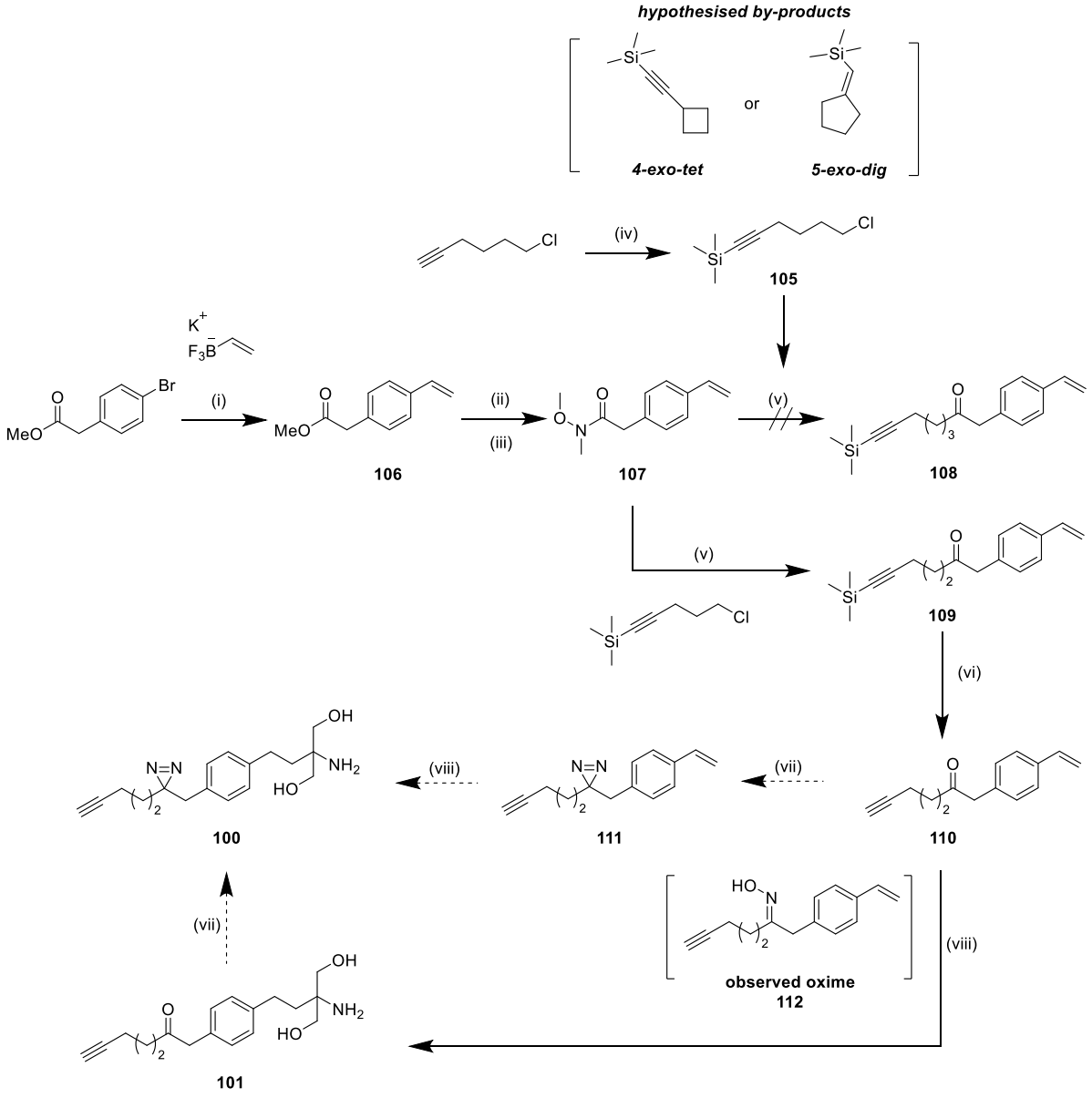


***Scheme 4.25: Reaction conditions:*** *(i) potassium vinyltrifluoroboronate (1.2 eq), $Cs_2CO_3$ (2.0 eq), $Pd(dppf)Cl_2 \bullet CH_2Cl_2$ (5 mol%), THF:$H_2O$ (9:1), 85 °C, 16 h, 76% (ii) LiOH (4.0 eq), 2MeTHF:MeOH (1:1), 70 °C, 2 h (iii) NHMeOMe•HCl (1.2 eq), HATU (1.2 eq), $Et_2N$ (2.0 eq), $CH_2Cl_2$, rt, 2 h, 81% over 2 steps (iv) nBuLi (1.1 eq), TMSCl (1.1 eq), $Et_2O$, −78 °C-rt, 16 h, 93% (v) Mg (8.0 eq), alkylBr (4.0 eq), $I_2$ (cat), 1,2-dibromoethane (cat), THF, −78-0 °C, 18 h, 32% for pentynyl (vi) $K_2CO_3$ (3.0 eq), MeOH, rt, 16 h, 48% (vii) $NH_3$ (sat), MeOH, −20 °C, 4 h then add HOSA (2.2 eq), rt, 16 h then $Et_3N$ (2.0 eq), $I_2$ (cat), MeOH, rt, 16 h.*

The ether-linked analogue of fingolimod, **113**, has demonstrated similar activity in immunomodulatory rat studies.[273] Therefore, in an attempt to generate a PAL probe comprised of an eight-atom chain length, comparable to that found in the parent compound, a new PAL probe **114** was designed incorporating this modality (Scheme 4.26). This phenolic alcohol would provide a more facile handle for functionalisation of the hydrophobic tail, avoiding the need for the problematic and low yielding *in situ* diazirine generation.

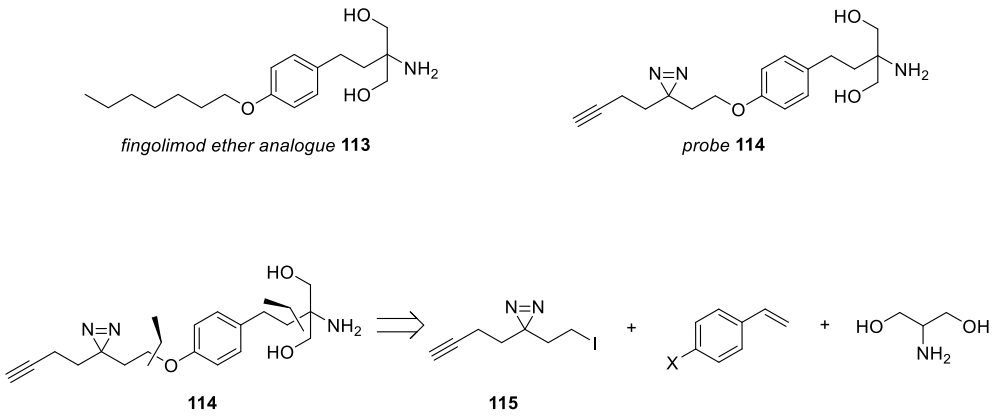


***Scheme 4.26: Fifth generation photoaffinity labelling probe design.*** *Photoaffinity probe **114** was derived from fingolimod's ether analogue, from Fujita et al.*[305] *Retrosynthetic analysis of probe **114**.*

Initially, the 4-bromostyrene derivative was explored as a start point for C-O bond formation due to its compatibility with the photocatalytic HAA (Scheme 4.27). A variety of conditions for Ullman-type cross-coupling or $SN_{Ar}$ with aryl bromide **116** were explored (Table 4.5), however, the milder conditions needed to avoid thermal decomposition of the diazirine (≤80°C) made this route incompatible with diazirine incorporation.[306]

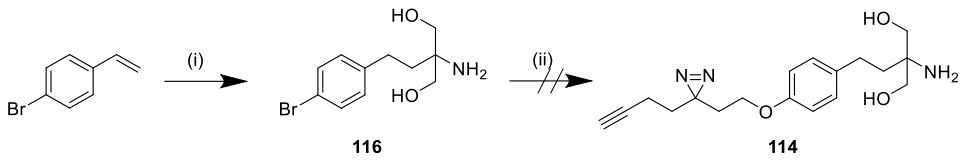


***Scheme 4.27: Reaction conditions:*** *(i) serinol (1.0 eq), 3DPA2FBN (1 mol%), [NBu4][N3] (10 mol%), DMF, 427 nm, rt, 20 h, 86% (ii) see* ***Table 4.5****.*

***Table 4.5: Reaction conditions for the attempted C-O formation between aryl bromide 116 and hydroxydiazirinealkyne.***

| *Entry* | *Conditions (ii)* | *Yield* |
|---|---|---|
| 1 | hydroxydiazirinealkyne (1.2 eq), CuI (5 mol%), $Me_4Phen$ (10 mol%), $Cs_2CO_3$ (1.5 eq) toluene, 80 °C | nr |
| 2 | hydroxydiazirinealkyne (1.2 eq), $Pd(OAc)_2$ (2 mol%), $Me_4{}^tBuXPhos$ (2.4 mol%), $Cs_2CO_3$ (1.5 eq), toluene, 80 °C | nr |
| 3 | hydroxydiazirinealkyne (1.2 eq), DMAP (cat), $Et_3N$ (1.2 eq), $CH_2Cl_2$, 50 °C | nr |

*nr = no reaction*

It was then decided to explore a phenol precursor, however, as the vinyl phenol alkene was too electron-rich to under ngo $\alpha$-amino radical attack under the photocatalytic HAA conditions, the phenol was alkylated first to give aryl ether **117** (Scheme 4.28). Under the photocatalytic HAA conditions, diaziridine **118** was isolated as the major product. There is no experimental evidence of the reduction potential of alkyl diazirines, but aryl diazirines demonstrate $E_{1/2}^{red} = -1.6$ V.[307] If alkyl diazirines exhibit a similar potential it would make this *in situ* reduction of the diazirine to the diaziridine feasible due to the strongly reductive power of the chosen photocatalyst 3DPA2FBN [$E_{1/2}$ (PC/PC$^{-\bullet}$) = −1.92 V].[308] Fortunately, this over-reduction was easily resolved by $I_2/Et_3N$-mediated oxidation of the diazirine to the desired alkyne PAL probe **114**, achieving a 7% overall yield over 3 steps.

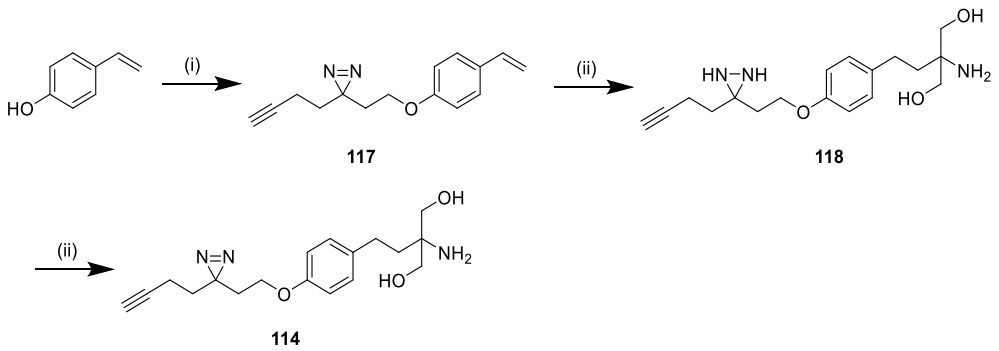


***Scheme 4.28: Reaction conditions:*** *(i) iododiazirinealkyne **115** (1.0 eq), $K_2CO_3$ (1.2 eq), DMF, 60 °C, 4 h, 35% (ii) serinol (1.0 eq), 3DPA2FBN (1 mol%), $[NBu_4][N_3]$ (10 mol%), DMF, 427 nm, rt, 20 h (iii) $I_2$ (cat), $Et_3N$ (2.0 eq), MeOH, rt, 2 h, 20% over 2 steps.*

In an attempt to improve the synthesis of the ether-linked PAL probe **5**, an alternative route involving HAA reaction of the boronic ester **119** and subsequent oxidation to the desired phenol **120** was devised (Scheme 4.29). The electron-withdrawing nature of the Bpin functionality made this substrate more suited towards the key HAA step, due to its stabilisation of the radical benzylic anion intermediate and enhancement of the electrophilicity of the alkene. Indeed, the conversion of pinacol boronic ester **119** into amino diol **120** proceeded in high yield. The resulting crude boronic ester could be oxidised to phenol **120** in 80% yield over the 2 steps. Using $K_2CO_3$ as a base, phenol **120** underwent selective alkylation with diazirine-containing iodide **115** to yield the desired ether-linked probe **5** in 40% yield over 3 steps, as confirmed by HMBC (Appendix VIII). This was a significant improvement compared to the previous route with a drastic improvement in overall yield and a streamlined synthetic pathway.

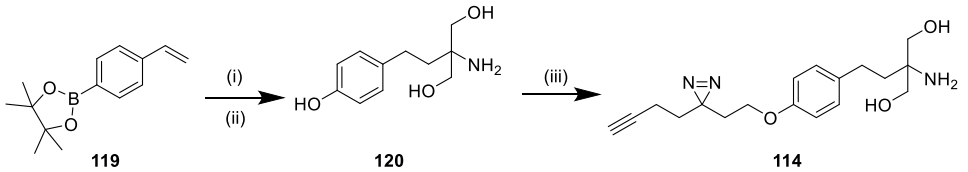


***Scheme 4.29: Reaction conditions:*** *(i) serinol (1.0 eq), 3DPA2FBN (1 mol%), [NBu4][N3] (10 mol%), DMF, 427 nm, rt, 20 h (ii) H2O2 (10 eq), 1M NaOH:THF (1:1), 0 °C, 2 h, 80% over 2 steps (iii) iododiazirinealkyne **115** (1.0 eq), $K_2CO_3$ (2.0 eq), DMF, rt, 18 h, 50%.*

## 4.5 Synthetic routes towards negative control analogues.

Truncated analogues **6** and **7** were synthesised using the same route that was optimised for fingolimod (Scheme 4.30). Methyl derivative **6** was synthesised in 13% overall yield, and butyl analogue **7** was synthesised in 22% overall yield.

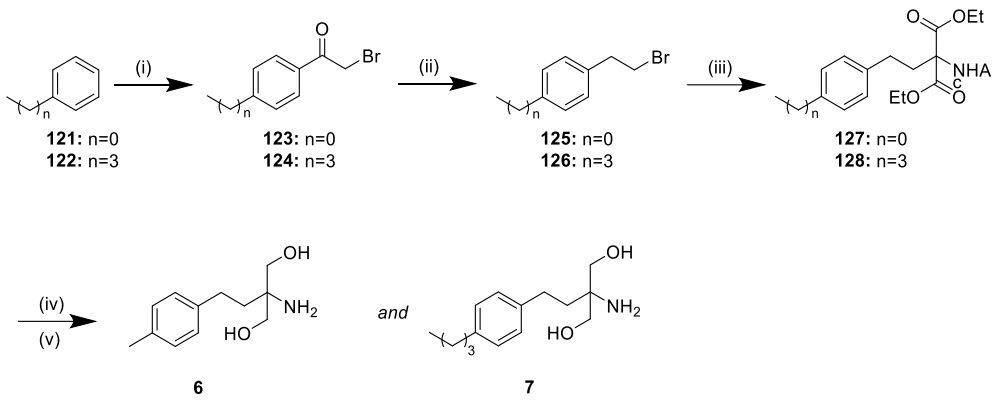


***Scheme 4.30: Reagents and conditions:*** *(i) $AlCl_3$ (1.4 eq), c-hexane, 10 °C-rt, 16 h;* ***123:*** *79%,* ***124:*** *96% (ii) $HSiEt_3$ (2.2 eq), TFA, 10 °C-rt, 16 h;* ***125:*** *87%,* ***126:*** *95% (iii) diethylacetamidomalonate (1.5 eq), $Cs_2CO_3$ (3.0 eq), DMSO, 60 °C, 24 h,* ***127:*** *31%,* ***128:*** *41% (vi) $NaBH_4$ (3.0 eq), THF, rt, 16 h (v) NaOH, MeOH, 70 °C, 5 h,* ***6:*** *63%,* ***7:*** *60% over 2 steps.*

The synthesis of the dimethylated analogue of fingolimod **8** was achieved *via* a HAA reaction between the previously reported *para*-octyl benzene **20** and the commercially available *O,O*-dimethylserinol **129** in 4 steps with an overall yield of 57% (Scheme 4.31).

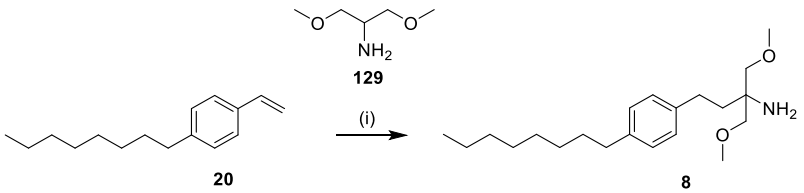


***Scheme 4.31: Reaction conditions:*** *(i) O,O*-dimethylserinol (1.0 eq), $[NBu_4][N_3]$ (10 mol%), 3DPA2FPN (1 mol%), DMF (0.15 M), rt, 427 nm, 20 h, 70%.

As previously emphasised, it is vital that any labelling experiments have the necessary controls to allow the distinction between true enrichment and background labelling. Therefore, it was essential that a structurally similar but functionally inactive derivative of the fingolimod PAL probe **114** was synthesised. To achieve this, it was previously rationalised that obstruction of the site of phosphorylation could ablate phenotypic activity (Figure 4.10).

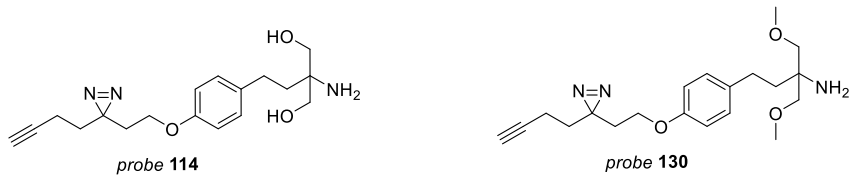


***Figure 4.10: Design for a structurally similar but functionally inactive negative control PAL probe 130.*** *The design incorporated methylation of the site of SPHK2-mediated phosphorylation.*

A familiar route to synthesise probe **130** was adopted whereby styrene boronic ester **119** underwent HAA with *O,O*-dimethyl serinol, followed by $H_2O_2$-mediated oxidative cleavage to form phenol **131**. Phenol **131** could then undergo alkylation with diazirine-containing iodide **115** to yield negative control probe **130** in 51% yield over 3 steps.

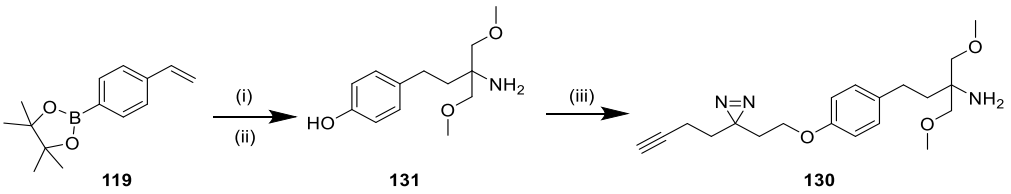


***Scheme 4.32: Reaction conditions:*** (i) *O,O*-dimethyl serinol (1.0 eq), 3DPA2FBN (1 mol%), $[NBu_4][N_3]$ (10 mol%), DMF, 427 nm, rt, 20 h (ii) $H_2O_2$ (10 eq), 1M NaOH:THF (1:1), 0 °C, 2 h, 85% over 2 steps (iii) iododiazirinealkyne **115** (1.0 eq), $K_2CO_3$ (2.0 eq), DMF, rt, 18 h, 60%.

Fingolimod and its analogues (**6-8**) were synthesised, along with a fingolimod-derived PAL probe (**114**) and a structure-matched negative control PAL probe (**130**). These designs were rationalised by fingolimod's known interactions with $S1PR_1$, and the observation that SPHK2-mediated phosphorylation is key for fingolimod's phenotypic effects of interest. However, the

binding mode of fingolimod to $S1PR_1$ does not necessarily correlate to its binding affinity towards its phenotypic targets. As such, it was essential to corroborate the functional effects of these synthesised analogues in both of the optimised phenotypic assays.

# Chapter 5

## Pharmacological Evaluation of Fingolimod's Immunomodulatory Phenotypic Effects

# 5 Pharmacological Evaluations of Fingolimod's Phenotypic Effects

## 5.1 Evaluation of the lymphangiogenic effect of fingolimod and its analogues

The lymphangiogenic sprouting (phenotypic) assay was also used to test the hypothesis that structural modification of fingolimod's hydrophobic tail (**6** & **7**) or polar headgroup (**8**) could interfere with its affinity towards its lymphangiogenic target (Figure 4.5). Reassuringly, the truncated fingolimod analogues (**6** & **7**) showed no pro-lymphangiogenic effect, confirming the hypothesis that the lipophilic tail of the parent compound plays a role in its affinity (Figure 5.1a). Similarly, the methylated analogue **8** was also inactive in the spheroid sprouting assay, providing further evidence that the phosphorylation of the pro-(*S*) alcohol is key to the phenotypic effect of fingolimod (Figure 5.1a). It was confirmed that the lack of effect observed by the control analogues was not due to compound toxicity (Appendix V). It was investigated whether the structural amendments made to fingolimod to facilitate its function as a PAL probe, could impact its pro-lymphangiogenic efficacy. PAL probe **114** induced sprouting, but with a slight loss in potency relative to the parent compound, with an observable $EC_{50}$ of 3.02 μM (Figure 5.1b), however this was not deemed statistically significant (P=0.0577). Despite this reduction in efficacy, PAL probe **114** could still serve its purpose as a phenotypically active photolytic fingolimod mimic. Furthermore, the proposed negative control probe **130**, which was derived from the inactive fingolimod analogue **8**, was also inactive in the spheroid sprouting assay (Figure 5.1b).

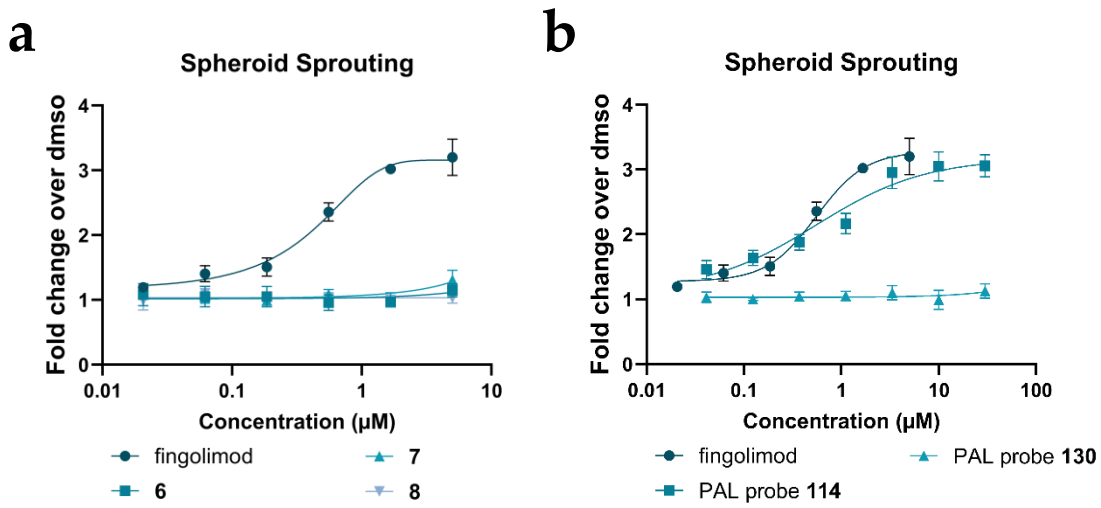


***Figure 5.1: Investigating pro-lymphangiogenic effects of fingolimod and its analogues.*** *(a) Observed fold change in sprouting per spheroid relative to DMSO control in response to fingolimod, its truncated analogues (**6** & **7**) and methylated analogue (**8**). N≥3 (b) Observed fold change in sprouting per spheroid relative to DMSO control in response to fingolimod, PAL probe **114** and negative control PAL probe **130**. N≥3. Error bars = sem. Statistical comparison using F-test, ns between fingolimod and probe **114**. P=0.0577.*

The optimised sprouting assay confirmed the pro-lymphangiogenic effect of fingolimod was sustained upon incorporation of alkyne and diazirine moieties to generate PAL probe **114**. The assay enabled the identification of three negative control analogues (**6-8**). Methylated analogue **8** was used as a foundation for the design of the inactive negative control PAL probe **130**. These observations established that the structure-matched PAL probes **114** and **130** could be used for future labelling studies.

Previous studies had shown that fingolimod's pro-lymphangiogenic effect was SPHK2-dependent, implying that Fing-P was the active form (Figure 4.5). As such, it was assessed whether PAL probe **114** also displayed a SPHK2 dependency. Co-dosing studies with a SPHK2 inhibitor showed an inhibition of probe **114**'s pro-lymphangiogenic phenotype

(Figure 5.2b), implying that the probe remains a substrate for SPHK2 and that its phosphorylation is key for activity.

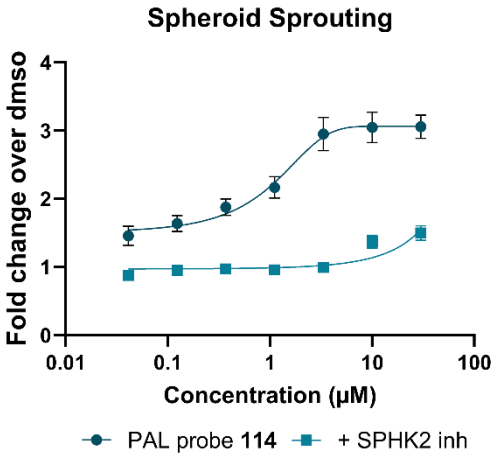


***Figure 5.2: Co-dosing lymphangiogenesis studies of PAL probe 114 with a SPHK2 inhibitor.*** *Observed fold change in sprouting per spheroid relative to DMSO control in response to a serial dilution of PAL probe* ***144*** *co-dosed with a selective SPHK2 inhibitor (2 μM). N=3. Error bars = sem.*

Fingolimod is canonically associated with agonism of the S1PR family of receptors ($S1PR_{1,3-5}$). It displays low nanomolar potency against each of its associated S1PRs ($S1P_1$, $S1P_4$, $S1P_5$: $EC_{50}$ ~ 0.3 – 0.6 nM) and $S1P_3$: $EC_{50}$ ~ 3 nM). [117, 130, 309] As such, the low micromolar activity ($EC_{50}$ = 1.67 μM) of fingolimod in the lymphangiogenic assay implies that it is likely acting through a different target, but, a differing activity profile could also be explained by a variety of factors (i.e. cell type, receptor expression levels, biochemical vs phenotypic readout). Therefore, it was ascertained whether fingolimod's pro-lymphangiogenic effect could be through agonism of a member of this family. Prior to any sprouting experiments it was confirmed by flow cytometry that the S1PR family were expressed on the surface of the commercial LECs (Appendix VI). A series of selective S1PR agonists were evaluated in the spheroid sprouting assay (Figure 5.3)[1-3] and none of them were able to induce lymphangiogenesis. This finding

supports the hypothesis that fingolimod is acting through a novel target, which is distinct from the S1PR family, to initiate lymphangiogenesis.

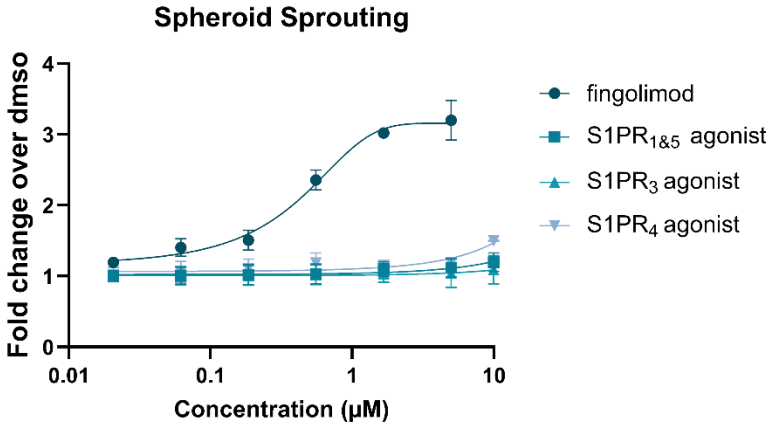


***Figure 5.3: Lymphangiogenesis studies with S1PR family agonists.*** *Observed fold change in sprouting per spheroid relative to DMSO control in response to a serial dilution of fingolimod, $S1PR_{1\&5}$ agonist (Siponimod)[1], $S1PR_3$ agonist (CYM5541)[2] and $S1PR_4$ agonist (CYM50308)[3]. N≥3. Error bars = sem.*

Due to fingolimod's affiliation with the S1PR family, and its lipid-like structure, it was hypothesised that fingolimod could be interacting with another G-protein coupled receptor (GPCR) to induce lymphangiogenesis. To investigate this theory, fingolimod was co-dosed with pertussis toxin (PTX), a bacterial exotoxin which interferes with GPCR signalling by trapping the G$\alpha$-protein in its inactive form.[310] Co-dosing with PTX completely inhibited fingolimod-induced sprouting (Figure 5.4a), suggesting that fingolimod's mechanism of action is *via* a GPCR with a $G_{i/o}$ dependency. This effect was also observed when PAL probe **114** was co-administered with PTX (Figure 5.4b).

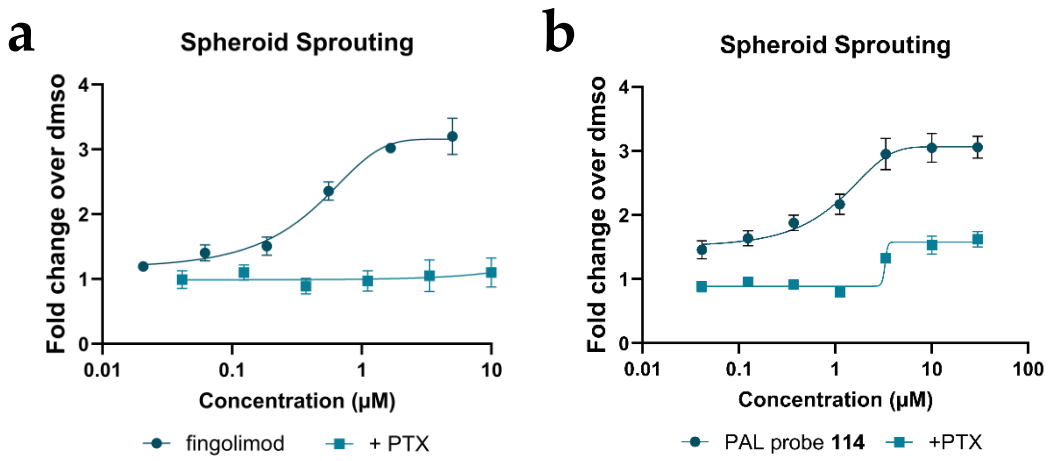


***Figure 5.4: Co-dosing lymphangiogenesis studies of fingolimod and PAL probe 114 with pertussis toxin (PTX).*** *(a) Observed fold change in sprouting per spheroid relative to DMSO control in response to a serial dilution of fingolimod co-dosed with PTX (200 ng/mL). N≥3 (b) Observed fold change in sprouting per spheroid relative to DMSO control in response to a serial dilution of PAL probe **114** co-dosed with PTX (200 ng/mL). N=3. Error bars = sem.*

To further investigate the hypothesis that fingolimod could be acting through a GPCR, a literature search was performed to explore any previously reported associations between fingolimod and non-S1PR GPCRs. Using the ChEMBL database, fingolimod (CHEMBL314854) and its analogous salts (hydrochloride & lauryl sulphate) were analysed (Figure 5.5a). Of the 763 assay records, 565 were for relevant bioactivity measurements (i.e. binding/functional assays). Of these 565 records, there were only 15 mammalian target proteins specified, excluding S1PRs and SPHKs. This list of 15 proteins was restricted to GPCRs which were expressed in the tissues of interest (i.e. lymphatics and T-lymphocytes) and also demonstrated a comparable activity profile to that observed in the phenotypic assay (%effect > 25% at μM dosage). These constraints produced a list of 8 proteins (Table 5.1). The majority of these targets were identified in a broad GPCR β-arrestin recruitment screen made available in the EUbOPEN Chemogenomic library. For each of these targets, a relevant

antagonist/agonist was synthesised (Appendix VII) or acquired, and evaluated in the spheroid sprouting assay (Figure 5.5b).

***Table 5.1: Known fingolimod targets identified in a ChEMBL screen.***

| *Target Protein* | *Abbrev.* | *Function* | *Modulator (MOA)* |
|---|---|---|---|
| Angiotensin II receptor type 1 | AT1 | cardiovascular function | Losartan (antagonist) |
| Apelin receptor | APLNR | cardiovascular function, fluid homeostasis, and energy metabolism | ML233 (agonist) |
| C5a anaphylatoxin chemotactic receptor 1 | C5aACR1 | inflammation and immune response | PMX53 (antagonist) |
| C-X3-C chemokine receptor 1 | CX3CR1 | cell adhesion, migration, and immune response | JMS-17-2* (antagonist) |
| G-protein coupled receptor 120 | GPR120 | regulating metabolism, inflammation, and insulin sensitivity | AH7614 (antagonist) |
| G-protein coupled receptor 183 | GPR183 | immune cell migration and function | GSK682753A (inverse agonist) |
| Lipoxin A4 receptor | LXA4 | regulating inflammation | BML111* (agonist) |
| Protein phosphatase 2A | PP2A | cell cycle regulation, immune cell function | LB100* (antagonist) |

**synthesised (Appendix VII)*

Three concentrations were tested per treatment: (i) the literature reported $EC_{50}$ against the target protein (ii) 10-fold above (iii) 10-fold below. The reported $EC_{50}$ concentrations were taken from cellular assays using endogenous GPCR levels.[311-316] Nevertheless, additional 10-fold disparity doses were opted for to account for any differing expression levels between cell types. LB100 (Table 5.1, Entry 8) demonstrated signs of cytotoxicity in LECs so its phenotypic activity was not evaluated any further (Appendix V). In this sprouting screen, only the apelin

receptor (APLNR) agonist ML233 demonstrated a noticeable pro-lymphangiogenic effect, which was dose-dependent (Figure 5.5c).

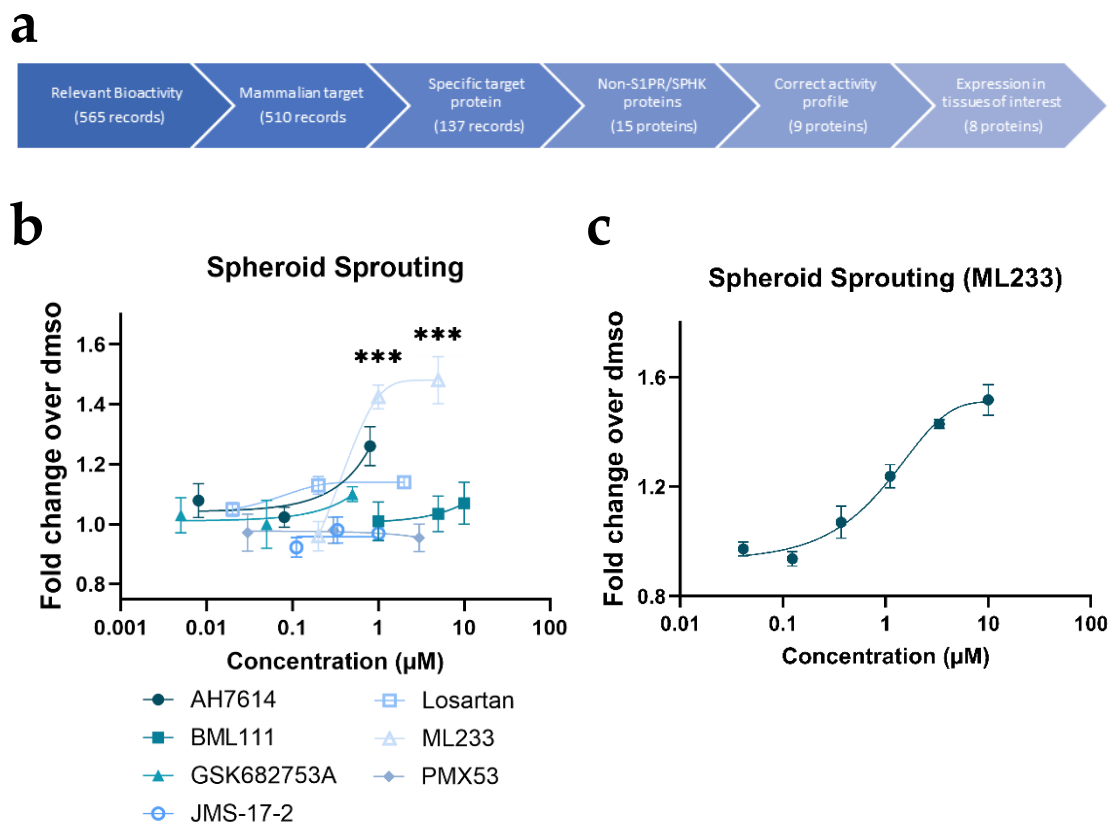


***Figure 5.5: Lymphangiogenesis screen of ChEMBL targets, identifying APLNR as a potential target of fingolimod.*** *(a) Workflow used to identify a shortlist of fingolimod targets to investigate further (b) Observed fold change in sprouting per spheroid relative to DMSO control in response to ChEMBL screen target treatments. N=3. Statistics were performed on raw data using a one-way ANOVA followed by multiple comparison tests, compared to DMSO-treated spheroids. *** = P<0.005. Error bars = sem (c) Observed fold change in sprouting per spheroid relative to DMSO control in response to ML223, a selective APLNR agonist. N=3. Error bars = sem.*

APLNR is a class A GPCR which has been previously linked to angiogenesis.[317] APLNR's endogenous ligand, apelin, has been shown to induce lymphangiogenesis in tumour metastasis models and is essential in early lymphatic development.[318, 319] In the context of cardiac injury, apelin overexpression ameliorates ischaemic injury, reducing matrix remodelling and inflammation.[320]

Of note however was the disparity between the magnitude of the pro-lymphangiogenic effect in response to fingolimod versus ML233. Fingolimod exhibited a 3-fold change increase in sprouting over DMSO, whereas ML233 was only observed to induce a 1.6-fold increase in sprouting. This disparity could be attributed to a different agonist profile (i.e. full vs partial vs allosteric agonism), consequently, the link between fingolimod and APLNR was investigated further.

A cellular thermal shift assay (CETSA) was performed to achieve biophysical evidence of fingolimod's interaction with APLNR. LECs treated with fingolimod demonstrated APLNR thermal stabilisation compared to DMSO treated LECs, suggesting that fingolimod interacts with APLNR, possibly to induce lymphangiogenesis (Figure 5.6).

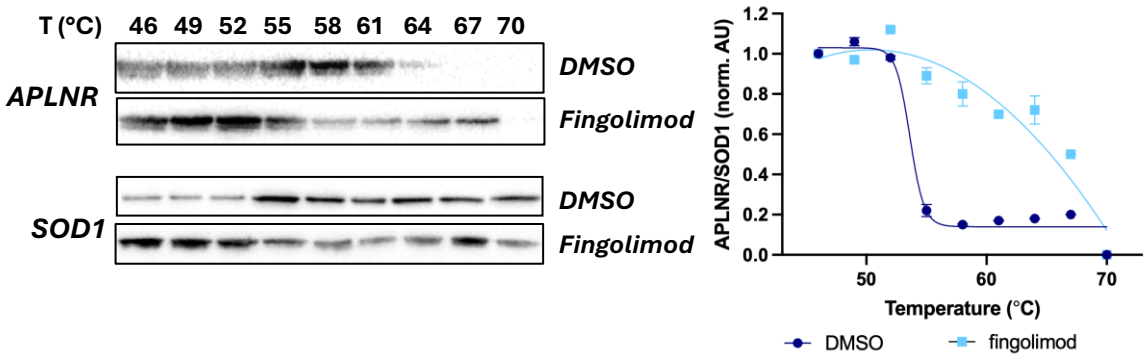


***Figure 5.6: Cellular thermal shift assay shows thermal stabilisation of APLNR when dosed with fingolimod.*** *Western blot analysis and quantification of soluble APLNR in LECs treated with 3 μM fingolimod or DMSO (0.1%). N=2. Error bars = SD.*

With evidence supporting fingolimod's interaction with APLNR, it was then necessary to corroborate whether this interaction was responsible for the pro-lymphangiogenic phenotype. It was initially investigated whether fingolimod's phenotypic effect could be outcompeted with a known APLNR inhibitor. When fingolimod was co-dosed with APLNR antagonists, protamine sulphate or ML221,[321, 322] its pro-lymphangiogenic effect was ablated (Figure 5.7a).

This observation supported the theory that fingolimod could be acting through APLNR to induce lymphangiogenesis. However, as the use of small molecules can be complicated by their selectivity, it was chosen to corroborate these findings with a more targeted approach. To enable this, siRNA-mediated knockdown (KD) of APLNR in LECs was carried out. APLNR protein levels were assessed by Western blot at 24, 48 and 72 h post-transfection (Figure 5.7b). 48 h post transfection, there was a significant decrease in APLNR protein levels in cells receiving siRNA targeting APLNR (siAPLNR KD), compared to non-targeting control siRNA (siCT) and non-transfected cells (no T) (Figure 5.7c). Accordingly, the extent of spheroid sprouting in response to fingolimod treatment was assessed in cells that had been transfected for 48 h. While there was a general reduction in sprouting observed with the transfected cells relative to non-transfected, there was a significant decrease in fingolimod induced sprouting in the siAPLNR KD LECs relative to both non-transfected (no T) and siCT transfected LECs (Figure 5.7d). To ensure that the decrease in sprouting was linked to APLNR KD and not an artifact of transfection, positive control compound SB431542 was also administered to the spheroids. SB431542 induces lymphangiogenic sprouting *via* an APLNR-independent mechanism.[323] SB431542 induced lymphangiogenesis to a similar level in siCT and siAPLNR KD spheroids. Whilst this was still to a lesser extent than in no T LEC spheroids, this observation improved the overall confidence in the hypothesis that the reduction in fingolimod-induced sprouting was linked to APLNR KD. To further validate the link between fingolimod and APLNR agonism, downstream pathways indicative of APLNR activation were explored. One such pathway is the robust translocation of histone deacetylase 5 (HDAC5),[324] whereby upon APLNR activation HDAC5 undergoes phosphorylation and rapidly (~1 h) translocates from the nucleus to the cytoplasm. To assess whether fingolimod could induce the same effect, LECs were dosed for 1 h, fixed and visualised with a nuclear

stain and HDAC5 antibody (Figure 5.7e). There appeared to be significant translocation of HDAC5 to the cytoplasm relative to the DMSO control. If true, this observation would suggest that APLNR is activated in response to fingolimod treatment. However, an alternative explanation for this observation is that the overall levels of HDAC5 were decreased upon fingolimod treatment, giving the appearance of translocation. As such, this could be followed up further with Western blot studies to evaluate the relative levels of HDAC5 and p-HDAC5 with and without fingolimod treatment.

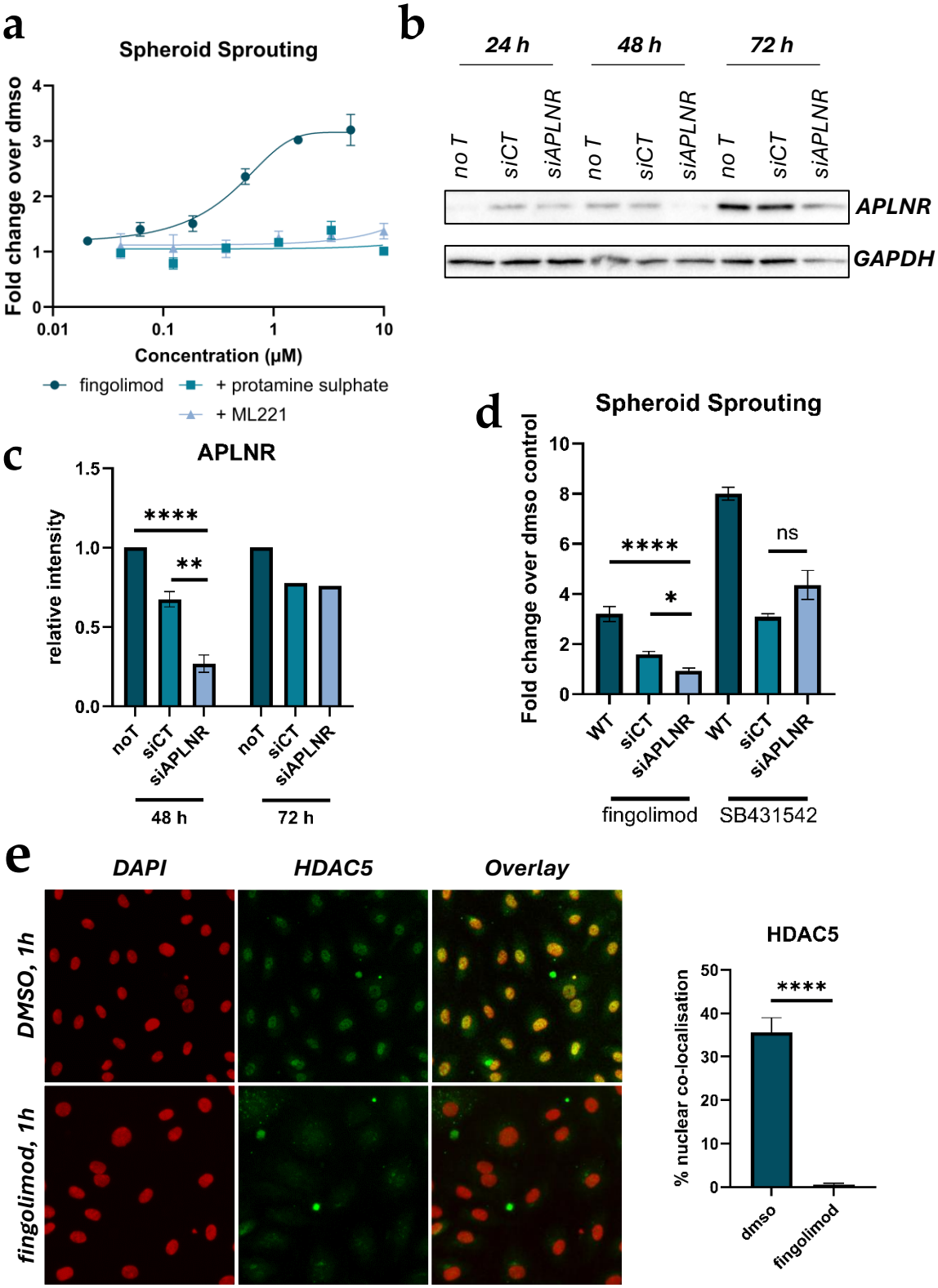
a
Spheroid Sprouting
Fold change over dmso
Concentration (μM)
fingolimod
+ protamine sulphate
+ ML221
b
24 h
48 h
72 h
no T
siCT
siAPLNR
APLNR
GAPDH
c
APLNR
relative intensity
****
**
noT
siCT
siAPLNR
48 h
72 h
d
Spheroid Sprouting
Fold change over dmso control
****
*
ns
WT
siCT
siAPLNR
fingolimod
SB431542
e
DAPI
HDAC5
Overlay
DMSO, 1h
fingolimod, 1h
HDAC5
% nuclear co-localisation
****
dmso
fingolimod

***Figure 5.7: Investigating the link between fingolimod and APLNR agonism.*** *(a) Observed fold change in sprouting per spheroid relative to DMSO control in response to a serial dilution of fingolimod co-dosed with APLNR antagonists: protamine sulphate (5 µg/mL) or ML221 (2 µM). N≥3. Error bars = sem. (b) Western blot analysis of APLNR expression in siRNA KD LECs 24-72 h after transfection (c) Quantification of 48 h and 72 h siRNA KD Western blots, relative to GAPDH and normalised to non-transfected LECs (no T). N=3. Statistical tests were performed using a one-way ANOVA followed by multiple comparison tests on unnormalised data. **** = P<0.001, ** = P<0.01 (d) Observed fold change in sprouting per spheroid relative to DMSO control in response to fingolimod (1.7 µM) or SB431542 (20 µM). N=3. Statistical tests were performed using a one-way ANOVA followed by multiple comparison tests on raw data. **** = P<0.001, ** = P<0.01, * = P<0.05, ns = P>0.05 (e) Immunostaining of LECs with DAPI (red) and HDAC5 (green) and their overlap (yellow) after treatment for 1 h with DMSO or fingolimod (1.7 µM). N=3. Quantified using ImageJ. Statistical tests using Student's t-test. **** = P<0.001.*

It had previously been observed in a study by Tatin *et al*,[320] that agonism of APLNR by its native peptide ligand, apelin, resulted in a 2.7-fold increase in SPHK2 mRNA levels in LECs. Therefore, it was investigated whether the increase in fingolimod-induced sprouting through APLNR was due to direct agonism of the receptor or through the indirect upregulation of SPHK2 levels and the subsequent increase in metabolism of fingolimod to its bioactive form, Fing-P. To investigate this, it was first necessary to confirm that the observations by Tatin *et al* translated on a protein level. Western blot analysis of SPHK2 protein levels was performed on untreated LECs, fingolimod-treated LECs and siAPLNR KD LECs. Fingolimod treatment did not significantly change SPHK2 protein levels compared to no T LECs. Conversely, in siAPLNR KD LECs there was a 60% decrease in SPHK2 protein levels relative to the non-targeting control (Fig 5.8).

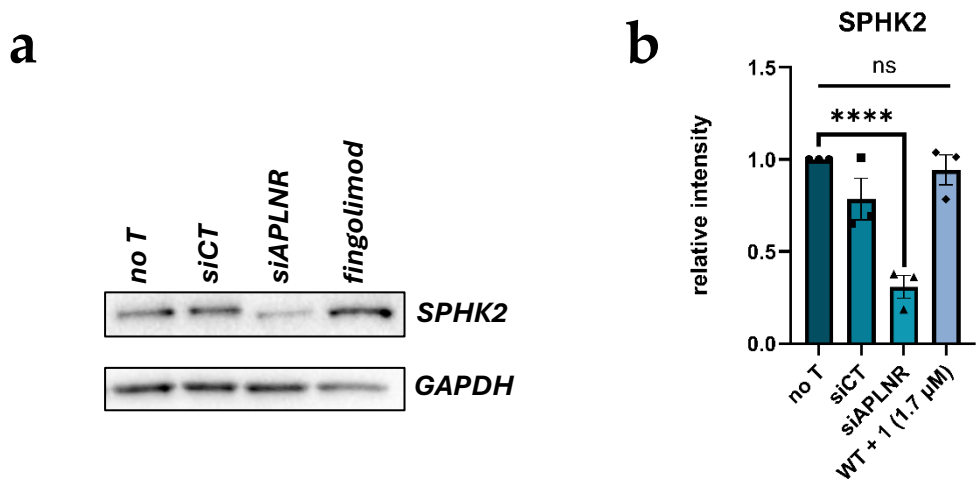


***Figure 5.8: SPHK2 protein level deviation in response to APLNR modulation.*** *(a) Western blot analysis of SPHK2 expression (b) Quantification of Western blots, relative to GAPDH and normalised to non-transfected LECs (no T). N=3. Statistical tests were performed using a one-way ANOVA followed by multiple comparison tests on unnormalised data. **** = P<0.001, ns = P>0.05*

However, it was unclear whether this was a biologically significant decrease in SPHK2 levels. It has been previously reported that human SPHK2 has a $K_M$ = 18.2 μM for fingolimod,[325] therefore, the saturation level of fingolimod for SPHK2 is much higher than the concentrations used in these experiments (<3 μM). To investigate whether APLNR KD reduced SPHK2-mediated phosphorylation of fingolimod, MS studies were performed to assess the relative levels of fingolimod versus Fing-P present in siAPLNR KD LECs compared to no T LECs. LECs were dosed with 3 μM fingolimod for 1 h before metabolism was arrested and metabolites were extracted for MS analysis. After 1 h, fingolimod could not be detected by MS in the cell extracts of either the no T or siAPLNR LECs (Figure 5.9). To ascertain whether this was because of extensive fingolimod metabolism, or a detection issue, co-treatment studies with a SPHK2 inhibitor were performed to determine if fingolimod detection could be restored. Co-treatment with a SPHK2 inhibitor resulted in the detection of comparable levels of fingolimod in both the no T and siAPLNR LECs (Figure 5.9), suggesting that the lack of

signal observed was due to the phosphorylation of fingolimod. In addition, there were similar levels of Fing-P detected in both no T and siAPLNR KD LECs, highlighting that the previously observed downregulation of SPHK2 has a negligible influence on the phosphorylation of fingolimod in the timeframe and at the concentrations used in these experiments (Figure 5.10).

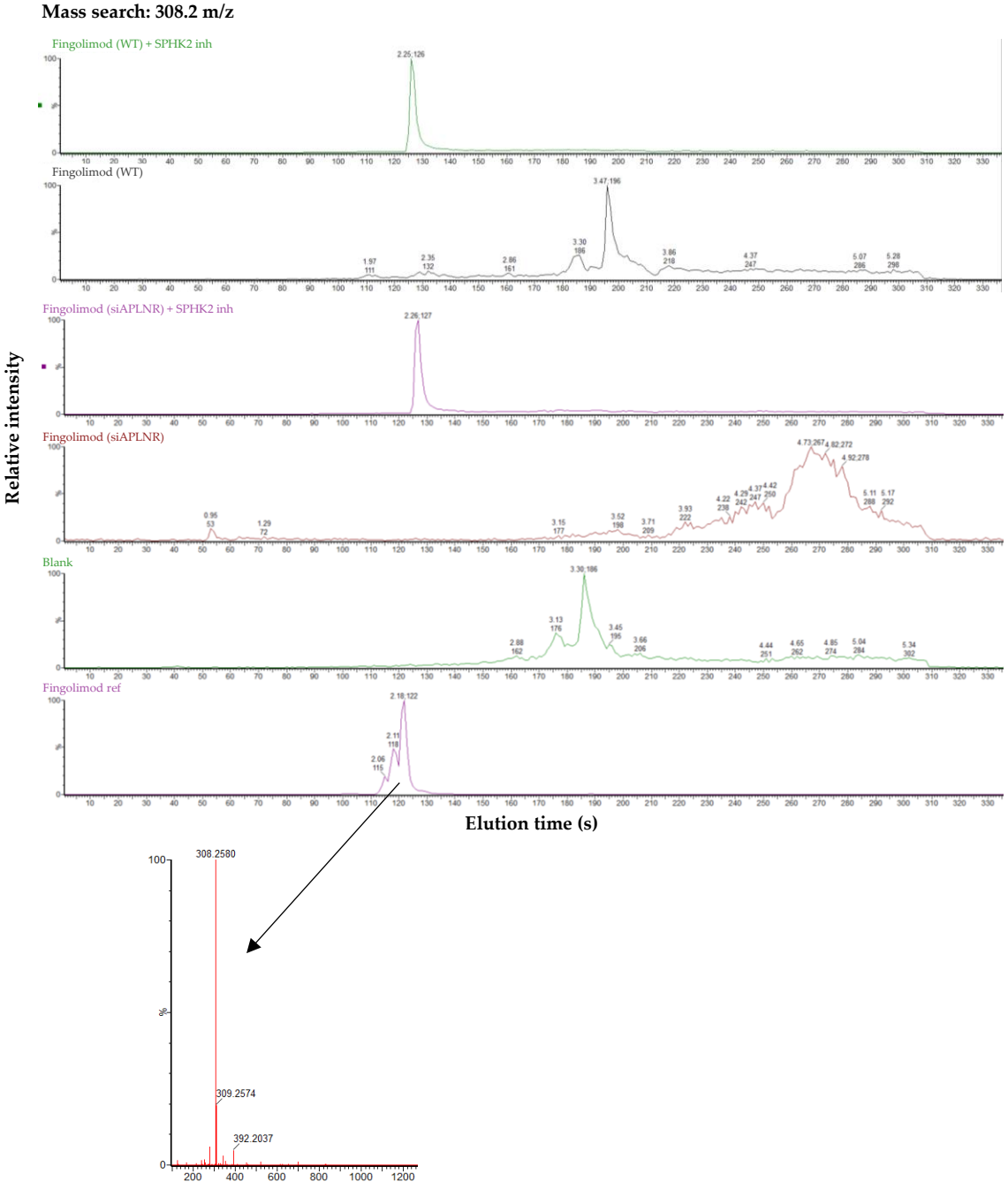


***Figure 5.9: UPLC-MS analysis of LEC cell extracts to assess the relative extent of fingolimod.*** *UPLC traces of cell extracts from fingolimod-treated (3 µM, 1 h) no T and siAPLNR LECs. Blank methanol trace and pure fingolimod trace for reference. All traces analysed with [M+H] 308.2 m/z search. MS obtained from pure fingolimod trace used as reference.*

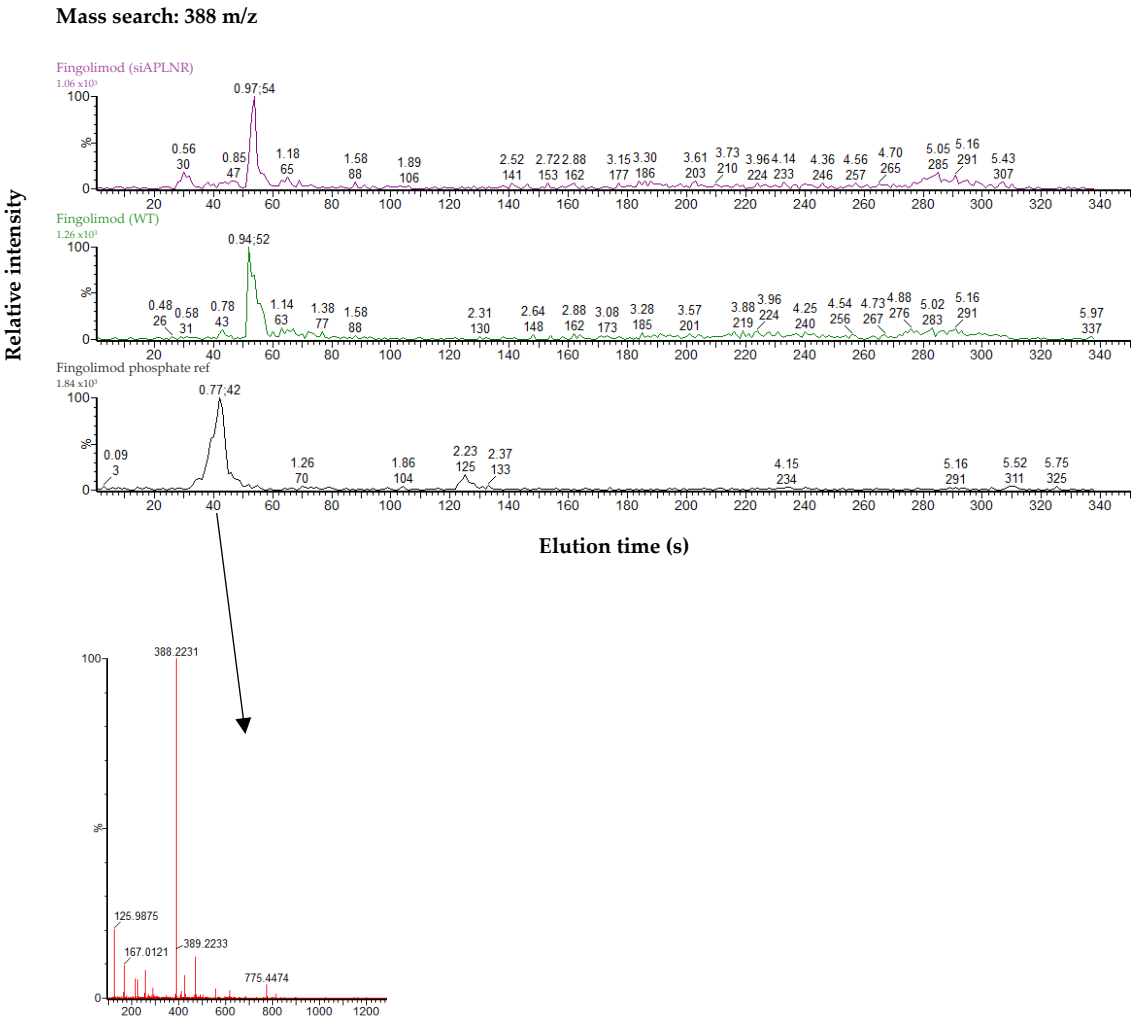


***Figure 5.10: UPLC-MS analysis of LEC cell extracts to assess the relative extent of fingolimod phosphate.*** *UPLC traces of cell extracts from fingolimod-treated (3 µM, 1 h) no T and siAPLNR LECs. Blank methanol trace and pure fingolimod phosphate trace for reference. All traces analysed with [M+H] 388 m/z search. MS obtained from pure fingolimod phosphate trace used as reference.*

To summarise, an in-depth pharmacological analysis of fingolimod was performed, using the optimised spheroid sprouting assay. It was identified that SPHK2-mediated phosphorylation of fingolimod to Fing-P was necessary for the lymphangiogenic phenotype. Targeted studies revealed that fingolimod's phenotypic target was not a member of the canonically associated S1PR family, but likely another GPCR. A ChEMBL screen identified the apelin receptor, APLNR, as a potential target, which was supported by CETSA, competition experiments,

siRNA KD studies and downstream pathway analysis. APLNR-mediated modulation of SPHK2 levels does not appear to be biologically significant, with no observable difference in Fing-P levels between no T and siAPLNR LECs. These findings support the hypothesis that fingolimod acts directly through APLNR to induce lymphangiogenesis. However, this pharmacological candidate approach does not preclude other potential fingolimod targets which could be uncovered *via* unbiased proteomics studies using the successfully validated PAL probes **114** and **130**.

Following on from the success of a pharmacologically driven approach towards the deconvolution of fingolimod's lymphangiogenic effect, the same tactic was applied to understand more about fingolimod's inhibitory effect upon T-lymphocyte migration.

## 5.2 Evaluation of the inhibitory effect of fingolimod and its analogues upon T-lymphocyte migration

With the inhibitory effect of fingolimod confirmed, the optimised migration assay was used to assess the effect of the synthesised analogues of fingolimod. It was discovered that fingolimod's truncated analogues, **6** & **7**, were active in the T-lymphocyte migration assay, demonstrating a comparable inhibitory effect to fingolimod (Figure 5.14). This observation was interesting as both these analogues had been phenotypically inactive in the lymphangiogenesis assay. This finding further supported the hypothesis that fingolimod was acting through unique and distinct targets to promote lymphangiogenesis versus the observed immunomodulatory effects on T-lymphocyte migration. Interestingly, the methylated fingolimod derivative **8** did not inhibit migration of T-lymphocytes in the Transwell assay (Figure 5.14). PAL probe **114** maintained fingolimod's phenotypic effect and inhibited migration of T-lymphocytes across the lymphatic endothelium, confirming its

capacity to be used in future labelling experiments. It was observed that PAL probe **114** inhibited migration up to 30 μM, in contrast to the loss of activity observed by fingolimod at higher micromolar concentrations (>1 μM). Whilst the exact reasoning behind this observation is unknown, some theories can be postulated. The structural modifications introduced to generate PAL probe **114** make the overall molecule less polarised, due to the introduction of heteroatoms on the lipophilic tail. If aggregation/micelle formation is the reasoning behind fingolimod's lack of efficacy at higher concentrations, then this could justify the sustained effect observed by PAL probe **114**. Additionally, it has been previously observed that small molecule agonism of GPCRs can result in differential effects on the desensitisation and internalisation of the receptor.[326, 327] If receptor desensitisation is indeed the explanation for

fingolimod's lack of efficacy at higher concentrations, then this could explain the different activity profiles observed.

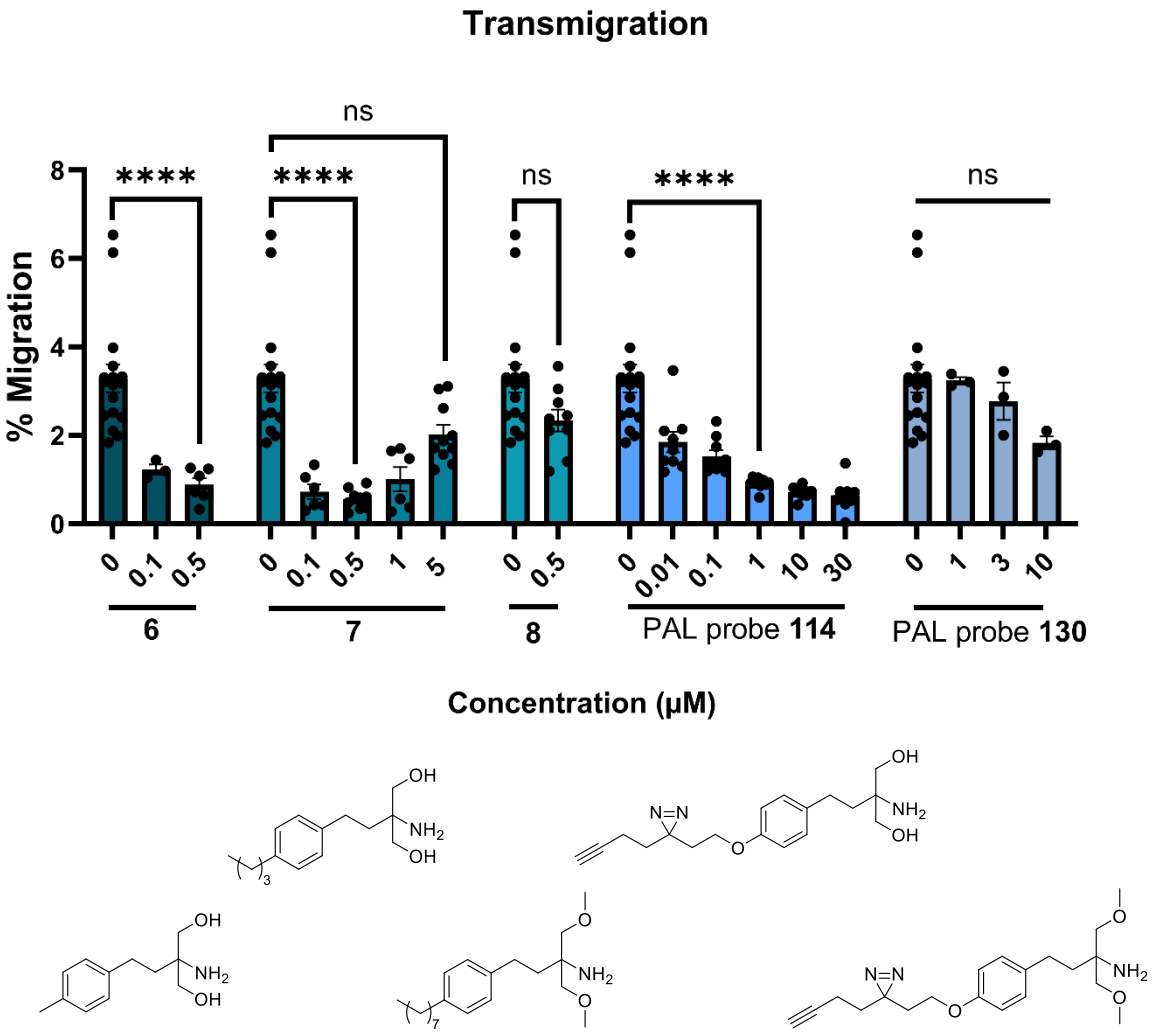


***Figure 5.11: T-lymphocyte migration in response to fingolimod analogues.*** *Migration of T-lymphocytes through LEC-coated Transwell inserts after 4 h, in response to fingolimod treatment. N≥3. Statistical tests using Student's t-test. **** = P<0.001, ns = P>0.05. Error bars = sem.*

To confirm that the observed inhibitory effects were not due to T-lymphocyte cell death, cell viability was assessed after a 6 h dosing of all compounds (Appendix V) and no cell death was observed. The PAL probe **130** showed no inhibitory effect upon T-lymphocyte migration, reaffirming its capacity as a negative control compound in labelling studies.

As previously stated, fingolimod is a known agonist of the S1PR family of GPCRs. To investigate whether fingolimod's inhibitory effect was through a S1PR, a screen of selective S1PR agonists were evaluated in the assay.[1-3] However, none of these selective agonists had a comparable inhibitory effect upon T-lymphocyte migration (Figure 5.15). To corroborate that this observation was not due to a lack of S1PRs present on the surface of Jurkats cells, their

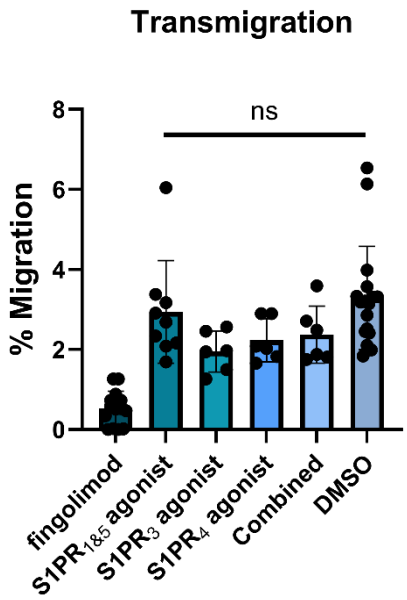


***Figure 5.12: Selective S1PR agonists do not inhibit T-lymphocyte migration to the same extent as fingolimod.*** *Migration of T-lymphocytes through LEC-coated Transwell inserts after 4 h, in response to treatment with of fingolimod (0.5 µM), S1PR$_{1\&5}$ agonist (Siponimod, 40 nM), S1PR$_3$ agonist (CYM5541, 500 nM) and S1PR$_4$ agonist (CYM50308, 100 nM). N≥3. Statistical tests using a one-way ANOVA. ns = P>0.05. Error bars = sem.*

expression was confirmed by FACS (Appendix II). The S1PR agonists were also administered as a combined treatment to confirm that fingolimod's effect was not due to pan-agonism of multiple members of the S1PR family, however, no inhibition of migration was observed. This further supported the theory that fingolimod's immunomodulatory effect is independent of the S1PR family, through a novel and distinct interaction partner.

Next it was investigated whether fingolimod's inhibitory influence upon T-lymphocyte migration could be mediated *via* another GPCR. Co-treatment with PTX also blocked

fingolimod's phenotypic effect (Figure 5.16), again suggesting that fingolimod is acting through a GPCR to enact its inhibitory effect.

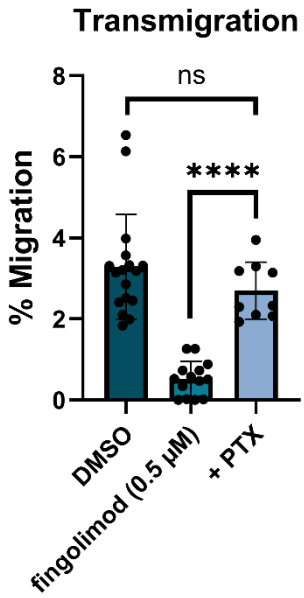


***Figure 5.13: Co-dosing fingolimod with pertussis toxin, inhibits its inhibitory effect on T-lymphocyte transmigration.*** *Migration of T-lymphocytes through LEC-coated Transwell inserts after 4 h, in response to fingolimod treatment co-dosed with PTX (200 ng/mL). N≥3. Statistical tests using a one-way ANOVA followed by multiple comparison tests. **** = P<0.001, ns = P>0.05. Error bars = sem. N≥3.*

To probe further into fingolimod's potential mechanism of action, the previously derived ChEMBL screen compounds (Table 5.1) were also tested in the Transwell migration assay. Whilst many of the targets had previously reported links to immune cell migration,[328-332] only JMS-17-2, a C-X3-C motif chemokine receptor 1 (CX3CR1) antagonist, demonstrated an inhibitory effect upon Jurkat transendothelial migration in a dose-dependent manner (Figure 5.17).

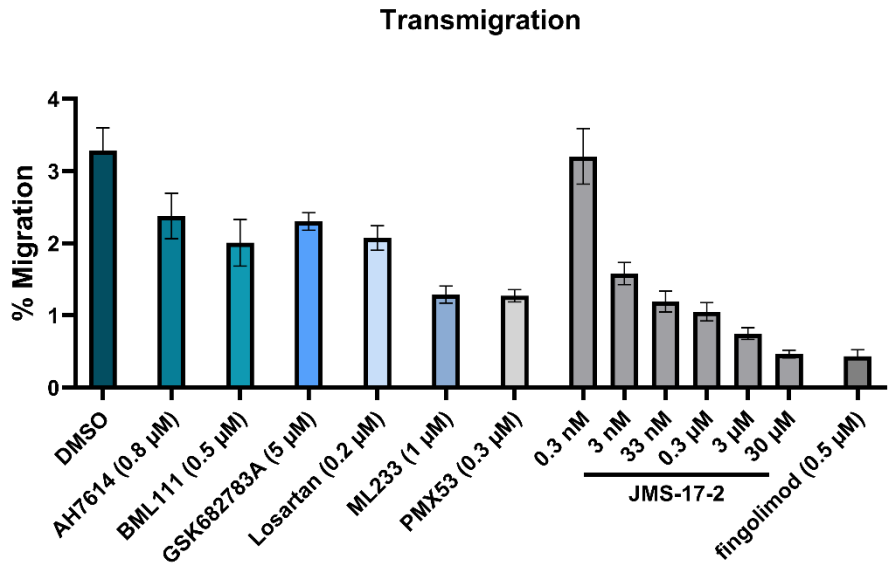


***Figure 5.14: ChEMBL screen identifies CX3CR1 antagonist as an inhibitor of T-lymphocyte migration through lymphatic endothelium.*** *Migration of T-lymphocytes through LEC-coated Transwell inserts after 4 h, in response to treatment. Error bars = sem.*

CX3CR1 is a GPCR expressed on a variety of immune cells, including T-lymphocytes, as well as on the lymphatic endothelium.[333] Upon pro-inflammatory cytokine activation, CX3CR1 can bind to its complementary ligand, C-X3-C motif chemokine ligand 1 (CX3CL1). CX3CL1 exists in two forms, its membrane-bound form, which mediates adhesion and migration, and its soluble form, which induces chemotaxis.[334, 335] Inhibition of CX3CR1 can prevent both CX3CL1-mediated and integrin-mediated migration of immune cells.[336] The CX3CR1/CX3CL1 axis plays a key role in dendritic cell migration through the lymphatic endothelium,[337] but to our knowledge there has been no link between CX3CR1 and $CD4^+$ T-lymphocyte ingression into afferent lymphatics.

To further validate the requirement for CX3CR1 in $CD4^+$ Jurkat migration across lymphatic endothelium, KD of CX3CR1 in both LECs and Jurkats was carried out. 24 h post transfection, CX3CR1 protein levels were successfully reduced in LECs (Figure 5.18a,b). In the Transwell

migration assay, baseline migration using siCX3CR1 KD LECs was significantly lower than with WT, and this level of migration was not reduced further by fingolimod dosing (Figure 5.18c). While this result does not conclusively link fingolimod with CX3CR1 antagonism it does reaffirm the importance of CX3CR1 in $CD4^+$ T-lymphocyte migration. Unfortunately, a CX3CR1 KD in Jurkat cells could not be produced. A variety of transfection reagents were trialled, but no downregulation of CX3CR1 levels in Jurkats could be achieved. This is a common limitation of Jurkats, their cell membrane is composed of low levels of heparin sulphate proteoglycans which weakens the entry of cationic nanoparticles, like Lipofectamine.[338] Coupled with the endosomal acidification in T-lymphocytes which hinders release of transfection agents,[338] Jurkats are difficult to transfect and require alternative methods such as electroporation.

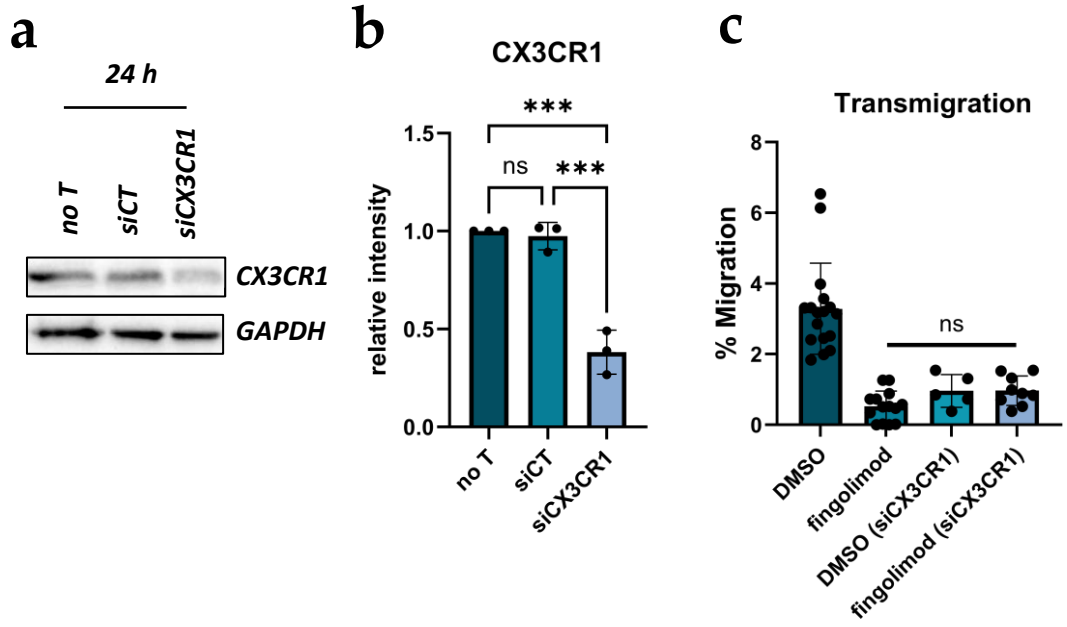


***Figure 5.15: CX3CR1 is necessary for T-lymphocyte migration through lymphatic endothelium.*** *(a) Western blot analysis of CX3CR1 expression in siRNA KD LECs 24 h after transfection (b) Quantification of 24 h siRNA KD Western blots, relative to GAPDH and normalised to non-transfected LECs (no T). N=3. Statistical tests were performed using a one-way ANOVA followed by multiple comparison tests, on unnormalised data. *** = P<0.005, ns = P>0.05. Error bars = SD (c) Migration of T-lymphocytes through noT or siCX3CR1 LEC coated Transwell inserts after 4 h, in response to treatment. Statistical tests were performed using a one-way ANOVA. ns = P>0.05. Error bars = SD.*

## 5.3 *In vivo* migration study

We next wanted to confirm that the inhibitory effect of fingolimod upon T-lymphocyte ingression observed in the *in vitro* assays, translated into *in vivo* studies. Ledgerwood *et al.* previously demonstrated that fingolimod-treated T-lymphocytes migrated into afferent lymphatics less than untreated cells when injected into the ear pinnae of mice.[339] Whilst attempting to recapitulate these results, it was also of interest to look at the effect of fingolimod at earlier time points (5 h vs. 15 h in Ledgerwood *et al.*) to observe the immediate intravasation events. Localised administration could also be used to investigate the effect of fingolimod administration upon the multiple tissue types present in the ear pinnae, rather than pre-treatment of T-lymphocytes independently.

To assess the *in vivo* effect of fingolimod, primary $CD3^+$ T-lymphocytes were isolated from the spleens of donor C57BL/6 mice and cultured in the presence of $\alpha$mCD3/CD28 antibodies and IL-2 to induce activation and proliferation (Figure 5.19a).[246, 340] The activated donor T-lymphocytes were dyed with CFSE and treated with vehicle or fingolimod (1 mg/kg). Our collaborator, Dr Voisin, injected the T-lymphocytes intradermally into the ear pinnae of C57BL/6 mice ($2.5 \times 10^6$ cells in 50 μL per ear). Each mouse received both a vehicle and fingolimod injection to ameliorate the comparability between the migratory data. After 5 h, the mice were sacrificed and the draining LNs and ears were harvested, fixed and stained. I imaged the LNs using confocal microscopy and Dr Benoit-Voisin imaged the site of injection and lymphatic capillaries in the ear pinnae. I analysed the resultant images to assess the extent of T-lymphocyte migration.

There appeared to be no difference in the number of T-lymphocytes still remaining in the tissue 5 h after administration, between vehicle and fingolimod-treated (Figure 5.19b).

Interestingly, there appeared to be a decrease in the number of T-lymphocytes which had ingressed into the peripheral lymphatic vessels in the fingolimod-treated ears, which was close to being statistically significant (P = 0.057). Additional repeats were attempted to increase the significance of this statistic, however, the LYVE1 staining used to distinguish lymphatic vasculature was weak which made it difficult to differentiate between lymphatic and blood vasculature. This could potentially be due to either a poor antibody signal or a decrease in LYVE1 expression, which has been observed under pro-inflammatory conditions.[341] Nevertheless, in the draining medullary LNs, there were significantly less CFSE-labelled T-lymphocytes present when administered with fingolimod treatment, relative to the vehicle control (Figure 5.19b-e). Collectively this data supports the *in vitro* observation that fingolimod inhibits T-lymphocyte intravasation and subsequent clearance to the LNs.

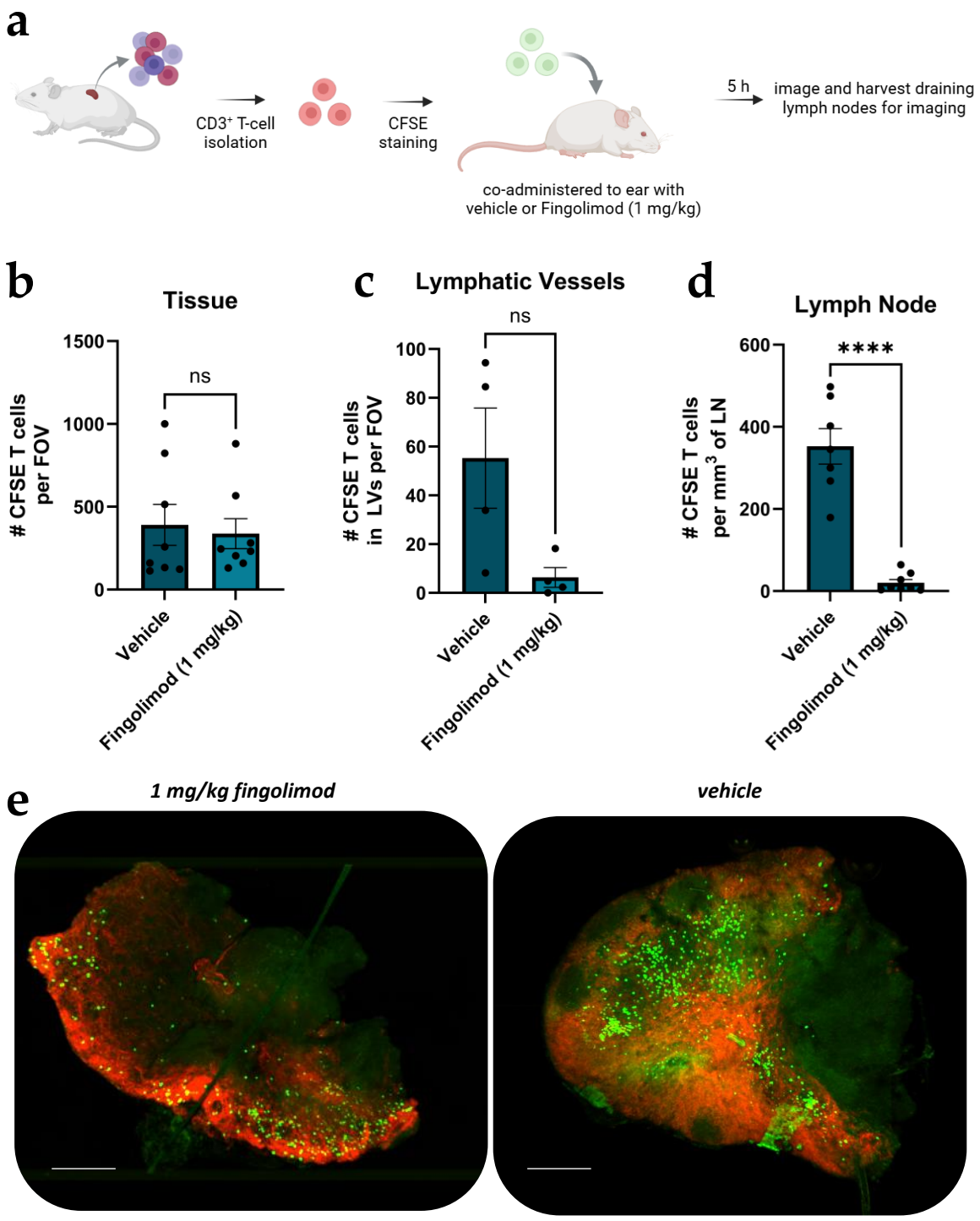


***Figure 5.16: Development of in vivo studies of T-lymphocyte migration in mice.*** *(a) Schematic depiction of in vivo experimental set-up performed in collaboration with Dr Beniot-Voisin. T-lymphocytes were isolated from the spleen of donor C57BL/6 mice and stained with CFSE. T-lymphocytes were administered to the ear with vehicle or fingolimod (1 mg/kg). After 5 h, the draining lymph nodes were harvested, fixed, stained, imaged and quantified. Quantification of CFSE T-lymphocytes observed in (b) tissue, (c) lymphatic vessels and (d) draining lymph nodes was performed. Statistical analysis was performed using a Mann-Whitney U-test. **** = P<0.001, ns = P>0.05 (e) Representative confocal images of draining auricular lymph node; red = LYVE1, green = T-lymphocytes. Scale bar is 250 µm.*

Upon closer inspection of the confocal images taken by Dr Voisin of the ear pinnae, some of the T-lymphocytes appeared to aggregate when treated with fingolimod (Figure 5.20). As such, it was hypothesised that the inhibitory effect of fingolimod upon T-lymphocyte migration could be due to aggregation preventing uptake into afferent lymphatics. It has previously been shown that clustering of T-lymphocytes lowers their motility,[342] however it has not been reported in the context of fingolimod. As these observations were only qualitative, it was necessary to investigate this further, as described below.

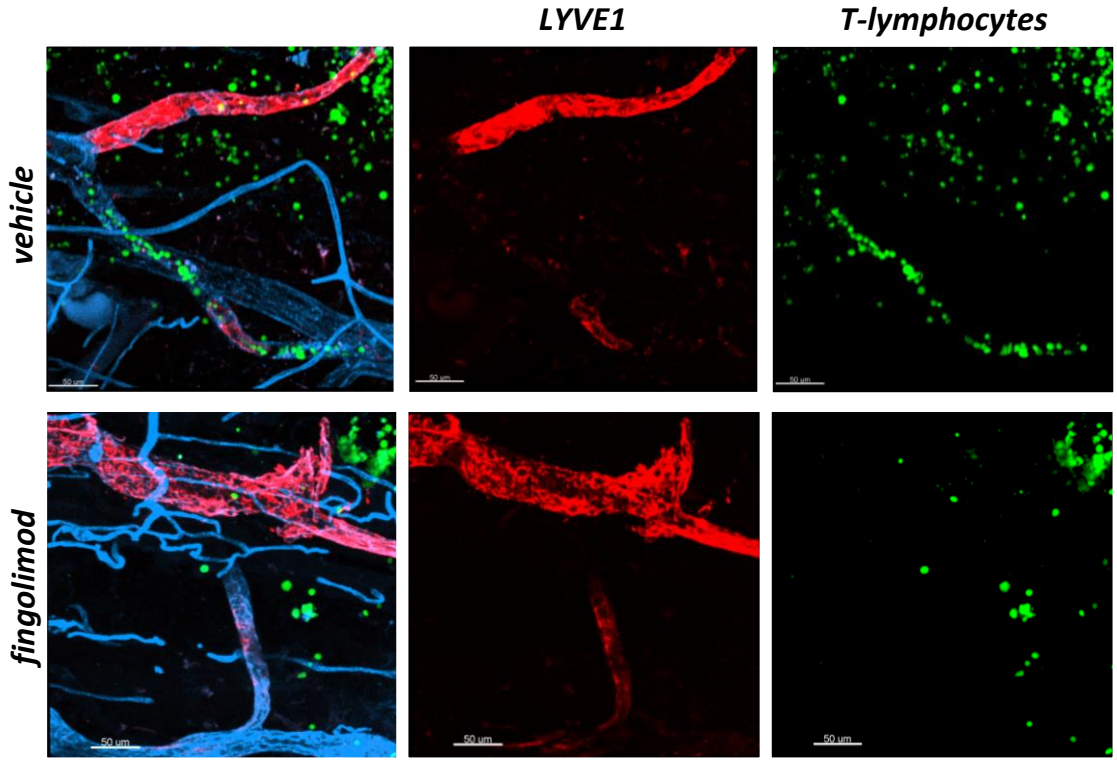


***Figure 5.17: Confocal microscopy of ear pinnae after exogenous CFSE-labelled T-lymphocyte administration.*** *Representative confocal images of ear pinnae fixed 5 h after CFSE-labelled T-lymphocyte administration with either vehicle or fingolimod (1 mg/kg). CFSE-labelled T-lymphocytes (green), LYVE1 (red), CD31 (blue). Scale bar = 50 µm. Images were obtained by Dr Benoit-Voisin.*

## 5.4 T-lymphocyte aggregation studies

To further investigate these *in vivo* observations of increased Jurkat aggregation, it was assessed whether these findings could be replicated *in vitro*, under a controlled setting. Jurkats were seeded with a serial dilution of fingolimod and imaged after 4 h. ImageJ was used to analyse the subsequent images to quantify the number of aggregates per treatment as well as the size of the aggregates (Figure 5.21a). No significant effect upon either the size or the number of Jurkat aggregates could be determined across concentrations (Figure 5.21b). As such, there was no *in vitro* evidence to support the theory that fingolimod induced aggregation of T-lymphocytes.

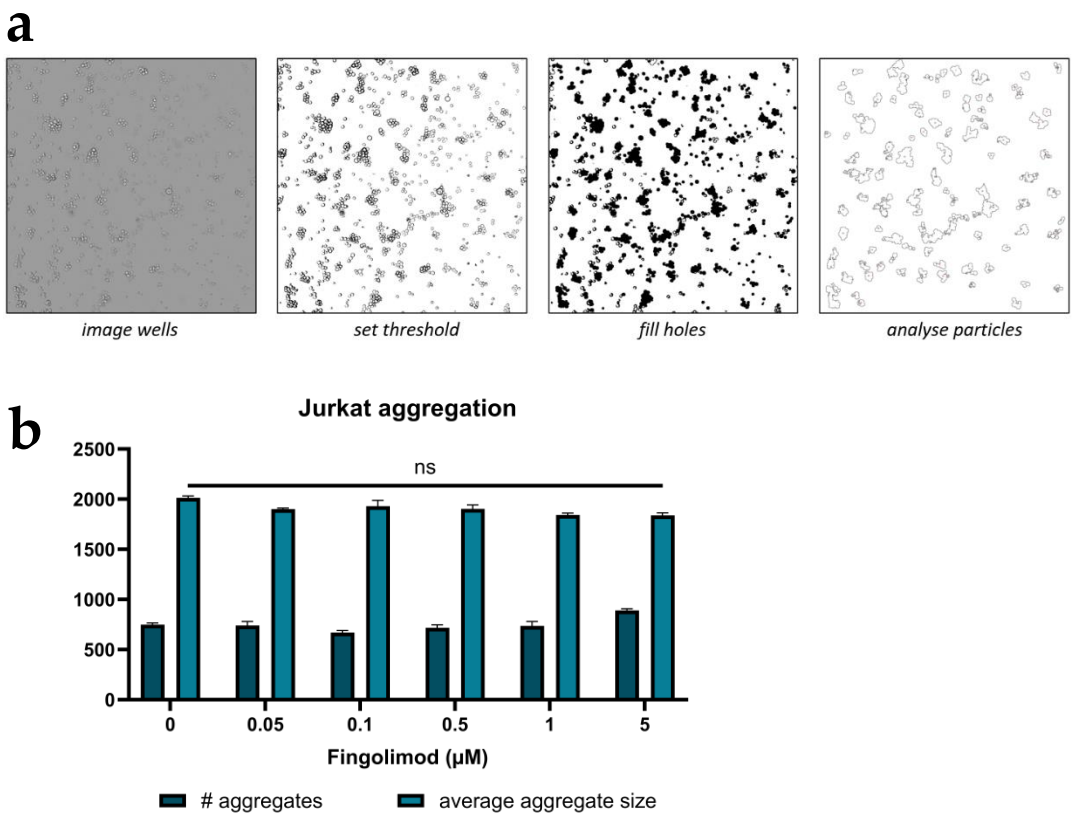


***Figure 5.18: Analysing Jurkat aggregation in response to treatment.*** *(a) Workflow followed to count number and size of aggregates per well using Fiji. A threshold was applied to the greyscale images to distinguish cells from background. Any outlines were filled to ensure clumped cells could be distinguished as an aggregate. Aggregates were then automatically counted and their surface area recorded using a pixel threshold to remove single cells (b) Average size and number of aggregates per well per treatment. Statistical analysis using one-way ANOVA. ns = P>0.05. Error bars = sem.*

Using the optimised Transwell migration assay, it was confirmed that fingolimod inhibited T-lymphocyte migration through the lymphatic endothelium in a dose-dependent manner. This inhibitory effect was supported by *in vivo* studies, but there was no evidence to support that inhibition of ingression was as a result of T-lymphocyte aggregation. To understand more about the role that fingolimod plays in both the lymphatic endothelium and T-lymphocytes to modulate its inhibitory effect, it was necessary to utilise the validated PAL probes to facilitate *in cellulo* labelling and proteomic target identification.

# Chapter 6

# Target Identification in Lymphatic Endothelial Cells Using Photoaffinity Probes

# 6 Target Identification in Lymphatic Endothelial Cells Using Photoaffinity Probes

## 6.1 Optimisation of photoaffinity labelling workflow

The initial investigations into fingolimod's immunomodulatory effects implied that its lymphangiogenic and migratory phenotype were occuring through distinct mechanisms. These unique phenotypic effects could potentially be as a result of tissue-specific action by fingolimod, with different targets and pathways being activated in Jurkats vs lymphatics. To investigate this, it was of interest to utilise the validated PAL probes to identify fingolimod's interactome in both cell types. The differing enrichment patterns could shine a light on the underlying mechanisms of fingolimod's phenotypes of interest. Therefore, attempts were made to optimise the photoaffinity labelling workflow in both Jurkats and lymphatic endothelial cells.

The underlying principle of the photoaffinity labelling technique requires the diazirine probe to undergo sufficient photolytic degradation to facilitate a measurable amount of proteome labelling. To ensure this photolysis occurs, an optimal length of sample irradiation is required; however, it is vital to avoid over-irradiation with UV light as this has been shown to induce the formation of free radicals which promote irreversible protein denaturation.[343, 344] Therefore, a 5 min UV irradiation window was chosen to avoid the potential loss of labelled sample while ensuring probe **114** photolysis, as confirmed by MS (Figure 6.1).

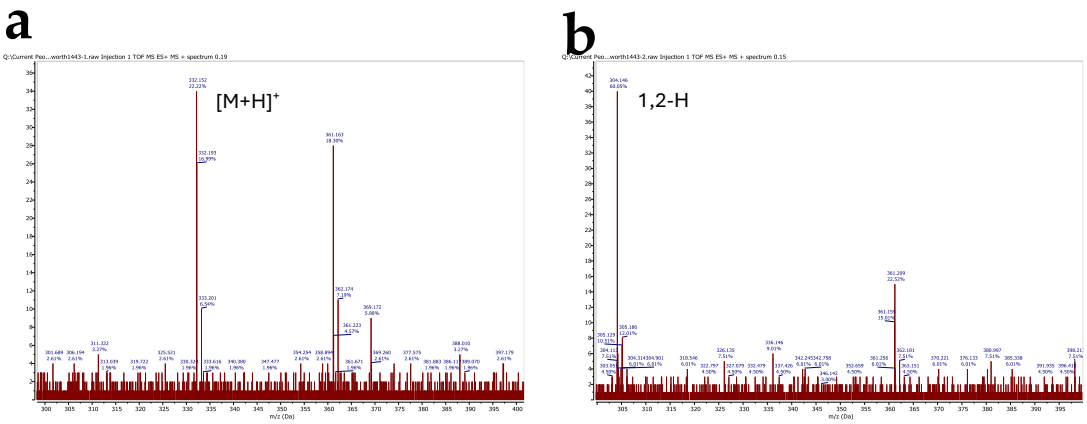


***Figure 6.1: Photolysis of photoaffinity probe 114 achieved after UV irradiation.*** *Mass spectra of 10 μM probe* ***114*** *in MeOH (a) before UV irradiation, where the molecular ion peak [M+H]⁺ of probe* ***114*** *is observed, and (b) after 5 min UV irradiation, where only the photolysed 1,2-H shift product is observed.*

With the irradiation timeframe confirmed, the labelling workflow could be further optimised in the cell lines of interest.

### 6.1.1 Optimisation of photoaffinity workflow in Jurkats

Due to the proliferative nature of Jurkats, optimisation in this cell line was attempted first. As Jurkats are a comparatively small cell (~10 μm),[345] it was decided to optimise the workflow using a large population (1 x $10^7$ cells) per condition to ensure a concentrated protein volume for SDS-PAGE analysis. The general workflow proceeded with Jurkats seeded in a T75 to ensure larger surface area coverage for maximal irradiation, before treatment for a preliminary 3 h timeframe (Figure 6.2a). PBS washes were performed to remove excess probe and reduce sample contamination from serum proteins in the incubation media, due to the high plasma protein binding potential of fingolimod (99.7%).[346] Jurkats were then UV irradiated in PBS, on ice, for 5 min before lysis. After sample normalisation, TAMRA-azide was conjugated using a CuAAC reaction and the samples were subjected to SDS-PAGE. An

initial dose response trial was performed to assess PAL probe **114** labelling (Figure 6.2b). Whilst there appeared to be a dose-dependent nature to the extent of labelling, the in-gel fluorescence wasn't clear. It was then hypothesised that the lack of signal could be improved by changing the lysis buffer.

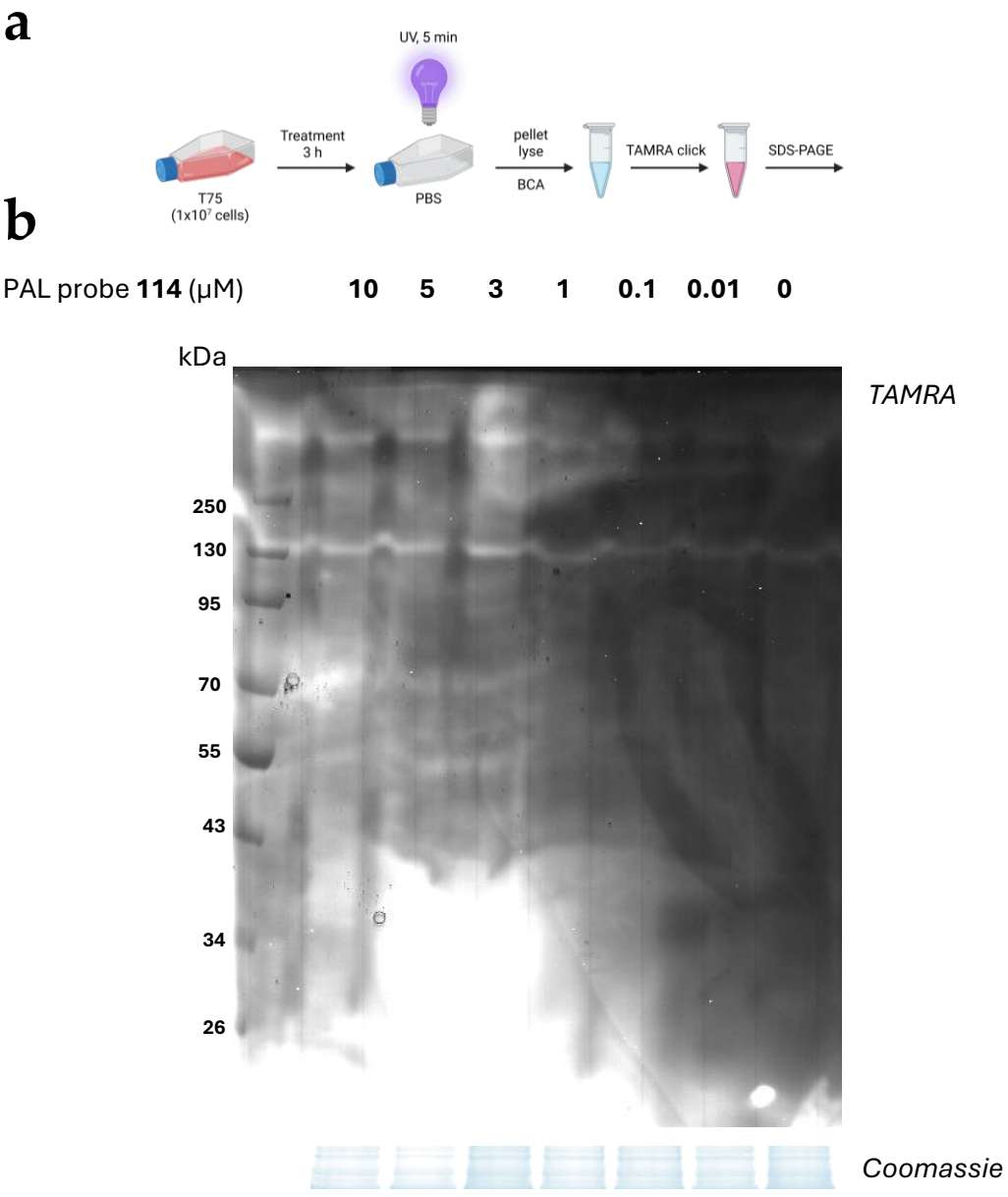


***Figure 6.2: Dose response of probe 114 labelling in Jurkats.*** *(a) Schematic depiction of labelling workflow in Jurkats (b) In-gel fluorescence of TAMRA-conjugated samples treated with probe **114** (3 h, 5 min UV irradiation). Coomassie used for total protein stain.*

Initially, RIPA had been used as the chosen lysis buffer in an attempt to follow previous lab protocols. However, RIPA is a Tris-based buffer, and the tris(hydroxymethyl)aminomethane salts can chelate Cu(I), hindering the necessary Click reaction. Therefore, PBS-based lysis buffers were used going forward.

The preliminary pharmacological evaluation of fingolimod's mechanism of action indicated that its protein target of phenotypic interest is a GPCR (Figures 5.4 & 5.15). All known GPCRs are membrane-bound proteins with 7 characteristic transmembrane (TM) helices.[347] The inherent hydrophobic nature of these TM regions is responsible for the propensity of GPCRs to aggregate during protein extraction and isolation. To prevent this aggregation, and to enable GPCR detection by Western blot analysis and MS, it is common practice to use additional surfactants to facilitate GPCR solubilisation. A screen of PBS-based lysis buffers was trialled to identify the most compatible surfactant (Figure 6.3). A selection of surfactants (SDS, CHAPS, Triton X-100, NP-40) was screened with no significant improvement in the clarity of the TAMRA bands, despite loading over 100 μg of protein per lane.

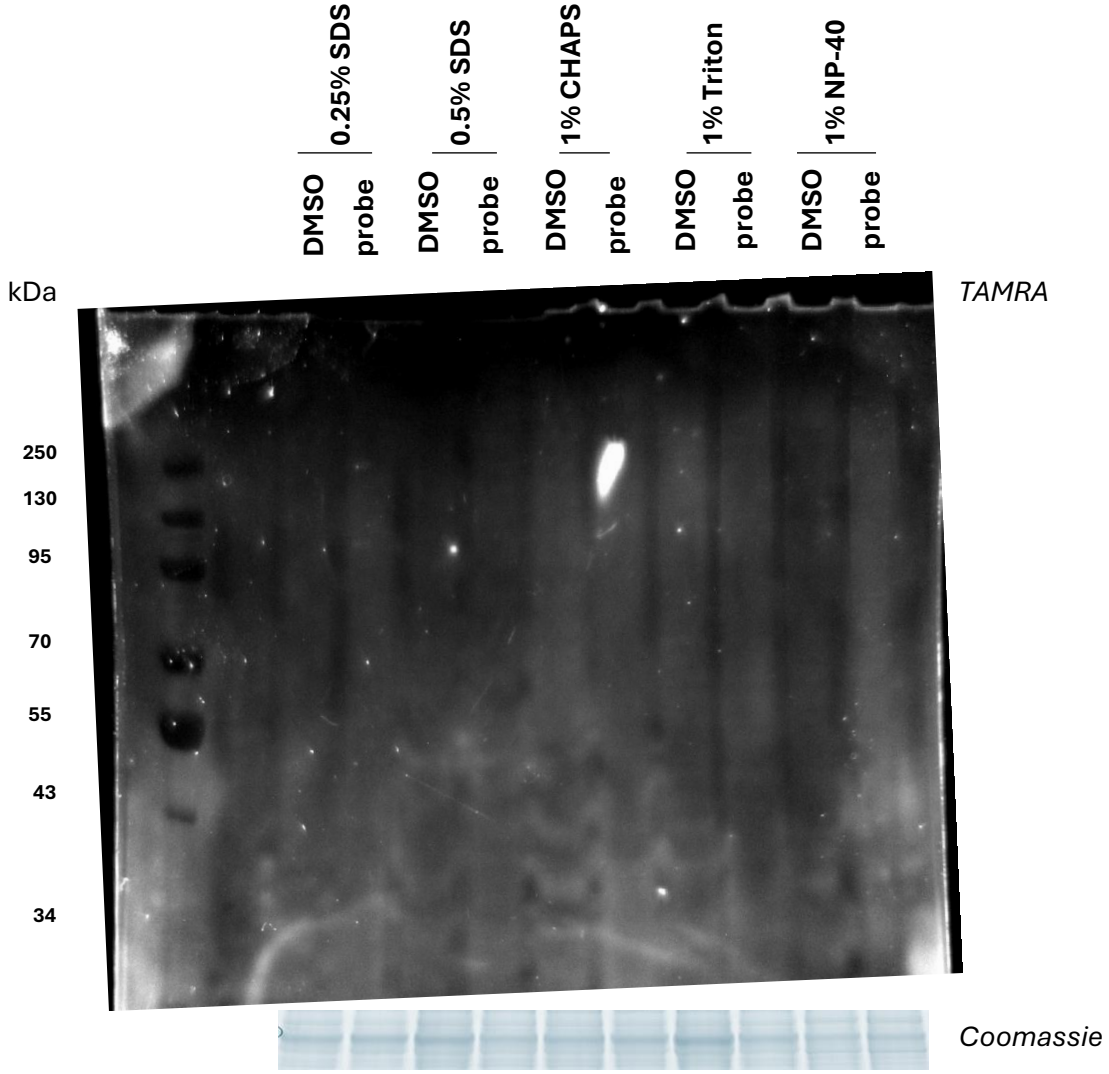


***Figure 6.3: Lysis buffer screen in Jurkats.*** *In-gel fluorescence of TAMRA-conjugated samples treated with probe* ***114*** *(3 μM, 3 h, 5 min UV irradiation). Coomassie used for total protein stain.*

It was then hypothesised that the serum proteins in the media could be sequestering the majority of probe **114**, resulting in minimal labelling; therefore, serum-free labelling conditions were trialled (Figure 6.4). In the absence of FBS during pre-irradiation probe treatment, significantly less labelling was observed by in-gel fluorescence. This finding made it clear that the presence of serum was necessary for probe uptake in Jurkats

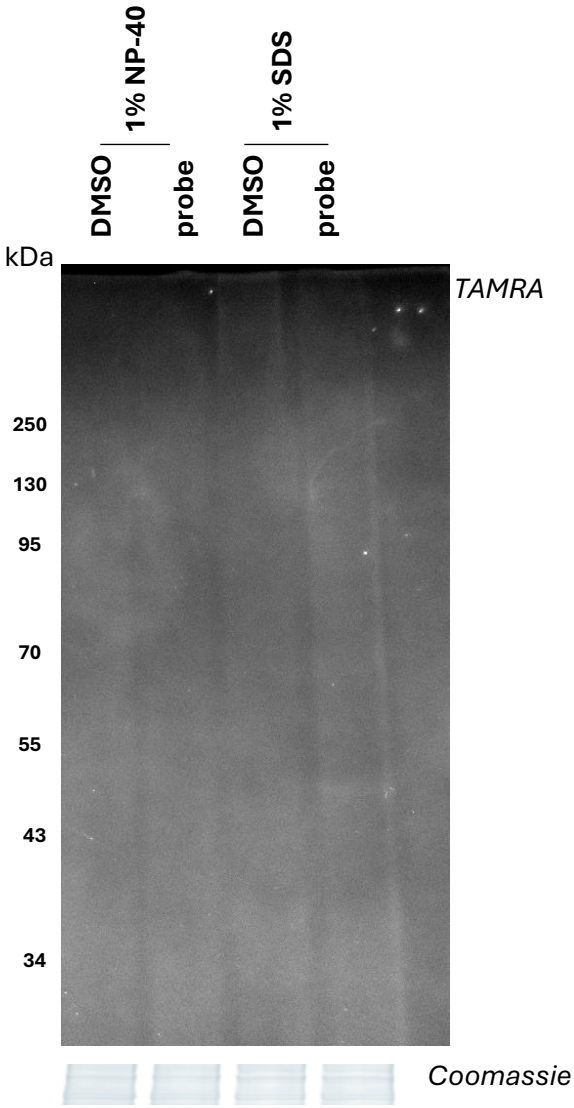


***Figure 6.4: Serum-free labelling conditions trialled in Jurkats.*** *In-gel fluorescence of TAMRA-conjugated samples treated with probe **114** (3 µM, 3 h, 5 min UV irradiation) in the absence of FBS. Coomassie used for total protein stain.*

With no observable improvements with the labelling in the Jurkat cell line, it was decided to prioritise optimisation of the LECs. In the future, alternative methods of Jurkat lysis (i.e. sonication) or alternative cell lines (i.e. primary human T-lymphocytes) could be explored to improve the labelling workflow. In addition, the efficiency of the Click chemistry could have been sub-optimal, explaining the lack of signal observed, as such a thorough analysis of the Click reagents could rectify this issue (i.e.TCEP pH).

### 6.1.2 Optimisation of the photoaffinity workflow in lymphatic endothelial cells

Guided by the attempted optimisation of the Jurkat workflow, the general LEC protocol proceeded in a confluent 10 cm dish (approx. 2-3 x $10^6$ cells), before treatment with probe **114** for a preliminary 3 h timeframe. Precautionary PBS washes were performed and the LECs were UV irradiated, on ice, for 5 min before lysis. After BCA normalisation, TAMRA-azide conjugation was performed and the samples were subjected to SDS-PAGE. There were similar issues with clarity of the in-gel fluorescence band (Figure 6.5a), however the excessive background fluorescence could be removed by running the gel longer to 'run off' the excess TAMRA-azide (Figure 6.5b). However, this still did not improve the lack of clear signal in the gels, so a screen of lysis buffers was performed.

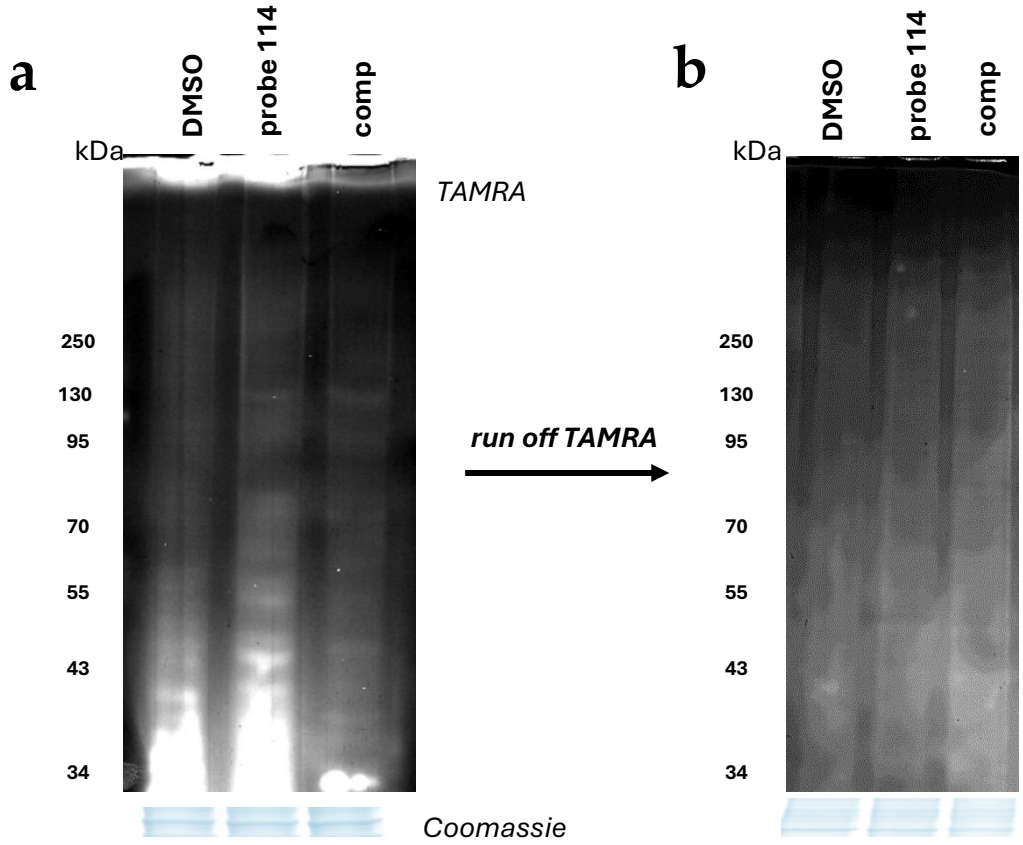


***Figure 6.5: Optimisation of TAMRA sample in-gel fluorescence.*** *SDS-PAGE gels of TAMRA-conjugated samples, imaged at 520 nm. Gels were loaded with lysates from cells treated with DMSO, 3 μM probe **114** and 3 μM probe **114** + 10 μM fingolimod (competition). Coomassie used for total protein stain.*

A variety of non-ionic (NP-40, Triton X-100), ionic (SDS) and zwitterionic (CHAPS) detergents were tested. Whilst all trialled lysis buffers demonstrated a significant improvement in signal clarity, relative to RIPA, NP-40 was chosen as the preferred surfactant moving forward, due to its broader scope solubilising potential (Figure 6.6).

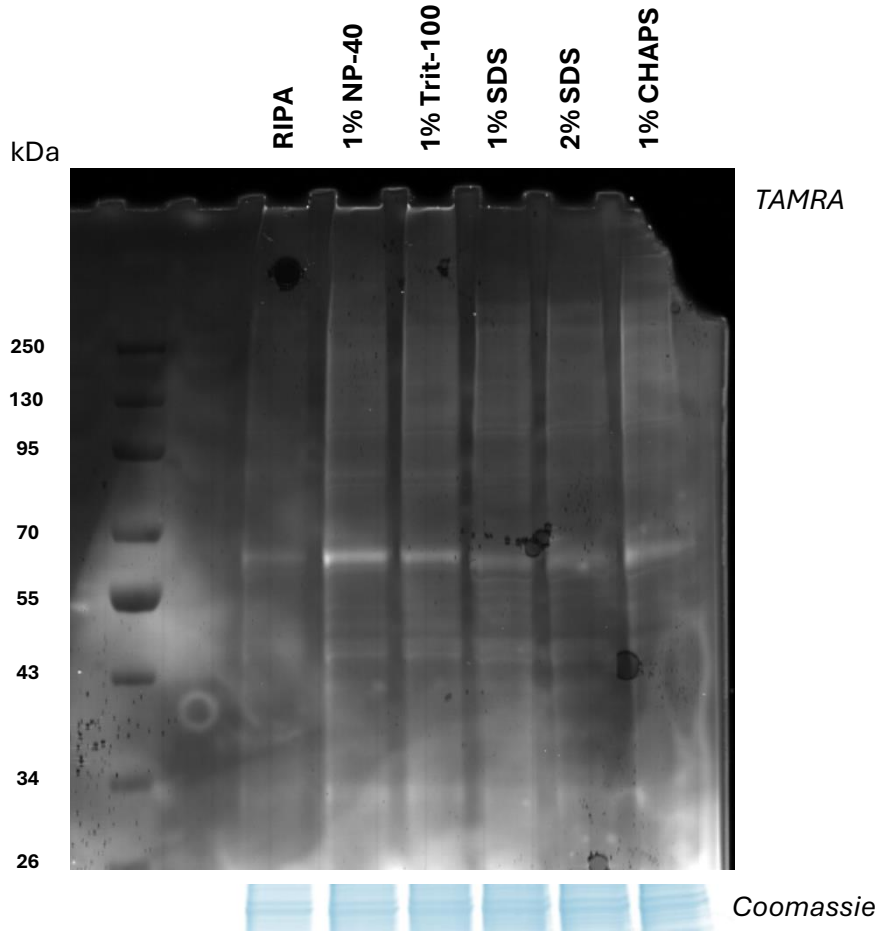


***Figure 6.6**: **Optimisation of lysis buffer conditions.** In-gel fluorescence of lysis buffer screen to identify optimal buffer conditions for improved TAMRA signal (1 μM **114** for 3 h, 5 min irradiation). RIPA is a Tris-based buffer, all other buffers were made up in PBS. Coomassie used for total protein stain.*

To further optimise the labelling protocol, a dose response of probe **114** (0.01 – 3 μM) was performed to assess the optimal concentration for labelling (Figure 6.7). Dose-dependent signal intensity was observed upon increasing probe **114** concentration, with the signal

plateauing at 1 μM. However, as the observable $EC_{50}$ of probe **114** in the phenotypic lymphangiogenesis screen was 3.02 μM (Figure 5.1), it was determined that an optimal dose of 3 μM would ensure capture of the phenotypic proteins of interest.

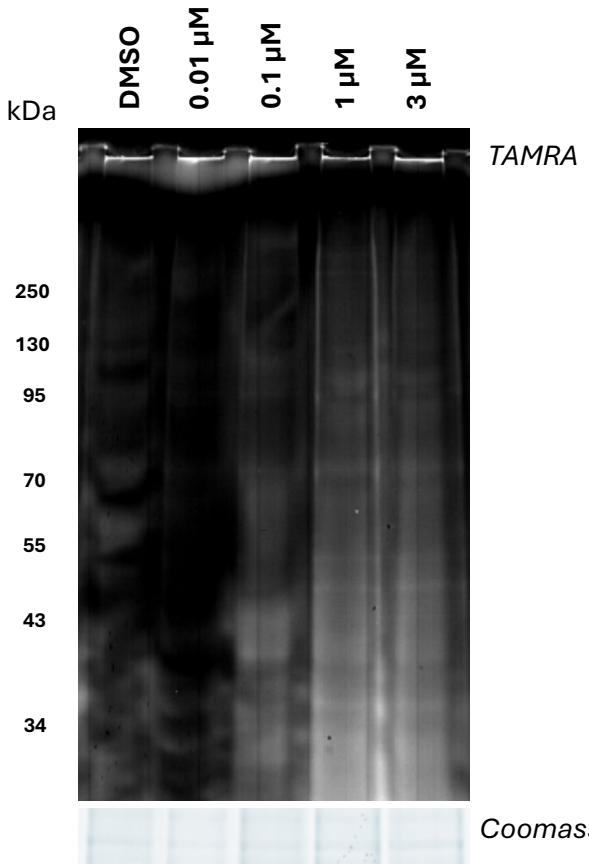


***Figure 6.7: Optimisation of probe dosage**. In-gel fluorescence of TAMRA-conjugated samples subjected to a serial dilution of probe **114** (3 h, 5 min UV irradiation). Coomassie used for total protein stain.*

It was also of interest to explore whether there was an optimal time frame to dose the LECs with probe **114,** before irradiation. It was essential that the probe had ample time to permeate the cells and undergo the key SPHK2-mediated phosphorylation that was necessary for its phenotypic activity. LECs were dosed with 3 μM probe **114** for 0.5, 1, 2 and 3 h time intervals before UV irradiation and sample preparation. There appeared to be no observable difference

in the bands labelled between the different time points by in-gel fluorescence of the TAMRA-conjugated samples (Figure 6.8).

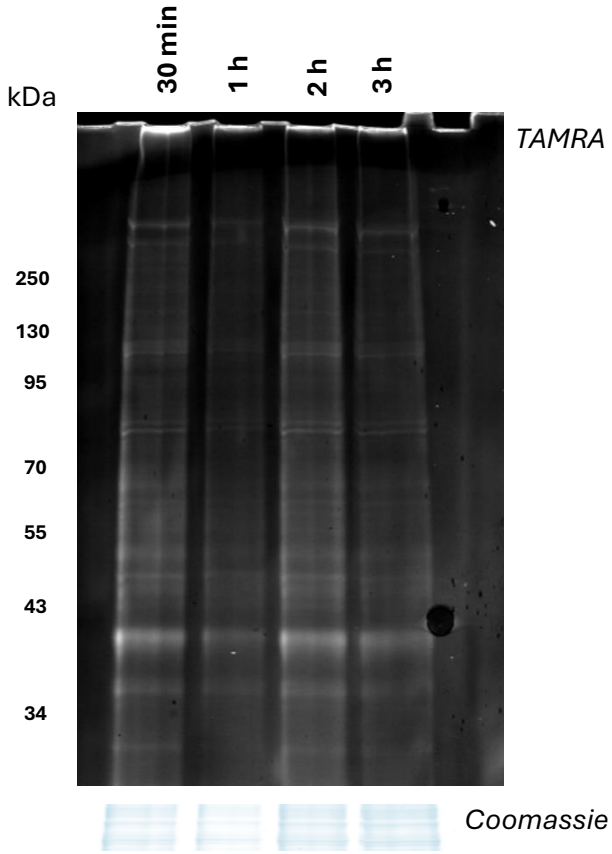


***Figure 6.8: Optimisation of labelling timeframe***. *In-gel fluorescence of TAMRA-conjugated samples treated over distinct time intervals (3 μM **114**, 5 min UV irradiation). Coomassie used for total protein stain.*

To confirm whether this observation correlated with the expected labelling of a known membrane target of fingolimod, the presence of $S1PR_1$ was assessed. A modified workflow was followed for biotin-conjugation of the labelled samples (Figure 6.9a). Western blot analysis showed the presence of $S1PR_1$ across all time points (Figure 6.9b). As the length of probe **114** pre-dosing did not appear to have any significant influence on labelling coverage, it was decided that a 1 h treatment would allow capture of fingolimod's initial interactome.

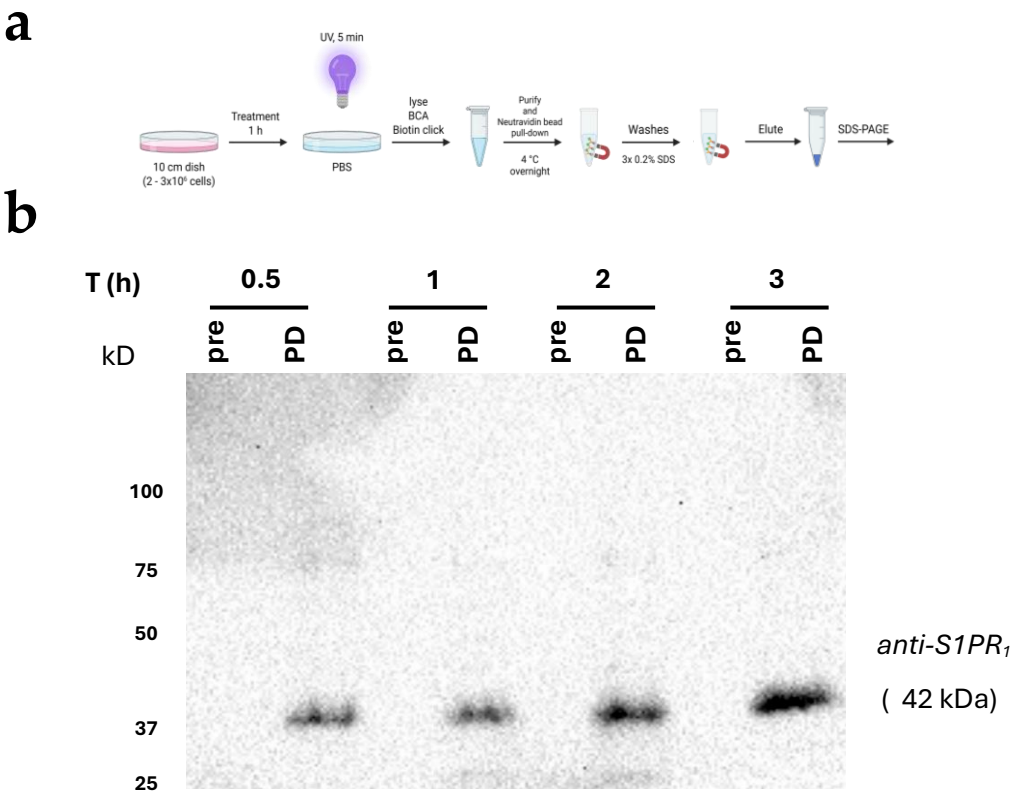


***Figure 6.9: Optimisation of labelling timeframe.*** *(a) Labelling workflow for neutravidin magnetic bead pull-down of biotinylated, labelled samples (1 h, 5 min UV irradiation) (b) Pre- and post-pull down (PD) biotin-conjugated protein samples treated over distinct time intervals (3 μM* ***114****, 5 min UV irradiation). Western blot analysis shows S1PR₁ labelling and capture across all time intervals.*

This observation also served as further validation of the photoaffinity labelling technique and the ability of probe **114** to mimic fingolimod's interactions. It is worth noting that the pull-down procedure used in Figure 6.9 was comprised of an optimised workflow compared to Figure 6.11, explaining the enhanced clarity. This optimisation will be discussed later in this chapter and is described in full detail in the Methods.

As previously stipulated, robust controls are essential to determine the identity of true probe-protein interactions, amongst the background probe labelling. Negative control probe **130** had previously demonstrated inactivity in both immunomodulatory phenotypic assays, and was therefore trialled as a control condition. It was also of interest to explore the use of fingolimod as a competitive ligand to indicate true interactions. The short time frame of the pre-dosing

allowed exploration of higher fingolimod doses, capturing initial interactions before inducing cytotoxicity (Appendix V). To ensure substantial competition with the PAL probe **114** (3 μM), both 10 and 30 μM fingolimod doses were trialled. In-gel fluorescence revealed that significantly more labelling had been achieved by the negative control probe **130**, relative to probe **114** (Figure 6.10). It was postulated that the more lipophilic nature of probe **130** could enhance cell permeability and non-specific protein interaction, compared to the more targeted interactions of probe **114**. The fingolimod co-treatment conditions gratifyingly appeared to outcompete some of the bands in the gel, an observation which was more defined in the 30 μM competition treatment.

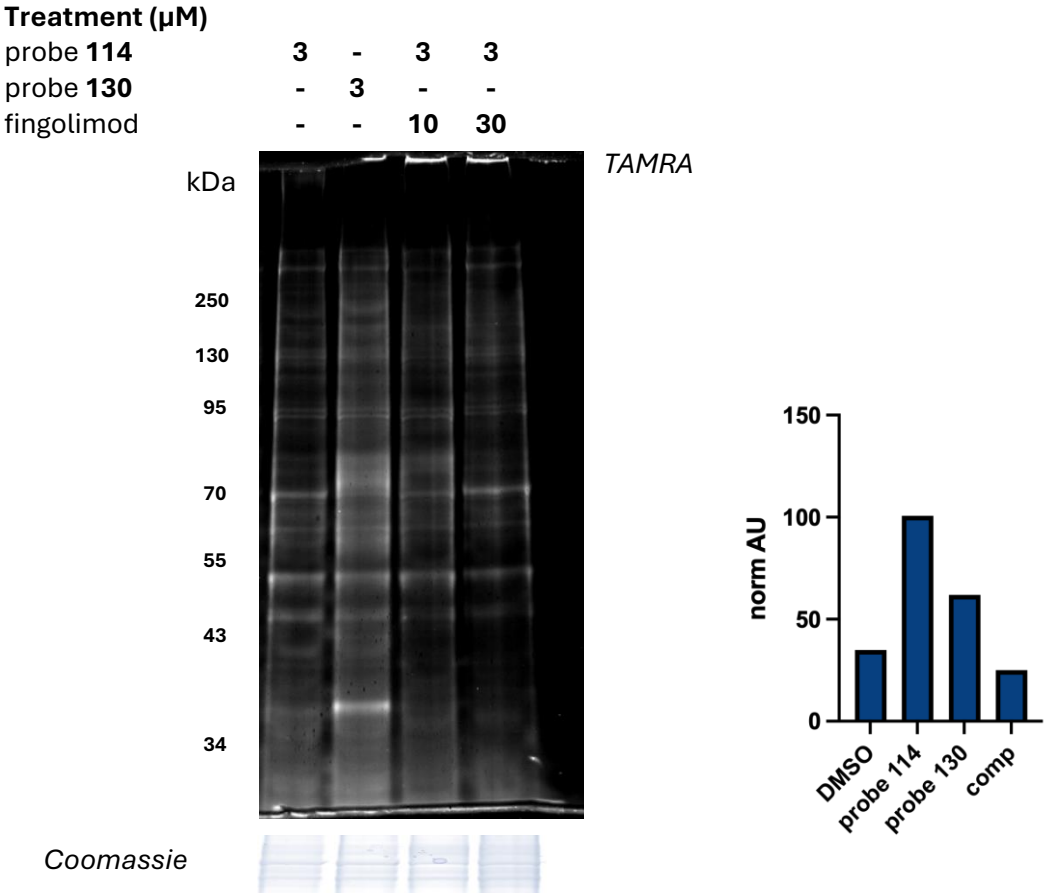


***Figure 6.10: Optimisation of labelling timeframe.*** *In-gel fluorescence of TAMRA-conjugated samples treated over distinct time intervals (3 μM **114**, 5 min UV irradiation). Coomassie used for total protein stain. The overall signal per lane relative to the Coomassie stain was quantified. N=1.*

Western blot analysis of the biotinylated pull-down samples showed enrichment for $S1PR_1$ relative to the pre-pulldown samples (Figure 6.11). There was also significantly more $S1PR_1$ present in the probe **114** treated samples relative to the DMSO control, which was promising. There appeared to be some labelling of $S1PR_1$ by the negative control probe **130**, but encouragingly, there was little $S1PR_1$ observed in both of the competition-treated pull-down samples.

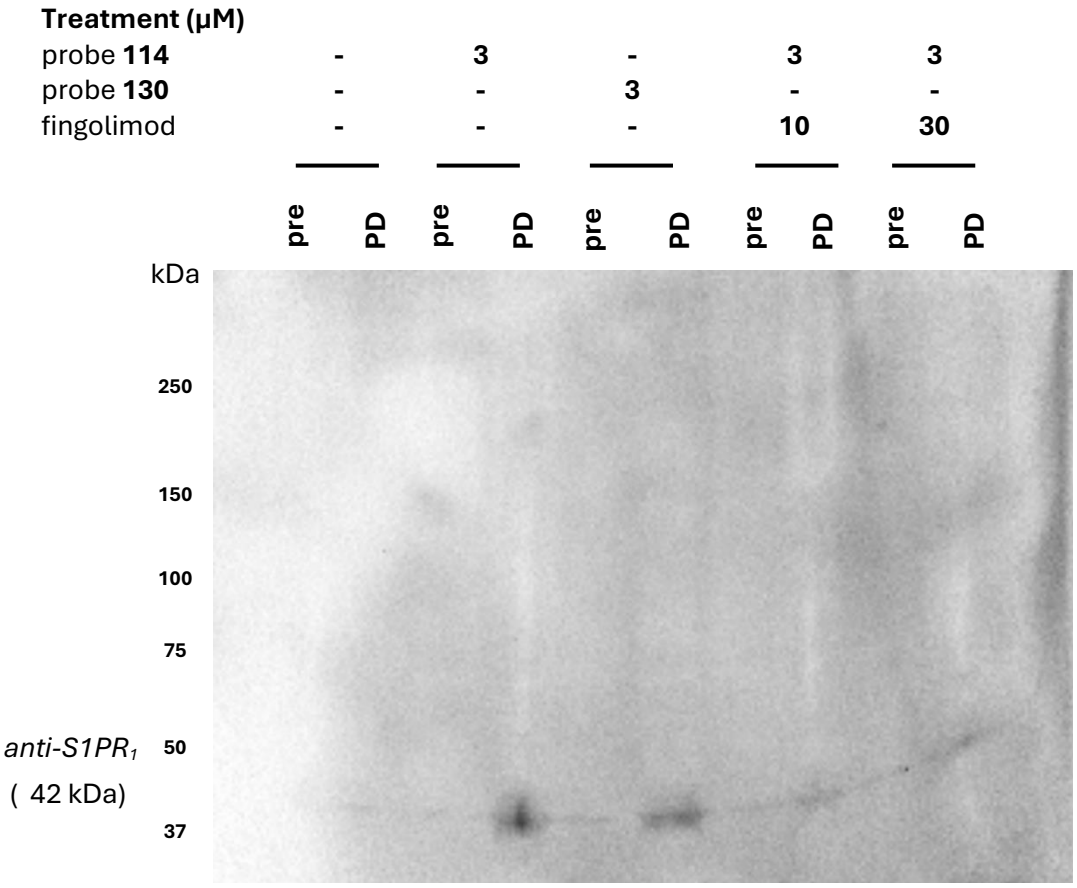


***Figure 6.11: Identifying a suitable control condition for photoaffinity labelling.*** *Pre and post pull-down (PD) biotin-conjugated protein samples (1 h, 5 min UV irradiation). Immunostained for $S1PR_1$.*

Whilst these initial results were promising, the signal intensity for $S1PR_1$ was very weak. In an attempt to improve the signal-to-noise ratio, and ensure maximum capture of fingolimod's labelled target proteins, a higher volume of beads per mg of protein was incorporated into the workflow (100 μL/mg -> 250 μL/mg). This modification would allow for the capture of more

protein per sample. However, with increased beads there is the inherent issue of increased non-specific binding. To combat this, a more thorough bead washing protocol was adopted (Figure 6.12a). These adjustments to the method significantly improved the signal of $S1PR_1$ in the pull-down samples (Figure 6.12b). Western blot analysis reaffirmed that negative control probe **130** was labelling $S1PR_1$. It was also revealed that, although initially promising, the 10 μM fingolimod competition dose did not significantly outcompete probe **114** binding to $S1PR_1$. Contrastingly, the 30 μM fingolimod competition appeared to completely outcompete probe **114** labelling of $S1PR_1$.

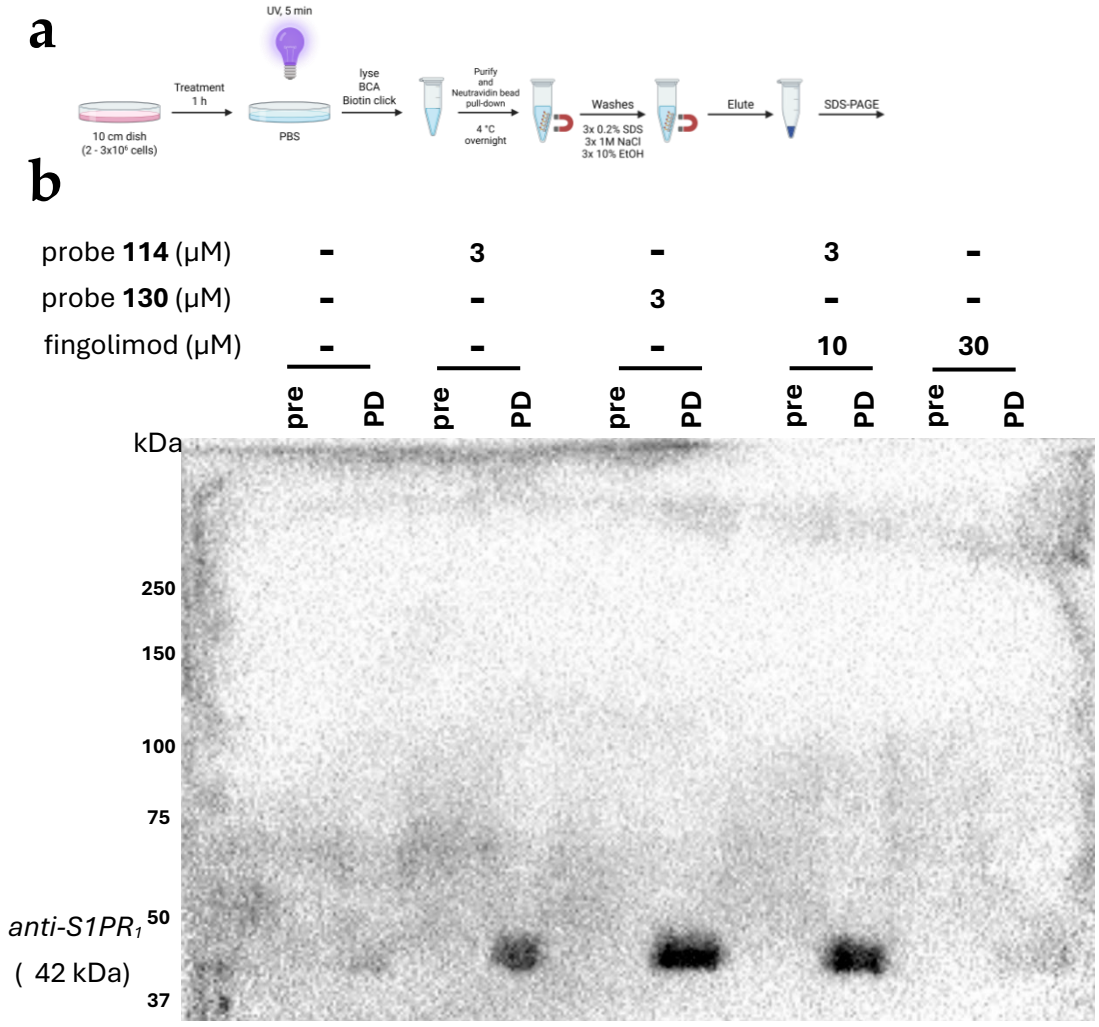


***Figure 6.12: Increased beads and robust washing improved the signal of S1PR$_1$ in pull-down.*** *(a) Optimised labelling workflow for neutravidin magnetic bead pull-down of biotinylated, labelled samples (1 h, 5 min UV irradiation) (b) Pre and post pull-down (PD) biotin-conjugated protein samples (1 h, 5 min UV irradiation). Immunostained for S1PR$_1$.*

To assess whether this pattern was consistent across the proteome, the levels of biotinylation within PD samples was investigated (Figure 6.13). Probe **114**-treated LECs appeared to have much more biotinylated proteins present within the PD samples, compared to DMSO-treated and competition.

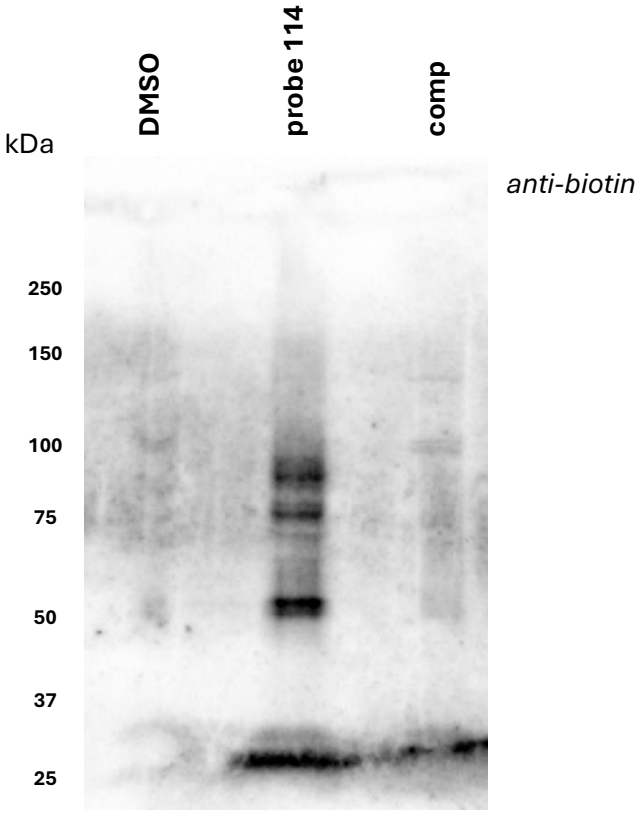


***Figure 6.13: Probe 114-treated LECs demonstrated increased sample biotinylation. P****ull-down (PD) biotin-conjugated protein samples (1 h, 5 min UV irradiation) from LECs treated with DMSO (0.1%), probe **114** (3 μM) or competition (3 μM probe **114** + 30 μM fingolimod). Immunostained for biotin.*

Despite the promising lack of phenotypic effect observed by negative control probe **130** in both the lymphangiogenesis and migration assays, significant labelling of $S1PR_1$ was still observed. It was shown that $S1PR_1$ is not the target responsible for these phenotypes (Figures 5.3 and 5.15), but phosphorylation of fingolimod is still necessary for $S1PR_1$ agonism.[119] The site of SPHK2-mediated phosphorylation on probe **130** was purposefully blocked in the design of the probe, highlighting the disconnection between affinity and efficacy. Control probe **130** must still exhibit an inherent affinity towards $S1PR_1$, whilst not exhibiting the necessary structural indication to induce agonism. Whilst avoiding making experimental assumptions based on a different target, the uncertainty surrounding the selectivity of control probe **130** was of concern. If control probe **130** maintained a non-functional affinity for other targets, then 'true' hits could be discarded due to poor enrichment relative to the control. This

justified the decision to use the 30 μM fingolimod competition control for future proteomics studies.

Unfortunately, a robust protocol for photoaffinity labelling in Jurkats was not achieved within the scope of this research; nonetheless, a workflow for PAL probe **114** -mediated labelling in LECs was optimised. A screen of detergents identified 1% NP-40 in PBS as a click-compatible lysis buffer, which facilitated distinct in-gel fluorescence imaging of TAMRA-conjugated samples. Preliminary labelling studies identified the optimal probe concentration (3 μM) and pre-irradiation treatment time (1 h) to enable capture of fingolimod's initial interaction partners. This was validated by using a known membrane-bound target of fingolimod, $S1PR_1$. The neutravidin bead pull-down workflow was optimised to increase the overall protein capture whilst reducing non-specific protein binding to the beads. And finally, a suitable control condition was chosen to enable necessary deconvolution of future proteomic data, thereby identifying the true interactome of fingolimod. This thorough workflow optimisation was vital to ensure the highest confidence in the samples generated for proteomic analysis.

## 6.2 Proteomic analysis of lymphatic endothelial cells treated with probe 114

### 6.2.1 Validation of proteomics workflow

With the labelling workflow optimised, it was in our interest to assess the MS workflow as well. Common sample preparation proceeds initially *via* protein denaturation and disulphide bond cleavage using reducing agents such as TCEP and DTT. The free cysteine thiols are then alkylated with iodoacetamide to prevent disulphide bridge reformation and protein refolding. The unfolded proteins then undergo enzymatic digestion from the neutravidin beads. The

most commonly used digestive enzyme for proteomics workflows is trypsin, a serine protease that cleaves peptide bonds exclusively at the *C*-terminal of lysine and arginine residues.[348] As it has previously been demonstrated, fingolimod's target of interest is likely a membrane bound GPCR. An inherent issue with GPCR tryptic digest is the scarcity of lysine and arginine residues present in their sequence due to the hydrophobic nature of their TM regions. This can make GPCR identification by proteomics problematic due to the reduced number of ionisable peptide fragments and low peptide coverage. Several other proteases have been identified that are more suited to membrane protein digestion. ProteinaseK is another serine protease that cleaves the exposed hydrophilic regions of membrane proteins.[349] However, proteinaseK has no defined recognition or cleavage pattern, which is unsuited to the complexity of whole cell proteomics. Despite these concerns, ExPASY *in silico* trypsin digestion predicted significant peptide coverage of $S1PR_1$ (90.8%).[350] Therefore, it was decided to perform a preliminary tryptic digest and LCMS analysis of a single PAL probe **114** labelled pull-down sample to assess the extent of membrane protein detection.

STRING analysis of the resultant protein list revealed a high level of membrane proteins, specifically those involved in focal adhesion and cell junctions (Figure 6.14a). This finding was corroborated by the observed enrichment of cadherin and cell adhesion binding proteins as well (Figure 6.14b).

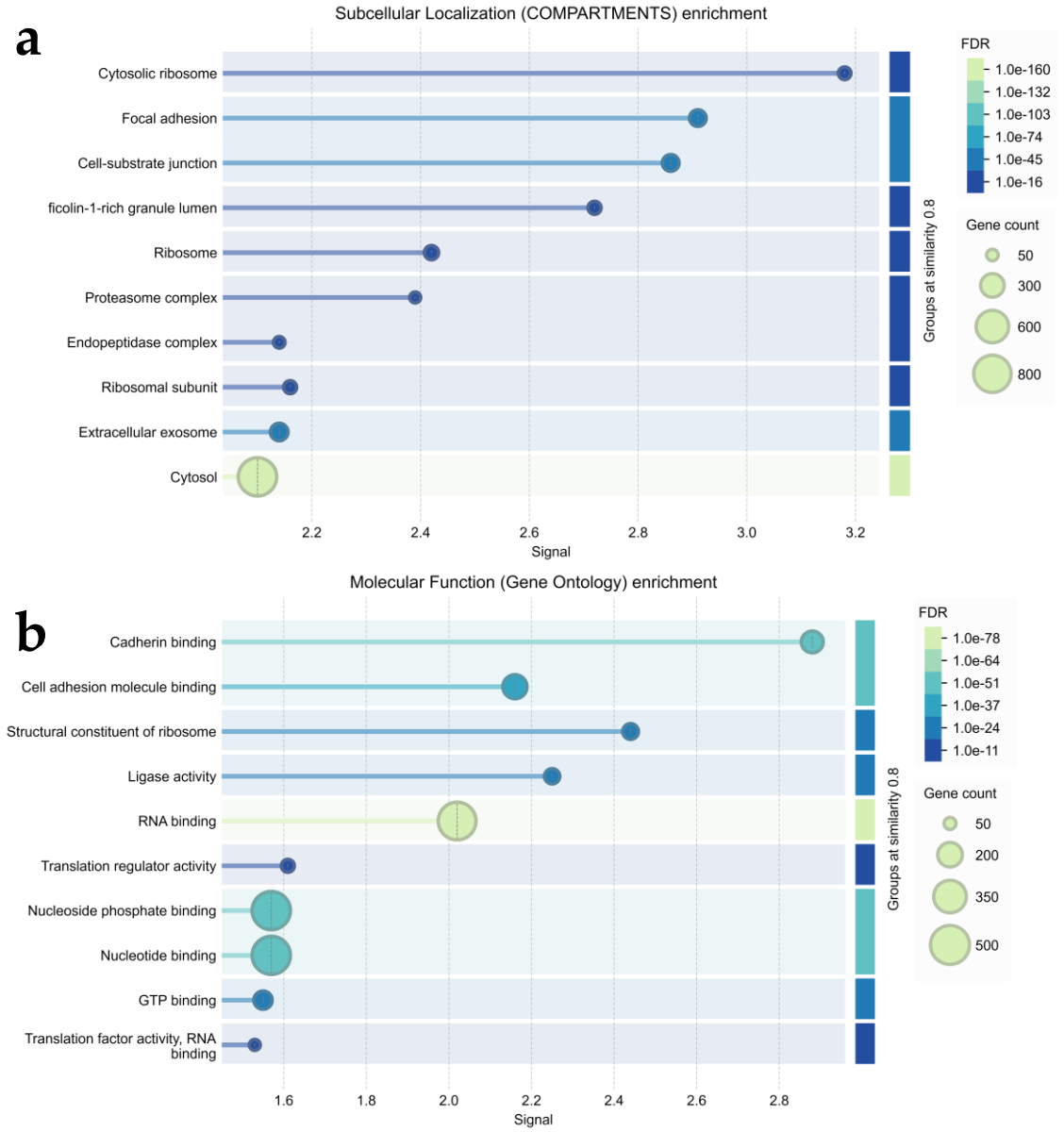


***Figure 6.14: STRING analysis of initial LCMS run on a single probe 114-labelled sample.*** *(a) Top subcellular localisation hits (b) Top molecular function hits.*

Amongst the identified proteins were several naturally biotinylated proteins, confirming the success of the neutravidin pull-down (Table 6.1). Also of note was the identification of several known targets of fingolimod, including the membrane bound $S1PR_1$ and TieI.

***Table 6.1: Known targets of fingolimod and naturally biotinylated proteins identified in the initial LCMS screen of a single probe 114-labelled pull-down sample***

| *Protein* | *Abbrev.* | *Subcellular localisation* |
|---|---|---|
| *Known targets of fingolimod:* | | |
| **Casein kinase I isoform delta** | CSNK1D | Cytosol |
| **Ceramide synthase 2** | CERS2 | ER |
| **Histone deacetylase 6** | HDAC6 | Cytosol, Nucleus |
| **Signal transducer and activator of transcription 3** | STAT3 | Cytosol, Nucleus |
| **Sphingosine-1-phosphate lyase** | SGPL1 | ER |
| **Sphingosine 1-phosphate receptor 1** | $S1PR_1$ | Membrane |
| **Tyrosine-protein kinase receptor 1** | TIE1 | Membrane |
| *Naturally biotinylated proteins:* | | |
| **Acetyl-CoA carboxylase 1** | ACACA | Cytosol |
| **Propionyl-CoA carboxylase** | PCCB | Mitochondria |

As these samples were run without fractionation or TMT-labelling, the proteome coverage is generally limited, with only the most enriched proteins meeting the detection threshold. Therefore, we would expect an even greater coverage in the intended 12-plex TMT-MS study. The DMSO and competition controls would also enable elimination of non-specific and very abundant proteins, permitting the identification of targets that are specifically enriched in probe **114**-labelled samples. These initial findings reaffirmed our confidence to continue with the larger scale proteomic experiment. Subsequently, the labelled samples (DMSO, probe **114** and competition) were prepared in quadruplicate, to enhance the statistical power of the bioinformatic analysis.

TMT-MS chemoproteomics is an expensive experiment to perform, therefore it is also worth acknowledging that there are alternative MS techniques which are compatible with chemoproteomics. The cheapest and therefore more accessible technique is label-free MS, which uses a simple workflow which can be used for large-scale sample analysis. However, it is very sensitive to technical variation between runs and samples which can lower the

statistical power of the data. Another technique is SILAC, which metabolically incorporates heavy isotope amino acids into cell culture allowing isotopic distinction between samples. This is a robust technique with high quantitatively accuracy, however multiplexing is limited to 2 or 3 samples unlike TMT-MS which can incorporate up to 35. Another limitation of SILAC is the non-native system which is adopted by the presence of heavy amino acids, as well as the risk of incomplete labelling or metabolic conversion of some amino acids which can skew data analysis. Therefore, it was decided to use TMT-MS proteomic techniques to quantify the interactome of probe **114**, in collaboration with Dr Kate Heesom at The University of Bristol.

### 6.2.2 TMT-proteomic analysis

The 12-plex TMT proteomic analysis yielded a list of 2839 identified proteins across the 12 samples. Of these proteins, 120 were significantly enriched (FC>1.5, P<0.05) in the probe **114**-treated LECs vs DMSO (Figure 6.15), including S1PR1. Some proteins of initial interest were stabilin-1 (STAB1), galectin-1 (LGALS1) and LYVE1, as all of these proteins have been implicated in the modulation of immune cell migration through lymphatic vessels.[22, 351-353] There were 12 significantly enriched (FC<0.067, P<0.05) proteins present in the DMSO-treated samples, the majority of which were known naturally biotinylated proteins (i.e. histones, carboxylases).

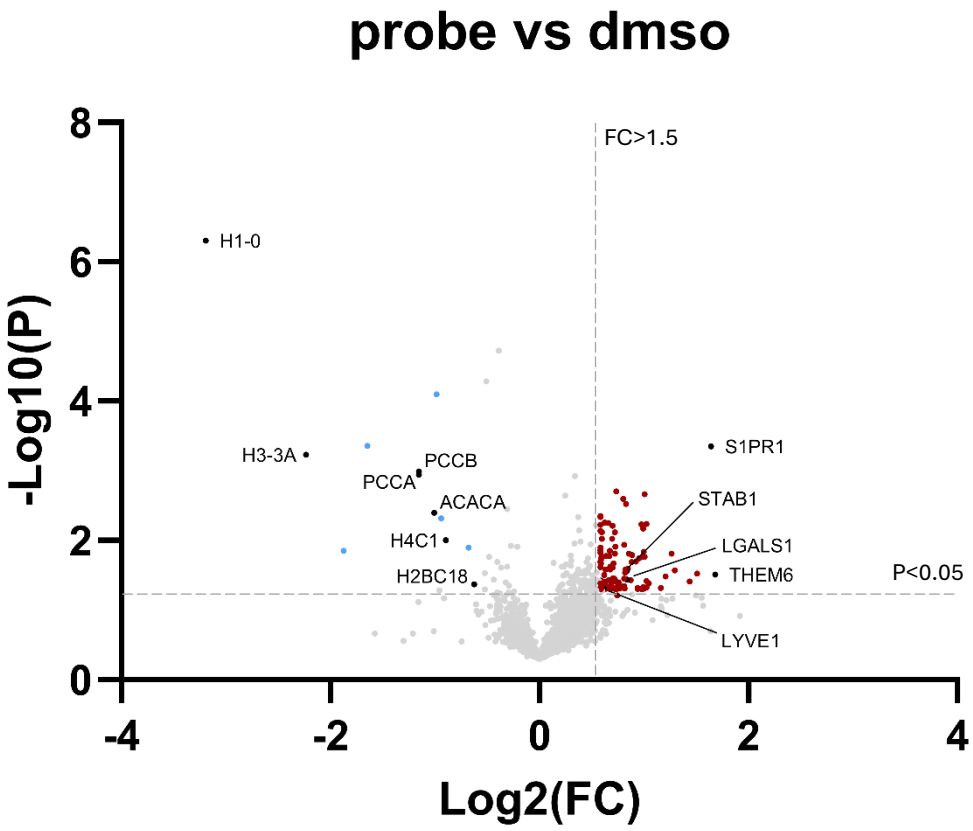


***Figure 6.15: Proteomic analysis of LECs treated with 3 μM PAL probe 114 relative to DMSO-treated control LECs.*** *Volcano plot of proteins enriched by 3 μM PAL probe **114** compared to control cells (0.1% DMSO). Red circles indicate significantly enriched proteins (FC>1.5, P<0.05), black circles indicate proteins of interest, blue circles indicate proteins enriched in the DMSO control cells.*

When comparing PAL probe **114**-treated lymphatics to the fingolimod competition cells (Figure 6.16), there were 186 significantly enriched proteins (FC>2, P<0.05). Amongst these enriched proteins were several known fingolimod interactors (i.e. $S1PR_1$, HDAC2, CerS2, SPNS2). The enrichment of these proteins increased the confidence in the proteomic data, ensuring that PAL probe **114** could capture true interactors of fingolimod.

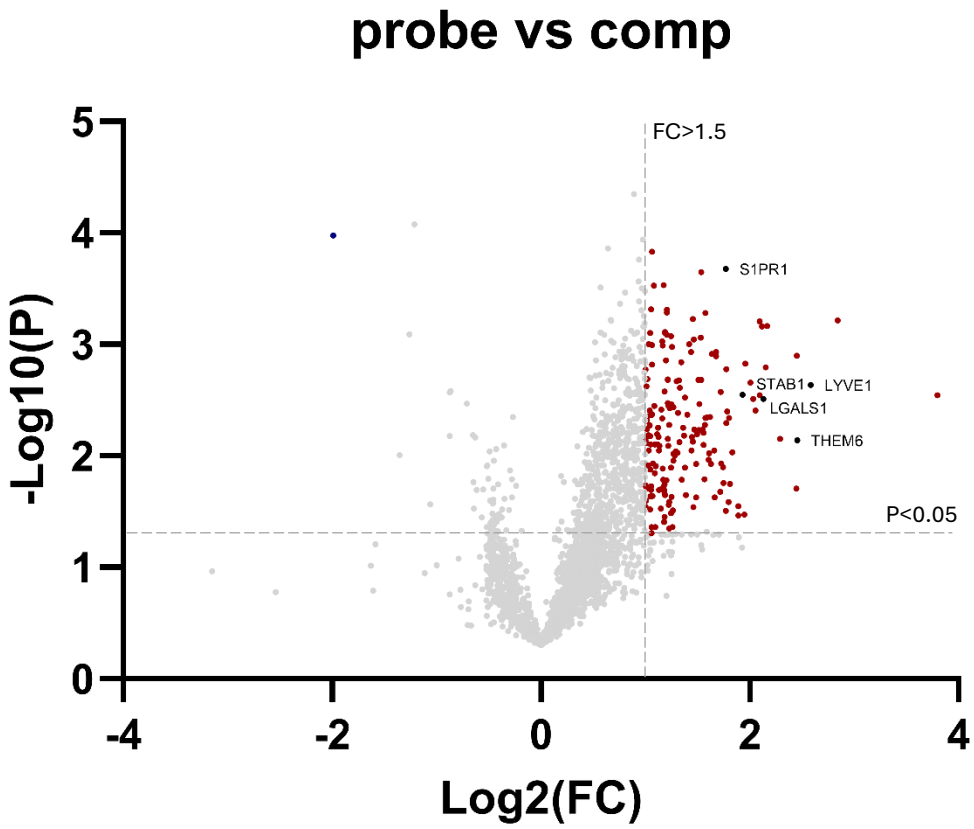


***Figure 6.16: Proteomic analysis of LECs treated with 3 μM PAL probe 114 relative to fingolimod competition LECs.*** *Volcano plot of proteins enriched by 3 μM PAL probe **114** compared to control cells (3 μM PAL probe **114** + 30 μM fingolimod). Red circles indicate significantly enriched proteins (FC>1.5, P<0.05), black circles indicate significantly enriched proteins of interest, blue circles indicate proteins enriched in the control cells.*

The presence of enriched $S1PR_1$ in probe **114**-treated pull-down samples had already been confirmed by Western blot analysis during the optimisation of the labelling protocol (Figure 6.12). Therefore, to further corroborate the findings of the proteomic analysis, THEM6 was

chosen as a substantially enriched protein to assess by Western blot. THEM6 is a thioesterase that plays a role in lipid homeostasis.[354] Probe **114**-treated LECs showed significant enrichment of THEM6 relative to both DMSO control and competition pull-down samples (Figure 6.17)

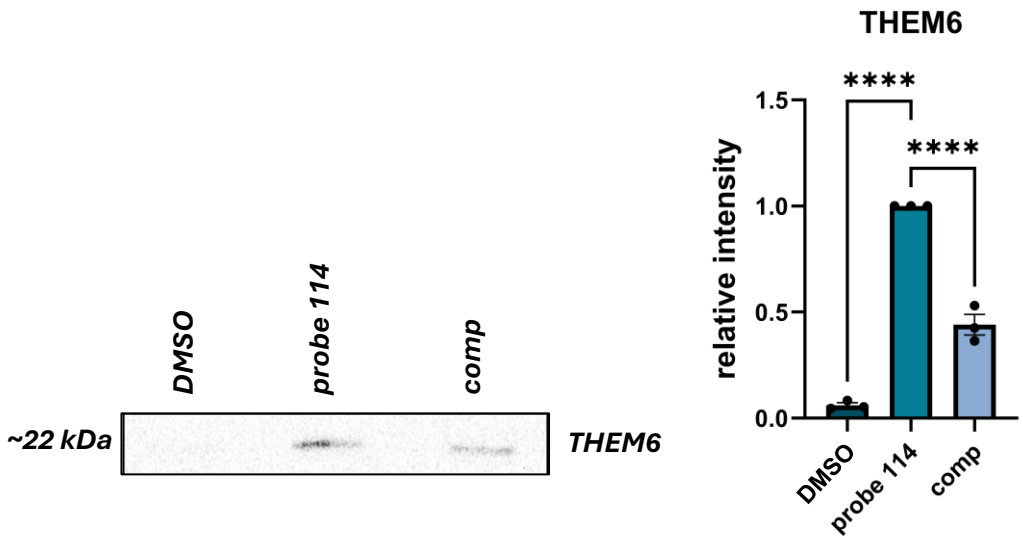


***Figure 6.17: Western blot analysis corroborates the enrichment of THEM6 in probe-treated LECs compared to controls.*** *Quantified Western blot analysis of THEM6 enrichment in 3 μM probe **114**-treated LECs compared to DMSO control cells and competition (3 μM probe **114** + 30 μM fingolimod). Statistical analysis was performed using one-way ANOVA and multiple comparison tests. **** = P<0.001. Error bars = sem. N=3.*

With established confidence in the proteomic data, a broader analysis of the proteins that were enriched relative to the competition cells revealed a huge proportion of proteins involved in mRNA processing, splicing and translation (Figure 6.18). Whilst, there is no prior knowledge of Fing-P directly regulating mRNA, another type of phospholipid, phosphoinositides, have been shown to directly bind to mRNA splicing, capping and transportation machinery.[355] However, the glycosylated nature of phosphoinositides makes them structurally different from Fing-P, therefore it would be unadvisable to make an assumption on Fing-P's activity based on phosphoinositide mechanisms. Another likely explanation for the relatively high proportion of mRNA related proteins is the generally high expression of these housekeeper

proteins present in the cell, particularly in response to a new stimulus (i.e. probe **114**). Coupled with the probable high plasma protein binding capability of the probe (Fing-P PPB> 99.7%),[346] there is likely a high probability of non-specific binding of the probe. A similar assessment could be made for the cytoskeletal and ribosomal proteins which are abundant within a human endothelial cell, all of which demonstrated a high false discovery rate (FDR).

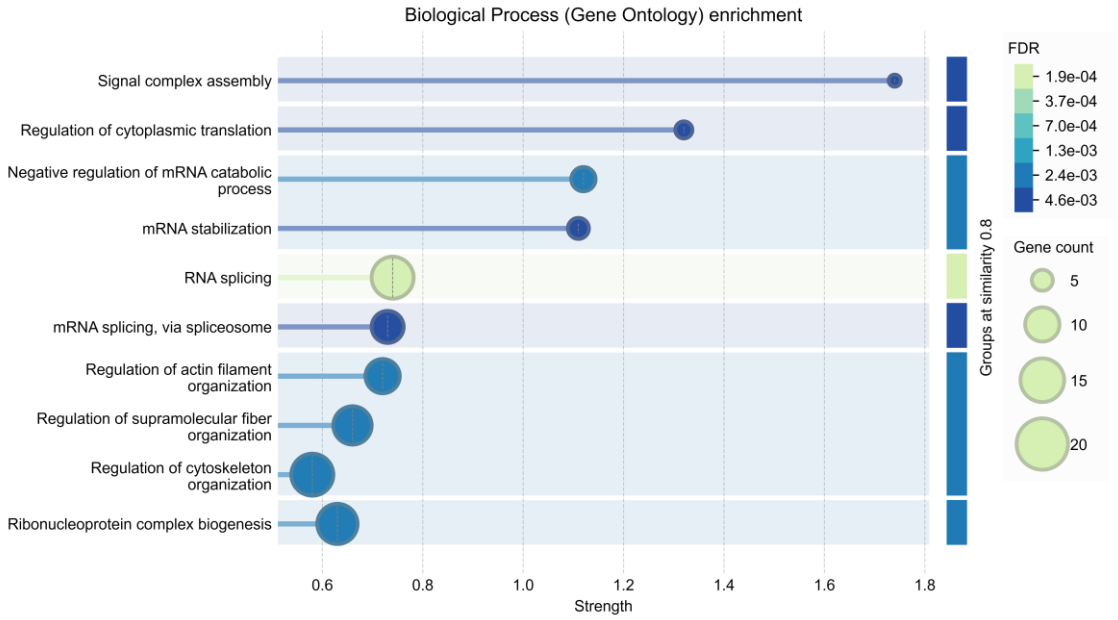


***Figure 6.18: Gene ontology analysis of proteins enriched in 3 μM PAL probe 114 relative to fingolimod competition LECs.*** *STRING GO analysis highlighting the top 10 biological processes associated with the enriched proteins.*

It was decided that a targeted insight into the enriched proteins of phenotypic relevance would be of great interest. Therefore, the 186 enriched proteins were shortlisted to 140, through the removal of ribosomal, spliceosomal and transcriptional machinery. Gene ontology analysis of these shortlisted proteins provided a more detailed account of the biological processes associated with these proteins (Figure 6.19). Gratifyingly, there were several clusters of enriched proteins with a low FDR, which exhibited associations with angiogenic and immunomodulatory processes, these connections will be explored later in this chapter.

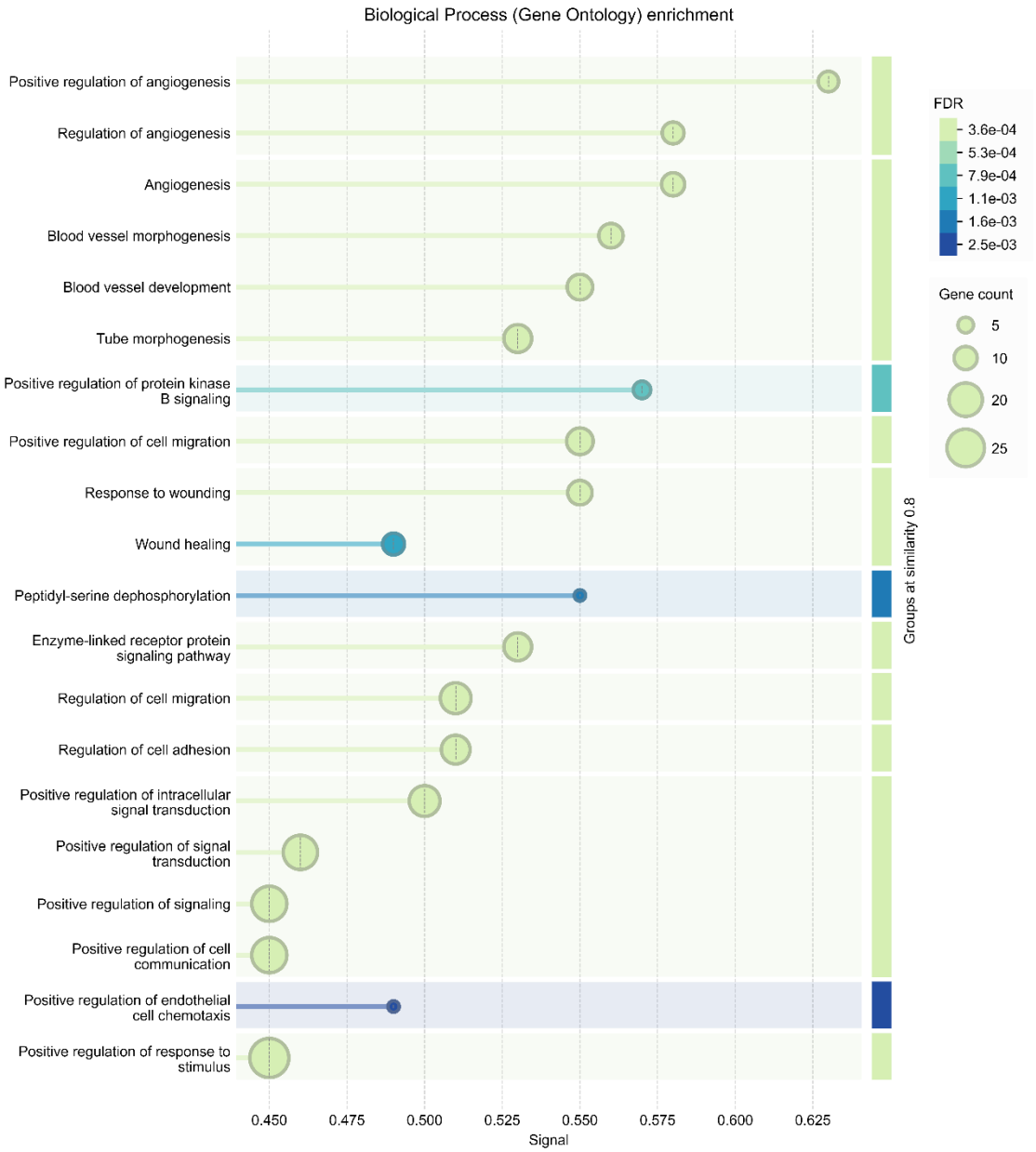


***Figure 6.19: Gene ontology analysis of shortlisted proteins which were enriched in 3 µM PAL probe 114 relative to fingolimod competition LECs.*** *STRING GO analysis of enriched proteins, which were shortlisted through the removal of 46 ribosomal, translational and spliceosomal proteins.*

Also of interest were the general proteome-wide differences which were observed in response to fingolimod treatment, which could potentially be attributed to indirect pathway perturbation versus direct interaction with probe **114**. To investigate this, pathway analysis

was performed on proteins which were enriched in competition samples relative to DMSO but not in probe **144**-treated samples relative to competition (Figure 6.20a).

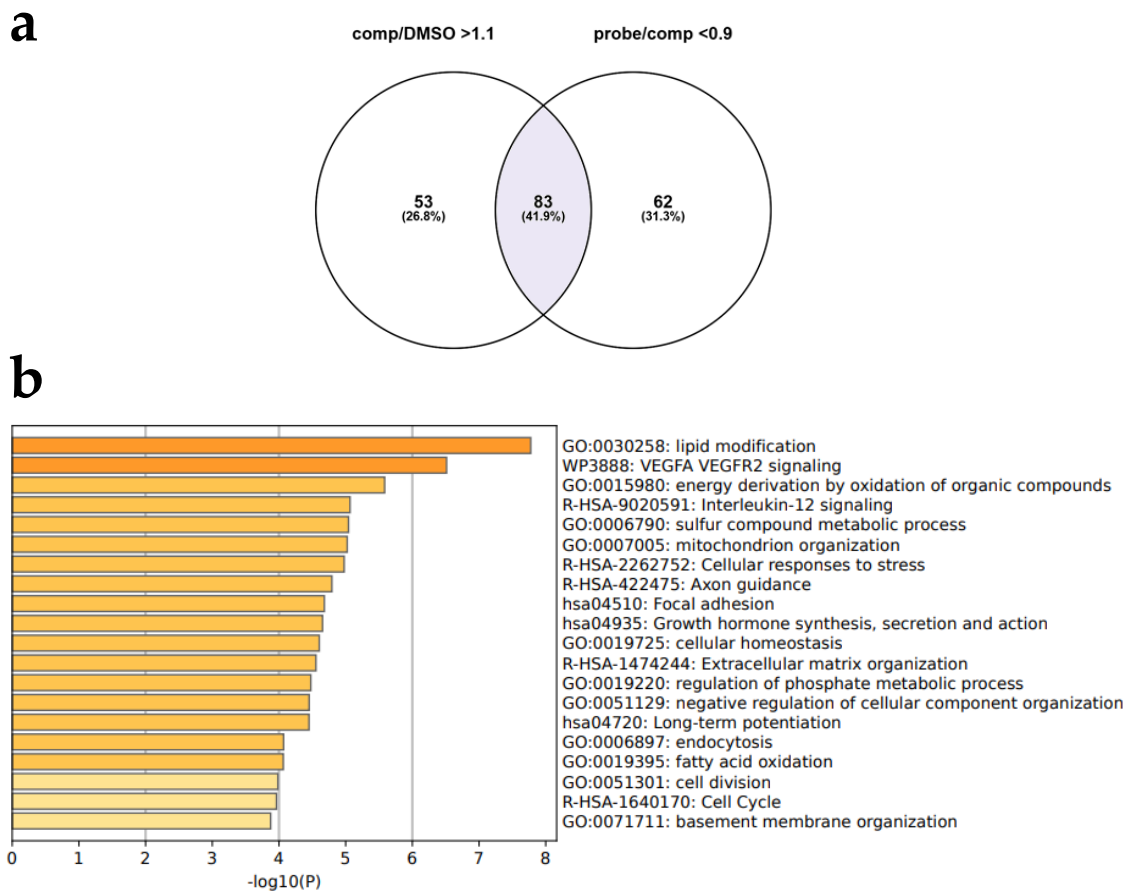


***Figure 6.20: Proteome perturbation in response to fingolimod treatment.*** *(a) Venn diagram highlighting proteins which were enriched in the competition (3 μM probe **114** and 30 μM fingolimod) relative to DMSO, but not enriched by probe **114**-treated samples compared to competition (b) Metascape gene ontology analysis of the 83 identified proteins which were enriched in the competition samples, coloured by p-values. P-values were calculated by a hypergeometric test with an applied Benjamini-Hochberg algorithm correction.*

Metascape gene ontology analysis highlighted some expected pathway enrichment related to lipid modification and fatty acid metabolism, which can be attributed to the lipid-like nature of fingolimod (Figure 6.20b). In addition, there were some pathways related to growth hormone secretion and VEGFR2 signalling which appeared to be enriched, which would be expected in a pro-lymphangiogenic environment in response to fingolimod treatment.

Similarly, ECM organisation and focal adhesion are processes which are necessary for lymphangiogenic growth and immune cell adhesion/migration.

Furthermore, transcription factor analysis indicated a cluster of TAZ-regulated proteins (Figure 6.21). This was intriguing, as TAZ-modulated transcriptional regulation has been associated with angiogenic signalling through (V)EGFRs.[356] Upregulated YAP/TAZ transcriptional regulation has also been observed in response to APLNR agonism in mice.[357] Downstream processes of TAZ-regulated transcription also include ECM remodelling and Rho GTPase-mediated actomyosin organisation.[356] As such future work could investigate YAP/TAZ-signalling in response to fingolimod treatment.

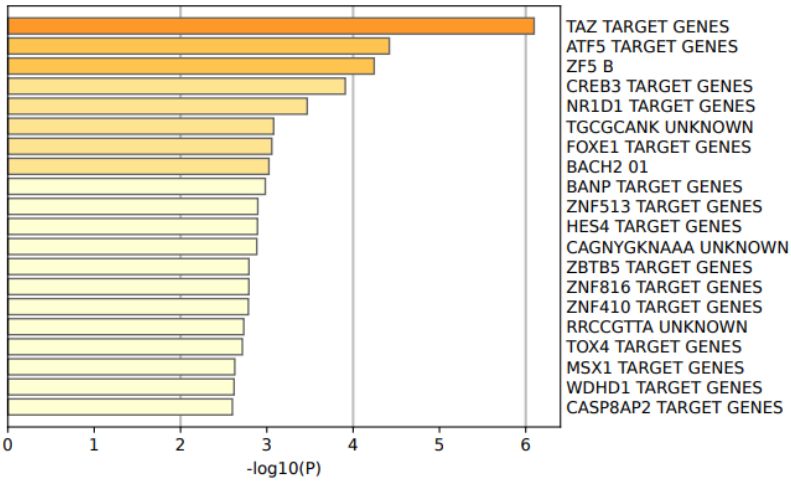


***Figure 6.21: Transcription factor analysis by Metascape.*** *Enrichment analysis in transcription factor targets, coloured by p-values. P-values were calculated by a hypergeometric test with an applied Benjamini-Hochberg algorithm correction.*

### 6.2.3 Analysis of (lymph)angiogenesis-related proteins

Examination of the probe **114**-enriched shortlisted proteins GO analysis revealed that a substantial proportion of enriched proteins were associated with endothelial vessel tube morphogenesis and angiogenesis (Figure 6.22).

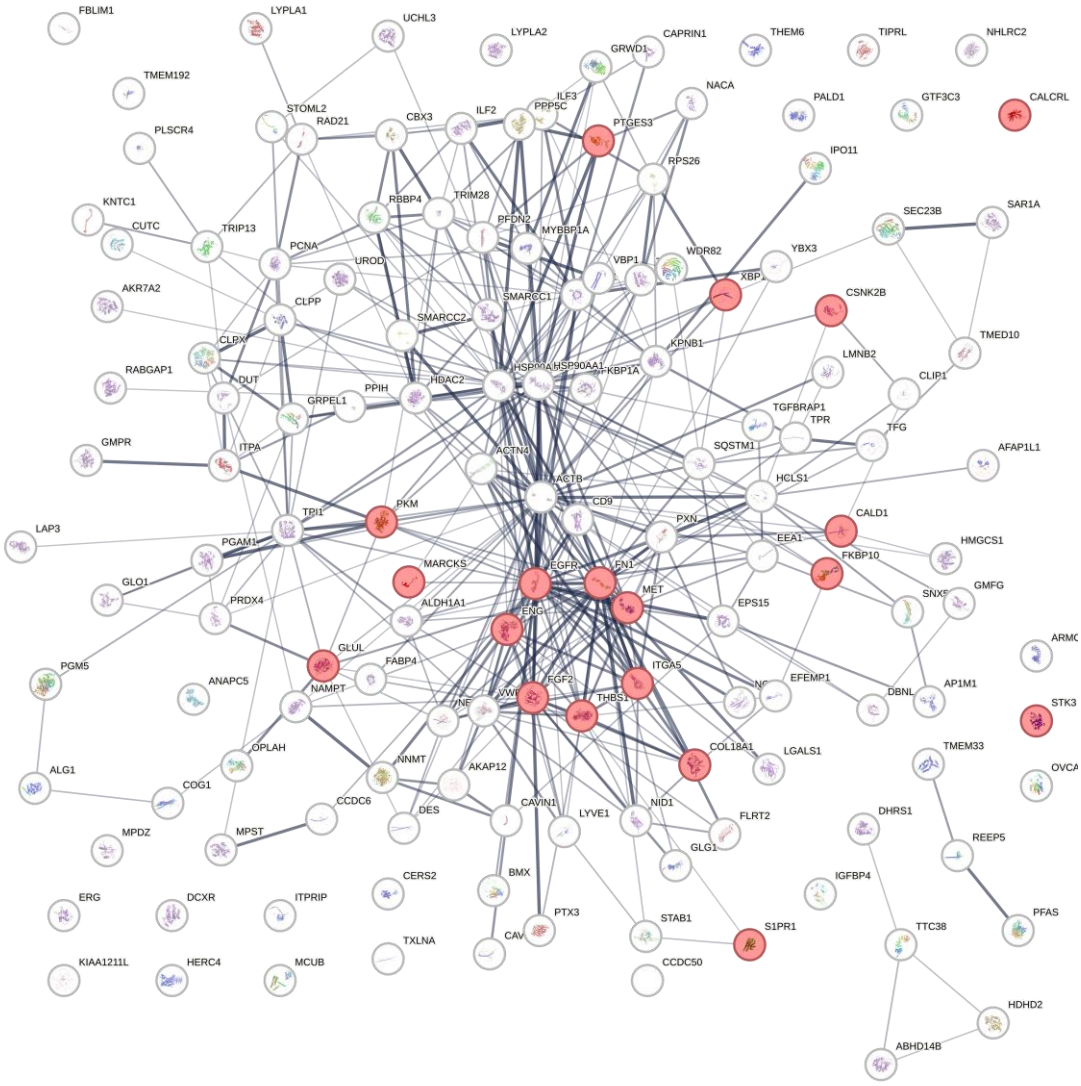


***Figure 6.22: A network of angiogenic proteins are enriched in probe 114-treated LECs relative to fingolimod competition LECs.*** *STRING network of 140 shortlisted proteins which are enriched in the probe treated cells versus competition cells. Red circles indicate proteins which have a documented association with angiogenesis and vessel morphology.*

A closer look at the clustering of these proteins revealed an interlinked network, involving many known regulators and inducers of lymphangiogenesis (Table 6.2). Of note was

calcitonin receptor-like receptor (CALCRL), a GPCR that forms a heterodimer with RAMP2 to enable adrenomedullin signalling, essential for normal lymphatic growth,[358] and has been linked to tumour-associated lymphangiogenesis.[359]

***Table 6.2: Identified enriched proteins which have a known role in lymphangiogenesis.***

| *Protein* | *Name* | *Role in lymphangiogenesis* | *Ref* |
|---|---|---|---|
| **ANGPT2** | angiopoietin-2 | Involved in the regulation of VEGFR3 cell surface expression in LECs. Required for normal lymphatic vessel development. | 360 |
| **CALCRL** | calcitonin receptor-like receptor | A GPCR for adrenomedullin signalling which promotes lymphatic growth | 358 |
| **COL18A1** | collagen XVIII | COL18A1 is cleaved by MMPs into several anti-lymphangiogenic factors | 361 |
| **EGFR** | epidermal growth factor receptor | Activation of EGFR promotes lymphangiogenesis | 362 |
| **FGF2** | fibroblast growth factor 2 | FGF2 plays a collaborative role with VEGFR3 in the promotion of lymphangiogenesis | 363 |
| **FN1** | fibronectin-1 | Promotes VEGFC expression and lymphangiogenesis | 364 |
| **ITGA5** | integrin $\alpha$5 | Downregulation of ITGA5 inhibits lymphangiogenesis | 365 |
| **MET** | hepatocyte growth factor receptor | Receptor for HGF, downstream signalling leads to lymphangiogenesis | 366 |
| **TMEM33** | transmembrane protein 33 | Essential for VEGF-mediated calcium signalling | 367 |

Unfortunately, APLNR was not detected in any sample by proteomics. This was surprising, as APLNR was enriched in the probe **114**-treated pull-down samples by Western blot (Figure 6.23). It was hypothesised that the lack of APLNR observed by MS was due to its lack of ionisable peptides after tryptic digestion, as to our knowledge APLNR has only been detected by proteomics previously after a combined Lys-C and trypsin digest.[368] There were several other membrane-bound fingolimod interactors which were not detected by TMT-MS (i.e. $S1PR_{3\text{-}5}$, TieII), which supported this hypothesis.

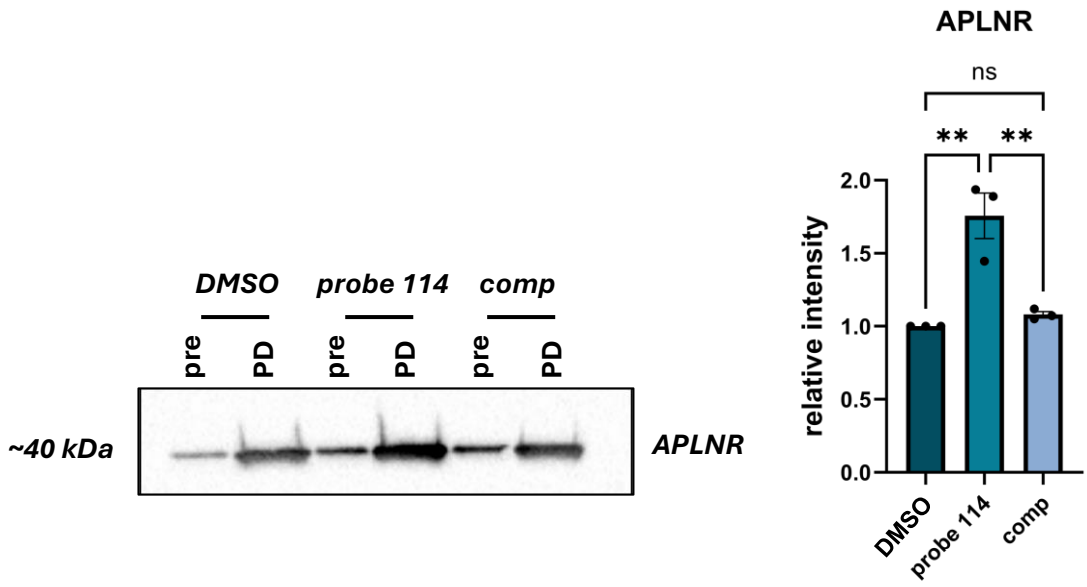


***Figure 6.23: Apelin receptor enrichment is observed in 3 μM probe 114-treated LECs.*** *Quantified Western blot analysis of APLNR enrichment in 3 μM probe **114**-treated LECS compared to DMSO control cells and competition (3 μM probe **114** + 30 μM fingolimod). Statistical analysis was performed using one-way ANOVA and multiple comparison tests. ** = P<0.01, ns = P>0.05. Error bars = sem.*

Despite the absence of APLNR in the proteomic data, there is still evidence to support its involvement as a receptor of fingolimod and a regulator of lymphangiogenesis.

### 6.2.4 Analysis of migration-related proteins

Amongst the highlighted GO terms associated with the probe-enriched proteins were clusters related to cell migration and cell adhesion. (Figure 6.24). Further investigation into these clustered proteins identified a number of proteins with a prior link to immune cell migration through lymphatic vasculature (Table 6.3). It was reaffirming that STAB1 and LGALS1 were seen to be enriched again, as was LYVE1, another protein linked to the transendothelial of immune cells.[22, 369] Macrophage mannose receptor 1 (MRC1) has also been observed to increase the adhesion of T-lymphocytes to lymphatic vessels, perpetuating them towards transendothelial migration.[370] Neither CX3CR1, nor any other chemokine receptor, were identified in the proteomic analysis, despite their known expression on LECs. Previous

identification of CX3CR1 by proteomics used substantially more detergent to facilitate protein solubilisation (5% SDS vs 0.1% SDS),[371] which could potentially explain the lack of CX3CR1 present in our samples if it is prone to aggregation. Nevertheless, the identification of these adhesion proteins within probe **114**-enriched LECs was promising and suggested that fingolimod could play a complimentary role in the lymphatic endothelium to induce its inhibition of T-lymphocyte ingression. Further validation of the functional connection between these receptors and fingolimod-mediated inhibition would be the focus of future studies.

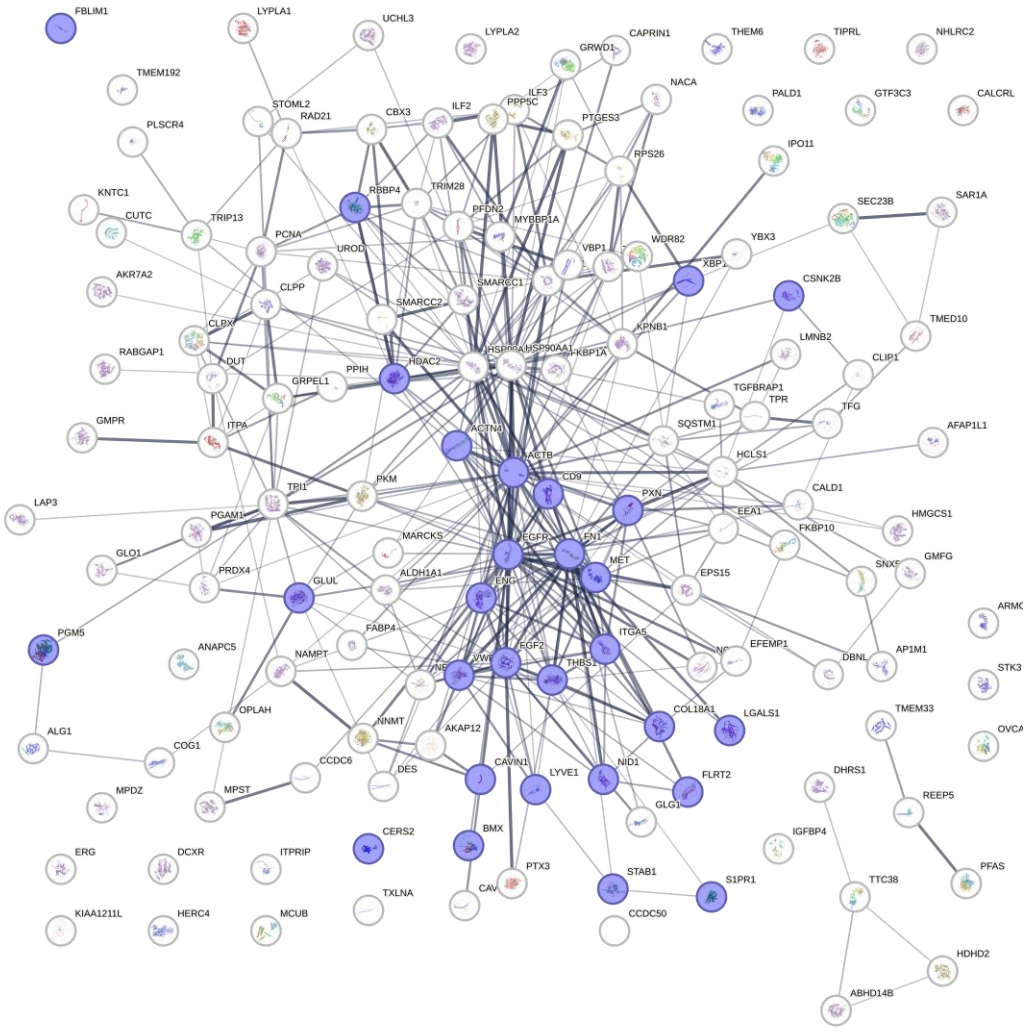


***Figure 6.24: A network of migration/adhesion proteins are enriched in probe 114-treated LECs relative to fingolimod competition LECs.*** *STRING network of 140 shortlisted proteins which are enriched in the probe treated cells versus competition cells. Blue circles indicate proteins which have an association with cell migration and cell adhesion.*

***Table 6.3: Identified enriched proteins which have a known role in immune cell trafficking in lymphatics.***

| *Protein* | *Name* | *Role in lymphangiogenesis* | *Ref* |
|---|---|---|---|
| **LGALS1** | galectin-1 | Inhibits T-lymphocyte migration through lymphatics | [372] |
| **LYVE1** | lymphatic vessel endothelial hyaluronan receptor 1 | Required for immune cell migration from heart into draining LNs | [22] |
| **MRC1** | macrophage mannose receptor 1 | Controls T-lymphocyte trafficking by increasing adhesion to lymphatics | [370, 373] |
| **STAB1** | common lymphatic endothelial and vascular endothelial receptor-1 | Mediates Treg migration across blood vasculature. Also mediates lymphocyte migration from tissue to draining LNs | [351, 374] |

Western blot analysis of the pull-down samples was performed to assess whether these identified receptors were 'true' interactions. LYVE1 was enriched in the probe **114**-treated samples compared to both the DMSO control sample and the competition sample (Figure 6.25)

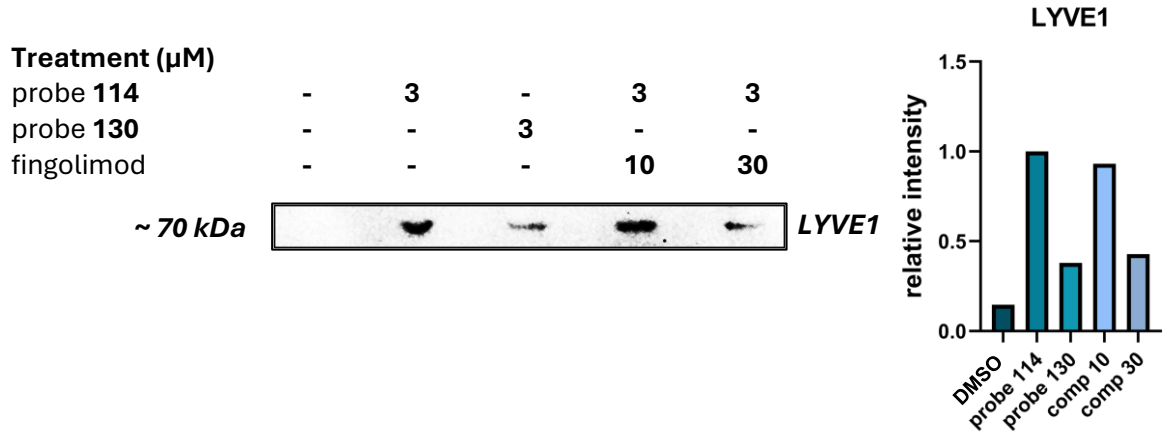


***Figure 6.25: Western blot analysis of LYVE1 expression in probe-treated LEC pull-down samples compared to controls.*** *Quantified Western blot analysis of LYVE1 enrichment in 3 μM probe **114**-treated LECs compared to control treatment. N=1.*

LYVE1 has been shown to be necessary for immune cell ingression into afferent lymphatics for clearance to LNs after an MI.[22] Whilst a LYVE1-dependent mechanism has only been confirmed for DCs, macrophages and leukocytes, its involvement has not yet been studied in the context of T-lymphocyte trafficking. As such, further studies into the role of LYVE1 in T-lymphocyte migration and fingolimod's involvement would be of interest.

Increased LGALS1 expression has been shown to inhibit T-lymphocyte migration across human umbilical vein endothelial cells (HUVECs). Therefore, its association with T-lymphocyte ingression into afferent lymphatics could be of interest and was investigated further. Western blot analysis of LGALS1 levels in pulldown samples from LECs highlighted that whilst enriched relative to DMSO, there appeared to be no substantial enrichment of probe **114**-treated samples compared to competition (Figure 6.26). This highlights the importance of thorough orthogonal validation during target identification and validation studies.

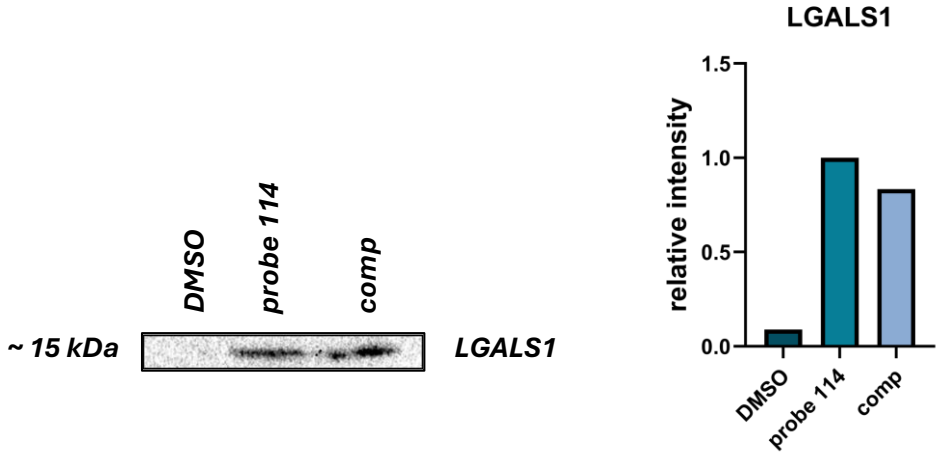


***Figure 6.26: Western blot analysis of LGALS1 expression in probe-treated LEC pull-down samples compared to controls.*** *Quantified Western blot analysis of LGALS1 enrichment in 3 µM probe **114**-treated LECs compared to DMSO control cells and competition (3 µM probe **114** + 30 µM fingolimod). N=1.*

### 6.2.5 Connections to fingolimod's adverse effects

Fingolimod treatment has also been linked to symptoms of hypertension in patients.[375] Thus far, this indication has been attributed to $S1PR_2$ and $S1PR_3$ signalling that induces vasoconstriction.[376, 377] There were a number of probe-enriched proteins with associations to hypertension: Type-I angiotensin II receptor-associated protein (ATRAP) and TieI are components of the Renin-Angiotensin-Aldosterone System (RAAS), which is the main

pathway responsible for inducing hypertension.[378] Furthermore, APLNR has been shown to interact with TieI upon activation,[379] in a cardioprotective manner which antagonises TieII-mediated hypertension.[380] However, other studies report contradictory findings, whereby APLNR activation enhances hypertension.[381-383] Moreover, some reported polymorphisms of APLNR correlate to an increased risk of hypertension in patients, which could explain, in part, the differential findings listed above.[384-386] As such, the true association between APLNR and hypertension remains unknown. In addition, β-adrenergic receptor kinase 1 (GRK2) was also enriched, and similarly has implications in hypertension, due to its upregulation of β-adrenergic receptors.[387] Whilst $S1PR_{2/3}$ still play a role in the manifestation of hypertension, there could be other contributing factors that have not yet been considered.

Furthermore, there have been numerous reports of increased carcinoma and melanoma risk in patients receiving fingolimod treatment.[388, 389] Among the probe **114**-enriched proteins were several families of cell-cycle modulators whose dysregulation has been linked to cancer progression: cyclin-dependent kinases (CDKs), protein phosphatases (PPs) and heterogeneous nuclear ribonucleoprotein (HNRNPs).[390-392] Additionally, transmembrane protein 192 (TMEM192) was also found to be enriched. TMEM192 is highly expressed in multiple cancers and plays a role in proliferation.[393] Also of note is the reported association of THEM6 with cancer cell survival.[394] Whilst these oncogenic mediators have been highlighted, there are many protein dysregulations which have been implemented in the progression of cancer and further studies would be required to understand which pathways could be modulated by fingolimod treatment. Similarly, fingolimod's pro-cancerous phenotype could be a side effect of its immunosuppressive and pro-lymphangiogenic effects.

### 6.2.6 Other observations

Metabolism of fingolimod proceeds *via* two differing biotransformations.[395] The first is mediated by CYP4F2, a cytochrome P450 isoform not detected in the proteomic analysis, likely due to its low abundance outside the liver. The second pathway proceeds *via* a still unknown acyltransferase, incorporating either a C16 or C18 fatty acid (Figure 6.27).[396]

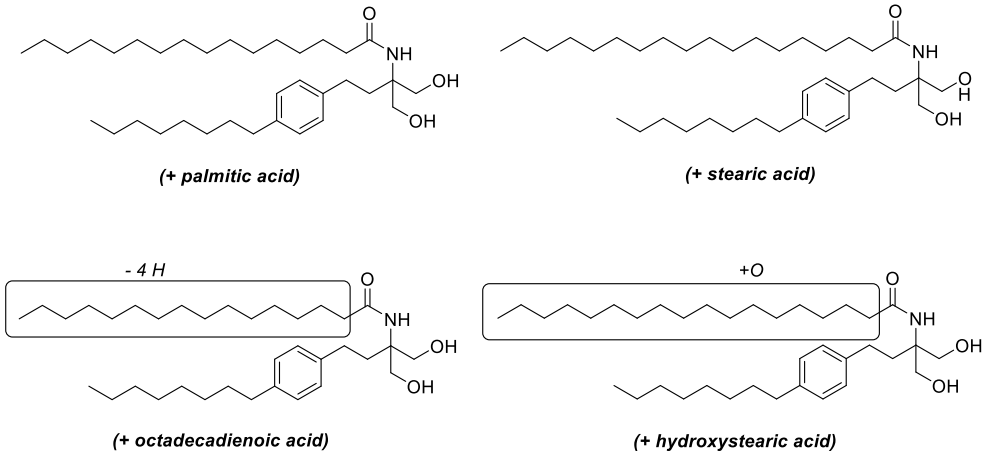


***Figure 6.27: Predicted metabolites of fingolimod, present in the blood by Huwiler et al.[397]*** *These metabolites were predicted using LC-MS/MS, assigned primarily based on their retention times, compared to metabolites characterized in rat blood. The metabolites are proposed to be products of amine acylation with endogenous fatty acids (in brackets) and hence analogous to ceramides.*

Amongst the probe enriched proteins were a selection of potential acyltransferases that could be involved in Fing-P metabolism (Table 6.4), as they are known to perform similar acyl transformations.[397-401]

***Table 6.4: Acyltransferases enriched in probe 114-treated samples, which could be involved in Fing-P metabolism***

| *Protein* | *Name* | *Function* |
|---|---|---|
| **AGPAT4** | 1-acylglycerol-3-phosphate O-acyltransferase 4 | Converts lysophosphatidic acid to phosphatidic acid |
| **LCLAT1** | lysocardiolipin acyltransferase 1 | Involved in phosphatidylinositol acyl-chain remodelling |
| **LPCAT4** | lysophosphatidylcholine acyltransferase 4 | Catalyses the conversion of lysophosphatidic acid to phosphatidic acid |
| **LPGAT1** | lysophosphatidylglycerol acyltransferase 1 | Catalyses the re-acylation of lysophosphatidylglycerol to phosphatidylglycerol |
| **MBOAT7** | lysophospholipid acyltransferase 7 | Involved in the re-acylation of phospholipids |

Also of note was a cluster of proteins relating to glycolysis, insulin signalling and fatty acid metabolism that were observed in the probe **114**-enriched samples (Figure 6.28). Fingolimod has been linked to improved outcomes in type II diabetes due to its ability to regenerate islet β-cells in mice.[402] This was proposed to be through agonism of S1PRs, however no KO/KD studies were performed to corroborate this statement. In addition to this regenerative effect, fingolimod has also been shown to improve glucose tolerance and insulin sensitivity in rodent disease models.[403, 404] Fingolimod's inhibition of CerS2 contributes to a therapeutic decrease in ceramide accumulation in the muscle.[404, 405] Moreover, fingolimod administration has also been shown to reduce the levels of di and triacylglycerol in skeletal tissue in mouse models,[39] potentially through its interaction with the plethora of metabolic enzymes highlighted below, which were enriched in probe-treated LECs (Figure 6.26). Fingolimod and its metabolites likely play a complex role in lipid modulation and signalling, that will have numerous effects in differing cellular processes.

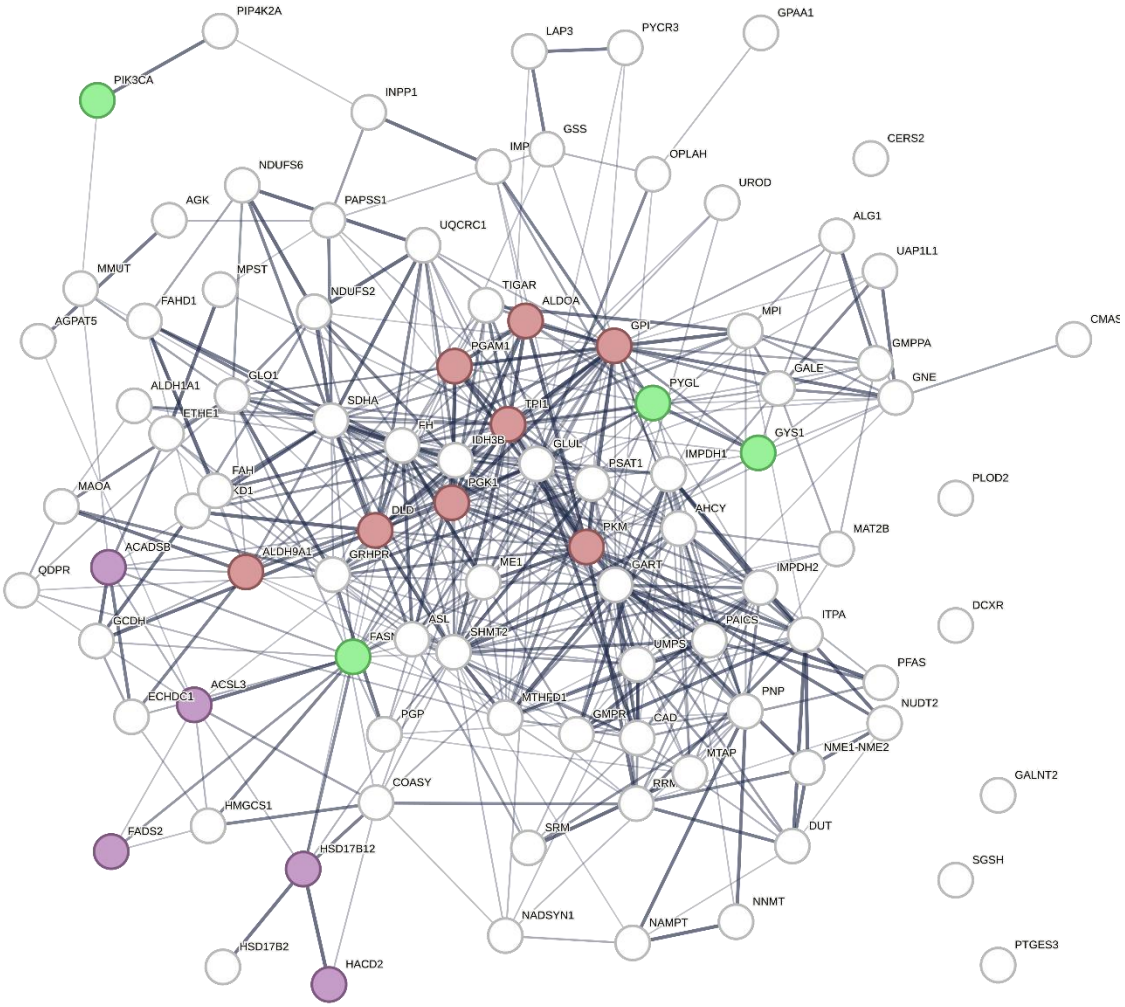


***Figure 6.28: Metabolic proteins enriched in probe 114-treated LECs compared to competition cells.*** *STRING network analysis of 140 shortlisted proteins, indicating metabolic proteins associated with insulin signalling (green), fatty acid metabolism (purple) and glycolysis/gluconeogenesis (red).*

Fingolimod has been linked to the amelioration of Alzheimer's disease (AD) progression.[406] In the competition-enriched proteins was a clustering associated with long-term potentiation (Figure 6.19). Long-term potentiation is a cellular mechanism involved in memory, characterised by a persistent increase in synaptic transmission, which is impaired in AD patients.[407] If fingolimod could play a role in long-term potentiation induction, it may contribute to the amelioration of AD symptoms observed with fingolimod treatment. Also of

note in the context of fingolimod's ties to AD, was the enrichment of ADAM10, a disintegrin protein, in probe-treated LECs. ADAM10 is a protein that has been linked to the $\alpha$-cleavage of amyloid precursor protein (APP) reducing neurotoxic amyloid-β (Aβ) production.[408] Different lipids have been reported to influence the effect of ADAM10, however it is still unknown if this is through direct or indirect mechanisms.[409, 410] Similarly, fingolimod could potentiate ADAM10 towards APP cleavage either directly or indirectly through its influence on cholesterol levels.[411] Moreover, fingolimod also enriched the insulin-degrading enzyme (IDE), another protein which has been associated with Aβ degradation.[406] Further studies into the causal link between fingolimod and Aβ deposition are required to better understand these effects.

Previous studies into fingolimod's alleviation of Niemann-Pick disease phenotypes revealed its ability to decrease free cholesterol levels. [148] This was postulated to be due to its upregulation of cholesterol transporter NPC1, in a SPHK2-independent manner. Analysis of the enriched proteins in probe-treated LECs identified NPC1 alongside other known modulators of free cholesterol, DHCR7 and NCEH1, which could potentially contribute to the phenotypic effect observed.

Proteomic analysis of the fingolimod-derived probe **114**-enriched LECs, relative to DMSO control cells and fingolimod competition treatment, revealed a plethora of proteins potentially involved in fingolimod's pleiotropic effects. The TMT-MS technique was limited by its lack of GPCR coverage, which could explain in the absence of APLNR, a hit which had demonstrated a promising association with fingolimod-derived lymphangiogenesis. Despite this, GO analysis identified a subpopulation of proteins associated with lymphangiogenesis, as well as immune cell migration and adhesion. However, these lymphatic adhesion and migration

receptors were not G-coupled. Previous PTX co-dosing studies had suggested that fingolimod's target was a GPCR, which implies that either (i) the true phenotypic target was not identified by MS or (ii) the transendothelial migration of T-lymphocytes into afferent lymphatics is a complex process involving multiple receptor pathways on both the lymphatic endothelium and T-lymphocytes. The GPCR-dependency of the migration could originate from the T-lymphocytes. As such, proteomic analysis of probe **114**-treated T-lymphocytes would enable further deconvolution of this biological process.

In short, the proteomics analysis was consistent with known immunomodulatory effects of fingolimod and also shed light on potential factors related to its observed side effects. A more in-depth study in disease-relevant tissue types is required to fully understand these findings.

# Chapter 7

## Discussion

# 7 Discussion

## 7.1 General Discussion

Despite the need for new therapeutic solutions to combat ischaemic injury and its progression towards chronic heart failure, there are no current treatments which target the root cause of adverse cardiac remodelling. Modulating our immune response towards subtle pro-inflammatory signalling and more reparative mechanisms has the potential to create an environment which is conducive to cardiac regeneration. This research broadened our understanding of these immunomodulatory mechanisms, using photoaffinity labelling technology to probe the Fing-P-mediated regulation of lymphangiogenesis and T-lymphocyte ingression. Novel interaction partners of fingolimod within lymphatics were discovered, shining a light on these immunomodulatory processes of interest.

### 7.1.1 Lymphangiogenesis

Pharmacological studies into the nuances of fingolimod's activity demonstrated that it induced lymphangiogenesis, in a SPHK2-dependent manner. Furthermore, it was determined that these immunomodulatory effects were independent of Fing-P's canonically associate S1PR family, but dependent on another GPCR. APLNR was identified as a potential GPCR responsible for Fing-Ps induction of lymphangiogenesis. APLNR is essential for lymphatic development,[412, 413] and remains strongly expressed in human lymphatic endothelial vasculature.[320, 414] The endogenous peptide of APLNR, apelin, has previously been implicated as a promotor of tumour-induced lymphangiogenesis.[318] In the context of cardiac lymphatic vasculature, apelin administration has been shown to hinder fibrosis, inflammation and pathological cardiac remodelling *in vivo* post-MI.[320] These indications implicate APLNR as a

potential therapeutic target in the context of cardiac regeneration. As such this research further assessed the connection between Fing-P and APLNR. Multiple, orthogonal studies were explored to investigate both the affinity and the functional efficacy of APLNR as Fing-P's target of interest in lymphangiogenic modulation. CETSA demonstrated a fingolimod-induced thermal stabilisation of APLNR in LECs, as biophysical evidence of their interaction. APLNR antagonism and siRNA KD of APLNR ablated Fing-P's lymphangiogenic effect. Similarly, fingolimod administration triggered a known downstream pathway of APLNR agonism, HDAC5 nuclear to cytoplasm translocation.[415] Photoaffinity probe **114**-treated samples demonstrated enrichment of APLNR by Western blot analysis, however this finding was not corroborated by TMT proteomic analysis of the enriched samples. It was hypothesised that this could be due to an insufficient level of ionisable peptides after tryptic digestion, a common problem associated with GPCRs.[416] Nevertheless, this research has provided substantial evidence to support the hypothesis that Fing-P acts *via* APLNR agonism to induce its lymphangiogenic effect.

In addition to the pharmacological evaluation of fingolimod's phenotypic effect, proteomic analysis of probe **114**-treated samples revealed a cluster of angiogenic proteins with known lymphangiogenic ties (ANGPT2, CALCRL, EGFR, FGF2, TMEM33), amongst which CALCRL was the only GPCR. CALCRL is necessary for normal lymphatic vessel development,[417] and forms part of the heterodimeric adrenomedullin receptor that has been shown to mediate lymphangiogenesis.[418] As such, this receptor would be an interesting target to focus future phenotypic studies on.

### 7.1.2 T-lymphocyte ingression

Additionally, this research discovered that fingolimod's inhibitory effect upon T-lymphocyte migration was also SPHK2-dependent and S1PR-independent. A bell-shaped inhibition was observed, whereby fingolimod lost its efficacy at higher concentrations. The underlying cause of this effect was investigated; waterLOGSY and SAXS experimentation found no conclusive evidence to support the hypothesis that fingolimod formed aggregates/micelles at higher concentrations. As such, the current theory postulates that Fing-P induces receptor desensitisation or internalisation at higher concentrations. This is an observation that has commonly been attributed to GPCRs.[419]

Further studies into Fing-P's immunomodulatory effect revealed that pertussis toxin co-administration resulted in a return to baseline migration, suggesting a GPCR-dependency. CX3CR1 was identified as a potential target responsible for the Fing-P-mediated inhibition of T-lymphocyte migration. CX3CR1 is a chemokine receptor which has been previously been associated with immune cell migration into inflamed tissue,[420] and undergoes internalisation *via* a regulatory mechanism.[421] However, there has been no prior association of CX3CR1 with $CD4^+$ T-lymphocyte ingress into lymphatics. Therefore, to further probe this relationship, siRNA KD of CX3CR1 in LECs was performed and was shown to hinder T-lymphocyte migration, highlighting the necessity of CX3CR1 expression on LECs for ingression.

Proteomic analysis of probe **114**-treated LECs provided an unbiased insight into fingolimod's potential immunomodulatory role upon the lymphatic endothelium. This revealed a clustering of surface receptors with reported links to T-lymphocyte ingress (LGALS1, LYVE1, MRC1, STAB1). Whilst these proteins are not GPCRs, the complex nature of immune cell migration means these receptors cannot be disregarded from their potential role in Fing-P-

mediated inhibition of ingression. The GPCR dependency of this process could originate from the T-lymphocytes or from an additional unidentified lymphatic receptor. Further validation of these clustered migratory receptors confirmed the enrichment of LYVE1 in probe-treated LECs, however, LGALS1 was shown to be a false positive hit which emphasised the importance of orthogonal validation. Nevertheless, LYVE1, MRC1 and STAB1 are all proteins of interest which will be followed up in future studies to confirm their affinity towards fingolimod, and whether their interaction has a causal link to the phenotypic inhibition of T-lymphocyte migration.

## 7.2 Research limitations

Despite extensive synthetic efforts, the fingolimod-derived photocatalytic probe could not be produced. Labelling studies and proteomic analysis with this photocatalytic probe could have provided a greater insight into subsequent fingolimod-mediated pathways. In addition, the use of photocatalytic probes would have enhanced the detection of low abundance proteins, which is an inherent limitation of the photoaffinity labelling technique.

Similarly, the photoaffinity labelling workflow could not be adapted to optimally label in Jurkat cells. As such, the intricate nature of T-lymphocyte transendothelial migration through the lymphatic endothelium could not be fully captured. Immune cell ingression is a complex process requiring multiple receptors on both the immune cell and lymphatic endothelium to mediate chemotaxis, adhesion and migration.[422] Therefore, more in-depth studies will be required to deconvolute the specific role Fing-P plays in either/both the lymphatic endothelium and T-lymphocytes.

While Jurkats are a practical T-lymphocyte cell line to use, there are limitations in their comparability to primary T-lymphocytes. As already stipulated, their genetic instability can lead to discrepancies in their behaviour over time and between research groups.[234] Also of concern are their differential signalling pathways, particularly Ag-receptor and PI3K signalling.[423] As the mechanism of Fing-P's activity in T-lymphocytes remains uncertain, it would be important to corroborate any findings in Jurkats, in primary T-lymphocytes as well. To account for this limitation, this research performed *in vivo* studies to corroborate some of the *in vitro* findings.

### 7.3 Future work

Whilst this research partially deconvoluted these immunomodulatory mechanisms, there are some proposed future studies which did not fall within the scope of this research, due to time and resource limitations.

APLNR was identified as a potential lymphangiogenic target, and several *in vitro* studies supported this hypothesis. However, it would be crucial to corroborate this finding *in vivo*, to assess whether Fing-P-mediated agonism of APLNR can induce biologically significant lymphangiogenesis, and enhance immune cell clearance. Moreover, as APLNR is expressed in both blood and lymphatic vasculature,[320, 414] it would be intriguing to investigate whether there is an observable preference in the angiogenic behaviour between to two systems. The combined effect of angiogenic reperfusion and lymphangiogenic immune cell clearance could be beneficial post-MI.[107, 424] If these future studies confirmed the therapeutic viability of small molecule modulation of APLNR, then a crystal structure of Fing-P bound to APLNR could provide crucial information in the drug development process to generate a more selective modality.

Proteomic analysis of probe **114** enrichment highlighted numerous additional targets of potential interest. However, affinity does not always correlate to a functional effect, as such, further validation of these targets would be required. CALCRL, a potential lymphangiogenic target, could be validated though CETSA/pulldown sample Western blot to confirm its interaction with Fing-P. Following this the lymphangiogenesis assay can be used to assess phenotype (i.e. antagonism, siRNA KD studies). Furthermore, analysis of downstream pathways (i.e. rapid ERK1/2 phosphorylation) could be interrogated in response to fingolimod treatment, relative to a known agonist (i.e. adrenomedullin).[358]

Similarly, the enriched migratory targets will also require thorough validation to confirm both their interaction and phenotypic effect. This could be achieved with CETSA or Western blot confirmation of their enrichment in probe **114**-treated samples, coupled with phenotypic assessment using the Transwell migration assay. Additionally, this research optimised the growth of a lymphatic microvessel-on-a-chip, co-cultured with T-lymphocytes, in collaboration with Dr Al Haj Zen. Unfortunately, these microvessels were not used to assess the migratory influence of Fing-P, however, future imaging of T-lymphocyte migration could provide insight into which aspects of migration are being hindered, in response to fingolimod treatment.

Despite the successful labelling studies performed in the lymphatic endothelium, to grasp a full understanding of the role of Fing-P in T-lymphocyte migration labelling studies must be performed in a T-lymphocyte cell line. Due to the aforementioned limitations of Jurkat cells, it would be preferable to perform these labelling studies in primary human T-lymphocytes. This proteomic analysis would also reveal if there are any tissue-specific differences in Fing-P's mechanistic effects.

Fingolimod has been shown to play a therapeutic role in a variety of diseases, including Alzheimer's disease,[425, 426] type II diabetes,[427] and Niemann-Pick disease.[428] This research identified several disease-related targets within LECs, as such, future labelling studies in relevant tissues or cell types, could further capture vital interactions which could be of therapeutic value.

**7.4 Final Conclusions**

To conclude, in this thesis the molecular basis of fingolimod's influence upon lymphangiogenesis and T-lymphocyte migration has been investigated. Targeted pharmacological analysis has highlighted a novel Fing-P-mediated pro-lymphangiogenic pathway through APLNR agonism. Moreover, this research has designed, synthesised, validated and utilised fingolimod-derived photoaffinity probes to identify previously unknown interaction partners with implications in lymphangiogenesis, immune cell migration, lipid metabolism, Alzheimer's disease and Niemann-Pick disease. These findings emphasise the importance of thorough small molecule target deconvolution, to enable the informed progression of therapeutic interventions. Small molecule agonism of APLNR could have beneficial implications in dampening the inflammatory response, enabling reparative and regenerative mechanisms to be adopted to aid cardiac repair post-ischaemic injury. Furthermore, the validated photoaffinity probe can be used in future labelling studies to decipher the full extent of fingolimod's influence upon T-lymphocytes, to identify new immunomodulatory targets which can be manipulated to aid endogenous cardiac regeneration.

# Chapter 8

# Chemistry Experimental

## 8 General Experimental

All reactions involving organometallic or other moisture-sensitive reagents were performed under a nitrogen or argon atmosphere using standard vacuum line techniques and glassware that was flame-dried and cooled under nitrogen before use. Anhydrous solvents were dried by passing over an activated alumina column, under an inert atmosphere, using a solvent purification system. All solvents were anhydrous unless specified otherwise. Water was purified by an Elix® UV-10 system. All other reagents were used as supplied (analytical or HPLC grade) without prior purification. Organic layers were dried over $Na_2SO_4$. Thin-layer chromatography was performed on aluminium plates coated with 60 F254 silica. Plates were visualised using UV light (254 nm), $KMnO_4$ (1% aq.), 10% ethanolic phosphomolybdic acid, and 10% ethanolic p-anisaldehyde. Normal phase flash column chromatography was performed either on Kieselgel 60 silica in a glass column or on a Biotage Isolera Four automated flash column chromatography platform. Reverse phase flash column chromatography was performed on a Biotage Selekt automated flash column chromatography platform. Melting points were recorded on SRS MPA120 EZ-Melt Melting Point Apparatus and are uncorrected. IR spectra were recorded on a Bruker Tensor 27 FT-IR spectrometer as a thin film. Selected characteristic peaks are reported in $cm^{-1}$ . NMR spectra were recorded on Bruker Avance spectrometers in the deuterated solvent stated. Spectra were recorded at rt unless otherwise stated. The field was locked by external referencing to the relevant deuterium resonance. Low-resolution mass spectra were recorded on either an Agilent 6120 Single Quadrupole or a Waters LCT Premier spectrometer. Accurate mass measurements were run on either a Bruker MicroTOF internally calibrated with polyalanine, or a Micromass GCT instrument fitted with a 162

Scientific Glass Instruments BPX5 column (15 m × 0.25 mm) using amyl acetate as a lock mass.

**General Procedure A**

To a solution of the arene (1.0 eq) in cyclohexane (0.6 M) at 10 °C was added 2-bromoacetyl chloride (1.4 eq) and $AlCl_3$ (1.4 eq) portionwise. The reaction was stirred at rt for 16 h. The reaction mixture was diluted with pentane, quenched with ice-cold water, and the aqueous layer extracted with EtOAc. The combined organic layers were dried ($Na_2SO_4$) and concentrated *in vacuo.* The crude product was further purified by flash column chromatography (silica gel).

**General Procedure B**

To a solution of the alpha bromo ketone (1.0 eq) in TFA (0.6 M) at 10 °C was added $HSiEt_3$ (2.2 eq). The reaction was stirred at rt overnight. The reaction mixture was neutralised with sat. aq. $NaHCO_3$, and the aqueous layer was extracted with pentane. The combined organic layers were dried ($Na_2SO_4$) and concentrated *in vacuo.* The crude product was further purified by flash column chromatography (silica gel).

**General Procedure C**

To a solution of the alkyl bromide (1.0 eq) in a DMSO was added $Cs_2CO_3$ (2.0 eq). The reaction was stirred at rt for 1.5 h before addition of diethylacetamidomalonate (2.0 eq). The reaction was stirred at 60 °C overnight. The reaction mixture was allowed to cool to rt, diluted with EtOAc and washed with water. The combined organic layers were dried ($Na_2SO_4$) and concentrated *in vacuo.* The crude product was further purified by flash column chromatography (silica gel).

**General Procedure D**

To a solution of the malonate (1.0 eq) in THF (0.6 M) at 0 °C was added $LiAlH_4$ (1 M in THF, 6.0 eq) dropwise. The reaction was heated to 55 °C and stirred for 16 h. The reaction mixture was allowed to cool to rt, then diluted with $Et_2O$, quenched with water and extracted with EtOAc three times. The combined organic layers were dried ($Na_2SO_4$) and concentrated *in vacuo.* To the resultant residue was added 4N HCl in 1,4-dioxane. The reaction mixture was stirred for 16 h at rt, filtered and washed with $Et_2O$ to yield the pure product as a chloride salt.

**General Procedure E**

To a flame-dried MW vial charged with $N_2$ was added the halobenzene (1.0 eq) and the alkyne (1.2 eq). The vial was degassed with $N_2$ again. $Et_3N$ (10 eq) and DMF (0.1 M) were added and the vial was degassed with $N_2$ again. CuI (0.2 eq) and $Pd(PPh_3)_4$ (0.4 eq) were added and the vial was degassed with $N_2$ again. The reaction was stirred at the specified temperature for the specified length of time. The reaction mixture was diluted with EtOAc and washed with 5% LiCl aq. solution. The organic layers were concentrated *in vacuo* and the crude material washed purified by flash column chromatography to yield the title compound.

**Fingolimod hydrochloride (1)**

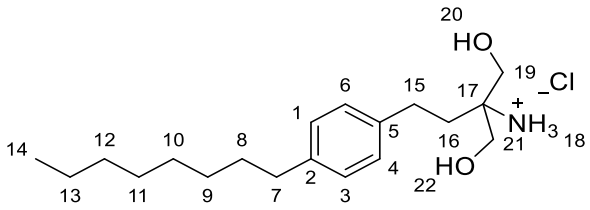


Following **General Procedure D, 1** was obtained from **12** (450 mg, 1.04 mmol) as a colourless crystalline solid (196 mg, 55% yield). **$^{1}$H NMR (400 MHz, MeOD):** δ 7.16 (d, *J* = 7.7 Hz, 2H, $H_{1,3}$), 7.09 (d, *J* = 7.7 Hz, 2H, $H_{4,6}$), 3.75 (s, 4H, $H_{19,21}$), 2.70-2.61 (m, 2H, $H_{15}$), 2.55 (t, *J* = 7.6 Hz, 2H, $H_{7}$), 2.03-1.95 (m, 2H, $H_{16}$), 1.63-1.52 (tt, *J* = 7.6, 7.3 Hz, 2H, $H_{8}$), 1.32-1.23 (m, 10H, $H_{9\text{-}13}$), 0.89 (t, *J* = 6.7 Hz, 3H, $H_{14}$) ppm. **$^{13}$C NMR (151 MHz,MeOD):** δ 140.5 ($C_{5}$), 139.2 ($C_{2}$), 128.1 ($C_{4,6}$), 128.0 ($C_{1,3}$), 62.1 ($C_{19,21}$), 58.5 ($C_{17}$), 34.8 ($C_{16}$), 32.5 ($C_{12}$), 31.3 ($C_{8}$), 31.1 ($C_{9}$), 28.7 ($C_{11}$), 28.1 ($C_{15}$), 22.1 ($C_{10}$), 16.1 ($C_{13}$), 13.9 ($C_{14}$) ppm. **HRMS ESI$^{+}$:** m/z 308.2579 $[M+H]^{+}$ *calc m/z 308.2584.* **IR (DMSO):** $\nu_{max}$ 3430 (O-$H_{inter}$), 2945 (N-$H_{salt}$), 1666 (C=$C_{arom}$), 1351 (O-H), 1090 (C-N), 1025 (C-O) $cm^{-1}$. This data was consistent with literature characterisation.[429]

**1-Hydroxy-2-(hydroxymethyl)-4-(p-tolyl)butan-2-aminium chloride (6)**

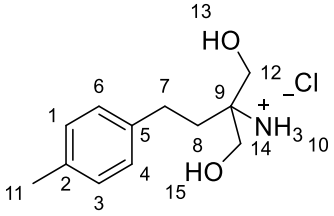

Following **General Procedure D, 6** was obtained from **126** (115 mg, 0.584 mmol) as a colourless crystalline solid (73 mg, 60% yield). **$^{1}$H NMR (400 MHz, MeOD):** δ 7.15-7.07 (m, 4H, $H_{1,3,4,6}$), 3.73 (s, 4H, $H_{12,14}$), 3.20-3.03 (m, 2H, $H_{7}$), 2.67-2.57 (m, 2H, $H_{8}$), 2.37 (s, 3H, $H_{11}$) ppm. **$^{13}$C NMR (101 MHz, MeOD):** δ 139.2 ($C_{5}$), 136.7.8 ($C_{2}$), 130.2 ($C_{4,6}$), 129.2 ($C_{1,3}$), 60.3 ($C_{12,14}$), 37.8 ($C_{9}$), 33.0 ($C_{8}$), 29.7 ($C_{7}$), 21.1 ($C_{11}$) ppm. **HRMS ESI$^{+}$:** m/z 210.1486 $[M+H]^{+}$ *calc 210.1489.* **IR (film):** $\nu_{max}$ 3359 (O-$H_{inter}$), 2925 (N-$H_{salt}$), 1601 (C=$C_{arom}$), 1457 (C-H), 1178 (C-N), 1058 (C-O), 683 (C-H) $cm^{-1}$. This data was consistent with literature characterisation.[430]

## 4-(4-Butylphenyl)-1-hydroxy-2-(hydroxymethyl)butan-2-aminium chloride (7)

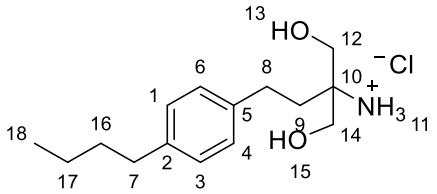


Following **General Procedure C, 7** was obtained from **127** (1.0 g, 2.6 mmol) as a colourless solid (470 mg, 63% yield). **$^{1}$H NMR (400 MHz, MeOD):** δ 7.13 (d, *J* = 7.8 Hz, 2H, $H_{1,3}$), 7.04 (d, *J* = 7.8 Hz, 2H, $H_{4,6}$), 3.74 (s, 4H, $H_{12,14}$), 3.15-3.05 (m, 2H, $H_{7}$), 2.66-2.57 (m, 2H, $H_{8}$), 2.51 (t, *J* = 7.7 Hz, 2H, $H_{9}$), 2.00-1.91 (m, 2H, $H_{16}$), 1.57-1.45 (m, 2H, $H_{17}$), 0.87 (t, *J* = 7.2 Hz, 3H, $H_{18}$) ppm. **$^{13}$C NMR (101 MHz, MeOD):** δ 141.7 ($C_{5}$), 139.6 ($C_{2}$), 129.5 ($C_{4,6}$), 129.2 ($C_{1,3}$), 66.8 ($C_{12,14}$), 60.3 ($C_{10}$), 37.8 ($C_{7}$), 36.1 ($C_{9}$), 34.9 ($C_{8}$), 33.0 ($C_{16}$), 23.2 ($C_{17}$), 14.3 ($C_{18}$) ppm. **HRMS ESI$^{+}$:** m/z 252.1959 $[M+H]^{+}$ *calc m/z 252.1958.* **IR (film):** $\nu_{max}$ 3350 (O-$H_{inter}$), 2957 (N-$H_{salt}$), 2857 (C-H), 1459 (C-H), 1420 (O-H), 1057 (C-O), 1024 (C-N) $cm^{-1}$. **mp:** 92-95 °C (MeCN)

**1-Methoxy-2-(methoxymethyl)-4-(4-octylphenyl)butan-2-amine (8)**

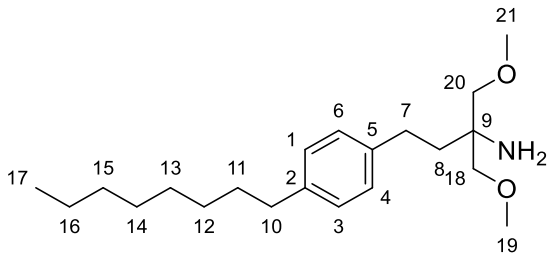


To a flame-dried MW vial under $N_2$ was added 1,3-dimethoxypropan-2-amine (150 μL, 1.2 mmol) and **20** (250 mg, 1.2 mmol) in degassed DMF (5 mL). The vial was sealed and degassed again. $[NBu_4][N_3]$ (33 mg in 100 μL MeCN, 10 mol%) and 3DPA2FBN (7.5 mg in 100 μL DMF, 1 mol%) were added and the reaction was stirred and irradiated by 427 nm light at rt for 20 h. The reaction was concentrated *in vacuo*. The crude material was purified by reverse-phase flash column chromatography (0 -> 10% MeOH in $CH_2Cl_2$) to yield **8** as a colourless solid (261 mg, 65%). **$^1$H NMR (400 MHz, $CDCl_3$):** δ 7.12 – 7.05 (m, 4H, $H_{1,3,4,6}$), 3.35 (s, 6H, $H_{19,21}$), 3.33 – 3.22 (m, 4H, $H_{18,20}$), 2.65 – 2.51 (m, 4H, $H_{7,10}$), 1.75 – 1.66 (m, 2H, $H_8$), 1.58 (*app* p, *J* = 8.0 Hz, 2H, $H_{11}$), 1.31 – 1.24 (m, 10H, $H_{12\text{-}16}$), 0.87 (t, *J* = 6.6 Hz, 3H, $H_{17}$) ppm. **$^{13}$C NMR (101 MHz, $CDCl_3$):** δ 140.4 ($C_5$), 139.9 ($C_2$), 128.5 ($C_{4,6}$), 128.3 ($C_{1,3}$), 66.0 ($C_{18,20}$), 59.4 ($C_{19,21}$), 55.1 ($C_9$), 37.6 ($C_{10}$), 35.7 ($C_8$), 32.0 ($C_{15}$), 31.8 ($C_{11}$), 29.6 ($C_7$), 29.5 ($C_{12}$), 29.4 ($C_{13}$), 29.3 ($C_{14}$), 22.8 ($C_{16}$), 14.3 ($C_{17}$) ppm. **LRMS ESI$^+$:** m/z 336 (100%, $[M+H]^+$), 693 (24%, $[2M+Na]^+$). **HRMS ESI$^+$:** m/z 336.2899 $[M+H]^+$ *calc. m/z 336.2897.* **IR (film):** $\nu_{max}$ 2928 (C-H), 1629 (N-H), 1222 (C-N), 1114 (C-O), 830 (C-H) $cm^{-1}$.

**Diethyl 2-acetamido-2-(4-octylphenethyl)malonate (9)**

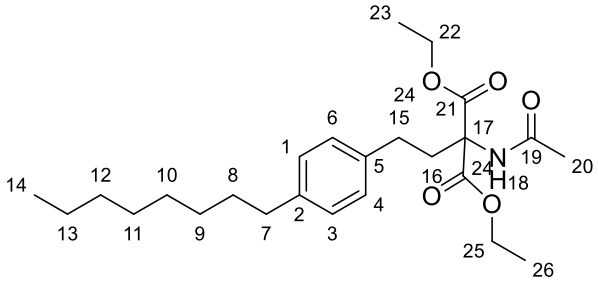


Following **General Procedure C, 9** was obtained from diethylacetoamidomalonate (440 mg, 2.0 mmol) and **19** (500 mg, 1.7 mmol). Purification by flash column chromatography (0% -> 50% EtOAc in pentane) yielded the title compound as a colourless oil (390 mg, 55%). **$^{1}$H NMR (600 MHz, $CDCl_3$):** δ 7.06 (m, 4H, $H_{1,3,4,6}$), 6.76 (s, 1H, $NH_{18}$), 4.20 (m, 4H, $H_{22,25}$), 2.70 – 2.66 (m, 2H, $H_{15}$), 2.57 – 2.52 (m, 2H, $H_7$), 2.48 – 2.43 (m, 2H, $H_{16}$), 1.97 (s, 3H, $H_{20}$), 1.59 – 1.53 (m, 2H, $H_8$), 1.33 – 1.27 (m, 10H, $H_{9\text{-}13}$), 1.24 (t, *J* = 7.1 Hz, 6H, $H_{23,26}$), 0.87 (t, *J* = 6.9 Hz, 3H, $H_{14}$) ppm. **$^{13}$C NMR (151 MHz, $CDCl_3$):** δ 169.3 ($C_{19}$), 168.2 ($C_{21,24}$), 140.9 ($C_5$), 137.8 ($C_2$), 128.6 ($C_{4,6}$), 128.5 ($C_{1,3}$), 66.6 ($C_{17}$), 62.7 ($C_{22,25}$), 35.7 ($C_7$), 33.5 ($C_{16}$), 32.1 ($C_{12}$), 31.8 ($C_8$), 29.9 ($C_{15}$), 29.6 ($C_9$), 29.5 ($C_{11}$), 29.4 ($C_{10}$), 23.1 ($C_{20}$), 22.8 ($C_{13}$), 14.2 ($C_{14}$), 14.1 ($C_{23,26}$) ppm. **LRMS ESI$^+$:** m/z 434 ([M+H$^+$], 97 %), 456 ([M+Na]$^+$, 87%). **HRMS ESI$^+$:** m/z 434.2892 [M+H]$^+$ *calc. m/z 434.2901.* **IR (film):** $\nu_{max}$ 2954 (C-H), 1741 (C=O), 1683 (C=O), 1514 (C=C), 1195 (C-O), 860 (C=C) $cm^{-1}$.

**2-Bromo-1-(4-octylphenyl)ethan-1-one (11)**

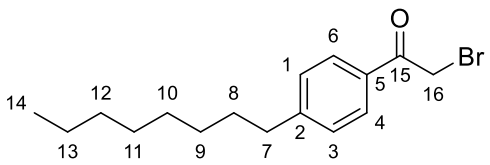


Following **General Procedure A, 11** was obtained from *n*-octyl benzene (1.0 mL, 8.9 mmol) and 2-bromoacetylchloride (1.0 mL, 13 mmol). Purification by flash column chromatography (0% -> 30% EtOAc in pentane) yielded the title compound as a brown oil (1.3 g, 79%). **$^{1}$H NMR (400 MHz, $CDCl_3$):** δ 7.89 (d, *J* = 8.3 Hz, 2H, $H_{4,6}$), 7.29 (d *J* = 8.3 Hz, 2H, $H_{1,3}$), 4.43 (s, 2H, $H_{16}$), 2.71-2.61 (m, 2H, $H_7$), 1.63 (tt, *J* = 7.4, 7.3 Hz, 2H, $H_8$), 1.33-1.22 (m, 10H, $H_{9\text{-}13}$), 0.88 (t, *J* = 7.0 Hz, $H_{14}$) ppm. **$^{13}$C NMR (101 MHz, $CDCl_3$):** δ 190.8 ($C_{15}$), 150.1 ($C_2$), 131.7 ($C_5$), 129.2 ($C_{4,6}$), 129.0 ($C_{1,3}$), 36.2 ($C_7$), 32.0 ($C_{12}$), 31.2 ($C_{16}$), 31.1 ($C_8$), 29.5 ($C_{9 \text{ or } 10 \text{ or } 11}$), 29.3 ($C_{9 \text{ or } 10 \text{ or } 11}$), 29.3 ($C_{9 \text{ or } 10 \text{ or } 11}$), 22.7 ($C_{13}$), 14.1 ($C_{14}$) ppm. **HRMS ESI$^+$:** m/z 333.0804 $[M+Na]^+$ *calc. m/z 333.0825.* **IR (film):** $\nu_{max}$ 1695 (C=O), 1814 (C-H), 1606 (C=C), 1465 (C-H, $CH_2$), 611 (C-Br) $cm^{-1}$. This data was consistent with literature characterisation.[431]

**2-(*tert*-Butyl) 1,1-diethyl 1-acetamidoethane-1,1,2-tricarboxylate (16)**

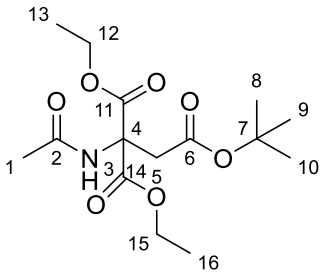

To a suspension of diethylacetamidomalonate (200 mg, 0.92 mmol) in EtOH (500 μL) was added NaOEt (70 mg, 0.92 mmol). The reaction mixture was stirred at rt for 1 h. 2-Bromoacetic acid (90 μL, 0.61 mmol) was added and the reaction was stirred at 65 °C overnight. The reaction was allowed to cool to rt, diluted with EtOAc (50 mL) and washed with water (2 x 100 mL). The combined organic layers were dried ($Na_2SO_4$) and concentrated *in vacuo*. The crude product was purified by flash column chromatography (0 -> 5% MeOH in $CH_2Cl_2$) to yield **16** (138 mg, 64%) as a yellow oil. The product was used without any further purification. **HRMS ESI$^+$:** m/z 354.1539 $[M+Na]^+$ *calc. m/z 354.1523.*

**3-Acetamido-4-ethoxy-3-(ethoxycarbonyl)-4-oxobutanoic acid (17)**

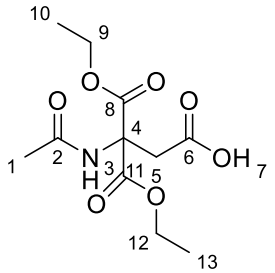


To a solution of **16** (100 mg, 0.30 mmol) in $CH_2Cl_2$ (1 mL) was added TFA (500 μL). The reaction was stirred at rt for 30 min. The reaction was quenched with water and basified with sat. aq. $Na_2CO_3$. The aqueous layer was washed with EtOAc (100 mL) and subsequently re-acidified with 1 M HCl. The aqueous layer was concentrated *in vacuo* to yield **17** (80 mg, 97%) as a colourless solid. **$^1$H NMR (400 MHz, *d*-DMSO):** δ 8.42 (s, 1H, $H_7$), 4.12 (q, *J* = 7.1, 4H, $H_{9,12}$), 3.17 (s, 2H, $H_5$), 1.90 (s, 3H, $H_1$), 1.13 (t, *J* = 7.1 Hz, 6H, $H_{10,13}$) ppm. **$^{13}$C NMR (101 MHz, *d*-DMSO):** δ 171.0 ($C_6$), 169.3 ($C_2$), 166.7 ($C_{8,11}$), 63.9 ($C_5$), 61.8 ($C_{9,12}$), 38.5 ($C_4$), 22.0 ($C_4$), 13.7 ($C_{10,13}$) ppm. **LRMS ESI$^+$:** m/z 298 ($[M+Na]^+$, 100%), 276 $(M+H)^+$, 41%).

**HRMS ESI$^-$:** m/z 274.0935 $[M-H]^-$ *calc. m/z 274.0932.* **IR (film):** $\nu_{max}$ 3353 (O-H), 2920 (C-H), 1756 (C=O), 1736 (C=O), 1715 (C=O), 1222 (C-O), 617 (C-H) $cm^{-1}$.

### 1-(2-Bromoethyl)-4-octylbenzene (19)

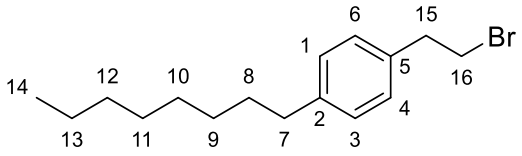


Following **General Procedure B, 19** was obtained from **11** (950 mg, 3.1 mmol). Purification by flash column chromatography (0% -> 10% EtOAc in pentane) yielded the title compound as a colourless oil (840 mg, 91%). **$^1$H NMR (400 MHz, $CDCl_3$):** δ 7.19-7.10 (m, 4H, $H_{1,3,4,6}$), 3.56 (t, *J* = 7.8 Hz, 2H, $H_{16}$), 3.15 (t, *J* = 7.8 Hz, 2H, $H_{15}$), 2.65-2.55 (m, 2H, $H_7$), 1.62 (tt, *J* = 7.5, 7.4 Hz, 2H, $H_8$), 1.37-1.25 (m, 10H, $H_{9-13}$), 0.90 (t, *J* = 7.0 Hz, 3H, $H_{14}$) ppm. **$^{13}$C NMR (101 MHz, $CDCl_3$):** δ 141.8 ($C_5$), 136.2 ($C_2$), 128.8 ($C_{4,6}$), 128.6 ($C_{1,3}$), 39.3 ($C_{16}$), 35.8 ($C_7$), 33.2 ($C_{15}$), 32.0 ($C_{12}$), 31.6 ($C_8$), 29.6 ($C_9$), 29.5 ($C_{11}$), 29.4 ($C_{10}$), 22.8 ($C_{13}$), 14.2 ($C_{14}$) ppm. **HRMS GC EI$^+$:** m/z 296.11396 $[M+H]^+$ *calc. m/z 296.11342.* **IR (film):** $\nu_{max}$ 3020 (C-H), 2926 (C-H), 2855 (C-H), 1514 (C=C), 1462, 805, 643 (C-Br). This data was consistent with literature characterisation.[432]

**1-Octyl-4-vinylbenzene (20)**

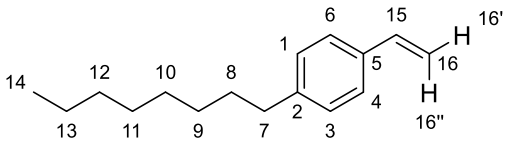


To a solution of **19** (1.0 g, 3.4 mmol) in EtOH was added 2 M NaOH (20 mL). The reaction was stirred at 80 °C for 16 h. The reaction mixture was diluted with pentane (100 mL), extracted and concentrated *in vacuo*. The crude material was purified by flash column chromatography (pentane) to yield **20** (660 mg, 90%) as colourless oil. **$^{1}$H NMR (400 MHz, $CDCl_3$):** δ 7.36 (d, J = 8.1 Hz, 2H, $H_{4,6}$), 7.17 (d, J = 8.1 Hz, 2H, $H_{1,3}$), 6.73 (dd, J = 17.6, 10.9 Hz, 1H, $H_{15}$), 5.74 (dd, J = 17.6, 1.0 Hz, 1H, $H_{16''}$), 5.22 (dd, J = 10.9, 1.0 Hz, 1H, $H_{16'}$), 2.66 – 2.60 (m, 2H, $H_7$), 1.64 (td, J = 8.8, 4.7 Hz, 2H, $H_8$), 1.41 – 1.24 (m, 10H, $H_{9\text{-}13}$), 0.93 (t, J = 7.0 Hz, 3H, $H_{14}$) ppm. **$^{13}$C NMR (101 MHz, $CDCl_3$):** δ 142.9 ($C_2$), 136.9 ($C_{15}$), 135.2 ($C_5$), 128.7 ($C_{1,3}$), 126.3 ($C_{4,6}$), 112.9 ($C_{16}$), 35.9 ($C_7$), 32.1 ($C_{12}$), 31.7 ($C_8$), 29.7 ($C_9$), 29.5 ($C_{10}$), 29.4 ($C_{11}$), 22.8 ($C_{13}$), 14.3 ($C_{14}$) ppm. **HRMS GC EI$^+$:** m/z 216.1878 [M+] *calc. m/z 216.1873.* This data was consistent with literature characterisation.[433]

Note: Polymerises when stored at room temperature. Can be stored at −20 °C in the dark for 3 months.

**2-Acetamido-3-ethoxy-3-oxopropanoic acid (22)**

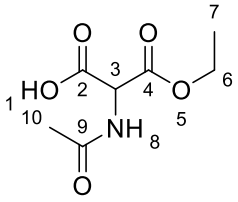

To a solution of diethylacetamidomalonate (1.0 g, 4.6 mmol) in 1,4-dioxane (15 mL) was added 1 M KOH (4.6 mmol) dropwise over 2 h. The reaction was stirred for another 2 h until completion. The organic solvent was evaporated and the aqueous layer was washed with EtOAc (10 mL). The aqueous layer was acidified with 1 M HCl, the crystals which formed were filtered and washed with $Et_2O$ to yield **22** as a colourless crystalline solid (760 mg, 87% yield). The compound was used without any further purification.

**1-Ethyl 3-(2,3,4,5-tetrafluorophenyl) 2-acetamidomalonate (23)**

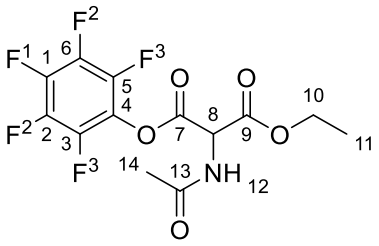


To a solution of pentafluorophenol (300 mg, 1.6 mmol) and DCC (240 mg, 1.2 mmol) in $CH_2Cl_2$ (10 mL) at 0 °C was added **22** (200 mg, 1.1 mmol). The reaction mixture was warmed to rt and stirred for 24 h. The reaction was diluted with $CH_2Cl_2$ (20 mL) and washed with water (10 mL). The combined organic layers were dried over $Na_2SO_4$ and concentrated *in vacuo.* The crude product was further purified by flash column chromatography (0 -> 10% MeOH in $CH_2Cl_2$) to yield **23** as a colourless solid (170 mg, 45%). **$^1$H NMR (400 MHz, $CDCl_3$):** δ 7.25 (d, *J* = 6.5 Hz, 1H, NH), 5.76 (d, *J* = 6.5 Hz, 1H, $H_8$), 4.68 – 4.55 (m, 2H, $H_{10}$), 2.39 (s, 3H, $H_{14}$), 1.60 (t, *J* = 7.2 Hz, 3H, $H_{11}$) ppm. **$^{13}$C NMR (101 MHz, $CDCl_3$):** δ 212.7 ($C_7$), 210.8 ($C_{13}$), 173.0 ($C_9$), 139.8 – 136.6 (m, $C_{2,3,5,6}$), 136.5 – 133.4 (m, $C_1$), 132.4 – 131.4 (m, $C_4$), 61.3 ($C_{10}$), 30.9 ($C_8$), 21.0 ($C_{14}$), 14.1 ($C_{11}$) ppm. **$^{19}$F NMR (377 MHz, $CDCl_3$):** δ -152.2 (d, *J* = 17.1 Hz, 2F, $F^3$), -156.9 (t, *J* = 21.8 Hz, 1F, $F^1$), -161.3 - -162.0 (m, 2F, $F^2$) ppm. **HRMS ESI$^+$:** m/z

356.0606 $[M+H]^+$ *calc. m/z 356.0552.* **IR (film):** $\nu_{max}$ 2934 (C-H), 1744 (C=O), 1660 (C=O), 1567 (C=C), 1271 (C-O), 1209 (C-O), 1029 (C-F) $cm^{-1}$. **mp:** 98-102 °C

**4-(Hydroxymethyl)-4-(4-octylphenethyl)oxazolidin-2-one (26)**

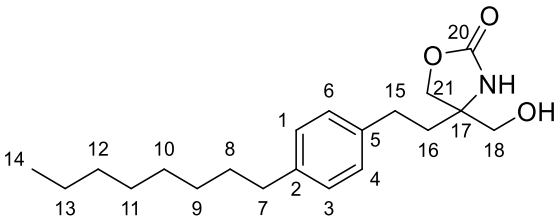


To a solution of fingolimod (150 mg, 0.49 mmol) in THF (200 μL) was added 6 M NaOH (1.0 mL). Diphosgene (90 μL, 0.75 mmol) was added dropwise. The reaction was stirred at rt for 3 h. The reaction mixture was extracted with EtOAc (20 mL) and concentrated *in vacuo* to yield **26** (138 mg, 82% yield). **$^1$H NMR (400 MHz, $CDCl_3$):** δ 7.14 – 7.03 (m, 4H, $H_{1,3,4,6}$), 4.28 (d, *J* = 8.7 Hz, 1H, $H_{21'}$), 4.16 (d, *J* = 8.7 Hz, 1H, $H_{21''}$), 3.67 (d, *J* = 11.6 Hz, 1H, $H_{18'}$), 3.54 (d, *J* = 11.6 Hz, 1H, $H_{18''}$), 3.33 (ddd, *J* = 7.4, 7.2, 7.0 Hz, 1H, $H_{15'}$), 3.15 (ddd, *J* = 7.4, 7.1, 7.0 Hz, 1H, $H_{15''}$), 2.73 – 2.46 (m, 4H, $H_{7,16',16''}$), 1.58 (tt, *J* = 7.5, 7.2 Hz, 2H, $H_8$), 1.31 – 1.23 (m, 10H, $H_{9\text{-}13}$), 0.87 (t, *J* = 6.5 Hz, 3H, $H_{14}$) ppm. **$^{13}$C NMR (101 MHz, $CDCl_3$):** δ 159.0 ($C_{20}$), 141.1 ($C_5$), 137.8 ($C_2$), 128.7 ($C_{4,6}$), 128.1 ($C_{1,3}$), 68.6 ($C_{21}$), 65.1 ($C_{18}$), 64.9 ($C_{17}$), 35.5 ($C_7$), 35.3 ($C_{16}$), 32.0 ($C_{12}$), 31.6 ($C_8$), 29.5 ($C_{15}$), 29.4 ($C_9$), 29.3 ($C_{11}$), 28.8 ($C_{10}$), 22.7 ($C_{13}$), 14.7 ($C_{14}$) ppm. **HRMS ESI$^-$:** m/z 332.2277 $[M-H]^-$ *calc m/z 332.2231.* **IR (film):** $\nu_{max}$ 3401 (O-H), 2926 (C-H), 1728 (C=O), 1422 (O-H), 1050 (C-O), 768 (C-H) $cm^{-1}$. The data was consistent with literature characterisation.[434]

**_tert_-Butyl-4-(hydroxymethyl)-4-(4-octylphenethyl)-2-oxooxazolidine-3-carboxylate (27)**

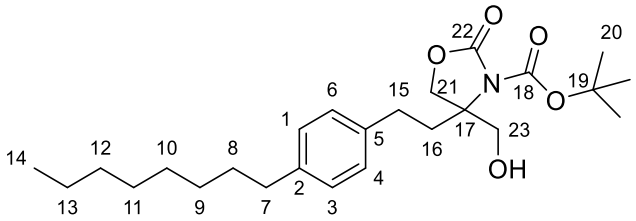


To a solution of **26** (130 mg, 0.39 mmol) in $CH_2Cl_2$ (1 mL) was added di-*tert*-butyl dicarbonate (85 mg, 0.40 mmol). The reaction was stirred at rt for 16 h. The reaction mixture was diluted with $CH_2Cl_2$ (10 mL), washed with water (5 mL) and concentrated *in vacuo*. The crude material was purified by flash column chromatography (10 -> 80% EtOAc in pentane) to yield **27** (84 mg, 49%) as a yellow oil. **$^1$H NMR (400 MHz, $CDCl_3$):** δ 7.13 – 7.05 (m, 4H, $H_{1,3,4,6}$), 4.54 (d, *J* = 11.3 Hz, 1H, $H_{21'}$), 4.46 (d, *J* = 11.3 Hz, 1H, $H_{21''}$), 4.35 (d, *J* = 3.3 Hz, 1H, $H_{23'}$), 4.32 (d, *J* = 2.7 Hz, 1H, $H_{23''}$), 3.97 (dd, *J* = 12.1, 7.0 Hz, 1H, $H_{15'}$), 3.81 (dd, *J* = 12.1, 7.2 Hz, 1H, $H_{15''}$), 2.69 (m, 2H, $H_{16}$), 2.55 (t, J = 7.5 Hz, 2H, $H_7$), 1.61-1.55 (m, 2H, $H_8$), 1.47 (s, 9H, $H_{20}$), 1.23 – 1.19 (m, 10H, $H_{9\text{-}13}$), 0.88 (t, J = 7.0 Hz, 3H, $H_{14}$) ppm. **$^{13}$C NMR (101 MHz, $CDCl_3$):** δ 157.9 ($C_{22}$), 153.2 ($C_{18}$), 141.2 ($C_5$), 137.3 ($C_2$), 128.8 ($C_{4,6}$), 128.1 ($C_{1,3}$), 85.2 ($C_{19}$), 83.1 ($C_{21}$), 68.3 ($C_{23}$), 62.8 ($C_{17}$), 35.7 ($C_7$), 35.5 ($C_{16}$), 31.9 ($C_{12}$), 31.6 ($C_8$), 29.5 ($C_{15}$), 29.4 ($C_9$), 29.3 ($C_{11}$), 28.6 ($C_{10}$), 27.7 ($C_{20}$), 22.7 ($C_{13}$), 14.6 ($C_{14}$) ppm. **LRMS ESI$^+$:** m/z 434 ([M+H]$^+$, 100%), 456 ([M+Na]$^+$, 14%). **HRMS ESI$^+$:** m/z 456.3026 [M+Na]$^+$ *calc. m/z 456.2720.* **IR (film):** $\nu_{max}$ 3469 (O-H), 2934 (C-H), 1811 (C=O), 1756 (C=O), 1213 (C-O), 1070 (C-O), 846 (C-H) cm$^{-1}$.

**2-Acetamido-2-(ethoxycarbonyl)-4-(4-octylphenyl)butanoic acid (30)**

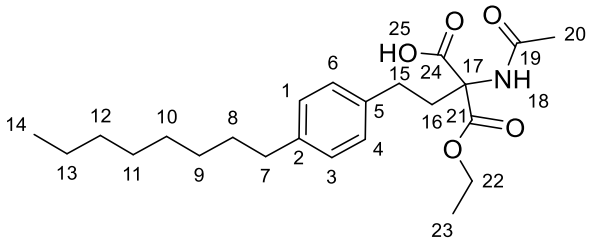


To a solution of **9** (200 mg, 0.46 mmol) in 1,4-dioxane (800 μL) was added 1 M KOH (500 μL) portionwise over 1 h. The reaction was stirred at rt for 16 h. The organic solvent was evaporated off and the aqueous solution was washed with EtOAc (50 mL). The aqueous layer was evaporated to yield **30** (180 mg, 87 %) as a crystalline solid. **$^{1}$H NMR (400 MHz, $CDCl_3$):** δ 7.09 – 7.02 (m, 4H, $H_{1,3,4,6}$), 6.92 (s, 1H, $H_{18}$), 4.29 – 4.16 (m, 2H, $H_{25}$), 2.74 – 2.58 (m, 2H, $H_{15}$), 2.53 (t, *J* = 7.7 Hz, 2H, $H_7$), 2.50 – 2.42 (m, 2H, $H_{16}$), 2.18 (s, 3H, $H_{28}$), 1.54 (tt, *J* = 8.1, 7.7 Hz, 2H, $H_8$), 1.34 – 1.24 (m, 10H, $H_{9\text{-}13}$), 0.87 (t, J = 6.9 Hz, 3H, $H_{14}$) ppm. **$^{13}$C NMR (101 MHz, $CDCl_3$):** δ 176.9 ($C_{24}$), 172.2 ($C_{21}$), 169.5 ($C_{19}$), 139.9 ($C_2$), 138.0 ($C_5$), 128.2 ($C_{4,6}$), 128.2 ($C_{1,3}$), 60.4 ($C_{17}$), 51.5 ($C_{22}$), 34.8 ($C_7$), 32.8 ($C_{16}$), 31.3 ($C_{12}$), 31.0 ($C_8$), 30.9 ($C_9$), 28.8 ($C_{10}$), 28.7 ($C_{15}$), 28.7 ($C_{11}$), 22.3 ($C_{20}$), 22.1 ($C_{13}$), 14.1 ($C_{14}$), 13.9 ($C_{23}$) ppm. **LRMS ESI$^+$:** m/z 444 ($[M+K]^+$, 100%). **HRMS ESI$^-$:** m/z 404.2353 $[M-H]^-$ *calc. m/z 404.2442.* **IR (film):** $\nu_{max}$ 3005 (O-H), 2939 (C-H), 1756 (C=O), 1064 (C-O), 716 (C-H) $cm^{-1}$.

**2-Acetamido-2-(hydroxymethyl)-4-(4-octylphenyl)butanoic acid (31)**

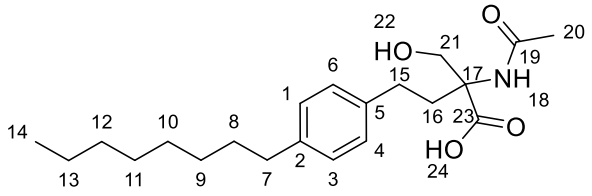

To a solution of **30** (50 mg, 0.12 mmol) in THF (2 mL) was added $LiBH_4$ (5.0 mg, 0.24 mmol). The reaction was stirred at rt for 6 h. The reaction was quenched with water, acidified with 1 M HCl, extracted with EtOAc (20 mL) and concentrated *in vacuo*. The crude material was purified by reverse-phase flash column chromatography (0 -> 100% MeCN in water) to yield **31** (20 mg, 44%) as a crystalline solid. **$^1$H NMR (400 MHz, $CDCl_3$):** δ 8.01 (s, 1H, $H_{24}$), 7.11 – 7.02 (m, 4H, $H_{1,3,4,6}$), 6.72 (s, 1H, $H_{18}$), 4.20 (d, *J* = 11.5 Hz, 1H, $H_{21'}$), 3.94 (d, *J* = 11.5 Hz, 1H, $H_{21''}$), 2.52 (m, 6H, $H_{7,15,16}$), 2.17 (s, 3H, $H_{20}$), 1.53 (tt, *J* = 7.4, 7.1 Hz, 1H, $H_8$), 1.34 – 1.20 (m, 10H, $H_{9\text{-}13}$), 0.92 – 0.84 (t, *J* = 7.0 Hz, 3H, $H_{14}$) ppm. **$^{13}$C NMR (101 MHz, $CDCl_3$):** δ 178.3 ($C_{23}$), 171.5 ($C_{19}$), 137.9 ($C_5$), 136.0 ($C_2$), 128.3 ($C_{4,6}$), 128.0 ($C_{1,3}$), 64.9 ($C_{21}$), 64.8 ($C_{17}$) 35.3 ($C_7$), 32.9 ($C_{16}$), 31.7 ($C_{12}$), 31.4 ($C_8$), 29.5 ($C_{15}$), 29.2 ($C_9$), 29.1 ($C_{11}$) 29.0 ($C_{10}$), 23.4 ($C_{20}$), 22.4 ($C_{13}$), 13.9 ($C_{14}$) ppm. **LRMS ESI$^+$:** m/z 749 (100%, $[2M+Na]^+$), 364 (70%, $[M+H]^+$), 386 (32%, $[M+Na]^+$). **HRMS ESI$^-$:** m/z 362.2349 $[M-H]^-$ *calc. m/z 362.2337.* **IR (film):** $\nu_{max}$ 3379 (O-H), 3100 (O-H), 1718 (C=O), 1644 (C=O), 1424 (O-H), 1375 (O-H), 1066 (C-O), 769 (C-H) $cm^{-1}$.

## ((Oxybis(ethane-2,1-diyl))bis(oxy))bis(ethane-2,1-diyl) dimethanesulfonate (33)

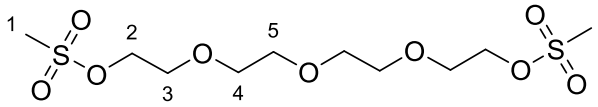


To a solution of tetraethyleneglycol (1.8 mL, 10 mmol) and triethylamine (3.2 mL, 24 mmol) in 2-MeTHF (15 mL) at 0 °C was added mesyl chloride (1.4 mL, 23 mmol). The reaction stirred at rt for 4 h. The solvent was evaporated and dissolved in EtOAc (50 mL), washed with water (20 mL) and sat. aq. $NH_4Cl$ (20 mL). The organic phases were concentrated *in vacuo* to yield **33** (2.6 g, 72%) as a colourless oil. **$^1$H NMR (400 MHz, $CDCl_3$):** δ 4.21 – 4.18

(m, 4H, $H_2$), 3.61 – 3.57 (m, 4H, $H_3$), 3.51 – 3.45 (m, 8H, $H_{4,5}$), 2.91 (s, 6H, $H_1$). ppm. **$^{13}$C NMR (101 MHz, $CDCl_3$):** δ 70.3 ($C_4$), 70.2 ($C_5$), 69.3 ($C_3$), 68.7 ($C_2$), 37.3 ($C_1$) ppm. **HRMS ESI$^+$:** m/z 351.0782 $[M+H]^+$ *calc. m/z 351.0778.* This data was consistent with literature characterisation.[435]

## 2-(2-(2-(2-Azidoethoxy)ethoxy)ethoxy)ethyl methanesulfonate (34)

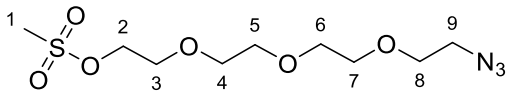


To a solution of **33** (2.6 g, 7.4 mmol) in EtOH (15 mL) was added sodium azide (530 mg, 8.2 mmol). The reaction was refluxed at 80 °C for 16 h. The reaction was diluted with EtOAc (35 mL) and washed with water (20 mL). The organic phases were concentrated *in vacuo* and purified by flash column chromatography (20 -> 80% EtOAc in pentane) to yield **34** (470 mg, 22% yield) as a colourless oil. **$^1$H NMR (400 MHz, $CDCl_3$):** δ 4.30 – 4.26 (m, 2H, $H_2$), 3.70 – 3.65 (m, 2H, $H_3$), 3.60 – 3.55 (m, 10H, $H_{4,-8}$), 3.30 (t, *J* = 5.0 Hz, 2H, $H_9$), 2.99 (s, 3H, $H_1$) ppm. **$^{13}$C NMR (101 MHz, $CDCl_3$):** δ 70.5 ($C_6$), 70.4 ($C_4$), 70.4 ($C_{5,8}$), 69.8 ($C_3$), 69.3 ($C_2$), 68.8 ($C_7$), 50.5 ($C_9$), 37.4 ($C_1$) ppm. **LRMS ESI$^+$:** m/z 320 ($[M+Na]^+$, 100%), 298 ($[M+H]^+$, 8%). **HRMS ESI$^+$:** m/z 298.1071 $[M+H]^+$ *calc. m/z 298.1067.* **IR (film):** $\nu_{max}$ 2874 (C-H), 2111 (N=N=N), 1352 (S=O), 1175 (S=O), 806 (C-H) $cm^{-1}$. This data was consistent with literature characterisation.[436]

**Methyl 1-azido-14-(tritylamino)-3,6,9,12-tetraoxapentadecan-15-oate (35)**

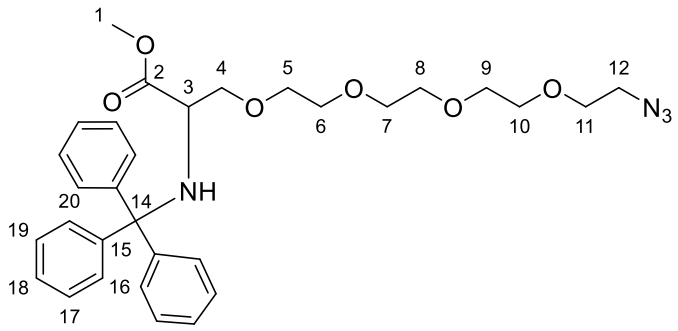


To a solution of methyl tritylserinate (1.0 g, 2.8 mmol) in DMF (8 mL) at 0 °C was added 60% NaH in mineral oil (130 mg, 3.3 mmol) followed by **34** (920 mg, 3.1 mmol). The reaction stirred at 40 °C for 6 h. The reaction was diluted with EtOAc (100 mL) and washed with 5% LiCl aq. Solution (2 x 30 mL). The organic phases were concentrated *in vacuo* and purified by flash column chromatography (10 -> 80% EtOAc in $CH_2Cl_2$) to yield **35** (790 mg, 49%) as a colourless oil. **$^1$H NMR (400 MHz, $CDCl_3$):** δ 7.54 – 7.48 (m, 6H, $H_{16,20}$), 7.30 – 7.23 (m, 6H, $H_{17,19}$), 7.22 – 7.17 (m, 3H, $H_{18}$), 4.39 – 4.35 (m, 2H, $H_{PEG}$), 3.78 – 3.74 (m, 2H, $H_{PEG}$), 3.69 – 3.62 (m, 13H, $H_{PEG}$), 3.38 (dd, *J* = 5.7, 4.6 Hz, 2H, $H_{12}$), 3.05 (s, 3H, $H_1$) ppm. **$^{13}$C NMR (101 MHz, $CDCl_3$):** δ 173.9 ($C_2$), 145.6 ($C_{15}$), 128.7 ($C_{16,20}$), 127.8 ($C_{17,19}$), 126.5 ($C_{18}$), 71.3 ($C_{PEG}$), 70.9 ($C_{PEG}$), 70.8 ($C_{PEG}$), 70.6 ($C_{PEG}$), 70.5 ($C_{PEG}$), 70.5 ($C_{PEG}$), 70.0 ($C_{PEG}$), 69.3 ($C_{PEG}$), 68.9 ($C_{PEG}$), 57.8 ($C_3$), 50.6 ($C_{12}$), 37.6 ($C_1$) ppm. **LRMS ESI$^+$:** m/z 243 ([Tr+H]$^+$, 100%), 585 ([M+Na]$^+$, 19%), 320 ([M-Tr+H]$^+$, 18%), 563 ([M+H]$^+$, 15%). **HRMS ESI$^+$:** m/z 563.2876 [M+H]$^+$ *calc m/z 563.2864.* **IR (film):** $\nu_{max}$ 3032 (N-H), 2110 ($N_3$), 1734 (C-O), 1175 (C-O), 1132 (C-N), 734 (C-H) cm$^{-1}$.

**14-Amino-1-azido-3,6,9,12-tetraoxapentadecan-15-ol (37)**

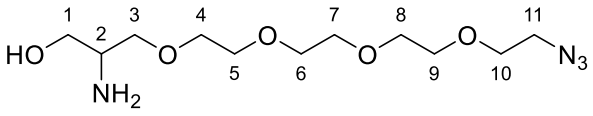


To a solution of **35** (50 mg, 0.089 mmol) in THF (1 mL) at 0 °C was added $LiBH_4$ (4 mg, 0.16 mmol). The reaction was stirred at rt for 4 h. The reaction was quenched with water and 2 M NaOH. The crude material was concentrated *in vacuo*, redissolved in $CH_2Cl_2$ (1.0 mL), filtered and transferred to a new flask. TFA (500 μL) was added and the reaction was stirred at rt for 1 h. The reaction was basified with 2 M NaOH, concentrated *in vacuo* and purified by reverse-phase flash column chromatography (0 -> 100% MeCN in 10 mM $NH_4Ac$) to yield a colourless oil (10 mg, 37%). **$^1$H NMR (400 MHz, $CDCl_3$):** δ 4.41 – 4.34 (m, 2H, $H_{10}$), 3.77 (ddd, *J* = 4.6, 2.8, 1.5 Hz, 2H, $H_8$), 3.67 – 3.60 (m, 15H, $H_{1,3\text{-}7,9,11}$), 3.58-3.52 (m, 1H, $H_{1'}$), 3.39 (m, 1H, $H_2$) ppm. **$^{13}$C NMR (101 MHz, CDCl3):** δ 71.5 ($C_{PEG}$), 70.8 ($C_{PEG}$), 70.8 ($C_{PEG}$), 70.8 ($C_{PEG}$), 70.6 ($C_{PEG}$), 70.5 ($C_{PEG}$), 70.2 ($C_{PEG}$), 69.4 ($C_{PEG}$), 69.2 ($C_{PEG}$), 50.8 ($C_2$), 37.8 ($C_{11}$) ppm. **LRMS ESI$^+$:** m/z 293 ([M+H]$^+$, 100%), 315 ([M+Na]$^+$, 13%). **IR (film):** $\nu_{max}$ 3345 (O-H), 3250 (N-H), 2143 (N=N=N), 1027 (C-O), 654 (C-H) cm$^{-1}$.

**2-(2-(2-(Benzylamino)ethoxy)ethoxy)ethan-1-ol (40)**

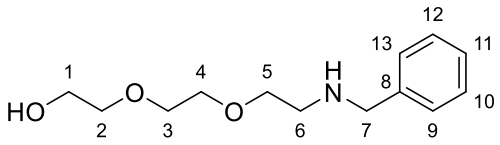


To a solution of amino-PEG3-alcohol (1.0 g, 6.8 mmol) in $CH_2Cl_2$ (7 mL) over 4Å molecular sieves was added benzaldehyde (820 μL, 8.0 mmol). The reaction was stirred at rt for 18 h.

The solvent was evaporated and the residue redissolved in EtOH (10 mL). $NaBH_4$ (550 mg, 14 mmol) was added portionwise and the reaction was stirred at rt for 3 h. The reaction was diluted with $Et_2O$ (20 mL), and quenched with $H_2O$ (2 mL) and aq. 6 M NaOH (550 μL). After stirring for 15 min, $MgSO_4$ (1 spatula) was added and stirred vigorously for another 15 min. The reaction mixture was filtered and the filtrate concentrated *in vacuo*. The crude was purified by flash column chromatography (0 -> 10% MeOH in $CH_2Cl_2$) to yield **40** (930 mg, 58%) as a colourless oil. **$^1$H NMR (400 MHz, $CDCl_3$):** δ 7.39 – 7.20 (m, 5H, $H_{9\text{-}13}$), 3.83 (s, 2H, $H_7$), 3.73 – 3.53 (m, 10H, $H_{1\text{-}5}$), 2.82 (td, *J* = 5.2, 2.2 Hz, 2H, $H_6$) ppm. **$^{13}$C NMR (101 MHz, $CDCl_3$):** δ 134.2 ($C_8$), 129.6 ($C_{10,12}$), 128.9 ($C_{9,13}$), 128.7 ($C_{11}$), 72.8 ($C_{PEG}$), 70.2 ($C_{PEG}$), 65.9 ($C_{PEG}$), 61.7 ($C_1$), 60.0 ($C_7$), 52.7 ($C_6$) ppm. **LRMS ESI$^+$:** m/z 276 ($[M+K]^+$, 100%), 240 ($[M+H]^+$, 58%), 262 ($[M+Na]^+$, 22%). **HRMS ESI$^+$:** m/z 262.1411 $[M+Na]^+$ *calc. m/z 262.1414.* **IR (film):** $\nu_{max}$ 3471 (O-H), 2872 (C-H), 1455 (C-H), 1351 (O-H), 1123 (C-N), 1071 (C-O), 701 (C-H) $cm^{-1}$.

**2-(2-(2-(Benzylamino)ethoxy)ethoxy)ethyl 4-methylbenzenesulfonate (41)**

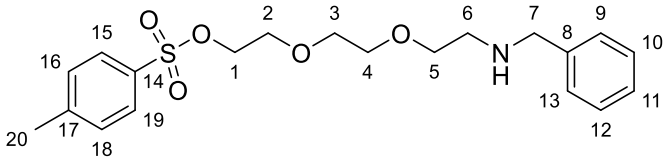


To a solution of **40** (500 mg, 2.1 mmol) and $Et_3N$ (590 μL, 4.2 mmol) in THF (10 mL) at 0 °C was added tosyl chloride (600 mg, 3.2 mmol). The reaction was stirred at rt for 4 h. The reaction was quenched with sat. aq. $NH_4Cl$ (5 mL), extracted with EtOAc (40 mL), dried over $MgSO_4$ and concentrated *in vacuo* to yield **41** (640 mg, 78%) as a colourless oil. **$^1$H NMR (400 MHz, $CDCl_3$):** δ 7.72 (d, *J* = 8.3 Hz, 2H, $H_{15,19}$), 7.32 – 7.23 (m, 7H, $H_{9\text{-}13,16,18}$), 4.36 (s, 2H, $H_7$), 3.69 – 3.65 (m, 2H, $H_1$), 3.54 – 3.47 (m, 4H, $H_{PEG}$), 3.41 – 3.35 (m, 4H, $H_{PEG}$), 3.28 (t, *J* = 6.1

Hz, 2H, $H_6$), 2.42 (s, 3H, $H_{20}$) ppm. **$^{13}$C NMR (101 MHz, $CDCl_3$):** δ 143.5 ($C_{17}$), 137.0 ($C_8$), 136.6 ($C_{14}$), 129.8 ($C_{16,18}$), 128.7 ($C_{10,12}$), 128.5 ($C_{9,13}$), 127.9 ($C_{15,19}$), 127.3 ($C_{11}$), 77.5 ($C_{PEG}$), 77.2 ($C_{PEG}$), 76.8 ($C_{PEG}$), 72.5 ($C_{PEG}$), 70.3 ($C_{PEG}$), 69.7 ($C_{PEG}$), 61.8 ($C_{PEG}$), 53.0 ($C_7$), 47.2 ($C_6$), 21.6 ($C_{20}$) ppm. **LRMS ESI$^+$:** m/z 411 (100%, $[M+Na]^+$), 394 (56%, $[M+H]^+$), 809 (50%, $[2M+Na]^+$). **HRMS ESI$^+$:** m/z 394.1686 $[M+H]^+$ *calc. m/z 394.1683.* **IR (film):** $\nu_{max}$ 3399 (N-H), 1339 (S=O), 1159 (S=O), 1011 (C-O), 701 (C-H) $cm^{-1}$.

## 1-Tosylaziridin-2-yl)methyl 4-methylbenzenesulfonate (43)

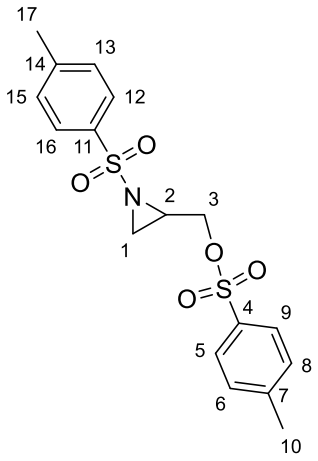


**Route A**

To a solution of 1-amino-3-chloro-propan-2-ol hydrochloride (250 mg, 1.7 mmol) in $CH_2Cl_2$:$H_2O$ (1:1, 10 mL) at 0 °C was added KOH (1.0 g) portionwise. Then tosyl chloride (700 mg, 3.7 mmol) was added and the reaction was stirred at rt for 2 h. Upon completion, the reaction was diluted with $CH_2Cl_2$ (50 mL) and washed with water (2 x 20 mL). The organic layers were extracted and concentrated *in vacuo* Purification by flash column chromatography (10% -> 80% EtOAc in pentane) yielded the title compound as a colourless oil (120 mg, 19%).

**Route B**

To a solution of 1-amino-3-chloro-propan-2-ol hydrochloride (2.1 g, 14 mmol) and $Et_3N$ (3.0 mL, 22 mmol) in $CH_2Cl_2$ (150 mL) was added tosyl chloride (3.3 g, 17 mmol) was added and the reaction was stirred at rt for 8 h until all starting material had been converted to the *N*-tosyl intermediate. Then $H_2O$ (150 mL) was added to the reaction mixture, followed by KOH (2.0 g) portionwise. Then an additional portion of tosyl chloride (3.3 g, 17 mmol) was added. The reaction was stirred at rt for 16 h, the crude material was concentrated *in vacuo* and purified by flash column chromatography (2% -> 40% EtOAc in pentane) yielded the title compound as a colourless oil (4.5 g, 81%). **$^1$H NMR (400 MHz, $CDCl_3$):** δ 7.99 – 7.94 (m, 4H, $H_{5,9,12,16}$), 7.38 – 7.32 (m, 4H, $H_{6,8,13,15}$), 3.88 (dd, *J* = 15.9, 5.3 Hz, 1H, $H_{3'}$), 3.76 (dd, *J* = 15.9, 4.8 Hz, 1H, $H_{3''}$), 3.20 (tdd, *J* = 5.0, 3.9, 2.5 Hz, 1H, $H_2$), 2.77 (dd, *J* = 4.7, 3.9 Hz, 1H, $H_{1'}$), 2.63 (dd, *J* = 4.8, 2.5 Hz, 1H, $H_{1''}$), 2.46 (s, 6H, $H_{10,17}$) ppm. **$^{13}$C NMR (101 MHz, $CDCl_3$):** δ 145.3 ($C_{7,14}$), 136.8 ($C_{4,11}$), 129.8 ($C_{6,8,13,15}$), 128.6 ($C_{5,9,12,16}$), 50.7 ($C_{2,3}$), 46.7 ($C_1$), 21.8 ($C_{10,17}$) ppm. **HRMS ESI$^+$:** m/z 382.0777 $[M+H]^+$ *calc. m/z 382.0777*. This data was consistent with literature characterisation.[437]

Note:- The pure aziridines polymerise at rt within a few days, but can be stored at –20 °C for 3 months.

**13-((4-Methylphenyl)sulfonamido)-1-phenyl-5,8,11-trioxa-2-azatetradecan-14-yl 4-methylbenzenesulfonate (44)**

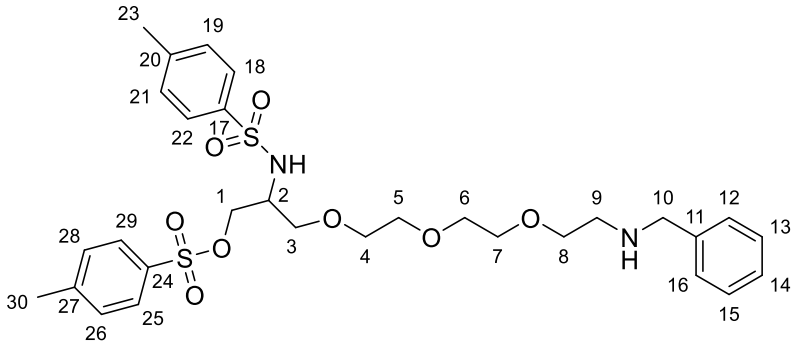


To a solution of **40** (380 mg, 1.6 mmol) in DMF (5 mL) was added 1 M KO$^t$Bu in THF (3.0 mmol) dropwise. The reaction was stirred at rt for 15 min, then **43** was added (610 mg, 1.6 mmol) and the reaction was refluxed at 120 °C for 16 h. The reaction was diluted with EtOAc (50 mL) and washed with 5% LiCl aq. solution (2 x 20 mL). The organic phases were concentrated *in vacuo* and purified by flash column chromatography (0 -> 10% MeOH in $CH_2Cl_2$) to yield **44** (100 mg, 16%) as a colourless oil. **$^1$H NMR (400 MHz, $CDCl_3$):** δ 7.91 (d, *J* = 8.4 Hz, 2H, $H_{18,22}$), 7.37 – 7.20 (m, 7H, $H_{12\text{-}16,19,21,25,26,28,29}$), 4.00 (dtd, *J* = 9.7, 6.0, 3.4 Hz, 1H, $H_2$), 3.82 (dd, *J* = 15.3, 6.0 Hz, 1H, $H_{1'}$), 3.74 – 3.67 (m, 2H, $H_{10}$), 3.66 – 3.35 (m, 11H, $H_{PEG}$), 2.76 (ddd, *J* = 14.1, 7.9, 4.2 Hz, 1H, $H_{3'}$), 2.68 – 2.48 (m, 3H, $H_{3'',9}$), 2.41 (s, 6H, $H_{23,30}$) ppm. **$^{13}$C NMR (101 MHz, $CDCl_3$):** δ 145.0 ($C_{20,27}$), 138.9 ($C_{11}$), 137.0 ($C_{17,24}$), 129.7 ($C_{19,21,26,28}$), 129.1 ($C_{13,15}$), 128.6 ($C_{18,22,25,29}$), 128.5 ($C_{12,16}$), 127.3 ($C_{14}$), 73.0 ($C_{PEG}$), 70.3 ($C_{PEG}$), 70.2 ($C_{PEG}$), 69.4 ($C_{PEG}$), 67.6 ($C_2$), 61.9 ($C_{10}$), 60.1 ($C_{PEG}$), 58.7 ($C_{PEG}$), 53.6 ($C_3$), 52.2 ($C_1$), 21.8 ($C_{23,30}$) ppm. **LRMS ESI$^+$:** m/z 621 ([M+H]$^+$, 100%), 643 ([M+Na]$^+$, 99%), 1263 ([2M+Na]$^+$, 42%), 1241 ([2M+H]$^+$, 32%). **HRMS ESI$^+$:** m/z 621.2306 [M+H]$^+$, *calc. m/z 621.2299*. **IR (film):** $\nu_{max}$ 3406 (N-H), 2838 (C-H), 1605 (N-H), 1349 (S=O), 1165 (S=O), 1021 (C-O), 704 (C-H) cm$^{-1}$.

**13-Amino-1-phenyl-5,8,11-trioxa-2-azatetradecan-14-ol (46)**

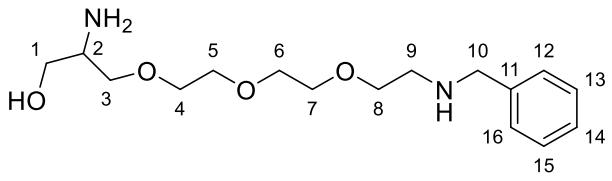


To a flame-dried MW vial under Ar was added Li (70 mg, 10 mmol) and naphthalene (1.3 g, 10 mmol). The vial was purged with Ar and degassed THF (5 mL) was added. The reaction was sonicated for 1 min until a dark green colour was observed. The reaction was stirred at rt for 2 h, until all the Li had disappeared. To a solution of **44** (200 mg, 0.3 mmol) in THF (5 mL) at −78 °C was added the freshly prepared lithium naphthalenide (10 eq) portionwise. The reaction was stirred at rt for 3 h. The reaction was acidified with 1 M HCl and washed with pentane (2 x 20 mL). The aqueous layer was concentrated *in vacuo* and purified by reverse-phase flash column chromatography (0 -> 100% MeCN in 10 mM $NH_4Ac$) to yield **46** (40 mg, 43%) as a colourless oil. **$^1$H NMR (400 MHz, $CDCl_3$):** δ 7.43 – 7.22 (m, 5H, $H_{12\text{-}16}$), 4.00 – 3.90 (m, 1H, $H_2$), 3.86 – 3.31 (m, 14H, $H_{1,4\text{-}8,10}$), 3.09 – 2.58 (m, 4H, $H_{3,9}$) ppm. **$^{13}$C NMR (101 MHz, $CDCl_3$):** δ 138.2 ($C_{11}$), 129.4 ($C_{12,16}$), 128.7 ($C_{13,15}$), 127.6 ($C_{14}$), 72.6 ($C_{PEG}$), 70.3 ($C_{PEG}$), 69.9 ($C_{PEG}$), 68.5 ($C_{PEG}$), 65.2 ($C_{PEG}$), 61.0 ($C_{PEG}$), 60.0 ($C_{PEG}$), 58.1 ($C_{PEG}$), 54.5 ($C_{10}$), 44.1 ($C_9$) ppm. **LRMS ESI$^+$:** 313 ([M+H]$^+$, 100%), 335 ([M+Na]$^+$, 71%), 625 ([2M+H]$^+$, 7%). **HRMS ESI$^+$:** m/z 313.2127 [M+H]$^+$ *calc. m/z 313.2122.* **IR (film):** $\nu_{max}$ 3380 (N-H), 2878 (C-H), 1575 (N-H), 1070 (C-O), 704 (C-H) cm$^{-1}$.

**13-Amino-13-(4-octylphenethyl)-1-phenyl-5,8,11-trioxa-2-azatetradecan-14-ol (47)**

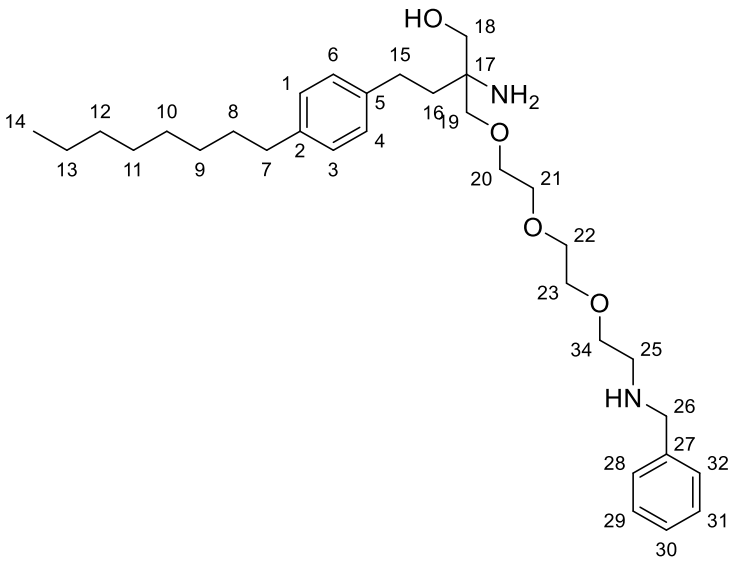


To a flame-dried MW vial under $N_2$ was added **46** (40 mg, 0.13 mmol) and **20** (30 mg, 0.13 mmol) in degassed DMF (1 mL). The vial was sealed and purged again. $[NBu_4][N_3]$ (4 mg in 100 μL MeCN, 10 mol%) and 3DPA2FBN (1 mg in 100 μL DMF, 1 mol%) were added and the reaction was stirred and irradiated by 427 nm light at rt for 20 h. The reaction was concentrated *in vacuo*. The crude material was purified by reverse-phase flash column chromatography (0 -> 100% MeCN in 10 mM $NH_4Ac$) to yield **47** as a colourless solid (0.5 mg, 1%). **LRMS ESI$^+$:** m/z 529 ($[M+H]^+$, 31%).

**Trimethyl(8-phenyloct-1-yn-1-yl)silane (54)**

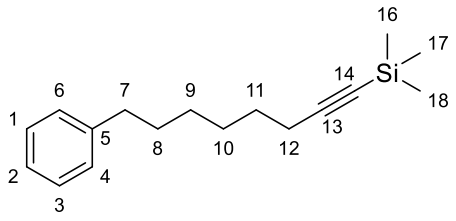

To a solution of TMS acetylene (1.4 mL, 9.9 mmol) in. THF (20 mL) under $N_2$ at −78 °C in flame-dried glassware was added 1.6 M *n*BuLi in THF (9.9 mmol) dropwise. The reaction was stirred at −78 °C for 1 h, then a solution of 1-bromo-6-phenylhexane (1.7 mL, 8.3 mmol) and HMPA (1.6 mL, 9.1 mmol) in THF (3 mL) was added and stirred for 1 h at −78 °C and then at rt for 16 h. The reaction was quenched with water (50 mL), and extracted with pentane (100 mL) twice. The organic layers were combined, dried ($Na_2SO_4$), and concentrated *in vacuo*. The crude material was further purified by flash column chromatography (0 -> 5% EtOAc in pentane) to yield the title compound a colourless oil (2.0 g, 96%). **$^1$H NMR (400 MHz, $CDCl_3$):** δ 7.27 – 7.19 (m, 2H, $H_{4,6}$), 7.16-7.09 (m, 3H, $H_{1-3}$), 2.65 (t, *J* = 7.7 Hz, 2H, $H_7$), 2.25 (t, *J* = 7.0, 2H, $H_{12}$), 1.74 – 1.62 (m, 2H, $H_8$), 1.61 – 1.33 (m, 6H, $H_{9-11}$), 0.30 – 0.16 (m, 9H, $H_{16-18}$) ppm. **$^{13}$C NMR (101 MHz, $CDCl_3$):** δ 142.6 ($C_5$), 128.4 ($C_{1,3}$), 128.3 ($C_{4,6}$), 125.5 ($C_2$), 107.7 ($C_{13}$), 84.3 ($C_{14}$), 36.0 ($C_7$), 31.4 ($C_8$), 28.7 ($C_9$), 28.7 ($C_{10}$), 28.6 ($C_{11}$), 20.0 ($C_{12}$), 0.3 ($C_{16-18}$) ppm. **HRMS APCI$^+$:** m/z 259.1878 $[M+H]^+$ *calc. m/z 259.1877*. **IR (film):** $\nu_{max}$ 2934 (C-H), 2172 (C≡C), 1454 (C-H), 842 (C-Si), 698 (C-H) $cm^{-1}$.

## Triisopropyl(8-phenyloct-1-yn-1-yl)silane (55)

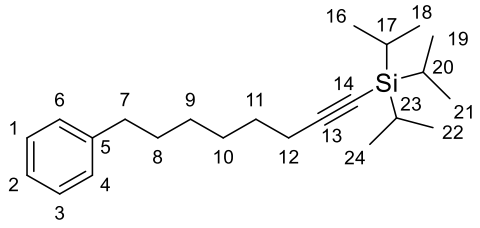


To a solution of TIPS acetylene (670 μL, 3.0 mmol) in THF (10 mL) under $N_2$ at −78 °C in flame-dried glassware was added 1.6 M *n*BuLi in THF (3.0 mmol) dropwise. The reaction was stirred at −78 °C for 1 h, then a solution of 1-bromo-6-phenylhexane (500 μL, 2.5 mmol)

and HMPA (480 μL, 2.7 mmol) in THF (1 mL) was added and stirred for 1 h at −78 °C and then at rt for 16 h. The reaction was quenched with water (50 mL), and extracted with pentane (100 mL) twice. The organic layers were combined, dried ($Na_2SO_4$), and concentrated i*n vacuo*. The crude material was further purified by flash column chromatography (0 -> 5% EtOAc in pentane) to yield the title compound a colourless oil (510 mg, 75%). **$^1$H NMR (400 MHz, $CDCl_3$):** δ 7.33 – 7.27 (m, 2H, $H_{4,6}$), 7.22 – 7.17 (m, 3H, $H_{1\text{-}3}$), 2.63 (t, *J* = 7.8 Hz, 2H, $H_7$), 2.27 (t, *J* = 6.8 Hz, 2H, $H_{12}$), 1.70 – 1.60 (m, 2H, $H_8$), 1.60 – 1.43 (m, 4H, $H_{9,10}$), 1.43 – 1.33 (m, 2H, $H_{11}$), 1.13 – 1.09 (m, 21H, $H_{16\text{-}23}$) ppm. **$^{13}$C NMR (101 MHz, $CDCl_3$):** δ 142.9 ($C_5$), 128.5 ($C_{1,3}$), 128.4 ($C_{4,6}$), 125.8 ($C_2$), 112.0 ($C_{13}$), 109.4 ($C_{14}$), 36.1 ($C_7$), 31.6 ($C_8$) 28.9 ($C_9$), 28.9 ($C_{10}$), 28.7 ($C_{11}$), 20.0 ($C_{12}$), 18.8 ($C_{16,18,19,21,22,24}$), 11.5 ($C_{17,20,23}$) ppm. **HRMS APCI$^+$:** m/z 343.2825 $[M+H]^+$ *calc. m/z 343.2816.* **IR (film):** $\nu_{max}$ 2941 (C-H), 2172 (C≡C), 1464 (C-H), 883 (C-Si), 677 (C-H) $cm^{-1}$.

**(6-Methoxyhexyl)benzene (57)**

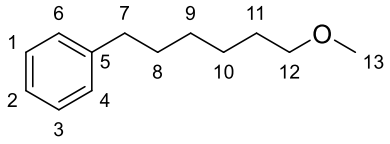


To a suspension of 60% NaH in mineral oil (450 mg, 11 mmol) in THF (20 mL) at 0 °C was added 6-phenyl-1-hexanol (1.0 g, 5.6 mmol) dropwise. The reaction was stirred at rt for 1 h, then MeI (1.4 mL, 22 mmol) was added dropwise. The reaction was stirred for 2 h at rt, quenched with water (20 mL), and extracted with EtOAc (100 mL). The combined organic layers were dried ($Na_2SO_4$) and concentrated *in vacuo*. The crude material was further purified by flash column chromatography (0 -> 10% EtOAc in pentane) to yield **57** (1.1 g,

quantitative) as a colourless oil. **$^{1}$H NMR (400 MHz, $CDCl_3$):** δ 7.31 – 7.24 (m, 2H, $H_{4,6}$), 7.20 – 7.13 (m, 3H, $H_{1\text{-}3}$), 3.36 (t, *J* = 6.6 Hz, 2H, $H_{12}$), 3.32 (s, 3H, $H_{13}$), 2.61 (dd, *J* = 8.7, 6.6 Hz, 2H, $H_7$), 1.68-1.52 (m, 4H, $H_{8,11}$), 1.42 – 1.32 (m, 4H, $H_{9,10}$) ppm. **$^{13}$C NMR (101 MHz, $CDCl_3$):** δ 142.9 ($C_5$), 128.5 ($C_{1,3}$), 128.3 ($C_{4,6}$), 125.7 ($C_2$), 73.0 ($C_{13}$), 58.7 ($C_{12}$), 36.0 ($C_7$), 31.6 ($C_{11}$), 29.7 ($C_8$), 29.3 ($C_{10}$), 26.2 ($C_9$) ppm. **HRMS ESI$^+$:** m/z 215.1400 $[M+Na]^+$ *calc. m/z 215.1406.* **IR (film):** $\nu_{max}$ 2932 (C-H), 1604 (C=$C_{arom}$), 1454 (C-H), 1120 (C-O), 698 (C-H) $cm^{-1}$.

**(6-(Allyloxy)hexyl)benzene (58)**

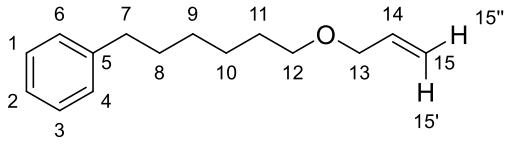


To a suspension of 60% NaH in mineral oil (270 mg, 6.7 mmol) in THF (20 mL) at 0 °C was added 6-phenyl-1-hexanol (1.0 g, 5.6 mmol) dropwise. The reaction was stirred at rt for 1 h, then allyl bromide (730 μL, 8.40 mmol) was added dropwise. The reaction was stirred for 2 h at rt, quenched with water (20 mL), and extracted with EtOAc (100 mL). The combined organic layers were dried ($Na_2SO_4$) and concentrated *in vacuo*. The crude material was further purified by flash column chromatography (0 -> 10% EtOAc in pentane) to yield **58** (1.1 g, 94%) as a colourless oil. **$^{1}$H NMR (400 MHz, $CDCl_3$):** δ 7.30 – 7.23 (m, 2H, $H_{4,6}$), 7.20 – 7.13 (m, 3H, $H_{1\text{-}3}$), 5.92 (ddt, *J* = 17.2, 10.4, 5.6 Hz, 1H, $H_{14}$), 5.31 (ddt, *J* = 17.2, 3.4, 1.5 Hz, 1H, $H_{15'}$), 5.21 (ddt, *J* = 10.5, 3.4, 1.3 Hz, 1H, $H_{15''}$) 3.95 (ddd, *J* = 5.6, 1.5, 1.3 Hz, 2H, $H_{13}$), 3.42 (t, *J* = 6.6 Hz, 2H, $H_{12}$), 2.65 – 2.56 (m, 2H, $H_7$), 1.67 – 1.54 (m, 4H, $H_{8,11}$), 1.45 – 1.33 (m, 4H, $H_{9,10}$) ppm. **$^{13}$C NMR (101 MHz, $CDCl_3$):** δ 142.8 ($C_5$), 135.2 ($C_{14}$), 128.5 ($C_{1,3}$), 128.3 ($C_{4,6}$), 125.7 ($C_2$), 116.7 ($C_{15}$), 71.9 ($C_{13}$), 70.5 ($C_{12}$), 36.0 ($C_7$), 31.6 ($C_{11}$), 29.8 ($C_8$), 29.3 ($C_{10}$), 26.1 ($C_9$)

ppm. **HRMS ESI$^+$:** m/z 219.1744 $[M+H]^+$ *calc. m/z 219.1743.* **IR (film):** $\nu_{max}$ 2932 (C-H), 1604 ($C=C_{arom}$), 1108 (C-O), 923 (C=C), 698 (C-H) $cm^{-1}$.

**Trimethyl(2-(((6-phenylhexyl)oxy)methoxy)ethyl)silane (59)**

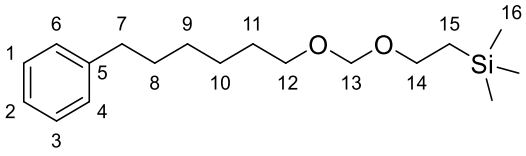


To a solution of 6-phenyl-1-hexanol (100 mg, 0.74 mmol) and DIPEA (520 μL, 3.0 mmol) in $CH_2Cl_2$ (3 mL) was added 2-(trimethylsilyl)ethoxymethyl chloride (390 μL, 2.2 mmol). The reaction mixture was stirred at rt for 1 h or until completion. The reaction was diluted with $Et_2O$ (50 mL) and washed with water (2 x 30 mL). The combined organic layers were dried ($Na_2SO_4$) and concentrated *in vacuo* to yield **59** as a colourless oil (190 mg, 96%). **$^1$H NMR (400 MHz, $CDCl_3$):** δ 7.28 – 7.20 (m, 2H, $H_{4,6}$), 7.17 – 7.11 (m, 3H, $H_{1-3}$), 4.64 (s, 2H, $H_{13}$), 3.63 – 3.55 (m, 2H, $H_{12}$), 3.50 (t, *J* = 6.6 Hz, 2H, $H_{14}$), 2.62 – 2.54 (m, 2H, $H_7$), 1.66-1.52 (m, 4H, $H_{8,11}$), 1.40-1.32 (m, 4H, $H_{9,10}$), 0.96 – 0.89 (m, 2H, $H_{15}$), 0.00 (s, 9H, $H_{16-18}$) ppm. **$^{13}$C NMR (101 MHz, $CDCl_3$):** δ 142.8 ($C_5$), 128.5 ($C_{1,3}$), 128.4 ($C_{4,6}$), 125.7 ($C_2$), 94.9 ($C_{13}$), 67.9 ($C_{12}$), 65.8 ($C_{14}$), 36.0 ($C_7$), 31.6 ($C_8$), 29.8 ($C_{11}$), 29.2 ($C_9$), 26.2 ($C_{10}$), 18.3 ($C_{15}$), -1.3 ($C_{16-18}$) ppm. **LRMS ESI$^+$:** m/z 331 ($[M+Na]^+$, 100%). **HRMS ESI$^+$:** m/z 331.2062 $[M+Na]^+$ *calc. m/z 331.2064.* **IR (film):** $\nu_{max}$ 2952 (C-H), 1941 (C-H), 1638 (C=C), 1146 (C-O), 1061 (C-O), 1249 (C-Si), 836 (C-Si) $cm^{-1}$.

**Trimethyl(2-(((6-phenylhexyl)oxy)methoxy)ethyl)silane (60)**

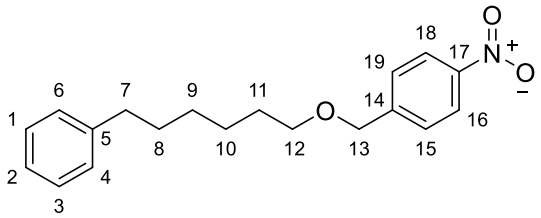


To a solution of 6-phenyl-1-hexanol (100 mg, 0.74 mmol) and 60% NaH in mineral oil (120 mg, 3.0 mmol) in THF (3 mL) was added 4-nitrobenzyl bromide (475 mg, 2.2 mmol). The reaction mixture was stirred at rt for 18 h. The reaction was diluted with $Et_2O$ (50 mL) and washed with water (2 x 30 mL). The combined organic layers were dried ($Na_2SO_4$) and concentrated *in vacuo* to yield **60** as a colourless oil (200 mg, 86%). **$^1$H NMR (400 MHz, $CDCl_3$):** δ 8.09 (d, *J* = 8.0 Hz, 2H, $H_{16,18}$), 7.49 (d, *J* = 8.0 Hz, 2H, $H_{15,19}$), 7.26 – 7.20 (m, 2H, $H_{4,6}$), 7.20 – 7.10 (m, 3H, $H_{1-3}$), 4.48 (s, 2H, $H_{13}$), 3.53 (t, *J* = 6.0 Hz, 2H, $H_{12}$), 2.63 (t, *J* = 7.9 Hz, 2H, $H_7$), 1.60-1.52 (m, 4H, $H_{8,11}$), 1.42-1.34 (m, 4H, $H_{9,10}$) ppm. **$^{13}$C NMR (101 MHz, $CDCl_3$):** δ 148.3 ($C_{17}$), 143.0 ($C_{14}$), 142.8 ($C_5$), 128.6 ($C_{1,3}$), 128.3 ($C_{4,6}$), 127.5 ($C_{15,19}$), 125.7 ($C_2$), 124.8 ($C_{16,18}$) 72.4 ($C_{13}$), 69.9 ($C_{12}$), 36.1 ($C_7$), 31.5 ($C_8$), 29.7 ($C_{11}$), 28.2 ($C_9$), 26.7 ($C_{10}$) ppm. **LRMS ESI$^+$:** m/z 314 ([M+H]$^+$, 100%). **HRMS ESI$^+$:** m/z 314.1750 [M+H]$^+$ *calc. m/z 314.1756.* **IR (film):** $\nu_{max}$ 2955 (C-H), 1061 (C-O), 1525 (N-O), 1313 (N-O), 742 (C-H) cm$^{-1}$.

***tert*-Butyldimethyl((6-phenylhexyl)oxy)silane (61)**

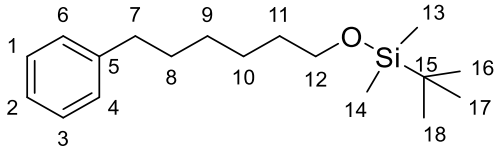

To a suspension of 6-phenyl-1-hexanol (130 mg, 0.98 mmol) and imidazole (80 mg, 1.2 mmol) in $CH_2Cl_2$ (3 mL) was added TBDMSCl (300 μL, 1.2 mmol). The reaction mixture was stirred for 2 h. The reaction was diluted with $Et_2O$ (50 mL) and washed with water (2 x 30 mL). The combined organic layers were dried ($Na_2SO_4$) and concentrated *in vacuo* to yield **61** as a colourless oil (370 mg, 99%). **$^1$H NMR (400 MHz, $CDCl_3$):** δ 7.26 – 7.20 (m, 2H, $H_{4,6}$), 7.16 – 7.09 (m, 3H, $H_{1\text{-}3}$), 3.55 (t, *J* = 6.5 Hz, 2H, $H_{12}$), 2.59 – 2.52 (m, 2H, $H_7$), 1.58 (tt, *J* = 7.6, 6.5 Hz, 2H, $H_{11}$), 1.47 (tt, *J* = 7.0, 6.7 Hz, 2H, $H_8$), 1.34 – 1.28 (m, 4H, $H_{9,10}$), 0.85 (s, 9H, $H_{16\text{-}18}$), 0.00 (s, 6H, $H_{13,14}$) ppm. **$^{13}$C NMR (101 MHz, $CDCl_3$):** δ 143.0 ($C_5$), 128.5 ($C_{1,3}$), 128.3 ($C_{4,6}$), 125.7 ($C_2$), 63.4 ($C_{12}$), 36.0 ($C_7$), 32.9 ($C_8$), 31.6 ($C_{11}$), 29.2 ($C_9$), 26.1 ($C_{16\text{-}18}$), 25.8 ($C_{10}$), 14.2 ($C_{15}$), -5.2 ($C_{13,14}$) ppm. **LRMS ESI$^+$:** m/z 315 ($[M+Na]^+$, 100%), 293 ($[M+H]^+$, 30%). **HRMS ESI$^+$:** m/z 293.2300 $[M+H]^+$ *calc. m/z 293.2295.* **IR (film):** $\nu_{max}$ 2931 (C-H), 1604 (C=C), 1259 (C-Si), 1098 (C-O), 1031 (O-Si), 835 (C=C) $cm^{-1}$.

**2-Bromo-1-(4-(6-methoxyhexyl)phenyl)ethan-1-one (62)**

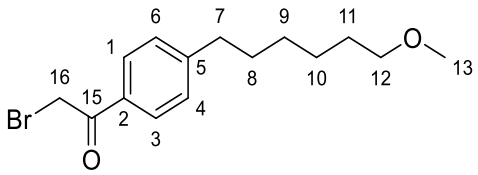


Following **General Procedure A, 62** was obtained from **57** (1.5 g, 7.8 mmol), 2-bromoacetylchloride (650 μL, 7.8 mmol) and $AlCl_3$ (1.1 g, 7.8 mmol). The reaction was stirred for 10 h. Purification by flash column chromatography (0% -> 30% EtOAc in pentane) yielded the title compound as a colourless oil (1.1 g, 44%). **$^1$H NMR (400 MHz, $CDCl_3$):** δ 7.90 (d, *J* = 8.3 Hz, 2H, $H_{1,3}$), 7.28 (d, *J* = 8.3 Hz, 2H, $H_{4,6}$), 4.43 (s, 2H, $H_{16}$), 3.35 (t, *J* = 6.5 Hz, 2H, $H_{12}$), 3.32 (s, 3H, $H_{13}$), 2.71 – 2.63 (m, 2H, $H_7$), 1.64 (m, 2H, $H_{11}$), 1.56 (m, 2H, $H_8$), 1.43 –

1.29 (m, 4H, $H_{9,10}$) ppm. **$^{13}$C NMR (101 MHz, $CDCl_3$):** δ 191.1 ($C_{15}$), 149.9 ($C_5$), 131.8 ($C_2$), 129.2 ($C_{1,3}$), 129.0 ($C_{4,6}$), 72.9 ($C_{12}$), 58.7 ($C_{14}$), 36.1 ($C_7$), 31.1 ($C_{16}$), 31.0 ($C_8$), 29.7 ($C_{11}$), 29.2 ($C_9$), 26.1 ($C_{10}$) ppm. **LRMS ESI$^+$:** m/z 337 ([$^{81}$BrM+Na]$^+$, 100%), 335 ([$^{79}$BrM+Na]$^+$, 91%), 315 ([$^{81}$BrM+H]$^+$, 12%), 313 ([$^{79}$BrM+H]$^+$, 6%). **HRMS ESI$^+$:** m/z 335.0611 [$^{81}$BrM+Na]$^+$ *calc. m/z 335.0617*. **IR (film):** $\nu_{max}$ 2933 (C-H), 1680 (C=O), 1606 (C=$C_{arom}$), 1117 (C-O), 690 (C-H), 605 (C-Br) $cm^{-1}$.

## 1-(4-(6-(Allyloxy)hexyl)phenyl)-2-bromoethan-1-one (63)

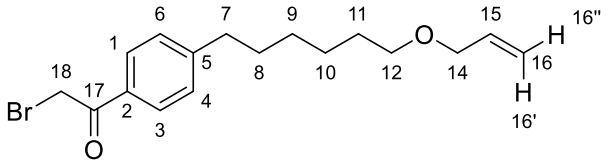


Following **General Procedure A, 63** was obtained from **58** (1.1 g, 5.0 mmol), 2-bromoacetylchloride (420 μL, 5.0 mmol) and $AlCl_3$ (680 mg, 5.0 mmol). The reaction was stirred for 10 h. Purification by flash column chromatography (0% -> 50% EtOAc in pentane) yielded the title compound as a colourless oil (700 mg, 41%). **$^1$H NMR (600 MHz, MeOD):** δ 7.98 – 7.91 (m, 2H, $H_{1,3}$), 7.37 – 7.33 (m, 2H, $H_{4,6}$), 5.89 (ddt, *J* = 17.3, 10.6, 5.6 Hz, 1H, $H_{15}$), 5.25 (ddt, *J* = 17.3, 3.4, 1.7 Hz, 1H, $H_{16'}$), 5.14 (ddt, *J* = 10.6, 3.4, 1.3 Hz, 1H, $H_{16''}$), 4.62 (s, 2H, $H_{18}$), 3.95 (dt, *J* = 5.6, 1.7, 1.3 Hz, 2H, $H_{14}$), 3.43 (t, *J* = 6.5 Hz, 2H, $H_{12}$), 2.71 (t, *J* = 7.7 Hz, 2H, $H_7$), 1.67 (tt, *J* = 7.7, 6.5 Hz, 2H, $H_{11}$), 1.57 (tt, *J* = 7.7, 7.0 Hz, 2H, $H_8$), 1.43 – 1.34 (m, 4H, $H_{9,10}$) ppm. **$^{13}$C NMR (151 MHz, $CDCl_3$):** δ 193.3 ($C_{17}$), 151.1 ($C_5$), 136.2 ($C_{15}$), 133.2 ($C_2$), 130.2 ($C_{1,3}$), 130.0 ($C_{4,6}$), 117.0 ($C_{16}$), 72.8 ($C_{14}$), 71.3 ($C_{12}$), 36.8 ($C_7$), 32.2 ($C_{18}$), 30.6 ($C_8$), 30.0 ($C_{11}$), 27.0 ($C_9$), 22.1 ($C_{10}$) ppm. **LRMS ESI$^+$:** m/z 361 ([M+Na]$^+$, 100%). **HRMS ESI$^+$:** m/z 339.0957 [M+H]$^+$

*calc. m/z 339.0954.* **IR (IPA):** $\nu_{max}$ 2935 (C-H), 1734 (C=O), 1648 (C=C), 1102 (C-O), 994 (C=C), 681 (C-Br) $cm^{-1}$.

**Diethyl 2-acetamido-2-(2-(4-(6-(allyloxy)hexyl)phenyl)-2-oxoethyl)malonate (64)**

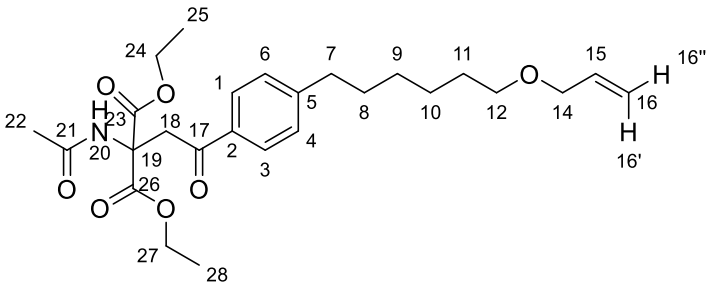


Following **General Procedure C, 64** was obtained from **63** (400 mg, 1.2 mmol) and diethylacetamidomalonate (520 mg, 2.4 mmol). The reaction was stirred at 65 °C overnight. Purification by flash column chromatography (0% -> 50% EtOAc in pentane) yielded the title compound as a colourless oil (145 mg, 25%). **$^{1}$H NMR (600 MHz, $CDCl_3$):** δ 7.90 – 7.85 (m, 2H, $H_{1,3}$), 7.27-7.23 (m, 2H, $H_{4,6}$), 7.11 (s, 1H, $NH_{20}$), 5.91 (ddt, *J* = 17.3, 10.4, 5.6 Hz, 1H, $H_{15}$), 5.26 (dq, *J* = 17.3, 1.3 Hz, 1H, $H_{16'}$), 5.16 (dt, *J* = 10.4, 1.3 Hz, 1H, $H_{16''}$), 4.26 (m, 4H, $H_{24,27}$), 4.24 (s, 2H, $H_{18}$), 3.95 (dt, *J* = 5.6, 1.5 Hz, 2H, $H_{14}$), 3.41 (t, *J* = 6.6 Hz, 2H, $H_{12}$), 2.66 (t, *J* = 7.7 Hz, 2H, $H_7$), 1.96 (s, 3H, $H_{22}$), 1.66 – 1.60 (m, 2H, $H_8$), 1.57 – 1.54 (m, 6H, $H_{9\text{-}11}$), 1.24 (t, *J* = 7.1 Hz, 6H, $H_{25,28}$) ppm. **$^{13}$C NMR (151 MHz, $CDCl_3$):** δ 196.7 ($C_{17}$), 169.6 ($C_{21}$), 167.5 ($C_{24,27}$), 149.6 ($C_5$), 135.2 ($C_{15}$), 134.0 ($C_2$), 128.9 ($C_{4,6}$), 128.5 ($C_{1,3}$), 116.9 ($C_{16}$), 72.0 ($C_{14}$), 71.5 ($C_{12}$), 70.5 ($C_{18}$), 63.0 ($C_{24,27}$), 42.4 ($C_{19}$), 36.1 ($C_7$), 31.1 ($C_8$), 29.8 ($C_{11}$), 29.1 ($C_9$), 26.0 ($c_{10}$), 23.1 ($C_{22}$), 14.1 ($C_{25,28}$) ppm. **LRMS ESI$^+$:** m/z 498 ([M+Na]$^+$, 100%), 476 ([M+H]$^+$, 40%). **HRMS ESI$^+$:** m/z 476.2653 [M+H]$^+$ *calc. m/z 476.2643.* **IR (film):** $\nu_{max}$ 2935 (C-H), 1747 (C=O), 1685 (C=O), 1447 (C-H), 1228 (C-O), 1196 (C-O) $cm^{-1}$.

**Diethyl 2-acetamido-2-(2-(4-(6-hydroxyhexyl)phenyl)-2-oxoethyl)malonate (65)**

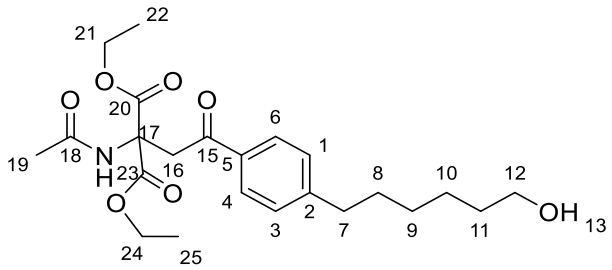


To a solution of **64** (200 mg, 0.42 mmol) in MeOH (2 mL) was added 1,3-dimethylbarbituric acid (130 mg, 0.84 mmol). The reaction vessel was purged with $N_2$. $Pd(PPh_3)_4$ (25 mg, 5 mol %) was added and the reaction was stirred at rt for 6 h. The reaction mixture was diluted with $CH_2Cl_2$ (50 mL), washed with water (2 x 30 mL) and concentrated *in vacuo*. The crude material was purified by flash column chromatography (10 -> 80% EtOAc:EtOH (3:1) + 2% $NH_4OH$ in pentane) to yield **65** (150 mg, 82%) as a yellow oil. **$^1$H NMR (400 MHz, $CDCl_3$):** δ 7.87 (d, *J* = 8.3 Hz, 2H, $H_{4,6}$), 7.26 (d, *J* = 8.3 Hz, 2H, $H_{1,3}$), 7.11 (s, 1H, NH), 4.27 (qd, *J* = 7.0, 1.4 Hz, 4H, $H_{21,24}$), 4.23 (s, 2H, $H_{16}$), 3.46 (t, *J* = 6.5 Hz, 2H, $H_{12}$), 2.65 (t, *J* = 7.6 Hz, 2H, $H_7$), 1.96 (s, 3H, $H_{19}$), 1.68 – 1.53 (m, 4H, $H_{8,11}$), 1.39 – 1.33 (m, 4H, $H_{9,10}$), 1.24 (t, *J* = 7.0 Hz, 6H, $H_{22,25}$) ppm. **$^{13}$C NMR (101 MHz, $CDCl_3$):** δ 196.7 ($C_{15}$), 169.6 ($C_{18}$), 167.5 ($C_{20,23}$), 149.6 ($C_2$), 134.0 ($C_5$), 128.9 ($C_{1,3}$), 128.5 ($C_{4,6}$), 71.5 ($C_{16}$), 64.2 ($C_{12}$), 63.0 ($C_{21,24}$), 42.4 ($C_{17}$), 36.1 ($C_7$), 31.1 ($C_8$), 29.6 ($C_{11}$), 26.0 ($C_9$), 23.1 ($C_{10}$), 21.9 ($C_{19}$), 14.1 ($C_{22,25}$) ppm. **LRMS ESI$^+$:** m/z 436 ($[M+H]^+$, 100%), 458 ($M+Na]^+$, 88%). **HRMS ESI$^+$:** m/z 436.2343 $[M+H]^+$ *calc. m/z 436.2330.* **IR (film):** $\nu_{max}$ 3628 (O-H), 2935 (C-H), 1747 (C=O), 1684 (C=O), 1607 (C=O), 1369 (O-H), 1053 (C-O), 746 (C-H) $cm^{-1}$.

**Diethyl 2-acetamido-2-(2-(4-(6-bromohexyl)phenyl)-2-oxoethyl)malonate (66)**

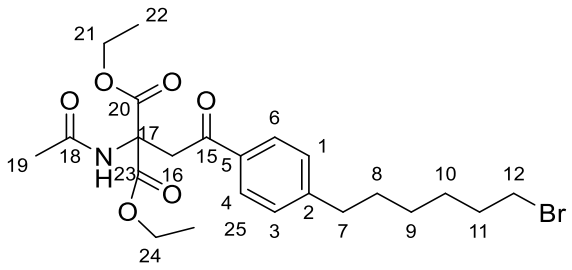


To a solution of **65** (100 mg, 0.23 mmol) in $CH_2Cl_2$ (1 mL) at 0 °C under $N_2$ was added $PPh_3$ (73 mg, 0.28 mmol) and $CBr_4$ (93 mg, 0.28 mmol). The reaction was stirred at rt for 24 h. The reaction mixture was filtered and washed with $CH_2Cl_2$ (50 mL). The filtrate was washed with water (20 mL) and the organic layers were concentrated *in vacuo*. The crude material was purified by flash column chromatography (10 -> 80% EtOAc in pentane) to yield **66** (17 mg, 15%) as a yellow oil. **$^1$H NMR (400 MHz, $CDCl_3$):** δ 7.88 (d, *J* = 8.3 Hz, 2H, $H_{4,6}$), 7.28 – 7.24 (d, *J* = 8.3 Hz, 2H, $H_{1,3}$), 7.11 (s, 2H, NH), 4.30 – 4.22 (m, 6H, $H_{21,24,16}$), 3.40 (t, *J* = 6.8 Hz, 2H, $H_{12}$), 2.67 (m, 2H, $H_7$), 1.97 (s, 3H, $H_{19}$), 1.85 (dq, *J* = 8.6, 6.9 Hz, 2H, $H_8$), 1.70 – 1.56 (m, 4H, $H_{8,11}$), 1.54 – 1.41 (m, 2H, $H_9$), 1.41 – 1.29 (m, 2H, $H_{10}$), 1.24 (t, *J* = 7.1 Hz, 6H, $H_{22,25}$) ppm. **$^{13}$C NMR (101 MHz, $CDCl_3$):** δ 196.7 ($C_{15}$), 169.6 ($C_{18}$), 167.5 ($C_{20,23}$), 149.4 ($C_2$), 134.1 ($C_5$), 128.9 ($C_{4,6}$), 128.6 ($C_{1,3}$), 64.2 ($C_{17}$), 63.0 ($C_{21,24}$), 42.4 ($C_{16}$), 36.0 ($C_7$), 34.0 ($C_{12}$), 32.8 ($C_{11}$), 31.0 ($C_8$), 28.4 ($C_9$), 28.1 ($C_{10}$), 23.1 ($C_{19}$), 14.1 ($C_{22,25}$) ppm. **LRMS ESI$^+$:** m/z 520 ([M+Na]$^+$, 100%), 498 ([M+H]$^+$, 79%). **HRMS ESI$^+$:** m/z 498.1509 [M+H]$^+$ *calc. m/z 498.1486.* **IR (film):** $\nu_{max}$ 2934 (C-H), 1746 (C=O), 1684 (C=O), 1229 (C-O), 672 (C-Br) cm$^{-1}$.

**Diethyl 2-acetamido-2-(2-(4-(6-iodohexyl)phenyl)-2-oxoethyl)malonate (67)**

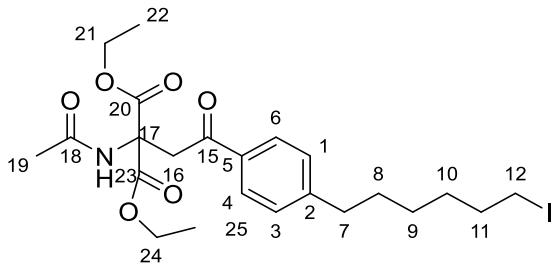


To a solution of **65** (100 mg, 0.23 mmol) in $CH_2Cl_2$ (1 mL) at 0 °C under $N_2$ was added $PPh_3$ (73 mg, 0.28 mmol) and imidazole (19 mg, 0.28 mmol), after 5 min $I_2$ (71 mg, 0.28 mmol) was added. The reaction was stirred at rt for 24 h. The reaction mixture was filtered and washed with $CH_2Cl_2$ (50 mL). The filtrate was washed with water (20 mL) and the organic layers were concentrated *in vacuo*. The crude material was purified by flash column chromatography (10 -> 80% EtOAc in pentane) to yield **67** (12.5 mg, 10%) as a yellow oil. **$^1$H NMR (400 MHz, $CDCl_3$):** δ 7.88 (d, *J* = 8.3 Hz, 2H, $H_{4,6}$), 7.26 (d, *J* = 8.3 Hz, 2H, $H_{1,3}$), 7.12 (s, 1H, NH), 4.30 – 4.22 (m, 6H, $H_{16,21,24}$), 3.17 (t, *J* = 6.9 Hz, 2H, $H_{12}$), 2.66 (t, *J* = 7.7 Hz, 2H, $H_7$), 1.96 (s, 3H, $H_{19}$), 1.81 (m, 2H, $H_{11}$), 1.69 – 1.57 (m, 2H, $H_8$), 1.52 – 1.43 (m, 4H, $H_{9,10}$), 1.25 (t, *J* = 6.7 Hz, 6H, $H_{22,25}$) ppm. **$^{13}$C NMR (101 MHz, $CDCl_3$):** δ 194.3 ($C_{15}$), 171.4 ($C_{18}$), 167.5 ($C_{20,23}$), 146.5 ($C_2$), 137.6 ($C_5$), 128.9 ($C_{1,3}$), 128.6 ($C_{4,6}$), 63.0 ($C_{21,24}$), 46.4 ($C_{12}$), 42.4 ($C_{16}$), 36.0 $C_7$), 30.9 ($C_8$), 30.4 ($C_{10}$), 28.2 ($C_9$), 23.1 ($C_{19}$), 14.1 ($C_{22,25}$) ppm. **LRMS ESI$^+$:** m/z 546 ([M+H]$^+$, 100%), 568 ([M+Na]$^+$, 46%). **HRMS ESI$^+$:** m/z 546.1353 [M+H]$^+$ *calc. m/z 546.1347.* **IR (film):** $\nu_{max}$ 2938 (C-H), 1747 (C=O), 1685 (C=O), 1176 (C-O), 921 (C=C) cm$^{-1}$.

**Diethyl 2-acetamido-2-(2-oxo-2-(4-(6-oxohexyl)phenyl)ethyl)malonate (69)**

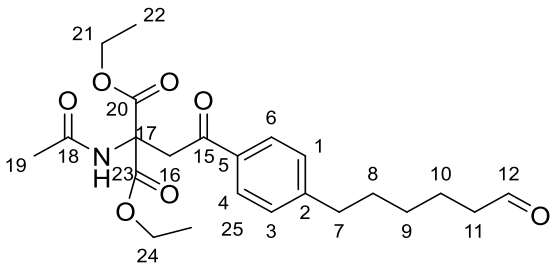


To a solution of **65** (16 mg, 0.036 mmol) in $CH_2Cl_2$ (200 μL) and DMSO (a few drops) was added PCC (30 mg, 0.072 mmol). The reaction vessel was stirred under $N_2$ at rt for 24 h. The reaction mixture was diluted with $CH_2Cl_2$ (20 mL), filtered through celite and concentrated *in vacuo*. The crude material was purified by flash column chromatography (0 -> 80% EtOAc in pentane) to yield **69** (15 mg, 96%) as a yellow oil. **$^1$H NMR (400 MHz, $CDCl_3$):** δ 9.76 (t, *J* = 1.7 Hz, 1H, $H_{12}$), 7.88 (d, *J* = 8.0 Hz, 2H, $H_{1,3}$), 7.25 (d, *J* = 8.0 Hz, 2H, $H_{4,6}$), 7.14 (s, 1H, NH), 4.32 – 4.21 (m, 6H, $H_{16,21,24}$), 2.67 (t, *J* = 7.7 Hz, 2H, $H_7$), 2.43 (td, *J* = 7.3, 1.7 Hz, 2H, $H_{11}$), 1.97 (s, 3H, $H_{19}$), 1.71 – 1.60 (m, 4H, $H_{8,10}$), 1.40 – 1.31 (m, 2H, $H_9$), 0.88 (t, *J* = 7.0 Hz, 6H, $H_{22,25}$) ppm. **$^{13}$C NMR (101 MHz, $CDCl_3$):** δ 202.6 ($C_{12}$), 196.7 ($C_{15}$), 169.7 ($C_{18}$), 167.5 ($C_{20,23}$), 149.2 ($C_2$), 134.1 ($C_5$), 132.2 ($C_{1,3}$), 128.7 ($C_{4,6}$), 64.2 ($C_{16}$), 63.0 ($C_{21,24}$), 42.4 ($C_{17}$), 35.9 ($C_7$), 30.9 ($C_8$), 29.2 ($C_{11}$), 28.8 ($C_9$), 23.1 ($C_{10}$), 22.0 ($C_{19}$), 14.2 ($C_{22,25}$) ppm. **LRMS ESI$^+$:** m/z 456 ($[M+Na]^+$, 100%), 434 ($[M+H]^+$, 38%). **HRMS ESI$^+$:** m/z 434.2163 $[M+H]^+$ *calc. m/z 434.2173.* **IR (film):** $\nu_{max}$ 3017 (C-H), 2939 & 2852 (C-H), 1745 (C=O), 1714 (C=O), 1687 (C=O), 1372 (C-H), 1197 (C-O), 697 (C-H) $cm^{-1}$.

**Dimethyl 2-acetamido-2-(2-(4-(hept-6-yn-1-yl)phenyl)-2-oxoethyl)malonate (70)**

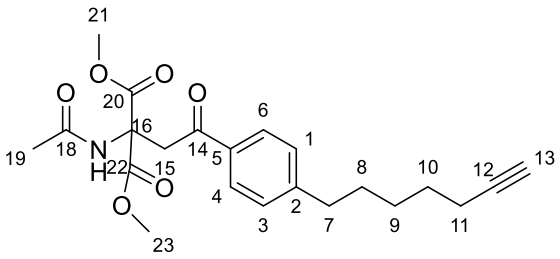


To a solution of **69** (15 mg, 0.030 mmol) in MeOH (200 μL) was added 10% dimethyl (1-diazo-2-oxo propyl) phosphonate in MeCN (63 μL, 0.033 mmol). The reaction vessel was stirred under $N_2$ at rt for 24 h. The reaction mixture was diluted with EtOAc (20 mL), washed with water (10 mL) and concentrated *in vacuo*. The crude material was purified by flash column chromatography (0 -> 80% EtOAc in pentane) to yield **70** (2 mg, 16% yield) as a yellow oil. **$^1$H NMR (600 MHz, $CDCl_3$):** δ 7.87 (d, *J* = 7.9 Hz, 2H, $H_{4,6}$), 7.43 (s, 1H, NH), 7.09 (d, *J* = 7.9 Hz, 2H, $H_{1,3}$), 4.24 (s, 2H, $H_{15}$), 3.80 (s, 6H, $H_{21,23}$), 3.39 (t, *J* = 5.0 Hz, 2H, $H_7$), 2.68 (m, 2H, $H_8$), 2.19 (dt, *J* = 6.7, 2.7 Hz, 2H, $H_{11}$), 1.97 (s, 3H, $H_{19}$), 1.94 (t, *J* = 2.7 Hz, 1H, $H_{13}$), 1.64 (p, *J* = 7.7 Hz, 2H, $H_{10}$), 1.45 (p, *J* = 8.0 Hz, 2H, $H_9$) ppm. **$^{13}$C NMR (151 MHz, $CDCl_3$):** δ 192.0 ($C_{14}$), 175.6 ($C_{18}$), 168.0 ($C_{20,22}$), 133.6 ($C_2$), 129.4 ($C_5$), 128.9 ($C_{4,6}$), 128.6 ($C_{1,3}$), 85.0 ($C_{12}$), 70.8 ($C_{13}$), 69.2 ($C_{16}$), 53.9 ($C_{21,23}$), 42.6 ($C_{15}$), 36.0 ($C_7$), 30.7 ($C_8$), 28.7 ($C_9$), 28.4 ($C_{10}$), 23.4 ($C_{19}$), 19.0 ($C_{11}$) ppm. **LRMS ESI$^+$:** m/z 424 ($[M+Na]^+$, 100%), 402 ($[M+H]^+$, 12%). **HRMS ESI$^+$:** m/z 402.1904 $[M+H]^+$ *calc. m/z 402.1911.*

**2-(Bromomethyl)-2-(4-(6-methoxyhexyl)phenyl)-1,3-dioxolane (72)**

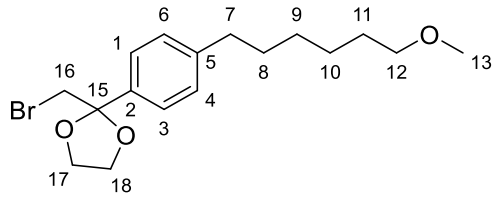


To a solution of **62** (500 mg, 1.6 mmol) in benzene (20 mL) with activated 3Å molecular sieves was added ethylene glycol (130 μL, 2.4 mmol) and *para*-toluene sulfonic acid (30 mg, 0.16 mmol). The reaction was refluxed for 48 h. Purification by flash column chromatography (0% -> 30% EtOAc in pentane) yielded the title compound as a colourless oil (480 mg, 85%). **$^{1}$H NMR (400 MHz, $CDCl_3$):** δ 7.40 (d, *J* = 8.1 Hz, 2H, $H_{1,3}$), 7.17 (d, *J* = 8.1 Hz, 2H, $H_{4,6}$), 4.22 – 4.15 (m, 2H, $H_{17',18'}$), 3.91 – 3.87 (m, 2H, $H_{17'',18''}$), 3.66 (s, 2H, $H_{16}$), 3.36 (t, *J* = 6.6 Hz, 2H, $H_{12}$), 3.32 (s, 3H, $H_{13}$), 2.64 – 2.56 (m, 2H, $H_7$), 1.67 – 1.50 (m, 4H, $H_{8,11}$), 1.44 – 1.32 (m, 4H, $H_{9,10}$) ppm. **$^{13}$C NMR (101 MHz, $CDCl_3$):** δ 143.7 ($C_5$), 137.0 ($C_2$), 128.5 ($C_{4,6}$), 126.0 ($C_{1,3}$), 107.4 ($C_{15}$), 73.0 ($C_{12}$), 65.9 ($C_{17,18}$), 58.7 ($C_{13}$), 38.5 ($C_{16}$), 35.7 ($C_7$), 31.4 ($C_8$), 29.7 ($C_{11}$), 29.29 ($C_9$), 26.1 ($C_{10}$) ppm. **LRMS ESI$^+$:** m/z 381 ([$^{81}$BrM+Na]$^+$, 100%), 397 ([$^{79}$BrM+Na]$^+$, 80%), 359 ([$^{81}$BrM+H]$^+$, 70%), 357 ([$^{79}$BrM+H]$^+$, 46%), 277 ([M-Br+H]•$^+$, 19%). **HRMS ESI$^+$:** m/z 357.1054 [M+H]$^+$, *calc. m/z 357.1060.* **IR (film):** $\nu_{max}$ 2930 (C-H), 1607 (C=C), 1463 (C-H), 1120 (C-O), 663 (C-H) cm$^{-1}$.

**1-(4-(3-Amino-4-hydroxy-3-(hydroxymethyl)butyl)phenyl)hept-6-yn-1-one (74)**

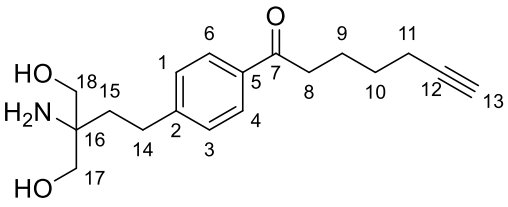

To a flame-dried MW vial under $N_2$ was added serinol (340 mg, 3.8 mmol) and **94** (800 mg, 3.8 mmol) in degassed DMF (20 mL). The vial was sealed and purged again. [$NBu_4$][$N_3$] (110 mg in 300 μL MeCN, 10 mol%) and 3DPA2FBN (24 mg in 500 μL DMF, 1.0 mol%) were added and the reaction was stirred and irradiated by 427 nm light at rt for 24 h. The reaction was concentrated *in vacuo*. The crude material was purified by reverse-phase flash column chromatography (2 -> 100% MeCN in 10mM $NH_4OAc$ aq.) to yield the title compound as a colourless solid (95 mg, 8%). **$^1$H NMR (400 MHz, MeOD):** δ 7.90 (d, *J* = 8.1 Hz, 2H, $H_{4,6}$), 7.36 (d, *J* = 8.1 Hz, 2H, $H_{1,3}$), 3.49 (*app* q, *J* = 10.9 Hz, 4H, $H_{17\text{-}18}$), 3.02 (t, *J* = 7.3 Hz, 2H, $H_8$), 2.79 – 2.69 (m, 2H, $H_{14}$), 2.26 – 2.17 (m, 3H, $H_{11,13}$), 1.81 (*app* p, *J* = 7.3 Hz, 2H, $H_9$), 1.73 – 1.66 (m, 2H, $H_{15}$), 1.59 (*app* p, *J* = 7.1 Hz, 2H, $H_{10}$) ppm. **$^{13}$C NMR (101 MHz, MeOD):** δ 202.3 ($C_7$), 150.3 ($C_2$), 136.0 ($C_5$), 129.8 ($C_{1,3}$), 129.5 ($C_{4,6}$), 84.7 ($C_{12}$), 69.7 ($C_{13}$), 66.4 ($C_{17\text{-}18}$), 56.9 ($C_{16}$), 38.8 ($C_8$), 37.2 ($C_{15}$), 30.5 ($C_{14}$), 29.2 ($C_{10}$), 24.7 ($C_9$), 18.9 ($C_{11}$) ppm. **LRMS ESI$^+$:** m/z 304 (100%, $[M+H]^+$), 607 (68%, $[2M+H]^+$). **HRMS ESI$^+$:** m/z 326.1724 $[M+Na]^+$ *calc. m/z 326.1727.* **IR (film):** $\nu_{max}$ 3262 (N-H), 2570 (O-H), 2073 (C≡C), 1679 (C=O), 1606 (N-H), 1355 (O-H), 1182 (C-N), 1063 (C-O), 804 (C-H) $cm^{-1}$.

**2-(Hex-5-yn-1-yl)-1,3-dioxolane (77)**

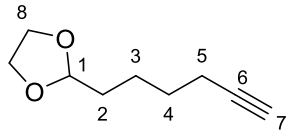


To a solution of **79** (500 mg, 4.5 mmol) in benzene (5 mL) at rt was added *para*-toluene sulfonic acid (80 mg, 0.45 mmol) and ethylene glycol (300 μL, 5.4 mmol). The reaction was stirred at 85 °C for 48 h. Upon completion by TLC, the reaction was concentrated *in vacuo*

(volatile compound, do not go below 700 mbar) to yield the title compound as a colourless oil (520 mg, 75%). **$^1$H NMR (400 MHz, $CDCl_3$):** δ 4.85 (t, *J* = 4.7 Hz, 1H, $H_1$), 3.98 – 3.91 (m, 2H, $H_{8',9'}$), 3.89 – 3.82 (m, 2H, $H_{8'',9''}$), 2.20 (td, *J* = 6.7, 2.7 Hz, 2H, $H_5$), 1.94 (t, *J* = 2.7 Hz, 1H, $H_7$), 1.73 – 1.64 (m, 2H, $H_2$), 1.63 – 1.47 (m, 4H, $H_{3,4}$) ppm. **$^{13}$C NMR (101 MHz, $CDCl_3$):** δ 104.6 ($C_1$), 84.5 ($C_6$), 68.5 ($C_7$), 65.0 ($C_8$), 33.5 ($C_2$), 28.5 ($C_4$), 23.3 ($C_3$), 18.5 ($C_5$) ppm. **IR (film):** $\nu_{max}$ 2951 (C-H), 2116 (C≡C), 1141 (C-O), 869 (C-H), 668 (C-H) $cm^{-1}$. This data was consistent with literature characterisation.[438]

## Hept-6-ynal (79)

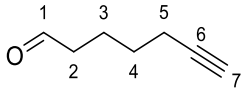


To a solution of heptyn-6-ol (500 mg, 4.5 mmol) in $CH_2Cl_2$ (14 mL) under $N_2$ was added PCC (1.9 g, 8.9 mmol). The reaction was stirred at rt for 16 h. Upon completion, the reaction was filtered over celite and concentrated *in vacuo* (volatile compound, do not go below 700 mbar). The crude material was purified by flash column chromatography (pentane) to yield the title compound as a colourless oil (500 mg, quantitative). **$^1$H NMR (400 MHz, $CDCl_3$):** δ 9.78 (s, 1H, $H_1$), 2.47 (dt, *J* = 7.2, 4.3 Hz, 2H, $H_2$), 2.23 (td, *J* = 7.0, 2.6 Hz, 2H, $H_5$), 1.96 (t, *J* = 2.7 Hz, 1H, $H_7$), 1.77 (m, 2H, $H_3$), 1.57 (p, *J* = 7.0 Hz, 2H, $H_4$) ppm. **$^{13}$C NMR (101 MHz, $CDCl_3$):** δ 202.1 ($C_1$), 83.6 ($C_6$), 68.6 ($C_7$), 53.5, 43.2 ($C_2$), 27.6 ($C_4$), 20.9 ($C_3$), 18.1 ($C_5$) ppm. **IR (film):** $\nu_{max}$ 3291 (O-H), 2867 (C-H), 2116 (C≡C), 1724 (C=O), 1449 (C-H), 765 (C-H) $cm^{-1}$. This data was consistent with literature characterisation.[439]

**2-Bromo-1-(4-bromophenyl)ethan-1-one (80)**

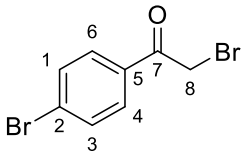


Following **General Procedure A, 80** was obtained from bromobenzene (1.0 mL, 9.4 mmol) and 2-bromoacetylchloride (1.1 mL, 11 mmol). Purification by flash column chromatography (0% -> 20% EtOAc in pentane) yielded the title compound as a yellow solid (860 mg, 35%). **$^{1}$H NMR (400 MHz, $CDCl_3$):** δ 7.85 (d, *J* = 8.7 Hz, 2H, $H_{4,6}$), 7.64 (d, *J* = 8.7 Hz, 2H, $H_{1,3}$), 4.40 (s, 3H, $H_8$) ppm. **$^{13}$C NMR (101 MHz, $CDCl_3$):** δ 190.6 ($C_7$), 132.8 ($C_5$), 132.4 ($C_{1,3}$), 130.6 ($C_{4,6}$), 129.5 ($C_2$), 30.5 ($C_8$) ppm. **IR (film):** $\nu_{max}$ 2950 (C-H), 1693 (C=O), 1396 (C-H), 710 (C-H), 644 (C-Br) $cm^{-1}$. This data was consistent with literature characterisation.[440]

**2-Bromo-1-(4-iodophenyl)ethan-1-one (81)**

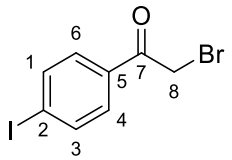


Following **General Procedure A, 81** was obtained from iodobenzene (1.8 mL, 4.9 mmol) and 2-bromoacetylchloride (500 μL, 5.9 mmol). Purification by flash column chromatography (0% -> 30% EtOAc in pentane) yielded the title compound as a yellow solid (1.3 g, 86%). **$^{1}$H NMR (400 MHz, $CDCl_3$):** δ 7.91 (d, *J* = 8.6 Hz, 2H, $H_{4,6}$), 7.74 (d, *J* = 8.6 Hz, 2H, $H_{1,3}$), 4.45 (s, 2H, $H_8$) ppm. **$^{13}$C NMR (101 MHz, $CDCl_3$):** δ 190.8 ($C_7$), 138.3 ($C_{1,3}$), 133.2 ($C_5$), 130.3 ($C_{4,6}$), 102.3 ($C_2$), 30.6 ($C_8$) ppm. **HRMS ESI$^+$:** m/z 346.8535 $[M+Na]^+$ *calc. m/z 346.8539.* This data was consistent with literature characterisation.[441]

**2-Bromo-1-(4-bromophenyl)ethan-1-one (82)**

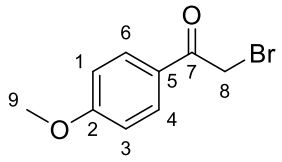


Following **General Procedure A, 82** was obtained from anisole (1.0 mL, 9.2 mmol) and 2-bromoacetylchloride (1.0 mL, 11 mmol). Purification by flash column chromatography (0% -> 20% EtOAc in pentane) yielded the title compound as a white solid (1.6 g, 76%). **$^1$H NMR (400 MHz, $CDCl_3$):** δ 7.95 (d, *J* = 9.0 Hz, 2H, $H_{4,6}$), 6.94 (d, *J* = 9.0 Hz, 2H, $H_{1,3}$), 4.39 (s, 2H, $H_8$), 3.87 (s, 3H, $H_9$) ppm. **$^{13}$C NMR (101 MHz, $CDCl_3$):** δ 190.0 ($C_7$), 164.2 ($C_2$), 131.4 ($C_{1,3}$), 127.0 ($C_5$), 114.2 ($C_{4,6}$), 55.7 ($C_8$), 30.9 ($C_9$) ppm. **HRMS:** m/z 228.9851$[M+H]^+$, *calc. m/z 228.9859.* This data was consistent with literature characterisation.[442]

**Diethyl 2-acetamido-2-(2-(4-bromophenyl)-2-oxoethyl)malonate (83)**

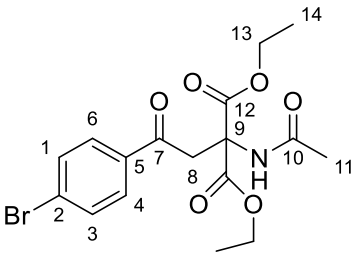


Following **General Procedure C, 83** was obtained from **80** (810 mg, 3.0 mmol) and diethylacetamidomalonate (770 mg, 3.6 mmol). The reaction was stirred at 65 °C overnight. Purification by flash column chromatography (0% -> 50% EtOAc in pentane) yielded the title compound as a colourless oil (370 mg, 30%). **$^1$H NMR (400 MHz, $CDCl_3$):** δ 7.78 (d, *J* = 8.4 Hz, 2H, $H_{4,6}$), 7.56 (d, *J* = 8.4 Hz, 2H, $H_{1,3}$), 7.11 (s, 1H, NH), 4.22 (q, *J* = 7.2 Hz, 4H, $H_{13}$),

4.19 (s, 2H, $H_8$), 1.94 (s, 3H, $H_{11}$), 1.20 (t, *J* = 7.2 Hz, 6H, $H_{14}$) ppm. **$^{13}$C NMR (101 MHz, $CDCl_3$):** δ 196.0 ($C_7$), 169.6 ($C_{10}$), 167.2 ($C_{12}$), 134.9 ($C_5$), 132.1 ($C_{1,3}$), 129.8 ($C_{4,6}$), 129.1 ($C_2$), 64.0 ($C_9$), 63.0 ($C_{13}$), 42.2 ($C_8$), 23.0 ($C_{11}$), 14.2 ($C_{14}$) ppm. **LRMS ESI$^+$:** m/z 851 ([2M($^{81}$Br)+Na]$^+$, 100%), 849 ([2M($^{79}$Br)+Na]$^+$, 61%), 436 ([M($^{79}$Br)+Na]$^+$, 48%), 438 ([M($^{81}$Br)+Na]$^+$, 43%), 416 ([M($^{81}$Br)+H]$^+$, 16%), 414 ([M($^{79}$Br)+Na]$^+$, 10%). **HRMS ESI$^+$:** m/z 414.0553 [M+H]$^+$ *calc. m/z 414.0547*. **IR (film):** $\nu_{max}$ 2940 (C-H), 1746 (C=O), 1688 (C=O), 1198 (C=O), 608 (C-Br) cm$^{-1}$.

## HU269 Diethyl 2-acetamido-2-(2-(4-iodophenyl)-2-oxoethyl)malonate (84)

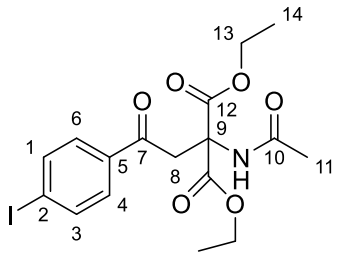


Following **General Procedure C, 84** was obtained from **81** (1.2 g, 3.7 mmol) and diethylacetamidomalonate (960 mg, 4.4 mmol). The reaction was stirred at 65 °C overnight. Purification by flash column chromatography (0% -> 50% EtOAc in pentane) yielded the title compound as a colourless oil (52 mg, 3%). **$^1$H NMR (400 MHz, $CDCl_3$):** δ 7.83 (d, *J* = 8.7 Hz, 2H, $H_{4,6}$), 7.66 (d, *J* = 8.7 Hz, 2H, $H_{1,3}$), 7.09 (s, 1H, NH), 4.26 (qd, *J* = 7.1, 1.0 Hz, 4H, $H_{14,17}$), 4.21 (s, 2H, $H_9$), 1.97 (s, 3H, $H_{12}$), 1.24 (t, *J* = 7.1 Hz, 6H, $H_{15,18}$) ppm. **$^{13}$C NMR (101 MHz, $CDCl_3$):** δ 196.5 ($C_8$), 170.0 ($C_{11}$), 167.3 ($C_{13,16}$), 138. 2 ($C_{1,3}$), 135.5 ($C_5$), 129.7 ($C_{4,6}$), 102.1 ($C_2$), 64.1 ($C_{10}$), 63.1 ($C_{14,17}$), 42.2 ($C_9$), 23.1, ($C_{12}$) 14.1 ($C_{15,18}$) ppm. **LRMS ESI$^+$:** m/z 945 ([2M+Na]$^+$, 100%), 462 ([M+H]$^+$, 36%), 484 ([M+Na]$^+$, 34%). **HRMS ESI$^+$:** m/z 462.0403 [M+H]$^+$ *calc. m/z 462.0408*. **IR (film):** $\nu_{max}$ 3381 (N-H), 2981 (C-H), 1743 (C=O), 1684 (C=O), 1223 (C-O), 810 (C-H) cm$^{-1}$.

**Diethyl 2-acetamido-2-(2-(4-methoxyphenyl)-2-oxoethyl)malonate (85)**

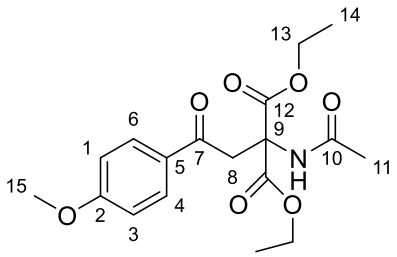

Following **General Procedure C, 85** was obtained from **82** (2.5 g, 11 mmol) and diethylacetamidomalonate (3.0 g, 14 mmol). The reaction was stirred at 60 °C overnight. Purification by flash column chromatography (10% -> 70% EtOAc in pentane) yielded the title compound as a colourless oil (2.8 g, 70%). **$^{1}$H NMR (400 MHz, $CDCl_3$)**: δ 7.85 (d, *J* = 8.9 Hz, 2H, $H_{4,6}$), 7.12 (s, 1H, NH), 6.85 (d, *J* = 8.9 Hz, 2H, $H_{1,3}$), 4.18 (qd, *J* = 7.1, 1.1 Hz, 4H, $H_{13}$), 4.13 (s, 2H, $H_8$), 3.78 (s, 3H, $H_{15}$), 1.89 (s, 3H, $H_{11}$), 1.16 (t, *J* = 7.1 Hz, 6H, $H_{14}$) ppm. **$^{13}$C NMR (101 MHz, $CDCl_3$):** δ 195.2 ($C_7$), 169.4 ($C_{10}$), 167.2 ($C_{12}$), 163.9 ($C_2$), 130.6 ($C_{1,3}$), 129.2 ($C_5$), 113.8 ($C_{4,6}$), 64.0 ($C_9$), 62.7 ($C_{13}$), 55.5 ($C_{15}$), 41.8 ($C_8$), 22.8 ($C_{11}$), 13.8 ($C_{14}$) ppm. **LRMS ESI$^+$:** m/z 753 ($[2M+Na]^+$, 100%), 366 ($[M+H]^+$, 93%), 388 ($[M+Na]^+$, 89%), 731 ($[2M+H]^+$, 29%). **HRMS ESI$^+$:** m/z 366.1561 $[M+H]^+$ *calc. m/z 366.1547*. **IR (film):** $\nu_{max}$ 2984 (C-H), 1745 (C=O), 1679 (C=O), 1601 (C=O), 1234 (C-O), 733 (C-H) $cm^{-1}$.

**Diethyl 2-acetamido-2-(4-bromophenethyl)malonate (86)**

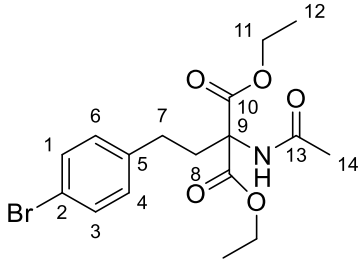

Following **General Procedure C, 86** was obtained from **83** (1.0 g, 3.8 mmol). The reaction was stirred at 70 °C. Purification by flash column chromatography (10% -> 80% EtOAc in pentane) yielded the title compound as a colourless oil (680 mg, 45%). **$^1$H NMR (400 MHz, $CDCl_3$):** δ 7.37 (d, *J* = 8.4 Hz, 2H, $H_{1,3}$), 7.02 (d, *J* = 8.4 Hz, 2H, $H_{4,6}$), 6.83 (s, 1H, NH), 4.21 (m, 4H, $H_{11}$), 2.72 – 2.61 (m, 2H, $H_7$), 2.49 – 2.42 (m, 2H, $H_8$), 2.00 (s, 3H, $H_{14}$), 1.25 (t, *J* = 7.1 Hz, 6H, $H_{12}$) ppm. **$^{13}$C NMR (101 MHz, $CDCl_3$):** δ 180.0 ($C_{13}$), 178.8 ($C_{10}$), 150.5 ($C_5$), 142.3 ($C_{1,3}$), 141.1 ($C_{4,6}$), 130.7 ($C_2$), 77.2 ($C_9$), 73.5 ($C_{11}$), 44.2 ($C_8$), 40.5 ($C_7$), 33.8 ($C_{14}$), 24.8 ($C_{12}$) ppm. **HRMS (ESI$^+$):** m/z 400.0741 $[M]^+$ *calc. m/z 400.0754.* This data was consistent with literature characterisation.[443]

**Diethyl 2-acetamido-2-(4-methoxyphenethyl)malonate (87)**

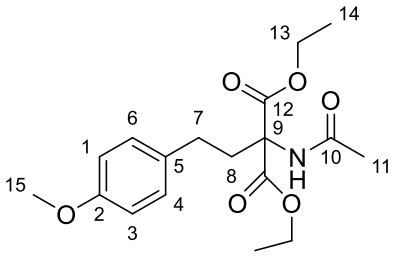


Following **General Procedure B, 87** was obtained from **85** (2.8 g, 7.7 mmol). The reaction was stirred at 70 °C. Purification by flash column chromatography (0% -> 50% EtOAc in pentane) yielded the title compound as a colourless oil (800 mg, 85%). **$^1$H NMR (400 MHz, $CDCl_3$**): δ 7.08 – 6.98 (m, 2H, $H_{4,6}$), 6.88 (s, 1H, NH), 6.80 – 6.72 (m, 2H, $H_{1,3}$), 4.16 (qt, *J* = 7.1, 3.6 Hz, 4H, $H_{13}$), 3.71 (s, 3H, $H_{15}$), 2.66 – 2.57 (m, 2H, $H_7$), 2.44 – 2.35 (m, 2H, $H_8$), 1.96 (s, 3H, $H_{11}$) ppm. **$^{13}$C NMR (101 MHz, $CDCl_3$):** δ 169.0 ($C_{10}$), 168.0 ($C_{12}$), 157.9 ($C_2$), 132.5 ($C_5$), 129.4 ($C_{4,6}$), 113.5 ($C_{1,3}$), 66.5 ($C_9$), 62.5 ($C_{13}$), 55.2 ($C_{15}$), 33.6 ($C_8$), 29.2 ($C_7$), 22.8 ($C_{11}$), 14.0 ($C_{14}$) ppm. **HRMS ESI$^+$:** m/z 374.1579 $[M+Na]^+$, *calc. m/z 374.1574.* **LRMS ESI$^+$:** m/z 725 (100%,

[2M+Na]$^+$), 352 (77%, [M+H]$^+$), 374 (8%, [M+Na]$^+$). **IR (film):** $\nu_{max}$ 3249 (N-H), 2980 (C-H), 1740 (C=O), 1643 (C=O), 1214 (C-O), 1034 (C-O), 827 (C-H) cm$^{-1}$.

**Diethyl 2-acetamido-2-(4-hydroxyphenethyl)malonate (88)**

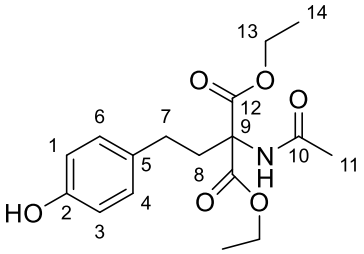


To a solution of **87** (680 mg, 1.9 mmol) in $CH_2Cl_2$ (10 mL) at −5 °C was added 1 M boron tribromide in $CH_2Cl_2$ (5.8 mmol) dropwise. The reaction was stirred at −5° C for 20 min, then warmed to rt for 18 h. The reaction was cooled in an ice bath, diluted with EtOAc (50 mL) and quenched with sat. aq. $NaHCO_3$ solution (20 mL). The organic layers were extracted and purified by reverse-phase flash column chromatography (0 -> 100% MeCN in 10 mM aq. $NH_4Ac$) yielded the title compound as a colourless oil (550 mg, 85%). **$^1$H NMR (400 MHz, $CDCl_3$)**: δ 6.97 (dd, *J* = 11.7, 8.5 Hz, 2H, $H_{4,6}$), 6.88 (s, 1H, NH), 6.75 (dd, *J* = 8.4, 6.0 Hz, 2H, $H_{1,3}$), 4.23 (qd, *J* = 7.2, 1.4 Hz, 4H, $H_{13}$), 2.72 – 2.63 (m, 2H, $H_7$), 2.44 – 2.34 (m, 2H, $H_8$), 2.00 (s, 3H, $H_{11}$), 1.25 (t, *J* = 7.2 Hz, 6H, $H_{14}$) ppm. **$^{13}$C NMR (101 MHz, $CDCl_3$):** δ 170.0 ($C_{11}$) 168.1 ($C_{12}$), 154.9 ($C_2$), 131.9 ($C_5$), 129.5 ($C_{4,6}$), 115.6 ($C_{1,3}$), 66.7 ($C_9$), 62.9 ($C_{13}$), 33.8 ($C_8$), 29.3 ($C_7$), 23.0 ($C_{11}$), 14.1 ($C_{14}$) ppm. **LRMS ESI$^+$:** m/z 338 (100%, [M+H]$^+$), 692 (82%, [2M+$NH_4$]$^+$), 675 (73%, [2M+H]$^+$), 697 (65%, [2M+Na]$^+$), 355 (40%, [M+$NH_4$]$^+$), 360 (29%, [M+Na]$^+$). **HRMS ESI$^+$:** m/z 338.1591 [M+H]$^+$, *calc. m/z 338.1598.* **IR (film):** $\nu_{max}$ 3317 (O-H), 1739 (C=O), 1637 (C=O), 1373 (O-H), 1070 (C-O), 773 (C-H) cm$^{-1}$.

**Diethyl 2-(4-(6-(1,3-dioxolan-2-yl)hex-1-yn-1-yl)phenethyl)-2-acetamidomalonate (84)**

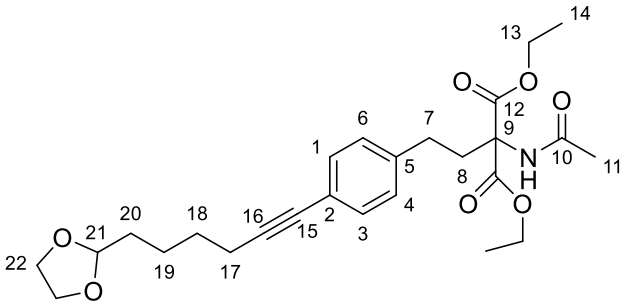


Following **General Procedure E, 90** was obtained from **86** (2.1 g, 5.3 mmol) and **71** (990 mg, 6.3 mmol). The reaction was stirred at 80 °C for 16 h. Purification by reverse-phase flash column chromatography (0% -> 100% MeCN in $H_2O$ + 0.1% formic acid) yielded the title compound as a yellow oil (260 mg, 10%). **$^1$H NMR (400 MHz, $CDCl_3$):** δ 7.28 (d, *J* = 8.2 Hz, 2H, $H_{1,3}$), 7.05 (d, *J* = 8.2 Hz, 2H, $H_{4,6}$), 6.75 (s, 1H, NH), 4.87 (t, *J* = 4.7 Hz, 1H, $H_{21}$), 4.27 – 4.12 (m, 4H, $H_{13}$), 3.99 – 3.92 (m, 2H, $H_{22'}$), 3.90 – 3.80 (m, 2H, $H_{22''}$), 2.71 – 2.62 (m, 2H, $H_7$), 2.49 – 2.43 (m, 2H, $H_8$), 2.40 (t, *J* = 6.9 Hz, 2H, $H_{17}$), 1.98 (s, 3H, $H_{11}$), 1.75 – 1.53 (m, 6H, $H_{18\text{-}20}$), 1.24 (t, *J* = 7.1 Hz, 6H, $H_{14}$) ppm. **$^{13}$C NMR (101 MHz, $CDCl_3$):** δ 169.3 ($C_{10}$), 168.1 ($C_{12}$), 140.2 ($C_5$), 131.7 ($C_{1,3}$), 128.5 ($C_{4,6}$), 121.9 ($C_2$), 104.7 ($C_{21}$), 89.8 ($C_{16}$), 80.7 ($C_{15}$), 66.5 ($C_{10}$), 65.0 ($C_{22}$), 62.8 ($C_{13}$), 33.6 ($C_{20}$), 33.3 ($C_8$), 30.2 ($C_7$), 28.8 ($C_{18}$), 23.6 ($C_{28}$), 23.1 ($C_{11}$), 19.5 ($C_{17}$), 14.1 ($C_{14}$) ppm. **LRMS ESI$^+$:** m/z 964 (100%, $[2M+NH_4]^+$), 491 (79%, $[M+NH_4]^+$), 474 (23%, $[M+H]^+$), 947 (23%, $[2M+H]^+$), 985 (8%, $[2M+K]^+$). **HRMS ESI$^+$:** m/z 474.2502 $[M+H]^+$ *calc. m/z 474.2486.* **IR (film):** $\nu_{max}$ 2981 (C-H), 2236 (C≡C), 1742 (C=O), 1211 (C-O), 1096 (C-O), 695 (C-H) $cm^{-1}$.

**_N_-(4-(4-(6-(1,3-Dioxolan-2-yl)hex-1-yn-1-yl)phenyl)-1-hydroxy-2-(hydroxymethyl)butan-2-yl) acetamide (91)**

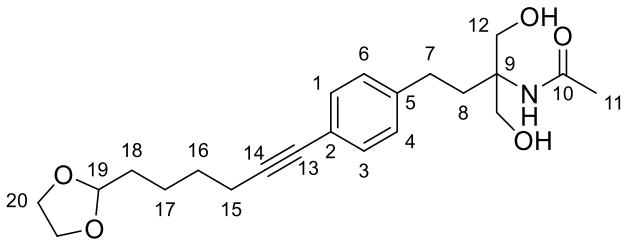


To a solution of **90** (220 mg, 0.47 mmol) in THF was added 60% RedAl in toluene (760 µL, 2.3 mmol). The reaction was stirred at 0 °C for 30 min. The reaction was diluted with $Et_2O$ (20 mL), and quenched with water (300 µL) and aq. 6 M NaOH (100 µL). After stirring for 15 min, $MgSO_4$ (500 mg) was added and stirred vigorously for another 15 min. The reaction mixture was filtered and the filtrate concentrated *in vacuo*. Purification by flash column chromatography (0% -> 10% MeOH in $CH_2Cl_2$) yielded the title compound as a colourless oil (30 mg, 16%). **$^1$H NMR (400 MHz, $CDCl_3$):** δ 7.35 (d, *J* = 8.1 Hz, 2H, $H_{1,3}$), 7.17 (d, *J* = 8.1 Hz, 2H, $H_{4,6}$), 4.87 (t, *J* = 4.7 Hz, 1H, $H_{19}$), 4.04 – 3.78 (m, 8H, $H_{12,20}$), 2.46 – 2.36 (m, 4H, $H_{7,15}$), 2.09 – 1.88 (m, 5H, $H_{8,11}$), 1.75 – 1.53 (m, 8H, $H_{16\text{-}18}$) ppm. **$^{13}$C NMR (101 MHz, $CDCl_3$):** δ 172.1 ($C_{10}$), 141.2 ($C_5$), 131.9 ($C_{1,3}$), 128.7 ($C_{4,6}$), 123.1 ($C_2$), 104.6 ($C_{19}$), 90.7 ($C_{14}$), 80.3 ($C_{13}$), 65.0 ($C_{12,20}$), 64.2 ($C_9$), 33.5 ($C_{18}$), 28.8 ($C_{16}$), 24.3 ($C_8$), 23.5 ($C_{11,17}$), 19.5 ($C_{7,15}$) ppm. **LRMS ESI$^+$:** m/z 412 (100%, $[M+Na]^+$), 428 (47%, $[M+K]^+$). **HRMS ESI$^+$:** m/z 390.2283 $[M+H]^+$ *calc. m/z 390.2275.* **IR (film):** $\nu_{max}$ 3330 (O-H), 2219 (C≡C), 1664 (C=O), 1016 (C-O), 764 (C-H) $cm^{-1}$.

**1-(4-Vinylphenyl)oct-7-yn-1-one (94)**

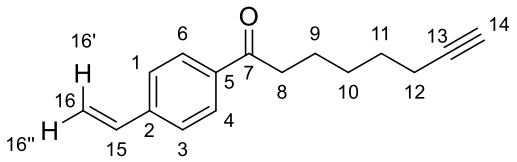


To a flame-dried MW vial under Ar was added magnesium turnings (400 mg, 19 mmol) and 2 small crystals of iodine (20 mg, 0.079 mmol). THF (3 mL) was added and the mixture was refluxed for 1 min and stirred at rt for 15 min. The activated magnesium was cooled to 0°C and 4-bromostyrene (1.0 mL, 7.7 mmol) was added dropwise over 30 min. The reaction was warmed to rt and stirred for 4 h. Then the Grignard reagent was cooled to 0 °C and **95** (1.6 g, 8.70 mmol) in THF (3 mL) was added dropwise. The reaction was warmed to rt and stirred for 18 h. The reaction was quenched with sat. aq. $NH_4Cl$ (10 mL), extracted with EtOAc (50 mL) and concentrated *in vacuo*. The crude material was purified by flash column chromatography (0 -> 10% EtOAc in pentane) to yield the title compound a colourless oil (350 mg, 20%). **$^1$H NMR (400 MHz, $CDCl_3$):** δ 7.91 (d, *J* = 8.2 Hz, 2H, $H_{4,6}$), 7.47 (d, *J* = 8.2 Hz, 2H, $H_{1,3}$), 6.75 (dd, *J* = 17.6, 10.9 Hz, 1H, $H_{15}$), 5.87 (d, *J* = 17.6 Hz, 1H, $H_{16'}$), 5.39 (d, *J* = 10.9 Hz, 1H, $H_{16''}$), 2.94 (t, *J* = 7.4 Hz, 2H, $H_8$), 2.21 (td, *J* = 6.9, 2.6 Hz, 2H, $H_{12}$), 2.02 (t, *J* = 2.6 Hz, 1H, $H_{14}$), 1.75 (*app* p, *J* = 7.4 Hz, 2H, $H_9$), 1.64 – 1.54 (m, 2H, $H_{11}$), 1.54 – 1.44 (m, 2H, $H_{10}$) ppm. **$^{13}$C NMR (101 MHz, $CDCl_3$):** δ 199.0 ($C_7$), 141.5 ($C_2$), 135.9 ($C_5$), 135.7 ($C_{15}$), 128.1 ($C_{4,6}$), 126.0 ($C_{1,3}$), 116.3 ($C_{16}$), 84.1 ($C_{13}$), 68.4 ($C_{14}$), 38.0 ($C_8$), 28.2 ($C_{10}$), 23.5 ($C_9$), 18.0 ($C_{12}$) ppm. **LRMS ESI$^+$:** m/z 249 ([M+Na]$^+$, 100%), 475 ([2M+Na]$^+$, 50%), 227 ([M+H]$^+$, 41%). **HRMS ESI$^+$:** m/z 249.1258 [M+Na]$^+$ *calc. m/z 249.1250.* **IR (film):** $\nu_{max}$ 2942 (C-H), 2116 (C≡C), 1672 (C=O), 1604 (C=C), 989 (C=C), 734 (C-H) cm$^{-1}$.

### *N*-Methoxy-*N*-methyloct-7-ynamide (95)

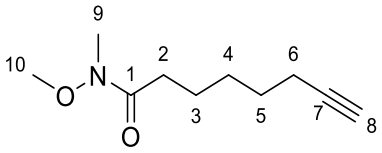


To a solution of **97** (1.4 g, 10 mmol) in $CH_2Cl_2$ (70 mL) at 0 °C was added *N*,*O*-dimethylhydroxylamine hydrochloride (1.2 g, 12 mmol), DMAP (cat.) and $Et_3N$ (1.7 mL, 12 mmol). Then EDC•HCl (2.3 g, 12 mmol) was added, and the reaction was stirred at rt for 16 h. The reaction was quenched with aq. 1 M HCl (10 mL), extracted and concentrated *in vacuo*. The crude material was purified by flash column chromatography (0 -> 25% EtOAc in pentane) to yield the title compound as a colourless oil (1.6 g, 87%). **$^1$H NMR (400 MHz, $CDCl_3$):** δ 3.63 (s, 3H, $H_{10}$), 3.13 (s, 3H, $H_9$), 2.38 (t, *J* = 7.6 Hz, 2H, $H_2$), 2.14 (td, *J* = 7.0, 2.6 Hz, 2H, $H_6$), 1.89 (t, *J* = 2.6 Hz, 1H, $H_8$), 1.60 (*app* p, *J* = 7.6 Hz, 2H, $H_3$), 1.56 – 1.47 (m, 2H, $H_5$), 1.47 – 1.34 (m, 2H, $H_4$) ppm. **$^{13}$C NMR (101 MHz, $CDCl_3$):** δ 176.8 ($C_1$), 84.5 ($C_7$), 68.2 ($C_8$), 61.2 ($C_9$), 33.8 ($C_{10}$), 31.7 ($C_2$), 28.5 ($C_4$), 28.3 ($C_5$), 24.1 ($C_3$), 18.3 ($C_6$) ppm. **LRMS ESI$^+$:** m/z 389 ([2M+Na]$^+$, 100%), 206 ([M+Na]$^+$, 62%), 184 ([M+H]$^+$, 58%). **HRMS ESI$^+$:** m/z 206.1151 [M+Na]$^+$ *calc. m/z 206.1152*. **IR (film):** $\nu_{max}$ 2940 (C-H), 2116 (C≡C), 1663 (C=O), 1463, 671 (C-H) cm$^{-1}$.

### Oct-7-ynoic acid (97)

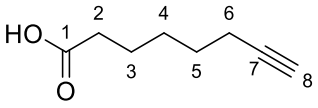

To a solution of 7-octyn-1-ol (2.0 g, 16 mmol) in acetone (16 mL) at 0 °C was added Jones reagent (7.6 mL, 19 mmol). The reaction was stirred at rt for 2 h. The reaction was quenched with water (20 mL), extracted with EtOAc/MeOH (3:1, 50 mL) and concentrated *in vacuo*. The crude material was purified by flash column chromatography (0 -> 100% EtOAc in pentane) to yield **97** as a colourless oil (1.7 g, 77%). **$^{1}$H NMR (400 MHz, $CDCl_3$):** δ 2.37 (t, *J* = 7.5 Hz, 2H, $H_2$), 2.20 (td, *J* = 6.9, 2.6 Hz, 2H, $H_6$), 1.94 (t, *J* = 2.6 Hz, 1H, $H_8$), 1.66 (p, *J* = 7.5 Hz, 2H, $H_3$), 1.61 – 1.52 (m, 2H, $H_5$), 1.51 – 1.41 (m, 2H, $H_4$) ppm. **$^{13}$C NMR (101 MHz, $CDCl_3$):** δ 220.7 ($C_1$), 84.4 ($C_7$), 68.5 ($C_8$), 34.0, 28.2, 28.2, 24.3, 18.4 ppm. **HRMS ESI$^-$:** m/z 139.0764 $[M-H]^-$ *calc. m/z 139.0764.* This data was consistent with literature characterisation.[444]

## *N*-(4-Vinylphenyl)hept-6-ynamide (99)

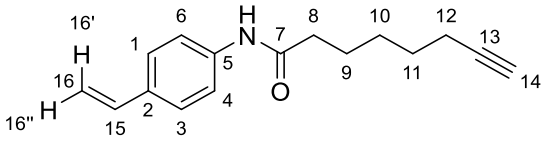


To a flame-dried MW vial under $N_2$ was added **94** (200 mg, 0.66 mmol), benzylamine (220 mg, 2.1 mmol) and $ZnCl_2$ (5.0 mg, 5 mol%) in degassed toluene (2 mL). The reaction was refluxed for 18 h. The reaction was cooled to rt, washed with water (5 mL), extracted with $Et_2O$ (20 mL) and concentrated *in vacuo*. The crude material was transferred to a flame-dried flask under $N_2$, redissolved in MeOH (2 mL) and cooled to −20 °C. $NH_3$ was condensed into the flask until saturated and HOSA (170 mg, 1.5 mmol) in MeOH (1 mL) was added. The reaction was stirred at −20 °C for 3 h and then at rt overnight. The reaction was filtered, washed with MeOH (10 mL), concentrated *in vacuo*. The crude material was purified by

flash column chromatography (2 -> 100% MeCN in 10mM $NH_4OAc$ aq.) to yield **99** as a colourless solid (95 mg, 60%). **$^1$H NMR (400 MHz, $CDCl_3$):** δ 8.92 (s, 1H, NH), 7.57 (d, *J* = 8.3 Hz, 2H, $H_{4,6}$), 7.42 (d, *J* = 8.5 Hz, 2H, $H_{1,3}$), 6.73 (dd, *J* = 17.5, 10.9 Hz, 1H, $H_{15}$), 5.79 (d, *J* = 17.5 Hz, 1H, $H_{16'}$), 5.29 (d, *J* = 10.9 Hz, 1H, $H_{16''}$), 2.81 (t, *J* = 7.7 Hz, 2H, $H_8$), 2.18 (td, *J* = 6.7, 2.6 Hz, 2H, $H_{12}$), 1.93 (t, *J* = 2.6 Hz, 1H, $H_{14}$), 1.65 – 1.43 (m, 4H, $H_{9,11}$), 1.37 – 1.18 (m, 2H, $H_{10}$) ppm. **$^{13}$C NMR (101 MHz, $CDCl_3$):** δ 159.5 ($C_7$), 138.6 ($C_5$), 136.4 ($C_{15}$), 135.1 ($C_2$) 126.6 ($C_{4,6}$) 126.5 ($C_{1,3}$), 114.8 ($C_{16}$), 84.6 ($C_{13}$), 68.4 ($C_{14}$), 29.0 ($C_8$), 28.3 ($C_{11}$), 26.0 ($C_{10}$), 18.4 ($C_9$), 14.2 ($C_{12}$) ppm. **LRMS ESI$^+$:** m/z 242 (100%, $[M+H]^+$), 505 (64%, $[2M+Na]^+$), 280 (38%, $[M+K]^+$), 521 (13%, $[2M+K]^+$). **IR (film):** $\nu_{max}$ 3304 (N-H), 2938 (C-H), 1629 (C=O), 1606 (C=C), 1512 (N-H), 737 (C-H) $cm^{-1}$.

**1-(4-(3-Amino-4-hydroxy-3-(hydroxymethyl)butyl)phenyl)hept-6-yn-2-one (101)**

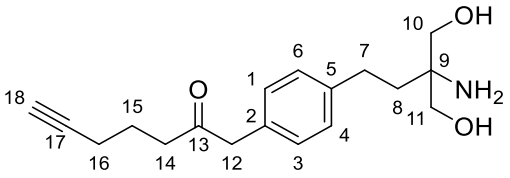


**110** (30 mg, 0.14 mmol), serinol (13 mg, 0.15 mmol), $[NBu_4][N_3]$ (4.0 mg, 20 mol%), 3DPA2FBN (1.0 mg, 1 mol%) in degassed DMF (950 μL) were stirred and irradiated at 427 nm at rt overnight. The crude reaction was concentrated *in vacuo* and purified by reverse-phase flash column chromatography (0 -> 100% MeCN in 10 mM $NH_4OAc$) to yield **101** (19 mg, 45%) as a colourless oil. **$^1$H NMR (400 MHz, MeOD):** δ 7.21 (d, *J* = 7.9 Hz, 2H, $H_{1,3}$), 7.14 (d, *J* = 7.9 Hz, 2H, $H_{4,6}$), 3.79 – 3.60 (m, 6H, $H_{10\text{-}12}$), 2.70 – 2.60 (m, 4H, $H_{7,14}$), 2.20 (t, *J* = 2.7 Hz, 1H, $H_{18}$), 2.14 (td, *J* = 6.9, 2.7 Hz, 2H, $H_{16}$), 1.98 – 1.94 (m, 2H, $H_8$), 1.71 (*app* p, *J* = 7.0 Hz, 2H, $H_{15}$) ppm. **$^{13}$C NMR (101 MHz, MeOD):** δ 210.7 ($C_{13}$) 141.2 ($C_5$), 131.8 ($C_2$), 130.8 ($C_{4,6}$), 129.6

($C_{1,3}$), 84.2 ($C_{17}$), 70.2 ($C_{18}$), 61.9 ($C_{10\text{-}11}$), 61.6 ($C_9$), 50.3 ($C_{12}$), 41.4 ($C_{14}$), 34.7 ($C_8$), 29.7 ($C_7$), 23.7 ($C_{15}$), 20.9 ($C_{16}$) ppm. **LRMS ESI$^+$:** m/z 342 (100%, $[M+Na]^+$), 304 (76%, $[M+H]^+$), 607 (55%, $[2M+H]^+$), 629 (41%, $[2M+Na]^+$). **HRMS ESI$^+$:** m/z 304.1917 $[M+H]^+$ *calc. m/z 304.1907.* **IR (film):** $\nu_{max}$ 3266 (O-H), 2937 (C-H), 2116 (C≡C), 1728 (C=O), 1061 (C-O), 706 (C-H) $cm^{-1}$.

## *N*-Methoxy-*N*-methylhept-6-ynamide (102)

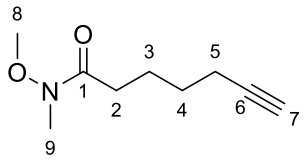


To a solution of 6-heptynoic acid (500 mg, 4.0 mmol) in $CH_2Cl_2$ (12 mL) at 0 °C was added *N*,*O*-dimethylhydroxylamine hydrochloride (420 mg, 4.4 mmol), DMAP (cat.) and $Et_3N$ (610 μL, 4.4 mmol). Then EDC•HCl (840 mg, 4.4 mmol) was added, and the reaction was stirred at rt for 16 h. The reaction was quenched with aq. 1 M HCl (10 mL), extracted with $CH_2Cl_2$ (50 mL) and concentrated *in vacuo*. The crude material was purified by flash column chromatography (0 -> 25% EtOAc in pentane) to yield the title compound as a colourless oil (130 mg, 19%). **$^1$H NMR (400 MHz, $CDCl_3$):** δ 3.68 (s, 3H, $H_8$), 3.18 (s, 3H, $H_9$), 2.45 (t, *J* = 7.4 Hz, 2H, $H_2$), 2.22 (td, *J* = 7.1, 2.7 Hz, 2H, $H_5$), 1.93 (t, *J* = 2.7 Hz, 1H, $H_7$), 1.77 (dd, *J* = 8.3, 7.4 Hz, 2H, $H_3$), 1.60 (dd, *J* = 8.3, 7.1 Hz, 2H, $H_4$) ppm. **$^{13}$C NMR (101 MHz, $CDCl_3$):** δ 171.4 ($C_1$), 84.4 ($C_6$), 68.7 ($C_7$), 61.5 ($C_8$), 60.6 ($C_9$), 28.4 ($C_2$), 24.0 ($C_4$), 18.5 ($C_3$), 14.4 ($C_5$) ppm. **LRMS ESI$^+$:** m/z 190 ($[M+H]^+$, 97%), 192 ($[M+Na]^+$, 11%), 138 ($[M-{}^\bullet OCH_3]^{+\bullet}$, 9%), 110 ($[M-{}^\bullet NCH_3OCH_3+H]^{+\bullet}$, 16%). **HRMS ESI$^+$:** m/z 192.1001 $[M+Na]^+$ *calc. m/z 192.0995.* **IR (film):** $\nu_{max}$ 2941 (C-H), 2116 (C≡C), 1656 (C=O), 1419, 661 (C-H) $cm^{-1}$.

**1-(Bromomethyl)-4-vinylbenzene (103)**

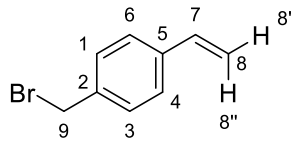


To a solution of (4-vinylphenyl)methanol (500 mg, 3.7 mmol) in $Et_2O$ (30 mL) at 0 °C under $N_2$ was added 1 M $PBr_3$ in $CH_2Cl_2$ (7.5 mmol) dropwise. The reaction was stirred at 0 °C for 1 h before an extra addition of 1 M $PBr_3$ in $CH_2Cl_2$ (7.5 mmol). The reaction was then stirred at rt overnight. The reaction was cooled with an ice bath, quenched with water (10 mL), extracted with $Et_2O$ (50 mL) and concentrated *in vacuo*. The crude material was purified by flash column chromatography (0 -> 30% EtOAc in pentane) to yield **103** (470 mg, 81%) as a colourless oil. **$^1$H NMR (400 MHz, $CDCl_3$):** δ 7.39 (*app* q, *J* = 8.4 Hz, 4H, $H_{1,3,4,6}$), 6.74 (dd, *J* = 17.6, 10.9 Hz, 1H, $H_7$), 5.80 (d, *J* = 17.6 Hz, 1H, $H_{8''}$), 5.31 (d, *J* = 10.9 Hz, 1H, $H_{8'}$), 4.51 (s, 2H, $H_9$) ppm. **$^{13}$C NMR (101 MHz, $CDCl_3$):** δ 137.8 ($C_2$), 137.3 ($C_5$), 136.2 ($C_7$), 129.4 ($C_{1,3}$), 126.7 ($C_{4,6}$), 114.7 ($C_8$), 33.6 ($C_9$) ppm. **HRMS EI$^+$:** m/z 195.98876 $[M+]^+$ *calc. m/z 195.98821.* This data was consistent with literature characterisation.[445]

**(6-Chlorohex-1-yn-1-yl)trimethylsilane (105)**

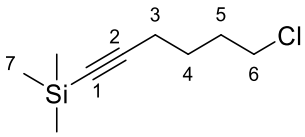


To a solution of 6-chloro-1-hexyne (500 mg, 4.3 mmol) in $Et_2O$ (9 mL) at −78 °C was added 1.6 M *n*BuLi in hexanes (4.7 mmol) dropwise. The reaction was stirred for 1 h before adding TMSCl (600 μL, 4.7 mmol). The reaction was allowed to warm to rt overnight. The reaction was quenched with water (10 mL), extracted with EtOAc (50 mL) and concentrated *in vacuo*.

The crude material was purified by flash column chromatography (0 -> 10% EtOAc in pentane) to yield the title compound as a colourless oil (750 mg, 93%). **$^1$H NMR (400 MHz, $CDCl_3$):** δ 3.57 (t, *J* = 6.6 Hz, 2H, $H_6$), 2.27 (t, *J* = 7.0 Hz, 2H, $H_3$), 1.95 – 1.81 (m, 2H, $H_5$), 1.73 – 1.63 (m, 2H, $H_4$), 0.15 (s, 9H, $H_7$) ppm. **$^{13}$C NMR (101 MHz, $CDCl_3$):** δ 106.7 ($C_2$), 85.4 ($C_1$), 44.8 ($C_6$), 31.8 ($C_5$), 26.0 ($C_4$), 19.4 ($C_3$), 0.4 ($C_7$) ppm. **IR (film):** $\nu_{max}$ 2959 (C-H), 2175 (C≡C), 1250 (C-Si), 844 (C-Si), 760 (C-Cl) $cm^{-1}$. This data was consistent with literature characterisation.[446]

## Methyl 2-(4-vinylphenyl)acetate (106)

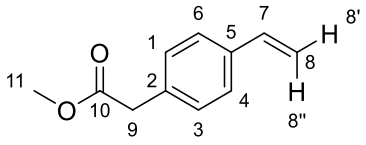


To a flame-dried MW vial purged with $N_2$ was added methyl 4-bromophenylacetate (1.0 g, 4.4 mmol), potassium vinyltrifluoroborate (600 mg, 4.5 mmol), $Cs_2CO_3$ (4.3 mg, 13 mmol) and Pd(dppf)$Cl_2$•$CH_2Cl_2$ (180 mg, 0.22 mmol). Degassed THF/$H_2O$ (9:1, 9 mL) was added and the reaction was stirred at 85 °C overnight. The mixture was then cooled, filtered over celite and washed with $Et_2O$ (50 mL). The organic layer was concentrated *in vacuo* and purified by flash column chromatography (0 -> 10% EtOAc in pentane) to yield **106** (460 mg, 59%) as a colourless oil. **$^1$H NMR (400 MHz, $CDCl_3$):** δ 7.40 – 7.33 (m, 2H, $H_{4,6}$), 7.24 (d, *J* = 8.2 Hz, 2H, $H_{1,3}$), 6.70 (dd, *J* = 17.6, 10.9 Hz, 1H, $H_7$), 5.73 (d, *J* = 17.6 Hz, 1H, $H_{8''}$), 5.24 (d, *J* = 10.9 Hz, 1H, $H_{8'}$), 3.69 (s, 3H, $H_{11}$), 3.62 (s, 2H, $H_9$) ppm. **$^{13}$C NMR (101 MHz, $CDCl_3$):** δ 172.1 ($C_{10}$), 136.7 ($C_7$), 136.5 ($C_5$), 133.6 ($C_2$), 129.6 ($C_{1,3}$), 126.6 ($C_{4,6}$), 114.0 ($C_8$), 52.2 ($C_{11}$), 41.1

($C_9$) ppm. **HRMS ESI$^+$:** m/z 177.0912 $[M+H]^+$ *calc. m/z 177.0910.* This data was consistent with literature characterisation.[447]

### *N*-Methoxy-*N*-methyl-2-(4-vinylphenyl)acetamide (107)

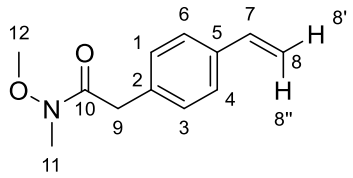


To a solution of **106** (480 mg, 2.7 mmol) in MeOH:2-Me THF (2:1, 8 mL) was added 1M LiOH (11 mL). The reaction was stirred at 50 °C for 1 h. The reaction crude was acidified with 1 M HCl, extracted in EtOAc (50 mL) and concentrated *in vacuo*. The crude material was redissolved in $CH_2Cl_2$ (8 mL). $Et_3N$ (800 μL, 5.5 mmol) and HATU (1.2 g, 3.3 mmol) were added and the reaction was stirred for 15 min before addition of NHMeOMe•HCl (320 mg, 3.3 mmol). The reaction was stirred at rt for 3 h. The reaction was washed with water (10 mL), extracted with $CH_2Cl_2$ (50 mL) and concentrated *in vacuo.* The crude material was purified by flash column chromatography (0 -> 30% EtOAc in pentane) to yield **107** (470 mg, 81%) as a colourless oil. **$^1$H NMR (400 MHz, $CDCl_3$):** δ 7.36 – 7.28 (m, 2H, $H_{4,6}$), 7.25 – 7.17 (m, 2H, $H_{1,3}$), 6.65 (dd, *J* = 17.6, 10.9 Hz, 1H, $H_7$), 5.68 (d, *J* = 17.6 Hz, 1H, $H_{8''}$), 5.18 (d, *J* = 11.0 Hz, 1H, $H_{8'}$), 3.72 (s, 2H, $H_9$), 3.56 (s, 3H, $H_{12}$), 3.14 (s, 3H, $H_{11}$) ppm. **$^{13}$C NMR (101 MHz, $CDCl_3$):** δ 172.3 ($C_{10}$), 136.5 ($C_7$), 136.2 ($C_5$), 134.6 ($C_2$), 129.5 ($C_{1,3}$), 126.4 ($C_{4,6}$), 113.6 ($C_8$), 61.3 ($C_{12}$), 39.2 ($C_9$), 32.3 ($C_{11}$) ppm. **LRMS ESI$^+$:** m/z 115 (100%, $[M+H+Na]^{2+}$), 228 (63%, $[M+Na]^+$), 206 (54%, $[M+H]^+$), 433 (54%, $[2M+Na]^+$). **HRMS ESI$^+$:** m/z 206.1174 $[M+H]^+$ *calc. m/z 206.1176.* **IR (film):** $\nu_{max}$ 2938 (C-H), 1666 (C=O), 1181 (C-N), 1002 (C-O), 728 (C-H) $cm^{-1}$.

**7-(Trimethylsilyl)-1-(4-vinylphenyl)ept-6-yn-2-one (109)**

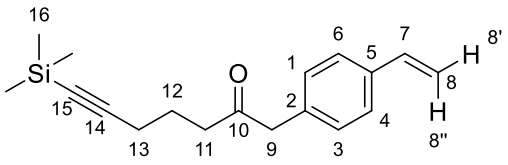


A flame-dried MW vial purged with $N_2$ was charged with etched Mg turnings (200 mg, 7.8 mmol), $I_2$ (3 balls, cat.), 1,2-dibromoethane (a few drops) and degassed THF (3 mL). The reaction was stirred at rt for 15 min before a couple drops of (5-chloro-1-pentynyl)trimethylsilane were added. The reaction was heated to reflux and the remaining (5-chloro-1-pentynyl)trimethylsilane (720 μL, 3.9 mmol) in THF (1 mL) was added dropwise over 30 min. The reaction was stirred at reflux for 3 h, then cooled to −78 °C before the addition of **107** (200 mg, 0.98 mmol) in THF dropwise. The reaction was allowed to warm to rt slowly and was stirred at rt overnight. The reaction was cooled with an ice bath, quenched with sat. aq. $NH_4Cl$ (10 mL) solution, extracted with $Et_2O$ (50 mL) and concentrated *in vacuo*. The crude material was purified by reverse-phase flash column chromatography (2 -> 100% MeCN in 10 mM $NH_4OAc$ aq.) to yield **109** (90 mg, 32%) as a colourless oil. **$^1$H NMR (400 MHz, $CDCl_3$):** δ 7.36 (d, *J* = 8.0 Hz, 2H, $H_{4,6}$), 7.17 (d, *J* = 8.0 Hz, 2H, $H_{1,3}$), 6.70 (dd, *J* = 17.6, 10.9 Hz, 1H, $H_7$), 5.73 (d, *J* = 17.6 Hz, 1H, $H_{8''}$), 5.23 (d, *J* = 10.8 Hz, 1H, $H_{8'}$), 3.68 (s, 2H, $H_9$), 2.58 (t, *J* = 7.2 Hz, 2H, $H_{11}$), 2.20 (t, *J* = 7.0 Hz, 2H, $H_{13}$), 1.75 (*app* p, *J* = 7.2, 7.0 Hz, 2H, $H_{12}$), 0.13 (s, 9H, $H_{16}$) ppm. **$^{13}$C NMR (101 MHz, $CDCl_3$):** δ 207.9 ($C_{10}$), 136.6 ($C_5$), 136.5 ($C_7$), 133.9 ($C_2$), 129.7 ($C_{1,3}$), 126.8 ($C_{4,6}$), 114.0 ($C_8$), 106.4 ($C_{14}$), 85.6 ($C_{15}$), 50.2 ($C_9$), 40.5 ($C_{11}$), 22.5 ($C_{13}$), 19.2 ($C_{12}$), 0.3 ($C_{16}$) ppm. **LRMS ESI$^+$:** m/z 591 (100%, $[2M+Na]^+$), 307 (89%, $[M+Na]^+$), 285 (74%, $[M+H]^+$). **HRMS ESI$^+$:** m/z 285.1672 $[M+H]^+$ *calc. m/z 285.1669.* **IR (film):** $\nu_{max}$ 2958 (C-H), 2174 (C≡C), 1714 (C=O), 1249 (C-Si), 843 (C-H) $cm^{-1}$.

**1-(4-Vinylphenyl)hept-6-yn-2-one (110)**

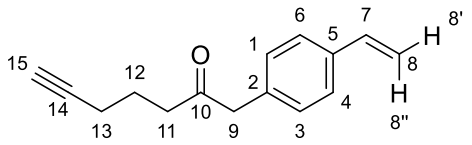


**109** (90 mg, 0.32 mmol) and $K_2CO_3$ (44 mg, 0.64 mmol) in MeOH (2 mL) were stirred at rt overnight. The crude reaction was concentrated *in vacuo* and purified by flash column chromatography (0 -> 10% $Et_2O$ in pentane) to yield **110** (30 mg, 48%) as a colourless oil. **$^1$H NMR (400 MHz, $CDCl_3$):** δ 7.37 (d, *J* = 8.1 Hz, 2H, $H_{4,6}$), 7.17 (d, *J* = 8.1 Hz, 2H, $H_{1,3}$), 6.70 (dd, *J* = 17.6, 10.8 Hz, 1H, $H_7$), 5.73 (d, *J* = 17.6 Hz, 1H, $H_{8''}$), 5.25 (d, *J* = 10.8 Hz, 1H, $H_{8'}$), 3.68 (s, 2H, $H_9$), 2.60 (t, *J* = 7.2 Hz, 2H, $H_{11}$), 2.19 (td, *J* = 6.9, 2.6 Hz, 2H, $H_{13}$), 1.93 (t, *J* = 2.6 Hz, 1H, $H_{15}$), 1.76 (*app* p, *J* = 7.0 Hz, 2H, $H_{12}$) ppm. **$^{13}$C NMR (101 MHz, $CDCl_3$):** δ 207.7 ($C_{10}$), 136.6 ($C_5$), 136.5 ($C_7$), 133.8 ($C_2$), 129.7 ($C_{1,3}$), 126.7 ($C_{4,6}$), 114.0 ($C_8$), 83.6 ($C_{14}$), 69.2 ($C_{15}$), 50.1 ($C_9$), 40.5 ($C_{11}$), 22.3 ($C_{13}$), 17.8 ($C_{12}$) ppm. **LRMS ESI$^+$:** m/z 235 (100%, $[M+Na]^+$), 213 (34%, $[M+H]^+$). **HRMS ESI$^+$:** m/z 235.1094 $[M+Na]^+$ *calc. m/z 235.1093.* **IR (film):** $\nu_{max}$ 2944 (C-H), 2116 (C≡C), 1715 (C=O), 987 (C=C), 757 (C-H) $cm^{-1}$.

**2-Amino-2-(4-(2-(3-(but-3-yn-1-yl)-3H-diazirin-3-yl)ethoxy)phenethyl)propane-1,3-diol – Photoaffinity labelling probe 114**

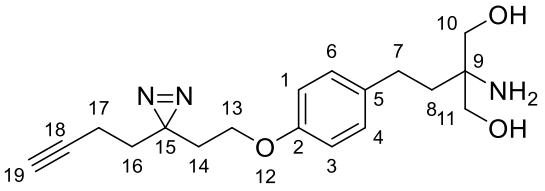

To a solution of **120** (50 mg, 0.24 mmol) and $K_2CO_3$ (66 mg, 0.48 mmol) in DMF (500 μL) was added 3-(but-3-yn-1-yl)-3-(2-iodoethyl)-3H-diazirine (60 mg, 0.24 mmol) in DMF (500 μL) dropwise. The reaction was stirred in the dark at 40 °C for 20 h. The crude reaction was cooled down, concentrated *in vacuo* and purified by reverse-phase flash column chromatography (0 -> 100% MeCN in 10 mM $NH_4OAc$) to yield **5** (1.3 mg, 2 %) as a colourless solid. **$^1$H NMR (400 MHz, $CDCl_3$):** δ 7.15 (d, *J* = 8.6 Hz, 2H, $H_{4,6}$), 6.84 (d, *J* = 8.6 Hz, 2H, $H_{1,3}$), 3.82 (t, *J* = 6.0 Hz, 2H, $H_{13}$), 3.70 – 3.63 (m, 4H, $H_{10,11}$), 2.65 – 2.57 (m, 2H, $H_7$), 2.26 (t, *J* = 2.7 Hz, 1H, $H_{19}$), 2.07 (td, *J* = 7.5, 2.7 Hz, 2H, $H_{17}$), 1.91 – 1.89 (m, 2H, $H_8$), 1.85 (t, *J* = 6.0 Hz, 2H, $H_{14}$), 1.68 (t, *J* = 7.5 Hz, 2H, $H_{16}$) ppm. **$^{13}$C NMR (101 MHz, $CDCl_3$):** δ 158.5 ($C_2$), 134.9 ($C_5$), 130.3 ($C_{4,6}$), 115.7 ($C_{1,3}$), 83.7 ($C_{18}$), 70.2 ($C_{19}$), 63.8 ($C_{13}$), 62.8 ($C_{10,11}$), 61.7 ($C_9$), 35.1 ($C_8$), 33.9 ($C_{14}$), 33.8 ($C_{16}$), 29.2 ($C_7$), 27.8 ($C_{15}$), 13.9 ($C_{17}$) ppm. **LRMS ESI$^+$:** m/z 685 (100%, $[2M+Na]^+$), 354 (69%, $[M+Na]^+$), 332 (9%, $[M+H]^+$). **HRMS ESI$^+$:** m/z 332.1957 $[M+H]^+$ *calc. m/z 332.1969.* **IR (film):** $\nu_{max}$ 3366 (N-H), 1566 (N=N), 1410 (O-H), 1017 (C-O), 658 (C-H) $cm^{-1}$.

## 2-Amino-2-(4-bromophenethyl)propane-1,3-diol (116)

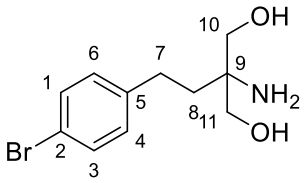


4-Bromo styrene (310 mg, 1.7 mmol), serinol (150 mg, 1.7 mmol), $[NBu_4][N_3]$ (50 mg, 20 mol%), 3DPA2FBN (10 mg, 1 mol%) and degassed DMF (11 mL) were stirred and irradiated at 427 nm at rt overnight. The crude reaction was concentrated *in vacuo* and purified by

reverse-phase flash column chromatography (0 -> 100% MeCN in 10 mM $NH_4OAc$) to yield **116** (400 mg, 86%) as a colourless oil. **$^1$H NMR (400 MHz, MeOD):** δ 7.42 (d, *J* = 8.4 Hz, 2H, $H_{1,3}$), 7.16 (d, *J* = 8.4 Hz, 2H, $H_{4,6}$), 3.68 – 3.58 (m, 4H, $H_{10}$), 2.72 – 2.58 (m, 2H, $H_7$), 1.88 – 1.81 (m, 2H, $H_8$) ppm. **$^{13}$C NMR (101 MHz, MeOD):** δ 142.2 ($C_5$), 132.6 ($C_{1,3}$), 131.3 ($C_{4,6}$), 120.7 ($C_2$), 63.6 ($C_{10}$), 60.5 ($C_9$), 35.3 ($C_8$), 29.6 ($C_7$) ppm. **LRMS ESI$^+$:** m/z 274 (100%, $[M+H]^+$), 571 (46%, $[2M+Na]^+$), 298 (40%, $[M+Na]^+$). **HRMS ESI$^+$:** m/z 274.0431 $[M+H]^+$ *calc. m/z 274.0437.* **IR (film):** $\nu_{max}$ 3284 (O-H), 2934 (C-H), 1558 (N-H), 1070 (C-O), 1012 (C-N), 656 (C-Br) $cm^{-1}$.

### 3-(But-3-yn-1-yl)-3-(2-(4-vinylphenoxy)ethyl)-3H-diazirine (117)

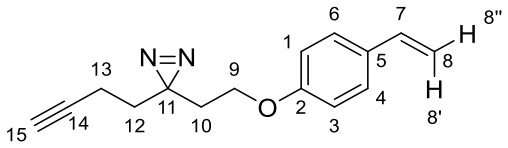


To a solution of 4-(vinyl)phenol (15 mg, 0.12 mmol) and $K_2CO_3$ (33 mg, 0.24 mmol) in DMF (500 μL) was added 3-(but-3-yn-1-yl)-3-(2-iodoethyl)-3H-diazirine (30 mg, 0.12 mmol) in DMF (500 μL) dropwise. The reaction was stirred in the dark at 40 °C for 20 h. The crude reaction was concentrated *in vacuo* and purified by reverse-phase flash column chromatography (0 -> 100% MeCN in 10 mM $NH_4OAc$) to yield **117** (10 mg, 35%) as a colourless oil. **$^1$H NMR (400 MHz, MeOD):** δ 7.35 (d, *J* = 8.8 Hz, 2H, $H_{4,6}$), 6.87 (d, *J* = 8.8 Hz, 2H, $H_{1,3}$), 6.66 (dd, *J* = 17.6, 10.9 Hz, 1H, $H_7$), 5.62 (dd, *J* = 17.6, 1.0 Hz, 1H, $H_{8'}$), 5.09 (dd, *J* = 10.9, 1.1 Hz, 1H, $H_{8''}$), 3.85 (t, *J* = 6.1 Hz, 2H, $H_9$), 2.26 (t, *J* = 2.7 Hz, 1H, $H_{15}$), 2.07 (td, *J* = 7.5, 2.7 Hz, 2H, $H_{13}$), 1.87 (t, *J* = 6.1 Hz, 2H, $H_{10}$), 1.69 (t, *J* = 7.5 Hz, 2H, $H_{12}$) ppm. **$^{13}$C NMR (101 MHz, MeOD):** δ δ 159.8 ($C_2$), 137.6 ($C_7$), 132.1 ($C_5$), 128.4 ($C_{4,6}$), 115.6 ($C_{1,3}$), 111.8 ($C_8$), 83.7

($C_{14}$), 70.3 ($C_{15}$), 63.8 ($C_9$), 33.9 ($C_{10}$), 33.8 ($C_{12}$), 27.8 ($C_{11}$), 13.8 ($C_{13}$) ppm. **IR (film):** $\nu_{max}$ 2919 (C-H), 2091 (C≡C), 1607 (C=C), 1042 (C-O), 642 (C-H) $cm^{-1}$.

**2-Amino-2-(4-hydroxyphenethyl)propane-1,3-diol (120)**

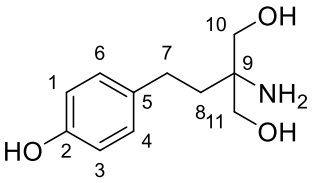


(4-Vinylphenyl)boronic acid pinacol ester (150 mg, 0.65 mmol), serinol (59 mg, 0.65 mmol), [$NBu_4$][$N_3$] (50 mg, 20 mol%), 3DPA2FBN (5.5 mg, 1 mol%) and degassed DMF (4.3 mL) were stirred and irradiated at 427 nm at rt overnight. The crude reaction was concentrated *in vacuo*, redissolved in THF:1 M NaOH (1:1, 25 mL) and 30% w/w $H_2O_2$ (480 μL, 4.80 mmol) was added at 0 °C. The reaction was stirred at rt for 1 h, quenched with sat. aq. $Na_2SO_3$ (10 mL), extracted with EtOAc:THF (2:1, 3 x 150 mL), concentrated *in vacuo* and purified by reverse-phase flash column chromatography (0 -> 100% MeCN in 10 mM $NH_4OAc$) to yield **120** (100 mg, 73%) as a colourless oil. **$^1$H NMR (400 MHz, MeOD):** δ 7.04 (d, *J* = 8.5 Hz, 2H, $H_{4,6}$), 6.70 (d, *J* = 8.5 Hz, 2H, $H_{1,3}$), 3.76 – 3.62 (m, 4H, $H_{10}$), 2.64 – 2.52 (m, 2H, $H_7$), 1.89 – 1.85 (m, 2H, $H_8$) ppm. **$^{13}$C NMR (101 MHz, MeOD):** δ 156.8 ($C_2$), 133.3 ($C_5$), 130.2 ($C_{4,6}$), 116.3 ($C_{1,3}$), 62.8 ($C_{10}$), 61.7 ($C_9$), 35.2 ($C_8$), 29.2 ($C_7$) ppm. **LRMS ESI$^+$:** m/z 234 (100%, $[M+Na]^+$), 445 (54%, $[2M+Na]^+$). **HRMS ESI$^+$:** m/z 212.1278 $[M+H]^+$ *calc. m/z 212.1281.* **IR (film):** $\nu_{max}$ 3120 (O-H), 3096 (N-H), 1555 (N-H), 1410 (O-H), 1066 (C-O), 656 (C-H) $cm^{-1}$.

**2-Bromo-1-(p-tolyl)ethan-1-one (123)**

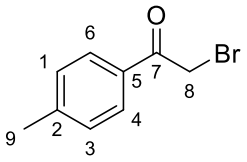


Following **General Procedure A, 123** was obtained from toluene (30 mL) and 2-bromoacetylchloride (1.0 mL, 13 mmol). Purification by re-crystallisation in pentane yielded the title compound as colourless crystals (2.09 g, 79%). **$^{1}$H NMR (400 MHz, $CDCl_3$):** δ 7.88 (d, *J* = 8.1 Hz, 2H, $H_{4,6}$), 7.28 (d, *J* = 8.1 Hz, 2H, $H_{1,3}$), 4.43 (s, 2H, $H_8$), 2.43 (s, 3H, $H_9$) ppm. **$^{13}$C NMR (101 MHz, $CDCl_3$):** δ 191.1 ($C_7$), 145.2 ($C_2$), 131.6 ($C_5$), 129.7 ($C_{4,6}$), 129.2 ($C_{1,3}$), 31.0 ($C_8$), 21.9 ($C_9$) ppm. **HMRS ESI$^+$:** m/z 212.9905 $[M+H]^+$ *calc m/z 212.9910.* This data was consistent with literature characterisation.[448]

**2-Bromo-1-(4-butylphenyl)ethan-1-one (124)**

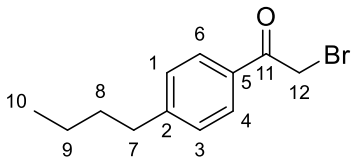


Following **General Procedure A, 124** was obtained from *n*-butyl benzene (1.0 mL, 6.4 mmol) and 2-bromoacetylchloride (1.4 mL, 8.9 mmol). Purification by flash column chromatography (0% -> 20% EtOAc in pentane) yielded the title compound as a brown oil (1.6 g, 96%). **$^{1}$H NMR (400 MHz, $CDCl_3$):** δ 7.90 (d, *J* = 8.3 Hz, 2H, $H_{1,3}$), 7.29 (d, *J* = 8.3 Hz, 2H, $H_{4,6}$), 4.43 (s, 3H, $H_{12}$), 2.71-2.63 (m, 2H, $H_7$), 1.67-1.55 (m, 2H, $H_8$), 1.41-1.29 (m, 2H, $H_9$), 0.93 (t, *J* = 7.3 Hz, 3H, $H_{10}$) ppm. **$^{13}$C NMR (101 MHz, $CDCl_3$):** δ 191.1 ($C_{11}$), 150.1 ($C_2$), 131.8 ($C_5$), 129.2 ($C_{4,6}$), 129.1 ($C_{1,3}$), 35.9 ($C_7$), 33.3 ($C_{12}$), 31.1 ($C_8$), 22.5 ($C_9$), 14.0 ($C_{10}$) ppm. **HRMS**

**ESI⁺:** m/z 255.0367 $[M+H]^+$ *calc m/z 255.0379.* **IR (film):** $\nu_{max}$ 2957 (C-H), 1680 (C=O), 1605 ($C=C_{arom}$), 845 ($C=C_{arom}$), 690 (C-H), 631 (C-Br) $cm^{-1}$. This data was consistent with literature characterisation.[449]

### 1-(2-Bromoethyl)-4-methylbenzene (125)

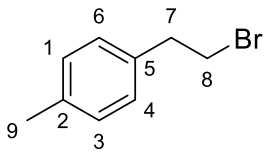


Following **General Procedure B, 125** was obtained from **123** (2.0 g, 9.4 mmol). Purification by flash column chromatography (0% -> 30% EtOAc in pentane) yielded the title compound as a colourless oil (1.6 g, 87%). **$^1$H NMR (400 MHz, $CDCl_3$):** δ 7.10-7.02 (m, 4H, $H_{1,3,4,6}$), 3.49 (t, *J* = 7.8 Hz, 2H, $H_8$), 3.06 (t, *J* = 7.8 Hz, 2H, $H_7$), 2.28 (s, 3H, $H_9$) ppm. **$^{13}$C NMR (101 MHz, $CDCl_3$):** δ 136.6 ($C_5$), 136.0 ($C_2$), 129.4 ($C_{4,6}$), 128.6 ($C_{1,3}$), 39.2 ($C_8$), 33.3 ($C_7$), 21.2 ($C_9$) ppm. **HRMS GC EI⁺:** m/z 198.00441 $[M+H]^+$ *calc m/z 198.00386.* **IR (film):** $\nu_{max}$ 3020 (C-H), 1899 (C-H), 1515, 1449 (C-H), 1209, 807 (C=C), 632 (C-Br) $cm^{-1}$. This data was consistent with literature characterisation.[450]

### 1-(2-Bromoethyl)-4-butylbenzene (126)

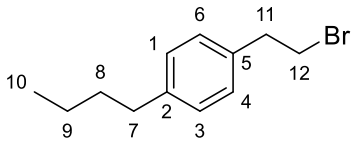

Following **General Procedure B, 126** was obtained from **124** (1.5 g, 5.9 mmol). Purification by flash column chromatography (0% -> 10% EtOAc in pentane) yielded the title compound as a colourless oil (1.4 g, 95%). **$^1$H NMR (400 MHz, $CDCl_3$):** δ 7.20-7.09 (m, 4H, $H_{1,3,4,6}$), 3.57 (t, *J* = 8.2 Hz, 2H, $H_{11}$), 3.15 (t, *J* = 8.2 Hz, 2H, $H_{12}$), 2.66-2.57 (m, 2H, $H_7$), 1.66-1.56 (m, 2H, $H_8$), 1.44-1.32 (m, 2H, $H_9$), 0.95 (t, *J* = 7.4 Hz, 3H, $H_{10}$) ppm. **$^{13}$C NMR (101 MHz, $CDCl_3$):** δ 141.8 ($C_5$), 136.3 ($C_2$), 128.9 ($C_{4,6}$), 128.7 ($C_{1,3}$), 39.4 ($C_{12}$), 35.5 ($C_7$), 33.9 ($C_{11}$), 33.3 ($C_8$), 22.6 ($C_9$), 14.2 ($C_{10}$) ppm. **HRMS GC EI$^+$:** m/z $[M]^+$ 240.05136 *calc m/z 240.05081.* **IR (film):** $\nu_{max}$ 2956 (C-H), 1652 (C=$C_{arom}$), 1464 (C-H), 739 (C=$C_{arom}$), 639 (C-Br) $cm^{-1}$.

## Diethyl 2-acetamido-2-(4-methylphenethyl)malonate (127)

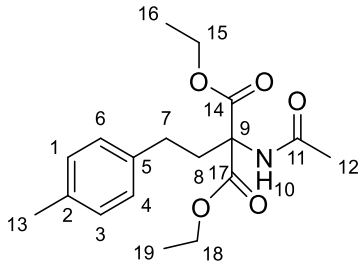


Following **General Procedure C, 127** was obtained from diethylacetoamidomalonate (2.1 g, 9.8 mmol) and **125** (1.6 g, 8.2 mmol). Purification by flash column chromatography (0% -> 50% EtOAc in pentane) yielded the title compound as a colourless oil (840 mg, 31%). **$^1$H NMR (600 MHz, MeOD):** δ 7.09 – 7.06 (m, 2H, $H_{1,3}$), 7.03 – 6.99 (m, 2H, $H_{4,6}$), 4.29 – 4.21 (m, 4H, $H_{15,18}$), 2.54 – 2.49 (m, 2H, $H_7$), 2.48 – 2.42 (m, 2H, $H_8$), 2.28 (s, 3H, $H_{13}$), 1.98 (s, 3H, $H_{12}$), 1.24 (t, *J* = 7.1 Hz, 6H, $H_{16,19}$) ppm. **$^{13}$C NMR (151 MHz, MeOD):** δ 172.5 ($C_{11}$), 169.2 ($C_{14,17}$), 139.1 ($C_5$), 136.7 ($C_2$), 130.1 ($C_{4,6}$), 129.3 ($C_{1,3,}$), 68.0 ($C_9$), 63.4 ($C_{15,18}$), 35.6 ($C_7$), 30.6 ($C_8$), 22.3 ($C_{12}$), 21.0 ($C_{13}$), 14.3 ($C_{16,19}$) ppm. **LRMS ESI$^+$:** m/z 378 ($[M+Na]^+$, 91%), 336 ($[M+H]^+$, 37%).

**HRMS ESI$^+$:** m/z 336.1807 $[M+H]^+$ *calc m/z 336.1806.* **IR (MeOH):** $\nu_{max}$ 2929 (C-H), 1740 (C=O), 1644 (C=O), 1515 (N-H), 1466 (C-H), 1191 (C-O), 808, 696 $cm^{-1}$.

## Diethyl 2-acetamido-2-(4-butylphenethyl)malonate (128)

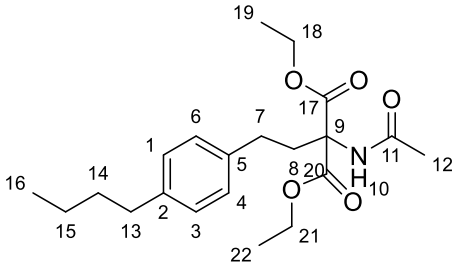


Following **General Procedure C, 128** was obtained from diethylacetoamidomalonate (1.5 g, 7.1 mmol) and **126** (1.4 g, 5.9 mmol). Purification by flash column chromatography (0% -> 50% EtOAc in pentane) yielded the title compound as a colourless oil (1.1 g, 41%). **$^1$H NMR (400 MHz, $CDCl_3$):** δ 7.07 – 6.97 (m, 4H, $H_{1,3,4,6}$), 6.82 (s, 1H, $NH_{10}$), 4.21 – 4.09 (m, 4H, $H_{18,21}$), 2.67 – 2.61 (m, 2H, $H_7$), 2.53 (t, *J* = 7.5 Hz, 2H, $H_{13}$), 2.47 – 2.38 (m, 2H, $H_8$), 1.99 (s, 3H, $H_{12}$), 1.52 (tt, *J* = 8.7, 7.5 Hz, 2H, $H_{14}$), 1.37 – 1.24 (m, 8H, $H_{15,19,22}$), 0.87 (t, *J* = 7.3 Hz, 3H, $H_{16}$). ppm. **$^{13}$C NMR (101 MHz, $CDCl_3$):** δ 169.0 ($C_{11}$), 168.0 ($C_{17,20}$), 140.5 ($C_5$), 137.6 ($C_2$), 128.3 ($C_{4,6}$), 128.2 ($C_{1,3}$), 66.4 ($C_9$), 62.4 ($C_{18,21}$), 35.1 ($C_{13}$), 33.7 ($C_8$), 33.3 ($C_7$), 29.6 ($C_{14}$), 22.8 ($C_{12}$), 22.3 ($C_{15}$), 13.9 ($C_{19,22}$), 13.9 ($C_{16}$) ppm. **LRMS ESI$^+$:** m/z 378 ($[M+H]^+$, 97%), 400 ($[M+Na]^+$, 40%). **HRMS ESI$^+$:** m/z 400.2111 $[M+Na]^+$ *calc. m/z 400.2094.* **IR (film):** $\nu_{max}$ 2935 (C-H), 1743 (C=O), 1679 (C=O), 1650 (C=O), 1515 (N-H), 1371 (C-O), 1268 (C-N), 1192 (C-O), 733 (C-H) $cm^{-1}$.

**4-(4-(2-(3-(But-3-yn-1-yl)-3H-diazirin-3-yl)ethoxy)phenyl)-1-methoxy-2-(methoxymethyl)butan-2-amine – Photoaffinity probe 130**

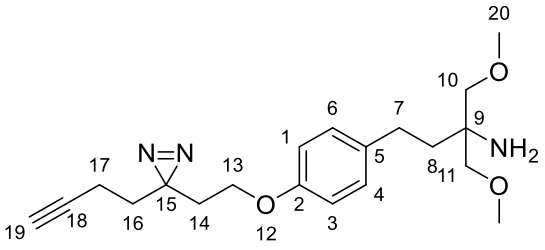


To a solution of **112** (50 mg, 0.20 mmol) and $K_2CO_3$ (55 mg, 0.40 mmol) in DMF (500 μL) was added 3-(but-3-yn-1-yl)-3-(2-iodoethyl)-3H-diazirine (50 mg, 0.20 mmol) in DMF (500 μL) dropwise. The reaction was stirred in the dark at 40 °C for 20 h. The crude reaction was concentrated *in vacuo* and purified by reverse-phase flash column chromatography (0 -> 100% MeCN in 10 mM $NH_4OAc$) to yield **12** (9.0 mg, 13%) as a colourless solid. **$^1$H NMR (400 MHz, MeOD):** δ 7.12 (d, *J* = 8.6 Hz, 2H, $H_{4,6}$), 6.85 (d, *J* = 8.6 Hz, 2H, $H_{1,3}$), 3.82 (t, *J* = 6.0 Hz, 2H, $H_{13}$), 3.54 – 3.46 (m, 4H, $H_{10}$), 3.41 (s, 6H, $H_{20}$), 2.62 – 2.56 (m, 2H, $H_7$), 2.26 (t, *J* = 2.7 Hz, 1H, $H_{19}$), 2.07 (td, *J* = 7.5, 2.7 Hz, 2H, $H_{17}$), 1.91 – 1.89 (m, 2H, $H_8$), 1.86 (t, *J* = 6.0 Hz, 2H, $H_{14}$), 1.68 (t, *J* = 7.5 Hz, 2H, $H_{16}$) ppm. **$^{13}$C NMR (101 MHz, MeOD):** δ 158.6 ($C_2$), 134.7 ($C_5$), 130.2 ($C_{4,6}$), 115.8 ($C_{1,3}$), 83.7 ($C_{18}$), 73.8 ($C_{10}$), 70.2 ($C_{19}$), 63.8 ($C_{13}$), 59.7 ($C_9$), 59.7 ($C_{13}$), 36.0 ($C_8$), 33.9 ($C_{16}$), 33.8 ($C_{14}$), 29.4 ($C_7$), 27.8 ($C_{15}$), 13.9 ($C_{17}$) ppm. **LRMS ESI$^+$:** m/z 360 (100%, $[M+H]^+$), 398 (78%, $[M+Na]^+$). **HRMS ESI$^+$:** m/z 360.2277 $[M+H]^+$ *calc. m/z 360.2282.* **IR (film):** $\nu_{max}$ 3398 (N-H), 1673 (N=N), 1204 (C-O), 1010 (C-O), 614 (C-H) $cm^{-1}$.

**4-(3-Amino-4-methoxy-3-(methoxymethyl)butyl)phenol (131)**

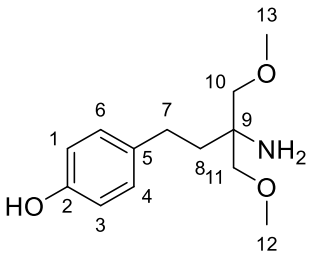


(4-Vinylphenyl)boronic acid pinacol ester (500 mg, 2.17 mmol), 1,3-dimethoxypropan-2-amine (260 mg, 2.2 mmol), $[NBu_4][N_3]$ (125 mg, 20 mol%), 3DPA2FBN (14 mg, 1 mol%) and degassed DMF (14 mL) were placed in a reaction flask and irradiated at 427 nm at rt overnight. The crude reaction was concentrated *in vacuo*, redissolved in THF:1 M NaOH (1:1, 25 mL) and 30% w/w $H_2O_2$ (1.2 mL, 11 mmol) was added at 0 °C. The reaction was stirred at rt for 1 h, quenched with $Na_2SO_3$ (2 mL), extracted with EtOAc (50 mL), concentrated *in vacuo* and purified by reverse-phase flash column chromatography (0 -> 100% MeCN in 10 mM $NH_4OAc$) to yield **131** (370 mg, 71%) as a colourless oil. **$^1$H NMR (400 MHz, MeOD):** δ 6.91 (d, *J* = 8.5 Hz, 2H, $H_{4,6}$), 6.61 (d, *J* = 8.5 Hz, 2H, $H_{1,3}$), 3.43 – 3.33 (m, 4H, $H_{10}$), 3.30 (s, 6H, $H_{12\text{-}13}$), 2.51 – 2.37 (m, 2H, $H_7$), 1.79 – 1.74 (m, 2H, $H_8$) ppm. **$^{13}$C NMR (101 MHz, MeOD):** δ 156.8 ($C_2$), 133.1 ($C_5$), 130.2 ($C_{4,6}$), 116.3 ($C_{1,3}$), 73.8 ($C_{10}$), 59.6 ($C_{12\text{-}13}$), 36.1 ($C_9$), 29.4 ($C_8$), 23.9 ($C_7$) ppm. **LRMS ESI$^+$:** m/z 501 (100%, $[2M+Na]^+$), 262 (57%, $[M+Na]^+$), 240 (34%, $[M+H]^+$). **HRMS ESI$^+$:** m/z 262.1401 $[M+Na]^+$ *calc. m/z 262.1414.* **IR (film):** $\nu_{max}$ 3372 (N-H), 2976 (C-H), 1252 (O-H), 1110 (C-O), 616 (C-H) $cm^{-1}$.

**(1*R*,2*S*,3*R*,4*R*)-3-(4-methylpiperazine-1-carbonyl)-7-oxabicyclo[2.2.1]heptane-2-carboxylic acid (LB-100, 132)**

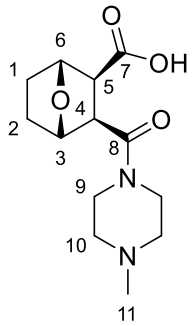


To a solution of norcantharidin (100 mg, 0.6 mmol) in benzene (2 mL), was added *N*-methylpiperazine (70 μL, 0.6 mmol). The reaction was stirred at rt overnight. The crude reaction was filtered and washed with toluene (10 mL) and acetone (10 mL) to yield LB-100 as a white solid (35 mg, 22%). **$^{1}$H NMR (400 MHz, $D_2O$):** δ 4.87 (d, *J* = 4.2 Hz, 1H, $H_6$), 4.73 (d, *J* = 4.5 Hz, 1H, $H_3$), 3.69 – 3.37 (m, 5H, $H_{9',9'',4}$), 3.26 (t, *J* = 5.3 Hz, 1H, $H_5$), 3.23 – 3.17 (m, 2H, $H_{10'}$), 3.06 – 3.00 (m, 2H, $H_{10''}$), 2.92 (s, 3H, $H_{11}$), 1.72 (tdd, *J* = 13.3, 7.1, 3.4 Hz, 2H, $H_{1',2'}$), 1.65 – 1.49 (m, 2H, $H_{1'',2''}$) ppm. **$^{13}$C NMR (101 MHz, $D_2O$):** δ 178.1 ($C_7$), 173.6 ($C_8$), 80.1 ($C_3$), 78.6 ($C_6$), 52.6 ($C_5$), 51.0 ($C_4$), 49.1 ($C_{10}$), 42.9 ($C_9$), 42.6 ($C_{11}$), 28.7 ($C_1$), 28.3 ($C_2$) ppm. **HRMS ESI$^-$:** m/z 267.1361 $[M-H]^-$ *calc. m/z 267.1350.* This data was consistent with literature characterisation.[451]

**Pyrrolo[1,2-a]quinoxalin-4(5H)-one (133)**

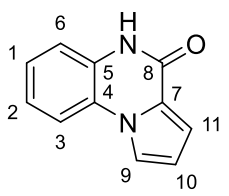

To a solution of 2-(1-pyrrolyl)benzoic acid (200 mg, 1.1 mmol) and DIPEA (370 μL, 2.1 mmol) in 2-MeTHF (80 mL) was added diphenylphosphonium azide (370 μL, 1.7 mmol). The reaction was stirred at 40 °C for 18 h. The reaction was allowed to cool, the precipitate was filtered off and washed with $CH_2Cl_2$ (20 mL) to yield **133** as a white solid (30 mg, 15%). **$^1$H NMR (400 MHz, $CDCl_3$):** δ 10.42 (s, 1H, NH), 7.72 (dd, *J* = 2.8, 1.5 Hz, 1H, $H_9$), 7.66 (d, *J* = 8.0 Hz, 1H, $H_3$), 7.32 – 7.27 (m, 3H, $H_{1,6,11}$), 7.23 (ddd, *J* = 8.8, 6.5, 2.4 Hz, 1H, $H_2$), 6.71 (dd, *J* = 4.0, 2.8 Hz, 1H, $H_{10}$) ppm. **$^{13}$C NMR (101 MHz, $CDCl_3$):** δ 157.2 ($C_8$), 128.1 ($C_5$), 125.8 ($C_1$), 123.5 ($C_{2,4}$), 123.4 ($C_7$), 117.3 ($C_9$), 117.1 ($C_6$), 114.5 ($C_3$), 113.4 ($C_{10}$), 112.9 ($C_{11}$) ppm. **HRMS ESI$^+$:** m/z 207.0532 $[M+Na]^+$ *calc. m/z 207.0529*. This data was consistent with literature characterisation.[452]

**5-(3-Chloropropyl)pyrrolo[1,2-a]quinoxalin-4(5H)-one (134)**

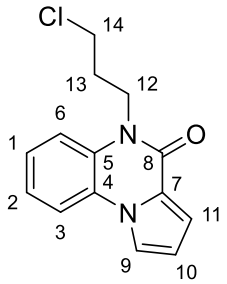


To a solution of **133** (30 mg, 0.16 mmol) in DMF (1 mL) was added $Cs_2CO_3$ (53 mg, 0.16 mmol) and stirred for 3 h at rt. 1-Bromo-3-chloropropane (32 μL, 0.33 mmol) was added and the reaction heated to 70 °C overnight. The reaction was cooled, diluted with EtOAc (25 mL) and washed with water (10 mL). The crude product was purified by flash column chromatography (0 -> 50% EtOAc in pentane) to yield **134** as a colourless film (17 mg, 45%). **$^1$H NMR (400 MHz, $CDCl_3$):** δ 7.71 (dd, *J* = 8.1, 1.4 Hz, 1H, $H_9$), 7.66 (dd, *J* = 2.8, 1.5 Hz, 1H,

$H_3$), 7.42 (dt, *J* = 8.4, 1.5 Hz, 1H, $H_{11}$), 7.35 (td, *J* = 7.8, 1.4 Hz, 1H, $H_6$), 7.28 – 7.21 (m, 2H, $H_{1,2}$), 6.67 (dd, *J* = 3.9, 2.8 Hz, 1H, $H_{10}$), 4.51 – 4.42 (m, 2H, $H_{12}$), 3.71 (t, *J* = 6.3 Hz, 2H, $H_{14}$), 2.29 – 2.21 (m, 2H, $H_{13}$) ppm. **$^{13}$C NMR (101 MHz, $CDCl_3$):** δ 155.7 ($C_8$), 129.3 ($C_5$), 125.9 ($C_1$), 124.3 ($C_4$), 123.2 ($C_{2,7}$), 116.2 ($C_9$), 115.6 ($C_6$), 115.0 ($C_3$), 113.5 ($C_{10}$), 112.9 ($C_{11}$), 42.8 ($C_{12}$), 39.2 ($C_{14}$), 30.6 ($C_{13}$) ppm. **HRMS ESI$^+$:** m/z 283.0613 $[M+Na]^+$ *calc. m/z 283.0609.* This data was consistent with literature characterisation.[453]

**5-(3-(4-(4-Chlorophenyl)piperidin-1-yl)propyl)pyrrolo[1,2-a]quinoxalin-4(5H)-one (JMS-17-2, 135)**

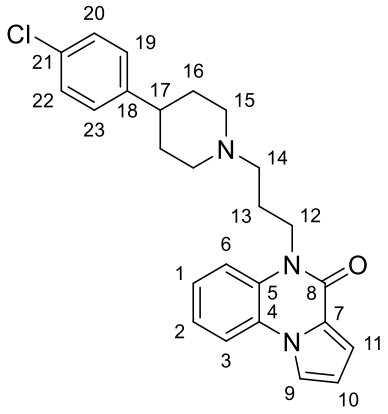


To a solution of **134** (17 mg, 0.065 mmol) in MeCN (1 mL) in a MW vial was added 4-(4-chlorophenyl)piperidine (16 mg, 0.078 mmol) and $K_2CO_3$ (18 mg, 0.13 mmol). The reaction was irradiated at 140 °C for 1 h. The crude material was filtered and purified by flash column chromatography (10 -> 100% EtOAc in pentane) to yield the title compound as a colourless oil (22 mg, 81%). **$^1$H NMR (400 MHz, $CDCl_3$):** δ 7.72 – 7.68 (dd, *J* = 8.1, 1.4 Hz, 1H, $H_9$), 7.67 – 7.66 (m, 1H, $H_3$), 7.47 (d, *J* = 8.3 Hz, 1H, $H_{11}$), 7.36 – 7.30 (t, *J* = 7.6 Hz, 1H, $H_6$), 7.29 – 7.19 (m, 4H, $H_{1,2,20,22}$), 7.14 (d, *J* = 8.3 Hz, 2H, $H_{19,23}$), 6.67 (t, *J* = 3.3 Hz, 1H, $H_{10}$), 4.36 (t, *J* = 7.4 Hz, 2H, $H_{12}$), 3.08 (d, *J* = 11.2 Hz, 2H, $H_{15'}$), 2.57 (t, *J* = 7.1 Hz, 2H, $H_{17}$), 2.48 (tt, *J* = 11.6,

4.3 Hz, 2H, $H_{14}$), 2.10 (dt, *J* = 12.3, 6.2 Hz, 2H, $H_{15''}$), 2.01 (t, *J* = 7.2 Hz, 2H, $H_{13}$), 1.89 – 1.71 (m, 4H, $H_{16',16''}$) ppm. **$^{13}$C NMR (101 MHz, $CDCl_3$):** δ 155.7 ($C_8$), 144.8 ($C_{18}$), 131.9 ($C_{21}$), 129.6 ($C_5$), 128.7 ($C_{20,22}$), 128.3 ($C_{19,23}$), 125.7 ($C_1$), 124.3 ($C_7$), 123.4 ($C_4$), 122.9 ($C_2$), 116.1 ($C_9$), 116.0 ($C_6$), 114.9 ($C_3$), 113.4 ($C_{11}$), 112.7 ($C_{10}$), 56.1 ($C_{14}$), 54.4 ($C_{15}$), 42.1 ($C_{12}$), 39.8 ($C_{17}$), 33.4 ($C_{16}$), 25.1 ($C_{13}$) ppm. **HRMS ESI$^+$:** m/z 420.1848 $[M+H]^+$ *calc. m/z 420.1837.* This data was consistent with literature characterisation.[454]

## Methyl (5*S*,6*R*,*E*)-5,6,7-trihydroxyhept-2-enoate (136)

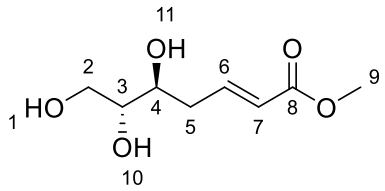


To a solution of 2-deoxy-D-ribose (100 mg, 0.75 mmol) in THF (9 mL) was added methyl (triphenylphosphoranylidene)acetate (300 mg, 0.90 mmol). The reaction was refluxed at 80 °C for 16 h. The solvent was evaporated and the crude material was purified by reverse-phase flash column chromatography ( 0 -> 100% MeCN + 0.1% formic acid in $H_2O$ + 0.1% formic acid) to yield the title compound as a colourless oil (73 mg, 51%). **$^1$H NMR (400 MHz, MeOD):** δ 7.07 (dt, *J* = 15.7, 7.3 Hz, 1H), 5.94 (d, *J* = 15.7 Hz, 1H), 3.77 – 3.61 (m, 5H), 3.58 (dd, *J* = 11.3, 6.2 Hz, 1H), 3.45 (ddd, *J* = 7.2, 6.2, 3.9 Hz, 1H), 2.65 – 2.57 (m, 1H), 2.36 (dddd, *J* = 14.8, 8.8, 7.6, 1.5 Hz, 1H) ppm. **$^{13}$C NMR (101 MHz, MeOD):** δ 168.61, 148.24, 123.74, 75.83, 72.21, 64.62, 51.90, 40.42, 37.15 ppm. **HRMS ESI$^+$:** m/z 191.0921 $[M+H]^+$ *calc. m/z 191.0914.* This data was consistent with literature characterisation.[455]

**Methyl (5S,6R)-5,6,7-trihydroxyheptanoate (BML-111, 137)**

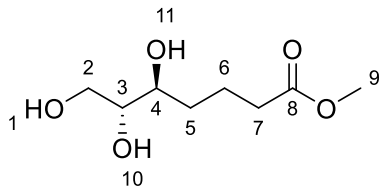


To a solution of **136** (73 mg, 0.38 mmol) in MeOH (5 mL) under $N_2$ was added a small spatula of palladium on activated charcoal. The reaction was placed under an atmosphere of $H_2$ and stirred for 1 h. The reaction was filtered through celite and purified by reverse-phase flash column chromatography (0 -> 100% MeCN + 0.1% formic acid in $H_2O$ + 0.1 % formic acid) to yield the title compound as a colourless oil (65 mg, 89%). **$^1$H NMR (400 MHz, MeOD):** δ 3.70 (td, *J* = 11.2, 3.6 Hz, 1H, $H_{2'}$), 3.66 (s, 3H, $H_9$), 3.56 (dd, *J* = 11.2, 6.4 Hz, 1H, $H_3$), 3.49 (ddd, *J* = 9.1, 6.4, 2.6 Hz, 1H, $H_4$), 3.43 (td, *J* = 6.4, 3.6 Hz, 1H, $H_{2''}$), 2.37 (m, 2H, $H_{7',7''}$), 1.90 – 1.79 (m, 1H, $H_{6'}$), 1.76 – 1.60 (m, 2H, $H_{5',6''}$), 1.49 – 1.36 (m, 1H, $H_{5''}$) ppm. **$^{13}$C NMR (101 MHz, MeOD):** δ 175.9 ($C_8$), 76.2 ($C_3$), 73.1 ($C_4$), 64.7 ($C_2$), 52.1 ($C_9$), 34.8 ($C_7$), 33.4 ($C_5$), 22.3 ($C_6$) ppm. **HRMS ESI$^+$:** m/z 193.1075 $[M+H]^+$ *calc. m/z 193.1071.* This data was consistent with literature characterisation.[456]

# Bibliography

(1) Pan, S.; Gray, N. S.; Gao, W.; Mi, Y.; Fan, Y.; Wang, X.; Tuntland, T.; Che, J.; Lefebvre, S.; Chen, Y.; et al. Discovery of BAF312 (Siponimod), a Potent and Selective S1P Receptor Modulator. *ACS Med Chem Lett* **2013**, *4* (3), 333–337. DOI: 10.1021/ml300396r From NLM.
(2) Jo, E.; Bhhatarai, B.; Repetto, E.; Guerrero, M.; Riley, S.; Brown, S. J.; Kohno, Y.; Roberts, E.; Schürer, S. C.; Rosen, H. Novel selective allosteric and bitopic ligands for the S1P(3) receptor. *ACS Chem Biol* **2012**, *7* (12), 1975–1983. DOI: 10.1021/cb300392z From NLM.
(3) Urbano, M.; Guerrero, M.; Velaparthi, S.; Crisp, M.; Chase, P.; Hodder, P.; Schaeffer, M.-T.; Brown, S.; Rosen, H.; Roberts, E. Discovery, synthesis and SAR analysis of novel selective small molecule S1P4-R agonists based on a (2Z,5Z)-5-((pyrrol-3-yl)methylene)-3-alkyl-2-(alkylimino)thiazolidin-4-one chemotype. *Bioorganic & Medicinal Chemistry Letters* **2011**, *21* (22), 6739–6745. DOI: https://doi.org/10.1016/j.bmcl.2011.09.049.
(4) JB, H. Clinical features of sudden obstruction of the coronary arteries. *JAMA* **1912**, *59*, 2015–2020.
(5) Reimer, K. A.; Jennings, R. B.; Tatum, A. H. Pathobiology of acute myocardial ischemia: metabolic, functional and ultrastructural studies. *Am J Cardiol* **1983**, *52* (2), 72a–81a. DOI: 10.1016/0002-9149(83)90180-7 From NLM.
(6) Jennings, R. B.; Steenbergen, C., Jr.; Reimer, K. A. Myocardial ischemia and reperfusion. *Monogr Pathol* **1995**, *37*, 47–80. From NLM.
(7) Gallucci, G.; Tartarone, A.; Lerose, R.; Lalinga, A. V.; Capobianco, A. M. Cardiovascular risk of smoking and benefits of smoking cessation. *J Thorac Dis* **2020**, *12* (7), 3866–3876. DOI: 10.21037/jtd.2020.02.47 From NLM.
(8) Mensink, R. P.; Katan, M. B. Effect of dietary fatty acids on serum lipids and lipoproteins. A meta-analysis of 27 trials. *Arteriosclerosis and thrombosis: a journal of vascular biology* **1992**, *12* (8), 911–919.
(9) Mente, A.; O'Donnell, M. J.; Rangarajan, S.; McQueen, M. J.; Poirier, P.; Wielgosz, A.; Morrison, H.; Li, W.; Wang, X.; Di, C. Association of urinary sodium and potassium excretion with blood pressure. *New england journal of medicine* **2014**, *371* (7), 601–611.
(10) McPherson, R.; Pertsemlidis, A.; Kavaslar, N.; Stewart, A.; Roberts, R.; Cox, D. R.; Hinds, D. A.; Pennacchio, L. A.; Tybjaerg-Hansen, A.; Folsom, A. R.; et al. A common allele on chromosome 9 associated with coronary heart disease. *Science* **2007**, *316* (5830), 1488–1491. DOI: 10.1126/science.1142447 From NLM.
(11) Schofield, J.; Ho, J.; Soran, H. Cardiovascular Risk in Type 1 Diabetes Mellitus. *Diabetes Ther* **2019**, *10* (3), 773–789. DOI: 10.1007/s13300-019-0612-8 From NLM.
(12) Sharifi, M.; Rakhit, R. D.; Humphries, S. E.; Nair, D. Cardiovascular risk stratification in familial hypercholesterolaemia. *Heart* **2016**, *102* (13), 1003–1008. DOI: 10.1136/heartjnl-2015-308845.
(13) Disease, G. B. o. *Global Burden of Disease estimates for 2021*. 2024. http://ghdx.healthdata.org/gbd-results-tool (accessed 2024).
(14) Stanley L Robbins, R. S. C. *Robbins & Cotran Pathologic Basis of Disease*; Elsevier, 2020.
(15) Pasotti, M.; Prati, F.; Arbustini, E. The pathology of myocardial infarction in the pre- and post-interventional era. *Heart* **2006**, *92* (11), 1552–1556. DOI: 10.1136/hrt.2005.086934 From NLM.
(16) Hotchkiss, R. S.; Strasser, A.; McDunn, J. E.; Swanson, P. E. Cell Death. *New England Journal of Medicine* **2009**, *361* (16), 1570–1583. DOI: doi:10.1056/NEJMra0901217.
(17) Yang, D.; Han, Z.; Oppenheim, J. J. Alarmins and immunity. *Immunological Reviews* **2017**, *280* (1), 41–56. DOI: https://doi.org/10.1111/imr.12577.

(18) DeLeon-Pennell, K. Y.; Meschiari, C. A.; Jung, M.; Lindsey, M. L. Matrix Metalloproteinases in Myocardial Infarction and Heart Failure. *Prog Mol Biol Transl Sci* **2017**, *147*, 75–100. DOI: 10.1016/bs.pmbts.2017.02.001 From NLM.
(19) Varda-Bloom, N.; Leor, J.; Ohad, D. G.; Hasin, Y.; Amar, M.; Fixler, R.; Battler, A.; Eldar, M.; Hasin, D. Cytotoxic T lymphocytes are activated following myocardial infarction and can recognize and kill healthy myocytes in vitro. *J Mol Cell Cardiol* **2000**, *32* (12), 2141–2149. DOI: 10.1006/jmcc.2000.1261 From NLM.
(20) Rog-Zielinska, E. A.; Norris, R. A.; Kohl, P.; Markwald, R. The Living Scar--Cardiac Fibroblasts and the Injured Heart. *Trends Mol Med* **2016**, *22* (2), 99–114. DOI: 10.1016/j.molmed.2015.12.006 From NLM.
(21) Frangogiannis, N. G. Regulation of the inflammatory response in cardiac repair. *Circ Res* **2012**, *110* (1), 159–173. DOI: 10.1161/circresaha.111.243162 From NLM.
(22) Vieira, J. M.; Norman, S.; Villa Del Campo, C.; Cahill, T. J.; Barnette, D. N.; Gunadasa-Rohling, M.; Johnson, L. A.; Greaves, D. R.; Carr, C. A.; Jackson, D. G.; et al. The cardiac lymphatic system stimulates resolution of inflammation following myocardial infarction. *J Clin Invest* **2018**, *128* (8), 3402–3412. DOI: 10.1172/jci97192 From NLM.
(23) Prabhu, S. D.; Frangogiannis, N. G. The Biological Basis for Cardiac Repair After Myocardial Infarction: From Inflammation to Fibrosis. *Circ Res* **2016**, *119* (1), 91–112. DOI: 10.1161/circresaha.116.303577 From NLM.
(24) Sangiuliano, B.; Pérez, N. M.; Moreira, D. F.; Belizário, J. E. Cell death-associated molecular-pattern molecules: inflammatory signaling and control. *Mediators Inflamm* **2014**, *2014*, 821043. DOI: 10.1155/2014/821043 From NLM.
(25) Mann, D. L.; Topkara, V. K.; Evans, S.; Barger, P. M. Innate immunity in the adult mammalian heart: for whom the cell tolls. *Trans Am Clin Climatol Assoc* **2010**, *121*, 34–50; discussion 50–31. From NLM.
(26) Mezzaroma, E.; Toldo, S.; Farkas, D.; Seropian, I. M.; Van Tassell, B. W.; Salloum, F. N.; Kannan, H. R.; Menna, A. C.; Voelkel, N. F.; Abbate, A. The inflammasome promotes adverse cardiac remodeling following acute myocardial infarction in the mouse. *Proc Natl Acad Sci U S A* **2011**, *108* (49), 19725–19730. DOI: 10.1073/pnas.1108586108 From NLM.
(27) Manz, M. G.; Boettcher, S. Emergency granulopoiesis. *Nature Reviews Immunology* **2014**, *14* (5), 302–314. DOI: 10.1038/nri3660.
(28) Yamashiro, S.; Kamohara, H.; Wang, J. M.; Yang, D.; Gong, W. H.; Yoshimura, T. Phenotypic and functional change of cytokine-activated neutrophils: inflammatory neutrophils are heterogeneous and enhance adaptive immune responses. *J Leukoc Biol* **2001**, *69* (5), 698–704. From NLM.
(29) Yan, X.; Anzai, A.; Katsumata, Y.; Matsuhashi, T.; Ito, K.; Endo, J.; Yamamoto, T.; Takeshima, A.; Shinmura, K.; Shen, W.; et al. Temporal dynamics of cardiac immune cell accumulation following acute myocardial infarction. *Journal of Molecular and Cellular Cardiology* **2013**, *62*, 24–35. DOI: 10.1016/j.yjmcc.2013.04.023 (accessed 2025/09/08).
(30) Vinten-Johansen, J. Involvement of neutrophils in the pathogenesis of lethal myocardial reperfusion injury. *Cardiovascular Research* **2004**, *61* (3), 481–497. DOI: 10.1016/j.cardiores.2003.10.011 (accessed 9/21/2025).
(31) Jolly, S. R.; Kane, W. J.; Hook, B. G.; Abrams, G. D.; Kunkel, S. L.; Lucchesi, B. R. Reduction of myocardial infarct size by neutrophil depletion: effect of duration of occlusion. *American heart journal* **1986**, *112* (4), 682–690.
(32) Askari, A. T.; Brennan, M.-L.; Zhou, X.; Drinko, J.; Morehead, A.; Thomas, J. D.; Topol, E. J.; Hazen, S. L.; Penn, M. S. Myeloperoxidase and plasminogen activator inhibitor 1 play

a central role in ventricular remodeling after myocardial infarction. *The Journal of experimental medicine* **2003**, *197* (5), 615–624.
(33) Chertov, O.; Ueda, H.; Xu, L. L.; Tani, K.; Murphy, W. J.; Wang, J. M.; Howard, O. M. Z.; Sayers, T. J.; Oppenheim, J. J. Identification of Human Neutrophil-derived Cathepsin G and Azurocidin/CAP37 as Chemoattractants for Mononuclear Cells and Neutrophils. *Journal of Experimental Medicine* **1997**, *186* (5), 739–747. DOI: 10.1084/jem.186.5.739 (accessed 9/21/2025).
(34) Lee, T. D.; Gonzalez, M. L.; Kumar, P.; Grammas, P.; Pereira, H. A. CAP37, a neutrophil-derived inflammatory mediator, augments leukocyte adhesion to endothelial monolayers. *Microvascular Research* **2003**, *66* (1), 38–48. DOI: https://doi.org/10.1016/S0026-2862(03)00010-4.
(35) Nahrendorf , M.; Swirski , F. K.; Aikawa , E.; Stangenberg , L.; Wurdinger , T.; Figueiredo , J.-L.; Libby , P.; Weissleder , R.; Pittet , M. J. The healing myocardium sequentially mobilizes two monocyte subsets with divergent and complementary functions. *Journal of Experimental Medicine* **2007**, *204* (12), 3037–3047. DOI: 10.1084/jem.20070885 (accessed 9/8/2025).
(36) Poon, I. K. H.; Lucas, C. D.; Rossi, A. G.; Ravichandran, K. S. Apoptotic cell clearance: basic biology and therapeutic potential. *Nature Reviews Immunology* **2014**, *14* (3), 166–180. DOI: 10.1038/nri3607.
(37) O'Rourke, S. A.; Dunne, A.; Monaghan, M. G. The Role of Macrophages in the Infarcted Myocardium: Orchestrators of ECM Remodeling. *Front Cardiovasc Med* **2019**, *6*, 101. DOI: 10.3389/fcvm.2019.00101 From NLM.
(38) Cohn, J. N.; Ferrari, R.; Sharpe, N. Cardiac remodeling—concepts and clinical implications: a consensus paper from an international forum on cardiac remodeling. *Journal of the American College of Cardiology* **2000**, *35* (3), 569–582. DOI: https://doi.org/10.1016/S0735-1097(99)00630-0.
(39) Ma, Y.; Mouton, A. J.; Lindsey, M. L. Cardiac macrophage biology in the steady-state heart, the aging heart, and following myocardial infarction. *Translational Research* **2018**, *191*, 15–28. DOI: https://doi.org/10.1016/j.trsl.2017.10.001.
(40) Sallusto, F.; Lanzavecchia, A. Mobilizing dendritic cells for tolerance, priming, and chronic inflammation. *The Journal of experimental medicine* **1999**, *189* (4), 611–614.
(41) Swirski, F. K.; Nahrendorf, M.; Etzrodt, M.; Wildgruber, M.; Cortez-Retamozo, V.; Panizzi, P.; Figueiredo, J.-L.; Kohler, R. H.; Chudnovskiy, A.; Waterman, P. Identification of splenic reservoir monocytes and their deployment to inflammatory sites. *Science* **2009**, *325* (5940), 612–616.
(42) Peng, Y.; Latchman, Y.; Elkon, K. B. Ly6Clow monocytes differentiate into dendritic cells and cross-tolerize T cells through PDL-1. *The Journal of Immunology* **2009**, *182* (5), 2777–2785.
(43) Van der Borght, K.; Scott, C. L.; Nindl, V.; Bouché, A.; Martens, L.; Sichien, D.; Van Moorleghem, J.; Vanheerswynghels, M.; De Prijck, S.; Saeys, Y.; et al. Myocardial Infarction Primes Autoreactive T Cells through Activation of Dendritic Cells. *Cell Rep* **2017**, *18* (12), 3005–3017. DOI: 10.1016/j.celrep.2017.02.079 From NLM.
(44) Anzai, A.; Anzai, T.; Fukuda, K. Abstract 61: Dendritic Cell Regulates Monocyte/Macrophage Polarization and Inflammatory Response After Myocardial Infarction in Mice. *Circulation Research* **2012**, *111* (suppl_1), A61–A61. DOI: doi:10.1161/res.111.suppl_1.A61.

(45) Naito, K.; Anzai, T.; Sugano, Y.; Maekawa, Y.; Kohno, T.; Yoshikawa, T.; Matsuno, K.; Ogawa, S. Differential effects of GM-CSF and G-CSF on infiltration of dendritic cells during early left ventricular remodeling after myocardial infarction. *J Immunol* **2008**, *181* (8), 5691–5701. DOI: 10.4049/jimmunol.181.8.5691 From NLM.
(46) Liao, Y. H.; Cheng, X. Autoimmunity in myocardial infarction. *Int J Cardiol* **2006**, *112* (1), 21–26. DOI: 10.1016/j.ijcard.2006.05.009 From NLM.
(47) Maisel, A.; Cesario, D.; Baird, S.; Rehman, J.; Haghighi, P.; Carter, S. Experimental autoimmune myocarditis produced by adoptive transfer of splenocytes after myocardial infarction. *Circ Res* **1998**, *82* (4), 458–463. DOI: 10.1161/01.res.82.4.458 From NLM.
(48) Van de Werf, F.; Bax, J.; Betriu, A.; Blomstrom-Lundqvist, C.; Crea, F.; Falk, V.; Filippatos, G.; Fox, K.; Huber, K.; Kastrati, A.; et al. [Management of acute myocardial infarction in patients presenting with persistent ST-segment elevation]. *G Ital Cardiol (Rome)* **2009**, *10* (7), 450–489. From NLM.
(49) Mi, L.-L.; Zhu, Y.; Lu, H.-Y. A crosstalk between type 2 innate lymphoid cells and alternative macrophages in lung development and lung diseases (Review). *Mol Med Rep* **2021**, *23* (6), 403. DOI: 10.3892/mmr.2021.12042.
(50) Engelbertsen, D.; Andersson, L.; Ljungcrantz, I.; Wigren, M.; Hedblad, B.; Nilsson, J.; Björkbacka, H. T-Helper 2 Immunity Is Associated With Reduced Risk of Myocardial Infarction and Stroke. *Arteriosclerosis, Thrombosis, and Vascular Biology* **2013**, *33* (3), 637–644. DOI: doi:10.1161/ATVBAHA.112.300871.
(51) Xu, J. Y.; Xiong, Y. Y.; Tang, R. J.; Jiang, W. Y.; Ning, Y.; Gong, Z. T.; Huang, P. S.; Chen, G. H.; Xu, J.; Wu, C. X.; et al. Interleukin-5-induced eosinophil population improves cardiac function after myocardial infarction. *Cardiovascular Research* **2021**, *118* (9), 2165–2178. DOI: 10.1093/cvr/cvab237 (accessed 9/8/2025).
(52) Xia, N.; Lu, Y.; Gu, M.; Li, N.; Liu, M.; Jiao, J.; Zhu, Z.; Li, J.; Li, D.; Tang, T.; et al. A Unique Population of Regulatory T Cells in Heart Potentiates Cardiac Protection From Myocardial Infarction. *Circulation* **2020**, *142* (20), 1956–1973. DOI: doi:10.1161/CIRCULATIONAHA.120.046789.
(53) Wang, Y.; Wang, C.; Shen, L.; Xu, D. The Role of Regulatory T Cells in Heart Repair After Myocardial Infarction. *Journal of Cardiovascular Translational Research* **2023**, *16* (3), 590–597. DOI: 10.1007/s12265-022-10290-5.
(54) Zhang, L.; Wang, Z.; Wang, D.; Zhu, J.; Wang, Y. CD8+CD28+ T cells might mediate injury of cardiomyocytes in acute myocardial infarction. *Molecular Immunology* **2018**, *101*, 74–79. DOI: https://doi.org/10.1016/j.molimm.2018.05.015.
(55) Sonoda, K. H.; Faunce, D. E.; Taniguchi, M.; Exley, M.; Balk, S.; Stein-Streilein, J. NK T cell-derived IL-10 is essential for the differentiation of antigen-specific T regulatory cells in systemic tolerance. *J Immunol* **2001**, *166* (1), 42–50. DOI: 10.4049/jimmunol.166.1.42 From NLM.
(56) Entman, M. L.; Youker, K.; Shoji, T.; Kukielka, G.; Shappell, S. B.; Taylor, A. A.; Smith, C. W. Neutrophil induced oxidative injury of cardiac myocytes. A compartmented system requiring CD11b/CD18-ICAM-1 adherence. *The Journal of Clinical Investigation* **1992**, *90* (4), 1335–1345. DOI: 10.1172/JCI115999.
(57) Gao, X.; Guo, Y.; Zhu, X.; Du, C.; Ma, B.; Cui, Y.; Wang, S. Factors related to cardiac rupture after acute myocardial infarction. *Front Cardiovasc Med* **2024**, *11*, 1401609. DOI: 10.3389/fcvm.2024.1401609 From NLM.
(58) Kong, P.; Christia, P.; Frangogiannis, N. G. The pathogenesis of cardiac fibrosis. *Cellular and molecular life sciences* **2014**, *71* (4), 549–574.

(59) Shiojima, I.; Sato, K.; Izumiya, Y.; Schiekofer, S.; Ito, M.; Liao, R.; Colucci, W. S.; Walsh, K. Disruption of coordinated cardiac hypertrophy and angiogenesis contributes to the transition to heart failure. *J Clin Invest* **2005**, *115* (8), 2108–2118. DOI: 10.1172/jci24682 From NLM.
(60) Tsuda, T. Clinical Assessment of Ventricular Wall Stress in Understanding Compensatory Hypertrophic Response and Maladaptive Ventricular Remodeling. *J Cardiovasc Dev Dis* **2021**, *8* (10). DOI: 10.3390/jcdd8100122 From NLM.
(61) Zhong, L.; Su, Y.; Yeo, S.-Y.; Tan, R.-S.; Ghista, D. N.; Kassab, G. Left ventricular regional wall curvedness and wall stress in patients with ischemic dilated cardiomyopathy. *American Journal of Physiology-Heart and Circulatory Physiology* **2009**, *296* (3), H573–H584. DOI: 10.1152/ajpheart.00525.2008.
(62) Chen, W.; Saxena, A.; Li, N.; Sun, J.; Gupta, A.; Lee, D.-W.; Tian, Q.; Dobaczewski, M.; Frangogiannis, N. G. Endogenous IRAK-M Attenuates Postinfarction Remodeling Through Effects on Macrophages and Fibroblasts. *Arteriosclerosis, Thrombosis, and Vascular Biology* **2012**, *32* (11), 2598–2608. DOI: doi:10.1161/ATVBAHA.112.300310.
(63) Dobaczewski, M.; Xia, Y.; Bujak, M.; Gonzalez-Quesada, C.; Frangogiannis, N. G. CCR5 signaling suppresses inflammation and reduces adverse remodeling of the infarcted heart, mediating recruitment of regulatory T cells. *Am J Pathol* **2010**, *176* (5), 2177–2187. DOI: 10.2353/ajpath.2010.090759 From NLM.
(64) de Lemos, J. A.; Morrow, D. A.; Blazing, M. A.; Jarolim, P.; Wiviott, S. D.; Sabatine, M. S.; Califf, R. M.; Braunwald, E. Serial measurement of monocyte chemoattractant protein-1 after acute coronary syndromes: results from the A to Z trial. *J Am Coll Cardiol* **2007**, *50* (22), 2117–2124. DOI: 10.1016/j.jacc.2007.06.057 From NLM.
(65) Cochain, C.; Auvynet, C.; Poupel, L.; Vilar, J.; Dumeau, E.; Richart, A.; Récalde, A.; Zouggari, Y.; Yin, K. Y. H. W.; Bruneval, P.; et al. The Chemokine Decoy Receptor D6 Prevents Excessive Inflammation and Adverse Ventricular Remodeling After Myocardial Infarction. *Arteriosclerosis, Thrombosis, and Vascular Biology* **2012**, *32* (9), 2206–2213. DOI: doi:10.1161/ATVBAHA.112.254409.
(66) Pfeffer, M. A.; Braunwald, E. Ventricular remodeling after myocardial infarction. Experimental observations and clinical implications. *Circulation* **1990**, *81* (4), 1161–1172. DOI: doi:10.1161/01.CIR.81.4.1161.
(67) Lai, L.; Leone, T. C.; Keller, M. P.; Martin, O. J.; Broman, A. T.; Nigro, J.; Kapoor, K.; Koves, T. R.; Stevens, R.; Ilkayeva, O. R.; et al. Energy metabolic reprogramming in the hypertrophied and early stage failing heart: a multisystems approach. *Circ Heart Fail* **2014**, *7* (6), 1022–1031. DOI: 10.1161/circheartfailure.114.001469 From NLM.
(68) Simmonds, S. J.; Cuijpers, I.; Heymans, S.; Jones, E. A. V. Cellular and Molecular Differences between HFpEF and HFrEF: A Step Ahead in an Improved Pathological Understanding. *Cells* **2020**, *9* (1), 242.
(69) Stewart, J.; Manmathan, G.; Wilkinson, P. Primary prevention of cardiovascular disease: A review of contemporary guidance and literature. *JRSM Cardiovasc Dis* **2017**, *6*, 2048004016687211. DOI: 10.1177/2048004016687211 From NLM.
(70) White, H. D.; Van de Werf, F. J. J. Thrombolysis for Acute Myocardial Infarction. *Circulation* **1998**, *97* (16), 1632–1646. DOI: doi:10.1161/01.CIR.97.16.1632.
(71) Cowled P, F. R. Pathophysiology of Reperfusion Injury. In *Mechanisms of Vacular Disease: A Reference Book for Vascular Specialists*, Fitridge R, T. M. Ed.; Vol. 18; University of Adelaide Press, 2011.

(72) Jordan, J. E.; Zhao, Z. Q.; Vinten-Johansen, J. The role of neutrophils in myocardial ischemia-reperfusion injury. *Cardiovasc Res* **1999**, *43* (4), 860–878. DOI: 10.1016/s0008-6363(99)00187-x From NLM.
(73) Lopaschuk, G. D.; Verma, S. Mechanisms of Cardiovascular Benefits of Sodium Glucose Co-Transporter 2 (SGLT2) Inhibitors: A State-of-the-Art Review. *JACC Basic Transl Sci* **2020**, *5* (6), 632–644. DOI: 10.1016/j.jacbts.2020.02.004 From NLM.
(74) Santos-Gallego, C. G.; Requena-Ibanez, J. A.; San Antonio, R.; Ishikawa, K.; Watanabe, S.; Picatoste, B.; Flores, E.; Garcia-Ropero, A.; Sanz, J.; Hajjar, R. J.; et al. Empagliflozin Ameliorates Adverse Left Ventricular Remodeling in Nondiabetic Heart Failure by Enhancing Myocardial Energetics. *Journal of the American College of Cardiology* **2019**, *73* (15), 1931–1944. DOI: https://doi.org/10.1016/j.jacc.2019.01.056.
(75) Byrne, N. J.; Matsumura, N.; Maayah, Z. H.; Ferdaoussi, M.; Takahara, S.; Darwesh, A. M.; Levasseur, J. L.; Jahng, J. W. S.; Vos, D.; Parajuli, N.; et al. Empagliflozin Blunts Worsening Cardiac Dysfunction Associated With Reduced NLRP3 (Nucleotide-Binding Domain-Like Receptor Protein 3) Inflammasome Activation in Heart Failure. *Circulation: Heart Failure* **2020**, *13* (1), e006277. DOI: doi:10.1161/CIRCHEARTFAILURE.119.006277.
(76) Verma, S.; Garg, A.; Yan, A. T.; Gupta, A. K.; Al-Omran, M.; Sabongui, A.; Teoh, H.; Mazer, C. D.; Connelly, K. A. Effect of Empagliflozin on Left Ventricular Mass and Diastolic Function in Individuals With Diabetes: An Important Clue to the EMPA-REG OUTCOME Trial? *Diabetes Care* **2016**, *39* (12), e212–e213. DOI: 10.2337/dc16-1312 (accessed 9/21/2025).
(77) Neal, B.; Perkovic, V.; Mahaffey, K. W.; Zeeuw, D. d.; Fulcher, G.; Erondu, N.; Shaw, W.; Law, G.; Desai, M.; Matthews, D. R. Canagliflozin and Cardiovascular and Renal Events in Type 2 Diabetes. *New England Journal of Medicine* **2017**, *377* (7), 644–657. DOI: doi:10.1056/NEJMoa1611925.
(78) Dapagliflozin and Cardiovascular Outcomes in Type 2 Diabetes. *New England Journal of Medicine* **2019**, *380* (19), 1880–1882. DOI: doi:10.1056/NEJMc1902837.
(79) Kmietowicz, Z. Survival rate after NHS heart surgery is higher than European average. *BMJ* **2010**, *341*, c6688. DOI: 10.1136/bmj.c6688.
(80) Wilhelm, M. J. Long-term outcome following heart transplantation: current perspective. *J Thorac Dis* **2015**, *7* (3), 549–551. DOI: 10.3978/j.issn.2072-1439.2015.01.46 From NLM.
(81) Macmahon, H. E. Hyperplasia and Regeneration of the Myocardium in Infants and in Children. *Am J Pathol* **1937**, *13* (5), 845–854.845. From NLM.
(82) Kilbride, H.; Way, G. L.; Merenstein, G. B.; Winfield, J. M. Myocardial infarction in the neonate with normal heart and coronary arteries. *Am J Dis Child* **1980**, *134* (8), 759–762. DOI: 10.1001/archpedi.1980.02130200029010 From NLM.
(83) Boulton, J.; Henry, R.; Roddick, L. G.; Rogers, D.; Thompson, L.; Warner, G. Survival after neonatal myocardial infarction. *Pediatrics* **1991**, *88* (1), 145–150. From NLM.
(84) Peeters, S.; Vandenplas, Y.; Jochmans, K.; Bougatef, A.; Waele, M. D.; Wolf, D. D. Myocardial infarction in a neonate with hereditary antithrombin III deficiency. *Acta Paediatrica* **1993**, *82* (6-7), 610–613. DOI: https://doi.org/10.1111/j.1651-2227.1993.tb12770.x.
(85) Saker, D. M.; Walsh-Sukys, M.; Spector, M.; Zahka, K. G. Cardiac Recovery and Survival After Neonatal Myocardial Infarction. *Pediatric Cardiology* **1997**, *18* (2), 139–142. DOI: 10.1007/s002469900133.
(86) Cesna, S.; Eicken, A.; Juenger, H.; Hess, J. Successful treatment of a newborn with acute myocardial infarction on the first day of life. *Pediatr Cardiol* **2013**, *34* (8), 1868–1870. DOI: 10.1007/s00246-012-0417-2 From NLM.

(87) Deutsch, M. A.; Cleuziou, J.; Noebauer, C.; Eicken, A.; Vogt, M.; Hoerer, J.; Lange, R.; Schreiber, C. Successful management of neonatal myocardial infarction with ECMO and intracoronary r-tPA lysis. *Congenit Heart Dis* **2014**, *9* (5), E169–174. DOI: 10.1111/chd.12117 From NLM.
(88) Haubner, B. J.; Schneider, J.; Schweigmann, U.; Schuetz, T.; Dichtl, W.; Velik-Salchner, C.; Stein, J.-I.; Penninger, J. M. Functional Recovery of a Human Neonatal Heart After Severe Myocardial Infarction. *Circulation Research* **2016**, *118* (2), 216–221. DOI: doi:10.1161/CIRCRESAHA.115.307017.
(89) Weinberger, M.; Riley, P. R. Animal models to study cardiac regeneration. *Nature Reviews Cardiology* **2024**, *21* (2), 89–105. DOI: 10.1038/s41569-023-00914-x.
(90) Porrello, E. R.; Mahmoud, A. I.; Simpson, E.; Hill, J. A.; Richardson, J. A.; Olson, E. N.; Sadek, H. A. Transient regenerative potential of the neonatal mouse heart. *Science* **2011**, *331* (6020), 1078–1080. DOI: 10.1126/science.1200708 From NLM.
(91) Angelone, D. F.; Wessels, M. R.; Coughlin, M.; Suter, E. E.; Valentini, P.; Kalish, L. A.; Levy, O. Innate immunity of the human newborn is polarized toward a high ratio of IL-6/TNF-$\alpha$ production in vitro and in vivo. *Pediatric research* **2006**, *60* (2), 205–209.
(92) Gordon, A.; Kozin, E. D.; Keswani, S. G.; Vaikunth, S. S.; Katz, A. B.; Zoltick, P. W.; Favata, M.; Radu, A. P.; Soslowsky, L. J.; Herlyn, M. Permissive environment in postnatal wounds induced by adenoviral-mediated overexpression of the anti-inflammatory cytokine interleukin-10 prevents scar formation. *Wound repair and regeneration* **2008**, *16* (1), 70–79.
(93) Lorant, D. E.; Li, W.; Tabatabaei, N.; Garver, M. K.; Albertine, K. H. P-selectin expression by endothelial cells is decreased in neonatal rats and human premature infants. *Blood, The Journal of the American Society of Hematology* **1999**, *94* (2), 600–609.
(94) Sattler, S.; Rosenthal, N. The neonate versus adult mammalian immune system in cardiac repair and regeneration. *Biochimica et Biophysica Acta (BBA) - Molecular Cell Research* **2016**, *1863* (7, Part B), 1813–1821. DOI: https://doi.org/10.1016/j.bbamcr.2016.01.011.
(95) Peng, H.; Shindo, K.; Donahue, R. R.; Gao, E.; Ahern, B. M.; Levitan, B. M.; Tripathi, H.; Powell, D.; Noor, A.; Elmore, G. A. Adult spiny mice (Acomys) exhibit endogenous cardiac recovery in response to myocardial infarction. *NPJ Regenerative Medicine* **2021**, *6* (1), 74.
(96) Qi, Y.; Dasa, O.; Maden, M.; Vohra, R.; Batra, A.; Walter, G.; Yarrow, J. F.; Aranda Jr, J. M.; Raizada, M. K.; Pepine, C. J. Functional heart recovery in an adult mammal, the spiny mouse. *International Journal of Cardiology* **2021**, *338*, 196–203.
(97) Poss, K. D.; Wilson, L. G.; Keating, M. T. Heart Regeneration in Zebrafish. *Science* **2002**, *298* (5601), 2188–2190. DOI: doi:10.1126/science.1077857.
(98) Lai, S.-L.; Marín-Juez, R.; Moura, P. L.; Kuenne, C.; Lai, J. K. H.; Tsedeke, A. T.; Guenther, S.; Looso, M.; Stainier, D. Y. R. Reciprocal analyses in zebrafish and medaka reveal that harnessing the immune response promotes cardiac regeneration. *eLife* **2017**, *6*, e25605. DOI: 10.7554/eLife.25605.
(99) Stockdale, W. T.; Lemieux, M. E.; Killen, A. C.; Zhao, J.; Hu, Z.; Riepsaame, J.; Hamilton, N.; Kudoh, T.; Riley, P. R.; van Aerle, R.; et al. Heart Regeneration in the Mexican Cavefish. *Cell Reports* **2018**, *25* (8), 1997–2007.e1997. DOI: https://doi.org/10.1016/j.celrep.2018.10.072.
(100) Riddle, M. R.; Aspiras, A. C.; Gaudenz, K.; Peuß, R.; Sung, J. Y.; Martineau, B.; Peavey, M.; Box, A. C.; Tabin, J. A.; McGaugh, S.; et al. Insulin resistance in cavefish as an adaptation to a nutrient-limited environment. *Nature* **2018**, *555* (7698), 647–651. DOI: 10.1038/nature26136.

(101) Panahi, M.; Papanikolaou, A.; Torabi, A.; Zhang, J.-G.; Khan, H.; Vazir, A.; Hasham, M. G.; Cleland, J. G. F.; Rosenthal, N. A.; Harding, S. E.; et al. Immunomodulatory interventions in myocardial infarction and heart failure: a systematic review of clinical trials and meta-analysis of IL-1 inhibition. *Cardiovascular Research* **2018**, *114* (11), 1445–1461. DOI: 10.1093/cvr/cvy145 (accessed 9/8/2025).
(102) Aspelund, A.; Robciuc, M. R.; Karaman, S.; Makinen, T.; Alitalo, K. Lymphatic System in Cardiovascular Medicine. *Circ Res* **2016**, *118* (3), 515–530. DOI: 10.1161/circresaha.115.306544 From NLM.
(103) Baluk , P.; Fuxe , J.; Hashizume , H.; Romano , T.; Lashnits , E.; Butz , S.; Vestweber , D.; Corada , M.; Molendini , C.; Dejana , E.; et al. Functionally specialized junctions between endothelial cells of lymphatic vessels. *Journal of Experimental Medicine* **2007**, *204* (10), 2349–2362. DOI: 10.1084/jem.20062596 (accessed 5/27/2025).
(104) Karkkainen, M. J.; Haiko, P.; Sainio, K.; Partanen, J.; Taipale, J.; Petrova, T. V.; Jeltsch, M.; Jackson, D. G.; Talikka, M.; Rauvala, H.; et al. Vascular endothelial growth factor C is required for sprouting of the first lymphatic vessels from embryonic veins. *Nature Immunology* **2004**, *5* (1), 74–80. DOI: 10.1038/ni1013.
(105) Secker, G. A.; Harvey, N. L. VEGFR signaling during lymphatic vascular development: From progenitor cells to functional vessels. *Developmental Dynamics* **2015**, *244* (3), 323–331. DOI: https://doi.org/10.1002/dvdy.24227.
(106) Balasubbramanian, D.; Mitchell, B. M. Lymphatics in Cardiovascular Physiology. *Cold Spring Harb Perspect Med* **2022**, *12* (8). DOI: 10.1101/cshperspect.a041173 From NLM.
(107) Vieira, J. M.; Norman, S.; Villa del Campo, C.; Cahill, T. J.; Barnette, D. N.; Gunadasa-Rohling, M.; Johnson, L. A.; Greaves, D. R.; Carr, C. A.; Jackson, D. G.; et al. The cardiac lymphatic system stimulates resolution of inflammation following myocardial infarction. *The Journal of Clinical Investigation* **2018**, *128* (8), 3402–3412. DOI: 10.1172/JCI97192.
(108) Novartis. *Novartis announces FDA approval of Gilenya® as the first disease-modifying therapy for pediatric relapsing multiple sclerosis*. 2018. https://www.novartis.com/news/media-releases/novartis-announces-fda-approval-gilenya-first-disease-modifying-therapy-pediatric-relapsing-multiple-sclerosis (accessed 2025).
(109) Fujita, T.; Inoue, K.; Yamamoto, S.; Ikumoto, T.; Sasaki, S.; Toyama, R.; Chiba, K.; Hoshino, Y.; Okumoto, T. Fungal metabolites. Part 11. A potent immunosuppressive activity found in Isaria sinclairii metabolite. *J Antibiot (Tokyo)* **1994**, *47* (2), 208–215. DOI: 10.7164/antibiotics.47.208 From NLM.
(110) Tetsuro Fujita, K. I., Satoshi Yamamoto, Takeshi Ikumoto,; Shigeo Sasaki, R. T., Masahiko Yoneta, Kenji Chiba, Yukio Hoshino and Takeki Okumoto. FUNGAL METABOLITES. Part 12. POTENT IMMUNOSUPPRESSANT,

1 4-DEOXOMYRIOGIN, (2*S*,3*R*,4*R*)-(*E*)AMINO-3,4-DIHYDROXY-2-HYDROXYMETHYLEICOS-6-ENOIC ACID AND STRUCTUREACTIVITY RELATIONSHIPS OF MYRIOCIN DERIVATIVES. *The Journal of antibiotics* **1994**, *47* (2), 216–224.
(111) Sasaki, S.; Hashimoto, R.; Kiuchi, M.; Inoue, K.; Ikumoto, T.; Hirose, R.; Chiba, K.; Hoshino, Y.; Okumoto, T.; Fujita, T. Fungal metabolites. Part 14. Novel potent immunosuppressants, mycestericins, produced by Mycelia sterilia. *J Antibiot (Tokyo)* **1994**, *47* (4), 420–433. DOI: 10.7164/antibiotics.47.420 From NLM.
(112) Fujita, T.; Yoneta, M.; Hirose, R.; Sasaki, S.; Inoue, K.; Kiuchi, M.; Hirase, S.; Adachi, K.; Arita, M.; Chiba, K. Simple compounds, 2-alkyl-2-amino-1,3-propanediols have potent

immunosuppressive activity. *Bioorganic & Medicinal Chemistry Letters* **1995**, *5* (8), 847–852. DOI: https://doi.org/10.1016/0960-894X(95)00126-E.
(113) Fujita, T.; Hirose, R.; Yoneta, M.; Sasaki, S.; Inoue, K.; Kiuchi, M.; Hirase, S.; Chiba, K.; Sakamoto, H.; Arita, M. Potent Immunosuppressants, 2-Alkyl-2-aminopropane-1,3-diols. *Journal of Medicinal Chemistry* **1996**, *39* (22), 4451–4459. DOI: 10.1021/jm9603911.
(114) Adachi, K.; Kohara, T.; Nakao, N.; Arita, M.; Chiba, K.; Mishina, T.; Sasaki, S.; Fujita, T. Design, synthesis, and structure-activity relationships of 2-substituted-2-amino-1,3-propanediols: Discovery of a novel immunosuppressant, FTY720. *Bioorganic & Medicinal Chemistry Letters* **1995**, *5* (8), 853–856. DOI: https://doi.org/10.1016/0960-894X(95)00127-F.
(115) Chiba, K.; Yanagawa, Y.; Masubuchi, Y.; Kataoka, H.; Kawaguchi, T.; Ohtsuki, M.; Hoshino, Y. FTY720, a novel immunosuppressant, induces sequestration of circulating mature lymphocytes by acceleration of lymphocyte homing in rats. I. FTY720 selectively decreases the number of circulating mature lymphocytes by acceleration of lymphocyte homing. *J Immunol* **1998**, *160* (10), 5037–5044. From NLM.
(116) Yanagawa, Y.; Sugahara, K.; Kataoka, H.; Kawaguchi, T.; Masubuchi, Y.; Chiba, K. FTY720, a novel immunosuppressant, induces sequestration of circulating mature lymphocytes by acceleration of lymphocyte homing in rats. II. FTY720 prolongs skin allograft survival by decreasing T cell infiltration into grafts but not cytokine production in vivo. *J Immunol* **1998**, *160* (11), 5493–5499. From NLM.
(117) Brinkmann, V.; Davis, M. D.; Heise, C. E.; Albert, R.; Cottens, S.; Hof, R.; Bruns, C.; Prieschl, E.; Baumruker, T.; Hiestand, P.; et al. The immune modulator FTY720 targets sphingosine 1-phosphate receptors. *J Biol Chem* **2002**, *277* (24), 21453–21457. DOI: 10.1074/jbc.C200176200 From NLM.
(118) Albert, R.; Hinterding, K.; Brinkmann, V.; Guerini, D.; Müller-Hartwieg, C.; Knecht, H.; Simeon, C.; Streiff, M.; Wagner, T.; Welzenbach, K.; et al. Novel immunomodulator FTY720 is phosphorylated in rats and humans to form a single stereoisomer. Identification, chemical proof, and biological characterization of the biologically active species and its enantiomer. *J Med Chem* **2005**, *48* (16), 5373–5377. DOI: 10.1021/jm050242f From NLM.
(119) Paugh, S. W.; Payne, S. G.; Barbour, S. E.; Milstien, S.; Spiegel, S. The immunosuppressant FTY720 is phosphorylated by sphingosine kinase type 2. *FEBS Lett* **2003**, *554* (1-2), 189–193. DOI: 10.1016/s0014-5793(03)01168-2 From NLM.
(120) Mechtcheriakova, D.; Wlachos, A.; Sobanov, J.; Bornancin, F.; Zlabinger, G.; Baumruker, T.; Billich, A. FTY720-phosphate is dephosphorylated by lipid phosphate phosphatase 3. *FEBS Lett* **2007**, *581* (16), 3063–3068. DOI: 10.1016/j.febslet.2007.05.069 From NLM.
(121) Budde, K.; Schütz, M.; Glander, P.; Peters, H.; Waiser, J.; Liefeldt, L.; Neumayer, H.-H.; Böhler, T. FTY720 (fingolimod) in renal transplantation. *Clinical Transplantation* **2006**, *20* (s17), 17–24. DOI: https://doi.org/10.1111/j.1399-0012.2006.00596.x.
(122) Foster, C. A.; Howard, L. M.; Schweitzer, A.; Persohn, E.; Hiestand, P. C.; Balatoni, B.; Reuschel, R.; Beerli, C.; Schwartz, M.; Billich, A. Brain Penetration of the Oral Immunomodulatory Drug FTY720 and Its Phosphorylation in the Central Nervous System during Experimental Autoimmune Encephalomyelitis: Consequences for Mode of Action in Multiple Sclerosis. *The Journal of Pharmacology and Experimental Therapeutics* **2007**, *323* (2), 469–476. DOI: 10.1124/jpet.107.127183 (accessed 2025/09/08).
(123) Balatoni, B.; Storch, M. K.; Swoboda, E. M.; Schönborn, V.; Koziel, A.; Lambrou, G. N.; Hiestand, P. C.; Weissert, R.; Foster, C. A. FTY720 sustains and restores neuronal function

in the DA rat model of MOG-induced experimental autoimmune encephalomyelitis. *Brain Res Bull* **2007**, *74* (5), 307–316. DOI: 10.1016/j.brainresbull.2007.06.023 From NLM.
(124) Fujino, M.; Funeshima, N.; Kitazawa, Y.; Kimura, H.; Amemiya, H.; Suzuki, S.; Li, X. K. Amelioration of experimental autoimmune encephalomyelitis in Lewis rats by FTY720 treatment. *J Pharmacol Exp Ther* **2003**, *305* (1), 70–77. DOI: 10.1124/jpet.102.045658 From NLM.
(125) Khatri, B.; Barkhof, F.; Comi, G.; Jin, J.; Francis, G.; Cohen, J. Fingolimod Treatment Increases the Proportion of Patients Who Are Free from Disease Activity in Multiple Sclerosis Compared to IFN-b1a: Results from a Phase 3, Active-Controlled Study (TRANSFORMS) (PD5.006). *Neurology* **2012**, *78* (1_supplement), PD5.006–PD005.006. DOI: doi:10.1212/WNL.78.1_supplement.PD5.006.
(126) O'Connor, P.; Comi, G.; Montalban, X.; Antel, J.; Radue, E. W.; de Vera, A.; Pohlmann, H.; Kappos, L. Oral fingolimod (FTY720) in multiple sclerosis: two-year results of a phase II extension study. *Neurology* **2009**, *72* (1), 73–79. DOI: 10.1212/01.wnl.0000338569.32367.3d From NLM.
(127) Kappos, L.; Antel, J.; Comi, G.; Montalban, X.; O'Connor, P.; Polman, C. H.; Haas, T.; Korn, A. A.; Karlsson, G.; Radue, E. W. Oral fingolimod (FTY720) for relapsing multiple sclerosis. *N Engl J Med* **2006**, *355* (11), 1124–1140. DOI: 10.1056/NEJMoa052643 From NLM.
(128) Hla, T. Physiological and pathological actions of sphingosine 1-phosphate. *Semin Cell Dev Biol* **2004**, *15* (5), 513–520. DOI: 10.1016/j.semcdb.2004.05.002 From NLM.
(129) Windh, R. T.; Lee, M.-J.; Hla, T.; An, S.; Barr, A. J.; Manning, D. R. Differential Coupling of the Sphingosine 1-Phosphate Receptors Edg-1, Edg-3, and H218/Edg-5 to the G<sub>i</sub>, G<sub>q</sub>, and G<sub>12</sub> Families of Heterotrimeric G Proteins *. *Journal of Biological Chemistry* **1999**, *274* (39), 27351–27358. DOI: 10.1074/jbc.274.39.27351 (accessed 2025/09/08).
(130) Mandala, S.; Hajdu, R.; Bergstrom, J.; Quackenbush, E.; Xie, J.; Milligan, J.; Thornton, R.; Shei, G.-J.; Card, D.; Keohane, C.; et al. Alteration of Lymphocyte Trafficking by Sphingosine-1-Phosphate Receptor Agonists. *Science* **2002**, *296* (5566), 346–349. DOI: doi:10.1126/science.1070238.
(131) Reeves, P. M.; Kang, Y.-L.; Kirchhausen, T. Endocytosis of Ligand-Activated Sphingosine 1-Phosphate Receptor 1 Mediated by the Clathrin-Pathway. *Traffic* **2016**, *17* (1), 40–52. DOI: https://doi.org/10.1111/tra.12343.
(132) Kono, M.; Mi, Y.; Liu, Y.; Sasaki, T.; Allende, M. L.; Wu, Y.-P.; Yamashita, T.; Proia, R. L. The Sphingosine-1-phosphate Receptors S1P<sub>1</sub>, S1P<sub>2</sub>, and S1P<sub>3</sub> Function Coordinately during Embryonic Angiogenesis *. *Journal of Biological Chemistry* **2004**, *279* (28), 29367–29373. DOI: 10.1074/jbc.M403937200 (accessed 2025/09/08).
(133) Mizugishi, K.; Yamashita, T.; Olivera, A.; Miller, G. F.; Spiegel, S.; Proia, R. L. Essential Role for Sphingosine Kinases in Neural and Vascular Development. *Molecular and Cellular Biology* **2005**, *25* (24), 11113–11121. DOI: 10.1128/MCB.25.24.11113-11121.2005.
(134) Forrest, M.; Sun, S. Y.; Hajdu, R.; Bergstrom, J.; Card, D.; Doherty, G.; Hale, J.; Keohane, C.; Meyers, C.; Milligan, J.; et al. Immune Cell Regulation and Cardiovascular Effects of Sphingosine 1-Phosphate Receptor Agonists in Rodents Are Mediated via Distinct Receptor Subtypes. *The Journal of Pharmacology and Experimental Therapeutics* **2004**, *309* (2), 758–768. DOI: 10.1124/jpet.103.062828 (accessed 2025/09/08).
(135) Walter, D. H.; Rochwalsky, U.; Reinhold, J.; Seeger, F.; Aicher, A.; Urbich, C.; Spyridopoulos, I.; Chun, J.; Brinkmann, V.; Keul, P.; et al. Sphingosine-1-Phosphate

Stimulates the Functional Capacity of Progenitor Cells by Activation of the CXCR<sub>4</sub>-Dependent Signaling Pathway via the S1P<sub>3</sub> Receptor. *Arteriosclerosis, Thrombosis, and Vascular Biology* **2007**, *27* (2), 275–282. DOI: doi:10.1161/01.ATV.0000254669.12675.70.

(136) Levkau, B.; Hermann, S.; Theilmeier, G.; van der Giet, M.; Chun, J.; Schober, O.; Schäfers, M. High-Density Lipoprotein Stimulates Myocardial Perfusion In Vivo. *Circulation* **2004**, *110* (21), 3355–3359. DOI: 10.1161/01.CIR.0000147827.43912.AE (accessed 2025/09/08).

(137) Keller, C. D.; Rivera Gil, P.; Tölle, M.; van der Giet, M.; Chun, J.; Radeke, H. H.; Schäfer-Korting, M.; Kleuser, B. Immunomodulator FTY720 Induces Myofibroblast Differentiation via the Lysophospholipid Receptor S1P<sub>3</sub> and Smad3 Signaling. *The American Journal of Pathology* **2007**, *170* (1), 281–292. DOI: 10.2353/ajpath.2007.060485 (accessed 2025/09/08).

(138) Graeler, M.; Goetzl, E. J. Activation-regulated expression and chemotactic function of sphingosine 1-phosphate receptors in mouse splenic T cells. *The FASEB Journal* **2002**, *16* (14), 1874–1878. DOI: https://doi.org/10.1096/fj.02-0548com.

(139) Wang, W.; Graeler, M. H.; Goetzl, E. J. Type 4 sphingosine 1-phosphate G protein-coupled receptor (S1P4) transduces S1P effects on T cell proliferation and cytokine secretion without signaling migration. *The FASEB Journal* **2005**, *19* (12), 1731–1733. DOI: https://doi.org/10.1096/fj.05-3730fje.

(140) Malek, R. L.; Toman, R. E.; Edsall, L. C.; Wong, S.; Chiu, J.; Letterle, C. A.; Van Brocklyn, J. R.; Milstien, S.; Spiegel, S.; Lee, N. H. Nrg-1 Belongs to the Endothelial Differentiation Gene Family of G Protein-coupled Sphingosine-1-phosphate Receptors *. *Journal of Biological Chemistry* **2001**, *276* (8), 5692–5699. DOI: 10.1074/jbc.M003964200 (accessed 2025/09/08).

(141) Im, D.-S.; Heise, C. E.; Ancellin, N.; O'Dowd, B. F.; Shei, G.-j.; Heavens, R. P.; Rigby, M. R.; Hla, T.; Mandala, S.; McAllister, G.; et al. Characterization of a Novel Sphingosine 1-Phosphate Receptor, Edg-8 *. *Journal of Biological Chemistry* **2000**, *275* (19), 14281–14286. DOI: 10.1074/jbc.275.19.14281 (accessed 2025/09/08).

(142) Walzer, T.; Chiossone, L.; Chaix, J.; Calver, A.; Carozzo, C.; Garrigue-Antar, L.; Jacques, Y.; Baratin, M.; Tomasello, E.; Vivier, E. Natural killer cell trafficking in vivo requires a dedicated sphingosine 1-phosphate receptor. *Nature Immunology* **2007**, *8* (12), 1337–1344. DOI: 10.1038/ni1523.

(143) van Doorn, R.; Lopes Pinheiro, M. A.; Kooij, G.; Lakeman, K.; van het Hof, B.; van der Pol, S. M.; Geerts, D.; van Horssen, J.; van der Valk, P.; van der Kam, E.; et al. Sphingosine 1-phosphate receptor 5 mediates the immune quiescence of the human brain endothelial barrier. *J Neuroinflammation* **2012**, *9*, 133. DOI: 10.1186/1742-2094-9-133 From NLM.

(144) Gesualdo, C.; Balta, C.; Platania, C. B. M.; Trotta, M. C.; Herman, H.; Gharbia, S.; Rosu, M.; Petrillo, F.; Giunta, S.; Della Corte, A.; et al. Fingolimod and Diabetic Retinopathy: A Drug Repurposing Study. *Frontiers in Pharmacology* **2021**, *Volume 12 - 2021*, Original Research. DOI: 10.3389/fphar.2021.718902.

(145) di Nuzzo, L.; Orlando, R.; Tognoli, C.; Di Pietro, P.; Bertini, G.; Miele, J.; Bucci, D.; Motolese, M.; Scaccianoce, S.; Caruso, A.; et al. Antidepressant activity of fingolimod in mice. *Pharmacology Research & Perspectives* **2015**, *3* (3), e00135. DOI: https://doi.org/10.1002/prp2.135.

(146) Pournajaf, S.; Dargahi, L.; Javan, M.; Pourgholami, M. H. Molecular Pharmacology and Novel Potential Therapeutic Applications of Fingolimod. *Frontiers in Pharmacology* **2022**, *Volume 13 - 2022*, Review. DOI: 10.3389/fphar.2022.807639.
(147) Martín-Montañez, E.; Pavia, J.; Valverde, N.; Boraldi, F.; Lara, E.; Oliver, B.; Hurtado-Guerrero, I.; Fernandez, O.; Garcia-Fernandez, M. The S1P mimetic fingolimod phosphate regulates mitochondrial oxidative stress in neuronal cells. *Free Radical Biology and Medicine* **2019**, *137*, 116–130. DOI: https://doi.org/10.1016/j.freeradbiomed.2019.04.022.
(148) Newton, J.; Hait, N. C.; Maceyka, M.; Colaco, A.; Maczis, M.; Wassif, C. A.; Cougnoux, A.; Porter, F. D.; Milstien, S.; Platt, N.; et al. FTY720/fingolimod increases NPC1 and NPC2 expression and reduces cholesterol and sphingolipid accumulation in Niemann-Pick type C mutant fibroblasts. *The FASEB Journal* **2017**, *31* (4), 1719–1730. DOI: https://doi.org/10.1096/fj.201601041R.
(149) **Lobaina M, S. E.** *Fingolimod*; StatPearls, 2024.
(150) Cohen, J. A.; Chun, J. Mechanisms of fingolimod's efficacy and adverse effects in multiple sclerosis. *Annals of Neurology* **2011**, *69* (5), 759–777. DOI: https://doi.org/10.1002/ana.22426.
(151) Rae-Grant, A.; Day, G. S.; Marrie, R. A.; Rabinstein, A.; Cree, B. A. C.; Gronseth, G. S.; Haboubi, M.; Halper, J.; Hosey, J. P.; Jones, D. E.; et al. Practice guideline recommendations summary: Disease-modifying therapies for adults with multiple sclerosis: Report of the Guideline Development, Dissemination, and Implementation Subcommittee of the American Academy of Neurology. *Neurology* **2018**, *90* (17), 777–788. DOI: 10.1212/wnl.0000000000005347 From NLM.
(152) Cervera, C. [Infections and fingolimod]. *Rev Neurol* **2012**, *55* (4), 227–237. From NLM.
(153) Ziemssen, T.; Lang, M.; Schmidt, S.; Albrecht, H.; Klotz, L.; Haas, J.; Lassek, C.; Lang, S.; Winkelmann, V. E.; Ettle, B.; et al. Long-term real-world effectiveness and safety of fingolimod over 5 years in Germany. *J Neurol* **2022**, *269* (6), 3276–3285. DOI: 10.1007/s00415-021-10931-w From NLM.
(154) Lindå, H.; von Heijne, A. A case of posterior reversible encephalopathy syndrome associated with gilenya(®) (fingolimod) treatment for multiple sclerosis. *Front Neurol* **2015**, *6*, 39. DOI: 10.3389/fneur.2015.00039 From NLM.
(155) Berger, J. R.; Cree, B. A.; Greenberg, B.; Hemmer, B.; Ward, B. J.; Dong, V. M.; Merschhemke, M. Progressive multifocal leukoencephalopathy after fingolimod treatment. *Neurology* **2018**, *90* (20), e1815–e1821. DOI: 10.1212/wnl.0000000000005529 From NLM.
(156) Koyrakh, L.; Roman, M. I.; Brinkmann, V.; Wickman, K. The Heart Rate Decrease Caused by Acute FTY720 Administration Is Mediated by the G Protein-Gated Potassium Channel IKACh. *American Journal of Transplantation* **2005**, *5* (3), 529–536. DOI: https://doi.org/10.1111/j.1600-6143.2005.00754.x.
(157) Mandal, P.; Gupta, A.; Fusi-Rubiano, W.; Keane, P. A.; Yang, Y. Fingolimod: therapeutic mechanisms and ocular adverse effects. *Eye (Lond)* **2017**, *31* (2), 232–240. DOI: 10.1038/eye.2016.258 From NLM.
(158) Ledgerwood, L. G.; Lal, G.; Zhang, N.; Garin, A.; Esses, S. J.; Ginhoux, F.; Merad, M.; Peche, H.; Lira, S. A.; Ding, Y.; et al. The sphingosine 1-phosphate receptor 1 causes tissue retention by inhibiting the entry of peripheral tissue T lymphocytes into afferent lymphatics. *Nature Immunology* **2008**, *9* (1), 42–53. DOI: 10.1038/ni1534.
(159) Shang, K.; He, J.; Zou, J.; Qin, C.; Lin, L.; Zhou, L. Q.; Yang, L. L.; Wu, L. J.; Wang, W.; Zhan, K. B.; et al. Fingolimod promotes angiogenesis and attenuates ischemic brain damage

via modulating microglial polarization. *Brain Res* **2020**, *1726*, 146509. DOI: 10.1016/j.brainres.2019.146509 From NLM.
(160) Gaengel, K.; Niaudet, C.; Hagikura, K.; Laviña, B.; Muhl, L.; Hofmann, Jennifer J.; Ebarasi, L.; Nyström, S.; Rymo, S.; Chen, Long L.; et al. The Sphingosine-1-Phosphate Receptor S1PR1 Restricts Sprouting Angiogenesis by Regulating the Interplay between VE-Cadherin and VEGFR2. *Developmental Cell* **2012**, *23* (6), 1264. DOI: https://doi.org/10.1016/j.devcel.2012.11.007.
(161) Alitalo, K.; Carmeliet, P. Molecular mechanisms of lymphangiogenesis in health and disease. *Cancer Cell* **2002**, *1* (3), 219–227. DOI: https://doi.org/10.1016/S1535-6108(02)00051-X.
(162) Zhu, Z.; Fu, Y.; Tian, D.; Sun, N.; Han, W.; Chang, G.; Dong, Y.; Xu, X.; Liu, Q.; Huang, D.; et al. Combination of the Immune Modulator Fingolimod With Alteplase in Acute Ischemic Stroke. *Circulation* **2015**, *132* (12), 1104–1112. DOI: doi:10.1161/CIRCULATIONAHA.115.016371.
(163) Fu, Y.; Zhang, N.; Ren, L.; Yan, Y.; Sun, N.; Li, Y.-J.; Han, W.; Xue, R.; Liu, Q.; Hao, J.; et al. Impact of an immune modulator fingolimod on acute ischemic stroke. *Proceedings of the National Academy of Sciences* **2014**, *111* (51), 18315–18320. DOI: doi:10.1073/pnas.1416166111.
(164) Taylor, L.; Christou, I.; Kapellos, T. S.; Buchan, A.; Brodermann, M. H.; Gianella-Borradori, M.; Russell, A.; Iqbal, A. J.; Greaves, D. R. Primary Macrophage Chemotaxis Induced by Cannabinoid Receptor 2 Agonists Occurs Independently of the CB2 Receptor. *Scientific Reports* **2015**, *5* (1), 10682. DOI: 10.1038/srep10682.
(165) Machleidt, T.; Woodroofe, C. C.; Schwinn, M. K.; Méndez, J.; Robers, M. B.; Zimmerman, K.; Otto, P.; Daniels, D. L.; Kirkland, T. A.; Wood, K. V. NanoBRET—A Novel BRET Platform for the Analysis of Protein–Protein Interactions. *ACS Chemical Biology* **2015**, *10* (8), 1797–1804. DOI: 10.1021/acschembio.5b00143.
(166) Jasper, J. R.; Lesnick, J. D.; Chang, L. K.; Yamanishi, S. S.; Chang, T. K.; Hsu, S. A. O.; Daunt, D. A.; Bonhaus, D. W.; Eglen, R. M. Ligand Efficacy and Potency at Recombinant $\alpha$2 Adrenergic Receptors: Agonist-Mediated [35s]gtp$\gamma$s Binding. *Biochemical Pharmacology* **1998**, *55* (7), 1035–1043. DOI: https://doi.org/10.1016/S0006-2952(97)00631-X.
(167) Handl, H. L.; Vagner, J.; Yamamura, H. I.; Hruby, V. J.; Gillies, R. J. Lanthanide-based time-resolved fluorescence of in cyto ligand-receptor interactions. *Anal Biochem* **2004**, *330* (2), 242–250. DOI: 10.1016/j.ab.2004.04.012 From NLM.
(168) Savitski, M. M.; Reinhard, F. B. M.; Franken, H.; Werner, T.; Savitski, M. F.; Eberhard, D.; Molina, D. M.; Jafari, R.; Dovega, R. B.; Klaeger, S.; et al. Tracking cancer drugs in living cells by thermal profiling of the proteome. *Science* **2014**, *346* (6205), 1255784. DOI: doi:10.1126/science.1255784.
(169) Gaetani, M.; Sabatier, P.; Saei, A. A.; Beusch, C. M.; Yang, Z.; Lundström, S. L.; Zubarev, R. A. Proteome Integral Solubility Alteration: A High-Throughput Proteomics Assay for Target Deconvolution. *Journal of Proteome Research* **2019**, *18* (11), 4027–4037. DOI: 10.1021/acs.jproteome.9b00500.
(170) Takakusagi, Y.; Takakusagi, K.; Sakaguchi, K.; Sugawara, F. Phage display technology for target determination of small-molecule therapeutics: an update. *Expert Opinion on Drug Discovery* **2020**, *15* (10), 1199–1211. DOI: 10.1080/17460441.2020.1790523.
(171) Wang, H.; Liu, L.; Zhang, Z.; Li, C.; Wang, K.; Gao, J.; Hu, Q.; Wang, W.; Li, H. Insights of affinity-based probes for target identification in drug discovery. *European Journal of Medicinal Chemistry* **2025**, *293*, 117711. DOI: https://doi.org/10.1016/j.ejmech.2025.117711.

(172) Chen, X.; Wong, Y. K.; Wang, J.; Zhang, J.; Lee, Y. M.; Shen, H. M.; Lin, Q.; Hua, Z. C. Target identification with quantitative activity based protein profiling (ABPP). *Proteomics* **2017**, *17* (3-4). DOI: 10.1002/pmic.201600212 From NLM.
(173) Anders, L.; Guenther, M. G.; Qi, J.; Fan, Z. P.; Marineau, J. J.; Rahl, P. B.; Lovén, J.; Sigova, A. A.; Smith, W. B.; Lee, T. I.; et al. Genome-wide localization of small molecules. *Nat Biotechnol* **2014**, *32* (1), 92–96. DOI: 10.1038/nbt.2776 From NLM.
(174) Tabei, Y.; Pauwels, E.; Stoven, V.; Takemoto, K.; Yamanishi, Y. Identification of chemogenomic features from drug-target interaction networks using interpretable classifiers. *Bioinformatics* **2012**, *28* (18), i487–i494. DOI: 10.1093/bioinformatics/bts412 From NLM.
(175) Kuhn, M.; Al Banchaabouchi, M.; Campillos, M.; Jensen, L. J.; Gross, C.; Gavin, A. C.; Bork, P. Systematic identification of proteins that elicit drug side effects. *Mol Syst Biol* **2013**, *9*, 663. DOI: 10.1038/msb.2013.10 From NLM.
(176) Takigawa, I.; Tsuda, K.; Mamitsuka, H. Mining Significant Substructure Pairs for Interpreting Polypharmacology in Drug-Target Network. *PLOS ONE* **2011**, *6* (2), e16999. DOI: 10.1371/journal.pone.0016999.
(177) Ruoho, A. E.; Kiefer, H.; Roeder, P. E.; Singer, S. J. The mechanism of photoaffinity labeling. *Proc Natl Acad Sci U S A* **1973**, *70* (9), 2567–2571. DOI: 10.1073/pnas.70.9.2567 From NLM.
(178) Yu, S.-H.; Boyce, M.; Wands, A. M.; Bond, M. R.; Bertozzi, C. R.; Kohler, J. J. Metabolic labeling enables selective photocrosslinking of O-GlcNAc-modified proteins to their binding partners. *Proceedings of the National Academy of Sciences* **2012**, *109* (13), 4834–4839. DOI: doi:10.1073/pnas.1114356109.
(179) Hulce, J. J.; Cognetta, A. B.; Niphakis, M. J.; Tully, S. E.; Cravatt, B. F. Proteome-wide mapping of cholesterol-interacting proteins in mammalian cells. *Nat Methods* **2013**, *10* (3), 259–264. DOI: 10.1038/nmeth.2368 From NLM.
(180) Liu, Y.; Zheng, W.; Zhang, W.; Chen, N.; Liu, Y.; Chen, L.; Zhou, X.; Chen, X.; Zheng, H.; Li, X. Photoaffinity labeling of transcription factors by DNA-templated crosslinking. *Chemical Science* **2015**, *6* (1), 745–751, 10.1039/C4SC01953A. DOI: 10.1039/C4SC01953A.
(181) Müller, R.; Citir, M.; Hauke, S.; Schultz, C. Synthesis and Cellular Labeling of Caged Phosphatidylinositol Derivatives. *Chemistry – A European Journal* **2020**, *26* (2), 384–389. DOI: https://doi.org/10.1002/chem.201903704.
(182) Trowbridge, A. D.; Seath, C. P.; Rodriguez-Rivera, F. P.; Li, B. X.; Dul, B. E.; Schwaid, A. G.; Buksh, B. F.; Geri, J. B.; Oakley, J. V.; Fadeyi, O. O.; et al. Small molecule photocatalysis enables drug target identification via energy transfer. *Proceedings of the National Academy of Sciences* **2022**, *119* (34), e2208077119. DOI: doi:10.1073/pnas.2208077119.
(183) Seath, C. P.; Burton, A. J.; Sun, X.; Lee, G.; Kleiner, R. E.; MacMillan, D. W. C.; Muir, T. W. Tracking chromatin state changes using nanoscale photo-proximity labelling. *Nature* **2023**, *616* (7957), 574–580. DOI: 10.1038/s41586-023-05914-y From NLM.
(184) Geri, J. B.; Oakley, J. V.; Reyes-Robles, T.; Wang, T.; McCarver, S. J.; White, C. H.; Rodriguez-Rivera, F. P.; Parker, D. L., Jr.; Hett, E. C.; Fadeyi, O. O.; et al. Microenvironment mapping via Dexter energy transfer on immune cells. *Science* **2020**, *367* (6482), 1091–1097. DOI: 10.1126/science.aay4106 From NLM.
(185) Bayley, H.; Knowles, J. R. Photogenerated reagents for membrane labeling. 2. Phenylcarbene and adamantylidene formed within the lipid bilayer. *Biochemistry* **1978**, *17* (12), 2420–2423. DOI: 10.1021/bi00605a026 From NLM.

(186) West, A. V.; Muncipinto, G.; Wu, H. Y.; Huang, A. C.; Labenski, M. T.; Jones, L. H.; Woo, C. M. Labeling Preferences of Diazirines with Protein Biomolecules. *J Am Chem Soc* **2021**, *143* (17), 6691–6700. DOI: 10.1021/jacs.1c02509 From NLM.
(187) Modarelli, D. A.; Morgan, S.; Platz, M. S. Carbene formation, hydrogen migration, and fluorescence in the excited states of dialkyldiazirines. *Journal of the American Chemical Society* **1992**, *114* (18), 7034–7041. DOI: 10.1021/ja00044a013.
(188) O'Brien, J. G. K.; Conway, L. P.; Ramaraj, P. K.; Jadhav, A. M.; Jin, J.; Dutra, J. K.; Evers, P.; Masoud, S. S.; Schupp, M.; Saridakis, I.; et al. Mechanistic differences between linear vs. spirocyclic dialkyldiazirine probes for photoaffinity labeling. *Chemical Science* **2024**, *15* (37), 15463–15473, 10.1039/D4SC04238G. DOI: 10.1039/D4SC04238G.
(189) West, A. V.; Amako, Y.; Woo, C. M. Design and Evaluation of a Cyclobutane Diazirine Alkyne Tag for Photoaffinity Labeling in Cells. *Journal of the American Chemical Society* **2022**, *144* (46), 21174–21183. DOI: 10.1021/jacs.2c08257.
(190) Trowbridge, A. D.; Seath, C. P.; Rodriguez-Rivera, F. P.; Li, B. X.; Dul, B. E.; Schwaid, A. G.; Buksh, B. F.; Geri, J. B.; Oakley, J. V.; Fadeyi, O. O.; et al. Small molecule photocatalysis enables drug target identification via energy transfer. *Proc Natl Acad Sci U S A* **2022**, *119* (34), e2208077119. DOI: 10.1073/pnas.2208077119 From NLM.
(191) Oakley, J. V.; Buksh, B. F.; Fernández, D. F.; Oblinsky, D. G.; Seath, C. P.; Geri, J. B.; Scholes, G. D.; MacMillan, D. W. C. Radius measurement via super-resolution microscopy enables the development of a variable radii proximity labeling platform. *Proceedings of the National Academy of Sciences* **2022**, *119* (32), e2203027119. DOI: doi:10.1073/pnas.2203027119.
(192) Stryker, Z. I.; Rajabi, M.; Davis, P. J.; Mousa, S. A. Evaluation of Angiogenesis Assays. *Biomedicines* **2019**, *7* (2), 37.
(193) Goodwin, A. M. In vitro assays of angiogenesis for assessment of angiogenic and anti-angiogenic agents. *Microvascular Research* **2007**, *74* (2), 172–183. DOI: https://doi.org/10.1016/j.mvr.2007.05.006.
(194) Kenyon, B. M.; Voest, E. E.; Chen, C. C.; Flynn, E.; Folkman, J.; D'Amato, R. J. A model of angiogenesis in the mouse cornea. *Invest Ophthalmol Vis Sci* **1996**, *37* (8), 1625–1632. From NLM.
(195) Hirakawa, S.; Hong, Y.-K.; Harvey, N.; Schacht, V.; Matsuda, K.; Libermann, T.; Detmar, M. Identification of Vascular Lineage-Specific Genes by Transcriptional Profiling of Isolated Blood Vascular and Lymphatic Endothelial Cells. *The American Journal of Pathology* **2003**, *162* (2), 575–586. DOI: https://doi.org/10.1016/S0002-9440(10)63851-5.
(196) García-Caballero, M.; Paupert, J.; Blacher, S.; Van de Velde, M.; Quesada, A. R.; Medina, M. A.; Noël, A. Targeting VEGFR-3/-2 signaling pathways with AD0157: a potential strategy against tumor-associated lymphangiogenesis and lymphatic metastases. *Journal of Hematology & Oncology* **2017**, *10* (1), 122. DOI: 10.1186/s13045-017-0484-1.
(197) Bruyère, F.; Melen-Lamalle, L.; Blacher, S.; Roland, G.; Thiry, M.; Moons, L.; Frankenne, F.; Carmeliet, P.; Alitalo, K.; Libert, C.; et al. Modeling lymphangiogenesis in a three-dimensional culture system. *Nature Methods* **2008**, *5* (5), 431–437. DOI: 10.1038/nmeth.1205.
(198) Navin Kumar Verma, S. M. P., Seow Theng Ong, Mobashar Hussain Urf Turabe Fazil, Madhavi Latha Somaraju Chalasani, Praseetha Prasannan et al. *T-Cell Motility*; Humana New York, NY, 2019. DOI: https://doi.org/10.1007/978-1-4939-9036-8.
(199) Oner, A.; Kobold, S. Transwell migration assay to interrogate human CAR-T cell chemotaxis. *STAR Protoc* **2022**, *3* (4), 101708. DOI: 10.1016/j.xpro.2022.101708 From NLM.

(200) Tavernaro, I.; Rodrigo, A. M.; Kandziora, M.; Kuntz, S.; Dernedde, J.; Trautwein, C.; Tacke, F.; Blas-Garcia, A.; Bartneck, M. Modulating Myeloid Immune Cell Migration Using Multivalently Presented Monosaccharide Ligands for Advanced Immunotherapy. *Advanced Therapeutics* **2019**, *2* (12), 1900145. DOI: https://doi.org/10.1002/adtp.201900145.
(201) Brown, M.; Johnson, L. A.; Leone, D. A.; Majek, P.; Vaahtomeri, K.; Senfter, D.; Bukosza, N.; Schachner, H.; Asfour, G.; Langer, B.; et al. Lymphatic exosomes promote dendritic cell migration along guidance cues. *J Cell Biol* **2018**, *217* (6), 2205–2221. DOI: 10.1083/jcb.201612051 From NLM.
(202) Phan, D. T. T.; Wang, X.; Craver, B. M.; Sobrino, A.; Zhao, D.; Chen, J. C.; Lee, L. Y. N.; George, S. C.; Lee, A. P.; Hughes, C. C. W. A vascularized and perfused organ-on-a-chip platform for large-scale drug screening applications. *Lab Chip* **2017**, *17* (3), 511–520. DOI: 10.1039/c6lc01422d From NLM.
(203) Human Induced Pluripotent Stem Cell-Derived Endothelial Cells for Three-Dimensional Microphysiological Systems. *Tissue Engineering Part C: Methods* **2017**, *23* (8), 474–484. DOI: 10.1089/ten.tec.2017.0133.
(204) Osaki, T.; Serrano, J. C.; Kamm, R. D. Cooperative Effects of Vascular Angiogenesis and Lymphangiogenesis. *Regen Eng Transl Med* **2018**, *4* (3), 120–132. DOI: 10.1007/s40883-018-0054-2 From NLM.
(205) Ahn, J.; Cho, C. S.; Cho, S. W.; Kang, J. H.; Kim, S. Y.; Min, D. H.; Song, J. M.; Park, T. E.; Jeon, N. L. Investigation on vascular cytotoxicity and extravascular transport of cationic polymer nanoparticles using perfusable 3D microvessel model. *Acta Biomater* **2018**, *76*, 154–163. DOI: 10.1016/j.actbio.2018.05.041 From NLM.
(206) Polacheck, W. J.; Kutys, M. L.; Yang, J.; Eyckmans, J.; Wu, Y.; Vasavada, H.; Hirschi, K. K.; Chen, C. S. A non-canonical Notch complex regulates adherens junctions and vascular barrier function. *Nature* **2017**, *552* (7684), 258–262. DOI: 10.1038/nature24998.
(207) Kim, S.; Chung, M.; Jeon, N. L. Three-dimensional biomimetic model to reconstitute sprouting lymphangiogenesis in vitro. *Biomaterials* **2016**, *78*, 115–128. DOI: https://doi.org/10.1016/j.biomaterials.2015.11.019.
(208) Cao, X.; Ashfaq, R.; Cheng, F.; Maharjan, S.; Li, J.; Ying, G.; Hassan, S.; Xiao, H.; Yue, K.; Zhang, Y. S. A Tumor-on-a-Chip System with Bioprinted Blood and Lymphatic Vessel Pair. *Advanced Functional Materials* **2019**, *29* (31), 1807173. DOI: https://doi.org/10.1002/adfm.201807173.
(209) Gong, M. M.; Lugo-Cintron, K. M.; White, B. R.; Kerr, S. C.; Harari, P. M.; Beebe, D. J. Human organotypic lymphatic vessel model elucidates microenvironment-dependent signaling and barrier function. *Biomaterials* **2019**, *214*, 119225. DOI: https://doi.org/10.1016/j.biomaterials.2019.119225.
(210) Livak, K. J.; Schmittgen, T. D. Analysis of Relative Gene Expression Data Using Real-Time Quantitative PCR and the 2−ΔΔCT Method. *Methods* **2001**, *25* (4), 402–408. DOI: https://doi.org/10.1006/meth.2001.1262.
(211) Bataille, C. J. R.; Rabbitts, T. H.; Claridge, T. D. W. NMR waterLOGSY as An Assay in Drug Development Programmes for Detecting Protein-Ligand Interactions-NMR waterLOGSY. *Bio Protoc* **2020**, *10* (13), e3666. DOI: 10.21769/BioProtoc.3666 From NLM.
(212) Jha, S. K.; Rauniyar, K.; Jeltsch, M. Key molecules in lymphatic development, function, and identification. *Annals of Anatomy - Anatomischer Anzeiger* **2018**, *219*, 25–34. DOI: https://doi.org/10.1016/j.aanat.2018.05.003.
(213) Kubota, Y.; Kleinman, H. K.; Martin, G. R.; Lawley, T. J. Role of laminin and basement membrane in the morphological differentiation of human endothelial cells into capillary-

like structures. *Journal of Cell Biology* **1988**, *107* (4), 1589–1598. DOI: 10.1083/jcb.107.4.1589 (accessed 3/15/2025).
(214) Lohela, M.; Bry, M.; Tammela, T.; Alitalo, K. VEGFs and receptors involved in angiogenesis versus lymphangiogenesis. *Current Opinion in Cell Biology* **2009**, *21* (2), 154–165. DOI: https://doi.org/10.1016/j.ceb.2008.12.012.
(215) Carpentier, G.; Berndt, S.; Ferratge, S.; Rasband, W.; Cuendet, M.; Uzan, G.; Albanese, P. Angiogenesis Analyzer for ImageJ - A comparative morphometric analysis of "Endothelial Tube Formation Assay" and "Fibrin Bead Assay". *Sci Rep* **2020**, *10* (1), 11568. DOI: 10.1038/s41598-020-67289-8 From NLM.
(216) Zahra, F. T.; Choleva, E.; Sajib, M. S.; Papadimitriou, E.; Mikelis, C. M. In Vitro Spheroid Sprouting Assay of Angiogenesis. *Methods Mol Biol* **2019**, *1952*, 211–218. DOI: 10.1007/978-1-4939-9133-4_17 From NLM.
(217) Leak, L. V.; Jones, M. Lymphangiogenesis in vitro: Formation of lymphatic capillary-like channels from confluent monolayers of lymphatic endothelial cells. *In Vitro Cellular & Developmental Biology - Animal* **1994**, *30* (8), 512–518. DOI: 10.1007/BF02631324.
(218) Pehrsson, M.; Mortensen, J. H.; Manon-Jensen, T.; Bay-Jensen, A.-C.; Karsdal, M. A.; Davies, M. J. Enzymatic cross-linking of collagens in organ fibrosis–resolution and assessment. *Expert Review of Molecular Diagnostics* **2021**, *21* (10), 1049–1064.
(219) Oka, M.; Iwata, C.; Suzuki, H. I.; Kiyono, K.; Morishita, Y.; Watabe, T.; Komuro, A.; Kano, M. R.; Miyazono, K. Inhibition of endogenous TGF-β signaling enhances lymphangiogenesis. *Blood* **2008**, *111* (9), 4571–4579. DOI: 10.1182/blood-2007-10-120337 (accessed 8/25/2025).
(220) Schwalm, S.; Beyer, S.; Hafizi, R.; Trautmann, S.; Geisslinger, G.; Adams, D. R.; Pyne, S.; Pyne, N.; Schaefer, L.; Huwiler, A.; et al. Validation of highly selective sphingosine kinase 2 inhibitors SLM6031434 and HWG-35D as effective anti-fibrotic treatment options in a mouse model of tubulointerstitial fibrosis. *Cell Signal* **2021**, *79*, 109881. DOI: 10.1016/j.cellsig.2020.109881 From NLM.
(221) Kharel, Y.; Morris, E. A.; Congdon, M. D.; Thorpe, S. B.; Tomsig, J. L.; Santos, W. L.; Lynch, K. R. Sphingosine Kinase 2 Inhibition and Blood Sphingosine 1-Phosphate Levels. *J Pharmacol Exp Ther* **2015**, *355* (1), 23–31. DOI: 10.1124/jpet.115.225862 From NLM.
(222) Pijuan, J.; Barceló, C.; Moreno, D. F.; Maiques, O.; Sisó, P.; Marti, R. M.; Macià, A.; Panosa, A. In vitro Cell Migration, Invasion, and Adhesion Assays: From Cell Imaging to Data Analysis. *Frontiers in Cell and Developmental Biology* **2019**, *7*, Protocols. DOI: 10.3389/fcell.2019.00107.
(223) Xiong, Y.; Brinkman, C. C.; Famulski, K. S.; Mongodin, E. F.; Lord, C. J.; Hippen, K. L.; Blazar, B. R.; Bromberg, J. S. A robust in vitro model for trans-lymphatic endothelial migration. *Sci Rep* **2017**, *7* (1), 1633. DOI: 10.1038/s41598-017-01575-w From NLM.
(224) Xiong, Y.; Brinkman, C. C.; Famulski, K. S.; Mongodin, E. F.; Lord, C. J.; Hippen, K. L.; Blazar, B. R.; Bromberg, J. S. A robust in vitro model for trans-lymphatic endothelial migration. *Scientific Reports* **2017**, *7* (1), 1633. DOI: 10.1038/s41598-017-01575-w.
(225) Erhard, H.; Rietveld, F. J.; Bröcker, E. B.; de Waal, R. M.; Ruiter, D. J. Phenotype of normal cutaneous microvasculature. Immunoelectron microscopic observations with emphasis on the differences between blood vessels and lymphatics. *J Invest Dermatol* **1996**, *106* (1), 135–140. DOI: 10.1111/1523-1747.ep12329708 From NLM.
(226) Schneider, U.; Schwenk, H. U.; Bornkamm, G. Characterization of EBV-genome negative "null" and "T" cell lines derived from children with acute lymphoblastic leukemia

and leukemic transformed non-Hodgkin lymphoma. *Int J Cancer* **1977**, *19* (5), 621–626. DOI: 10.1002/ijc.2910190505 From NLM.
(227) Weiss, A.; Wiskocil, R. L.; Stobo, J. D. The role of T3 surface molecules in the activation of human T cells: a two-stimulus requirement for IL 2 production reflects events occurring at a pre-translational level. *J Immunol* **1984**, *133* (1), 123–128. From NLM.
(228) Linette, G. P.; Li, Y.; Roth, K.; Korsmeyer, S. J. Cross talk between cell death and cell cycle progression: BCL-2 regulates NFAT-mediated activation. *Proc Natl Acad Sci U S A* **1996**, *93* (18), 9545–9552. DOI: 10.1073/pnas.93.18.9545 From NLM.
(229) Gibson, S.; August, A.; Branch, D.; Dupont, B.; Mills, G. M. Functional LCK Is required for optimal CD28-mediated activation of the TEC family tyrosine kinase EMT/ITK. *J Biol Chem* **1996**, *271* (12), 7079–7083. DOI: 10.1074/jbc.271.12.7079 From NLM.
(230) Yang, M.; Yu, Z.; Ping, J.; Duan, Y.; Tang, J.; Liu, W.; He, Q.; Lai, Y.; Lam, S. M.; Tang, H.; et al. Targeting lipid scrambling potentiates ferroptosis and triggers tumor immune rejection. *Science Advances* **2025**, *11* (33), eadx6587. DOI: doi:10.1126/sciadv.adx6587.
(231) Ma, Y. R.; Ma, Y. H. MIP-1$\alpha$ enhances Jurkat cell transendothelial migration by up-regulating endothelial adhesion molecules VCAM-1 and ICAM-1. *Leuk Res* **2014**, *38* (11), 1327–1331. DOI: 10.1016/j.leukres.2014.08.019 From NLM.
(232) Sonmez, U. M.; Wood, A.; Justus, K.; Jiang, W.; Syed-Picard, F.; LeDuc, P. R.; Kalinski, P.; Davidson, L. A. Chemotactic Responses of Jurkat Cells in Microfluidic Flow-Free Gradient Chambers. *Micromachines (Basel)* **2020**, *11* (4). DOI: 10.3390/mi11040384 From NLM.
(233) Gioia, L.; Siddique, A.; Head, S. R.; Salomon, D. R.; Su, A. I. A genome-wide survey of mutations in the Jurkat cell line. *BMC Genomics* **2018**, *19* (1), 334. DOI: 10.1186/s12864-018-4718-6.
(234) Wilson, A.; Dasyam, N.; O'Hagan, F.; Farrell, D.; Turner, C.; Jay, A.; Schmidt, A.; Beddow, R.; Lillis, T.; Chin, T.; et al. Jurkat T-cell lines exhibit marked genomic instability affecting karyotype, mutational profile, gene expression, immunophenotype and function. *Scientific Reports* **2025**, *15* (1), 22426. DOI: 10.1038/s41598-025-95903-0.
(235) Justus, C. R.; Marie, M. A.; Sanderlin, E. J.; Yang, L. V. Transwell In Vitro Cell Migration and Invasion Assays. *Methods Mol Biol* **2023**, *2644*, 349–359. DOI: 10.1007/978-1-0716-3052-5_22 From NLM.
(236) Partridge, J.; Flaherty, P. An in vitro FluoroBlok tumor invasion assay. *J Vis Exp* **2009**, (29). DOI: 10.3791/1475 From NLM.
(237) Poissonnier, A.; Legembre, P. Boyden Chamber Assay to Study of Cell Migration Induced by Metalloprotease Cleaved-CD95L. In *CD95: Methods and Protocols*, Legembre, P. Ed.; Springer New York, 2017; pp 117–123.
(238) Iino, J.; Osada, M.; Kurano, M.; Kaneko, M.; Ohkawa, R.; Satoh, Y.; Okubo, S.; Ozaki, Y.; Tozuka, M.; Tsuno, N.; et al. Platelet-derived sphingosine 1-phosphate induces migration of Jurkat T cells. *Lipids in health and disease* **2014**, *13*, 150. DOI: 10.1186/1476-511X-13-150.
(239) Gardeta, S. R.; García-Cuesta, E. M.; D'Agostino, G.; Soler Palacios, B.; Quijada-Freire, A.; Lucas, P.; Bernardino de la Serna, J.; Gonzalez-Riano, C.; Barbas, C.; Rodríguez-Frade, J. M.; et al. Sphingomyelin Depletion Inhibits CXCR4 Dynamics and CXCL12-Mediated Directed Cell Migration in Human T Cells. *Frontiers in Immunology* **2022**, *13*, Original Research. DOI: 10.3389/fimmu.2022.925559.
(240) Zepeda-Moreno, A.; Saffrich, R.; Walenda, T.; Hoang, V. T.; Wuchter, P.; Sánchez-Enríquez, S.; Corona-Rivera, A.; Wagner, W.; Ho, A. D. Modeling SDF-1–induced

mobilization in leukemia cell lines. *Experimental Hematology* **2012**, *40* (8), 666–674. DOI: https://doi.org/10.1016/j.exphem.2012.05.001.
(241) Johnson , L. A.; Clasper , S.; Holt , A. P.; Lalor , P. F.; Baban , D.; Jackson , D. G. An inflammation-induced mechanism for leukocyte transmigration across lymphatic vessel endothelium. *Journal of Experimental Medicine* **2006**, *203* (12), 2763–2777. DOI: 10.1084/jem.20051759 (accessed 3/18/2025).
(242) Luster, A. D.; Alon, R.; von Andrian, U. H. Immune cell migration in inflammation: present and future therapeutic targets. *Nat Immunol* **2005**, *6* (12), 1182–1190. DOI: 10.1038/ni1275 From NLM.
(243) Berard, M.; Tough, D. F. Qualitative differences between naïve and memory T cells. *Immunology* **2002**, *106* (2), 127–138. DOI: 10.1046/j.1365-2567.2002.01447.x From NLM.
(244) Ceuppens, J. L.; Baroja, M. L.; Lorre, K.; Van Damme, J.; Billiau, A. Human T cell activation with phytohemagglutinin. The function of IL-6 as an accessory signal. *J Immunol* **1988**, *141* (11), 3868–3874. From NLM.
(245) Nian, M.; Lee, P.; Khaper, N.; Liu, P. Inflammatory Cytokines and Postmyocardial Infarction Remodeling. *Circulation Research* **2004**, *94* (12), 1543–1553. DOI: doi:10.1161/01.RES.0000130526.20854.fa.
(246) Sedwick, C. E.; Morgan, M. M.; Jusino, L.; Cannon, J. L.; Miller, J.; Burkhardt, J. K. TCR, LFA-1, and CD28 play unique and complementary roles in signaling T cell cytoskeletal reorganization. *The Journal of Immunology* **1999**, *162* (3), 1367–1375.
(247) González-Amaro, R.; Cortés, J. R.; Sánchez-Madrid, F.; Martín, P. Is CD69 an effective brake to control inflammatory diseases? *Trends in molecular medicine* **2013**, *19* (10), 625–632.
(248) Loetscher, M.; Geiser, T.; O'Reilly, T.; Zwahlen, R.; Baggiolini, M.; Moser, B. Cloning of a human seven-transmembrane domain receptor, LESTR, that is highly expressed in leukocytes. *Journal of Biological Chemistry* **1994**, *269* (1), 232–237.
(249) Maksym, R. B.; Tarnowski, M.; Grymula, K.; Tarnowska, J.; Wysoczynski, M.; Liu, R.; Czerny, B.; Ratajczak, J.; Kucia, M.; Ratajczak, M. Z. The role of stromal-derived factor-1—CXCR7 axis in development and cancer. *European journal of pharmacology* **2009**, *625* (1-3), 31–40.
(250) Décaillot, F. M.; Kazmi, M. A.; Lin, Y.; Ray-Saha, S.; Sakmar, T. P.; Sachdev, P. CXCR7/CXCR4 heterodimer constitutively recruits β-arrestin to enhance cell migration. *Journal of Biological Chemistry* **2011**, *286* (37), 32188–32197.
(251) Ott, T. R.; Pahuja, A.; Lio, F. M.; Mistry, M. S.; Gross, M.; Hudson, S. C.; Wade, W. S.; Simpson, P. B.; Struthers, R. S.; Alleva, D. G. A high-throughput chemotaxis assay for pharmacological characterization of chemokine receptors: Utilization of U937 monocytic cells. *Journal of Pharmacological and Toxicological Methods* **2005**, *51* (2), 105–114. DOI: https://doi.org/10.1016/j.vascn.2004.10.001.
(252) Oner, A.; Kobold, S. Transwell migration assay to interrogate human CAR-T cell chemotaxis. *STAR Protocols* **2022**, *3* (4), 101708. DOI: https://doi.org/10.1016/j.xpro.2022.101708.
(253) Zhang, R.; Liu, L. Assaying antigen-specific T cell trans-endothelial migration in vitro with the Transwell system: application in tumor immunology. *Biophys Rep* **2025**, *11* (3), 156–163. DOI: 10.52601/bpr.2024.240032 From NLM.
(254) Davis, C. T.; Rao, A. V.; Guadalupe, E.; Christensen, D. J.; Weinberg, J. B. Fingolimod Is Cytotoxic in Acute Myeloid Leukemia Independent of Additional Chemotherapeutic Agents. *Blood* **2016**, *128* (22), 5126–5126. DOI: 10.1182/blood.V128.22.5126.5126 (accessed 6/18/2025).

(255) Bilgehan, A.; Şeker, Z.; Qaoud, M. T.; Özhan, G. In vitro investigation of the toxicological mechanisms of Fingolimod (S)-phosphate in HEPG2 cells. *Toxicol Res (Camb)* **2025**, *14* (3), tfaf064. DOI: 10.1093/toxres/tfaf064 From NLM.
(256) Swain, J.; Mohapatra, M.; Borkar, S. R.; Aidhen, I. S.; Mishra, A. K. Study of aqueous phase aggregation of FTY720 (fingolimod hydrochloride) and its effect on DMPC liposomes using fluorescent molecular probes. *Phys Chem Chem Phys* **2013**, *15* (41), 17962–17970. DOI: 10.1039/c3cp53148a From NLM.
(257) Thomas J. Bruno, P. D. N. S.

*CRC Handbook of Basic Tables for Chemical Analysis*; CRC Press, 2020. DOI: https://doi.org/10.1201/b22281.
(258) Parsi, K. Interaction of detergent sclerosants with cell membranes. *Phlebology* **2015**, *30* (5), 306–315. DOI: 10.1177/0268355514534648 From NLM.
(259) Bataille, C. J. R.; Rabbitts, T. H.; Claridge, T. D. W. NMR waterLOGSY as An Assay in Drug Development Programmes for Detecting Protein-Ligand Interactions–NMR waterLOGSY. *Bio-protocol* **2020**, *10* (13), e3666. DOI: 10.21769/BioProtoc.3666.
(260) Baluk, P.; McDonald, D. M. Buttons and Zippers: Endothelial Junctions in Lymphatic Vessels. *Cold Spring Harb Perspect Med* **2022**, *12* (12). DOI: 10.1101/cshperspect.a041178 From NLM.
(261) Angeli, V.; Lim, H. Y. Biomechanical control of lymphatic vessel physiology and functions. *Cellular & Molecular Immunology* **2023**, *20* (9), 1051–1062. DOI: 10.1038/s41423-023-01042-9.
(262) Selahi, A.; Fernando, T.; Chakraborty, S.; Muthuchamy, M.; Zawieja, D. C.; Jain, A. Lymphangion-chip: a microphysiological system which supports co-culture and bidirectional signaling of lymphatic endothelial and muscle cells. *Lab Chip* **2021**, *22* (1), 121–135. DOI: 10.1039/d1lc00720c From NLM.
(263) Leak, L. V. Electron microscopic observations on lymphatic capillaries and the structural components of the connective tissue-lymph interface. *Microvasc Res* **1970**, *2* (4), 361–391. DOI: 10.1016/0026-2862(70)90031-2 From NLM.
(264) Frenkel, N.; Poghosyan, S.; Alarcón, C. R.; García, S. B.; Queiroz, K.; van den Bent, L.; Laoukili, J.; Rinkes, I. B.; Vulto, P.; Kranenburg, O.; et al. Long-Lived Human Lymphatic Endothelial Cells to Study Lymphatic Biology and Lymphatic Vessel/Tumor Coculture in a 3D Microfluidic Model. *ACS Biomaterials Science & Engineering* **2021**, *7* (7), 3030–3042. DOI: 10.1021/acsbiomaterials.0c01378.
(265) Xu, Z.; Ikuta, T.; Kawakami, K.; Kise, R.; Qian, Y.; Xia, R.; Sun, M.-X.; Zhang, A.; Guo, C.; Cai, X.-H.; et al. Structural basis of sphingosine-1-phosphate receptor 1 activation and biased agonism. *Nature Chemical Biology* **2022**, *18* (3), 281–288. DOI: 10.1038/s41589-021-00930-3.
(266) Adamian, L.; Naveed, H.; Liang, J. Lipid-binding surfaces of membrane proteins: Evidence from evolutionary and structural analysis. *Biochimica et Biophysica Acta (BBA) - Biomembranes* **2011**, *1808* (4), 1092–1102. DOI: https://doi.org/10.1016/j.bbamem.2010.12.008.
(267) Wang, Z.; Min, X.; Xiao, S.-H.; Johnstone, S.; Romanow, W.; Meininger, D.; Xu, H.; Liu, J.; Dai, J.; An, S.; et al. Molecular Basis of Sphingosine Kinase 1 Substrate Recognition and Catalysis. *Structure* **2013**, *21* (5), 798–809. DOI: https://doi.org/10.1016/j.str.2013.02.025.
(268) Pashikanti, S.; Foster, D. J.; Kharel, Y.; Brown, A. M.; Bevan, D. R.; Lynch, K. R.; Santos, W. L. Sphingosine Kinase 2 Inhibitors: Rigid Aliphatic Tail Derivatives Deliver Potent and

Selective Analogues. *ACS Bio & Med Chem Au* **2022**, *2* (5), 469–489. DOI: 10.1021/acsbiomedchemau.2c00017.
(269) Wang, J.; Knapp, S.; Pyne, N. J.; Pyne, S.; Elkins, J. M. Crystal Structure of Sphingosine Kinase 1 with PF-543. *ACS Med Chem Lett* **2014**, *5* (12), 1329–1333. DOI: 10.1021/ml5004074 From NLM.
(270) Kiuchi, M.; Adachi, K.; Kohara, T.; Teshima, K.; Masubuchi, Y.; Mishina, T.; Fujita, T. Synthesis and biological evaluation of 2,2-disubstituted 2-aminoethanols: analogues of FTY720. *Bioorganic & Medicinal Chemistry Letters* **1998**, *8* (1), 101–106. DOI: https://doi.org/10.1016/S0960-894X(97)10188-3.
(271) Stepanovska, B.; Zivkovic, A.; Enzmann, G.; Tietz, S.; Homann, T.; Kleuser, B.; Engelhardt, B.; Stark, H.; Huwiler, A. Morpholino Analogues of Fingolimod as Novel and Selective S1P1 Ligands with In Vivo Efficacy in a Mouse Model of Experimental Antigen-Induced Encephalomyelitis. *International Journal of Molecular Sciences* **2020**, *21* (18), 6463.
(272) Lee, A. G. How lipids affect the activities of integral membrane proteins. *Biochimica et Biophysica Acta (BBA)-Biomembranes* **2004**, *1666* (1-2), 62–87.
(273) Kiuchi, M.; Adachi, K.; Kohara, T.; Minoguchi, M.; Hanano, T.; Aoki, Y.; Mishina, T.; Arita, M.; Nakao, N.; Ohtsuki, M.; et al. Synthesis and Immunosuppressive Activity of 2-Substituted 2-Aminopropane-1,3-diols and 2-Aminoethanols. *Journal of Medicinal Chemistry* **2000**, *43* (15), 2946–2961. DOI: 10.1021/jm000173z.
(274) Askey, H. E.; Grayson, J. D.; Tibbetts, J. D.; Turner-Dore, J. C.; Holmes, J. M.; Kociok-Kohn, G.; Wrigley, G. L.; Cresswell, A. J. Photocatalytic Hydroaminoalkylation of Styrenes with Unprotected Primary Alkylamines. *Journal of the American Chemical Society* **2021**, *143* (39), 15936–15945. DOI: 10.1021/jacs.1c07401.
(275) Li, H.; Hou, Y.; Liu, C.; Lai, Z.; Ning, L.; Szostak, R.; Szostak, M.; An, J. Pentafluorophenyl esters: highly chemoselective ketyl precursors for the synthesis of $\alpha$, $\alpha$-dideuterio alcohols using SmI2 and D2O as a deuterium source. *Organic letters* **2020**, *22* (4), 1249–1253.
(276) Peng, M.; Li, H.; Qin, Z.; Li, J.; Sun, Y.; Zhang, X.; Jiang, L.; Do, H.; An, J. Pentafluorophenyl Group as Activating Group: Synthesis of $\alpha$-Deuterio Carboxylic Acid Derivatives via Et3N Catalyzed H/D Exchange. *Advanced Synthesis & Catalysis* **2022**, *364* (13), 2184–2189. DOI: https://doi.org/10.1002/adsc.202200258.
(277) McKillop, A.; McLaren, L.; Taylor, R. J. K.; Watson, R. J.; Lewis, N. J. The total synthesis of the diepoxycyclohexanone antibiotic aranorosin and novel synthetic analogues. *Journal of the Chemical Society, Perkin Transactions 1* **1996**, (12), 1385–1393, 10.1039/P19960001385. DOI: 10.1039/P19960001385.
(278) Abraham, E.; Brock, E. A.; Candela-Lena, J. I.; Davies, S. G.; Georgiou, M.; Nicholson, R. L.; Perkins, J. H.; Roberts, P. M.; Russell, A. J.; Sánchez-Fernández, E. M.; et al. Asymmetric synthesis of N,O,O,O-tetra-acetyl d-lyxo-phytosphingosine, jaspine B (pachastrissamine), 2-epi-jaspine B, and deoxoprosophyllinevialithium amide conjugate addition. *Organic & Biomolecular Chemistry* **2008**, *6* (9), 1665–1673, 10.1039/B801671B. DOI: 10.1039/B801671B.
(279) Rannard, S. P.; Davis, N. J.; Herbert, I. Synthesis of Water Soluble Hyperbranched Polyurethanes Using Selective Activation of AB2 Monomers. *Macromolecules* **2004**, *37* (25), 9418–9430. DOI: 10.1021/ma0489218.
(280) al., R. e. WO2005/21503. 2005.
(281) al, P. e. CN109836392. China 2017.

(282) Yadav, G. D.; Pawar, S. V. Novelty of immobilized enzymatic synthesis of 3-ethyl-1,3-oxazolidin-2-one using 2-aminoalcohol and dimethyl carbonate: Mechanism and kinetic modeling of consecutive reactions. *Journal of Molecular Catalysis B: Enzymatic* **2014**, *109*, 62–69. DOI: https://doi.org/10.1016/j.molcatb.2014.08.001.
(283) Wu, K.; Che, C.-M. Iron-catalysed intramolecular C(sp3)–H amination of alkyl azides. *Chemical Communications* **2024**, *60* (95), 13998–14011, 10.1039/D4CC04169K. DOI: 10.1039/D4CC04169K.
(284) Yang, Y.-Z.; Xue, Q.; Xiong, Z.-Q.; Li, Y.; Ouyang, X.-H.; Hu, M.; Li, J.-H. Divergent [2 + n] Heteroannulation of β-CF3-1,3-enynes with Alkyl Azides via Hydrogen Atom Transfer and Radical Substitution. *Organic Letters* **2024**, *26* (4), 889–894. DOI: 10.1021/acs.orglett.3c04041.
(285) Sabir, S.; Kumar, G.; Verma, V. P.; Jat, J. L. Aziridine Ring Opening: An Overview of Sustainable Methods. *ChemistrySelect* **2018**, *3* (13), 3702–3711. DOI: https://doi.org/10.1002/slct.201800170.
(286) West, A. V.; Muncipinto, G.; Wu, H.-Y.; Huang, A. C.; Labenski, M. T.; Jones, L. H.; Woo, C. M. Labeling Preferences of Diazirines with Protein Biomolecules. *Journal of the American Chemical Society* **2021**, *143* (17), 6691–6700. DOI: 10.1021/jacs.1c02509.
(287) Oh, K.; Kim, H.; Cardelli, F.; Bwititi, T.; Martynow, A. M. Synthesis of Cyclic Thioethers through Tandem C(sp3)−S and C(sp2)−S Bond Formations from α,β′-Dichloro Vinyl Ketones. *The Journal of Organic Chemistry* **2008**, *73* (6), 2432–2434. DOI: 10.1021/jo702457t.
(288) Martens, H.; Hoornaert, G.; Toppet, S. Spectral correlations for β-chlorovinyl ketones. *Tetrahedron* **1973**, *29* (24), 4241–4249. DOI: https://doi.org/10.1016/0040-4020(73)80265-0.
(289) Rai, K. M. L.; Musad, E. A.; Jagadish, R. L.; Shivakumar, K. N. Convenient Method for the Friedel–Crafts Acylation of Benzene Derivatives Using Silver Nitrate as Catalyst. *Synthetic Communications* **2011**, *41* (7), 953–955. DOI: 10.1080/00397911003707139.
(290) Protection for the Hydroxyl Group, Including 1,2- and 1,3-Diols. In *Greene's Protective Groups in Organic Synthesis*, 2006; pp 16–366.
(291) Valente, C.; Çalimsiz, S.; Hoi, K. H.; Mallik, D.; Sayah, M.; Organ, M. G. The Development of Bulky Palladium NHC Complexes for the Most-Challenging Cross-Coupling Reactions. *Angewandte Chemie International Edition* **2012**, *51* (14), 3314–3332. DOI: https://doi.org/10.1002/anie.201106131.
(292) Gilbert, J. C.; Weerasooriya, U. Diazoethenes: their attempted synthesis from aldehydes and aromatic ketones by way of the Horner-Emmons modification of the Wittig reaction. A facile synthesis of alkynes. *The Journal of Organic Chemistry* **1982**, *47* (10), 1837–1845. DOI: 10.1021/jo00349a007.
(293) Schmitz, E. Diaziridine. In *Dreiringe mit Zwei Heteroatomen: Oxaziridine · Diaziridine Cyclische Diazoverbindungen*, Schmitz, E. Ed.; Springer Berlin Heidelberg, 1967; pp 67–113.
(294) Tachrim, Z. P.; Wang, L.; Murai, Y.; Hashimoto, M. New Trends in Diaziridine Formation and Transformation (a Review). *Molecules* **2021**, *26* (15), 4496.
(295) Uyanik, M.; Ishihara, K. 6.14 Functional Group Transformations via Carbonyl Derivatives. In *Comprehensive Organic Synthesis (Second Edition)*, Knochel, P. Ed.; Elsevier, 2014; pp 573–597.
(296) Ganguly, N. C.; Mondal, P. Efficient Iodine-Mediated Beckmann Rearrangement of Ketoximes to Amides under Mild Neutral Conditions. *Synthesis* **2010**, *2010* (21), 3705–3709. DOI: 10.1055/s-0030-1258217.

(297) Fernandez, A. B.; Lezcano-Gonzalez, I.; Boronat, M.; Blasco, T.; Corma, A. Study of the Beckmann rearrangement of acetophenone oxime over porous solids by means of solid state NMR spectroscopy. *Physical Chemistry Chemical Physics* **2009**, *11* (25), 5134–5141, 10.1039/B816276J. DOI: 10.1039/B816276J.
(298) Lepage, M. L.; Gras, E. The Versatility of Diazirines: Properties, Synthetic and Modern Applications. *Chemistry – A European Journal n/a* (n/a), e202500414. DOI: https://doi.org/10.1002/chem.202500414.
(299) Baker, K. V.; Brown, J. M.; Hughes, N.; Skarnulis, A. J.; Sexton, A. Mechanical activation of magnesium turnings for the preparation of reactive Grignard reagents. *The Journal of Organic Chemistry* **1991**, *56* (2), 698–703. DOI: 10.1021/jo00002a039.
(300) Kozhushkov, S. I.; Wagner-Gillen, K.; Khlebnikov, A. F.; de Meijere, A. Productive Syntheses of 1-Ethynylcyclopropylamine and 1-Ethynylcyclobutylamine. *Synthesis* **2010**, *2010* (23), 3967–3973. DOI: 10.1055/s-0030-1258964.
(301) van der Louw, J.; van der Baan, J. L.; Komen, C. M. D.; Knol, A.; de Kanter, F. J. J.; Bickelhaupt, F.; Klumpp, G. W. Intramolecular zinc-ene reactions of alkynes; preparation of 1,5-annulated 4-methylenecyclopentenes. *Tetrahedron* **1992**, *48* (29), 6105–6122. DOI: https://doi.org/10.1016/S0040-4020(01)89858-6.
(302) Ibert, Q.; Cauwel, M.; Glachet, T.; Tite, T.; Le Nahenec-Martel, P.; Lohier, J.-F.; Renard, P.-Y.; Franck, X.; Reboul, V.; Sabot, C. One-Pot Synthesis of Diazirines and 15N2-Diazirines from Ketones, Aldehydes and Derivatives: Development and Mechanistic Insight. *Advanced Synthesis & Catalysis* **2021**, *363* (18), 4390–4398. DOI: https://doi.org/10.1002/adsc.202100679.
(303) Fang, G.; Bi, X. Silver-catalysed reactions of alkynes: recent advances. *Chemical Society Reviews* **2015**, *44* (22), 8124–8173, 10.1039/C5CS00027K. DOI: 10.1039/C5CS00027K.
(304) Trifan, D. S.; Bartlett, P. D. Iodine and Styrene. I. Four Reactions between Iodine and Styrene. *Journal of the American Chemical Society* **1959**, *81* (21), 5573–5581. DOI: 10.1021/ja01530a016.
(305) Fujita, T.; Hirose, R.; Yoneta, M.; Sasaki, S.; Inoue, K.; Kiuchi, M.; Hirase, S.; Chiba, K.; Sakamoto, H.; Arita, M. *Journal of Medicinal Chemistry* **1996**, *39* (22), 4451–4459. DOI: 10.1021/jm9603911.
(306) Jennings, B. M.; Liu, M. T. H. Mechanism of thermal decomposition of diazirine. Evidence for diazomethane intermediate. *Journal of the American Chemical Society* **1976**, *98* (20), 6416–6417. DOI: 10.1021/ja00436a073.
(307) Ping, J.; Gao, F.; Chen, J. L.; Webster, R. D.; Steele, T. W. J. Adhesive curing through low-voltage activation. *Nature Communications* **2015**, *6* (1), 8050. DOI: 10.1038/ncomms9050.
(308) Speckmeier, E.; Fischer, T. G.; Zeitler, K. A Toolbox Approach To Construct Broadly Applicable Metal-Free Catalysts for Photoredox Chemistry: Deliberate Tuning of Redox Potentials and Importance of Halogens in Donor–Acceptor Cyanoarenes. *Journal of the American Chemical Society* **2018**, *140* (45), 15353–15365. DOI: 10.1021/jacs.8b08933.
(309) Brinkmann, V.; Davis, M. D.; Heise, C. E.; Albert, R.; Cottens, S.; Hof, R.; Bruns, C.; Prieschl, E.; Baumruker, T.; Hiestand, P.; et al. The Immune Modulator FTY720 Targets Sphingosine 1-Phosphate Receptors*. *Journal of Biological Chemistry* **2002**, *277* (24), 21453–21457. DOI: https://doi.org/10.1074/jbc.C200176200.
(310) Mangmool, S.; Kurose, H. G(i/o) protein-dependent and -independent actions of Pertussis Toxin (PTX). *Toxins (Basel)* **2011**, *3* (7), 884–899. DOI: 10.3390/toxins3070884 From NLM.

(311) Kiyohito Yagi, M. S., Minori Hashizume, Leonard S. Shimba,; Miura, S. K. a. Y. *BIOCHEMICAL AND BIOPHYSICAL RESEARCH COMMUNICATIONS* **1991**, *180* (3), 1200–1206.
(312) Shen, F.; Zhang, Y.; Jernigan, D. L.; Feng, X.; Yan, J.; Garcia, F. U.; Meucci, O.; Salvino, J. M.; Fatatis, A. Novel Small-Molecule CX3CR1 Antagonist Impairs Metastatic Seeding and Colonization of Breast Cancer Cells. *Mol Cancer Res* **2016**, *14* (6), 518–527. DOI: 10.1158/1541-7786.Mcr-16-0013 From NLM.
(313) Sparks, S. M.; Chen, G.; Collins, J. L.; Danger, D.; Dock, S. T.; Jayawickreme, C.; Jenkinson, S.; Laudeman, C.; Leesnitzer, M. A.; Liang, X.; et al. Identification of diarylsulfonamides as agonists of the free fatty acid receptor 4 (FFA4/GPR120). *Bioorganic & Medicinal Chemistry Letters* **2014**, *24* (14), 3100–3103. DOI: https://doi.org/10.1016/j.bmcl.2014.05.012.
(314) Karasu, E.; Demmelmaier, J.; Kellermann, S.; Holzmann, K.; Köhl, J.; Schmidt, C. Q.; Kalbitz, M.; Gebhard, F.; Huber-Lang, M. S.; Halbgebauer, R. Complement C5a Induces Pro-inflammatory Microvesicle Shedding in Severely Injured Patients. *Frontiers in Immunology* **2020**, *Volume 11 - 2020*, Original Research. DOI: 10.3389/fimmu.2020.01789.
(315) Benned-Jensen, T.; Smethurst, C.; Holst, P. J.; Page, K. R.; Sauls, H.; Sivertsen, B.; Schwartz, T. W.; Blanchard, A.; Jepras, R.; Rosenkilde, M. M. Ligand modulation of the Epstein-Barr virus-induced seven-transmembrane receptor EBI2: identification of a potent and efficacious inverse agonist. *J Biol Chem* **2011**, *286* (33), 29292–29302. DOI: 10.1074/jbc.M110.196345 From NLM.
(316) Hong, C. S.; Ho, W.; Zhang, C.; Yang, C.; Elder, J. B.; Zhuang, Z. LB100, a small molecule inhibitor of PP2A with potent chemo- and radio-sensitizing potential. *Cancer Biol Ther* **2015**, *16* (6), 821–833. DOI: 10.1080/15384047.2015.1040961 From NLM.
(317) Helker, C. S.; Eberlein, J.; Wilhelm, K.; Sugino, T.; Malchow, J.; Schuermann, A.; Baumeister, S.; Kwon, H. B.; Maischein, H. M.; Potente, M.; et al. Apelin signaling drives vascular endothelial cells toward a pro-angiogenic state. *Elife* **2020**, *9*. DOI: 10.7554/eLife.55589 From NLM.
(318) Berta, J.; Hoda, M. A.; Laszlo, V.; Rozsas, A.; Garay, T.; Torok, S.; Grusch, M.; Berger, W.; Paku, S.; Renyi-Vamos, F.; et al. Apelin promotes lymphangiogenesis and lymph node metastasis. *Oncotarget* **2014**, *5* (12), 4426–4437. DOI: 10.18632/oncotarget.2032 From NLM.
(319) Kim, J. D.; Kang, Y.; Kim, J.; Papangeli, I.; Kang, H.; Wu, J.; Park, H.; Nadelmann, E.; Rockson, S. G.; Chun, H. J.; et al. Essential role of Apelin signaling during lymphatic development in zebrafish. *Arterioscler Thromb Vasc Biol* **2014**, *34* (2), 338–345. DOI: 10.1161/atvbaha.113.302785 From NLM.
(320) Tatin, F.; Renaud-Gabardos, E.; Godet, A. C.; Hantelys, F.; Pujol, F.; Morfoisse, F.; Calise, D.; Viars, F.; Valet, P.; Masri, B.; et al. Apelin modulates pathological remodeling of lymphatic endothelium after myocardial infarction. *JCI Insight* **2017**, *2* (12). DOI: 10.1172/jci.insight.93887 From NLM.
(321) Yeganeh-Hajahmadi, M.; Mehrabani, M.; Esmaili, M.; Farokhi, M. S.; Sanjari, M. Protamine as a barrier against the angiogenic effect of insulin: a possible role of apelin. *Scientific Reports* **2023**, *13* (1), 17267. DOI: 10.1038/s41598-023-44639-w.
(322) Maloney, P. R.; Khan, P.; Hedrick, M.; Gosalia, P.; Milewski, M.; Li, L.; Roth, G. P.; Sergienko, E.; Suyama, E.; Sugarman, E.; et al. Functional antagonists of the Apelin (APJ) receptor. In *Probe Reports from the NIH Molecular Libraries Program*, National Center for Biotechnology Information (US), 2010.

(323) James, J. M.; Nalbandian, A.; Mukouyama, Y. S. TGFβ signaling is required for sprouting lymphangiogenesis during lymphatic network development in the skin. *Development* **2013**, *140* (18), 3903–3914. DOI: 10.1242/dev.095026 From NLM.
(324) Kang, Y.; Kim, J.; Anderson, J. P.; Wu, J.; Gleim, S. R.; Kundu, R. K.; McLean, D. L.; Kim, J.-d.; Park, H.; Jin, S.-w.; et al. Apelin-APJ Signaling Is a Critical Regulator of Endothelial MEF2 Activation in Cardiovascular Development. *Circulation Research* **2013**, *113* (1), 22–31. DOI: doi:10.1161/CIRCRESAHA.113.301324.
(325) Billich, A.; Bornancin, F.; Dévay, P.; Mechtcheriakova, D.; Urtz, N.; Baumruker, T. Phosphorylation of the Immunomodulatory Drug FTY720 by Sphingosine Kinases *. *Journal of Biological Chemistry* **2003**, *278* (48), 47408–47415. DOI: 10.1074/jbc.M307687200 (accessed 2025/07/25).
(326) Cawston, E. E.; Redmond, W. J.; Breen, C. M.; Grimsey, N. L.; Connor, M.; Glass, M. Real-time characterization of cannabinoid receptor 1 (CB1) allosteric modulators reveals novel mechanism of action. *British Journal of Pharmacology* **2013**, *170* (4), 893–907. DOI: https://doi.org/10.1111/bph.12329.
(327) January, B.; Seibold, A.; Whaley, B.; Hipkin, R. W.; Lin, D.; Schonbrunn, A.; Barber, R.; Clark, R. B. β2-Adrenergic Receptor Desensitization, Internalization, and Phosphorylation in Response to Full and Partial Agonists*. *Journal of Biological Chemistry* **1997**, *272* (38), 23871–23879. DOI: https://doi.org/10.1074/jbc.272.38.23871.
(328) Lee, M.; Lee, Y.; Song, J.; Lee, J.; Chang, S. Y. Tissue-specific Role of CX(3)CR1 Expressing Immune Cells and Their Relationships with Human Disease. *Immune Netw* **2018**, *18* (1), e5. DOI: 10.4110/in.2018.18.e5 From NLM.
(329) Gerard, N. P.; Gerard, C. The chemotactic receptor for human C5a anaphylatoxin. *Nature* **1991**, *349* (6310), 614–617. DOI: 10.1038/349614a0 From NLM.
(330) Kjær, V. M. S.; Daugvilaite, V.; Stepniewski, T. M.; Madsen, C. M.; Jørgensen, A. S.; Bhuskute, K. R.; Inoue, A.; Ulven, T.; Benned-Jensen, T.; Hjorth, S. A.; et al. Migration mediated by the oxysterol receptor GPR183 depends on arrestin coupling but not receptor internalization. *Science Signaling* **2023**, *16* (779), eabl4283. DOI: doi:10.1126/scisignal.abl4283.
(331) Lee, T. H.; Horton, C. E.; Kyan-Aung, U.; Haskard, D.; Crea, A. E. G.; Spur, B. W. Lipoxin A4 and Lipoxin B4 Inhibit Chemotactic Responses of Human Neutrophils Stimulated by Leukotriene B4 and N-Formyl-l-Methionyl-l-Leucyl-l-Phenylalanine. *Clinical Science* **1989**, *77* (2), 195–203. DOI: 10.1042/cs0770195 (accessed 6/23/2025).
(332) Nguyen-Jackson, H.; Panopoulos, A. D.; Zhang, H.; Li, H. S.; Watowich, S. S. STAT3 controls the neutrophil migratory response to CXCR2 ligands by direct activation of G-CSF-induced CXCR2 expression and via modulation of CXCR2 signal transduction. *Blood* **2010**, *115* (16), 3354–3363. DOI: 10.1182/blood-2009-08-240317 From NLM.
(333) K Clark, A.; A Staniland, A.; Malcangio, M. Fractalkine/CX3CR1 signalling in chronic pain and inflammation. *Current pharmaceutical biotechnology* **2011**, *12* (10), 1707–1714.
(334) Fong, A. M.; Robinson, L. A.; Steeber, D. A.; Tedder, T. F.; Yoshie, O.; Imai, T.; Patel, D. D. Fractalkine and CX3CR1 mediate a novel mechanism of leukocyte capture, firm adhesion, and activation under physiologic flow. *The Journal of experimental medicine* **1998**, *188* (8), 1413–1419.
(335) Al-Aoukaty, A.; Rolstad, B.; Giaid, A.; Maghazachi, A. MIP-3alpha, MIP-3beta and fractalkine induce the locomotion and the mobilization of intracellular calcium, and activate the heterotrimeric G proteins in human natural killer cells. *Immunology* **1998**, *95* (4), 618.

(336) D'Haese, J. G.; Demir, I. E.; Friess, H.; Ceyhan, G. O. Fractalkine/CX3CR1: why a single chemokine-receptor duo bears a major and unique therapeutic potential. *Expert opinion on therapeutic targets* **2010**, *14* (2), 207–219.
(337) Johnson, L. A.; Jackson, D. G. The chemokine CX3CL1 promotes trafficking of dendritic cells through inflamed lymphatics. *J Cell Sci* **2013**, *126* (Pt 22), 5259–5270. DOI: 10.1242/jcs.135343 From NLM.
(338) Shen, Y. Understanding the biological barriers to Jurkat Transfection using non-viral peptides. Queen's University Belfast, 2022.
(339) Ledgerwood, L. G.; Lal, G.; Zhang, N.; Garin, A.; Esses, S. J.; Ginhoux, F.; Merad, M.; Peche, H.; Lira, S. A.; Ding, Y.; et al. The sphingosine 1-phosphate receptor 1 causes tissue retention by inhibiting the entry of peripheral tissue T lymphocytes into afferent lymphatics. *Nat Immunol* **2008**, *9* (1), 42–53. DOI: 10.1038/ni1534 From NLM.
(340) Katzen, D.; Chu, E.; Terhost, C.; Leung, D. Y.; Gesner, M.; Miller, R. A.; Geha, R. S. Mechanisms of human T cell response to mitogens: IL 2 induces IL 2 receptor expression and proliferation but not IL 2 synthesis in PHA-stimulated T cells. *J Immunol* **1985**, *135* (3), 1840–1845. From NLM.
(341) Johnson, L. A.; Prevo, R.; Clasper, S.; Jackson, D. G. Inflammation-induced Uptake and Degradation of the Lymphatic Endothelial Hyaluronan Receptor LYVE-1*♦. *Journal of Biological Chemistry* **2007**, *282* (46), 33671–33680. DOI: https://doi.org/10.1074/jbc.M702889200.
(342) Hunter, M. C.; Teijeira, A.; Montecchi, R.; Russo, E.; Runge, P.; Kiefer, F.; Halin, C. Dendritic Cells and T Cells Interact Within Murine Afferent Lymphatic Capillaries. *Front Immunol* **2019**, *10*, 520. DOI: 10.3389/fimmu.2019.00520 From NLM.
(343) Ruzza, P.; Honisch, C.; Hussain, R.; Siligardi, G. Free Radicals and ROS Induce Protein Denaturation by UV Photostability Assay. *Int J Mol Sci* **2021**, *22* (12). DOI: 10.3390/ijms22126512 From NLM.
(344) Kerwin, B. A.; Remmele, R. L., Jr. Protect from light: photodegradation and protein biologics. *J Pharm Sci* **2007**, *96* (6), 1468–1479. DOI: 10.1002/jps.20815 From NLM.
(345) Rosenbluth, M. J.; Lam, W. A.; Fletcher, D. A. Force microscopy of nonadherent cells: a comparison of leukemia cell deformability. *Biophys J* **2006**, *90* (8), 2994–3003. DOI: 10.1529/biophysj.105.067496 From NLM.
(346) Kacirova, I.; Kusnirikova, Z. K.; Pesakova, V.; Hradilek, P.; Brozmanova, H.; Grundmann, M. Whole blood concentrations of fingolimod and its pharmacologically active metabolite fingolimod phosphate obtained during routine health care of patients with multiple sclerosis. *Multiple Sclerosis and Related Disorders* **2025**, *93*, 106246. DOI: https://doi.org/10.1016/j.msard.2024.106246.
(347) Weis, W. I.; Kobilka, B. K. The Molecular Basis of G Protein-Coupled Receptor Activation. *Annu Rev Biochem* **2018**, *87*, 897–919. DOI: 10.1146/annurev-biochem-060614-033910 From NLM.
(348) Olsen, J. V.; Ong, S.-E.; Mann, M. Trypsin cleaves exclusively C-terminal to arginine and lysine residues. *Molecular & cellular proteomics* **2004**, *3* (6), 608–614.
(349) Wu, C. C.; MacCoss, M. J.; Howell, K. E.; Yates, J. R. A method for the comprehensive proteomic analysis of membrane proteins. *Nature Biotechnology* **2003**, *21* (5), 532–538. DOI: 10.1038/nbt819.
(350) Wilkins, M. R.; Lindskog, I.; Gasteiger, E.; Bairoch, A.; Sanchez, J. C.; Hochstrasser, D. F.; Appel, R. D. Detailed peptide characterization using PEPTIDEMASS--a World-Wide-

Web-accessible tool. *Electrophoresis* **1997**, *18* (3-4), 403–408. DOI: 10.1002/elps.1150180314 From NLM.
(351) Shetty, S.; Weston, C. J.; Oo, Y. H.; Westerlund, N.; Stamataki, Z.; Youster, J.; Hubscher, S. G.; Salmi, M.; Jalkanen, S.; Lalor, P. F.; et al. Common lymphatic endothelial and vascular endothelial receptor-1 mediates the transmigration of regulatory T cells across human hepatic sinusoidal endothelium. *J Immunol* **2011**, *186* (7), 4147–4155. DOI: 10.4049/jimmunol.1002961 From NLM.
(352) Karikoski, M.; Irjala, H.; Maksimow, M.; Miiluniemi, M.; Granfors, K.; Hernesniemi, S.; Elima, K.; Moldenhauer, G.; Schledzewski, K.; Kzhyshkowska, J.; et al. Clever-1/Stabilin-1 regulates lymphocyte migration within lymphatics and leukocyte entrance to sites of inflammation. *Eur J Immunol* **2009**, *39* (12), 3477–3487. DOI: 10.1002/eji.200939896 From NLM.
(353) Auvynet, C.; Moreno, S.; Melchy, E.; Coronado-Martínez, I.; Montiel, J. L.; Aguilar-Delfin, I.; Rosenstein, Y. Galectin-1 promotes human neutrophil migration. *Glycobiology* **2013**, *23* (1), 32–42. DOI: 10.1093/glycob/cws128 From NLM.
(354) Blomme, A.; Peter, C.; Mui, E.; Rodriguez Blanco, G.; An, N.; Mason, L. M.; Jamieson, L. E.; McGregor, G. H.; Lilla, S.; Ntala, C.; et al. THEM6-mediated reprogramming of lipid metabolism supports treatment resistance in prostate cancer. *EMBO Molecular Medicine* **2022**, *14* (3), e14764. DOI: https://doi.org/10.15252/emmm.202114764.
(355) Barlow, C. A.; Laishram, R. S.; Anderson, R. A. Nuclear phosphoinositides: a signaling enigma wrapped in a compartmental conundrum. *Trends Cell Biol* **2010**, *20* (1), 25–35. DOI: 10.1016/j.tcb.2009.09.009 From NLM.
(356) Hooglugt, A.; van der Stoel, M. M.; Boon, R. A.; Huveneers, S. Endothelial YAP/TAZ Signaling in Angiogenesis and Tumor Vasculature. *Front Oncol* **2020**, *10*, 612802. DOI: 10.3389/fonc.2020.612802 From NLM.
(357) Li, W.; Xu, P.; Kong, L.; Feng, S.; Shen, N.; Huang, H.; Wang, W.; Xu, X.; Wang, X.; Wang, G. Elabela-APJ axis mediates angiogenesis via YAP/TAZ pathway in cerebral ischemia/reperfusion injury. *Translational Research* **2023**, *257*, 78–92.
(358) Fritz-Six, K. L.; Dunworth, W. P.; Li, M.; Caron, K. M. Adrenomedullin signaling is necessary for murine lymphatic vascular development. *J Clin Invest* **2008**, *118* (1), 40–50. DOI: 10.1172/jci33302 From NLM.
(359) Karpinich, N. O.; Kechele, D. O.; Espenschied, S. T.; Willcockson, H. H.; Fedoriw, Y.; Caron, K. M. Adrenomedullin gene dosage correlates with tumor and lymph node lymphangiogenesis. *Faseb j* **2013**, *27* (2), 590–600. DOI: 10.1096/fj.12-214080 From NLM.
(360) Korhonen, E. A.; Murtomäki, A.; Jha, S. K.; Anisimov, A.; Pink, A.; Zhang, Y.; Stritt, S.; Liaqat, I.; Stanczuk, L.; Alderfer, L.; et al. Lymphangiogenesis requires Ang2/Tie/PI3K signaling for VEGFR3 cell-surface expression. *J Clin Invest* **2022**, *132* (15). DOI: 10.1172/jci155478 From NLM.
(361) Kojima, T.; Azar, D. T.; Chang, J.-H. Neostatin-7 regulates bFGF-induced corneal lymphangiogenesis. *FEBS Letters* **2008**, *582* (17), 2515–2520. DOI: https://doi.org/10.1016/j.febslet.2008.06.014.
(362) Marino, D.; Angehrn, Y.; Klein, S.; Riccardi, S.; Baenziger-Tobler, N.; Otto, V. I.; Pittelkow, M.; Detmar, M. Activation of the epidermal growth factor receptor promotes lymphangiogenesis in the skin. *J Dermatol Sci* **2013**, *71* (3), 184–194. DOI: 10.1016/j.jdermsci.2013.04.024 From NLM.
(363) Cao, R.; Ji, H.; Feng, N.; Zhang, Y.; Yang, X.; Andersson, P.; Sun, Y.; Tritsaris, K.; Hansen, A. J.; Dissing, S.; et al. Collaborative interplay between FGF-2 and VEGF-C

promotes lymphangiogenesis and metastasis. *Proc Natl Acad Sci U S A* **2012**, *109* (39), 15894–15899. DOI: 10.1073/pnas.1208324109 From NLM.
(364) Morita, Y.; Hata, K.; Nakanishi, M.; Omata, T.; Morita, N.; Yura, Y.; Nishimura, R.; Yoneda, T. Cellular fibronectin 1 promotes VEGF-C expression, lymphangiogenesis and lymph node metastasis associated with human oral squamous cell carcinoma. *Clin Exp Metastasis* **2015**, *32* (7), 739–753. DOI: 10.1007/s10585-015-9741-2 From NLM.
(365) Wang, X.; Huang, J.; You, R.; Hou, D.; Liu, J.; Wu, L.; Yao, M.; Yang, F.; Huang, H. Downregulation of ITGA5 inhibits lymphangiogenesis and cell migration and invasion in male laryngeal squamous cell carcinoma. *Protoplasma* **2023**, *260* (6), 1569–1580. DOI: 10.1007/s00709-023-01873-3 From NLM.
(366) Kajiya, K.; Hirakawa, S.; Ma, B.; Drinnenberg, I.; Detmar, M. Hepatocyte growth factor promotes lymphatic vessel formation and function. *Embo j* **2005**, *24* (16), 2885–2895. DOI: 10.1038/sj.emboj.7600763 From NLM.
(367) Savage, A. M.; Kurusamy, S.; Chen, Y.; Jiang, Z.; Chhabria, K.; MacDonald, R. B.; Kim, H. R.; Wilson, H. L.; van Eeden, F. J. M.; Armesilla, A. L.; et al. tmem33 is essential for VEGF-mediated endothelial calcium oscillations and angiogenesis. *Nat Commun* **2019**, *10* (1), 732. DOI: 10.1038/s41467-019-08590-7 From NLM.
(368) Bai, B.; Wang, X.; Li, Y.; Chen, P.-C.; Yu, K.; Dey, K. K.; Yarbro, J. M.; Han, X.; Lutz, B. M.; Rao, S.; et al. Deep Multilayer Brain Proteomics Identifies Molecular Networks in Alzheimer's Disease Progression. *Neuron* **2020**, *105* (6), 975–991.e977. DOI: https://doi.org/10.1016/j.neuron.2019.12.015.
(369) Johnson, L. A.; Jackson, D. G. Hyaluronan and Its Receptors: Key Mediators of Immune Cell Entry and Trafficking in the Lymphatic System. *Cells* **2021**, *10* (8). DOI: 10.3390/cells10082061 From NLM.
(370) Salmi, M.; Karikoski, M.; Elima, K.; Rantakari, P.; Jalkanen, S. CD44 binds to macrophage mannose receptor on lymphatic endothelium and supports lymphocyte migration via afferent lymphatics. *Circ Res* **2013**, *112* (12), 1577–1582. DOI: 10.1161/circresaha.111.300476 From NLM.
(371) Lloyd, A. F.; Martinez-Muriana, A.; Davis, E.; Daniels, M. J. D.; Hou, P.; Mancuso, R.; Brenes, A. J.; Sinclair, L. V.; Geric, I.; Snellinx, A.; et al. Deep proteomic analysis of microglia reveals fundamental biological differences between model systems. *Cell Reports* **2024**, *43* (11), 114908. DOI: https://doi.org/10.1016/j.celrep.2024.114908.
(372) He, J.; Baum, L. G. Endothelial cell expression of galectin-1 induced by prostate cancer cells inhibits T-cell transendothelial migration. *Laboratory Investigation* **2006**, *86* (6), 578–590. DOI: 10.1038/labinvest.3700420 (accessed 2025/09/12).
(373) Marttila-Ichihara, F.; Turja, R.; Miiluniemi, M.; Karikoski, M.; Maksimow, M.; Niemelä, J.; Martinez-Pomares, L.; Salmi, M.; Jalkanen, S. Macrophage mannose receptor on lymphatics controls cell trafficking. *Blood* **2008**, *112* (1), 64–72. DOI: 10.1182/blood-2007-10-118984 (accessed 9/12/2025).
(374) Karikoski, M.; Irjala, H.; Maksimow, M.; Miiluniemi, M.; Granfors, K.; Hernesniemi, S.; Elima, K.; Moldenhauer, G.; Schledzewski, K.; Kzhyshkowska, J.; et al. Clever-1/Stabilin-1 regulates lymphocyte migration within lymphatics and leukocyte entrance to sites of inflammation. *European Journal of Immunology* **2009**, *39* (12), 3477–3487. DOI: https://doi.org/10.1002/eji.200939896.
(375) Kappos, L.; Radue, E.-W.; O'Connor, P.; Polman, C.; Hohlfeld, R.; Calabresi, P.; Selmaj, K.; Agoropoulou, C.; Leyk, M.; Zhang-Auberson, L.; et al. A Placebo-Controlled Trial of

Oral Fingolimod in Relapsing Multiple Sclerosis. *New England Journal of Medicine* **2010**, *362* (5), 387–401. DOI: doi:10.1056/NEJMoa0909494.
(376) Igarashi, J.; Michel, T. Sphingosine-1-phosphate and modulation of vascular tone. *Cardiovascular Research* **2009**, *82* (2), 212–220. DOI: 10.1093/cvr/cvp064 (accessed 9/13/2025).
(377) Schuchardt, M.; Tölle, M.; Prüfer, J.; van der Giet, M. Pharmacological relevance and potential of sphingosine 1-phosphate in the vascular system. *British Journal of Pharmacology* **2011**, *163* (6), 1140–1162. DOI: https://doi.org/10.1111/j.1476-5381.2011.01260.x.
(378) te Riet, L.; van Esch, J. H. M.; Roks, A. J. M.; van den Meiracker, A. H.; Danser, A. H. J. Hypertension. *Circulation Research* **2015**, *116* (6), 960–975. DOI: doi:10.1161/CIRCRESAHA.116.303587.
(379) Siddiquee, K.; Hampton, J.; McAnally, D.; May, L. T.; Smith, L. H. The apelin receptor inhibits the angiotensin II type 1 receptor via allosteric trans-inhibition. *British journal of pharmacology* **2013**, *168* (5), 1104–1117.
(380) Siddiquee, K.; Hampton, J.; Khan, S.; Zadory, D.; Gleaves, L.; Vaughan, D. E.; Smith, L. H. Apelin protects against angiotensin II-induced cardiovascular fibrosis and decreases plasminogen activator inhibitor type-1 production. *Journal of Hypertension* **2011**, *29* (4).
(381) Andersen, C. U.; Hilberg, O.; Mellemkjær, S.; Nielsen-Kudsk, J. E.; Simonsen, U. Apelin and pulmonary hypertension. *Pulm Circ* **2011**, *1* (3), 334–346. DOI: 10.4103/2045-8932.87299 From NLM.
(382) Kagiyama, S.; Fukuhara, M.; Matsumura, K.; Lin, Y.; Fujii, K.; Iida, M. Central and peripheral cardiovascular actions of apelin in conscious rats. *Regulatory Peptides* **2005**, *125* (1), 55–59. DOI: https://doi.org/10.1016/j.regpep.2004.07.033.
(383) Zhang, Q.; Yao, F.; Raizada, M. K.; O'Rourke, S. T.; Sun, C. Apelin Gene Transfer Into the Rostral Ventrolateral Medulla Induces Chronic Blood Pressure Elevation in Normotensive Rats. *Circulation Research* **2009**, *104* (12), 1421–1428. DOI: 10.1161/CIRCRESAHA.108.192302 (accessed 2025/09/23).
(384) Falcone, C.; Bozzini, S.; Schirinzi, S.; Buzzi, M. P.; Boiocchi, C.; Totaro, R.; Bondesan, M.; Pelissero, G. APJ polymorphisms in coronary artery disease patients with and without hypertension. *Mol Med Rep* **2012**, *5* (2), 321–325. DOI: 10.3892/mmr.2011.685 From NLM.
(385) Jin, W.; Su, X.; Xu, M.; Liu, Y.; Shi, J.; Lu, L.; Niu, W. Interactive association of five candidate polymorphisms in Apelin/APJ pathway with coronary artery disease among Chinese hypertensive patients. *PLoS One* **2012**, *7* (12), e51123. DOI: 10.1371/journal.pone.0051123 From NLM.
(386) Liu, R.; Zhao, H.; Wang, Y.; Wang, Y.; Lu, C.; Xiao, Y.; Jia, N.; Wang, B.; Niu, W. The contributory role of angiotensin receptor-like 1 gene multiple polymorphisms in hypertension among northeastern Han Chinese. *PLoS One* **2014**, *9* (1), e86095. DOI: 10.1371/journal.pone.0086095 From NLM.
(387) Zhang, F.; Armando, I.; Jose, P. A.; Zeng, C.; Yang, J. G protein-coupled receptor kinases in hypertension: physiology, pathogenesis, and therapeutic targets. *Hypertension Research* **2024**, *47* (9), 2317–2336. DOI: 10.1038/s41440-024-01763-y.
(388) Robinson, C. L.; Guo, M. Fingolimod (Gilenya) and melanoma. *BMJ Case Rep* **2016**, *2016*. DOI: 10.1136/bcr-2016-217885 From NLM.
(389) Jia, A.; Kuramoto, L.; Khakban, A.; Sio, W. S.; Traboulsee, A.; De Vera, M. A.; Oh, J.; Loree, J.; Tam, R.; Lynd, L. D.; et al. Fingolimod and risk of skin cancer among individuals with multiple sclerosis: a population-based cohort study protocol. *BMJ Open* **2025**, *15* (1), e088924. DOI: 10.1136/bmjopen-2024-088924.

(390) Ghafouri-Fard, S.; Khoshbakht, T.; Hussen, B. M.; Dong, P.; Gassler, N.; Taheri, M.; Baniahmad, A.; Dilmaghani, N. A. A review on the role of cyclin dependent kinases in cancers. *Cancer Cell International* **2022**, *22* (1), 325. DOI: 10.1186/s12935-022-02747-z.
(391) Ruvolo, P. P. Role of protein phosphatases in the cancer microenvironment. *Biochim Biophys Acta Mol Cell Res* **2019**, *1866* (1), 144–152. DOI: 10.1016/j.bbamcr.2018.07.006 From NLM.
(392) Li, H.; Liu, J.; Shen, S.; Dai, D.; Cheng, S.; Dong, X.; Sun, L.; Guo, X. Pan-cancer analysis of alternative splicing regulator heterogeneous nuclear ribonucleoproteins (hnRNPs) family and their prognostic potential. *J Cell Mol Med* **2020**, *24* (19), 11111–11119. DOI: 10.1111/jcmm.15558 From NLM.
(393) Nguyen, T. L.; Schneppenheim, J.; Rudnik, S.; Lüllmann-Rauch, R.; Bernreuther, C.; Hermans-Borgmeyer, I.; Glatzel, M.; Saftig, P.; Schröder, B. Functional characterization of the lysosomal membrane protein TMEM192 in mice. *Oncotarget* **2017**, *8* (27).
(394) Zanivan, S. R. THEM6-mediated lipid remodelling sustains stress resistance in cancer. 2021.
(395) Volpi, C.; Orabona, C.; Macchiarulo, A.; Bianchi, R.; Puccetti, P.; Grohmann, U. Preclinical discovery and development of fingolimod for the treatment of multiple sclerosis. *Expert Opinion on Drug Discovery* **2019**, *14* (11), 1199–1212. DOI: 10.1080/17460441.2019.1646244.
(396) Huwiler, A.; Zangemeister-Wittke, U. The sphingosine 1-phosphate receptor modulator fingolimod as a therapeutic agent: Recent findings and new perspectives. *Pharmacology & Therapeutics* **2018**, *185*, 34–49. DOI: https://doi.org/10.1016/j.pharmthera.2017.11.001.
(397) Zhukovsky, M. A.; Filograna, A.; Luini, A.; Corda, D.; Valente, C. The Structure and Function of Acylglycerophosphate Acyltransferase 4/ Lysophosphatidic Acid Acyltransferase Delta (AGPAT4/LPAATδ). *Front Cell Dev Biol* **2019**, *7*, 147. DOI: 10.3389/fcell.2019.00147 From NLM.
(398) Cao, J.; Liu, Y.; Lockwood, J.; Burn, P.; Shi, Y. A novel cardiolipin-remodeling pathway revealed by a gene encoding an endoplasmic reticulum-associated acyl-CoA:lysocardiolipin acyltransferase (ALCAT1) in mouse. *J Biol Chem* **2004**, *279* (30), 31727–31734. DOI: 10.1074/jbc.M402930200 From NLM.
(399) Eto, M.; Shindou, H.; Yamamoto, S.; Tamura-Nakano, M.; Shimizu, T. Lysophosphatidylethanolamine acyltransferase 2 (LPEAT2) incorporates DHA into phospholipids and has possible functions for fatty acid-induced cell death. *Biochemical and Biophysical Research Communications* **2020**, *526* (1), 246–252.
(400) Sato, T.; Umebayashi, S.; Senoo, N.; Akahori, T.; Ichida, H.; Miyoshi, N.; Yoshida, T.; Sugiura, Y.; Goto-Inoue, N.; Kawana, H.; et al. LPGAT1/LPLAT7 regulates acyl chain profiles at the sn-1 position of phospholipids in murine skeletal muscles. *J Biol Chem* **2023**, *299* (7), 104848. DOI: 10.1016/j.jbc.2023.104848 From NLM.
(401) Shindou, H.; Shimizu, T. Acyl-CoA:Lysophospholipid Acyltransferases*. *Journal of Biological Chemistry* **2009**, *284* (1), 1–5. DOI: https://doi.org/10.1074/jbc.R800046200.
(402) Zhao, Z.; Choi, J.; Zhao, C.; Ma, Z. A. FTY720 Normalizes Hyperglycemia by Stimulating β-Cell in Vivo Regeneration in db/db Mice through Regulation of Cyclin D3 and p57KIP2*. *Journal of Biological Chemistry* **2012**, *287* (8), 5562–5573. DOI: https://doi.org/10.1074/jbc.M111.305359.
(403) Kendall, M. R.; Hupfeld, C. J. FTY720, a sphingosine-1-phosphate receptor modulator, reverses high-fat diet–induced weight gain, insulin resistance and adipose tissue

inflammation in C57BL/6 mice. *Diabetes, Obesity and Metabolism* **2008**, *10* (9), 802–805. DOI: https://doi.org/10.1111/j.1463-1326.2008.00910.x.
(404) Bruce, C. R.; Risis, S.; Babb, J. R.; Yang, C.; Lee-Young, R. S.; Henstridge, D. C.; Febbraio, M. A. The Sphingosine-1-Phosphate Analog FTY720 Reduces Muscle Ceramide Content and Improves Glucose Tolerance in High Fat-Fed Male Mice. *Endocrinology* **2013**, *154* (1), 65–76. DOI: 10.1210/en.2012-1847 (accessed 9/13/2025).
(405) Lahiri, S.; Park, H.; Laviad, E. L.; Lu, X.; Bittman, R.; Futerman, A. H. Ceramide synthesis is modulated by the sphingosine analog FTY720 via a mixture of uncompetitive and noncompetitive inhibition in an Acyl-CoA chain length-dependent manner. *J Biol Chem* **2009**, *284* (24), 16090–16098. DOI: 10.1074/jbc.M807438200 From NLM.
(406) Wang, M.-T.; Hu, Z.-C.; Xiang, Y.; Zeng, X.-Q.; Fei, Z.-C.; Chen, J.; Li, X.-P.; Zhu, Y.-P.; Wang, J.; Wang, Y.-J.; et al. Fingolimod ameliorates amyloid deposition and neurodegeneration in APP/PS1 mouse model of Alzheimer's disease. *The Journal of Prevention of Alzheimer's Disease* **2025**, *12* (7), 100131. DOI: https://doi.org/10.1016/j.tjpad.2025.100131.
(407) Prieto, G. A.; Trieu, B. H.; Dang, C. T.; Bilousova, T.; Gylys, K. H.; Berchtold, N. C.; Lynch, G.; Cotman, C. W. Pharmacological Rescue of Long-Term Potentiation in Alzheimer Diseased Synapses. *J Neurosci* **2017**, *37* (5), 1197–1212. DOI: 10.1523/jneurosci.2774-16.2016 From NLM.
(408) Kuhn, P. H.; Wang, H.; Dislich, B.; Colombo, A.; Zeitschel, U.; Ellwart, J. W.; Kremmer, E.; Rossner, S.; Lichtenthaler, S. F. ADAM10 is the physiologically relevant, constitutive alpha-secretase of the amyloid precursor protein in primary neurons. *Embo j* **2010**, *29* (17), 3020–3032. DOI: 10.1038/emboj.2010.167 From NLM.
(409) Grimm, M. O.; Rothhaar, T. L.; Grösgen, S.; Burg, V. K.; Hundsdörfer, B.; Haupenthal, V. J.; Friess, P.; Kins, S.; Grimm, H. S.; Hartmann, T. Trans fatty acids enhance amyloidogenic processing of the Alzheimer amyloid precursor protein (APP). *J Nutr Biochem* **2012**, *23* (10), 1214–1223. DOI: 10.1016/j.jnutbio.2011.06.015 From NLM.
(410) Eckert, G. P.; Chang, S.; Eckmann, J.; Copanaki, E.; Hagl, S.; Hener, U.; Müller, W. E.; Kögel, D. Liposome-incorporated DHA increases neuronal survival by enhancing non-amyloidogenic APP processing. *Biochim Biophys Acta* **2011**, *1808* (1), 236–243. DOI: 10.1016/j.bbamem.2010.10.014 From NLM.
(411) Endres, K.; Deller, T. Regulation of Alpha-Secretase ADAM10 In vitro and In vivo: Genetic, Epigenetic, and Protein-Based Mechanisms. *Front Mol Neurosci* **2017**, *10*, 56. DOI: 10.3389/fnmol.2017.00056 From NLM.
(412) Karpinich, N. O.; Caron, K. M. Apelin signaling: new G protein-coupled receptor pathway in lymphatic vascular development. *Arterioscler Thromb Vasc Biol* **2014**, *34* (2), 239–241. DOI: 10.1161/atvbaha.113.302905 From NLM.
(413) Kim, J.-D.; Kang, Y.; Kim, J.; Papangeli, I.; Kang, H.; Wu, J.; Park, H.; Nadelmann, E.; Rockson, S. G.; Chun, H. J.; et al. Essential Role of Apelin Signaling During Lymphatic Development in Zebrafish. *Arteriosclerosis, Thrombosis, and Vascular Biology* **2014**, *34* (2), 338–345. DOI: doi:10.1161/ATVBAHA.113.302785.
(414) Kleinz, M. J.; Skepper, J. N.; Davenport, A. P. Immunocytochemical localisation of the apelin receptor, APJ, to human cardiomyocytes, vascular smooth muscle and endothelial cells. *Regul Pept* **2005**, *126* (3), 233–240. DOI: 10.1016/j.regpep.2004.10.019 From NLM.
(415) Kang, Y.; Kim, J.; Anderson, J. P.; Wu, J.; Gleim, S. R.; Kundu, R. K.; McLean, D. L.; Kim, J. D.; Park, H.; Jin, S. W.; et al. Apelin-APJ signaling is a critical regulator of endothelial

MEF2 activation in cardiovascular development. *Circ Res* **2013**, *113* (1), 22–31. DOI: 10.1161/circresaha.113.301324 From NLM.
(416) Han, J.; Schey, K. L. Proteolysis and Mass Spectrometric Analysis of an Integral Membrane: Aquaporin 0. *Journal of Proteome Research* **2004**, *3* (4), 807–812. DOI: 10.1021/pr049945w.
(417) Hoopes, S. L.; Willcockson, H. H.; Caron, K. M. Characteristics of multi-organ lymphangiectasia resulting from temporal deletion of calcitonin receptor-like receptor in adult mice. **2012**.
(418) Norrmén, C.; Tammela, T.; Petrova, T. V.; Alitalo, K. Biological Basis of Therapeutic Lymphangiogenesis. *Circulation* **2011**, *123* (12), 1335–1351. DOI: doi:10.1161/CIRCULATIONAHA.107.704098.
(419) Calebiro, D.; Godbole, A. Internalization of G-protein-coupled receptors: Implication in receptor function, physiology and diseases. *Best Pract Res Clin Endocrinol Metab* **2018**, *32* (2), 83–91. DOI: 10.1016/j.beem.2018.01.004 From NLM.
(420) Hamon, P.; Loyher, P.-L.; Baudesson de Chanville, C.; Licata, F.; Combadière, C.; Boissonnas, A. CX3CR1-dependent endothelial margination modulates Ly6Chigh monocyte systemic deployment upon inflammation in mice. *Blood* **2017**, *129* (10), 1296–1307. DOI: 10.1182/blood-2016-08-732164 (accessed 9/24/2025).
(421) Neel, N. F.; Schutyser, E.; Sai, J.; Fan, G.-H.; Richmond, A. Chemokine receptor internalization and intracellular trafficking. *Cytokine & Growth Factor Reviews* **2005**, *16* (6), 637–658. DOI: https://doi.org/10.1016/j.cytogfr.2005.05.008.
(422) Hampton, H. R.; Chtanova, T. Lymphatic Migration of Immune Cells. *Front Immunol* **2019**, *10*, 1168. DOI: 10.3389/fimmu.2019.01168 From NLM.
(423) Astoul, E.; Cantrell, D. A.; Edmunds, C.; Ward, S. G. PI 3-K and T-cell activation: limitations of T-leukemic cell lines as signaling models. *Trends in Immunology* **2001**, *22* (9), 490–496. DOI: https://doi.org/10.1016/S1471-4906(01)01973-1.
(424) Wu, X.; Reboll, M. R.; Korf-Klingebiel, M.; Wollert, K. C. Angiogenesis after acute myocardial infarction. *Cardiovasc Res* **2021**, *117* (5), 1257–1273. DOI: 10.1093/cvr/cvaa287 From NLM.
(425) Wencel, P. L.; Blecharz-Klin, K.; Piechal, A.; Pyrzanowska, J.; Mirowska-Guzel, D.; Strosznajder, R. P. Fingolimod Modulates the Gene Expression of Proteins Engaged in Inflammation and Amyloid-Beta Metabolism and Improves Exploratory and Anxiety-Like Behavior in Obese Mice. *Neurotherapeutics* **2023**, *20* (5), 1388–1404. DOI: 10.1007/s13311-023-01403-2 From NLM.
(426) Angelopoulou, E.; Piperi, C. Beneficial Effects of Fingolimod in Alzheimer's Disease: Molecular Mechanisms and Therapeutic Potential. *Neuromolecular Med* **2019**, *21* (3), 227–238. DOI: 10.1007/s12017-019-08558-2 From NLM.
(427) Li, J.; Nan, X.; Ma, Y.; Wang, Z.; Fang, H. Therapeutic Potential of Fingolimod in Diabetes Mellitus and Its Chronic Complications. *Diabetes, Metabolic Syndrome and Obesity* **2024**, *17* (null), 507–516. DOI: 10.2147/DMSO.S385016.
(428) Newton, J.; Hait, N. C.; Maceyka, M.; Colaco, A.; Maczis, M.; Wassif, C. A.; Cougnoux, A.; Porter, F. D.; Milstien, S.; Platt, N.; et al. FTY720/fingolimod increases NPC1 and NPC2 expression and reduces cholesterol and sphingolipid accumulation in Niemann-Pick type C mutant fibroblasts. *Faseb j* **2017**, *31* (4), 1719–1730. DOI: 10.1096/fj.201601041R From NLM.
(429) Calzavara, J.; McNulty, J. A convergent synthesis of the immunosuppressant FTY720 employing aqueous Wittig chemistry. *Tetrahedron Letters* **2011**, *52* (43), 5672–5675. DOI: https://doi.org/10.1016/j.tetlet.2011.08.100.

(430) Liu, Y.; Ge, H. Site-selective C–H arylation of primary aliphatic amines enabled by a catalytic transient directing group. *Nature Chemistry* **2017**, *9* (1), 26–32. DOI: 10.1038/nchem.2606.
(431) Limited, N. P. WO2014/111949. 2014.
(432) Abel, S. e. a. United States 2002.
(433) Liu, Z.; MacRitchie, N.; Pyne, S.; Pyne, N. J.; Bittman, R. Synthesis of (S)-FTY720 vinylphosphonate analogues and evaluation of their potential as sphingosine kinase 1 inhibitors and activators. *Bioorganic & Medicinal Chemistry* **2013**, *21* (9), 2503–2510. DOI: https://doi.org/10.1016/j.bmc.2013.02.042.
(434) Albert, R.; Hinterding, K.; Brinkmann, V.; Guerini, D.; Müller-Hartwieg, C.; Knecht, H.; Simeon, C.; Streiff, M.; Wagner, T.; Welzenbach, K.; et al. Novel Immunomodulator FTY720 Is Phosphorylated in Rats and Humans To Form a Single Stereoisomer. Identification, Chemical Proof, and Biological Characterization of the Biologically Active Species and Its Enantiomer. *Journal of Medicinal Chemistry* **2005**, *48* (16), 5373–5377. DOI: 10.1021/jm050242f.
(435) Lahav, D.; Liu, B.; van den Berg, R. J. B. H. N.; van den Nieuwendijk, A. M. C. H.; Wennekes, T.; Ghisaidoobe, A. T.; Breen, I.; Ferraz, M. J.; Kuo, C.-L.; Wu, L.; et al. A Fluorescence Polarization Activity-Based Protein Profiling Assay in the Discovery of Potent, Selective Inhibitors for Human Nonlysosomal Glucosylceramidase. *Journal of the American Chemical Society* **2017**, *139* (40), 14192–14197. DOI: 10.1021/jacs.7b07352.
(436) Willemsen, J. S.; van Hest, J. C. M.; Rutjes, F. P. J. T. Aqueous reductive amination using a dendritic metal catalyst in a dialysis bag. *Beilstein Journal of Organic Chemistry* **2013**, *9*, 960–965. DOI: 10.3762/bjoc.9.110.
(437) Bergmeier, S. C.; Seth, P. P. Formation of Scalemic Aziridines via the Nucleophilic Opening of Aziridines. *The Journal of Organic Chemistry* **1997**, *62* (8), 2671–2674. DOI: 10.1021/jo962307f.
(438) MacAlpine, G. A.; Warkentin, J. Thermolysis of Δ3-1,3,4-oxadiazolin-2-ones and 2-phenylimino-Δ3-1,3,4-oxadazolines derived from α,β-epoxyketones. An alternative method for the convers of α,β-epoxyketones to alkynones and alkynals. *Canadian Journal of Chemistry* **1978**, *56* (3), 308–315. DOI: 10.1139/v78-048.
(439) Rode, K.; Palomba, M.; Ortgies, S.; Rieger, R.; Breder, A. Aerobic Allylation of Alcohols with Non-Activated Alkenes Enabled by Light-Driven Selenium-π-Acid Catalysis. *Synthesis* **2018**, *50* (19), 3875–3885. DOI: 10.1055/s-0037-1609938.
(440) Sharma, Y.; Pawar, G. P.; Chaudhari, V. D. One-Pot Domino Reaction: Direct Access to Polysubstituted 1,4-Benzothiazine 1,1-Dioxide via Water–Gas Shift Reaction Utilizing DMF/H2O. *The Journal of Organic Chemistry* **2023**, *88* (1), 701–710. DOI: 10.1021/acs.joc.2c02171.
(441) Lapointe, D.; Markiewicz, T.; Whipp, C. J.; Toderian, A.; Fagnou, K. Predictable and Site-Selective Functionalization of Poly(hetero)arene Compounds by Palladium Catalysis. *The Journal of Organic Chemistry* **2011**, *76* (3), 749–759. DOI: 10.1021/jo102081a.
(442) Xing, Y.; Zhang, M.; Ciccarelli, S.; Lee, J.; Catano, B. AuIII-Catalyzed Formation of α-Halomethyl Ketones from Terminal Alkynes. *European Journal of Organic Chemistry* **2017**, *2017* (4), 781–785. DOI: https://doi.org/10.1002/ejoc.201601416.
(443) Hamada, M.; Nakamura, M.; Kiuchi, M.; Marukawa, K.; Tomatsu, A.; Shimano, K.; Sato, N.; Sugahara, K.; Asayama, M.; Takagi, K.; et al. Removal of Sphingosine 1-Phosphate Receptor-3 (S1P3) Agonism is Essential, But Inadequate to Obtain Immunomodulating 2-

Aminopropane-1,3-diol S1P1 Agonists with Reduced Effect on Heart Rate. *Journal of Medicinal Chemistry* **2010**, *53* (8), 3154–3168. DOI: 10.1021/jm901776q.
(444) Dienemann, J.-N.; Chen, S.-Y.; Hitzenberger, M.; Sievert, M. L.; Hacker, S. M.; Prigge, S. T.; Zacharias, M.; Groll, M.; Sieber, S. A. A Chemical Proteomic Strategy Reveals Inhibitors of Lipoate Salvage in Bacteria and Parasites. *Angewandte Chemie International Edition* **2023**, *62* (31), e202304533. DOI: https://doi.org/10.1002/anie.202304533.
(445) Ding, L.-G.; Yao, B.-J.; Wu, W.-X.; Yu, Z.-G.; Wang, X.-Y.; Kan, J.-L.; Dong, Y.-B. Metalloporphyrin and Ionic Liquid-Functionalized Covalent Organic Frameworks for Catalytic CO2 Cycloaddition via Visible-Light-Induced Photothermal Conversion. *Inorganic Chemistry* **2021**, *60* (16), 12591–12601. DOI: 10.1021/acs.inorgchem.1c01975.
(446) Stadtmüller, H.; Vaupel, A.; Tucker, C. E.; Stüdemann, T.; Knochel, P. Stereoselective Preparation of Polyfunctional Cyclopentane Derivatives by Radical Nickel- or Palladium-Catalyzed Carbozincations. *Chemistry – A European Journal* **1996**, *2* (10), 1204–1220. DOI: https://doi.org/10.1002/chem.19960021006.
(447) Boulos, R. A.; Man, N. Y. T.; Lengkeek, N. A.; Hammer, K. A.; Foster, N. F.; Stemberger, N. A.; Skelton, B. W.; Wong, P. Y.; Martinac, B.; Riley, T. V.; et al. Inspiration from Old Dyes: Tris(stilbene) Compounds as Potent Gram-Positive Antibacterial Agents. *Chemistry – A European Journal* **2013**, *19* (52), 17980–17988. DOI: https://doi.org/10.1002/chem.201303119.
(448) Chai, Y.-M.; Zou, Q.; Guo, Z.-X.; Qin, Y.-J.; Zhang, P. A mild oxidative bromination of ketones with the combination of KBr/Fe(NO3)3·9H2O. *Tetrahedron Letters* **2023**, *122*, 154517. DOI: https://doi.org/10.1016/j.tetlet.2023.154517.
(449) Hu, S.; Liu, D.; Yan, C.; Cai, M. An efficient heterogeneous gold (I)-catalyzed hydration of haloalkynes leading to $\alpha$-halomethyl ketones. *Synthetic Communications* **2018**, *48* (23), 2983–2991.
(450) Burke, C. P.; Shi, Y. Enantioselective epoxidation of nonconjugated cis-olefins by chiral dioxirane. *Organic letters* **2009**, *11* (22), 5150–5153.
(451) BEAT, G. R. COMPOUNDS, COMPOSITIONS AND METHODS FOR CONTROLLING INVERTEBRATE PESTS. 2008.
(452) Vaillard, V. A.; Rossi, R. A.; Martín, S. E. Synthesis of pyrrole and indole quinoxalinone and oxazinone derivatives by intramolecular copper-catalyzed reactions. *Organic & Biomolecular Chemistry* **2011**, *9* (13), 4927–4935, 10.1039/C1OB05269A. DOI: 10.1039/C1OB05269A.
(453) UNIVERSITY, D. Methods of Inhibiting Metastasis from Cancer. 2012.
(454) L, F. A. U. S. J. M. U. M. O. U. G. W. Compounds useful for inhibiting metastasis from cancer and methods using same. US 2013.
(455) Ravelo, J.; Regueiro, A.; Rodríguez, E.; de Vera, J.; Martín, J. D. Synthetic studies towards ciguatoxin via acetal/$\gamma$-oxovinyl stannane condensation: A convergent approach. *Tetrahedron Letters* **1996**, *37* (16), 2869–2872. DOI: https://doi.org/10.1016/0040-4039(96)00409-1.
(456) Rodríguez, A.; Nomen, M.; Spur, B. W.; Godfroid, J. J.; Lee, T. H. Total synthesis of lipoxin A4 and lipoxin B4 from butadiene. *Tetrahedron Letters* **2000**, *41* (6), 823–826. DOI: https://doi.org/10.1016/S0040-4039(99)02201-7.

# Appendix

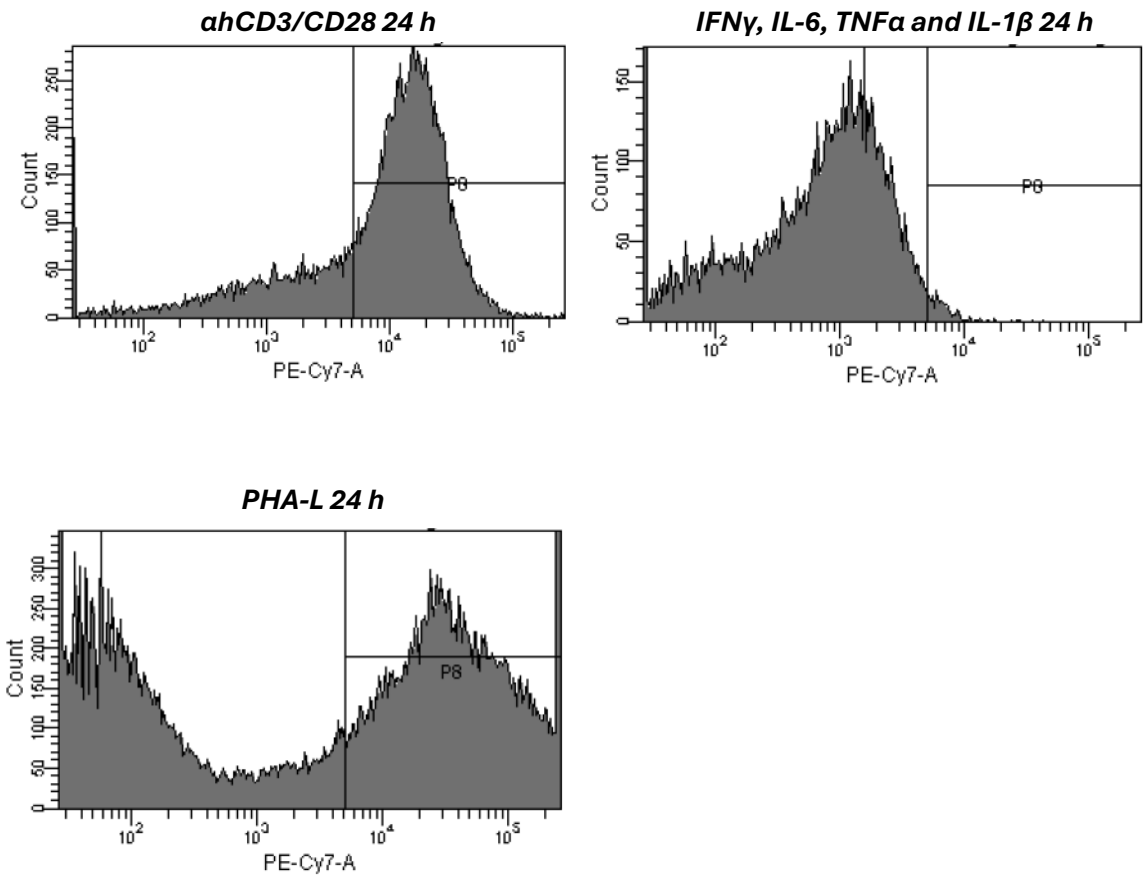


***Appendix I: Jurkat T-lymphocyte activation after 24 h, as measured by CD69 expression by FACS.***

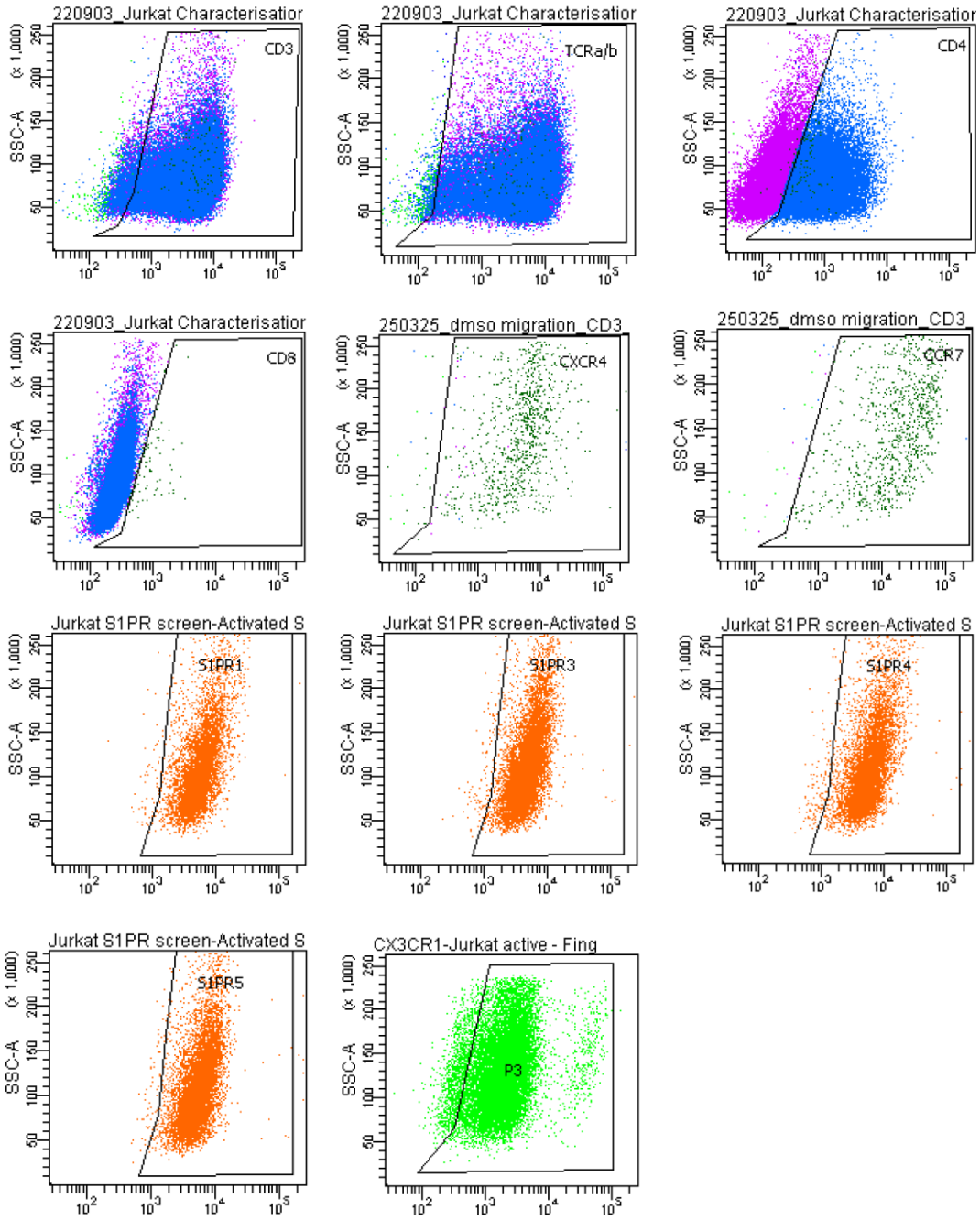


***Appendix II: Flow cytometry characterisation of the Jurkat E6.1 cells***

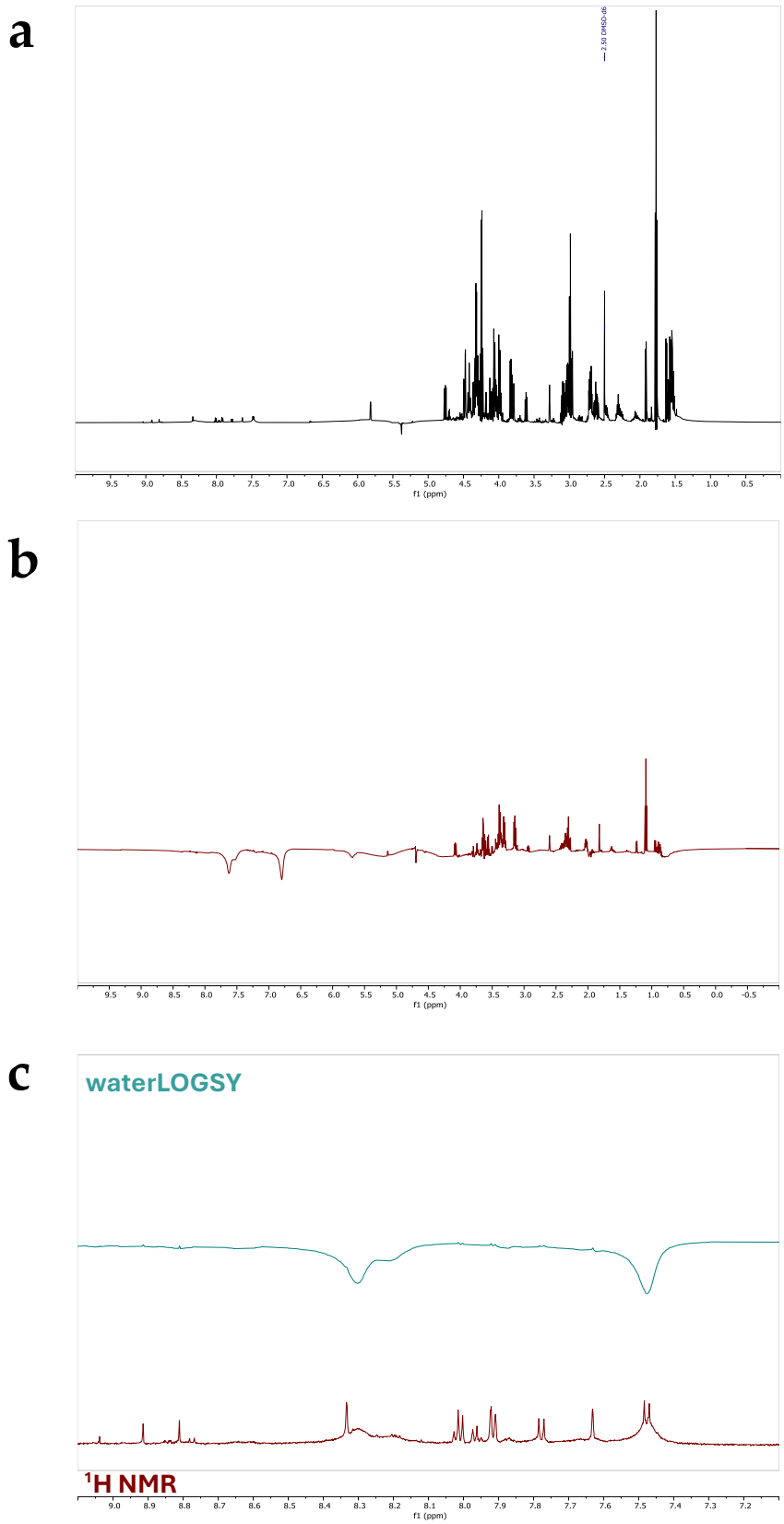


***Appendix III: WaterLOGSY experiment to investigate fingolimod aggregation in EGM-2MV media.*** *(a) $^1$H NMR spectra (32 scans) of fingolimod (500 µM) in EGM-2MV media (b) waterLOGSY spectra (1024 scans) of fingolimod (500 µM) in EGM-2MV media (c) stacked spectra of $^1$H NMR and waterLOGSY in the aromatic region (7.0-9.1 ppm) indicating significant background noise.*

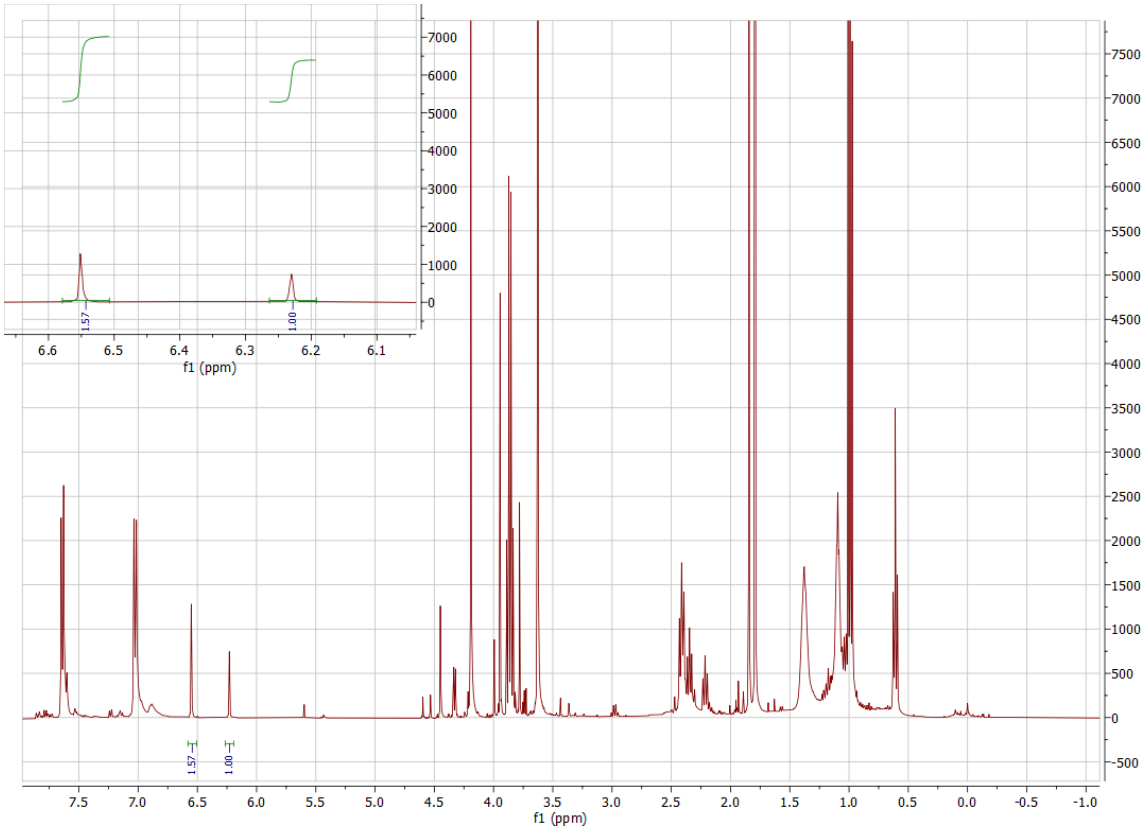


***Appendix IV: $^{1}$H NMR of β-chlorovinyl ketone 56 side product.***

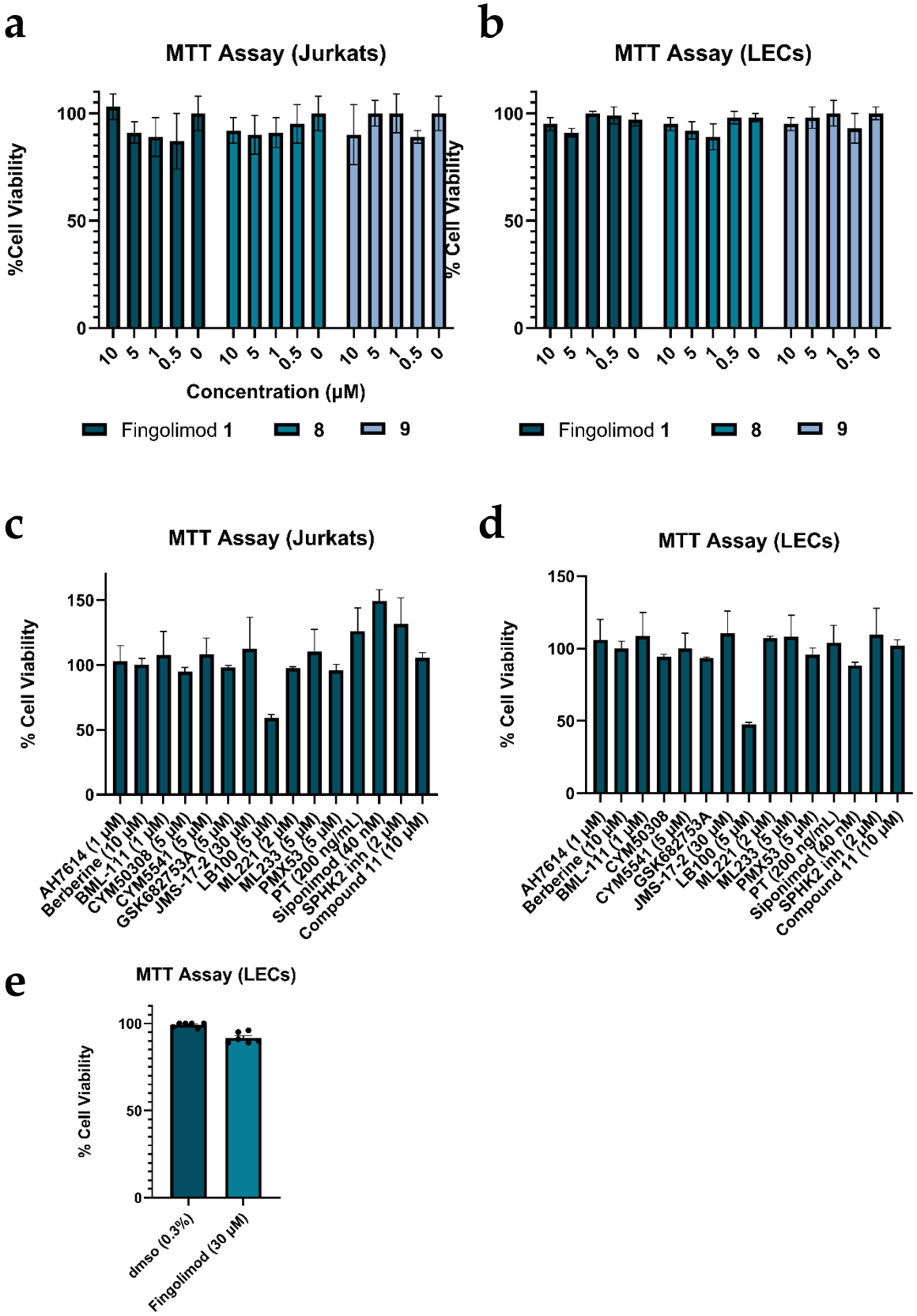


***Appendix V: Cytotoxicity Assay of all compounds in Jurkats and LECs.*** *MTT assays after 6 h treatment with fingolimod and negative control analogues **8** & **9** in (a) Jurkats and (b) LECs. MTT assays after 6 h treatment with all compounds at their highest tested dose in (c) Jurkats and (d) LECs. (e) MTT assay after 1 h treatment of LECs with fingolimod. Error bars = sem. All data normalised to 0.1% dmso treated cell viability.*

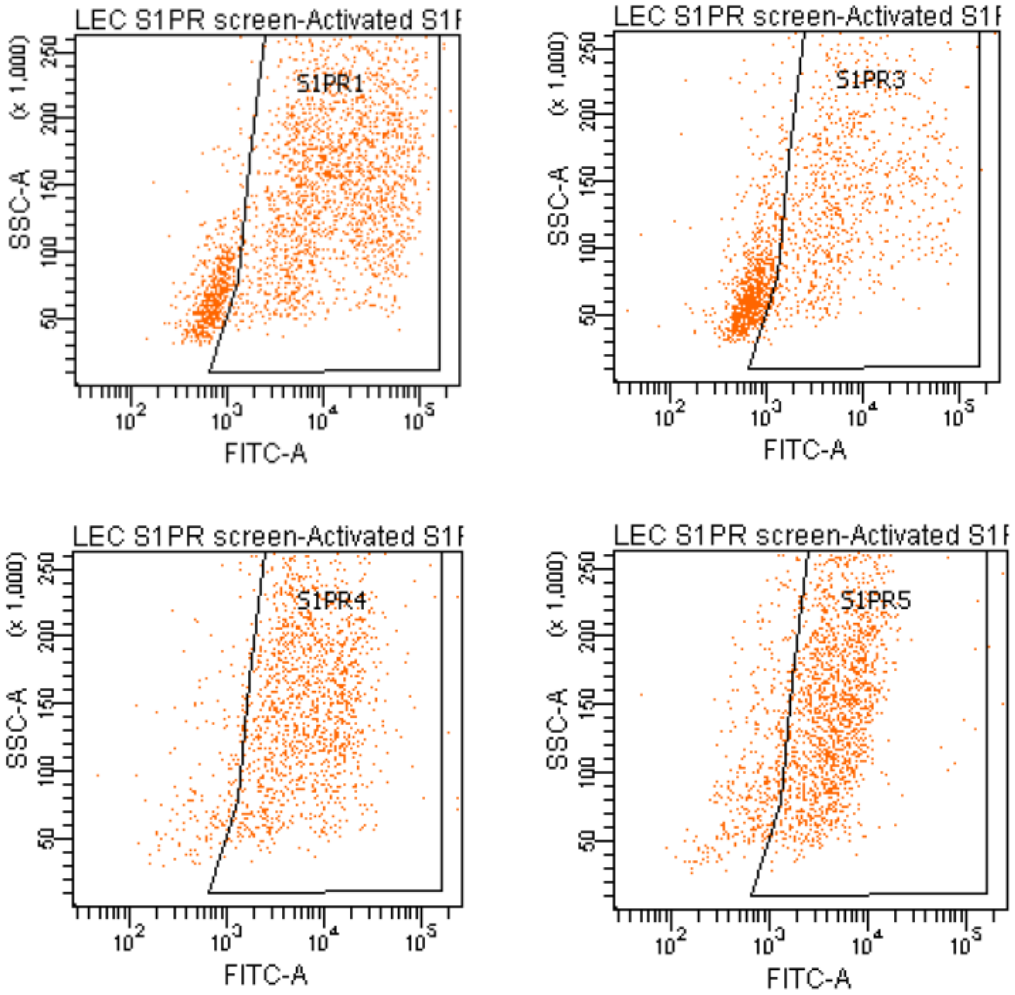


***Appendix VI: S1PR expression levels on lymphatic endothelial cells.*** *Flow cytometry was used to assess the surface expression levels of $S1PR_{1,3-5}$. % of the population expressing each marker was $S1PR_1$ = 76.5%; $S1PR_3$ = 52.1%; $S1PR_4$ = 88.0%; $S1PR_5$ = 79.7%.*

**Appendix VII: Synthetic routes to ChEMBL screen compounds, BML-111, JMS-17-2, LB-100**

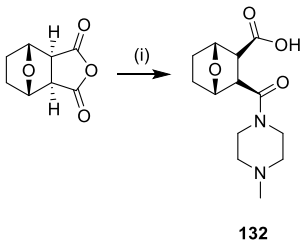


132

***Scheme S1: BML-100 synthetic route. Reaction conditions:*** *norcantharidin (1.0 eq), N-methylpiperazine (1.0 eq), benzene, rt, 18 h, 22% yield.*

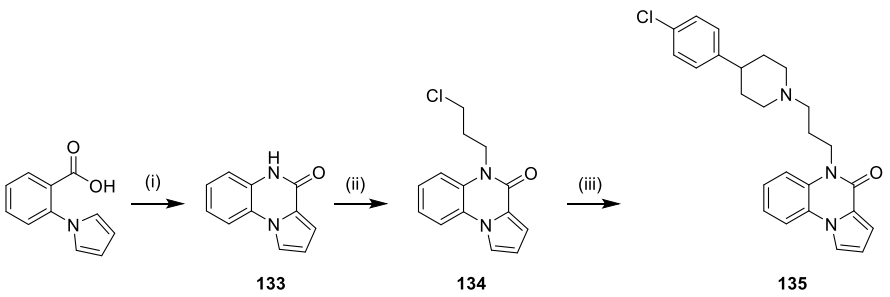


133 134 135

***Scheme S2: JMS-17-2 synthetic route. Reaction conditions:*** *(i) DIPEA (2.0 eq), DPPA (1.6 eq), 2-MeTHF, 40 °C, 18 h, 15% yield (ii) $Cs_2CO_3$ (1.0 eq), 1-bromo-3-chloropropane (2.0 eq), DMF, 70 °C, 18 h, 45% yield (iii) 4-(4-chlorophenyl)piperidine (1.2 eq), $K_2CO_3$ (2.0 eq), MeCN, MW, 140 °C, 1 h, 81% yield.*

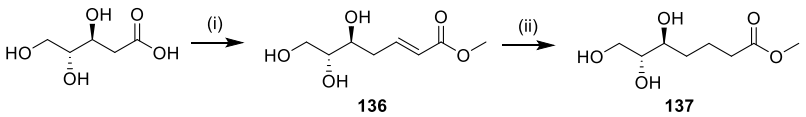


136 137

***Scheme S3: LB-100 synthetic route. Reaction conditions:*** *(i) methyl (triphenylphosphoranylidene)acetate (1.2 eq), THF, 80 °C, 16 h, 51% yield (ii) Pd/C (cat.), $H_2$, MeOH, 89% yield.*

NMRs for fingolimod:

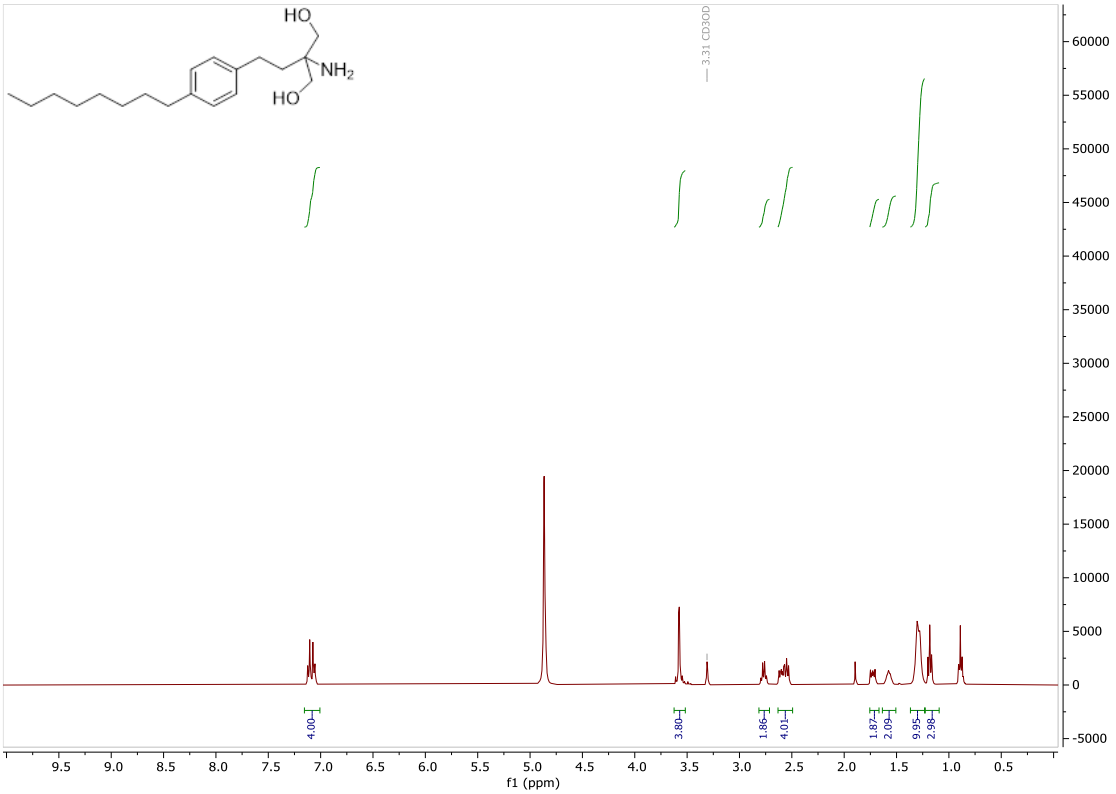


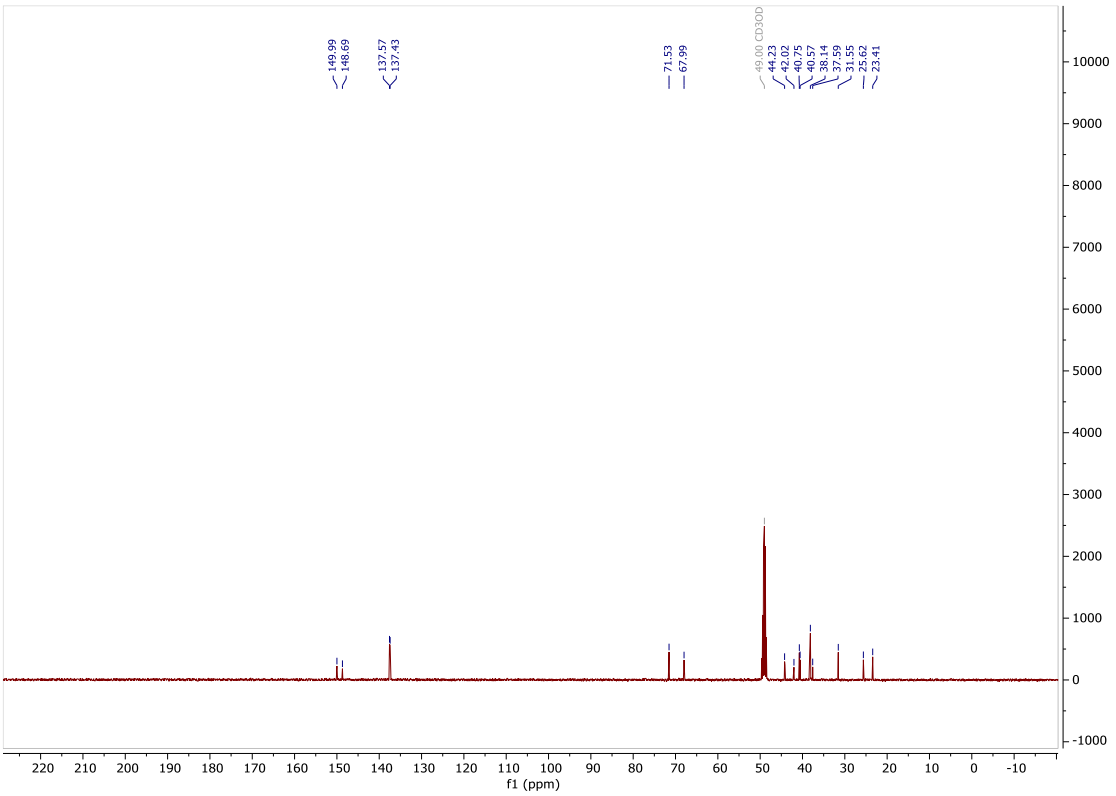

NMRs for Compound **6**:

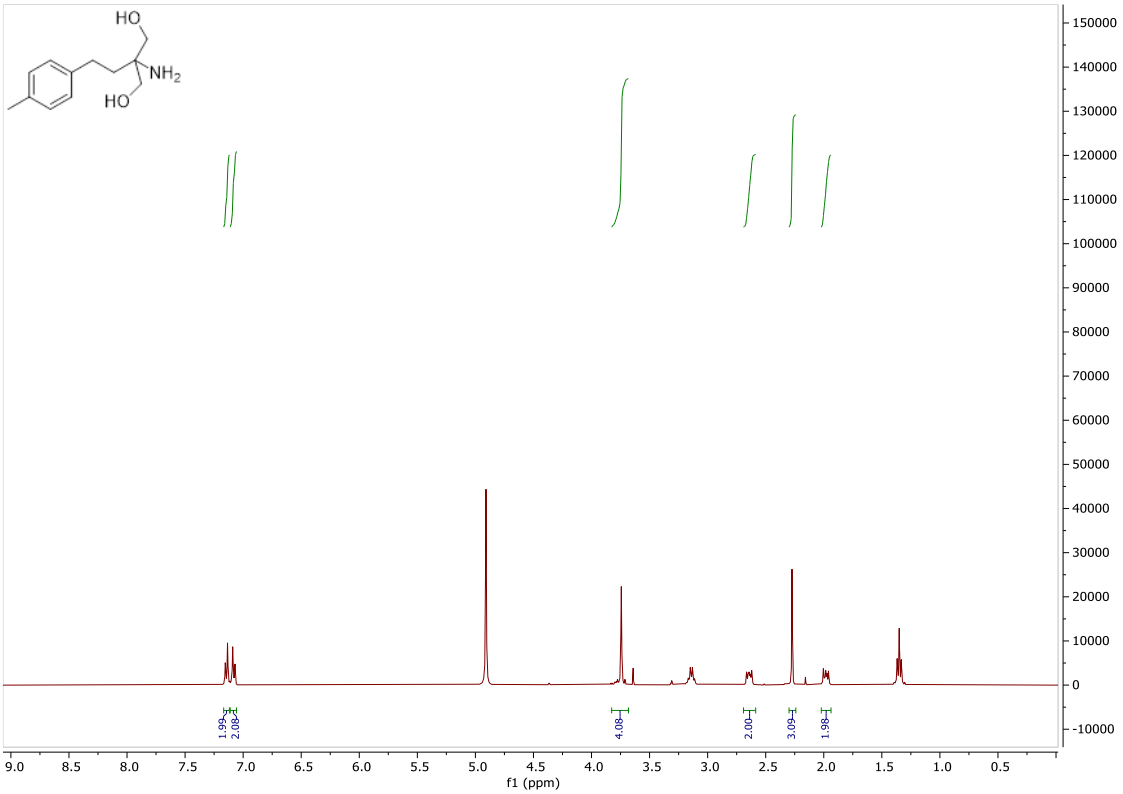


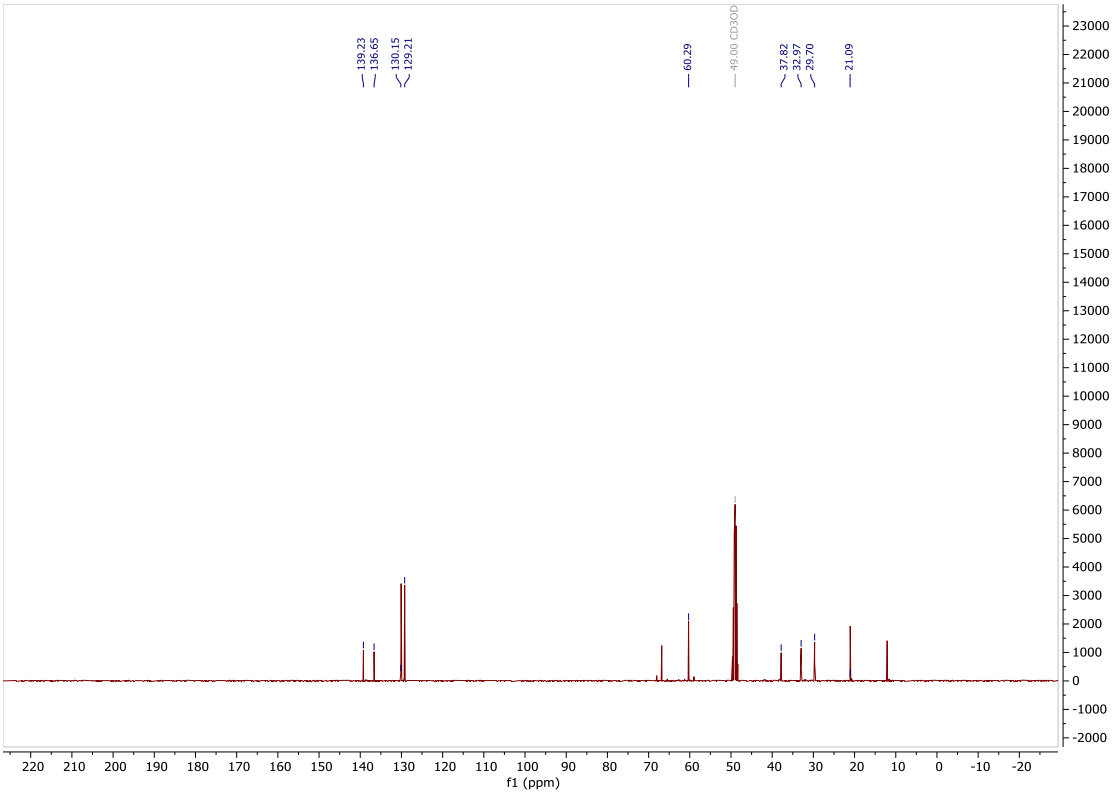

NMRs for Compound **7**:

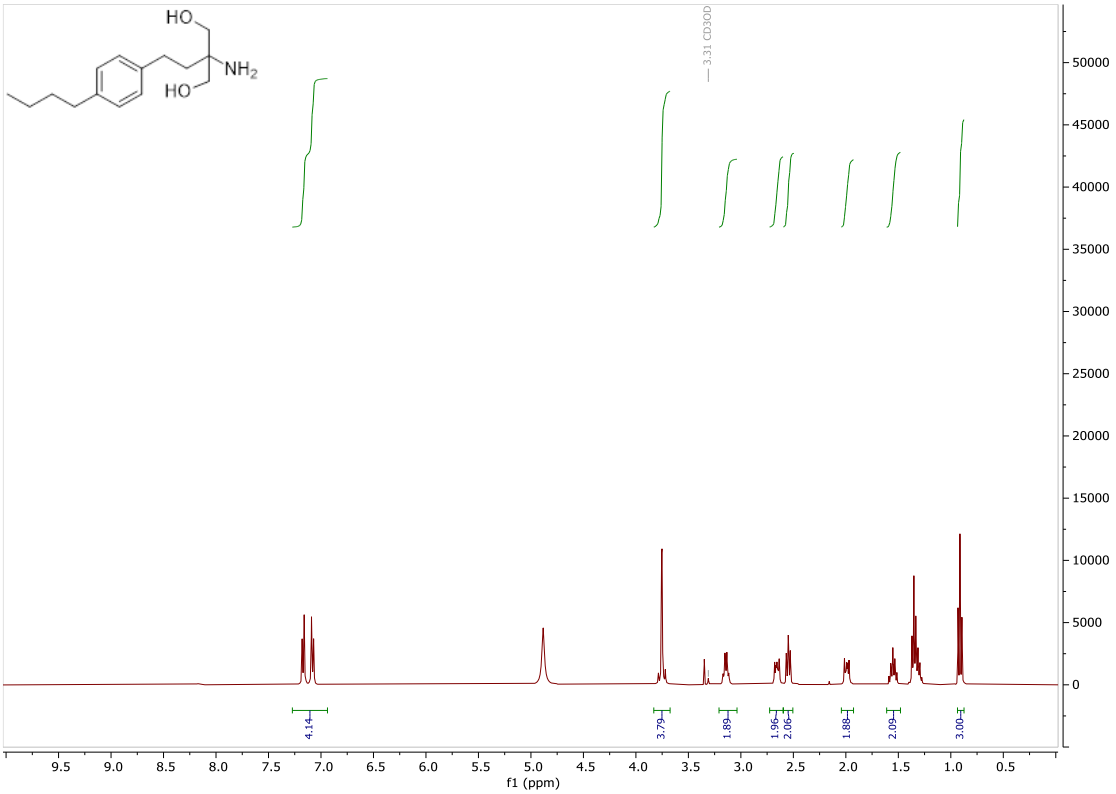


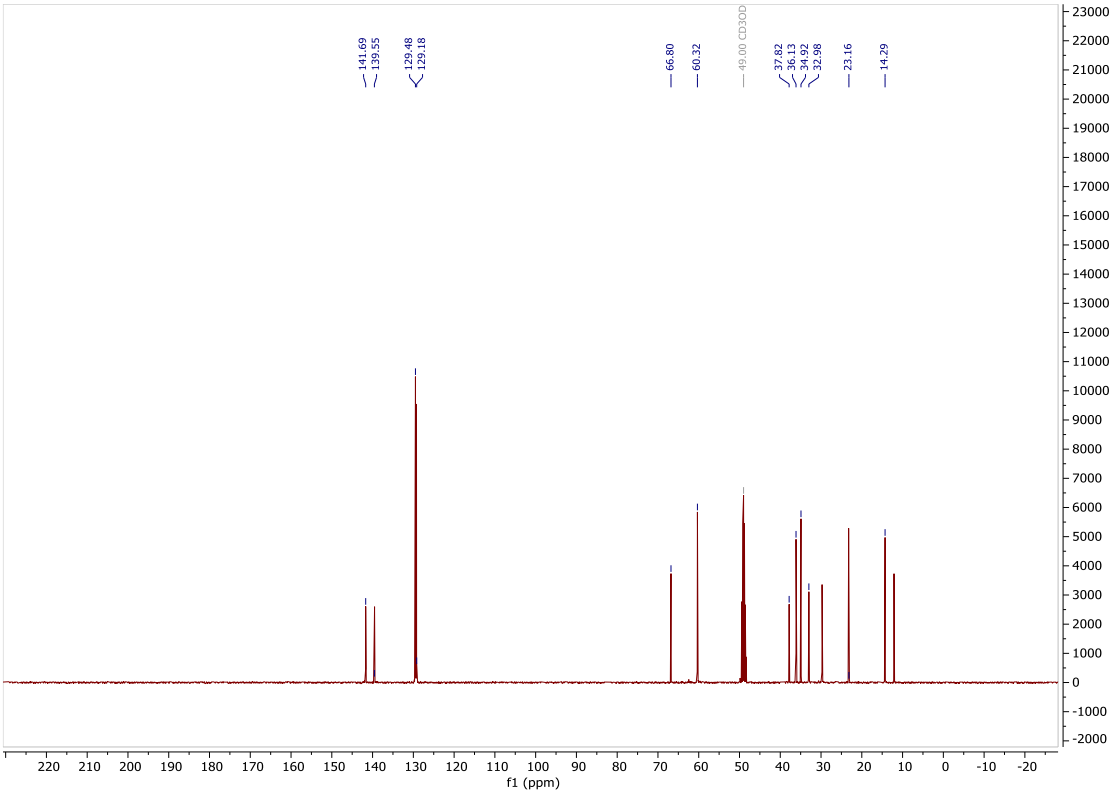

NMRs for Compound **8**:

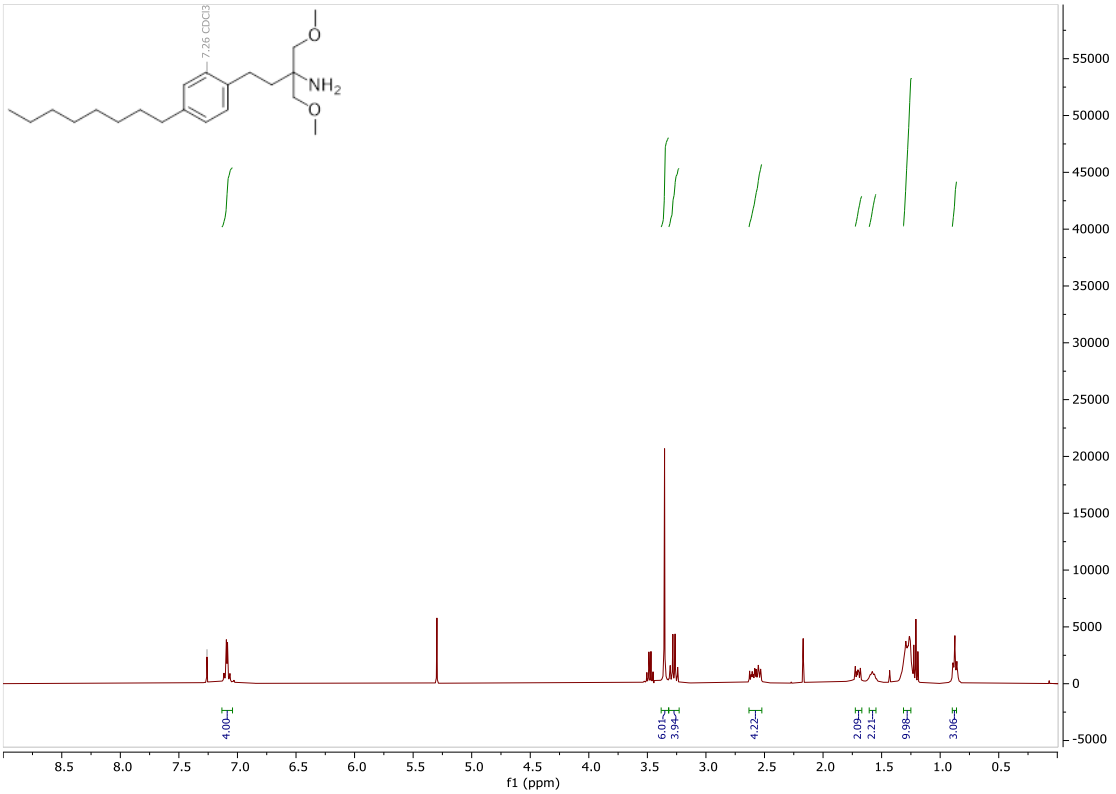


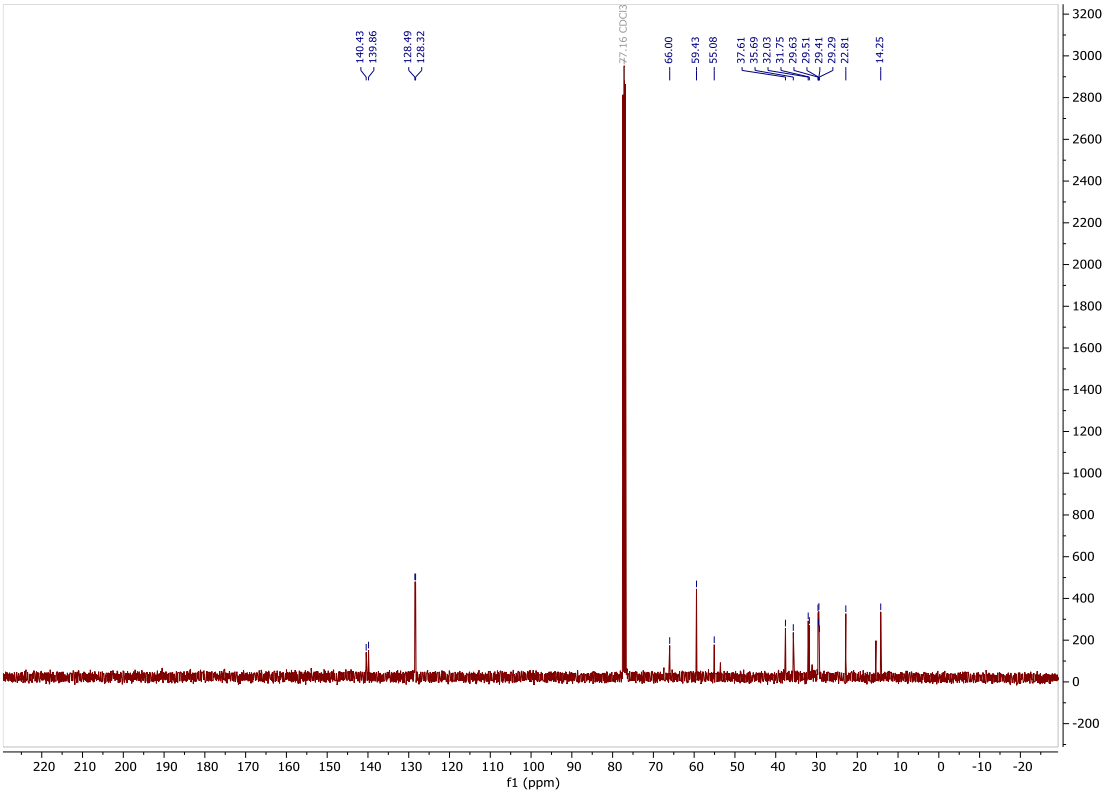

NMRs for PAL probe **114**:

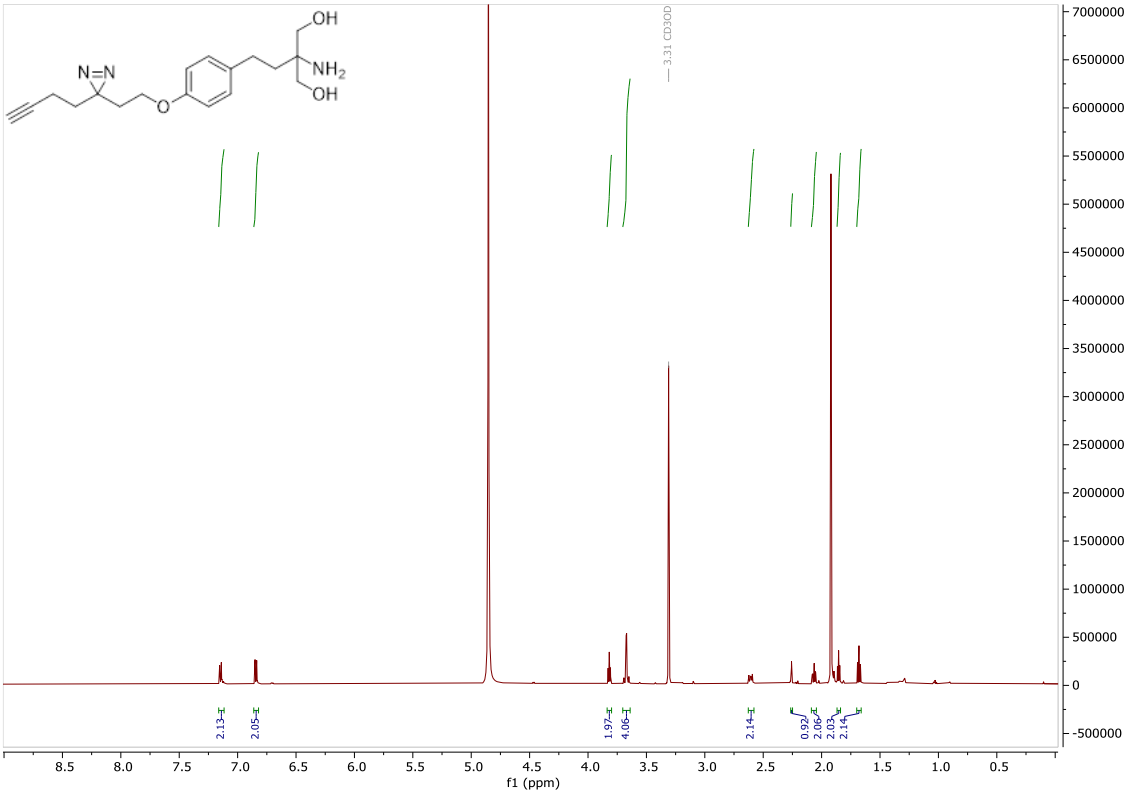


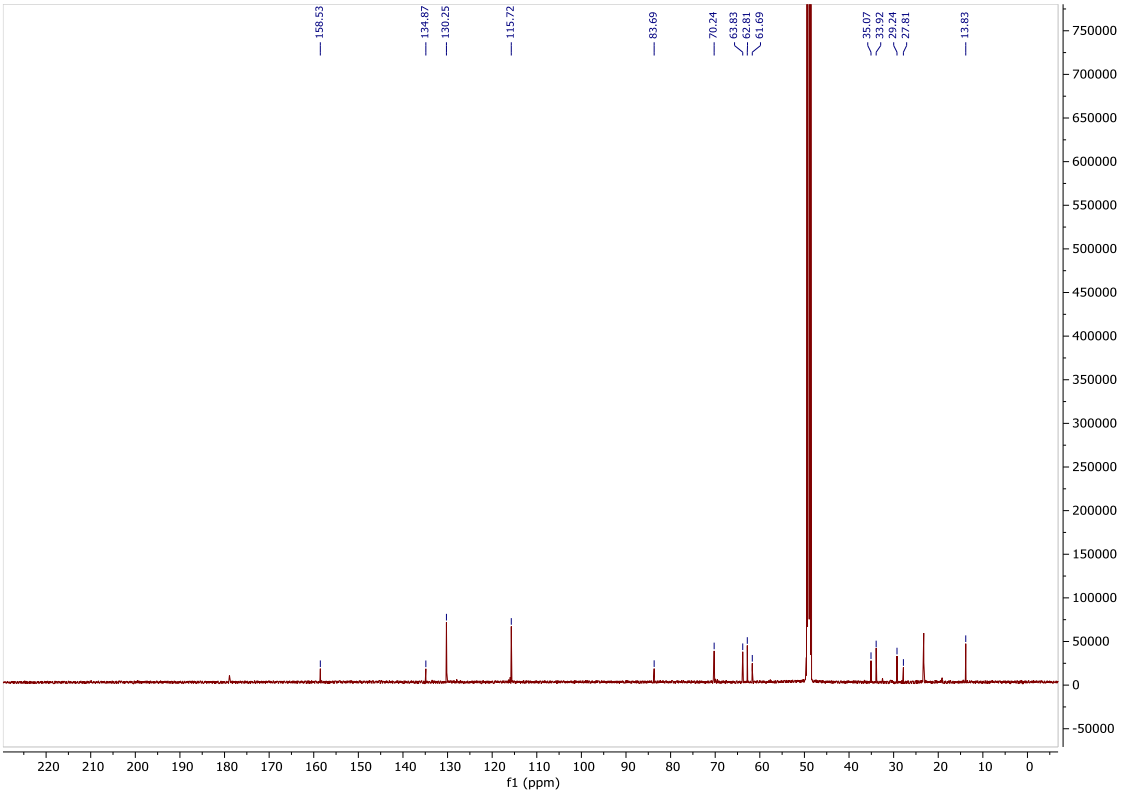

HMBC Spectra of PAL probe **114**:

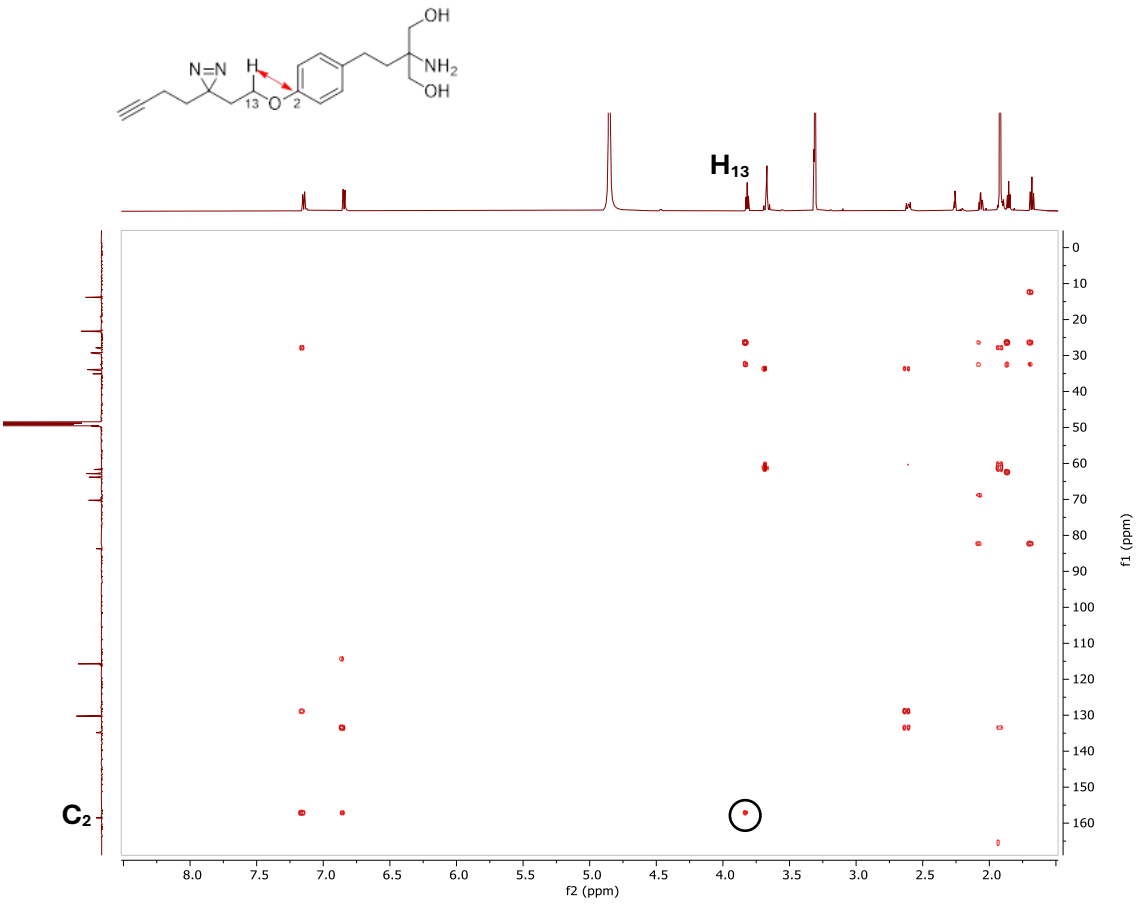

NMRs for PAL probe **130**:

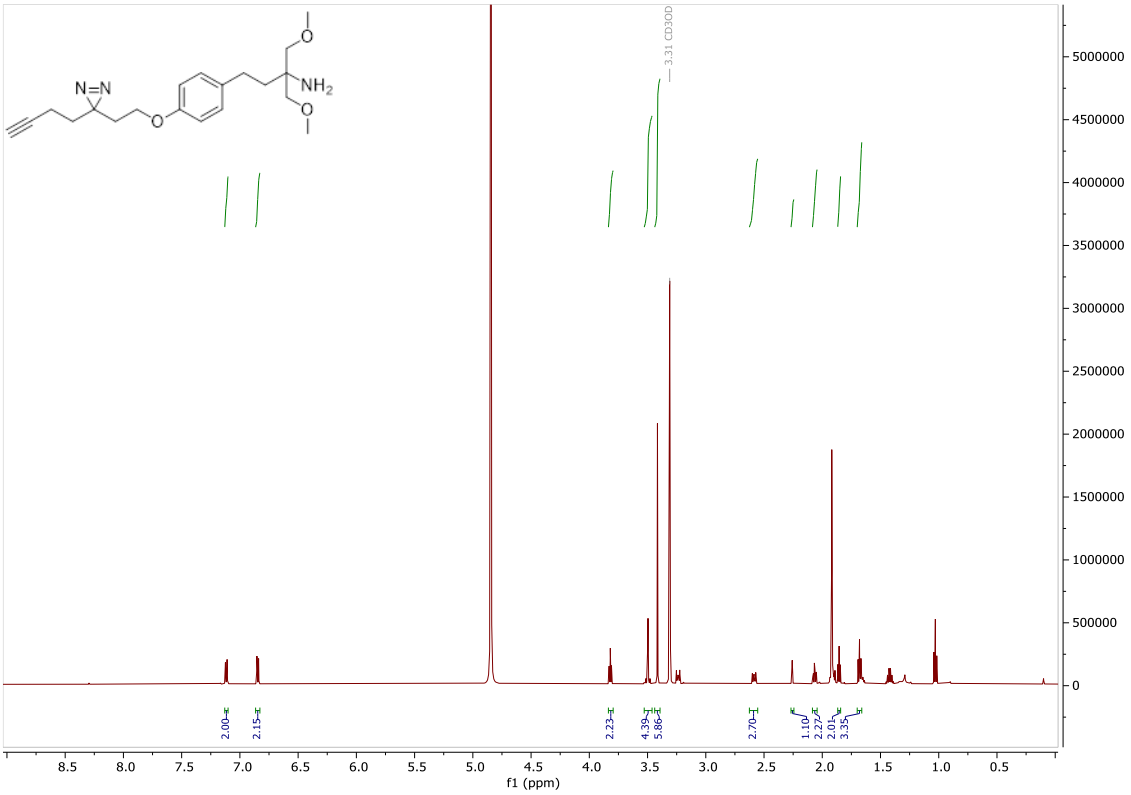


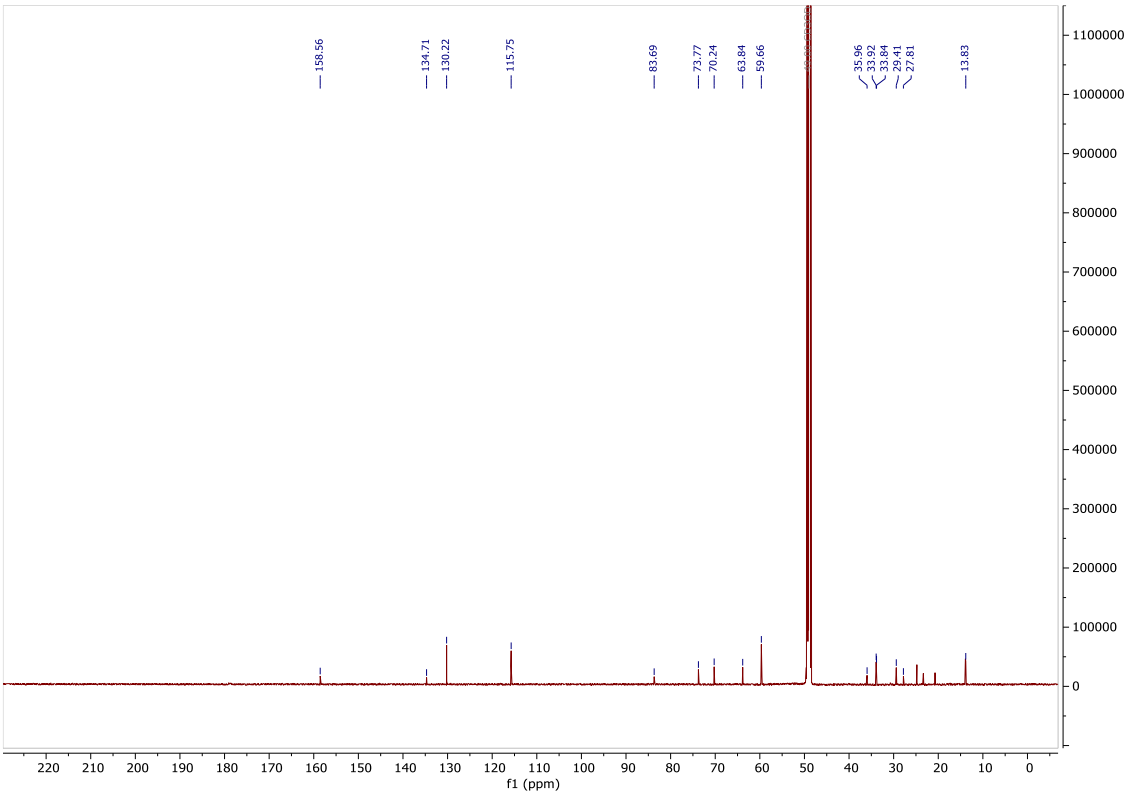

HMBC Spectra of PAL probe **130**:

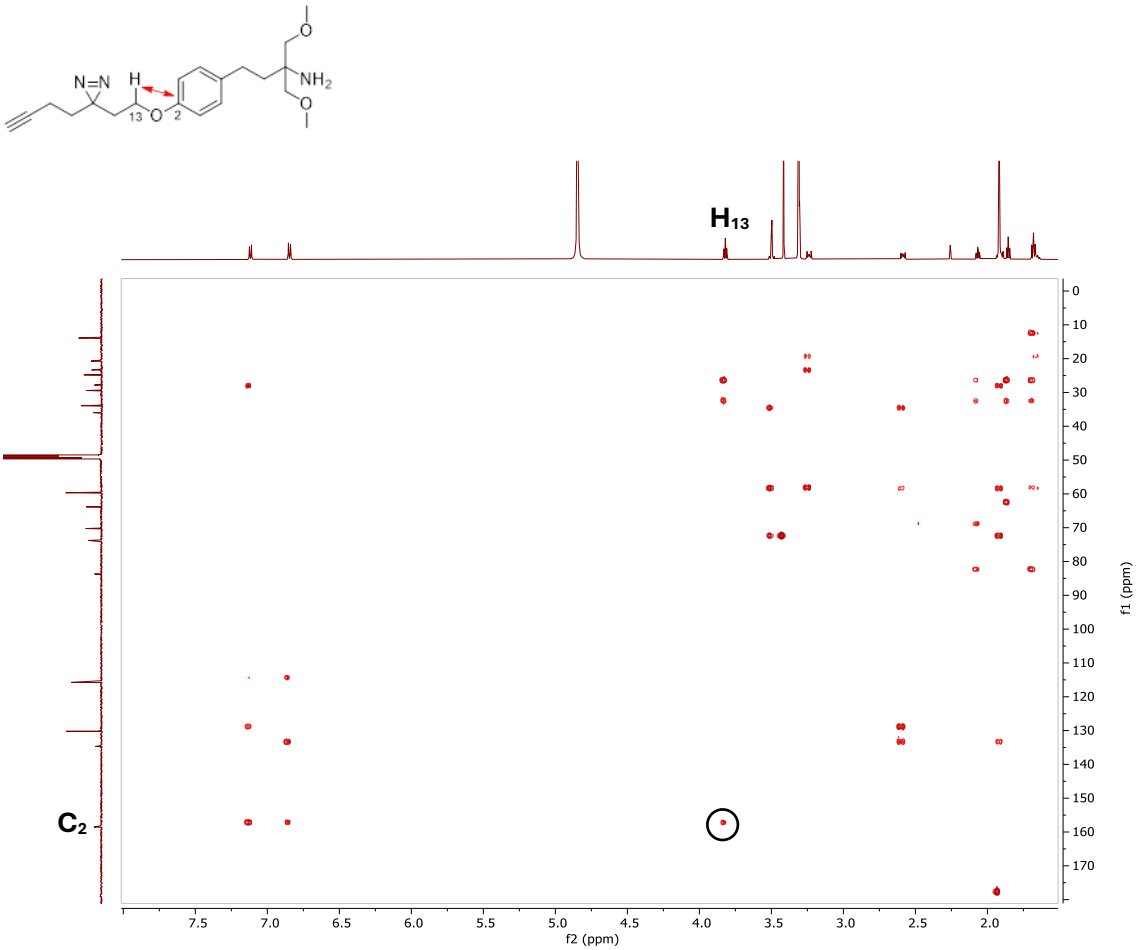

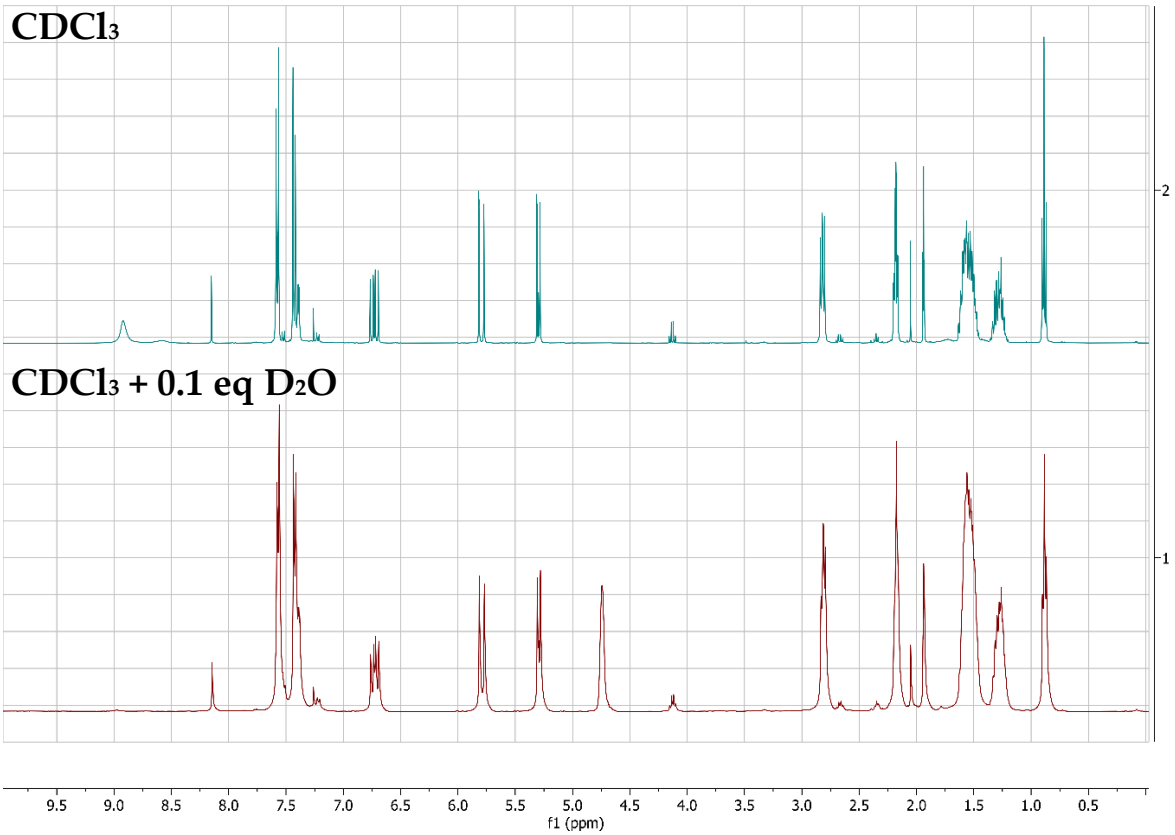


**Appendix IX: Characterisation of side product 99.** $^{1}$H NMR spectra of side product **99** in $CDCl_3$, before (above) and after (below) a $D_2O$ shake. The overlayed spectra clearly display the disappearance of a broad singlet at 8.9 ppm in the presence of $D_2O$. This observation indicates the presence of an exchangeable proton, supporting the interpretation that **99** is an amide.

## Appendix X – Detailed preparation of LEC microvessel-on-a-chip

### Gel preparation

1. Add 50 μL PBS in all the used observation wells.
2. Prepare the collagen gel mixture (3 mg/ml) in a 2 ml Eppendorf tube.

| Name | Amount (total 200 μL) | Notes |
|---|---|---|
| 1M HEPES | 20 μL | Mix them very well w/o introducing bubbles |
| 37 mg/ml $NaHCO_3$ pH:9.5 | 20 μL | |
| Sterile $H_2O$ | 40 μL | Add to mixture and mix them well |
| 5 mg/ml collagen gel | 120 μL | Finally, add collagen gel and mix them w/o introducing bubbles. |

3. Prepare Matrigel-collagen gel mixture in a 2 ml Eppendorf tube

| Name | Amount (total 100 μL) | Notes |
|---|---|---|
| GELTREX LDEV FREE HESC | 65 μL | Mix them very well w/o introducing bubbles |
| Sterile $H_2O$ | 10 μL | Add to mixture and mix them well |
| 3 mg/ml collagen gel mixture | 25 μL | Finally, add collagen gel and mix them w/o introducing bubbles. |

4. Inject 1.68 ul/ chip Matrigel-collagen gel mixture into the gel inlet.
5. Check two lines in the observation well for each well under the microscope.
6. Place the plate in the incubator (37°C and 5% $CO_2$) for 15 min to allow the gel to solidify.
7. Add 40 μL of 10 μg/ml fibronectin into the left and right outlets of lymphatic vessel channel and incubate the plate at 37°C overnight**.**
8. Aspirate 40 μL fibronectin suspension from the gel inlet in the plate and wash twice with 50 μL PBS and 1 time with 50 μL EGM2 MV.
9. Aspirate the media

### LEC tubule formation

10. Harvest 1 T75 flask LEC and resuspend the cells in 100 μL.
11. Inject 3 μL cell mixture in one inlet of the endothelial cell channel.
12. Add 50 μL EGM2 MV media in outlet channels of opposite LEC channels.
13. Check the cells under the microscope.
14. Place the plate on its side on the Mimetas plate stand for 2-3hours in the incubator to allow the cells in the perfusion channel to settle onto the ECM gel and attach
15. Add 50 μL EGM2 MV media into the inlet and outlet of LEC channels.
16. Place the plate on the OrganoFlow in a humidifier incubator and adjust it to 14° Inclination and 8 min intervals.

17. Refresh the medium every 2 days by replacing the medium from perfusion inlets and outlets (50 μL in each).
18. Incubate for 4-5 days at 37°C %5 humidifier chamber on the OrganoFlow to have a complete endothelial tubule (14° Inclination and 8 min intervals).

**Lymphatic endothelial cell activation**

19. After the formation of the complete endothelial tube, remove the EGM2 MV from the inlet and outlet of endothelial perfusion channels.
20. Add the 50 μL EGM2 MV media containing 1 ng/ml TNF$\alpha$ inlet and outlet of endothelial perfusion channels.
21. Incubate the plate on the OrganFlow (14° Inclination and 8 min intervals) in the incubator overnight.

**Jurkat cell activation**

22. Coat two wells in a 12-well plate with $\alpha$hCD3 (1 μL in 1 ml PBS for each well) for 2 h at 37°C and 5% $CO_2$.
23. Remove PBS
24. Add 1x$10^6$ Jurkat cells in 1 mL RPMI media containing 5 μL $\alpha$hCD28.
25. Incubate the cells for 48 h at 37°C and 5% $CO_2$.

**Jurkat cell seeding**

26. Collect the cells by pipetting up and down
27. Centrifuge the cells for 5 min at 200 xg and resuspend in 30 μL EGM2 MV media.
28. Mix the cells with 15 mg $ml^{-1}$ matrigel (1:1) (GELTREX LDEV FREE HESC) to achieve a final concentration of 90000 activated Jurkat cells per chip.
29. Remove all media from the perfusion channels.
30. Inject 4 μL Matrigel with cell into the inlet channel of the opposite side of the endothelial channel. Then inject 4 μL into the outlet channel.
31. Add the 50 μL EGM2 MV inlet and outlet of endothelial perfusion channels.
32. Incubate 15 min at 37°C and 5% $CO_2$.
33. Add the 50 μL EGM2 MV media inlet and outlet of the opposite side of endothelial perfusion channels.
34. Incubate the plate on the OrganoFlow (14° Inclination and 8 min intervals) in the incubator for 3 days.

**Jurkat cell gating strategy for flow cytometry:**

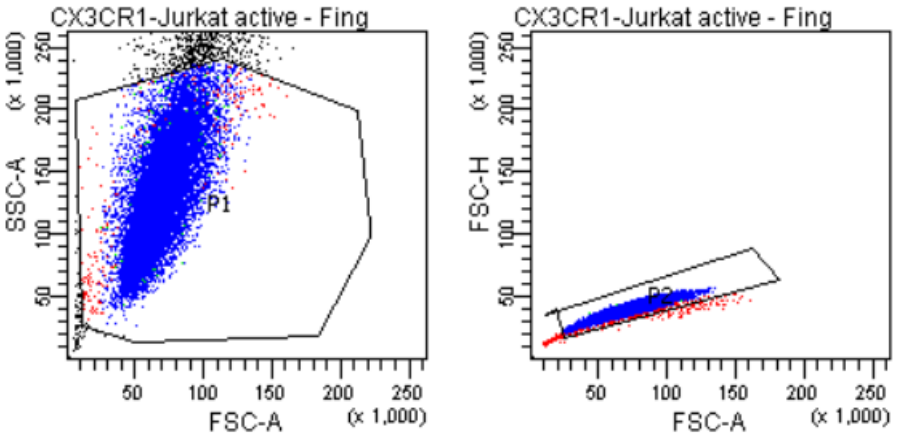


**Lymphatic cell gating strategy for flow cytometry:**